NATIONAL RESEARCH CENTRE "KURCHATOV INSTITUTE"
B. P. Konstantinov Petersburg Nuclear Physics Institute

PNPI

High Energy Physics Division

MAIN SCIENTIFIC ACTIVITIES 2007–2012

GATCHINA
2013

ISBN 978-5-86763-324-0

PREFACE

This edition presents a summary of the scientific activities of the High Energy Physics Division in the period 2007–2012. It can be considered as a continuation of the previous editions:

High Energy Physics Division. Main scientific activities 1971–1996, Gatchina (1997);
High Energy Physics Division. Main scientific activities 1997–2001, Gatchina (2002);
High Energy Physics Division. Main scientific activities 2002–2006, Gatchina (2007).

The main directions of the HEP Division scientific activities are experimental studies in nuclear and particle physics at accelerators, as well as some applications of the nuclear methods, in medicine in particular. As in the previous years, the HEP Division strategy was, on one hand, to exploit in a maximal possible way the accelerator facilities available at PNPI and, on the other hand, to maintain active international cooperation in fundamental research in the world's most advanced accelerator centres.

The PNPI 1-GeV proton synchrocyclotron with its proton, neutron, pion, and muon beams remains a valuable instrument for nuclear physics, for solid state physics, for medical applications, as well as for radiation studies of various materials and equipment. The medical 1 GeV proton beam was successfully used for neurosurgery. An important step in medical applications is related to the construction at PNPI of a new 80-MeV high-intensity proton cyclotron. This accelerator will be specialized on production of various radioactive isotopes, including production of generators of positron emitting isotopes for applications in the positron emission tomography.

During the reviewed period, the HEP Division participated in experiments at the leading accelerator centres: CERN, FNAL (USA), BNL (USA), PSI (Switzerland), DESY (Germany), GSI (Germany), FZ-Juelich (Germany), as well as at the accelerators in the Universities in Jyvaskyla (Finland), in Bonn (Germany), in Mainz (Germany), and at the accelerator at ITEP (Moscow).

Our main efforts were concentrated on experiments at the Large Hadron Collider (LHC) at CERN. PNPI participates in all major collider experiments at the LHC: CMS, ATLAS, LHCb, ALICE with essential contributions to the design, construction, and maintenance of these experiments. The tremendous success of the LHC experiments is well known. More than 300 physics papers were published by the end of 2012. A great amount of new results have been obtained, crowned by the discovery of the Higgs boson. At present, PNPI participates in preparations for further studies at the LHC with the increased energy and intensity of the colliding beams.

Very successful was also our traditional cooperation with the nuclear centre PSI in Switzerland, where we have a possibility to use the world's best muon beams of the "meson factory". Deep studies of the muon catalyzed *dd*- and *dt*-fusion, performed in the previous years, now are followed by high precision measurements of the muon capture by protons and by light nuclei.

The future plans of the HEP Division include participations in the experiments at the accelerator complex FAIR, which is under construction at GSI (Germany). Also, we plan to create a special complex (project IRIN) at the high flux neutron reactor PIK at PNPI for studies of neutron-rich nuclei far from the stability region.

Alexey Vorobyov
Head of the High Energy Physics Division

Status of the Accelerator Facilities at PNPI

STATUS OF THE PNPI PROTON SYNCHROCYCLOTRON

E.M. Ivanov, G.F. Mikheev, G.A. Riabov and the accelerator staff

1. Introduction

The PNPI synchrocyclotron (Fig. 1) for the proton energy of 1000 MeV was put into operation in 1970 and is intended for researches in the field of nuclear physics, elementary particle physics, solid state physics, as well as for an applied program. Main parameters of the synchrocyclotron are presented in Table 1.

Fig. 1. The PNPI synchrocyclotron

Table 1

Main parameters of the synchrocyclotron

Proton energy	1000 MeV
Energy spread, $\Delta E / E$	1 %
Intensity of the internal beam	≤ 3 mkA
Intensity of the extracted beam	≤ 1 mkA
Beam repetition rate	45–50 Hz
Duty factor	Up to 85 %

The construction of the Gatchina synchrocyclotron was started later than other synchrocyclotrons, and the progress in the accelerator technology and in the accelerator physics achieved to that moment was taken into account in its design and up-grading. The design and construction of the accelerator required some new and original technical decisions, such as high quality shimming of the magnetic field, a new scheme of the frequency variator with a system of symmetric coupling, a feedback of the high frequency generator, and so on. As a result of an extensive improvement program after it was put into operation, essential improvements of synchrocyclotron parameters were achieved:

- a new electrostatic focusing in the central region provides a significant increasing of the beam intensity [1];
- a new high aperture extraction system provides a record (for synchrocyclotrons) extraction efficiency of 30 %, and a high intensity and good quality external proton beam [2, 3];
- a new resonance long burst operation system provides a record beam duty cycle [4];
- a one turn deflection of the beam on an internal target made possible to generate a pulsed neutron beam and to develop a TOF neutron spectrometer [5].

In spite of the fact that modern "meson factories" exceed considerably the PNPI SC in the beam intensity, nevertheless, due to some accelerator features, there is a significant area of researches which is not overlapped by other facilities. The PNPI SC accelerates protons up to the energy of 1000 MeV, which is higher than that at the meson factories. The energy of 1000 MeV is optimal for nuclear physics of intermediate energies, in particular, for investigation of nuclear density distributions by measuring proton-nucleus scattering. It appeared possible to study production of K^+- and η-mesons at proton and pion beams, respectively. The proton energy of 1000 MeV is also considered to be optimal for transmutation researches. Due to higher energy of the primary beam, the energy of secondary π-meson beams of the SC is higher than that of the meson factories, which is essential for partial wave analyses of pion-nucleon scattering and for baryon spectroscopy investigations.

2. Beam lines and the experimental complex of the PNPI synchrocyclotron

Beam lines of the PNPI SC are shown in Fig. 2, and the beam parameters are presented in Tables 2–4.

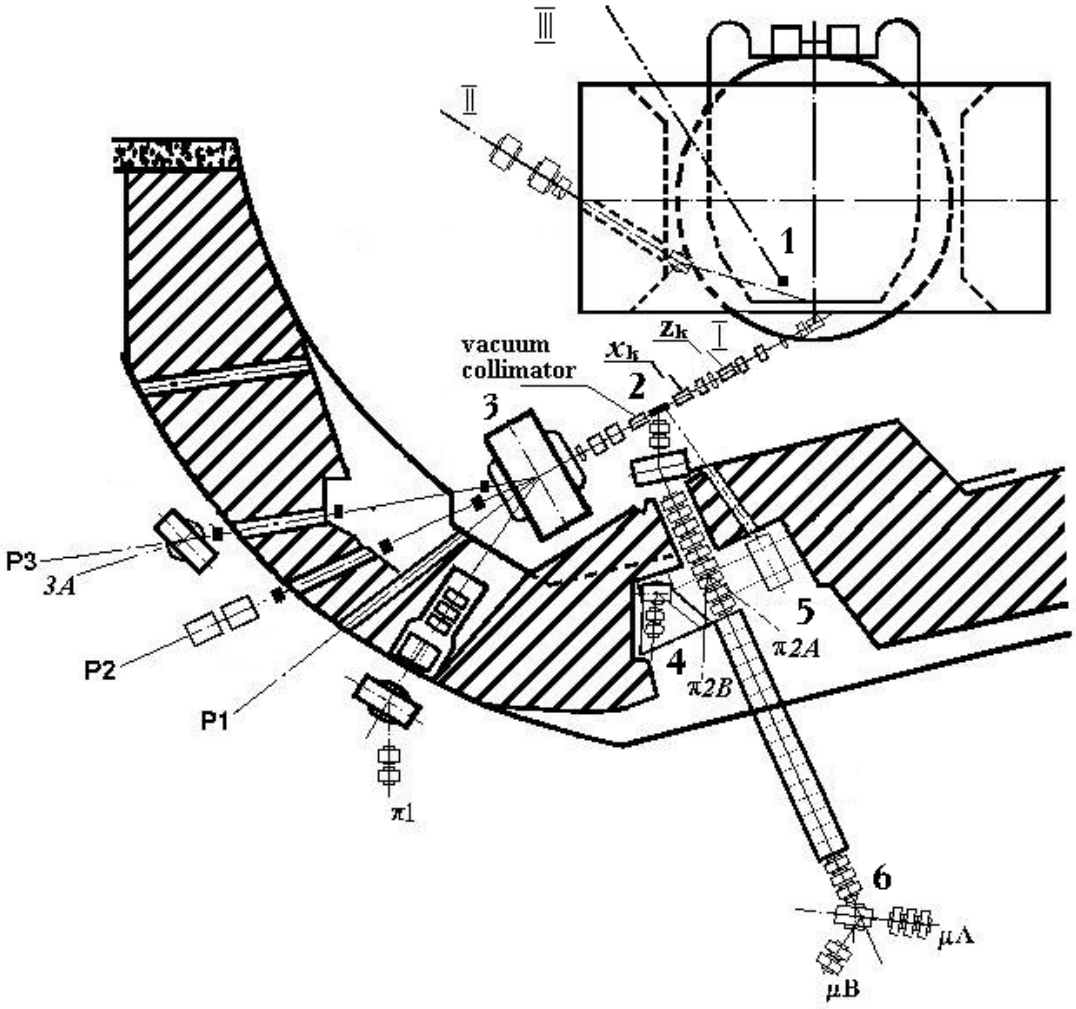

Fig. 2. Beam lines of the PNPI SC: I – primary proton beam; II – additional small intensity proton beam; III – neutron beam; P1, P2, P3 – directions of the proton beams; 1 – neutron production target; 2 – meson production target; 3 – distributing magnet of the proton beam; π1 – high energy meson channel; 4, 5 – removable platform with a magnet for π2A and π2B low energy meson beams; 6 – separated μ-meson beams μA and μB

Table 2

Parameters of the PNPI synchrocyclotron proton beams

Proton beams				
Energy, MeV	ΔE/E, %	Intensity, s^{-1}	Channel	Comment
1000	1	6×10^{12}	P1, P2, P3	Primary proton beam
1000	1	10^8	P2	Medical beam Ø 3–5 mm
1000	1	10^{10}	II	Second extracted proton beam
1000	3×10^{-3}	10^{10}	P2	Spectrometric beam
200–1000	1.0–14	10^7–10^{12}	P3	Variable energy proton beam

Table 3

Secondary particle beams

Particle	Momentum, MeV/*c*	Δ*p*/*p*, %	Intensity, s^{-1}	Beam line	Comments
π^+ π^-	450 450	6 6	10^6 3×10^5	π1-channel	Achromatic mode
π^+ π^- μ^+	250 250 29	2.5–12 2.5–12 12	3×10^5–10^7 10^5–5×10^6 3×10^4	π2-channel	Achromatic mode “Surface” mesons
μ^+ μ^-	170 160	10 10	3×10^5 9×10^4	μ-channel	Separated beams

Table 4

Neutron beam intensity at the GNEIS neutron production target

Energy, MeV	Intensity, s^{-1}	Pulse duration, ns	Frequency, Hz
10^{-2} eV – 10^2 MeV	3×10^{14}	10	50

The reference literature [6–9] contains more detailed information on the beam parameters, while new proton and neutron beams developed for radiation tests of electronics components are described in chapter 4. Some experimental facilities listed below are disposed in special annexes to the main SC building.

The IRIS facility. The IRIS facility is aimed at investigations of short lived isotopes far from the β-stability line. New types of targets for a high production rate of rare isotopes have been developed at PNPI in collaboration with scientists from Italy, France and Canada. The IRIS Laboratory is a well known world research centre. This laboratory is working in cooperation with other centres, such as ISOLDE at CERN.

The neutron time-of-flight facility. The neutron time-of-flight spectrometer GNEIS has a 10 ns spark pulse and a 48.5 m flight base. The neutron beam is used for investigations of neutron interaction cross sections. The cross sections for inelastic neutron-nucleus interaction in the case of heavy nuclei were measured. Recently, a special neutron beam for radiation tests was developed on the basis of the spectrometer GNEIS (see below).

The proton therapy facility. The proton therapy facility was developed at the PNPI SC in collaboration with the specialized medical institute Russian Scientific Centre of Radiology and Surgical Technology – RSCRST. The main peculiarity of the Gatchina facility is application of the 1000-MeV proton beam for irradiation of intracranial targets in human brain. By present, more than 1385 patients have been treated [10].

Original experimental installations were constructed at PNPI, and world level physics results were obtained:

- a set-up in the π1-beam line to investigate πN scattering and πN interaction in the region of low-energy pion-nucleon resonances;
- a spectrometer MAP with 10^{-3} energy resolution to investigate the behaviour of the nucleon inside the nuclear matter by using quasi-elastic scattering method;
- an ionization spectrometer IKAR to investigate nuclear matter distributions in exotic nuclei with a neutron halo by measuring small-angle proton elastic scattering in inverse kinematics;
- a crystal-diffraction spectrometer to investigate exotic atoms;
- an experimental set-up to investigate muon catalysis physics of the DD and DT nuclear synthesis;
- an experimental set-up in the muon-channel to investigate new nano-materials by using the μSR (muon spin rotation) method.

3. SC operation in 2007–2012

During this period, the PNPI SC was in operation for physical research and an applied program ~ 2500 hours per year. The accelerator time was distributed between the following physics experiments:

- investigation of short-lived isotopes;
- μSR experiments;
- spectrometer GNEIS;
- baryon spectroscopy;
- beam channeling and reflection by bent crystals.

The applied program consisted from

- radiation tests of electronics components in proton and neutron beams;
- proton therapy;
- tests of experimental equipment developed in PNPI for international experiments at high energy accelerators and colliders.

The PNPI SC had a support from the Russian Academy of Sciences and from the Ministry of Science and Education.

In 2007–2012, the SC users published 124 papers and reports including 61 articles on the accelerator technology, 3 candidate and 1 doctor theses were defended.

4. New experimental facilities at the PNPI SC

In parallel with a routine SC operation, a development of new facilities and an upgrade of the existing ones was performed in 2007–2012. The recent trends are towards to applied and commercial applications including

- building of a new electronics radiation resistance test centre with proton and neutron beams;
- development of a universal nuclear medicine centre including traditional proton therapy at the 1000 MeV proton beam and commissioning of the new isochronous cyclotron SC-80 with the proton beam energy of 80 MeV and beam current of 100 μA for medicine isotopes production and organization of a melanoma treating facility.

4.1. Test centre for radiation resistance

An advance in the space and aviation equipment is largely bound up with an extensive use of modern micro- and nano-electronics. One of the main requirements specified for this type of electronics is its

capability to reliably function in radiation fields of space and the upper atmosphere. The present-day norms of Russia and leading countries include standards for compulsory radiation tests of aviation and space electronics equipment. Such tests can be carried out at a new test centre using proton and neutron beams.

4.1.1. Proton beam tests

Last years, a proton beam was used to test electronics, and contracts with specialized organizations on radiation tests occupied nearly 10–15 % of the accelerator time schedule. In 2007–2012, a work station in the P2 beam line (see Fig. 2) was built for tests. Two modes of operation of the quadruple lenses were found to obtain a narrow beam (30 mm in diameter) and a wide beam (230 mm in diameter). Beam parameters, the beam density uniformity, and the neutron and secondary particles background were investigated. The work station was equipped with a proton beam monitor – a dosimeter and a device for absolute measurements of the proton beam flux. A state license was received for this proton test beam [11].

4.1.2. Neutron beam tests

The JEDEC Standard (Measurement and Reporting of Alpha Particles and Terrestrial Cosmic Ray-Induced Soft Errors in Semiconductor Devices) [1] prescribes testing of electronics and radio components in neutron fluxes with a spectrum similar to that of neutrons in the atmosphere with energies varying over a wide range from low energies to 1 GeV. The spectrum of neutrons above New York City (the United States) was accepted by the JEDEC Standard as a reference. The only test facility in which the neutron spectrum is close to the standard one in the energy range of 0.1–750 MeV is LANSCE at the Los Alamos National Laboratory on the basis of LAMPF. Linear proton accelerators are used by aviation and space companies of the United States, Europe, and Asia to test their electronic equipment. In contrast to the test facilities in Los Alamos and Uppsala (Sweden), the PNPI test facility was developed on the basis of an internal target of the synchrocyclotron, the infrastructure of the GNEIS neutron time-of-flight spectrometer available at PNPI being used. The scheme of the GNEIS spectrometer is presented in Fig. 3.

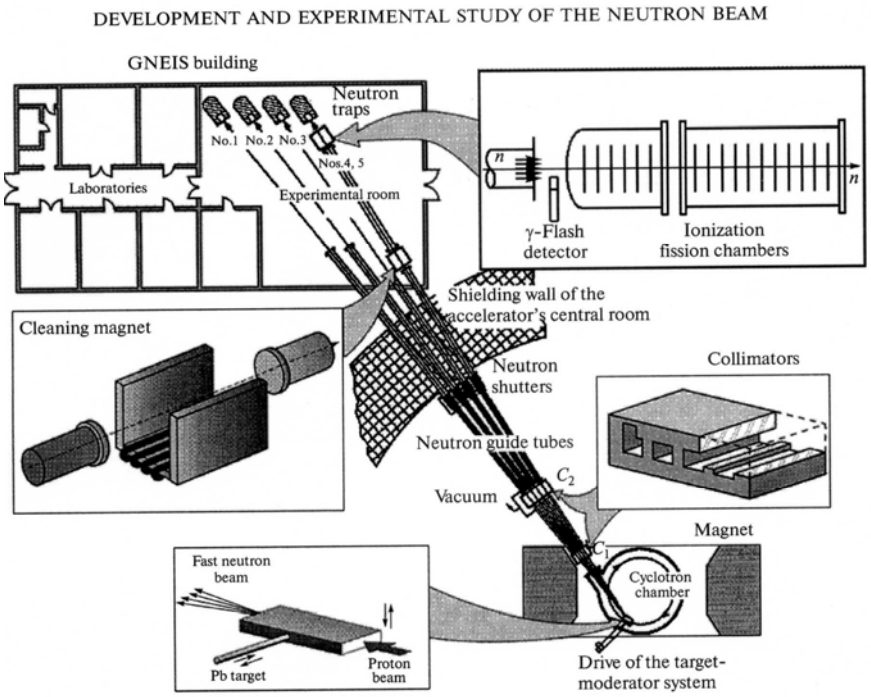

Fig. 3. The scheme of the time-of-flight PNPI neutron spectrometer GNEIS

Our approach to use the available infrastructure of the GNEIS spectrometer and its internal target for obtaining a wide neutron spectrum stretching up to 1000 MeV with an energy distribution similar to the atmospheric neutron spectrum is much simpler than that to use an external target. Concerning our and Los Alamos neutron beams, we would like to note the following:

1. Instead of a moderator used in GNEIS as a neutron source, a thick target for the neutron test beam should be used as a source to obtain a wide neutron spectrum.

2. The accelerator, the neutron guide tubes, the target, and the building of the GNEIS spectrometer (see Fig. 3) are located in such a way that the neutron beam selection angle is 27–32°, as at Los Alamos.

3. The distance between the target and the equipment in the GNEIS room is 30–40 m, which is comparable to the distance of 12 m at Los Alamos. A proton beam with a current of up to 1.7 μA is used in radiation tests at the Los Alamos laboratory.

Before experimental measurements, preliminary calculations for the GNEIS neutron source were performed using the GEANT-4 software package. We calculated the neutron yield from a lead target irradiated by a 1000 MeV proton beam with an intensity of 1.8×10^{13} neutrons/s inside the chamber of the PNPI synchrocyclotron. The target length down stream of the beam was 40 cm. The distance from the "observation point" was taken to be 30.5 m, and the range of the selected angles was 20–35°. It was shown that the calculated energy spectrum of neutrons is close in shape to the standard one, and differs from that of Los Alamos in the flux value at energies larger than 1 MeV only by 20 % or less.

Experimental measurements were performed with a target without a moderator in the beam tube number 5 of the spectrometer at distances of 48.5 and 36.0 m from the target. The neutron beam passed in evacuated sections of the neutron guide tube through the wall in the main hall of the synchrocyclotron and entered the GNEIS spectrometer building. A system of steel, brass, and lead collimators formed 50 and 180 mm in diameter beams with flight paths of 36.0 and 48.5 m, respectively. Measurements at a flight path of 48.5 m were carried out using a "cleaning" magnet located at a distance of 36 m from the target used as a neutron source. This magnet is intended for cleaning the neutron beam from charged particles produced on the collimators and filters of the neutron beam.

The neutron spectrum measured in the energy range of 1–1000 MeV is presented in Fig. 4. This figure also shows the calculated spectrum, the standard spectrum recommended for testing electronics components according to the JEDEC international standard, and the neutron spectrum obtained at Los Alamos. The parameters of the neutron sources based on the PNPI synchrocyclotron and LANSCE are presented in Table 5 for comparison [12].

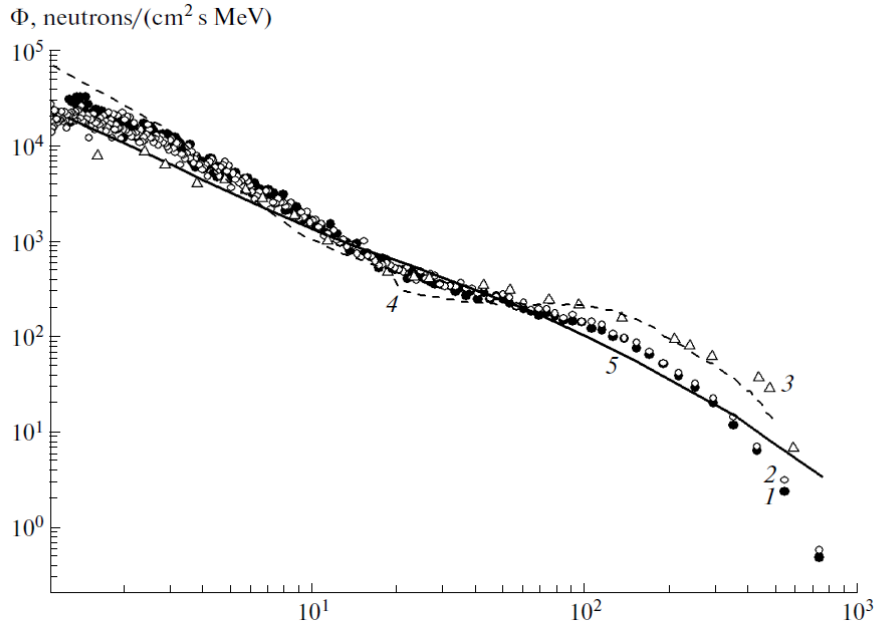

Fig. 4. Neutron spectra in the energy range of 1–1000 MeV: 1, 2 – GNEIS, experimental data for the U^{238} and U^{235} targets, respectively; 3 – spectrum of LANSCE in Los Alamos; 4 – GNEIS, calculated spectrum, and 5 – JEDEC standard spectrum

Table 5

Parameters of the LANSCE and PNPI neutron sources

Neutron source	LANSCE	PNPI synchrocyclotron
Target material	Tungsten	Lead
Proton energy, MeV	800	1000
Maximum neutron intensity for 4 π, neutrons/s	20×10^{14}	3×10^{14}
Burst frequency	200	50
Neutron flux at the test set-up, neutrons/(s cm^2)	1.7×10^5	1×10^5

Today, the PNPI specialists are engaged in organizing a test set-up, infrastructure, and necessary equipment for carrying out mass tests of aviation and space electronics equipment in the neutron beam.

As a result, a new unique centre for radiation resistance tests at a dedicated neutron beam, as well as at a proton one, was built at PNPI.

4.2. Nuclear medicine program

Since 1975, a centre of proton therapy at the 1000 MeV proton beam is in operation at PNPI. More than 1385 patients have been treated in this centre. The patient's treatment is carried out by the specialized medical institute Russian Scientific Centre of Radiology and Surgical Technology – RSCRST. Prominent results on about 80 % of remission of patients with pituitary adenomas and arteriovenous malformations have been obtained. In 2007–2012, the patient's treatment was continued and some upgrade of the equipment was performed. In particular, a computer control of the magnetic elements of the medicine beam line was put into operation.

Another direction of the nuclear medicine in PNPI is a design and construction of a 40–80 MeV H^- ion isochronous cyclotron with the beam current of 100 μA. Realization of the project will allow to produce high quality radioisotopes and radioactive preparations for medicine. An eye melanoma treatment facility will be built at the cyclotron extracted beam. Recent years, an impressive progress in this project has been achieved. More detailed information on the present status of the cyclotron construction and the planned facility for production of medical isotopes is presented in special articles of this book.

5. Conclusion

The PNPI synchrocyclotron is in operation since 1970 for researches in nuclear physics experiments in the range of intermediate energies up to 1000 MeV. A rich arsenal of experimental installations and the availability of world-rate experts and scientists allow us to carry out at the PNPI synchrocyclotron a wide spectrum of fundamental and applied research programs and to fulfil competitive scientific programs. Recent years, there is a trend to applied programs. Development of new proton and neutron beams and construction of a new test set-up have considerably extended the potential in radiation researches of the PNPI synchrocyclotron, and offer a chance for PNPI to establish a unique European centre for radiation tests of aviation and space electronics equipment in compliance with high requirements of international standards. Realization of the nuclear medicine program will provide medicine isotopes for needs of all North-West region.

References

1. N.K. Abrossimov *et al*., Proc. of RUPAC-6, Dubna 1978, v. **1**, 277 (1979).
2. N.K. Abrossimov *et al*., Journ. Techn. Phys. **40**, 2593 (1970).
3. N.K. Abrossimov *et al*., Proc. of RUPAC-2, Moscow 1970, v. **2**, 182 (1970).
4. N.K. Abrossimov *et al*., Proc. of RUPAC-3, Moscow 1972, v. **2**, 94 (1972).
5. N.K.Abrossimov *et al*., NIM A **242**, 121 (1985).
6. N.K. Abrossimov *et al*., Proc. of RUPAC-7, Dubna 1980, v. **2**, 75 (1981).
7. N.K. Abrossimov *et al.*, Abstracts of 6th Meeting on Applied Accelerators, Leningrad, 1988, CNII Atominform, p. 5.
8. N.K. Abrossimov *et al*., Proc. of RUPAC-5, Dubna 1976, v. **1**, 183 (1978).
9. V. Volchenkov *et al*., Preprint PNPI-**612**, Leningrad (1980).
10. N.K. Abrossimov *et al*., Transaction on Atomic Science and Technology, series "Electro-physics equipment", issue **23**, 61 (1987).
11. N.K. Abrossimov *et al*., Transaction "STOIKOST'-2003", Moscow, issue **6**, 165 (2003).
12. N.K. Abrossimov *et al*., Transaction "STOIKOST'-2009", Moscow, issue **12**, 223 (2009).

STATUS OF THE PNPI C-80 CYCLOTRON

PNPI participants: D.A. Amerkanov, S.A. Artamonov, G.I. Gorkin, V.P. Gres, E.M. Ivanov, G.F. Mikheev, G.A. Riabov

D.V. Efremov NIIEFA participants: Yu.N. Gavrish, V.G. Mudrolyubov, A.P. Strokach

The C-80 cyclotron system is intended to produce proton beams with an energy ranging from 40 to 80 MeV and current up to 200 μA.

Over a number of years, studies on designing a cyclotron for acceleration of H^- ions up to 80 MeV were carried out at PNPI in cooperation with NIIEFA specialists [1–4]. Since September 2010, NIIEFA and PNPI have been carrying out works on building the C-80 cyclotron system intended for production of isotopes, proton therapy of eye diseases and superficial oncologic diseases, as well as for fundamental and applied research. In addition, the cyclotron is supposed to be used as an injector for the C-230 synchrotron to ensure an additional acceleration of the extracted proton beam up to approximately 230 MeV. This will allow the procedures based on the Bragg peak to be applied in the proton therapy of oncologic patients.

The development of modern methods in nuclear medicine resulted in high demand for radioisotopic products used both in diagnostics and therapy. A rapid growth is observed of the PET diagnostics which uses radiopharmaceuticals based on radioisotopes with a half-life from several seconds up to several minutes. It is evident that the PET diagnostics can be performed only in direct vicinity of functioning cyclotron systems, that is, in large regional centres. The situation can be changed by using Sr-Rb generators, which can be produced at 70–90 MeV cyclotrons under irradiation of ^{85}Rb targets with protons. The parent isotope, ^{82}Sr with a half-life of 25.3 days, decays and produces a daughter positron emitter ^{82}Rb used in the production of radiopharmaceuticals for PET. Thus, if ^{82}Sr is available, a PET centre can function in hospitals located sufficiently far from the cyclotron system.

The parameters of the C-80 cyclotron (Table 1) make possible realization of the proton radiation therapy of eye diseases and superficial oncologic diseases, as well as implementation of a research program aimed at the development of innovative methods of the proton therapy and promising radionuclides for diagnostics and therapy. A long-term fruitful cooperation of specialists from PNPI and medical specialists from the Research centre for Radiology and Surgical Technology, St. Petersburg, in treatment of patients using the functioning at PNPI SC-1000 accelerator is of great importance in this matter.

Table 1

Main characteristics of the C-80 cyclotron

Systems/Parameters	Characteristics
Accelerated particles	H^-
Extracted particles	H^+
Beam energy, variable, MeV	40–80
Beam current, μA	≤ 200
Electromagnet – type – pole diameter, mm – mass, t	 E-shaped 2050 245
RF-generator power, kW	80
Ion source	external
Operating mode	Continuous/pulsed
Total power consumption, kW – with the beam on – in the stand-by mode	 ≤ 500 ≤ 200

The major unit of the cyclotron, the electromagnet, has been designed using the model of the magnet of the SC-1000 synchrocyclotron. This electromagnet has a traditional design with an E-shaped magnet yoke. The system to move upward the magnet upper part (the half-yoke) was worn-out and outdated. Therefore, it has been replaced with 4 pairs of ball bearings and screws equipped with servomechanisms and position sensors. The maximum height of the half-yoke lifting is about 600 mm, the setting accuracy is better than 50 μm. Figure 1 shows the magnet with the half-yoke lifting system. Based on the magnetic measurements, new magnet sectors have been designed and manufactured. To form the magnetic field, 17 packs of iron plates have been assembled on each sector.

Fig. 1. Electromagnet

The resonance accelerating system (Fig. 2) is located completely inside the vacuum chamber. The system consists of two symmetrical quarter-wave resonators. An inner conductor of each resonator consists of a 60º dee and a stem. The dees in the vicinity of the magnet centre are galvanically coupled. The accelerating system is equipped with two capacitors for frequency tuning, an AFT trimmer and an RF-probe. The operating frequency of the accelerating system RF oscillations is 41.2 MHz. The range for the frequency tuning with the AFT trimmer is 220 kHz. The active loss power is about 29 kW in each resonator at the RF-voltage amplitude of 60 kV.

Fig. 2. Resonance System

The RF power supply system consists of a stabilization and control module (designed in NIIEFA) and an RF-power amplifier (the "Coaxial Power System" firm, Great Britain). The stabilization and control module of the RF-power supply system is intended for generation of the main frequency of 41.2 MHz, measuring and stabilization of the dee acceleration voltage amplitude, manipulation of the acceleration voltage and its synchronization with the operation of the rest systems of the cyclotron, tuning and stabilization of the resonance system natural frequency, automatic tuning of the resonance system frequency to the supply voltage frequency. Structurally the module consists of mother and daughter cards built into an industrial computer housed in an RF-power amplifier cabinet. The RF-power amplifier shall ensure an output power of 80 kW at a frequency of 41.2 MHz. The amplifier with power supply units is also located in the cabinet installed in the experimental hall basement. The RF-power is transmitted to the resonance system via a flexible coaxial feeder.

The external injection system serves for generation, shaping and transport of the H^- ion beam from an external source into the cyclotron through an axial opening in the pole. The system is located under the magnet. It consists of a plasma ion source with electrostatic optics, a beam line with two focusing lenses and two correcting electromagnets, an inflector and diagnostics devices.

The cyclotron is equipped with a stripping device, 2 standard and 3 diagnostic probes. The stripping device is equipped with a mechanism to adjust the radial and angular position of the carbon foil to provide a required range of final ion energies. The head of the stripping device is made as a "three-fingered fan", onto which three thin carbon foils are fixed. Remote rotation of the head is provided, which allows any of these 3 foils to be placed under the beam.

The power supply system of the cyclotron includes the main switchboard and systems for consumers secondary power supply. The electric power to the external injection system is provided from power supplies produced by the Lambda and Spellman firms. The power supplies are housed in 2 cabinets. The power supply system of the BRUKER firm serves to power the main electromagnet, and magnets and lenses of the 1^{st} section of the beam transport system.

To achieve high vacuum in the cyclotron chamber, two Velco 322 cryopumps of the HSR firm, Liechtenstein, are used. Turbo-molecular pumps (Edwards, Great Britain) are used in the external injection and beam transport systems.

The water cooling system is intended to remove the heat, totally of about 500 kW, from the heat-loaded components and units of the cyclotron, and stabilize the working coolant temperature at the input to these components within 1–2°, a double-circuit system being used. Distilled water (the heat carrier) circulates in the inner circuit, and process water (the coolant) is used in the outer circuit. The heat removed by the heat carrier from heat-loaded components is transferred to the coolant in a plate-type heat-exchanger. To dissipate the heat released in the process of the cyclotron operation in the atmosphere, the outer circuit is connected to the circulating water cooling system of the building. At the atmospheric air temperature of 25 °C, the heat is removed through a water-water chiller.

A distributed automatic control system is used. It consists of Mitsubishi and Fastwel IO controllers and computers, each being responsible for the control of one or several sub-systems of the cyclotron. The main unit of the control system is an industrial (host) computer, which inquires slave controllers and transmits the acquired information to computers of the operator workstation, receives commands from the operator workstation and performs their arbitration and distribution. Data exchange is realized via network interfaces of three types: the Ethernet, an upper level network, and the ProfiBus DP and RS-485, low-level networks. The Ethernet networks the host Mitsubishi controller, the host computer, computers of the operator workstation, a computer of the beam current measuring system and an industrial computer, which controls the RF system. The ProfiBus DP links the host controller, controllers of devices of the cyclotron and a beam-forming system, a vacuum system, a power switchboard, power supply cabinets of the external injection system, a water cooling system, as well as control units of the power supply system for magnets and lenses. The RS-485 networks the host computer, vacuum measuring units and controllers of turbomolecular pumps, as well as the computer of the beam current measuring system and drivers of step motors of the devices for measuring the beam current density. In addition, the RS-485 links the controller of the cyclotron and beam-forming system devices with the drivers of the step motors of the probes and the stripping device.

The experimental complex of the cyclotron consists of a system for production of radioactive isotopes located in the basement, a unit for the radiation ophthalmology installed in the experimental hall, and a unit for radiation tests of electronic components and devices. Figure 3 shows the layout of the cyclotron and experimental system in the experimental hall.

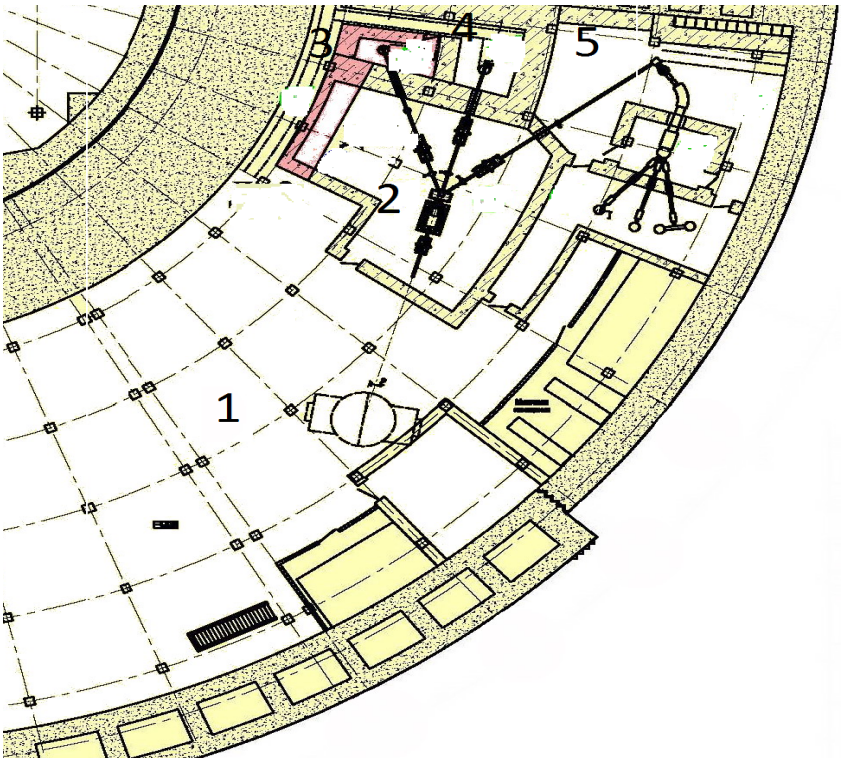

Fig. 3. Cyclotron layout: 1 – cyclotron; 2 – switching magnet; 3, 4 – targets for production of isotopes; 5 – target for electromagnetic separation of isotopes

The beam transport system of the C-80 cyclotron is intended to transport the extracted proton beam to interaction chambers and radio-therapeutic units for proton therapy. To date, the equipment for the 1st section of the system (Fig. 4) has been designed and manufactured: a matching magnet, a correcting electromagnet, a quadrupole lens doublet, and diagnostics devices comprising a Faraday cup and beam profile monitors. The equipment for the 2nd section of the system, which serves to transport the proton beam to target devices for production of radionuclides, has been designed and is under manufacturing. In this section, a switching magnet is installed, which directs the beam to several beamlines. When the switching magnet power is off, the beam is directed to a system of two bending magnets, which transport the beam to the second switching magnet installed in the basement (Fig. 3, № 2) and further to one of three target devices (Fig. 3, № 3, 4 and 5). For the beam focusing and control of its parameters, 5 quadrupole lens doublets, 4 correcting magnets and 2 diagnostic devices are installed in the 2nd section of the beam transport system.

When the power is on, the magnet directs the proton beam of ultra-low intensity and high stability to the beamlines for the proton therapy of eye diseases and superficial oncologic diseases. When the polarity of the magnet is changed, the beam is directed to the beamline intended for studying radiation resistance of radioelectronic devices. These beamlines will be designed in 2013.

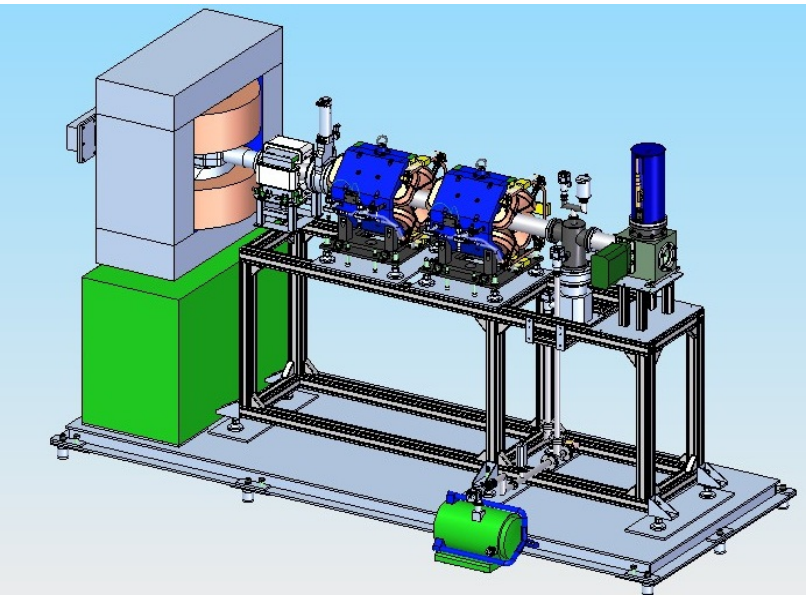

Fig. 4. First section of the beam transport system

To date, the reconstruction of the hall and rooms housing the cyclotron equipment has been completed. New sectors, shims and sector iron plates have been manufactured, and the magnetic field has been formed. The equipment of the cyclotron and the 1st section of the beam transport system has been manufactured and installed in the experimental hall, in the basement and in the corresponding rooms. In compliance with the schedule, the SC-80 cyclotron physical start-up is planned for the end of 2013.

References

1. N.K. Abrossimov, S.A. Artamonov, P.V. Bogdanov *et al.*, Proc. of XIII Intern. Cyclotron Conference, Vancouver, Canada, July 1992, 58.
2. N.K. Abrossimov *et al.*, Proc. of XIII Conference on Accelerators, Dubna, v. **2**, 205 (1993).
3. N.K. Abrossimov *et al.*, Proc. of XIV Conference on Accelerators, Protvino, v. **4**, 5 (1994).
4. N.K. Abrossimov *et al.*, Proc. of V Intern. Cyclotron Conference, Caen, France, June 1998, 58.

STATUS OF THE PNPI ELECTROSTATIC ACCELERATOR

PNPI participants: V.M. Lebedev, V.A. Smolin, B.B. Tokarev, A.G. Krivshitch, and G.E. Gavrilov
Ioffe Phisical-Technical Institute of RAS participants: E.I. Terukov, Yu.K. Undalov, V.Kh. Kudoyarova, and V.K. Gusev
Kurnakov Institute of General and Inorganic Chemistry of RAS participant S.A. Kozyukhin

1. Analytical complex on the base of the electrostatic accelerator

There are two working small accelerators in PNPI: an ElectroStatic Accelerator (ESA) [1, 2] and a neutron generator. The machines of such a type are used widely both in scientific and in applied investigations. Researches in the fields of solid state physics, semiconductors, and element analyses of the matter are carried out at these accelerators. The ESA is shown in Fig. 1. Its main parameters are given in Table 1. The ion tract with the length of 15 m has ion-optics elements, beam control devices, and an analysing magnet that makes it possible to form and to lead to the target an ion beam with the desired size and intensity, as well as to stabilize its energy [1, 2].

An experimental installation for element analyses was installed at the PNPI electrostatic accelerator. The installation consists of a target chamber (Fig. 2), Si(Li) and crystal-diffraction spectrometers for detection of *X*-rays [3], planar Si detectors for detection of ions, and a Ge(Li)-spectrometer for detection of γ-rays. Spectra from detectors are collected with CAMAC electronics. Parameters of the experimental installation are also given in Table 1.

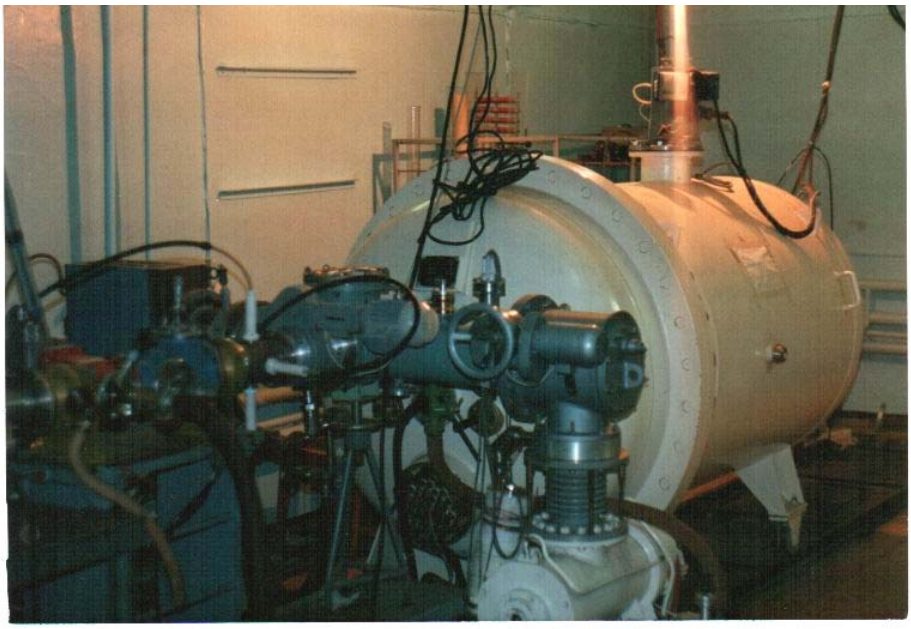

Fig. 1. The electrostatic accelerator

2. Methods of nuclear microanalysis on the ESA beams

Beams of light ions were used for microanalyses of solids by means of nuclear physics techniques: the Proton Induced *X*-ray Emission (PIXE), the Nuclear Reaction Analysis (NRA), and the Rutherford Backscattering Spectrometry (RBS). The element composition of bulk materials, the structure of films and outer layers of solids, and the concentration profiles are generally considered in the microanalysis of solids (Fig. 3).

Nuclear physics techniques are nondestructive, high sensitive and precise. However, the possibilities of the PIXE, RBS, and NRA methods for detection of elements with low and high atomic numbers and for measurements of their contents in samples are different. The RBS is more sensitive to heavy elements

Table 1

Parameters of the analytical complex on the base of the ESA

Parameter	Value
Accelerating particles	Protons, deuterons
Ion energy	(0.3–1.3) MeV
Energy resolution $\Delta E/E$	10^{-4}
Energy spread of the beam	~ 100 eV
Beam intensity on a sample	$(0.1–3 \cdot 10^4)$ nA
Precision of beam intensity measurements	~ 1 %
Beam diameter on the sample	(1–8) mm
Vacuum in the target chamber	10^{-6} Torr
Energy resolution of the spectrometers	
Crystal-diffraction at E_X = 6.4 keV	30 eV
Si(Li) at E_X = 6.4 keV	190 eV
Ge(Li) at E_γ = 1.33 MeV	2.1 keV
For charge particles at E_α = 2.5 MeV	8 keV

Table 2

Nuclear reactions used to determine the isotope composition

Nucleus	Nuclear reaction	Q_R-value, MeV	Incident beam energy, keV	Cross section, mb/sr
^{2}H	$D(d, p)^{3}H$	4.033	950	6.0
^{6}Li	$^{6}Li(d, \alpha)^{4}He$	22.374	900	4.5
^{7}Li	$^{7}Li(p, \alpha)^{4}He$	17.347	670	0.4
^{10}B	$^{10}B(d, \alpha_0)^{8}Be$	17.822	900	~ 0.38
^{11}B	$^{11}B(p, \alpha_0)^{8}Be$ $^{11}B(p, \alpha_1)^{8}Be$	8.586 5.650	700 700	0.12 (α_0) 90 (α_1)
^{12}C	$^{12}C(d, p)^{13}C$	2.722	1000	30
^{13}C	$^{13}C(d, p)^{14}C$	5.947	640	0.4
^{14}N	$^{14}N(d, p)^{15}N$ $^{14}N(d, \alpha_0)^{12}C$ $^{14}N(d, \alpha_1)^{12}C$	1.305 13.579 9.146	970 900 900	6.1 (p_5) 0.07 (α_0) 0.86 (α_1)
^{15}N	$^{15}N(p, \alpha)^{12}C$	4.864	800	~ 15
^{16}O	$^{16}O(d, p_0)^{17}O$ $^{16}O(d, p_1)^{17}O$ $^{16}O(d, \alpha)^{14}N$	1.918 1.049 3.111	900 900 900	0.74 (p_0) 4.5 (p_1) 5.1
^{18}O	$^{18}O(p, \alpha)^{15}N$	3.980	730	15
^{19}F	$^{19}F(p, \alpha)^{16}O$	8.114	1250	0.5
^{19}F	$^{19}F(p, \alpha\gamma)^{16}O$	8.114	1250	Resonance reaction

(with the atomic number Z greater than 30). In favorable cases, 10^{12} at/cm^2 can be detected. In spite of lower sensitivity for high Z elements, the PIXE can give better element resolution than the RBS. Nuclear reactions are efficient for detection of low Z ($Z < 14$) impurities, and hence complement the RBS and PIXE (Table 2). The RBS and NRA techniques can give the depth distribution of elements in a sample. The simultaneous usage of these methods allows one to obtain detail and precise information on the element composition from one experiment. Analytical characteristics of the nuclear techniques are given in Table 3.

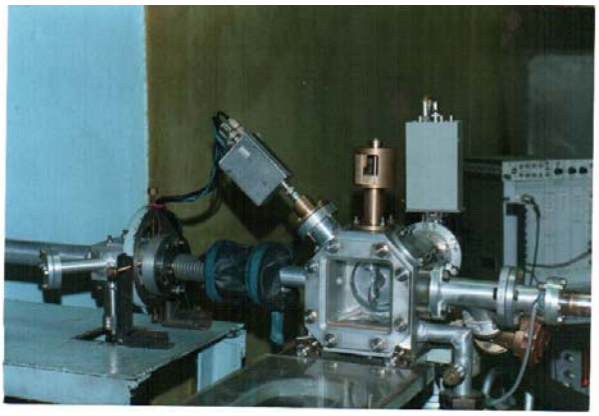

Fig. 2. The target chamber

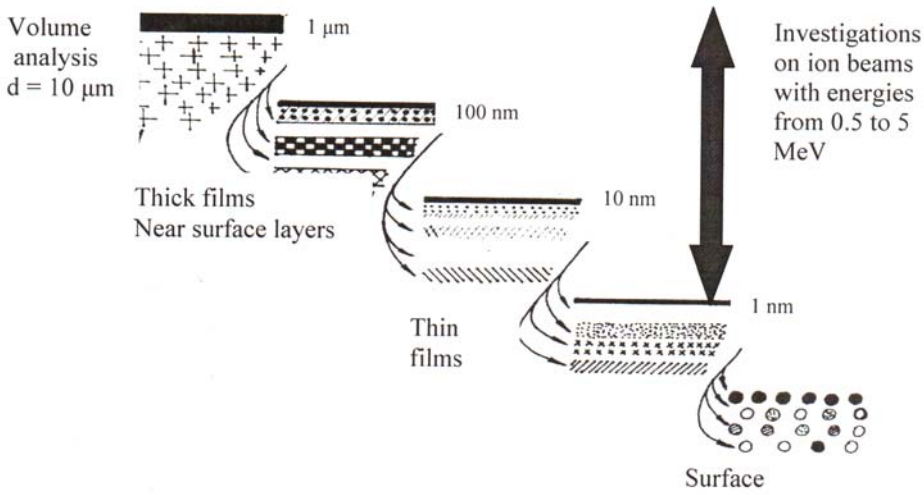

Fig. 3. Typical sphere of the microanalysis using nuclear physics methods with ions

Table 3

Analytical characteristics of the nuclear microanalysis techniques

Parameter	Value
Elements identified	^{2}H, Li – U
Element resolution ΔZ	1
Sensitivity	$(10^{-1} – 10^{-5})$ %
Precision	(3–5) %
Thickness of the investigated layers	(0.01–10) μm
Depth resolution	< 10 nm
Lateral resolution	± 0.5 mm

3. Main results of investigations on the ion beams

The main results of investigations of solids carried out at these accelerators during last 6 years include:

- aging investigations of straw drift-tubes, proposed for experiments at the LHC [4, 5];
- investigations of the composition, morphology and structure of mixed layers deposited onto surfaces after a preliminary carboboronization procedure (B/C:H layers deposition) and subsequent deuterium plasma-wall interaction in different areas of the Globus-M spherical tokamak after more than 8000 pulses (more than 800 s) [6–8];
- studying of the composition and photoluminescence of amorphous hydrogenised silicon films doped with erbium and oxygen (α–SiO_X:H<Er, O>) [9, 10];
- studying of the synthesis, composition and surface composition of the amorphous As_2Se_3 and As_2S_3, modified with complex compounds $Ln(thd)_3$ (Ln = Eu, Tb, Er, Yb) [11–13];
- investigations of doping influence on the structure and optical characteristics of $Ge_2Sb_2Te_5$ amorphous films [14].

References

1. V.B. Andrienko, A.N. Dyumin, V.M. Lebedev *et al*., Preprint LNPI-**872**, Leningrad (1983).
2. V.M. Lebedev *et al*., Proc. of XIII International Conference on Electrostatic Accelerators. Obninsk, Russia, 1999, p. 60.
3. V.B. Andrienko, A.N. Dyumin, V.M. Lebedev *et al*., Prib. Tekhn. Eksp. **3**, 51 (1991).
4. V.K. Gusev *et al*., Journ. of Nucl. Materials **386–388**, 708 (2009).
5. V.K. Gusev *et al*., Nuclear Fusion **49**, 095022 (2009).
6. V.K. Gusev *et al.,* Nuclear Fusion **49**, 104021 (2009).
7. V.M. Lebedev *et al.*, Bulletin of the Russian Academy of Sciences: Physics **71**, 1327 (2007).
8. A.G. Krivchitch, V.M. Lebedev, Nucl. Instr. Meth. A **381**, 167 (2007).
9. Yu.K. Undalov *et al.*, Semiconductors **42**, 1327 (2008).
10. Yu.K. Undalov *et al*., Semiconductors **45**, 1604 (2011).
11. S.A. Kozyukhin *et al*., Physics and Chemistry of Solids **68**, 1117 (2007).
12. V.Kh. Kudoyarova *et al.,* Semiconductors **41**, 914 (2007).
13. V.Kh. Kudoyarova *et al*., Physica Status Solidi C **7**, 881 (2010).
14. S.A. Kozyukhin *et al*., Physica Status Solidi C **8**, 2688 (2011).

Elementary Particles Physics

EXPERIMENT CMS AT THE LHC

A.A. Vorobyov, B.V. Bochin, S.A. Gets, V.L. Golovtsov, Yu.M. Ivanov, V.T. Kim, P.M. Levchenko, V.A. Murzin, V.A. Oreshkin, L.A. Schipunov, I.B. Smirnov, V.V. Sulimov, V.I. Tarakanov, L.N. Uvarov, S.A. Vavilov, S.S. Volkov, An.A. Vorobyov

1. Introduction

The observation of a particle with characteristics closely matching those predicted for the Standard Model (SM) Higgs boson was announced by the CMS and ATLAS experiments in July 4, 2012. This was a turning point for the experiments at the CERN Large Hadron Collider (LHC), especially because one of the main purposes of building the LHC and the CMS and ATLAS detectors was that of discovering the Higgs boson and understanding the origin of the electroweak symmetry breaking.

As it was officially stated at the European Physical Society conference in July 2013, the observed 125 GeV/c^2 resonance is indeed the Standard Model Higgs boson, though still many questions remain unanswered. The study of properties of the new 125 GeV/c^2 particle will constitute a new chapter of particle physics, one which will take the next decades to write.

In parallel with the Higgs boson discovery, the CMS experiment has kept expanding our knowledge of frontier particle physics with precise measurements of electroweak physics observables, and with the search for new particles and phenomena beyond the Standard Model.

The PNPI team is involved in the CMS project through a significant contribution to the design, construction, and maintenance of the Endcap Muon System. Also, PNPI physicists take part in the data analysis. This report presents a brief summary of the PNPI team activity in the CMS experiment, as well as some selected physics results published by the CMS Collaboration.

2. CMS detector

The Compact Muon Solenoid (CMS) is a collider detector (Fig. 1) designed to study physics of proton-proton collisions at the centre-of-mass energy up to 14 TeV at the full LHC luminosity [1].

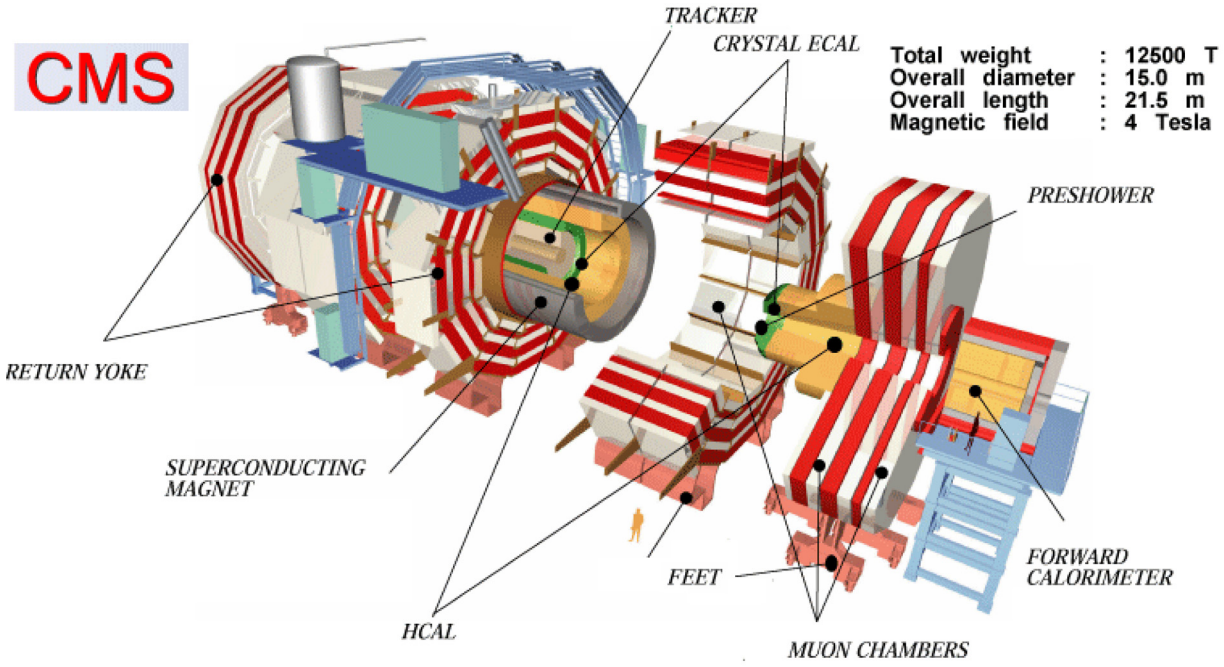

Fig. 1. Schematic view of the CMS detector

The basic element of the CMS detector is a superconducting solenoid of 6 m internal diameter, which provides a magnetic field of 3.8 T. Within the field volume, there are: the silicon pixel/strip tracker, the lead-tungsten crystal Electromagnetic CALorimeter (ECAL), and the brass/scintillator Hadron CALorimeter (HCAL). Muons are measured in gas-ionization detectors embedded in the steel flux-return yoke. The muon system consists of four stations in the barrel and in the endcap regions. Each muon station in the barrel region consists of twelve drift-tube layers, except for the outermost station, which has eight layers. In the endcap regions, each muon station consists of six planes of cathode strip chambers.

The CMS detector is operated by a collaboration of more than 4000 physicists and engineers from 182 institutions representing 42 countries. After installation and commissioning in 2007–2008, the CMS experiment started in November 2009 with the proton-proton centre-of-mass energy of 2.36 TeV and the LHC luminosity of 10^{28} $cm^{-2}s^{-1}$. By the end of 2012, after 3 years of continuous improvements, the LHC increased the *pp* centre-of-mass energy up to 8 TeV and the luminosity by more than 5 orders of magnitude up to $7.7 \cdot 10^{33}$ cm^{-2} s^{-1}. The experimental data corresponding to about 25 fb^{-1} of an integrated luminosity (about 5 fb^{-1} at 7 TeV and 20 fb^{-1} at 8 TeV, respectively) have been collected by the CMS Collaboration during this period. In February 2013, the LHC was stopped for the first Long Shutdown (LS1) for nearly two years with the goal to increase the *pp* centre-of-mass energy up to 14 TeV and to increase the luminosity up to $2 \cdot 10^{34}$ cm^{-2} s^{-1}. To optimize the performance of the CMS detector in these new conditions, the CMS Phase 1 upgrade program was launched to be implemented during LS1. A major part of this program is related with the upgrade of the Endcap Muon System.

3. PNPI participation in the design, construction, maintenance, operation, and upgrade of the CMS Endcap Muon System

3.1. Muon chambers. Status before the LS1 shutdown

The design and construction of the Endcap Muon System (EMU) was performed with an active participation of the PNPI team. Each of the two endcaps in the EMU system contains four detecting stations: ME1, ME2, ME3, ME4 (shown in red in Fig. 2). M1 station is divided into three regions: ME1/1, ME1/2, and ME1/3. The other stations are divided into two regions each: ME2,3,4/1 and ME2,3,4/2. Muons are detected with specially designed Cathode Strip Chambers (CSCs) which can measure the *r*-φ coordinates and the arrival time of each muon. The CSCs are six-plane chambers of trapezoidal shape. The cathode planes are formed by honeycomb panels with copper clad FR4 skins. Strips run radially in the endcap geometry and provide the φ-coordinate of muon hits with an accuracy of ~ 100 μm. Wires are stretched across the strips and, for readout purposes, are grouped in bunches from 5 to 16 wires. They provide the radial coordinate of the muon hits with a few cm precision.

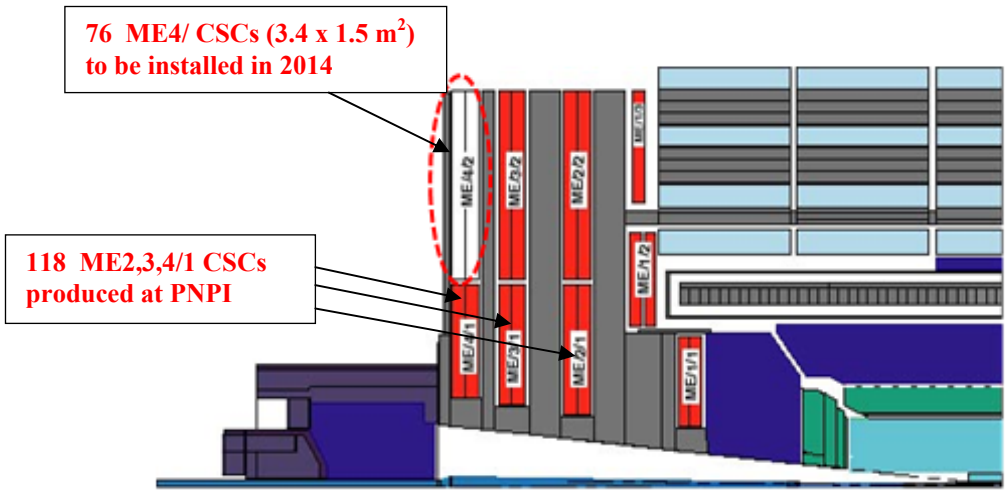

Fig. 2. Structure of the Endcap Muon System

In total, the EMU design comprised 540 CSCs, which contain 273024 cathode channels and about 2.5 million wires grouped into 210816 anode channels. However, because of finance restrictions, it was decided to postpone the construction of the ME4/2 region (72 CSCs) until the first LHC shutdown in 2013–2014.

The mass production of the chambers was distributed between three laboratories: PNPI, FNAL (USA), and IHEP (China). PNPI was responsible for assembling and testing of ME2/1, ME3/1, and ME4/1 chambers. In total, 120 CSCs (40 chambers of each type) were produced at a special facility (a muon chamber factory) prepared at PNPI to accomplish this task. The mass production of muon chambers at PNPI was started in October 2001. Full installation of these chambers in the CMS detector was completed in the end of 2007. This period of construction, testing, transportation to CERN, and installation of the CSCs is described in detail in our previous edition "HEPD Main scientific activities in 2002–2006" [2].

During the whole LHC running period in 2009–2012, the EMU system demonstrated very efficient and reliable performance even at the highest achieved luminosity $L \approx 8 \cdot 10^{33}$ cm^{-2} s^{-1}.

3.2. Muon chambers. The upgrade during LS1

The previous running period showed that the Endcap CSCs could operate without serious problems at the increased luminosity and energy planned for the running period after LS1 in 2015–2017. Therefore, a decision was taken to build CSCs for the missing station ME4/2 and to install them during the shutdown period LS1 [3]. This should considerably increase the redundancy of the Endcap Muon system. In total, 76 large area six-layers CSCs should be installed. In fact, the same type CSCs were assembled before at FNAL for stations ME2/2 and ME3/2.

Fig. 3. "Muon chamber factory" in building 904 at CERN

For several reasons, the ME4/2 chambers were to be assembled at CERN, all the materials and tooling needed for the chamber construction being supplied from FNAL. For this purpose, a "muon chamber factory" was organized in building 904 at CERN in 2011 (Fig. 3). The "factory" occupied 2000 m^2 area. It was equipped with two clean rooms, with an automated wiring machine, an automated wire soldering machine, an automated wire pitch and tension measuring machine, and with other tooling and equipment to perform chamber assembling and control on various steps of the assembling procedure.

Fig. 4. PNPI engineers played the leading role in all stages of the CSCs assembling and testing.
From left to right:
B.V. Bochin, An.A. Vorobyov, V.L. Golubev, V.V. Sulimov, S.A. Gets, V.I. Tarakanov

As a matter of fact, the ME4/2 chamber assembling technology is similar to that used earlier at PNPI to assemble ME2,3,4/1 chambers. That is why PNPI engineers (Fig. 4) were invited to participate in setting up the chamber assembling facility at CERN and to lead in production and testing ME4/2 chambers. Following the assembling of three prototype chambers for development of the assembling technology, the mass production was started in 2012. The production rate was 3 chambers per month at the initial stage. Then it was increased up to 4–5 chambers per month. The assembled chambers had to pass various controls, including gas leak tests and high voltage tests. Then they were kept under high voltage during one month, the leak currents being measured. After that, the chambers were dressed with the on-chamber electronics and tested at the cosmic muon test stand. Then they were stored under continuous gas flow expecting installation in the pit during the LS1 shutdown. This work strictly followed the production schedule according to which the production of all ME4/2 chambers should be completed by February 2014. The installation and commissioning of the chambers in the pit will be started in October 2013 with participation of the PNPI team.

3.3. High voltage system. The upgrade during LS1

The EMU CSCs require a rather complicated high voltage supply. At present, the EMU system comprises 468 six-plane muon chambers. Each plane should be provided with a high voltage line. Moreover, the HV line in each layer is subdivided into several sections (5 sections in chambers ME2/2, ME3/2 and 3 sections in all other chambers). So, in total there are more than 9000 sections with independent HV lines. This increases essentially the redundancy of the EMU system as, in case of problems, only one section will be switched off, which will not deteriorate noticeably the performance of the whole EMU system. Such a design dictated development of a special multichannel HV supply, which could satisfy the requirements of the CMS experiment. This problem was solved by joint efforts of specialists from PNPI and the University of Florida [2]. By the end of 2006, a 10000-channel HV system was designed, constructed, and delivered to CERN. The system provided independent voltage and current control in each channel. The maximal current in each channel is 100 μA. This HV system demonstrated reliable operation during all running periods in 2009–2012.

The construction of new CSCs for the ME4/2 station required additional HV supplies. The decision was to produce another 2400-channel HV system at PNPI with most of materials provided by the Florida University. The block diagram of the designed HV system is presented in Fig. 5. The high voltage from the Primary HV power supply is distributed for about 2400 HV lines with independent regulations of the voltage in each line. Also, the current in each line is under control with a possibility to switch off any line by burning off a fuse, if necessary. The HV distribution is done in two stages. Firstly, it is distributed by nine Master Boards into 72 HV lines with the HV regulation from 0 to 4 kV. These lines go *via* ~ 100 meter long cables to 72 Remote Distribution Boards. Each such board has 30 or 36 outputs going directly to the muon chambers. Including the spares, there are 96 modules to be constructed and tested: 86 Remote Distribution Boards and 10 Master Boards. The comprehensive test of the modules takes into account the requirements of the upgrade of the CMS Muon System concerning the increased LHC luminosity. The production of the 2400-channel system was started in the end of 2012, and the HV system will be finished and transported to CERN by February 2014.

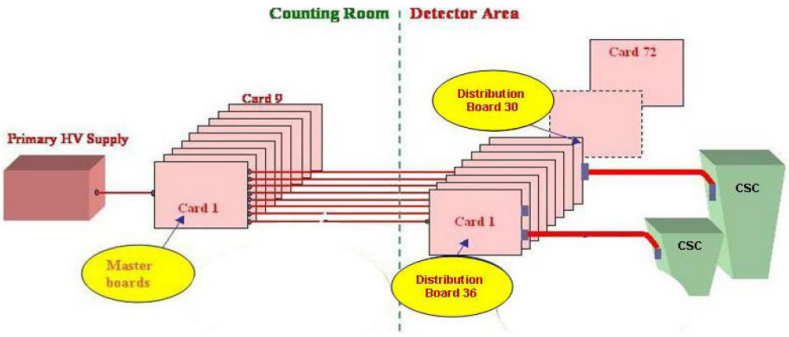

Fig. 5. Block diagram of the 2400-channel HV system

3.4. Track Finding Processor and the upgrade of the Level-1 Muon Trigger

The Track Finding Processor (TFP) is an essential part of the existing EMU trigger system. It links track segments from the individual muon stations into complete tracks, measures the transfer momentum from the sagitta induced by the magnetic bending, and reports the number and quality of the tracks to the Level-1 global trigger. The TFP (Fig. 6) was designed by PNPI engineers in cooperation with the University of Florida [2]. It is implemented as 12 processors working in parallel. Each of them should identify up to three best muons in the corresponding 60° azimuthal sectors. The design of the TFP is based on the most advanced Field Programmable Gate Array (FPGA) chips, each of them containing more than one million logical elements. The TFP was fabricated in the US industry, while testing and commissioning of this system was done by PNPI engineers in cooperation with specialists from the University of Florida. The TFP demonstrated reliable performance during the 2009–2012 running periods.

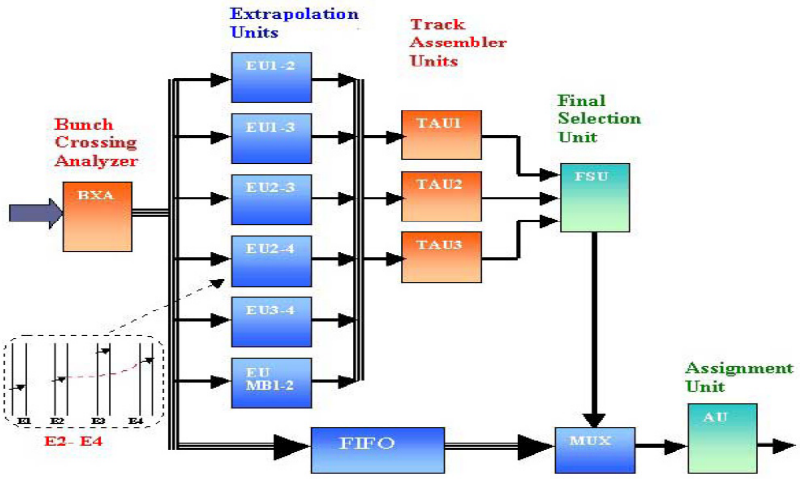

Fig. 6. Block diagram of the Track Finding Processor

The global Level-1 Muon Trigger operated with the required high efficiency in 2009–2012. However, the envisaged further increase of the LHC beam energy and luminosity creates serious problems for the trigger system. Therefore, the upgrade of the trigger system is considered as the most important part of the CMS upgrade program. For that reason, the CMS Collaboration has prepared a Technical Design Report [4] with a conceptual design of an improved muon trigger system able to select interesting collisions in this new high intensity regime.

The overall strategy is to merge the detector information from different muon sub-detector systems at the input to the muon track-finder and to form a combined track-finder layer. This substantial change to the design of the muon trigger is planned to proceed through several stages, so that commissioning of the upgrade can proceed in parallel with the running current trigger. The first step is to make several changes to the data links providing muon trigger data. The next step is to deploy the new Muon Track Finder that will be partitioned into barrel, endcap, and overlap regions. It will be commissioned in parallel with the running current trigger in 2015 using the full set of parallel inputs from the CSC and RPC systems and a subset of duplicated inputs from the DT system. The algorithms developed initially will be similar to the current trigger, but will be expanded over time to fully replace the separate CSC, DT, and RPC trigger systems. After the track-finder layer, a further layer is necessary to merge and remove duplicate muon candidates from the different track finders and also to sort the muons. The Global Muon Trigger will also be upgraded to receive more muon candidates.

The successful collaboration between PNPI and the University of Florida on the first generation muon trigger has resulted in the development of the Track-Finding Processor, which served CMS well for the first LHC runs. The PNPI team will participate also in the Muon Trigger upgrade with the responsibility to design and build the new Barrel/Endcap Overlap Track-Finding Processor.

4. Selected physics results

4.1. Search for the Higgs boson

In July 4, 2012, CMS jointly with ATLAS announced [5] that a new particle with the mass $m \approx 125$ GeV/c^2 was observed with characteristics compatible with those expected for the Standard Model Higgs boson. It was detected in its decays to bosons (photon pairs, *WW*- and *ZZ*-pairs) using 5.1 fb^{-1} at $\sqrt{s} = 7$ TeV and 5 fb^{-1} at $\sqrt{s} = 8$ TeV, respectively. The next updates [6–10], were presented in November and December 2012, and in March and May 2013, and at the European Physical Society (EPS) conference in July 2013. These results were based on 19.6 fb^{-1} at $\sqrt{s} = 8$ TeV. Also, they included decays to fermions: $\tau\tau$- and $b\bar{b}$-pairs. At the EPS conference, the new 125 GeV/c^2 resonance was officially established as the SM Higgs boson.

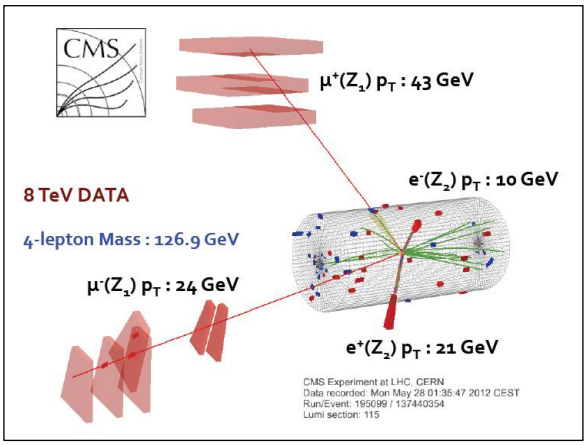

Fig. 7. Four-leptons event, a candidate for the Higgs boson decay with a mass 126.9 GeV/c^2. One of the muons is detected by the Endcap Muon System

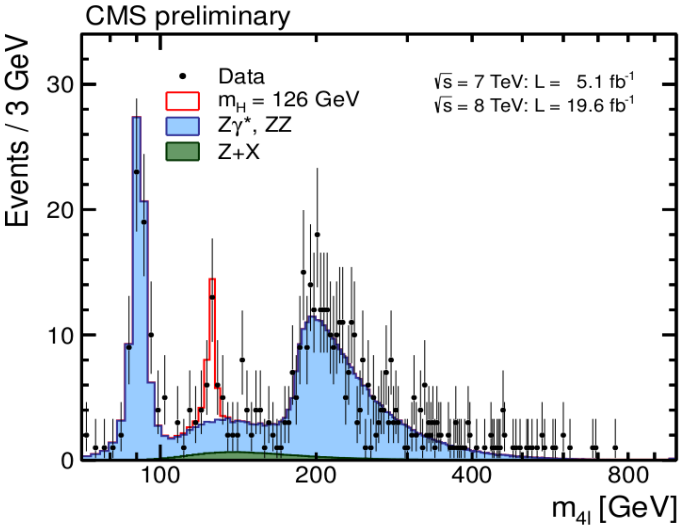

Fig. 8. Four-leptons mass distribution

The Standard Model predicted the Higgs boson existence with its mass between 115 GeV/c^2 and 140 GeV/c^2. Also, the SM predicted the production cross sections for the Higgs boson in *pp*-collisions and the branching ratios of the Higgs boson decay to various channels. The search for the Higgs boson in the CMS experiment was driven by these predictions. The cleanest signal of the Higgs boson was observed in the four-leptons decay modes, though the branching ratios to these channels are very small: Br ($H \rightarrow ZZ^* \rightarrow 4l$) $\approx 10^{-4}$ for a 125 GeV/c^2 Higgs (here, l = μ, e). Figure 7 shows one condidate for the four-leptons Higgs decay observed in the CMS experiment, and Fig. 8 presents the four-leptons mass distribution with full statistics collected by CMS. It was concluded from an analysis of this spectrum that a new particle with the mass $m_H = 125.6 \pm 0.5$ (stat.) $\pm$ 0.2 (syst.) GeV/c^2 is observed with the local significance of 6.8 standard deviations above the expected background. The width of the observed resonance was determined as $\Gamma \leq 3.4$ GeV/c^2 at the 95% CL. The signal strength μ, relative to the expectation for the Standard Model Higgs boson, is found to be $\mu = 0.91 + 0.30 - 0.24$ at the measured mass.

The $H \rightarrow \gamma\gamma$ decay is one of the most sensitive channels for the Higgs search in the mass region around 125 GeV/c^2 due to its relatively high expected branching fraction of the order of ~ 0.2 %. However, a serious problem in this case is the background. The search results were based on the Multi-Variate-Analysis (MVA) techniques for both photon identification and event classification which extracts the signal from the background using a fit to the diphoton mass spectrum shown in Fig. 9. The following results were obtained from that analysis: $m_H = 125.4 \pm 0.5$ (stat.) $\pm$ 0.6 (syst.) GeV/c^2, $\mu = 0.78 + 0.28 - 0.26$. The local significance of the observed peak at 125.4 GeV/c^2 is 3.2 standard deviations above the background.

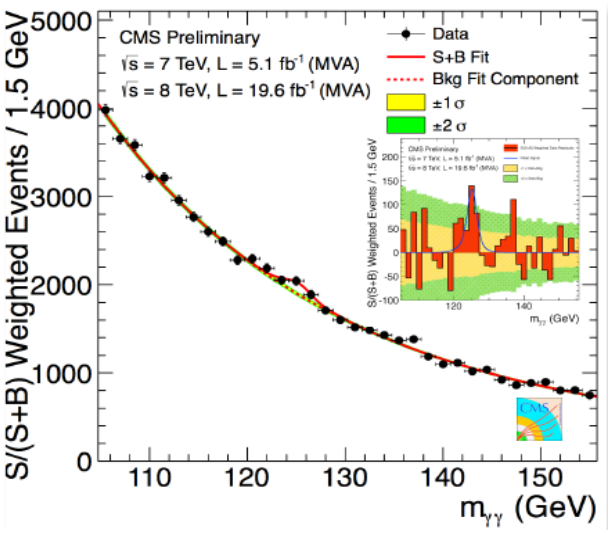

Fig. 9. Two-gammas mass distribution measured in the CMS experiment

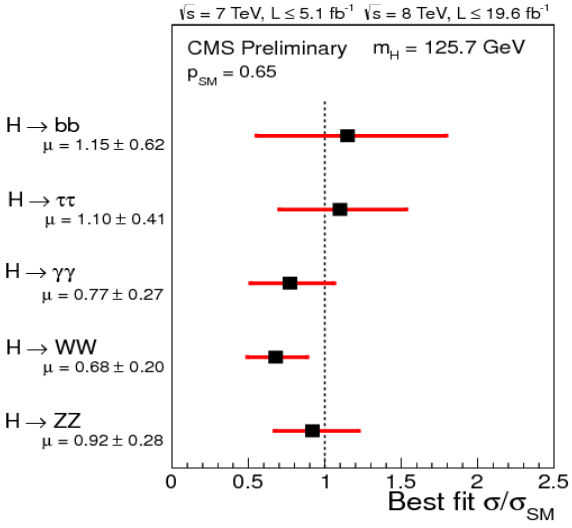

Fig. 10. Ratio of the measured yields in various decay channels of the Higgs boson to those predicted by the Standard Model

Besides the observation of the Higgs boson *via* channels $H \to ZZ^* \to 4l$ and $H \to \gamma\gamma$, the CMS Collaboration has reported also on observation of Higgs signals in $H \to WW$, $H \to bb$, and $H \to \tau\tau$ channels with the signal strengths compatible with those predicted by the Standard Model (Fig. 10). These observations are of special importance as they provide control of the SM predictions [11] both in vector boson and fermion couplings (Fig. 11).

The spin-parity of the SM Higgs boson should be 0^+ (that is it is a scalar particle). Spin 1 is excluded by the fact that the observed particle decays into two gammas. The analysis of the angular distributions of the four leptons showed that the pure scalar hypothesis is consistent with the observation when compared to six other spin-parity hypotheses. The data disfavour the pure pseudoscalar hypothesis 0^- with a CLs value of 0.16 % (Fig. 12) and disfavour the pure spin 2 hypothesis of a narrow resonance with minimal couplings to the vector bosons with a CLs value of 1.5 %.

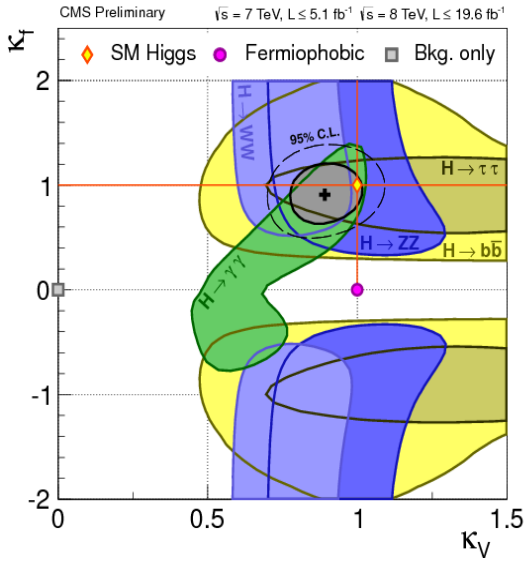

Fig. 11. The measured fermion and boson couplings in the observed channels

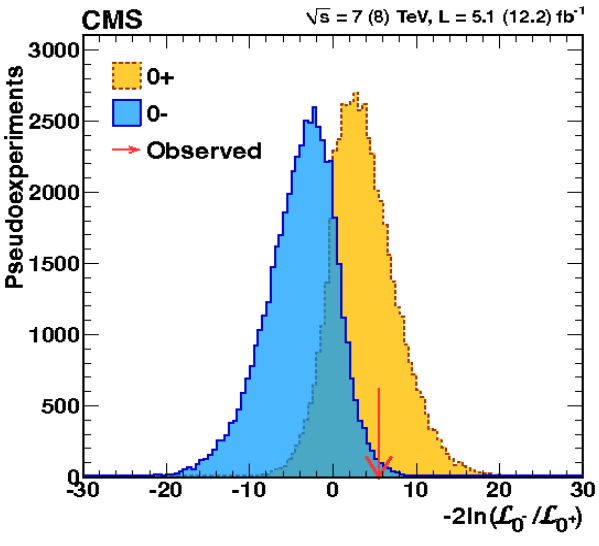

Fig. 12. Spin-parity properties: expected distribution of $-2 \cdot \ln(L0^- / L0^+)$ under the pure pseudoscalar and scalar hypotheses; the red arrow shows the observed value

To summarize, the new discovered 125 GeV/c^2 particle is compatible with the SM Higgs boson properties. It is seen beyond doubts in three boson decay channels. Fermionic decays in $b\bar{b}$ - and ττ-channels are observed, and they are in agreement within the uncertainties with the SM predictions. The two high-resolution modes allowed independent determinations of the Higgs boson mass: m_H = (125.8 ± 0.6) GeV/c^2 in $H \to ZZ \to 4l$ and m_H = (125.4 ± 0.8) GeV/c^2 in $H \to \gamma\gamma$. There is no evidence for non-SM decays and for additional Higgs bosons at higher or lower masses. ***The observed spin-parity properties and the measured couplings allow to establish the observed particle as the SM Higgs boson.***

4.2. Search for "new physics". Rare decays $B_s \to \mu^+\mu^-$ and $B_d \to \mu^+\mu^-$

The search for "new physics" beyond the Standard Model was among the main goals of the CMS experiment. One way was to make an attempt to see directly new particles (sypersymmetric partners, heavy bosons, leptoquarks, *etc*.) produced in *pp* collisions at the LHC. Various channels were tested where these new particles could be produced. However, the result was negative. So, the conclusion was that the mass of these particles (if they exist) should be higher than ~ 1 TeV/c^2. A hope still remains that such particles could be discovered in the next runs when the energy of the LHC will be increased to $\sqrt{s}$ = 14 TeV.

Another (inderect) way to see the presence of "new physics" was studies of rare decays of B mesons. From this point of view, the most promising was the decay of B_s and B_d mesons to two muons. The Standard Model predicts very low branching fractions for these decays:

$$\mathcal{B}(B_s \to \mu^+\mu^-) = (3.2 \pm 0.2) \times 10^{-9}, \quad \mathcal{B}(B_d \to \mu^+\mu^-) = (1.0 \pm 0.1) \times 10^{-10}.$$

On the other hand, "new physics" (in particular, some supersymmetric models) could drastically increase probabilities of these decays. That is why investigation of these decays attracted so much attention in the LHC experiments (LHCb and CMS). The CMS Collaboration presented results of a search for the rare decays $B_s \to \mu^+\mu^-$ and $B_d \to \mu^+\mu^-$ in *pp* collisions at $\sqrt{s}$ = 7 TeV and $\sqrt{s}$ = 8 TeV based on data samples corresponding to integrated luminosities of 5 fb^{-1} and 20 fb^{-1}, respectively [12]. An excess of $B_s \to \mu^+\mu^-$ decays was observed above the background predictions (Fig. 13).

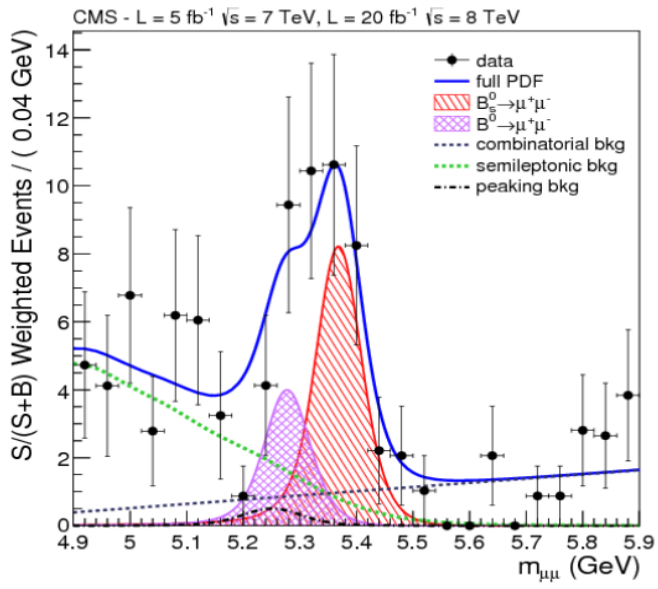

Fig. 13. Dimuon weighted mass distribution

The measured decay-time integrated branching fraction from the fit is

$$\mathcal{B}(B_s \to \mu^+\mu^-) = (3.0 + 1.0 - 0.9) \times 10^{-9},$$

where the uncertainty includes both the statistical and systematic components, but is dominated by the statistical uncertainties. The significance of the observed decay is 4.7 standard deviations. The measured branching fraction is consistent with the expectation from the SM. No excess is observed for $B_d \to \mu^+\mu^-$, with the upper limit

$$\mathcal{B}(B_d \to \mu^+\mu^-) < 1.1 \times 10^{-9}$$

at the 95 % confidence level.

Similar results were obtained in the LHCb experiment (see a special article in this edition). The fact that the measured $\mathcal{B}(B_s \to \mu^+\mu^-)$ corresponds to the SM prediction puts strong limitations for proposed models of "new physics". In particular, it excludes some of the supersymmetric models.

4.3. Ridge effect in *pp*-, *pA*- and *AA*-collisions

The first groundbreaking result at the LHC was announced by the CMS Collaboration in 2010 with the observation of long-range near-side angular correlations in *pp* collisions with high multiplicities at $\sqrt{s}$ = 7 TeV [13]. The CMS has measured the two-particle correlation function in azimuthal and pseudorapidity two-dimensional space. In high multiplicity events (N > 110), a pronounced structure ("ridge") emerges in the two-dimensional correlation function for particle pairs with intermediate p_T-values of 1–3 GeV/c, 2.0 < |Δη| < 4.8, and Δφ ≈ 0 (Fig. 14). This was the first observation of such a long-range, near-side feature in two-particle correlation functions in hadron-hadron collisions. Such a correlation was observed earlier in central heavy-ion collisions at RHIC (BNL). The heavy-ion ridge effect found at RHIC at $\sqrt{s_{NN}}$ = 0.2 TeV was interpreted as a manifestation of formation of a new state of the superdense hot nuclear matter and, hence, it should not be observed in *pp* collisions. Later, the ridge effect was observed at the LHC also in *pA*- ($\sqrt{s_{NN}}$ = 5.02 TeV) and *AA*- ($\sqrt{s_{NN}}$ = 2.76 TeV) collisions (Fig. 14). The interpretation of the ridge effect is still under discussion, and it requires further theoretical and experimental studies to test numerious models [14].

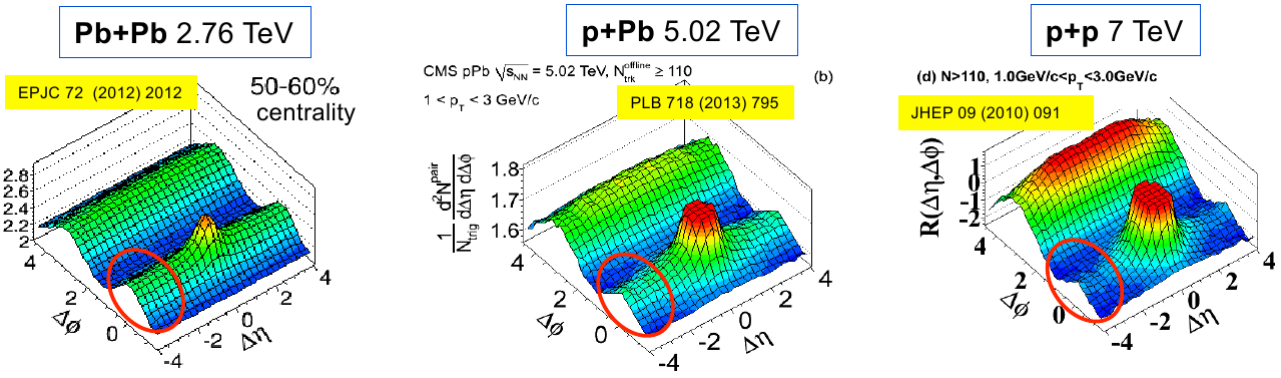

Fig. 14. Two-particle correlation functions versus Δη and Δφ for *pp*-, *pA*- and *AA*-collisions at the CMS. The cycles show the locations of the near-side ridge structures

4.4. Search for electroweak production of *Z* bosons with two forward-backward jets

The CMS has performed the first measurement of the electroweak production cross section of a *Z* boson with two forward jets (*Zjj*) in *pp* collisions at $\sqrt{s}$ = 7 TeV with an integrated luminosity of 5 fb^{-1} [15]. This process was studied in the context of rapidity intervals in hadron collisions as a probe of anomalous triple-gauge-boson couplings and as a background to Higgs boson searches in Vector Boson Fusion (VBF) processes. There are three classes of diagrams to be considered in the EW production of *W* and *Z* bosons with two forward jets: VBF processes, bremsstrahlung, and multiperipheral processes (Fig. 15). A full calculation reveals a large negative interference between the pure VBF process and the other two categories.

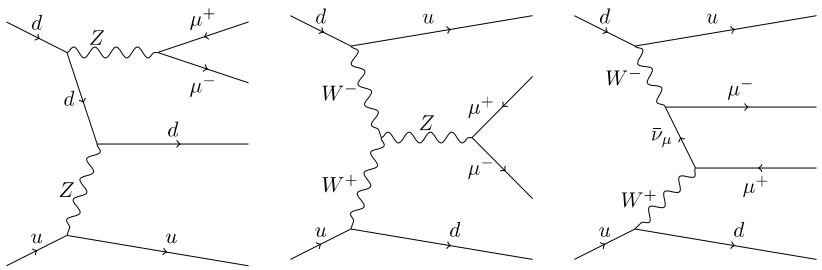

Fig. 15. Representative Feynman diagrams for electroweak *llqq'* production processes. Bremstrahlung (left); vector boson fusion (centre); peripheral (right)

The VBF Higgs boson production in *pp* collisions at the LHC has been extensively investigated as a way to discover the Higgs boson and to measure its couplings. Recent searches by the ATLAS and CMS Collaborations for the SM Higgs boson include analyses of the VBF final states. In particular, the study of the processes shown in Fig. 15 can improve our understanding of selection of the tagging jets, as well as that of vetoing additional parton radiation between forward-backward jets in VBF searches. The measurement of the electroweak production of the *Zjj* final state is also a precursor to the measurement of elastic vector boson pair scattering at high energy, an important physics goal for future analyses of LHC data.

The cross section is measured for the *lljj* ($l = e$, μ) final state in the kinematic region $m_{ll} > 50$ GeV/c^2, forward dijet $m_{jj} > 120$ GeV/c^2, jet transverse momenta $p_T > 25$ GeV/c, and the jet pseudorapidity $|\eta| < 4.0$. This measurement, combining the muon and electron channels, yields σ = (154 ± 24 (stat.) ± 46 (exp. syst.) ± 27 (th. syst.) ± 3 (lum.)) fb, in agreement with the SM prediction (~ 166 fb) for the cross section. The hadronic activity in the rapidity interval between the jets is also measured. A significance of 2.6 standard deviations has been obtained for the observation of EW production of the *Z* boson with two tagging jets. This first measurement of the *Z* boson with two jets at the hadron collider by the CMS constitutes an important foundation for a more general study of vector boson fusion processes of relevance for Higgs boson searches and for measurements of electroweak gauge couplings and vector-boson scattering.

4.5. Search for BFKL effects in forward jets

Measurements of inclusive jet production in *pp* collisions provide an important testing ground for the Standard Model. At the LHC energies, the inclusive production of jets with large transverse momentum in the central rapidity region is well described by the perturbative quantum chromodynamics (QCD) using the Gribov – Lipatov – Altarelli – Parisi – Dokshitzer (GLAPD) evolution. However, the dominant kinematical regime for jet production at the LHC energies is extended for a very wide rapidity domain. At very high energies, this dominant kinematic regime is expected to be described by the Balitsky – Fadin – Kuraev – Lipatov (BFKL) evolution [16, 17]. The BFKL-effects may dominate for the QCD background in searches for new heavy extra-dimension gravitons with forward dijets at the LHC [18, 19].

The results presented below illustrate attempts to see some evidence of the BFKL effects already at the LHC energies. For these studies, the dijet events were chosen. The events were classified as follows. The events with at least one pair of jets with $p_T > p_T^{min}$ are denoted as "inclusive". The inclusive dijets with the jets most forward and backward in the rapidity, *i.e.*, dijets with the maximal rapidity separation between the jets, are the so called Mueller – Navelet (MN) jets. Events with exactly one pair of jets with $p_T > p_T^{min}$ are called "exclusive". The ratio of the dijet production cross section for "inclusive" events to that for "exclusive" events, $R^{incl} = \sigma^{incl} / \sigma^{excl}$ (the dijet "*K*-factor"), as a function of the rapidity separation $|\Delta y|$ between two jets, may be a sensitive probe of BFKL-effects [20]. Analogously, one can consider the ratio $R^{MN} = \sigma^{MN} / \sigma^{excl}$.

The CMS performed the first measurement of the ratios R^{incl} and R^{MN} in a wide range of the rapidity separation, up to $|\Delta y| = 9.2$, in *pp* collisions at $\sqrt{s} = 7$ TeV [21]. A dedicated forward dijet trigger allowed to enhance the registration rate of the dijets by a factor of ~ 150 in the forward region. The results are shown in Fig. 16. A moderate rise of the ratios R^{incl} and R^{MN} as a function of $|\Delta y|$ is observed. In comparisons of theoretical values of R^{incl} and R^{MN} with the experimental data, three GLAPD based MC event generators were used: PYTHIA6, PYTHIA8, and HERWIG++, improved by polar angle ordering (*i.e.*, by colour coherence effects) in the parton shower. The predictions of the PYTHIA6 and PYTHIA8 generators agree with the measurements, while the predictions of the HERWIG++ generator are larger than the measurements, especially at large $|\Delta y|$ values. The BFKL-motivated generators in the leading logarithm (LL) approximation, CASCADE and HEJ+ARIADNE, predict for these ratios a significantly stronger rise than the observed one. The moderate rise of the measured dijet ratios indicates that either the BFKL effects are not dominant for jets with $p_T > p_T^{min} = 35$ GeV/c at the collision energy $\sqrt{s} = 7$ TeV, or the BFKL effects are canceled in the ratios.

There is another way to study the dynamics of hadron jets in *pp* collisions, which yields important information about underlying partonic processes. The azimuthal decorrelation of jets with a large rapidity separation might show effects beyond the GLAPD description. In the kinematic region where BFKL-effects are important, the azimuthal angle decorrelations will increase with the rapidity separation increasing.

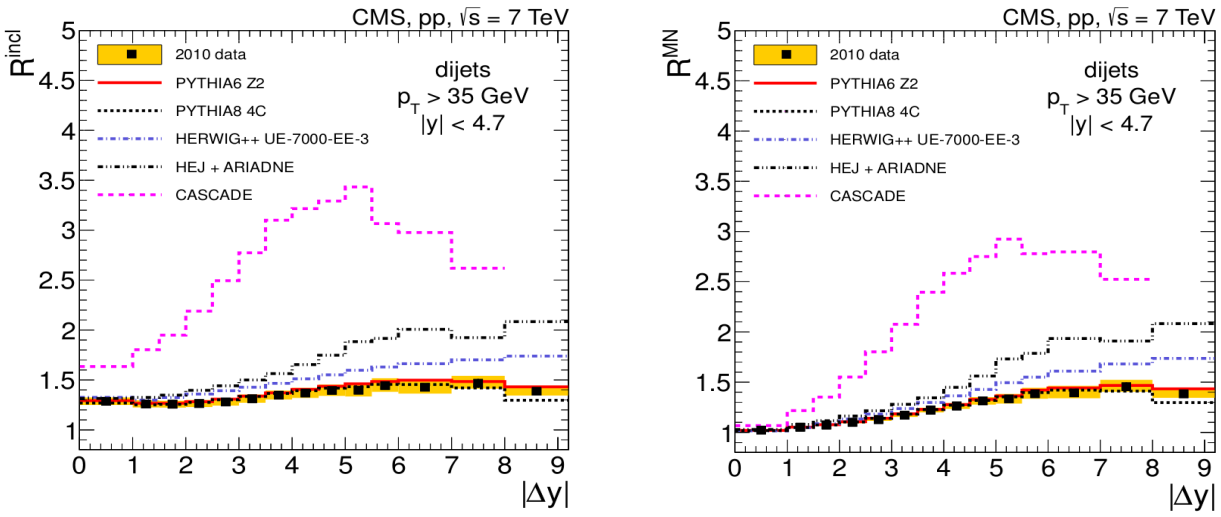

Fig. 16. First measurement of dijet raios $R^{\mathrm{incl}} = \sigma^{\mathrm{incl}}/\sigma^{\mathrm{excl}}$ (left) and $R^{\mathrm{MN}} = \sigma^{\mathrm{MN}}/\sigma^{\mathrm{excl}}$ (right) as a function of the rapidity separation between jets up to $|\Delta y| = 9.2$ at the LHC [20]

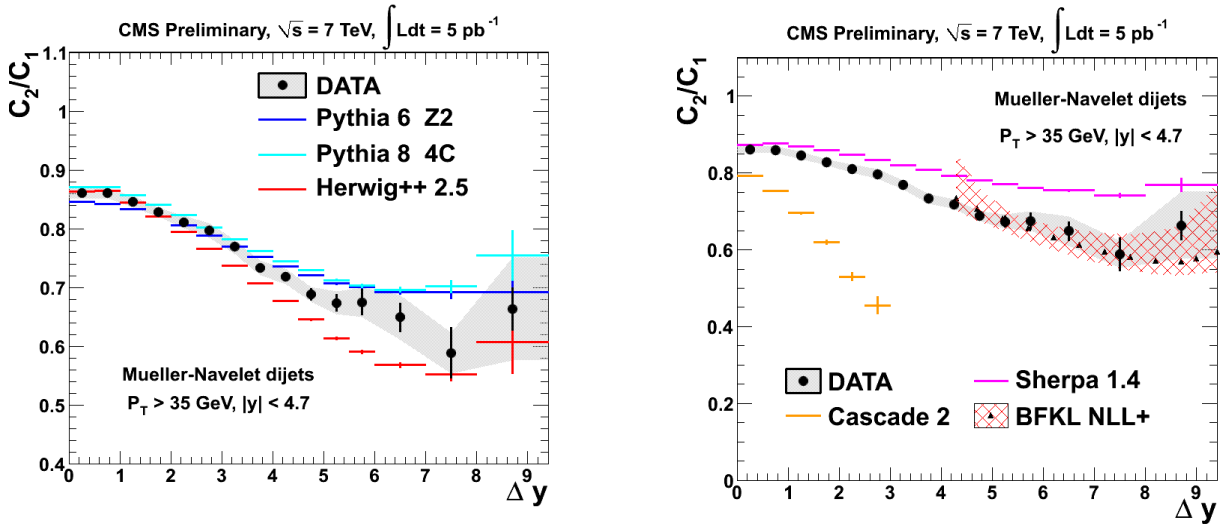

Fig. 17. First measurement of the azimuthal angle decorrelations at *pp* collisions as a function of the rapidity separation between jets up to $|\Delta y| = 9.4$ in CMS at the LHC. The ratio of average cosines $C_2 / C_1 = \langle\cos(2(\pi - \Delta\varphi))\rangle / \langle\cos(\pi - \Delta\varphi)\rangle$ is shown *vs* GLAPD MC generators (left) and *vs* BFKL predictions (right)

The first measurement of the azimuthal angle decorrelations of Mueller – Navelet dijets with a rapidity separation of up to $\Delta y = 9.4$, in proton-proton collisions at $\sqrt{s} = 7$ TeV, was performed by CMS [22]. The results are presented in Fig. 17. The average cosine ratios are particularly sensitive to details of parton showering and multiparton interaction: without implementing polar angle ordering in parton showering and multiparton interactions the considered GLAPD MC generators show significant deviations from the data. CASCADE 2, which incorporates essential elements of LL BFKL but is missing some elements of collinear factorization of the GLAPD approach, predicts too strong azimuthal decorrelations. Analytical BFKL calculations [23] performed at the next-to-leading logarithmic (NLL) approximation [24] provide a satisfactory description of the data for the average cosine ratios. The observed disagreement of the LL GLAPD MC generators without the polar angle ordering in parton showering may be considered as a hint that the kinematical domain of the present study lies in the transition between the regions described by the GLAPD and BFKL approaches. For further investigations of possible manifestations of BFKL effects, data at higher energies are needed.

5. Summary

The CMS experiment, one of the most ambitious projects in fundamental particle physics, has demonstrated at the first stage of the LHC running its extraordinary capabilities to extend the high-energy physics frontier. The main result so far is the discovery of the 125 GeV/c^2 Higgs boson, a quantum of the scalar fundamental vacuum field, which is responsible for spontaneous symmetry breaking of electroweak forces and the particle mass origin. In addition, the CMS experiment performed a large number of new precise measurements of the Standard Model physics observables, and also measurements aimed to discover new particles and phenomena beyond the Standard Model. These measurements proved to be a strong confirmation of the Standard Model with no indication of signs of "new physics" in the investigated mass region up to ~ 1 TeV/c^2.

The PNPI team has made a significant contribution to the design, construction and maintenance of the Endcap Muon System of the CMS detector. At present, the PNPI team is actively involved in the upgrade of the Endcap Muon System of the CMS detector for the challenging high luminosity beam conditions at the next stage of the LHC operation. PNPI physicists have contributed to the CMS data analysis, in particular in searches for the Higgs boson in vector boson fusion production, in studies of the electroweak *Z*-boson production with forward jets, and for BFKL physics in forward dijets as a novel QCD dynamics in a new energy domain.

In total, the CMS Collaboration has published 242 physics papers in the period 2010 – July 2013. The list of authors in the CMS physics publications includes PNPI physicists and engineers: A.A. Vorobyev, Yu.M. Ivanov, V.L. Golovtsov, V.T. Kim, P.M. Levtchenko, V.A. Murzin, V.A. Oreshkin, I.B. Smirnov, V.V. Sulimov, L.N. Uvarov, S.A. Vavilov, An.A. Vorobyev.

References

1. CMS Collaboration, JINST **3**, S08004 (2008).
2. A.A. Vorobyov *et al.*, PNPI HEPD Main Scientific Activities, 2002–2006, PNPI, 2007, pp. 26–34.
3. CMS Collaboration, CMS U1 TDR, June 2011.
4. CMS Collaboration, CERN-LHCC-2013-011, CMS-TDR-012, June 2013.
5. CMS Collaboration, Phys. Lett. B **716**, 30 (2012).
6. CMS Collaboration, CMS-PAS-HIG-13-002, March 2013.
7. CMS Collaboration, JHEP **06**, 081 **(**2013).
8. CMS Collaboration, Phys. Rev. Lett. **110**, 081803 (2013).
9. CMS Collaboration, CMS-PAS-HIG-13-016, July 2013.
10. CMS Collaboration, CMS-PAS-HIG-13-005, April 2013.
11. V.T. Kim, Nucl. Phys. Proc. Suppl. **198**, 223 (2010).
12. CMS Collaboration, Phys. Rev. Lett. **111**, 101804 (2013).
13. CMS Collaboration, JHEP **1009**, 091 (2010).
14. I.M. Dremin and V.T. Kim, Pis'ma ZhETF **92**, 720 (2010) [JETP Lett. **92**, 652 (2010)].
15. CMS Collaboration, CMS-PAS-FSQ-12-019, November 2012, JHEP (2013), in press.
16. E.A. Kuraev, L.N. Lipatov, and V.S. Fadin, ZhETF **72**, 377 (1977) [JETP **45**, 199 (1977)].
17. I.I. Balitsky and L.N. Lipatov, Yad. Fiz. **28**, 1597 (1978) [Sov. J. Nucl. Phys. **28**, 822 (1978)].
18. V.T. Kim *et al*. Nucl. Phys. Proc. Suppl. **198**, 220 (2010).
19. V.T. Kim and V.A. Oreshkin, Nucl. Phys. Proc. Suppl. **219–220**, 235 (2011).
20. V.T. Kim and G.B. Pivovarov, Phys. Rev. D **53**, 6 (1996).
21. CMS Collaboration, Eur. Phys. J. C **72**, 2216 (2012).
22. CMS Collaboration, CMS-PAS-FSQ-12-002, April 2013.
23. S.J. Brodsky *et al*., Pis'ma ZhETF **70**, 161 (1999) [JETP Lett. **70**, 155 (1999)].
24. B. Ducloue, L. Szymanowski, and S. Wallon, JHEP **1305**, 096 (2013).

EXPERIMENT ATLAS AT THE LHC

PNPI participants of the ATLAS Collaboration: O.L. Fedin, S.V. Katunin, S.V. Kovalenko, N.V. Klopov, L.G. Kudin, V.P. Maleev, A.V. Nadtochi, S.B. Oleshko, S.K. Patrichev, Yu.F. Ryabov, V.A. Schegelsky, E.V. Sedykh, D.M. Seliverstov, V.M. Solovyev, Yu.K. Zalite

1. Introduction

ATLAS is a particle physics experiment at the Large Hadron Collider (LHC) at CERN. The ATLAS detector [1] is searching for new discoveries in the proton-proton collisions of extraordinarily high energy. ATLAS investigates a wide range of physics including searches for the Higgs boson, extra dimensions, and particles that could make up dark matter.

ATLAS is an international collaboration of about 3000 physicists from 174 institutions. PNPI was involved in the ATLAS experiment through the design and construction of the Transition Radiation Tracker (TRT) from the beginning of the conceptual detector design. The TRT is one of three sub-systems of the ATLAS Inner Detector (ID) (Fig. 1), which is composed of the silicon-based Pixel and Semiconductor Tracker (SCT) detectors, and the gaseous drift tube Transition Radiation Tracker. The TRT is the outermost of the three sub-systems.

At present, PNPI physicists participate in the TRT detector operation and in the data analysis including QCD and electroweak physics studies, and heavy bosons searches.

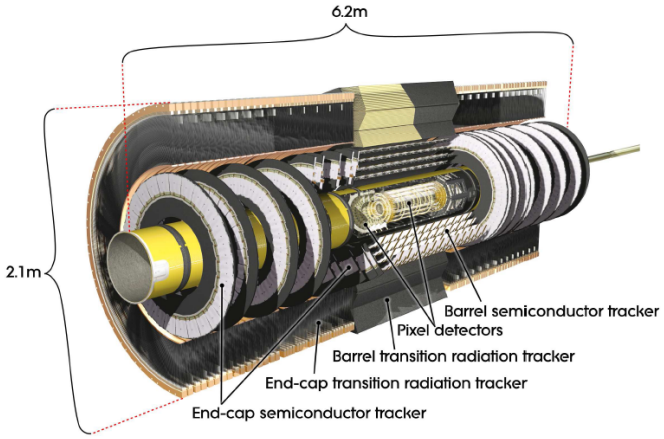

Fig. 1. General view of the Inner Detector of the ATLAS detector

2. Transition Radiation Tracker

The TRT detector was designed for two purposes: extended tracking to provide high resolution of a track transverse momentum measurement and the particle identification based on Transition Radiation (TR). These tasks became possible to realize due to a unique combination of the precision drift time measurement with straws as base elements of the detector, and the registration of soft *X*-rays emitted by relativistic particles in the radiator filling the space between the straws.

To meet requirements for spatial and momentum resolutions, the initial requirement for the straw hit resolution was set ~ 170 μm with the single straw efficiency ~ 95 % [2]. This should provide ~ 30 μm track resolution in the middle of the detector with ~ 35 measurement points (hits) per track. The TRT makes a crucial contribution to the track measurement. In Fig. 2, the momentum resolution and the impact parameter measurement accuracy obtained in the cosmic ray commissioning performed in 2008–2009 [3] are presented. It is seen that the TRT provides a significant improvement, especially for $p_T > 20$ GeV/c. A difference between the simulation and the full ID data indicates mainly remaining intrinsic misalignments. The following alignment [4] has allowed to reach a significant improvement of the spatial resolution. The single

straw hit position resolution of 120 μm for the TRT barrel and 135 μm for the TRT end-caps has been achieved (see Fig. 3).

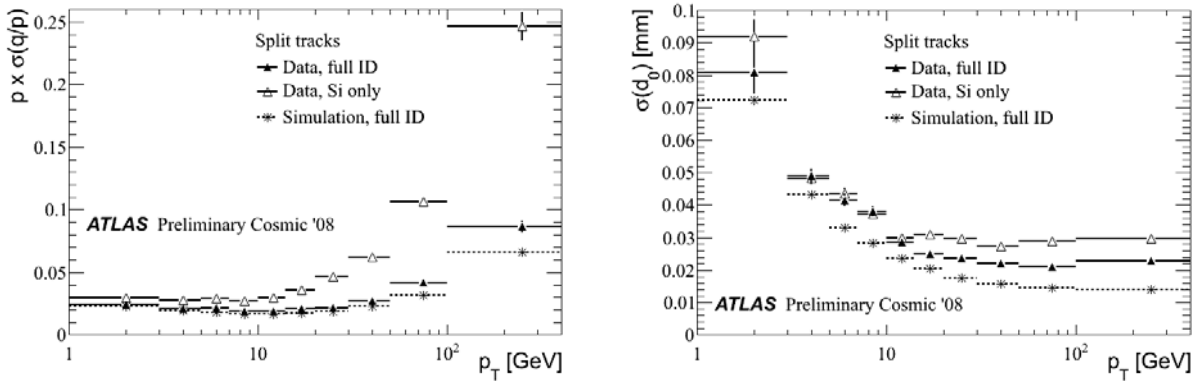

Fig. 2. Momentum resolution (left) and accuracy of the impact parameter measurement (right) as a function of the transverse momentum of the particle. Black dots – simulation, open triangles – combined measurements by the Pixel and SCT detectors, filled triangles – full ID measurement. The difference between simulations and the full ID measurement indicates the remaining misalignment

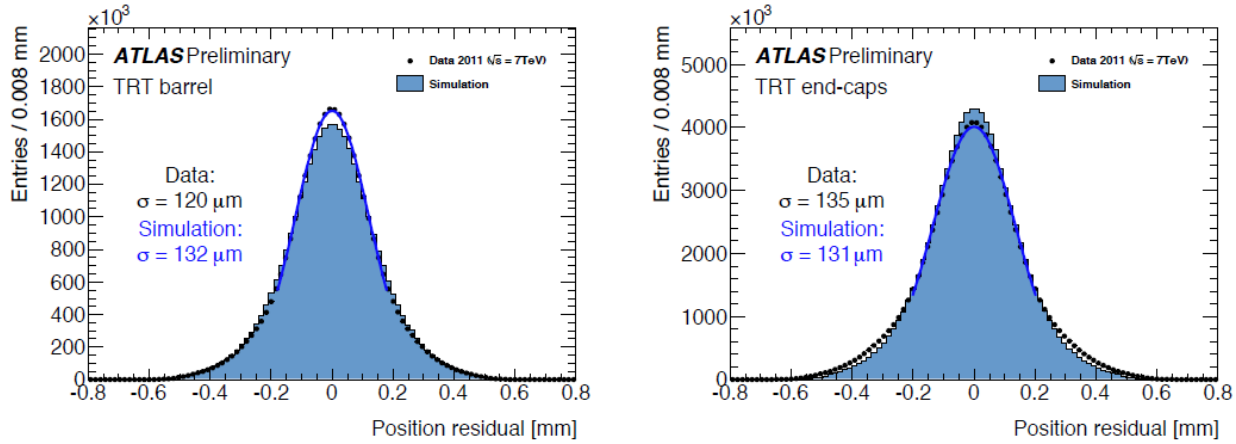

Fig. 3. Single straw spatial resolution after the latest alignment for the TRT barrel (left) and the TRT end-caps (right) obtained with 2011 proton-proton collision data (points) and with simulations (filled histograms)

In addition to its tracking capabilities, the TRT provides discrimination between electrons and pions over the energy range between 1 and 200 GeV by utilizing transition radiation. Transition radiation is emitted when a highly relativistic charged particle with the Lorentz factor $\gamma = E/m \sim 10^3$ traverses boundaries between materials of different dielectric constants. The TR photons (soft *X*-rays) emitted in the radiator are absorbed in the gas inside straw tubes, which serve as detecting elements both for tracking and for particle identification.

In Fig. 4, the TR photon observation probability depending on the charged particle Lorentz factor ("turn-on" curve) is presented. A pure sample of electrons with high values of γ (above γ = 1000) is obtained from the data using photon conversions. For low values of γ, all selected tracks in the event are used with an assumption that these particles are pions. As expected, the probability of a high threshold hit increases for particles with the Lorentz factor above 1000, which enables the TRT to separate electrons from pions over a momentum range between 1 GeV/*c* and 200 GeV/*c*. It is seen that the onset of TR from the lower plateau (corresponding to the probability of producing high-energy delta-rays) and the upper plateau (corresponding to saturation of the transition radiation production in the geometry chosen for the TRT radiators foils and straw tubes) in the end-cap is steeper than that for the barrel. Small difference between TRT barrel and end-

cups is expected because of different radiator materials used for the barrel (irregularly spaced fibers) and end-caps (regularly spaced foils).

The results agree with those obtained in the minimum bias Monte Carlo simulations for almost all values of the Lorentz factor and provide the TRT detector with an excellent starting point to study and optimize its particle identification properties. The simulation of the transition radiation has so far been tuned on the data collected with the barrel modules only in 2004 on a test beam set-up and can now be improved by using new results from collision data.

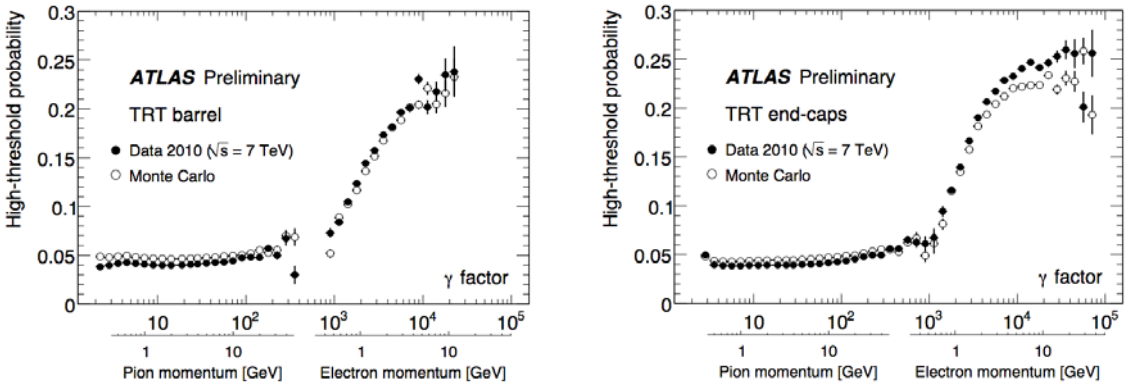

Fig. 4. The probability of a TRT high-threshold hit in the TRT barrel (left) and TRT end-caps (right) as a function of the Lorentz factor γ for the TRT barrel and end-cap regions, as measured in 7 TeV collision events

Another way to distinguish between different types of particles can be based on dE/dx measurements. Though the TRT detector was not designed for this purpose and not equipped with amplitude measuring electronics, discriminators based on TRT timing information can be used for a particle identification since the measured Time over Threshold (ToT) is correlated with the ionization deposit within the straws. For the purpose of dE/dx measurements, the ToT is defined as the number of bits above the threshold in the largest single group of bits above the threshold. Figure 5 shows the ToT distributions for electron and pion candidates (left) and the track-averaged ToT distribution, as a function of the track momenta (right).

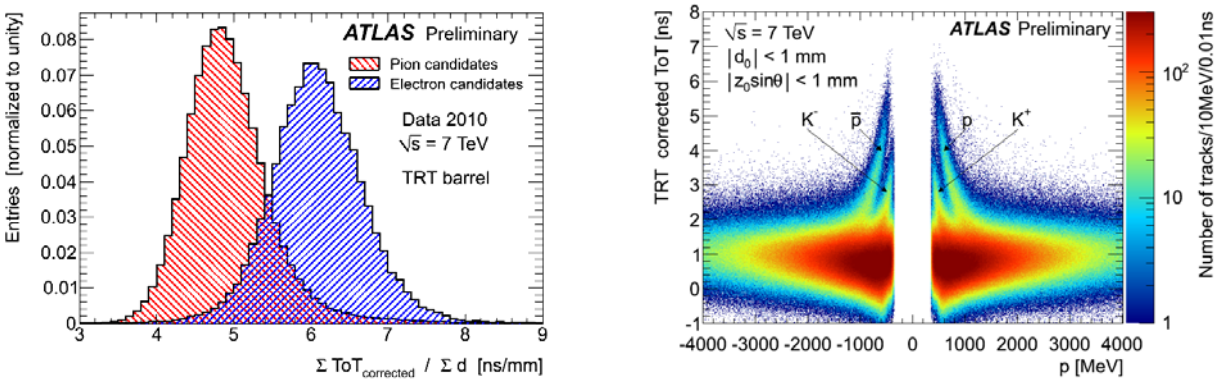

Fig. 5. The average Time over Threshold (ToT corrected), divided by the average transverse track path length inside the straw (left) and the track-averaged ToT distribution, as a function of the track momenta (right)

To compare the performance in collision data with the expected performance reported in the ATLAS Technical Design Report [5], the performance of a selection criterion that gives 90 % electron efficiency is used as a reference. A criterion that gives a 90 % electron efficiency was determined in different momentum bins and applied to the pion sample to determine the efficiency for pions to pass the same criterion. Figure 6 shows the pion misidentification probability $p_{\pi\to e}$ at 90 % electron efficiency as a function of the momentum. The uncertainties were estimated by varying the selection criteria in such a way that the electron efficiency changed by ± 2 %. It should be noted that any contamination of the pion sample with electrons above

the TR threshold will systematically bias the estimate of $p_{\pi\to e}$ by roughly the same amount. As seen in Fig. 6, the ToT-based selection improves the pion rejection at $p < 10$ GeV/c [6].

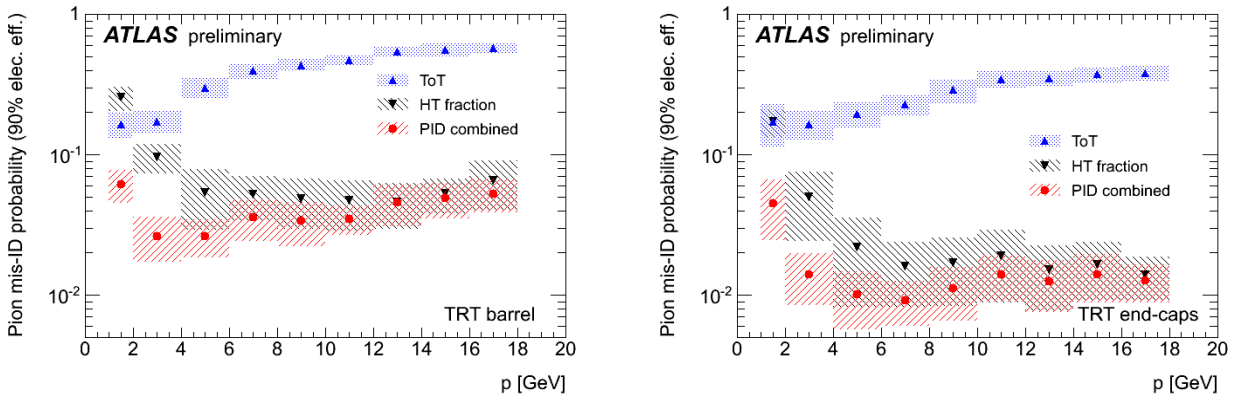

Fig. 6. The pion misidentification probability for a selection criteria that gives 90 % electron efficiency as a function of the momentum for the barrel (left) and end-cap (right) region of the detector

3. Physics results

Figure 7 (left) shows the integrated luminosities recorded by the ATLAS detector during Run I (2010–2012 years data taking periods). In total, ATLAS has recorded data corresponding to about 25 fb^{-1}. ATLAS data taking efficiency was about 94 %. The instantaneous luminosity delivered by the LHC accelerator was increased from $0.5 \cdot 10^{33}\,\mathrm{cm^{-2}s^{-1}}$ in 2010 up to $7.7 \cdot 10^{33}\,\mathrm{cm^{-2}s^{-1}}$ in 2012. It is close to initial design luminosity $10^{34}\,\mathrm{cm^{-2}s^{-1}}$. The average number of interactions per crossing (pile-up) dramatically increases with the luminosity, and it goes rapidly from average 5–7 interaction in 2011 data to 20–25 in 2012 data, as it is shown in Fig. 7 (right). Despite the fact that the ATLAS detector has been nominally designed for lower pile-up (~ 22), the detector performance remained excellent in high pile-up conditions (> 30).

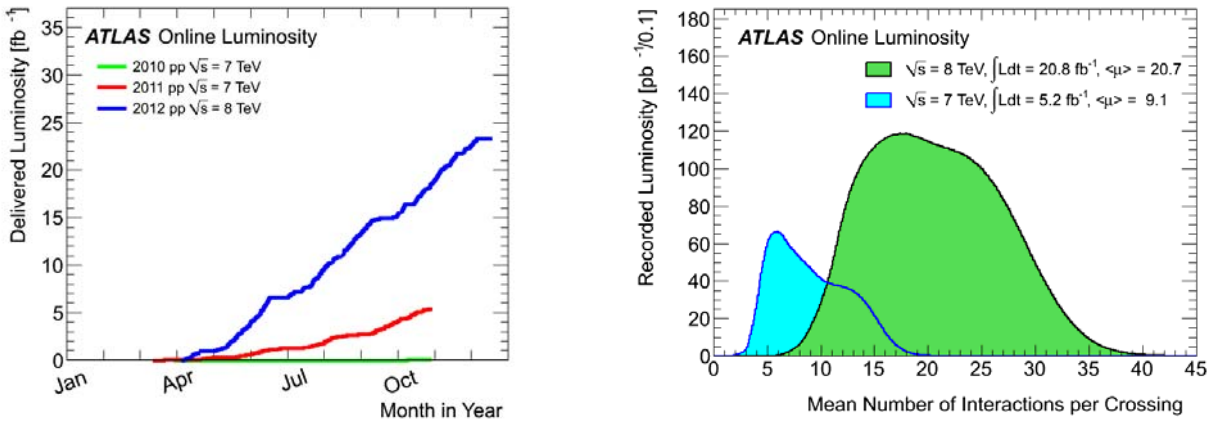

Fig. 7. Integrated luminosity delivered in the ATLAS experiment as a function of time during 2012 (blue), 2011 (red) and 2010 (green) data taking periods (left). The luminosity-weighted distribution of the mean number of interactions per crossing (pile-up) for the 2011 and 2012 data (right)

Using data recorded during Run I, ATLAS has performed a wide range of physics analyses. The major ATLAS result is the discovery of a Higgs-like boson, which is compatible with the Standard Model (SM) Higgs Boson. Unfortunately, no new physics beyond the SM (SUSY, new heavy bosons, *etc*.) has been observed despite great efforts to find it. The predictions of the Standard Model stand firm!

3.1. Discovery of the Higgs boson

The Higgs boson is the only particle of the Standard Model that was not observed previously. During the summer of 2012, both the ATLAS and CMS Collaborations have reported the observation of a Higgs-like particle with a mass of approximately 125 GeV [7, 8]. Note that the electroweak theory does not predict directly the Higgs mass.

SM Higgs analyses with the ATLAS detector were performed for various possible decay modes. The observation of a new boson is well established in the two-photon channel [9], in the four-lepton decay channel [10], as well as in the *WW* channel [11]. Invariant mass distributions for $H \to \gamma\gamma$ and $H \to ZZ \to 4l$ are shown in Fig. 8.

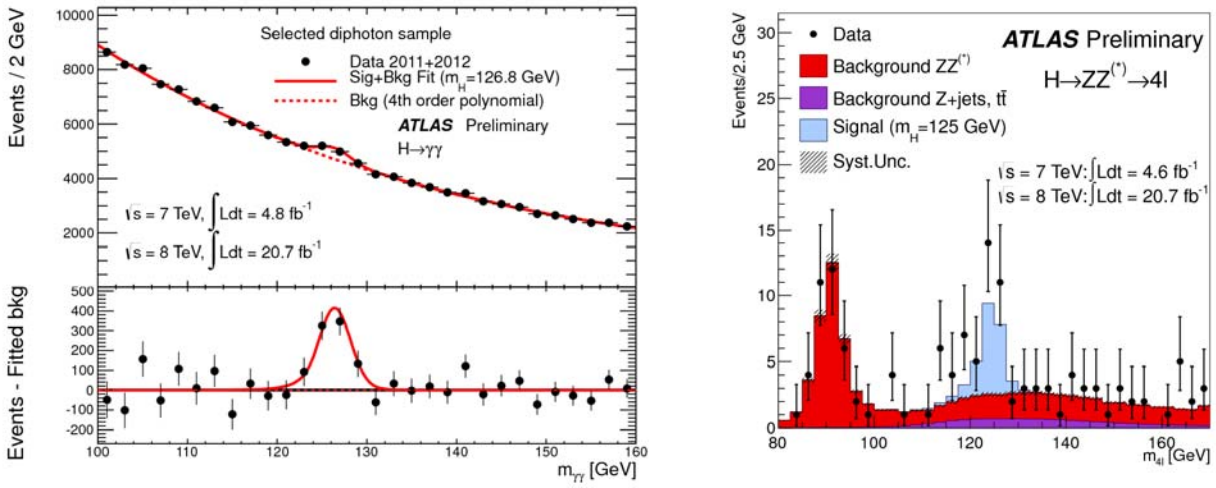

Fig. 8. Invariant mass distribution of diphoton candidates (left) for the combined √s = 7 TeV and √s = 8 TeV data samples. The result of a fit to the data of the sum of a signal component fixed to m_H = 126.8 GeV and a background component described by a fourth-order Bernstein polynomial is superimposed**.** The distribution of the four-lepton invariant mass (right), for the selected candidates in the four-lepton channel compared to the background expectation for the combined √s = 8 TeV and √s = 7 TeV datasets. The signal expectation for the m_H = 125 GeV hypothesis is also shown (right)

In the $H \to \gamma\gamma$ decay channel, an excess of events is observed with a local significance of 7σ. The measured mass of the boson is 126.8 ± 0.2 (stat) ± 0.7 (syst) GeV. The signal strength (the ratio of the observed cross section to the expected SM cross section) is $1.65\ ^{+0.24}_{-0.24}$ (stat) $^{+0.25}_{-0.18}$ (syst) for m_H = 126.8 GeV, which corresponds to a 2.3σ deviation from the SM prediction. The diphoton invariant mass and the angular distribution of the photons in the resonance rest frame are used to separate the signal and background, and to distinguish between the tested spin hypotheses. The data are in good agreement with the spin-0 hypothesis. The hypothesis of a spin-2 particle produced by gluon fusion is excluded at 99% CL, which corresponds to the expected exclusion.

A clear excess of events over the background is observed with the local significance of 6.6 σ in the $H \to ZZ \to 4l$ decay channel, corresponding to a background fluctuation probability of $2.7 \cdot 10^{-11}$. The mass of the Higgs-like boson is measured to be $m_H = 124.3\ ^{+0.6}_{-0.5}$ (stat) $^{+0.5}_{-0.3}$ (syst) GeV, and the signal strength at this mass is found to be $1.7\ ^{+0.5}_{-0.4}$. A spin-parity analysis is performed using the events with the reconstructed four-lepton invariant mass satisfying 115 GeV < m_{4l} < 130 GeV. The Higgs-like boson is found to be compatible with the SM expectation of 0^+ when compared pair-wise with 0^-, 1^+, 1^-, 2^+, and 2^-. The 0^- and 1^+ states are excluded at the 97.8 % confidence level or higher using CL's in favour of 0^+.

The combined measurement [12] of the global signal strength (see Fig. 9, left) for the final states $H \to \gamma\gamma$, $H \to ZZ^* \to 4l$, $H \to WW^* \to l\nu l\nu$, $H \to bb$, and $H \to \tau\tau$ results in a value of 1.30 ± 0.13 (stat) ± 0.14 (syst) obtained at the mass of 125.5 GeV. The couplings determination of the Higgs-like boson for the three most sensitive channels is shown in Fig. 9 (right).

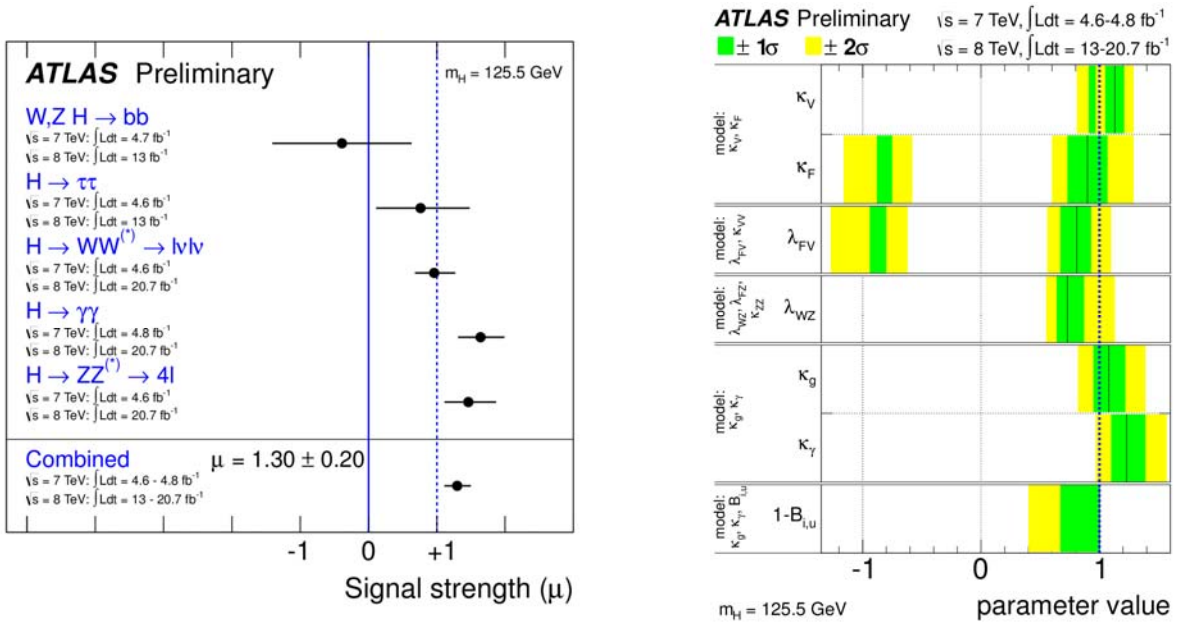

Fig. 9. Measurements of the signal strength parameter (left) at m_{H} = 125.5 GeV for the individual channels and for their combination (left). Summary of the coupling scale factor measurements (right). The best-fit values are represented by the solid vertical line

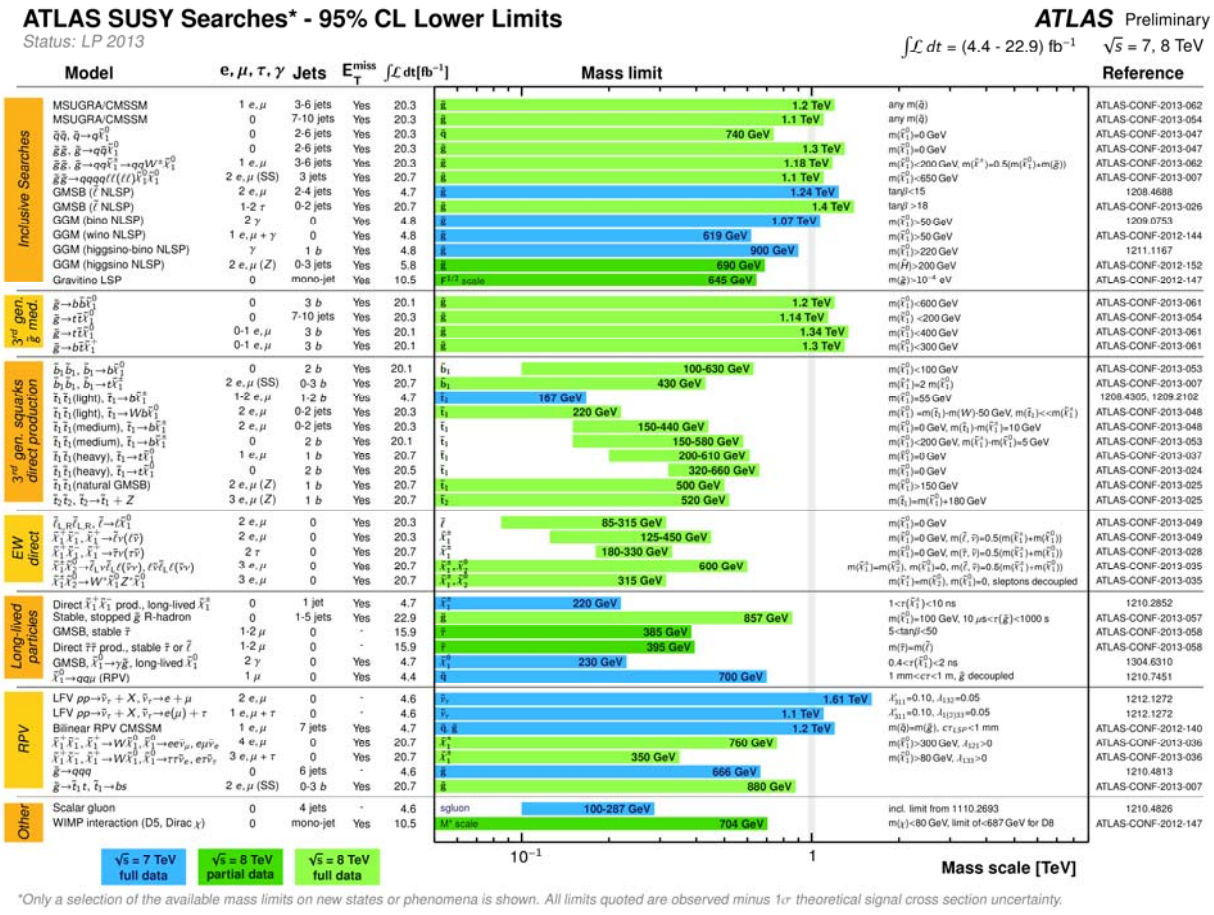

Fig. 10. Mass reach of the ATLAS searches for the Supersymmetry. Only a representative selection of the available results is shown

3.2. SUSY searches

The SUperSYmmetry (SUSY) is one of the most promising theories beyond the Standard Model, proposing solutions for some of the most important open questions of the SM, such as the hierarchy problem and unification of the gauge couplings. It also provides a natural cancellation of corrections to the Higgs mass. In addition, this theory provides suitable Dark Matter candidates compatible with astrophysics and astro-particle physics observations such as the WMAP3 measurements of the cosmic microwave background. For these reasons, the search for the SUSY is one the most important goals of the ATLAS experiment with about 50 different analyses performed in 2011–2012. In the absence of any evidence of the signal, they provide new exclusion limits for various models, such as the minimal SUperGRAvity (mSUGRA), the Gauge-Mediated Supersymmetry Breaking (GMSB), the phenomenological minimal Supersymmetric Standard Model, and others. A summary of the mass limits obtained in the ATLAS SUSY searches is presented in Fig. 10.

3.3. Search of heavy gauge and excited bosons

Although the Standard Model (SM) of strong and electroweak interactions is remarkably consistent with particle physics observations to date, the high-energy collisions at the CERN LHC provide new opportunities to search for physics beyond it. New heavy spin-1 gauge bosons are predicted by many extensions of the SM. They are generically called Z' and W' bosons. The Z' bosons are associated with additional U(1)′ gauge symmetries and W' bosons arise in models with an extra SU(2) gauge [13].

In addition to the gauge bosons, another type of spin-1 bosons may exist, which have only a Pauli-like anomalous coupling to fermions instead of the gauge one. This model was proposed by JINR theorists [14]. The anomalous couplings mix both left-handed and right-handed fermions, and therefore these bosons carry a nonzero chiral charge. The associated gauge bosons are labeled as Z^* and W^*. As these bosons are coupled to the tensor quark currents, they can be considered as excited states, and therefore they are also called excited bosons.

PNPI physicists participate in searches of heavy gauge and excited boson, playing a key role in an analysis of decays into the final state with an electron, *i.e.* $Z'/Z^* \to e^+e^-$ and $W'/W^* \to e\nu$. The results presented here use the full data sample recorded by ATLAS in 2011, corresponding to a total integrated luminosity of ~ 5.0 fb^{-1}.

The event selection and the lepton identification for the process $Z'/Z^* \to \ell\ell$ are discussed in detail in [15]. Figure 11 shows the invariant mass distribution for the dielectron and dimuon final states after final selections. The expected Z^* signal for three mass hypotheses is shown in Fig. 11. The dilepton invariant mass distributions are well described by the SM. For both channels, the dominant and irreducible background is due to the Z/γ^* (Drell – Yan) process, characterized by the same final state as the signal. Small contributions from $t\bar{t}$ and diboson (WW, WZ and ZZ) production are also present in both channels. Semileptonic decays of b and c quarks into the e^+e^- and $\mu^+\mu^-$ pairs, plus a mixture of photon conversions and hadrons faking electrons in the e^+e^- sample, are backgrounds that are referred to as the QCD background. Jets accompanying W bosons (W + jets) may similarly produce dilepton candidates. The expected signal and backgrounds, with the exception of those from QCD and W^+ jets, are evaluated with simulated samples and are rescaled using the most precise available cross section predictions. The total SM prediction is then normalized to the data in an invariant mass interval around the Z peak (70–110 GeV/c^2). In the electron channel, the rescaling is done after adding the QCD multijet and W + jets backgrounds evaluated directly from the data.

In the absence of a signal, the upper limits on the number of events produced by the decay of a new resonance are determined at the 95% CL. Figure 12 (left) shows the 95% CL for the observed and expected exclusion limits on the combination of the electron and muon channels for Z'_{SSM} and for the lowest and highest value of σB (cross section multiplied by the branching ratio) of the E_6-motivated Z' models. The rising of the σB limit at very high masses is due to a slight acceptance decrease: contrary to the acceptance as a function of the dilepton masses, which tends to increase at high mass, the acceptance as a function of the

pole mass slightly decreases due to a faster fall of the parton luminosity at very high masses, which distorts the Breit – Wigner resonance shape and enhances the relative contribution of low-mass signal events. The right plot in Fig. 12 shows the 95% CL for the observed and expected exclusion limits on $\sigma B(Z^* \to \ell^+\ell^-)$, as well as the value of σB expected from theory. The parameters of the model are fixed by requiring that the total and partial decay widths of W^*, the charged partner of Z^*, should be the same as those of the W'_{SSM} boson with the same mass. As a result, the corresponding 95% CL limits on the mass of the dilepton resonance was set at 2.22 TeV/c^2 for the Z'_{SSM} model and 2.20 TeV/c^2 for the Z^* model. Figure 13 displays the difference between the data and the expectation for both electron and muon channels. Local significance nowhere exceeds two standard deviations. The data are consistent with the SM prediction in this search.

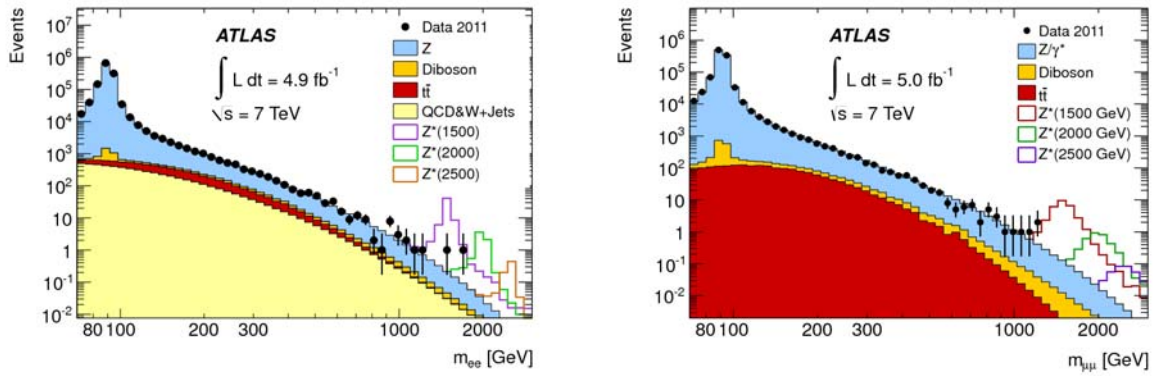

Fig. 11. The dielectron (left) and dimuon (right) invariant mass ($m_{\ell\ell}$) distribution after final selections, compared to the stacked sum of all expected backgrounds, with three example Z^* signals overlaid. The bin width is constant in log($m_{\ell\ell}$)

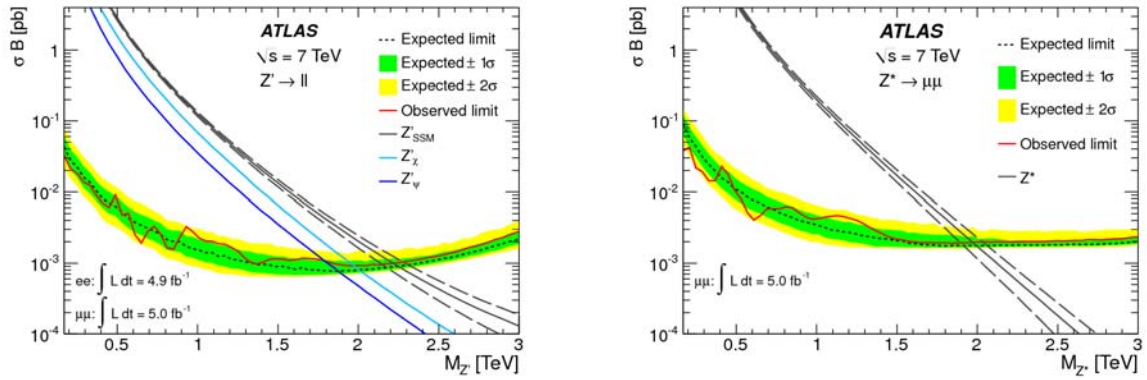

Fig. 12. Expected and observed 95% CL limits on the cross section multiplied by the branching ratio (σB) and the expected value of σB for Z'_{SSM} production and the two E_6-motivated Z' models with the lowest and highest σB for the combination of the dielectron and dimuon channels (left) and for Z^* boson production for the combination of dielectron and dimuon channels (right). The dashed lines around the Z^* and around the Z'_{SSM} theory curve represent theoretical uncertainties

A search is also performed for the charged partners of Z'/Z^*, denoted as W' and W^*. The event selection and the lepton identification are described in detail in [16]. The same reconstruction and event selection are applied to the data and the simulated samples. Figure 14 shows the m_{T} spectra for events with $m_{\mathrm{T}} > 200$ GeV/c^2 in each channel after the event selection. The data, the expected background, and three examples of W' signals at different masses are shown. The main background to the $W'/W^* \to l\nu$ signal comes from the high-m_{T} tail of the SM W boson decay to the same final state. Other backgrounds are Z bosons decaying into two leptons where one lepton is not reconstructed, W or Z decaying to τ-leptons where a τ subsequently decays to an electron or muon, and diboson production. These are collectively referred to as the electroweak background. In addition, there is a background contribution from $t\bar{t}$ and single-top production which is most important for the lowest W'/W^* masses considered here, where it constitutes about 15 % of the background after the event selection. Other strong-interaction background sources, where a light or heavy

hadron decays semileptonically or a jet is misidentified as an electron or muon, are estimated from the data to be 10 % at most of the total background in the electron channel and a negligible fraction in the muon channel. These are called QCD background.

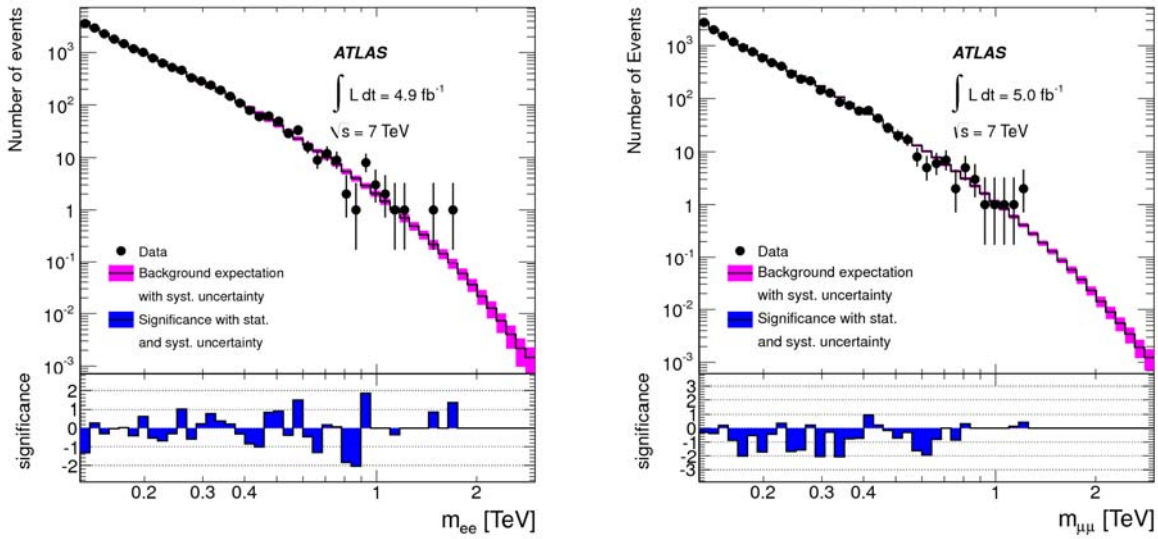

Fig. 13. Differences between data and expectation in the electron (left) and muon (right) channels. The mass range goes from 128 GeV/c^2 to 3 TeV/c^2. Both statistical and systematic uncertainties have been taken into account

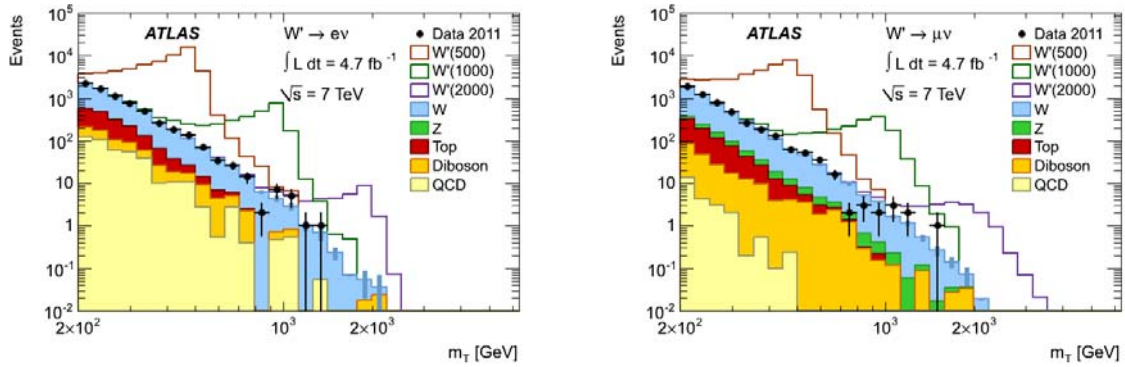

Fig. 14. Spectra of m_T for the electron (left) and muon (right) channels for events with $m_T > 200$ GeV/c^2 after event selection. The points represent the data, and the filled histograms show the stacked backgrounds. Open histograms for W'/ $W^* \rightarrow l\nu$ signals added to the background with masses in GeV are indicated in parentheses in the legend. The QCD backgrounds estimated from the data are also shown. The signal and other background samples are normalized using the integrated luminosity of the data and the NNLO cross sections

The σB limits are evaluated independently for both W' and W^*. The observed number of events N_{obs} is the count after the final selection including the requirement $m_T > m_T^{min}$, with the thresholds chosen separately for each of the masses and decay channels to maximize the sensitivity. None of the observations for any mass in either channel or their combination has a significance above three standard deviations, so there is no evidence for the observation of $W' \rightarrow l\nu$ or $W^* \rightarrow l\nu$ decays. Figure 15 presents the 95% CL observed for the combined limits on σB for both $W' \rightarrow l\nu$ and $W^* \rightarrow l\nu$. A W' boson with the Sequential SM couplings is excluded at the 95 % credibility level for masses up to 2.55 TeV/c^2. Excited chiral bosons (W^*) with the equivalent coupling strength are excluded for masses up to 2.42 TeV/c^2.

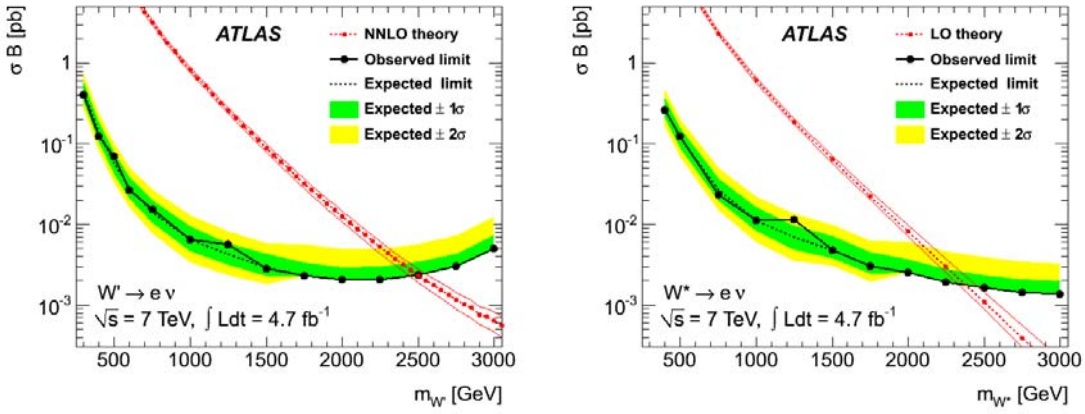

Fig. 15. Expected and observed combined limits on σB for $W' \to l\nu$ (left) and $W^* \to l\nu$ (right) obtained by assuming the same branching fraction for both channels. The NNLO calculated cross section and its uncertainty are also shown

3.4. Observation of inclusive electrons

A precise measurement of inclusive electrons production at the LHC could lead to quantitative comparisons with theory for the production of charm and beauty hadrons. It is also required to understand the basic processes which will be the main sources of backgrounds to measurements and searches involving one electron with high transverse energy E_T in the final state, in particular the observation and early measurements of $W \to e\nu$ decays and, at a somewhat later stage, of semileptonic decays of top quarks and possible signals from decays of supersymmetric particles.

PNPI physicists participate in developing and validation of electron reconstruction and identification algorithms. These algorithms are designed to achieve both a large background rejection and a high and uniform efficiency for isolated electrons over the full acceptance of the detector, for transverse energies above 20 GeV. These electrons need to be separated from hadrons in QCD jets and from secondary electrons originating mostly from photon conversions in the tracker material. The baseline electron identification algorithm in ATLAS relies on variables which deliver good separation between isolated electrons and fake signatures from QCD jets. These variables include information from the calorimeter, the tracker, and matching between the tracker and the calorimeter. The TRT detector built at PNPI as a part of the ATLAS tracker provides a substantial discriminating power between electrons and pions over a wide energy range between 0.5 and 100 GeV.

Based on an integrated luminosity of 13.8 nb^{-1} obtained with stable beams and very loose electron trigger requirements, the properties of a total of 67124 electron candidates with $E_T > 7$ GeV and $|\eta| < 2.0$ passing an optimized set of identification cuts was studied [17]. The preselection requires that the electron candidates lie within the pseudorapidity coverage of the TRT, $|\eta| < 2.0$, and outside the transition region between the barrel and end-cap calorimeters, $1.37 < |\eta| < 1.52$. Only reconstructed electron candidates with a raw cluster transverse energy above 4 GeV and a calibrated offline cluster transverse energy above 7 GeV are considered. This choice is the result of a balance between the high statistics required for the analysis and the requirement of a high and uniform trigger efficiency. The preselected electrons are also required to be associated to tracks containing at least ten TRT hits and four hits in the Pixel and SCT detectors. Preselected electron candidates were selected further using the medium identification criteria, which consist of requirements on their energy deposits in the strip layer of the ElectroMagnetic (EM) calorimeter and on the track quality and the track-cluster matching. Figure 16 displays the transverse energy and pseudorapidity spectra for these electron candidates. The prompt electrons comprise mostly non-isolated electrons from the charm and beauty hadron decay in this low-energy range, and only a very small fraction of them is expected to be isolated electrons from W/Z-boson decay. The distributions were compared between the data and simulations. The Monte Carlo distributions are normalized to the same number of electron candidates passing the medium identification criteria as in the data. The transverse energy and pseudorapidity spectra of the signal are in agreement in shape between the data and predictions from leading-order parton shower

Monte Carlo simulations (Fig. 16). The breakdown of electron candidates in the Monte Carlo simulation according to their origin is the following: 69.6 ± 0.1 % hadrons, 20.2 ± 0.2 % secondary electrons (conversions), and 10.1 ± 0.1 % prompt electrons.

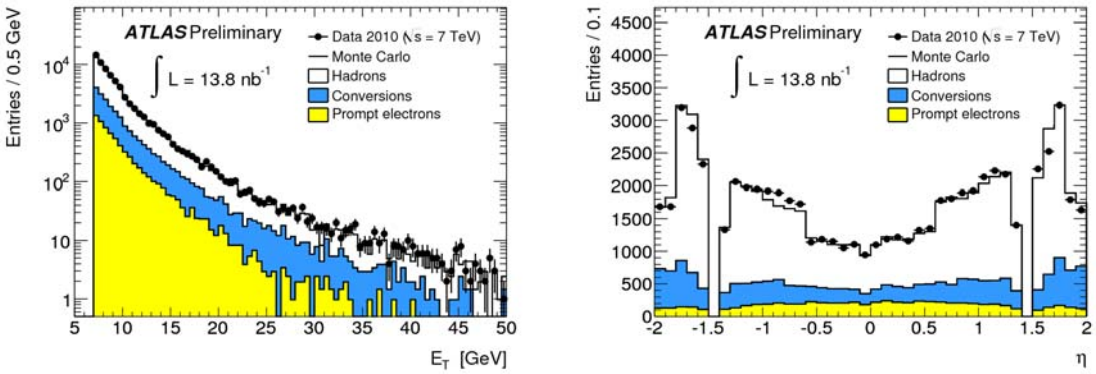

Fig. 16. Distributions of cluster transverse energy E_T (left), and pseudorapidity η (right), for electron candidates passing the medium identification cuts

A signal of 9920 ± 160 (stat.) ± 990 (syst.) electrons, predominantly from heavy flavour production, is measured within this sample. Further analysis is required to extract differential cross-sections for production of electrons from heavy flavour at the LHC.

3.5 Bose – Einstein correlation parameters from the ATLAS experiment

One of the ways to study the space-time picture of hadronic interaction is to measure correlations between two identical particles which momenta are close to each other – the so called Bose – Einstein Correlations (BEC). The general definition of a correlation function for two variables p_1 and p_2 can be written as

$$C_2(p_1, p_2) = \frac{P(p_1, p_2)}{P_{ref}(p_1, p_2)},$$

where $P(p_1, p_2)$ is the probability to observe particles with the momenta p_1 and p_2. The proximity in the phase space between final state particles with 4-momenta p_1 and p_2 can be quantified by $Q^2 = (p_1 - p_2)^2$. The BEC effect is observed as an enhancement at low Q values, $Q \sim 300$ MeV. To extract the effect one can compare the measured Q-spectra with the reference ones without BEC. Then the ratio

$$R(Q) = \frac{\frac{dN}{dQ} - \frac{dN_{ref}}{dQ}}{\frac{dN_{ref}}{dQ}}$$

can be fitted with an appropriate formula $R(Q) = F(rQ) + a + bQ$. Here, $F(rQ)$ is the Fourier transform of the spatial distribution of the emission region with an effective size $< r >$. The function $F(rQ)$ can be parameterized as a linear exponent $F(rQ) = C \cdot \exp(-r_e Q)$ or a Gaussian $F(rQ) = C \cdot \exp(-r_g^2 Q^2)$. For the same value of $< r >$, there is quite a simple relation between these two cases: $r_e = \pi^{1/2} r_g$.

ATLAS has collected large event samples of multi-particles production at low intensity LHC runs with beam energies 2.76 and 7 TeV. The number of collisions was ~ 1 per beam crossing. Under such conditions it is possible to make precise measurements of QCD processes. The size of the particle radiation zone was determined from the observed Bose – Einstein correlation (Fig. 17). As it was predicted by Gribov – Regge theory, the interaction radius is slowly rising with the energy. At the same time, the size of the radiation zone at moderate multiplicities depends only from the multiplicity, and its rise with the energy is connected with the multiplicity increase. Such a rise should be limited because of a finite radius of the colliding particles. In

the runs with the beam energy 2.76 TeV, a special trigger was implemented to collect events with high multiplicities in the final state. It occurs that the radius rise is saturated indeed at high multiplicities and this saturation happens at a higher value of the multiplicity as soon as the beam energy increases. Such an effect has been observed for the first time in the ATLAS data.

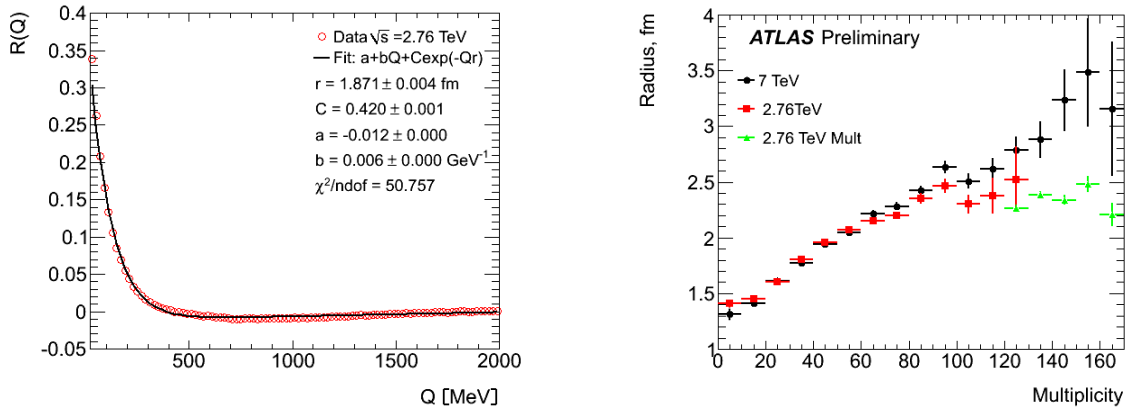

Fig. 17. Bose – Einstein correlation parameters from the ATLAS experiments. The measured value of $R(Q)$ for 2.76 TeV data (left). The radiation zone radius $r = < r >$ as a function of the multiplicity (right). The data obtained with a special trigger to collect high multiplicity events at the beam energy 2.76 TeV are shown in green colour

4. Summary

The ATLAS experiment successfully operated during Run I (2010–2012). The ATLAS detector was working well with a high data taking efficiency ~ 97 %. A number of physics results have been obtained these years, which have been published in about 240 papers and many more in the pipeline. Only a part of the collected data has been analysed. The data analysis will be continued till the new start-up of the LHC in 2015.

The discovery of a Higgs boson with the mass of ~ 125 GeV was a great result for the more than 20 years old LHC project. Now we should answer the question – is this the Minimal Standard Model Higgs? Answering this question will take time and will require to measure more precisely as many characteristics of the Higgs boson as possible. With the Higgs mass known, the MSM couplings can now be calculated and compared with the experimental results. The SUSY theory is also affected by the Higgs discovery. The measured value of the Higgs mass at the LHC may give indirect evidence for the existence of different SUSY scenarios. With the new LHC physics run in 2015, there will be another round of searches for SUSY and other "new physics".

According to the plans, the LHC and the ATLAS detector in 2018 will undergo the Phase-1 upgrade to the full energy (14 TeV) and to the design luminosity – 2×10^{34} $s^{-1}cm^{-2}$ with 25 ns bunch spacing. In the physics run which will follow, ATLAS will record about 350 fb^{-1} of data. It has been estimated that with ~ 300 fb^{-1} of data, the spin-parity of Higgs will be known to ~ 5 σ level, and the ratios of couplings will be known to within 30–50 %. PNPI will take an active part in this upgrade program.

There is a possibility that with an increase of the *pp* collision energy from 8 TeV to 13 TeV in 2015, we will cross a threshold above which we will observe new particles, too heavy to have been observed so far. This would be really interesting.

References

1. ATLAS Collaboration, G. Aad *et al.*, *The ATLAS Experiment at the CERN Large Hadron Collider*, JINST **3**, S08003 (2008).
2. ATLAS Collaboration, G. Aad *et al.*, *Atlas Inner Detector Technical Design Report*. **1**, ATLAS TDR **4**, CERN-LHCC-97-16, CERN (1997).
3. ATLAS Collaboration, G. Aad *et al.*, *The ATLAS Inner Detector Commissioning and Calibration*, Eur. Phys. J. C **70**, 787 (2010).
4. ATLAS Collaboration, G. Aad *et al.*, *Alignment of the ATLAS Inner Detector Tracking System with 2010 LHC Proton-Proton Collisions at* $\sqrt{s}$ *= 7 TeV*, ATLAS-CONF-2011-012, CERN (2011).
5. ATLAS Collaboration, G. Aad *et al.*, *ATLAS Detector and Physics Performance*: Technical Design Report, **1**, ATLAS Note CERN-LHCC-99-014.
6. ATLAS Collaboration, G. Aad *et al.*, *Particle Identification Performance of the ATLAS Transition Radiation Tracker*, ATLAS-CONF-2011-128, CERN (2011).
7. ATLAS Collaboration, G. Aad *et al.*, *Observation of a New Particle in the Search for the Standard Model Higgs Boson with the ATLAS Detector at the LHC*, Phys. Lett. B **716**, 1 (2012).
8. CMS Collaboration, S. Chatrchyan *et al.*, *Observation of a New Boson at a Mass of 125 GeV with the CMS Experiment at the LHC*, Phys. Lett. B **716**, 1 (2012).
9. ATLAS Collaboration, G. Aad *et al.*, *Measurements of the Properties of the Higgs-Like Boson in the Two Photon Decay Channel with the ATLAS Detector Using 25* fb^{-1} *of Proton-Proton Collision Data*, ATLAS-CONF-2013-012, CERN (2013).
10. ATLAS Collaboration, G. Aad *et al.*, *Measurements of the Properties of the Higgs-Like Boson in the Four Lepton Decay Channel with the ATLAS Detector Using 25* fb^{-1} *of Proton-Proton Collision Data*, ATLAS-CONF-2013-013, CERN (2013).
11. ATLAS Collaboration, G. Aad *et al., Measurements of the Properties of the Higgs-Like Boson in the* $WW^{(*)} \rightarrow \ell\nu\ell\nu$ *Decay Channel with the ATLAS Detector Using 25* fb^{-1} *of Proton-Proton Collision Data*, ATLAS-CONF-2013-030, CERN (2013).
12. ATLAS Collaboration, G. Aad *et al., Combined Coupling Measurements of the Higgs-Like Boson with the ATLAS Detector Using up to 25* fb^{-1} *of Proton-Proton Collision Data*, ATLAS-CONF-2013-034, CERN (2013).
13. D. London and J. L. Rosner, *Extra Gauge Bosons in E(6)*, Phys. Rev. D **34**, 1530 (1986).
14. M. Chizhov, V. Bednyakov, and J. Budagov, *Proposal for Chiral-Boson Search at LHC via Their Unique New Signature*, Phys. At. Nucl. **71**, 2096 (2008).
15. ATLAS Collaboration, G. Aad *et al.*, *Search for High-Mass Resonances Decaying to Dilepton Final states in pp Collisions at sqrt(s) = 7 TeV with the ATLAS Detector*, arXiv:1209.2535.
16. ATLAS Collaboration, G. Aad *et al.*, *ATLAS Search for a Heavy Gauge Boson Decaying to a Charged Lepton and a Neutrino in pp Collisions at* $\sqrt{s}$ *= 7 TeV*, arXiv:1209.4446.
17. ATLAS Collaboration, G. Aad *et al.*, *Observation of Inclusive Electrons in the ATLAS Experiment at* $\sqrt{s}$ *= 7 TeV*, ATLAS-CONF-2010-073.

EXPERIMENT LHCb AT THE LHC

A.A. Vorobyev, G.D. Alkhazov, B.V. Bochin, N.F. Bondar, S.V. Bondarev, V.L. Golovtsov, S.A. Guets, A.A. Dzyuba, N.B. Isaev, A.P. Kashchuk, O.E. Maev, P.V. Neustroev, N.R. Sagidova, Yu.A. Shcheglov, E.M. Spiridenkov, S.S. Volkov, An.A. Vorobyev

1. Introduction

The main physics goals of the LHCb experiment at the Large Hadron Collider (LHC) at CERN are studies of CP violation effects in various decays of *B* and *D* mesons and also searches for rare *B* decays suppressed in the Standard Model (SM). The PNPI group made important contributions to the design of the LHCb detector and especially to the design and construction of the LHCb Muon system, as it was described in the previous PNPI HEPD report for 2002–2006.

Below we describe shortly the performance of the LHCb Muon system and present some of the LHCb results from experimental data collected in 2010–2012, including the results of studies of the $B_s^0 \to \mu^+\mu^-$ decay, where the PNPI group took an active part.

2. Present status of the LHCb Muon system

Muon triggering is a major part of the LHCb lowest level trigger providing fast information on high transverse momentum muons. Prompt and accurate muon identification is an important part of the high level trigger and a strong requirement for most of branches in the off-line analysis. Muons are present in final states of many CP-sensitive *B* decays. Also, they play a major role in CP asymmetry and oscillation measurements since muons from semi-leptonic *b* decays provide a tag of the initial state flavour of the accompanying neutral *B* mesons. In addition, a study of rare *B* decays, such as the flavour-changing neutral current decay $B_s^0 \to \mu^+\mu^-$, may reveal new physics beyond the SM.

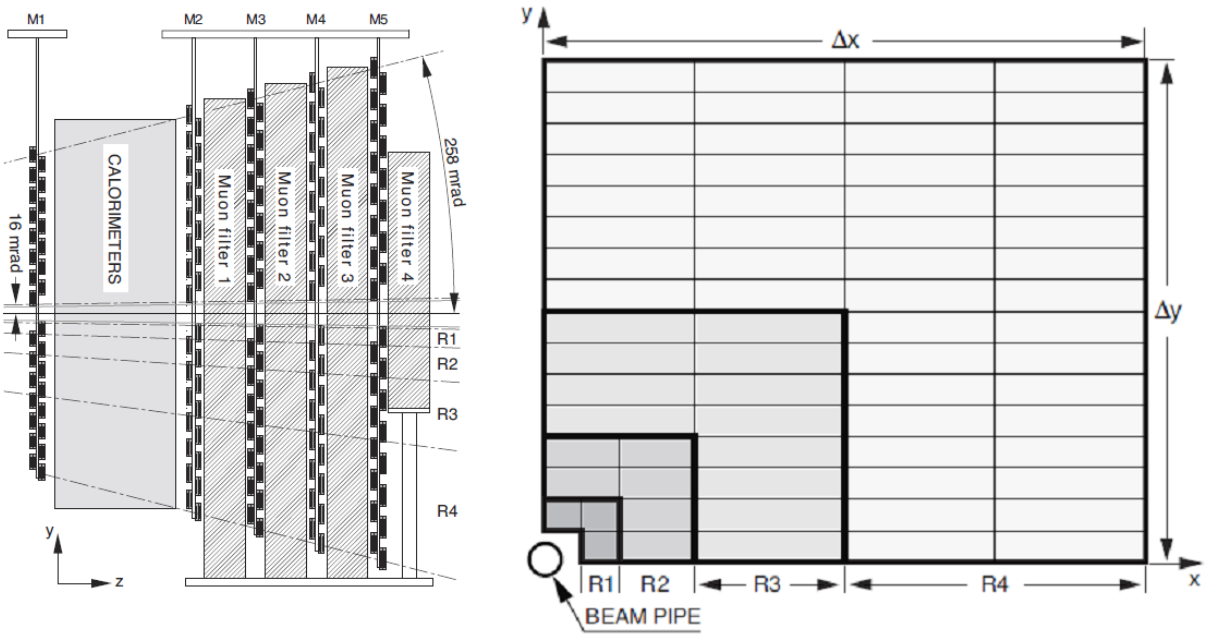

Fig. 1. Side view of the muon system (left). Front view of a quadrant of a muon station (right). Each rectangle represents one chamber. Each station contains 276 chambers

The muon system [1], shown in Fig. 1, consists of five stations M1–M5 of rectangular shape, placed along the beam axis. Each Muon station is subdivided into four regions, R1 to R4, with increasing distance from the beam axis. The linear dimensions of regions R1, R2, R3, R4 and their segmentations scale in the ratio 1 : 2 : 4 : 8. With this geometry, the particle flux and channel occupancy are expected to be roughly the same over the four regions of a given station. The full muon system comprises 12 GEMs (region M1R1) and 1368 four-gaps (two-gaps in M1) Multi-Wire Proportional Chambers (MWPCs), and it covers a total area of 435 m^2.

PNPI has constructed 660 MWPCs for region R4 in stations M2–M4. The sensitive areas of these chambers range from 120 × 25 cm^2 (M2R4) to 140 × 29 cm^2 (M4R4). The anode wires were wound along the short side of the chambers. In total, these chambers contain 1500000 anode wires with 2 mm wire spacing. The wires are grouped in wire pads. The wire pad size is constant within each region. For example, it is 5 × 4270 mm^2 for region M3R4. The MWPCs in region R3 contain cathode pads. The MWPCs in regions R2 and R1 have both anode and cathode pads, the crossovers of which determine "logical pads" of proper sizes. The chambers operate in the double-gap mode, where the pads from the neighbour gaps are joint together in one readout channel. The designed detection efficiency in a 20 ns time window should be at least 95 % for one double gap and at least 99 % for two double gaps at the nominal High Voltage (HV) around 2.6 kV.

An essential element of the Muon system is the multi-channel HV system. In total, the LHCb Muon system contains about 5000 MWPC gaps. For better redundancy, each of these gaps should have an independent HV line. In 2005, the LHCb Collaboration decided that the R3 and R4 regions in stations M2–M5 should be equipped with the HV system developed at PNPI. The total number of the MWPC gaps in these regions is about 4000. However, taking into account financial limitations, it was decided to build the HV system in two stages. At the first stage, a 2000-channel HV system was constructed at PNPI and installed in the LHCb detector in the end of 2007. The remaining 2000-channel system was constructed at PNPI in 2012 and prepared for installation during the LHC long shutdown period LS1 in 2013.

The PNPI group played a major role in assembling and commissioning of the LHCb Muon system. After initial start up of the LHC, the PNPI group participated in maintenance and technical support of the Muon system, as well as in the data analysis. The operational status of the Muon system is demonstrated in the efficiency plots from the 2011 data (Fig. 2). One can see that the measured efficiency in each station is close to 99 %. During the whole running period up to the LHC stop in February 2013, the Muon system showed a reliable operation, being one of the best operating subsystems in the LHCb detector.

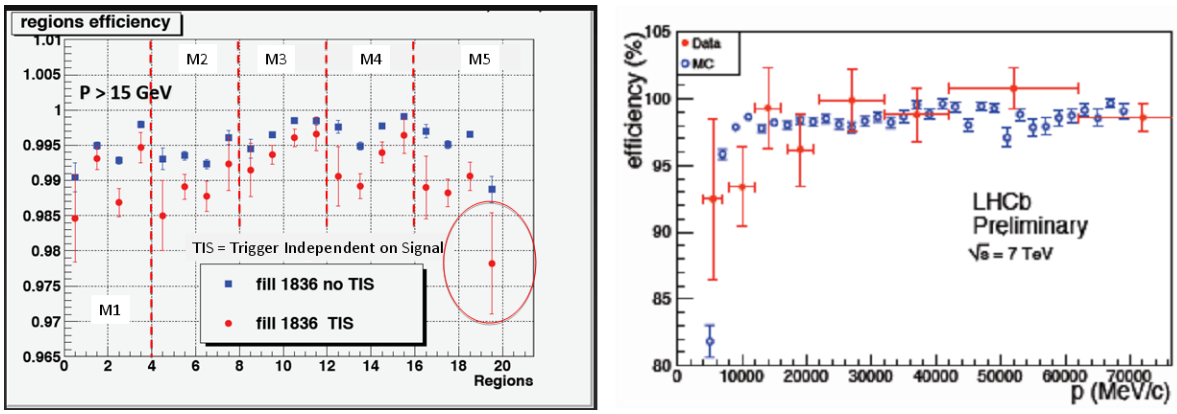

Fig. 2. Efficiency in Muon stations and regions (p > 15 GeV) (left). Efficiency of the whole Muon system versus momentum (right). The data are from 2011 runs

3. Plans for upgrades of the LHCb Muon system

The analysis of the data collected in 2010–2012 show that the LHCb detector is robust and is functioning well at the designed luminosity $L = 2 \cdot 10^{32}$ $cm^{-2}s^{-1}$. Moreover, it was demonstrated that LHCb can operate at

higher luminosities up to $L = 4 \cdot 10^{32}$ cm^{-2}s^{-1}. This regime was kept during the 2012 running period until March 2013, and it will remain the same in 2015–2016 after the LS1 shutdown, when the energy of the colliding beams will be increased up to 7 TeV + 7 TeV. During the LS1 shutdown period in 2013–2014, the new PNPI 2000-channel HV system should be installed in the Muon detector. No other major upgrades in the LHCb Muon system are foreseen for this period.

The main goal of the second long shutdown LS2 in 2017 is to increase the LHC luminosity by an order of magnitude. All LHC detectors are preparing plans for upgrades, which could allow to use such high luminosities. Such a plan is under consideration also in the LHCb Collaboration. The aim is to operate the LHCb detector at luminosities up to $L = 2 \cdot 10^{33}$ cm^{-2}s^{-1}. To reach this goal, some subsystems of the LHCb detector should be essentially modified. Also, the readout electronics and the DAQ system should be rebuilt allowing to increase the maximal trigger rate from 1 MHz at present to 40 MHz.

For the Muon system, the planned upgrade consists mainly in changes of the off-detector electronics. Apart from these changes, some modifications of the muon chambers are under discussions. Running LHCb at the luminosities up to $L = 2 \cdot 10^{33}$ cm^{-2}s^{-1} brings station M1 and the central regions in stations M2 and M3 (M2R1, M2R2, and M3R1) to the rates exceeding the maximal permissible rate, which is 1 MHz per physical pad. As concerns station M1, the Muon system can operate without this station with slightly worth but still acceptable momentum resolution. Several solutions have been proposed to improve the situation in regions M2R1, M2R2, and M3R1. The most realistic ones are construction of new MWPCs for region M2R2 with smaller pad size and replacement of the MWPCs in regions M2R1 and M3R1 by GEM chambers.

4. Physics results

Figure 3 shows the integrated luminosities recorded by the LHCb detector during the running periods in 2010, 2011, and 2012. Note that the colliding beams energy was 3.5 TeV + 3.5 TeV in the 2010 and 2011 runs, and it was 4.0 TeV + 4.0 TeV in the 2012 runs. In total, LHCb has collected 3.19 fb^{-1} of data. An analysis of the data was continuously going on. About 100 papers had been published by the end of 2012, though only a part of the collected data had been analysed by that time. The intense analysis will be continued till the new start up of the LHC in 2015 with the colliding beams energy increased to 7.0 TeV + 7.0 TeV.

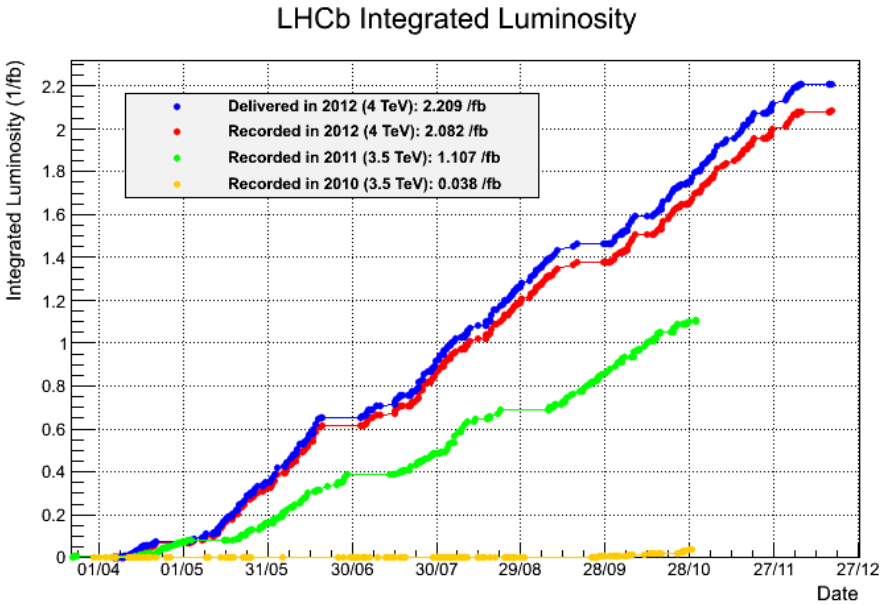

Fig. 3. Integrated luminosities delivered in 2012 (blue) and recorded by the LHCb detector during the running periods in 2010 (yellow), 2011 (green), and 2012 (red)

The excellent performance of the LHCb detector showed that it is the most powerful *B*-factory to date. The number of $b\bar{b}$ and $c\bar{c}$ pairs produced within the LHCb acceptance during this period was $2.6 \cdot 10^{11}$ and $5.9 \cdot 10^{12}$, respectively. A powerful particle identification system and a high mass resolution of the LHCb detector are important advantages of this detector. This helped the LHCb Collaboration to produce many new results on a record level of precision and sensitivity. Some of these results are presented below.

4.1. Study of $B_s^0 \leftrightarrow \overline{B}_s^0$, $B_d^0 \leftrightarrow \overline{B}_d^0$, and $D^0 \leftrightarrow \overline{D}^0$ oscillations

One of the goals of the LHCb experiment was to perform a precise measurement of the $B_s^0 \leftrightarrow \overline{B}_s^0$ oscillation frequency, that is the frequency with which the B_s^0 meson turns from particle to antiparticle and then back. The oscillation frequency in the $B_s^0 - \overline{B}_s^0$ system is given by the mass difference Δm_s between the heavy and light B_s mass eigenstates. For the first time, the $B_s^0 \leftrightarrow \overline{B}_s^0$ oscillation was observed by the D0 and CDF experiments. The oscillation frequency measured by CDF was $\Delta m_s = 17.77 \pm 0.10 \pm 0.07$ ps^{-1}. The LHCb experiment was able to reproduce this result already at an early stage with 36 pb^{-1} of data collected in 2010 in *pp* collisions at $\sqrt{s} = 7$ TeV. The B^0_s meson decays into $D^-_s\pi^+$ and $D^-_s\pi^+\pi^-\pi^+$ were used with D^-_s decays into five different channels. All reconstructed decays are flavour-specific final states, thus the flavour of B^0_s at the time of its decay is given by the charges of the final state particles of the decay. A combination of tagging algorithms was used to identify the B^0_s flavour at production. A total of 1381 $B_s^0 \to D_s^-\pi^+$ and $B_s^0 \to D_s^-\pi^+\pi^-\pi^+$ decays were reconstructed with the average decay time resolution of 44 fs and 36 fs, respectively. An oscillation signal was observed, and the oscillation frequency was determined: $\Delta m_s = 17.63 \pm 0.11$ (stat) $\pm$ 0.02 (syst) ps^{-1}, in agreement with the measurement reported by CDF. Later on, the analysis was repeated [2] with 1 fb^{-1} of data collected in 2011. In total, 34000 $B_s^0 \to D_s^-\pi^+$ signals were detected with the time distribution shown in Fig. 4.

This analysis resulted in the highest-precision value of the oscillation frequency in the $B_s^0 - \overline{B}_s^0$ ***system*:**

$$\Delta m_s = 17.768 \pm 0.023 \pm 0.006 \text{ ps}^{-1}.$$

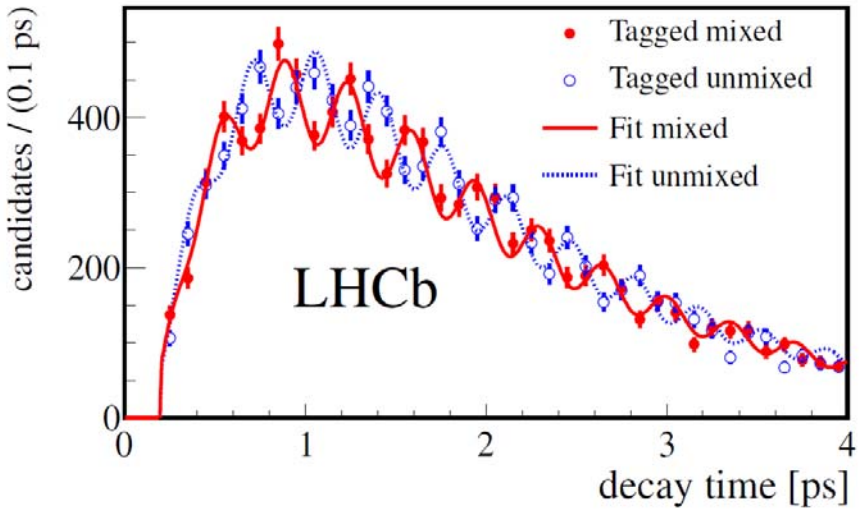

Fig. 4. Time dependence of $B_s^0 \to D_s^-\pi^+$ signals with two kinds of flavour tagging: when the production flavour is equal to the flavour at decay (tagged unmixed) and when the production flavour is opposite to the flavour at decay (tagged mixed)

Also, the world's highest precision was achieved in the measurement of the oscillation frequency in the $B_d^0 \leftrightarrow \overline{B}_d^0$ ***system*** **[3].**

This measurement was based on an analysis of a data set corresponding to the integrated luminosity of 1 fb^{-1} of *pp*-collisions at $\sqrt{s} = 7$ TeV using the decay channels $B^0 \to D^-\pi^+$ and $B^0 \to J/\psi\, K^*$.

Figure 5 shows the time dependent mixing asymmetry $A(t) = [N_{\text{unmixed}}(t) - N_{\text{mixed}}(t)] / [N_{\text{unmixed}}(t) + N_{\text{mixed}}(t)]$. The analysis of this time distribution gives the oscillation frequency Δm_d :

$$\boldsymbol{\Delta m_d = 0.5156 \pm 0.0051 \pm 0.0033\ \text{ps}^{-1}.}$$

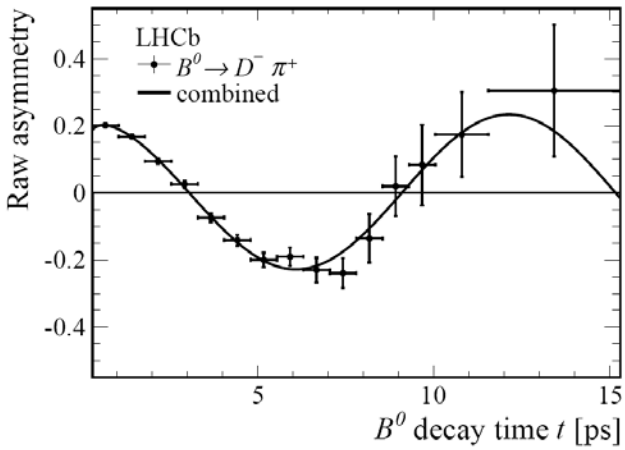

Fig. 5. Time dependence of the mixing asymmetry $A(t)$ in tagged $B^0 \to D^- \pi^+$ decays

From these two measurements it follows that $\boldsymbol{\Delta m_s / \Delta m_d = 34.4}$ with 1.2 % precision, this ratio being of special interest for theory.

Finally, the LHCb Collaboration reported [4] on the first observation of $D^0 \leftrightarrow \overline{D}^0$ oscillations by measuring the time dependence of the ratio of $D^0 \to K^+ \pi^-$ to $\overline{D}^0 \to K^- \pi^+$ yields (Fig. 6). The oscillation rate in this case proved to be very low. Nevertheless, it was observed on a high confidence level.

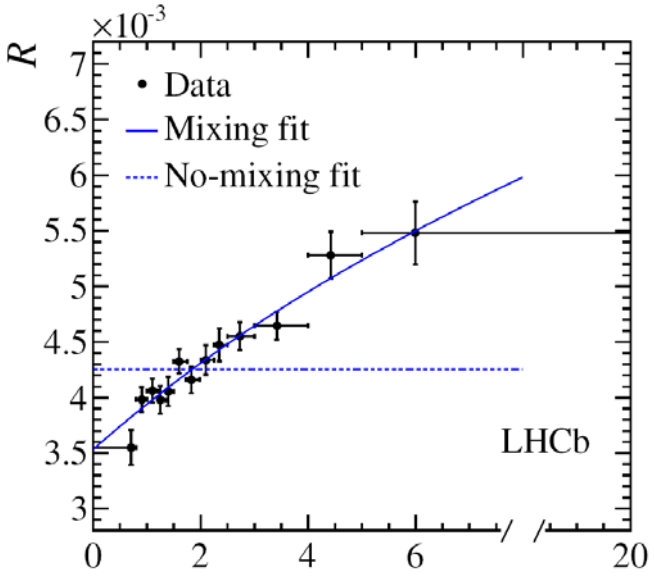

Fig. 6. Decay-time evolution of the ratio of the $D^0 \to K^+ \pi^-$ to $D^0 \to K^- \pi^+$ yields. The horizontal dotted line represents the prediction for the case with no mixing. This hypothesis is excluded at 9.1 standard deviations

4.2. CP violation in decays of *B* mesons

One of the main goals of the LHCb experiment was to study CP violation in *B* meson decays. The CP violation was discovered in 1964 in decays of neutral *K* mesons and was rewarded with the 1980 Nobel Prize in Physics for James Cronin and Val Fitch. In 1973, M. Kobayashi and T. Maskawa proposed a mechanism which could incorporate CP violation within the Standard Model with not less than 6 quarks. In 2001, CP violation was observed in the decay of B^0 mesons. The SM mechanism of CP violation was confirmed, and therefore Kobayashi and Maskawa were rewarded with the 2008 Nobel Prize in Physics. The LHCb Collaboration extended these studies for other *B* decays.

4.2.1. CP asymmetries in decays of charged *B* mesons

In March 2012, the LHCb Collaboration reported an observation of CP violation in charged $B^{\pm}$ meson decays into $DK^{\pm}$ with 5.8 σ significance [5]. Large CP asymmetries were observed also in three-body charmless decays of charged *B* mesons, $B^{\pm} \to K^{\pm}\pi^{+}\pi^{-}$ and $B^{\pm} \to \pi^{\pm}K^{+}K^{-}$:

$$\boldsymbol{A_{CP}(B^{\pm} \to \pi^{\pm}\pi^{+}\pi^{-}) = + 0.120 \pm 0.020 \pm 0.019,}$$
$$\boldsymbol{A_{CP}(B^{\pm} \to \pi^{\pm}K^{+}K^{-}) = - 0.153 \pm 0.046 \pm 0.019.}$$

A remarkable feature of these results is that the CP violation effects appear to arise in some special kinematical regions that are not dominated by contributions from narrow resonances. For example, in $B^{\pm} \to \pi^{\pm}K^{+}K^{-}$ decays the CP asymmetry is especially large at $m^2_{K^+K^-} < 1.5$ GeV^2, as one can see in Fig. 7. This points to some interesting hadronic dynamics that could generate the observed direct CP violation. The results from these analyses will also establish whether the observed CP violation is consistent with the expectations of the Standard Model or it has a more exotic origin.

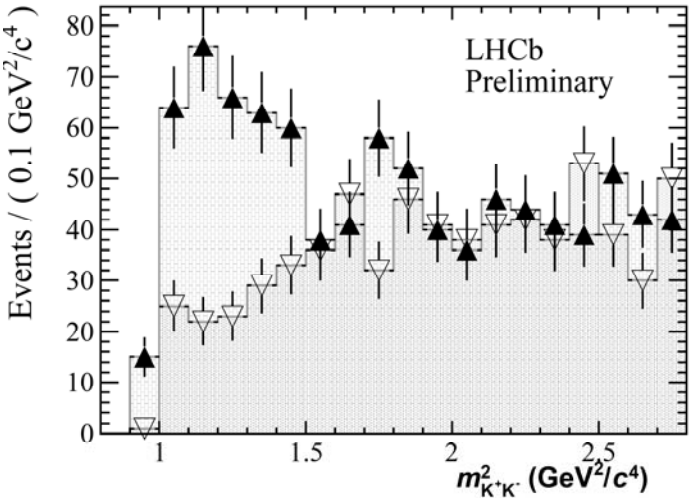

Fig. 7. Invariant mass $m^2_{K^+K^-}$ distribution of $B^+ \to \pi^+K^+K^-$ decays (filled triangles) and $B^- \to \pi^-K^+K^-$ decays (open triangles)

4.2.2. First observation of CP violation in decays of B^0_s mesons

The direct CP violation in the $B^0 \to K^+\pi^-$ decay was first observed in 2004 in the BaBar experiment. This observation raised the question of whether the effect could be accommodated by the SM or it was due to non-SM physics. The answer to this question was expected from comparison with the direct CP violation in $B^0_s \to K^-\pi^+$ decay. Several attempts to perform such measurements were made, but only the LHCb experiment could observe this effect with more than 5 σ significance. In this experiment, the CP asymmetry was measured simultaneously in $B^0 \to K^+\pi^-$ and $B^0_s \to K^-\pi^+$ decays. Figure 8a – d shows the invariant mass spectra obtained for the $B^0 \to K^+\pi^-$ and $B^0_s \to K^-\pi^+$ decays. The analysis was based on the data corresponding to an integrated luminosity of 1 fb^{-1} of *pp*-collisions at $\sqrt{s} = 7$ TeV. The mass resolution was 22 MeV in these measurements. The number of the detected events was 41420 ± 300 for the $B^0 \to K^+\pi^-$ decay and 1065 ± 55 for the $B^0_s \to K^-\pi^+$ decay. As a result, the CP asymmetries were determined [6]:

$$\boldsymbol{A_{CP}(B^0 \to K^+\pi^-) = - 0.080 \pm 0.007 \pm 0.003,}$$
$$\boldsymbol{A_{CP}(B^0_s \to K^-\pi^+) = + 0.27 \pm 0.04 \pm 0.01.}$$

The former is the most precise measurement of $A_{CP}(B^0 \to K^+\pi^-)$ to date, whereas the latter represents the first observation of CP violation in decays of B^0_s mesons with the significance exceeding 5 σ.

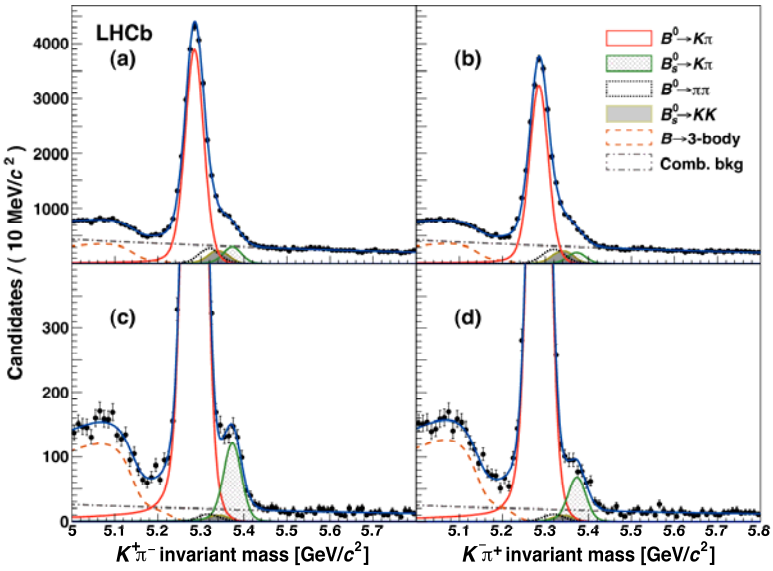

Fig. 8. Invariant mass spectra obtained using the event selection optimal for the $B^0 \to K^+\pi^-$ decay {plots (a) and (b)} and for $B^0{}_s \to K^-\pi^+$ decay {plots (c) and (d)}

These results allow a stringent test of validity of the relation between $A_{CP}(B^0 \to K^+\pi^-)$ and $A_{CP}(B^0{}_s \to K^-\pi^+)$ given in the SM: $\Delta_{SM} = A_{CP}(B^0 \to K^+\pi^-) / A_{CP}(B^0{}_s \to K^-\pi^+) + \mathcal{B}(B^0{}_s \to K^-\pi^+)\tau_d] / / \mathcal{B}(B^0 \to K^+\pi^-)\tau_s = 0$, where $\mathcal{B}(B^0 \to K^+\pi^-)$ and $\mathcal{B}(B^0{}_s \to K^-\pi^+)$ are CP-averaged branching fractions, and τ_d and τ_s are the B^0 and $B^0{}_s$ mean lifetimes, respectively. The experimental value of Δ_{SM} proved to be quite close to this prediction:

$$\mathbf{\Delta_{exp} = -0.02 \pm 0.05 \pm 0.04},$$

where the first uncertainty is from the measurements of the CP asymmetries and the second one is from the input values of the branching fractions and the lifetimes.

The observation of CP violation in the B_s decays was recognized at CERN as "an important milestone in the history of particle physics", extending the family of subatomic particles known to exhibit such behaviour.

4.3. Search for CP violation in charm decays

In the Standard Model, CP violation in the charm sector is expected to be very small, whereas new physics effects could generate essential enhancements. The LHCb Collaboration studied the CP asymmetry $A_{CP} = [N(D^0 \to f) - N(\overline{D}{}^0 \to f)]/[N(D^0 \to f) + N(\overline{D}{}^0 \to f)]$, where f is the CP eigenstate K^-K^+ or $\pi^-\pi^+$. As a matter of fact, it was decided to measure the difference in the asymmetries $\Delta A_{CP} = A_{CP}(K^-K^+) - A_{CP}(\pi^-\pi^+)$ to eliminate some systematic errors, while the effect of new physics should be doubled as the induced asymmetries should have opposite signs in these two decay modes. The first result reported by the LHCb Collaboration in November 2011 showed a 3.5 σ evidence for CP violation in the charm sector: $\Delta A_{CP} = = (-0.82 \pm 0.21 \pm 0.11)$ %. This result triggered an intensive theoretical and experimental activity. The CDF and Belle Collaborations presented their results: $\Delta A_{CP} = (-0.62 \pm 0.21 \pm 0.10)$ % and $\Delta A_{CP} = (-0.87 \pm 0.41 \pm \pm 0.06)$ %, respectively, thus supporting the LHCb result.

In all these studies, $D^{*+} \to D^0\pi^+$ decays were used as the source of the D^0 sample, and the emitted pion was used to determine the flavour of the neutral meson. Later, the LHCb Collaboration repeated this analysis with a larger data set and with better background rejection [7]. The obtained result was $\Delta A_{CP} = (-0.34 \pm 0.15 \pm 0.10)$ %, which is much closer to zero than the previous ones. In addition, the LHCb Collaboration presented results of a second independent analysis in which the D^0 and $\overline{D}{}^0$ mesons were selected using the semileptonic B decays, $B^{+(-)} \to \mu^{+(-)}\,\nu\,D^0(\overline{D}{}^0)$. In this analysis, the flavour of

the D^0 meson was identified by the sign of the detected muons. The second analysis resulted in the following value of the asymmetry: ΔA_{CP} = (+ 0.49 ± 0.30 ± 0.14) %. A combination of the two LHCb results gives:

$$\mathbf{\Delta A_{CP} = (-0.15 \pm 0.16)\ \%.}$$

The two new LHCb results are consistent with each other at the 2σ level and do not confirm the previous evidence for CP violation in the charm sector.

4.4. Measurement of the CP-violating phase φ_s and the difference in the lifetimes of B_s mass eigenstates

The mass difference $\Delta m_s = m_H - m_L$ between the B_s mass eigenstates B_H and B_L was determined with high precision from the $B_s^0 \leftrightarrow \overline{B}_s^0$ oscillation frequency. Also, it was known from previous measurements that there is some difference $\Delta\Gamma_s \equiv \Gamma_L - \Gamma_H$ in the lifetimes of the B_H and B_L states, though the sign of this difference was not determined. The CP properties of the B_H and B_L states depend on the value of the CP-violating phase φ_s. The previous studies (dominated by the LHCb experiment) of the $B_s \to J/\psi\varphi$ decays showed that the CP violation effect in the B_s system is rather small. The value of φ_s proved to be close to zero or to π, depending on the unknown sign of $\Delta\Gamma_s$. So, there were two options: $\Delta\Gamma_s > 0$, $\varphi_s \approx 0$, and $\Delta\Gamma_s < 0$, $\varphi_s \approx \pi$. To resolve this ambiguity, the LHCb Collaboration investigated interference between the K^+K^- *S*-wave and *P*-wave amplitudes in $B_s \to J/\psi K^+K^-$ decays with the K^+K^- pairs in the regions around the φ(1020) resonance. It was concluded from this analysis [8] that $\Delta\Gamma_s > 0$ with high significance, and the most precise results on φ_s, Γ_s and $\Delta\Gamma_s$ were presented:

$$\mathbf{\varphi_s = 0.07 \pm 0.09 \pm 0.01\ rad,}$$
$$\mathbf{\Gamma_s = (\Gamma_L + \Gamma_H)/2 = 0.663 \pm 0.005 \pm 0.006\ ps^{-1},}$$
$$\mathbf{\Delta\Gamma_s = \Gamma_L - \Gamma_H = 0.100 \pm 0.016 \pm 0.003\ ps^{-1}.}$$

These results are plotted in Fig. 9 together with the results from the D0 and CDF experiments. One can see that LHCb not only has resolved the ambiguity but also has improved considerably the precision of the measurements.

The obtained results show that the lightest B_s mass eigenstate B_L decays faster and its state is almost CP = +1, while the heavier B_s mass eigenstate B_H is almost CP = –1 and it lives longer.

The LHCb results proved to be close to the SM predictions:

$$\varphi_s = -0.036 \pm 0.002\ \text{rad},\ \ \Delta\Gamma_s = 0.082 \pm 0.021\ \text{ps}^{-1}.$$

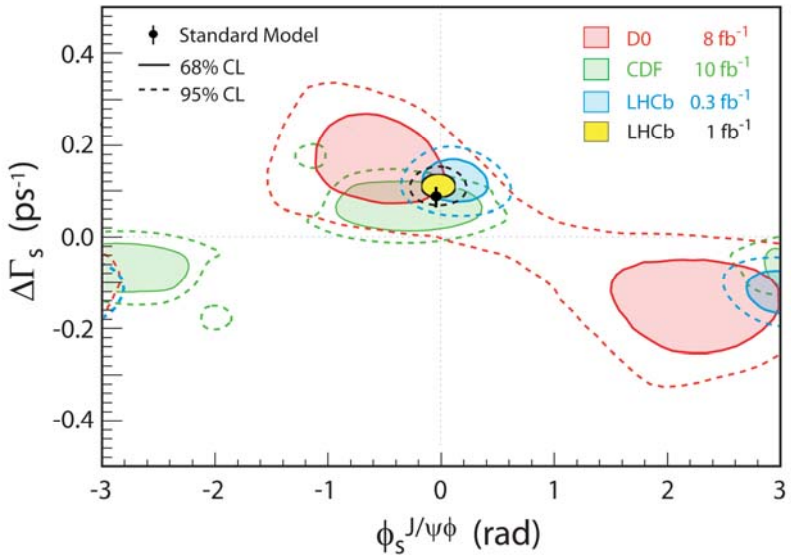

Fig. 9. Results of CDF, D0, and LHCb on measurements of the difference $\Delta\Gamma_s$ in the lifetimes of the B_s mass eigenstates B_H and B_L and determination of the CP-violating phase φ_s.
The LHCb results have resolved the ambiguity and also have improved considerably the precision of the measurements, confirming the Standard Model

4.5. Study of exotic hadronic states

An important advantage of the LHCb experiment is a possibility to study exotic hadronic states with various quark combinations. This is not only because proton-proton collisions at the LHC energies are a rich source of such states, but also due to a powerful particle identification system and a high momentum resolution of the LHCb detector. Below we present two examples of such studies.

4.5.1. First observation of excited states of Λ_b

The excited states were previously observed for the $\Lambda(uds)$ and $\Lambda_c(udc)$ baryons. The LHCb Collaboration has made first observations [9] of two excited states of $\Lambda_b(udb)$.

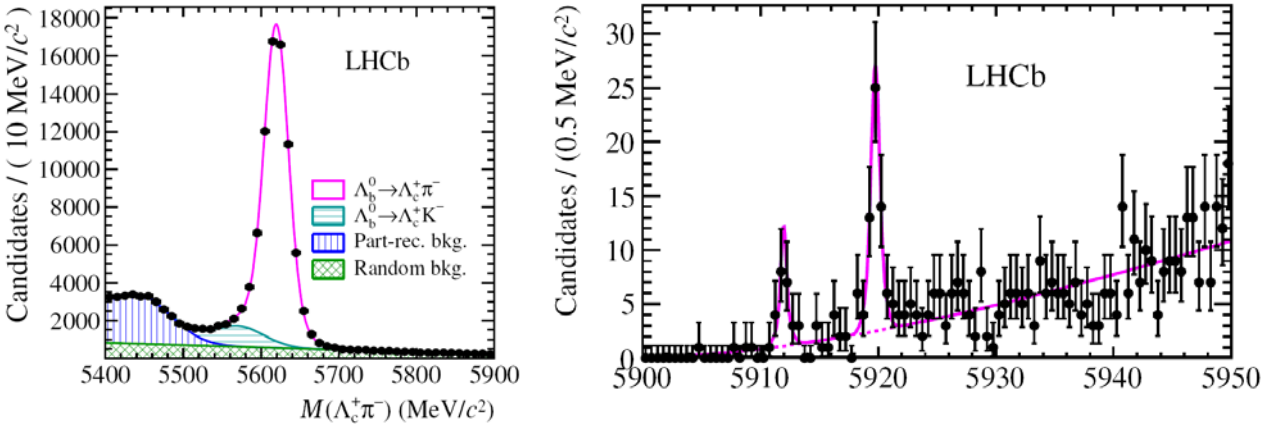

Fig. 10. Observation of Λ_b ground state (left panel) and two Λ_b excited states (right panel)

The Λ_b excited states were reconstructed in three steps. In the first step, the Λ_c^+ particles were reconstructed through their decay into a proton p, a negative K^- meson and a positive π^+ meson. In the second step, the Λ_c particles were combined with negative π^- mesons in order to form the Λ_b particles. The Λ_b signal is clearly seen as an enhancement in the left panel of Fig. 10 showing the $\Lambda_c^+\pi^-$ invariant mass spectrum. Finally, the Λ_b particles were combined with a pair of opposite sign pions $\pi^+\pi^-$. In the right panel of Fig. 10, two enhancements are clearly seen, corresponding to two Λ_b excited states with masses of 5912 MeV and 5920 MeV.

4.5.2. Study of the exotic state $X(3872)$

Some 10 years ago, the BELLE Collaboration observed a narrow state at the mass 3872 MeV. It was discovered in B^+ meson decay into an $X(3872)$ and a K^+ meson. Its existence was confirmed later by the CDF, D0, and BaBar experiments. An analysis of the CDF Collaboration has limited possible values for the quantum numbers J^{PC} of $X(3872)$ to either 1^{++} or 2^{-+}. The LHCb experiment has observed the $X(3872)$ particle in the decay of a B^+ meson into an $X(3872)$ and a K^+ meson. A peak at the mass of 3872 MeV was observed in the invariant mass of a J/ψ particle and a $\pi^+\pi^-$ pair, J/ψ being identified from its decay into a $\mu^+\mu^-$ pair. Figure 11 presents the difference between the invariant mass of the $\pi^+\pi^- J/\psi$ combination and J/ψ showing clearly the $X(3872)$ and $\psi(2S)$ enhancements over the smooth background distribution. These results were obtained in an analysis of the 2011 data.

A sophisticated analysis [10] of the whole B^+ decay chain in 5 dimensions allowed to determine unambiguously the quantum numbers of $X(3872)$ to be 1^{++}. The other previously allowed assignment of 2^{-+} was rejected with the statistical significance over 8 σ. The exotic nature of $X(3872)$ would be unambiguously determined if its quantum numbers could not be described by the quark-antiquark combination. However, this is not the case. In fact, the mass of 3872 MeV is located in a region in which many charm quark-antiquark states (of charmonium) are present. $X(3872)$ has the quantum numbers of an as yet unobserved

charmonium state called $\chi_{c1}(2^3P_1)$. However, the charmonium spectrum is very well understood and the mass of 3872 MeV makes this assignment very unlikely.

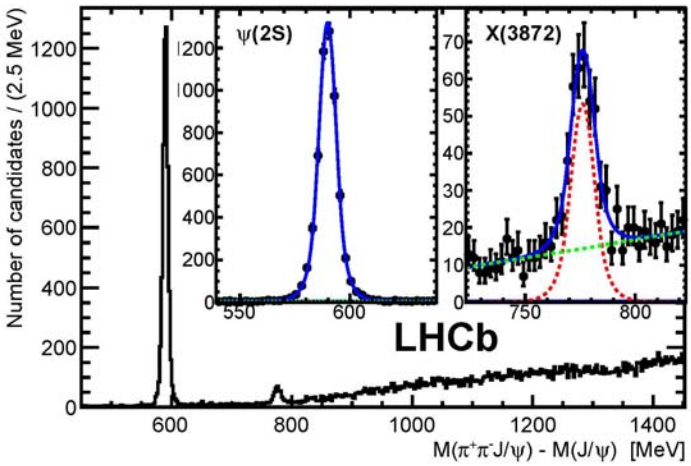

Fig. 11. Observation of the $X(3872)$ state in the B^+ decay into J/ψ and $\pi^+\pi^-$

Possible explanations of the X(3872) nature include the observation of a tetraquark state.

4.6. First evidence for the $B^0_s \to \mu^+\mu^-$ decay

Flavour changing neutral current processes are highly suppressed in the Standard Model. There are precise SM predictions for the branching fractions of the $B_{s(d)} \to \mu^+\mu^-$ decays: $\mathrm{Br}(B_s \to 2\mu) = (3.2 \pm 0.2) \cdot 10^{-9}$, $\mathrm{Br}(B_d \to 2\mu) = (1.0 \pm 0.1) \cdot 10^{-10}$. This makes these modes stringent probes in the search for deviations from the SM, since contributions from some new processes or new heavy particles can significantly modify these values. The search of the $B_{s(d)} \to 2\mu$ decays was initiated at the Tevatron at FNAL. The upper limits for the branching fraction of the $B_s \to 2\mu$ decays reached in these experiments by 2012 exceeded the SM value by more than an order of magnitude, thus leaving some room for «new physics». The CDF Collaboration even declared a possible observation of the $B_s \to 2\mu$ signals on a level of $\mathrm{Br}(B_s \to 2\mu) = (18^{+11}/_{-9}) \cdot 10^{-9}$, giving some hopes for observation of "new physics". However, these results were disproved by the LHCb experiment. The analysis of the experimental data collected in 2011 with the integrated luminosity of 1 fb^{-1} of *pp*-collisions at $\sqrt{s}$ = 7 TeV allowed to push down these upper limits to $\mathrm{Br}(B_s \to 2\mu) < 4.5 \cdot 10^{-9}$ and $\mathrm{Br}(B_d \to 2\mu) < 1.0 \cdot 10^{-9}$. These results were published in June 2012 [11]. The further analysis included a part of the data collected in 2012. The data sample comprised 1.1 fb^{-1} of *pp*-collisions at $\sqrt{s}$ = 8 TeV and 1.0 fb^{-1} at $\sqrt{s}$ = 7 TeV. The events were selected with the BDT method to classify data into bins with different ratios of $B^0_s \to 2\mu$ decays and background contributions. The $\mu^+\mu^-$ invariant mass spectrum for the bins with the smallest background contribution is shown in Fig. 12. The solid blue line shows that the data distribution presented as black dots is well understood and can be separated into different components presented with the help of different colour lines. The dashed red narrow distribution shows the $B^0_s \to 2\mu$ contribution around the B^0_s mass of 5366 MeV/c^2. The green dashed distribution shows a possible $B^0_d \to 2\mu$ contribution around the B^0_d mass of 5280 MeV/c^2.

A small excess of data around the B^0_d mass over the background and the Standard Model rate is observed, but it is consistent with the SM expectation. This gives an upper limit for the branching fraction of the $B_d \to 2\mu$ decays. LHCb has set the following limit for this branching ratio:

$$\mathbf{Br}(B^0_d \to 2\mu) < 9.4 \cdot 10^{-10} \text{ at } 95\% \text{ CL.}$$

On the other hand, the excess of signals in the region of the B^0_s mass is interpreted as the first observation of the $B^0_s \to 2\mu$ decay with the branching fraction

$$\mathbf{Br}(B^0_s \to 2\mu) = (3.2^{+1.5}_{-1.2}) \cdot 10^{-9}.$$

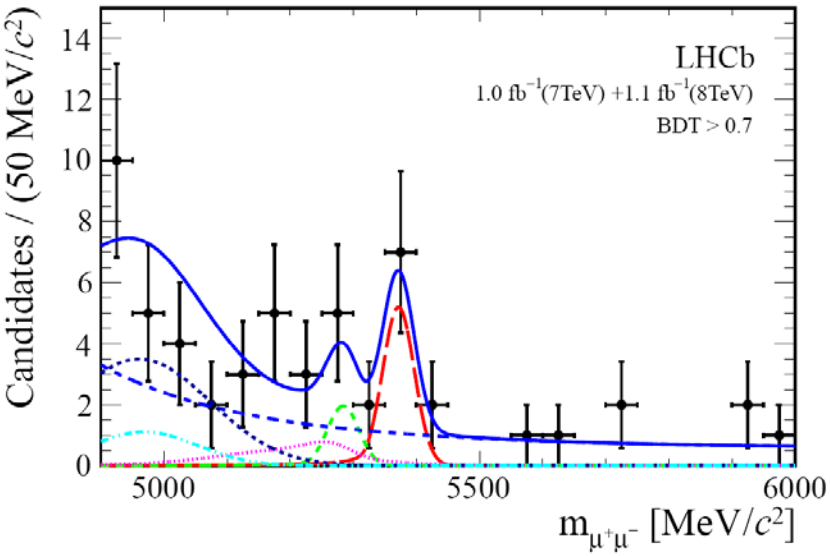

Fig. 12. The $\mu^+\mu^-$ invariant mass distribution of the selected ($B^0_s \to 2\mu$) candidates

The significance of this measurement is 3.5 σ, and therefore this result is classified as ***the first evidence for the $B^0_s \to \mu^+\mu^-$ decay***, in agreement with the Standard Model.

These results were first presented at the Kioto conference in November 2012 and then published in PRL [12].

At CERN, these results are considered among the most important achievements of the LHC experiments, while the editorial board of PRL selected this article into the category of "exceptional research". The obtained results put quite strong limits for existence of supersymmetric partners in certain regions of the SSM parameters.

Figure 13 illustrates this statement for the case of the Constrained Minimal Super Symmetric Model (CMSSM). This figure shows a two-dimensional plot of the CMSSM parameters $\{m_0, m_{1/2}\}$ with the other two parameters fixed to $\tan\beta = 50$ and $A_0 = 0$. One can see that in this particular case the limits coming from the LHCb data are much stronger than those from the direct search. Note, however, that this statement is valid only for $\tan\beta > 30$.

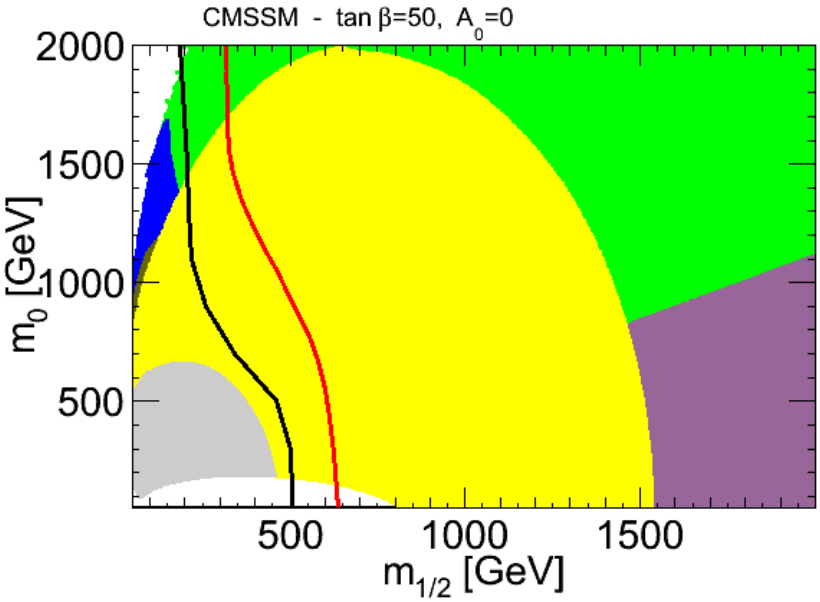

Fig. 13. The regions in the two-dimensional plot of the CMSSM parameters $\{m_0, m_{1/2}\}$ excluded by the LHCb $B^0_s \to 2\mu$ data (yellow) and by the direct search in the CMS experiment (to the left from the red line)

5. Summary

The LHCb experiment demonstrated that it is the most powerful *B*-factory to date. Already during the first years of operation in 2010–2012, most of the previous results in this domain were exceeded in precision and many new observations were reported. The main outcome of these studies was strong quantitative confirmation of the validity of the Standard Model in various aspects including CP violation in the *B* sector. Also, some stringent limits were set on possible contributions from "new physics" (in particular, from some supersymmetry models) in the energy region explored by the LHC. Very promising areas for the LHCb experiment proved to be rare decay studies, as well as studies of exotic states of mesons and baryons.

The LHCb detector showed a very effective and reliable performance. This made it possible to perform measurements at the luminosity of $L = 4 \cdot 10^{32}$ cm^{-2} s^{-1}, twice exceeding the designed value. Plans for further upgrades of the LHCb detector are under considerations at present. The goal is to increase the luminosity up to $L = 2 \cdot 10^{33}$ cm^{-2} s^{-1}. This will require some serious modifications in various subsystems of the detector including the Muon system and the Tracking system. PNPI will take an active part in this upgrade program.

References

1. *LHCb Technical Design Report*, CERN/LHCC 203-30, LHCb TDR9, September 2003.
2. R. Aaij *et al*. (LHCb Collaboration), *Precision measurement of the* $B^0_s \leftrightarrow B^0_s$*_bar oscillation frequency with the decay* $B^0_s \to D^-_s\pi^+$, New J. Phys. **15**, 053021 (2013).
3. R. Aaij *et al*. (LHCb Collaboration), *Measurement of the* $B^0 \leftrightarrow B^0$*_bar oscillation frequency* Δm_d *with the decays* $B^0 \to D^-\pi^+$ *and* $B^0 \to J/\psi K^{0*}$, Phys. Lett. B **719**, 318 (2013).
4. R. Aaij *et al*. (LHCb Collaboration), *Observation of* $D^0 \leftrightarrow D^0$*_bar oscillations*, Phys. Rev. Lett. **110**, 101802 (2013).
5. R. Aaij *et al*. (LHCb Collaboration), *Observation of CP violation in* $B^\pm \to DK^\pm$ *decays*, Phys. Lett. B **712**, 203 (2012).
6. R. Aaij *et al*. (LHCb Collaboration), *First observation of CP violation in decays of* B^0_s *mesons*, Phys. Rev. Lett. **110**, 221601 (2013).
7. R. Aaij *et al*. (LHCb Collaboration), *Search for direct CP violation in* $D^0 \to h^+h^-$ *modes using semileptonic B decays*, Phys. Lett. B **723**, 33 (2013).
8. R. Aaij *et al*. (LHCb Collaboration), *Measurement of CP violation and* B^0_s *meson decay width difference*, arXiv:1304.2600 [hep-ex].
9. R. Aaij *et al*. (LHCb Collaboration), *Observation of excited* Λ^0_b *baryons*, Phys. Rev. Lett. **109**, 172003 (2012).
10. R. Aaij *et al*. (LHCb Collaboration), *Determination of the X*(3872) *meson quantum numbers*, arXiv:1302.6269 [hep-ex].
11. R. Aaij *et al*. (LHCb Collaboration), *Strong constraints on the rare decays* $B^0_s \to \mu^+\mu^-$ *and* $B^0 \to \mu^+\mu^-$, Phys. Rev. Lett. **108**, 231801 (2012).
12. R. Aaij *et al*. (LHCb Collaboration), *First evidence for the decay* $B_s \to \mu^+\mu^-$, Phys. Rev. Lett. **110**, 021801 (2013).

In total, the LHCb Collaboration has published 116 physics papers in the period 2011 – June 2013. The list of the authors includes the following members of the PNPI team: G.D. Alkhazov, N.F. Bondar, A.A. Dzyuba, O.E. Maev, N.R. Sagidova, Yu.A. Shcheglov, A.A. Vorobyev.

EXPERIMENT ALICE AT THE LHC

PNPI participants of the ALICE Collaboration: V.M. Samsonov, V.A. Guzey, V.S. Ivanov, E.L. Kryshen, A.V. Khanzadeev, M.V. Malaev, V.N. Nikulin, V.G. Ryabov, Yu.G. Ryabov, M.B. Zhalov

1. Introduction

Last decades, a study of one of the most exciting problems of high energy physics – properties of the extreme state of the nuclear matter created in collisions of ultrarelativistic heavy ions – were on the top of priority at the Relativistic Heavy Ion Collider (RHIC) at Brookhaven at the energy of colliding nuclei $s_{NN}^{1/2}$ = 200 GeV. A huge bulk of data was accumulated and processed by joint efforts of four collaborations (STAR, PHENIX, BRAHMS and PHOBOS). This allowed one to investigate a wide spectrum of observables in heavy ion collisions ranging from the global characteristics like multiplicity distributions of the produced particles and ratios of their integral yields to detailed studies of the Hanbury – Brown – Twiss (HBT) correlations, elliptic flows of different particles, and quenching of jets escaping from the hot medium produced in the central collisions. From a combined analysis of all these results it was stated that the hot gluon dominated medium was formed in the volume of about 150 fm^3 in collisions of ultrarelativistic heavy ions at $s_{NN}^{1/2}$ = 200 GeV. Even within the conservative estimates, this medium is characterized by the energy density of more than 5 GeV/fm^3, and by the lifetime of the order of 6 fm/c. Contrary to the QCD based expectations to find at high temperature a deconfined gas of weakly interactive quarks and gluons (Qaurk-Gluon Plasma), the medium created at RHIC appeared to resemble almost perfect parton liquid with very low shear viscosity. This exciting observation was mainly validated by three cornerstone phenomena discovered at RHIC: a large elliptic flow of the produced particles which was found to be close to the hydrodynamic limit of the ideal liquid, quark number scaling properties of the flowing particles at small transverse momenta, and strong quenching of jets due to the parton energy loss in the deconfined colour medium created in the central zone of ion interactions. So, before the start of the heavy ion program at the Large Hadron Collider (LHC) in 2010, the top priority question was how the properties of the medium created in the central collisions can change when the energy of the colliding ions is increased up to 1380 GeV/N, which is higher by more than one order in comparison to the energy 100 GeV/N of beams at RHIC. The ALICE detector [1] was designed and built to answer this question.

2. The ALICE detector

To perform a detailed study of the properties of the extreme state of the nuclear matter created in collisions of ultrarelativistic heavy ions at the LHC, the ALICE detector comprises a number of dedicated subsystems (Fig. 1).

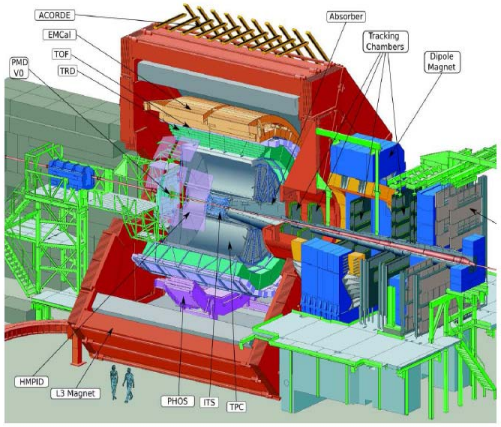

Fig. 1. Layout of the ALICE detector

Central barrel subdetectors – an Inner Tracking System (ITS), a Time Projection Chamber (TPC), a Transition Radiation Detector (TRD), and a Time-of-Flight (TOF) detector – cover the full azimuthal angle range at midrapidities $|\eta| < 0.9$. The calorimeters EmCal and PHOS have partial coverage at midrapidities. V0 detectors from both sides measure the charged particle multiplicity in the forward and backward directions at $-3.7 < \eta < -1.7$ and $2.8 < \eta < 5.1$ and are also used for triggering and centrality determination. Two Zero Degree Calorimeters are placed at a distance of about 114 m from the interaction zone to measure neutral particles, mainly neutrons.

The PNPI team in ALICE is responsible for the Muon Spectrometer system, which is placed in the forward direction and measures yields of muons from decays of the produced particles. The layout of the ALICE Muon spectrometer is shown in Fig. 2. The detector consists of an absorber, five tracking stations (ST1–ST5), two Trigger Stations (TS1 and TS2), a dipole magnet, and an iron wall. The selection of muons is based on their high penetrating power: most of particles other than muons are stopped inside the 4.3 m long composite absorber ($X_0 \approx 60$, $\lambda_{int} \approx 10$). The passed through particles are bent by the magnetic field of the dipole magnet. The tracking stations measure the particle track deviation: ST1 and ST2 measure the input angle, ST4 and ST5 measure the output direction, and ST3 gives track coordinates inside the dipole magnet. The dipole magnet (3 Tm field integral) is used for a momentum analysis. The iron wall located between the tracking and trigger parts of the detector makes an additional cleanup from non-muon components. The trigger Resistive Plate Chambers (RPCs) provide the tracklet information, thus one can easily estimate the transverse momentum of the particle. The trigger electronics performs an analysis of the data, and within 800 ns produces a trigger signal taking into account the threshold on the transverse momentum (1 GeV/c to select J/ψ and 5 GeV/c to select Υ).

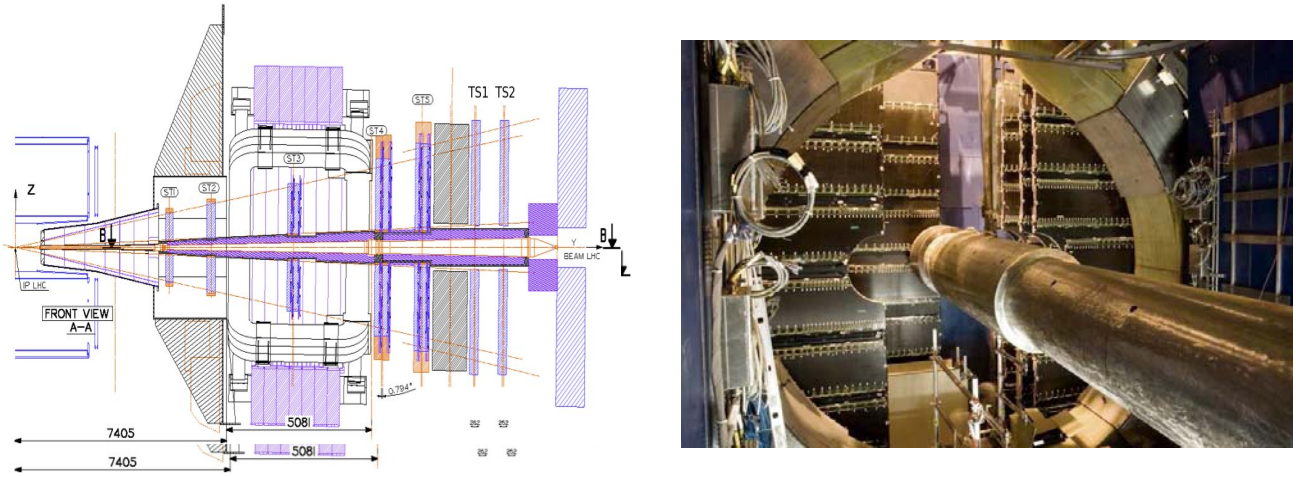

Fig. 2. Muon spectrometer longitudinal section and the layout of stations 3 and 4 (slat design) and the beam-shield tube

Large (up to 6 m), high granularity (capable to detect several hundred hits per plane per event), high resolution (better than 100 microns in the bending plane) detectors were built. The PNPI team participation in the Muon spectrometer hardware can be summarized as follows:

(i) Designing and building prototypes: the conception of the slat chambers (a plane composed of long rectangular detector elements was proposed by the PNPI team). The chamber prototypes were successfully tested at the CERN PS beam.

(ii) Manufacturing: a quarter of the tracking modules for ST3, ST4 and ST5 were assembled at PNPI. The PNPI team also built the tooling for production of the modules (machines for high precision trimming of the printed circuit boards for Cagliari and Kolkata, a wire stress measurement device, a radioactive source scanning system, a HV test-bench).

(iii) Commissioning and maintenance: participation in the final tests and chamber assembly at CERN, installation of the chambers in the cave, elimination of the electronic noise, repairing of faulty components during technical stops, participation in shifts at the expert level.

Segmented cathode pad chambers with about 1.09 millions readout channels were used in order to achieve the required performance. The on-board signal encoding and zero suppression enable a fast readout procedure. Up to 1200 channels are daisy-chained and organized in data buses, which come to the readout system. The readout crate can read up to 50 data buses at a rate up to 1 kHz. The system includes 20 crates. In order to align the tracking modules, their positions in the first approximation were measured by means of the photogrammetry method (a PNPI representative participated in the ALICE survey group). The final alignment procedure was done using particle tracks in the absence of the magnetic field. Simulations have shown that the mass resolution of about 75 MeV/c^2 for J/ψ and about 150 MeV/c^2 for Υ can be achieved.

3. Upgrade plans

The LHC has recently entered a two-year period of Long Shutdown 1 dedicated to increasing the energy of the accelerated particles to the designed value of 7 TeV per beam. ALICE will take this opportunity to complete the approved detector design and consolidate the detector performance. In 2015–2017, ALICE is going to fulfill the initially approved plans and to collect about 1 nb^{-1} of Pb-Pb data at the full LHC energy. This data taking period will be followed by Long Shutdown 2 aimed to upgrade the LHC luminosity capabilities by a factor of 10 and, hence, to reach the Pb-Pb interaction rates of about 50 kHz.

ALICE is going to take full advantage of the high-luminosity LHC [2]. The intent is to explore 10^{10} minimum bias events, a factor of 100 more than it was planned before the upgrade. This would allow one to perform multi-dimensional analyses of rare low-p_T observables (*e.g.*, charm baryons) with unprecedented statistical and systematic accuracy. This ambitious goal relies on the development of a new data acquisition system based on pipeline readout and a high-level trigger with online event reconstruction and selection. In addition, the readout electronics of all detector subsystems has to be upgraded, and new GEM-based readout chambers will be installed in TPC to meet the high rate requirements. Besides, in order to exploit low-p_T and charm physics, ALICE is going to install a smaller radius beam pipe and a new inner tracking system with a pipeline readout, the reduced material budget of only 0.3 % of the radiation length and smaller pixel sizes providing the hit resolution of the order of 4 μm and improving the vertexing precision by a factor of 3.

Another essential part of the upgrade project is the Muon Forward Tracker (MFT), a silicon pixel detector will be added in the Muon Spectrometer upstream of the hadron absorber [3]. The MFT will provide reliable measurements of the muon track offsets with respect to the primary vertex of the interaction and enhance the ALICE capabilities for detecting muons at the forward rapidity. The presence of the MFT detector will give an access to new observables like prompt/displaced J/ψ separation and charm/beauty separation, in both cases at very low transverse momentum.

The PNPI team actively participates in the upgrade activities, namely in the construction and integration of the MFT support structures and in the development of the new trigger system allowing one to combine old hardware triggers with the foreseen pipeline readout architecture.

4. Global observables from the first ALICE results on heavy ion collisions

During the 2010–2013 runs at proton-proton, ion-ion and ion-proton beams, a large volume of data was collected with general purpose triggers, and additionally some specialized hard interaction triggers were also used to study in more details specific processes with relatively small cross sections. The information on major data taking periods is shown in Table 1.

Table 1

Summary of the data sets recorded with ALICE [4]

System	$s_{NN}^{1/2}$, TeV	Year	Min. bias triggers, M	Int. luminosity
pp	7	2010	800	17 μb^{-1}
pp	7	2011	800	2 pb^{-1}
pp	2.76	2011	70	20 nb^{-1}
pp	8	2012	500	5 pb^{-1}
Pb-Pb	2.76	2011	30	4 μb^{-1}
Pb-Pb	2.76	2012	9	80 μb^{-1}
p-Pb	5.02	2013	140	12 μb^{-1}

Already the first result obtained and published by ALICE [5] after the run at $s_{NN}^{1/2}$ = 2.76 TeV/N in 2010 revealed a pronounced effect due to increasing the energy of collisions in comparison with the energies at RHIC. The charge particle multiplicity density measured in the central lead-lead collisions scaled by the number of the nucleon pairs participating in the collision appeared to rise steeper than the charge particle multiplicity density in *pp* interactions at the same energy (Fig. 3). From the HBT correlations of charged hadrons, the transverse radius of the produced medium was found to be $R_t \approx 6$ fm, the medium volume exceeding the RHIC value by a factor of about 1.5–2.

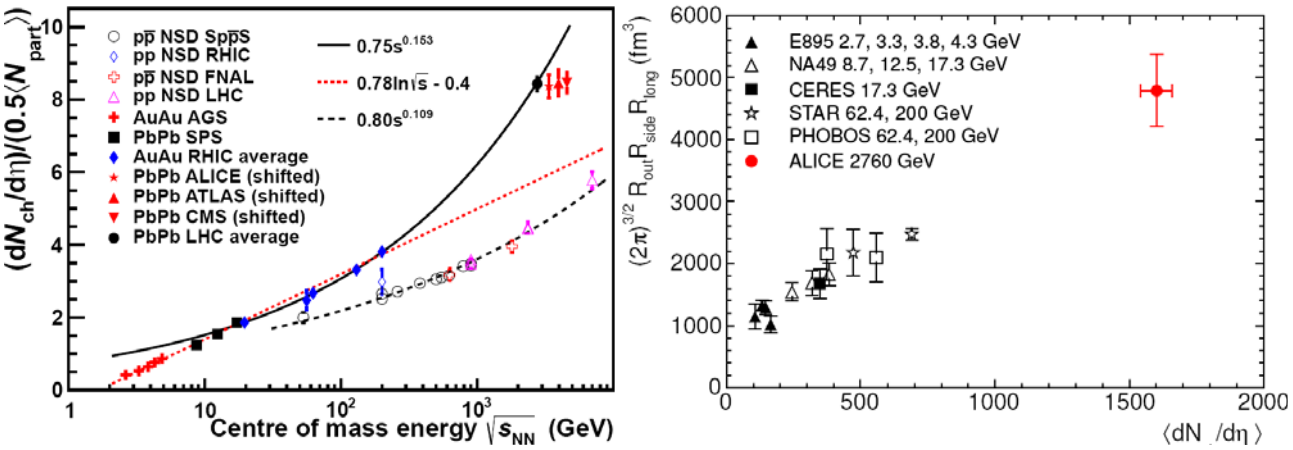

Fig. 3. Charged particle multiplicity density and the volume of the medium created in the central PbPb collisions measured in the ALICE experiment

The measured value $dN_{ch}/d\eta \approx 1600$ allowed one to estimate the energy density using as a guess the Bjorken model formula. Assuming the same formation time $\tau_{form} \approx 1$ fm/c at the RHIC and LHC energies, this leads to the value $\varepsilon \approx 15$ GeVfm^{-3}, exceeding the value found at RHIC at least by a factor of about 3. On the assumption of establishing the state of the thermodynamics equilibration, the corresponding increase of the temperature would be by 30 % above the RHIC value. One has to note that the same Bjorken formula gives an estimate of the energy density deposited during the time of the ion interaction ($\Delta\tau_{int} \approx 2R_A/\gamma_L \approx$ ≈ 0.01 fm/c) on the level of 1500 GeV/fm^3. This rises a question about the mechanism driving the equilibration of the created medium with so high initial energy density during a rather short time of the order of 1 fm/c.

A detailed analysis of the charged particle yields shows [6] that the developed elliptic flows at the LHC energies are close to that found at RHIC (Fig. 4). A slight increase of the parameter v_2 characterizing the elliptic flow is mainly due to an increase of the average transverse momentum of particles at the LHC energies. Note that in the case of formation of the weakly interactive Quark-Gluon Plasma (QGP) at the LHC one should expect a decrease of the elliptic flows.

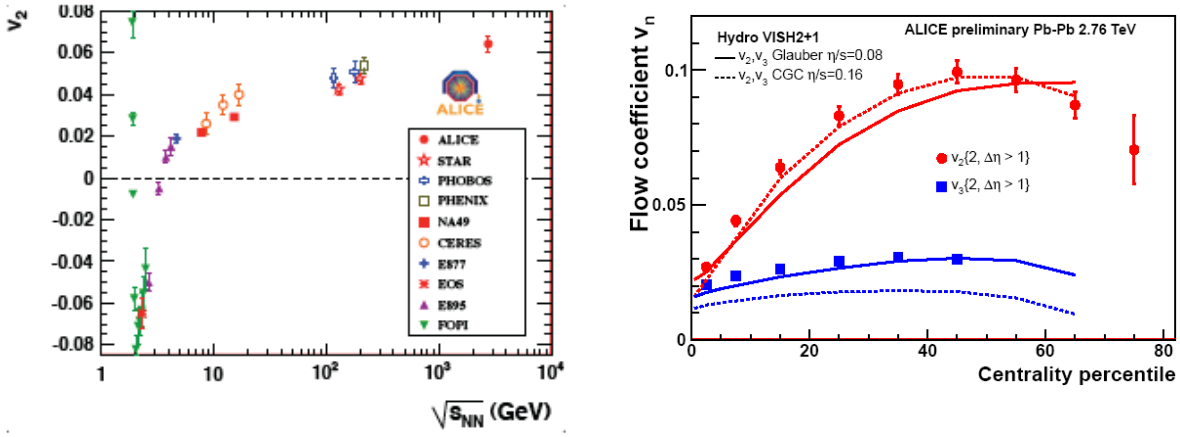

Fig. 4. Dependence of the integral elliptic flow coefficient on the energy (left), description of the measured by ALICE elliptic and triangular flow coefficients by the hydrodynamical model with different values of the shear viscosity (right)

In Fig. 4 (right side), it is seen that the elliptic flow coefficient can be reasonably described by hydrodynamics with a small ratio of shear viscosity to enthropy $\eta/s \approx 0.08$–0.16, close to the unitarity limit $\eta/s \approx 1/4\pi$ obtained for this ratio from the Anti-De-Sitter/Conformal-Field-Theory correspondence. This is a clear indication that the medium formed in Pb + Pb collisions at the LHC energies has the properties of

the almost perfect liquid. Even on the face of it, the behaviour of the elliptic flow coefficients for different hadrons at small transverse momenta (Fig. 5, left side) hints that the difference between the flowing of mesons and baryons can be removed if one takes into account that these hadrons comprise different numbers of the valence quarks. Indeed, after scaling of the value of these coefficients and transverse momenta of hadrons by the numbers of quarks (Fig. 5, right side), the partial coefficients become very similar, while, contrary to the picture found at RHIC, some difference still persists. Such scaling property means that the elliptic flow is mainly formed at the early stage of the expansion when the created medium is still in the partonic state. A more detailed analysis of the particle flows including studies of the hadrons comprising heavy quarks and the behaviour of the higher harmonics is under progress to get better understanding of the observed difference in the scaling properties and of the influence of fluctuations on the hydrodynamic properties of the created medium.

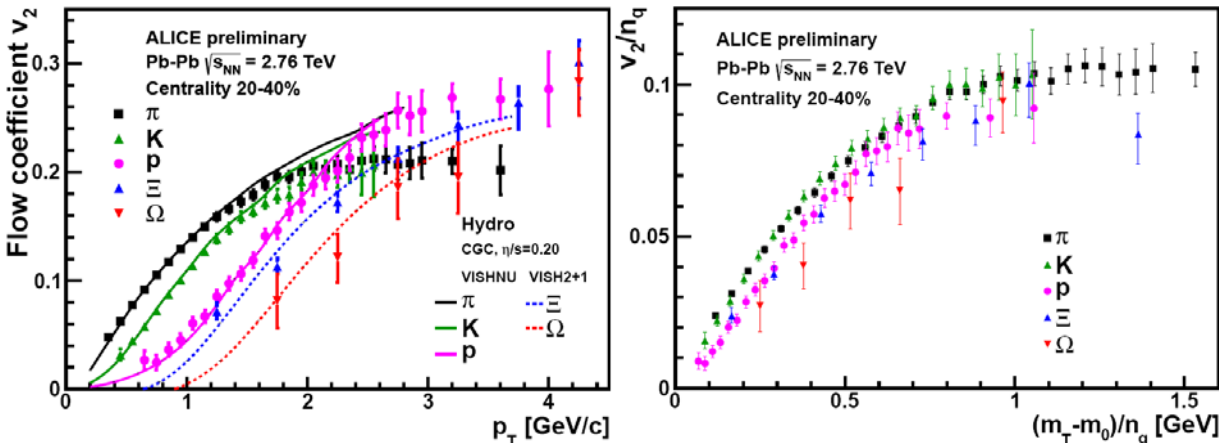

Fig. 5. Scaling of the elliptic flow coefficients for different hadrons by the number of quarks they are composed of

The third cornerstone phenomenon, jet quenching and parton recombination, is considered among the main signatures of the quark-gluon plasma. In ultrarelativistic heavy ion collisions they manifest themselves in suppression of high-p_T hadron production and in enhancement of baryon production at intermediate values of p_T. Experimental study of these effects is important for understanding and numerical estimation of the plasma transport properties and its time-spatial evolution.

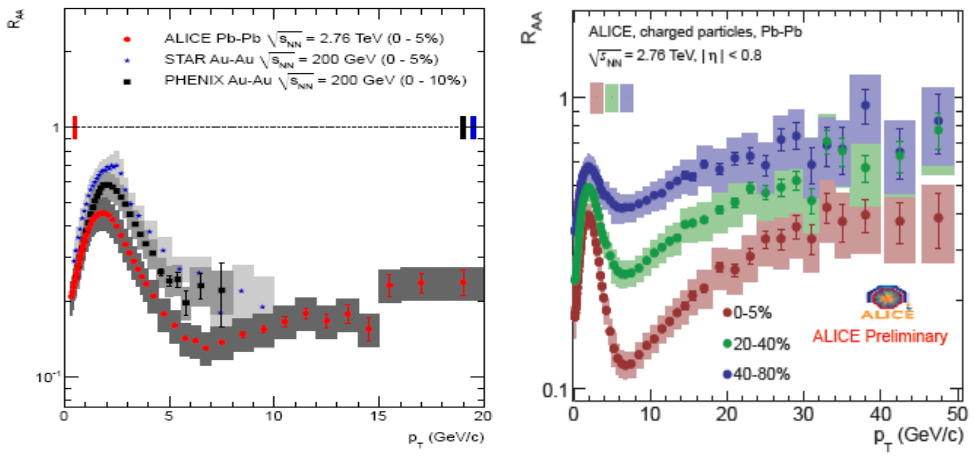

Fig. 6. Factor of nuclear modification of leading hadrons observed at ALICE in comparison with RHIC results

It is generally accepted to characterize the effect of jet quenching by the ratio R_{AA} of the leading hadron yield in nucleus-nucleus collision to that in proton-proton scaled by the number of the interacting nucleon pairs. From the analysis of the RHIC data it was found that three main phenomena can contribute to

the modification of the leading hadron yield in nucleus-nucleus collisions – Cronin effect, shadowing of the quark and gluons in the initial state, and the energy loss of fast partons crossing the created medium. However, a very strong suppression can be explained only if one takes into account the energy loss of the fast coloured parton which crosses the deconfined medium consisting of quarks and gluons. The nuclear modification factor measured with the ALICE detector [7] at the invariant energy 2.76 TeV is compared to that determined at RHIC energies, Fig. 6. Up to the transverse momenta of about 7 GeV/c, the results are in close agreement, thus confirming the strong jet quenching effect due to the parton energy losses in the coloured media at the energies of the LHC.

To achieve an unambiguous interpretation of the nuclear modification effects and to discriminate between theoretical models, one needs to measure production of identified hadrons containing light (u, d), strange (s) and heavy (c, b) quarks at intermediate and high transverse momenta.

5. Heavy quarks: hints of thermalization?

Charm quarks are abundantly produced at the LHC providing a powerful tool to study both the properties of the medium and the transport properties of the charm quarks. In-medium energy loss for heavy quarks is expected to be smaller than that for light quarks and gluons due to the colour charge and gluon-bremsstrahlung dead cone effects. Figure 7 (left) presents ALICE results [8] on the nuclear modification factors for D^0, D^+ and D^{*+} mesons. The observed suppression is similar for different meson species and reaches a factor of 5 at $p_T \sim 10$ GeV/c, being very close to the average charged particle suppression and providing an indication of no strong colour charge dependence of the in-medium energy loss. A similar suppression pattern was also observed in semi-leptonic decay channels of heavy flavours.

The observed elliptic flow of prompt D^0 mesons, shown in Fig. 7 (right), is also comparable with v_2 of light hadrons in favour of possible thermalization of charm quarks in the hot QCD medium created in heavy-ion collisions at the LHC.

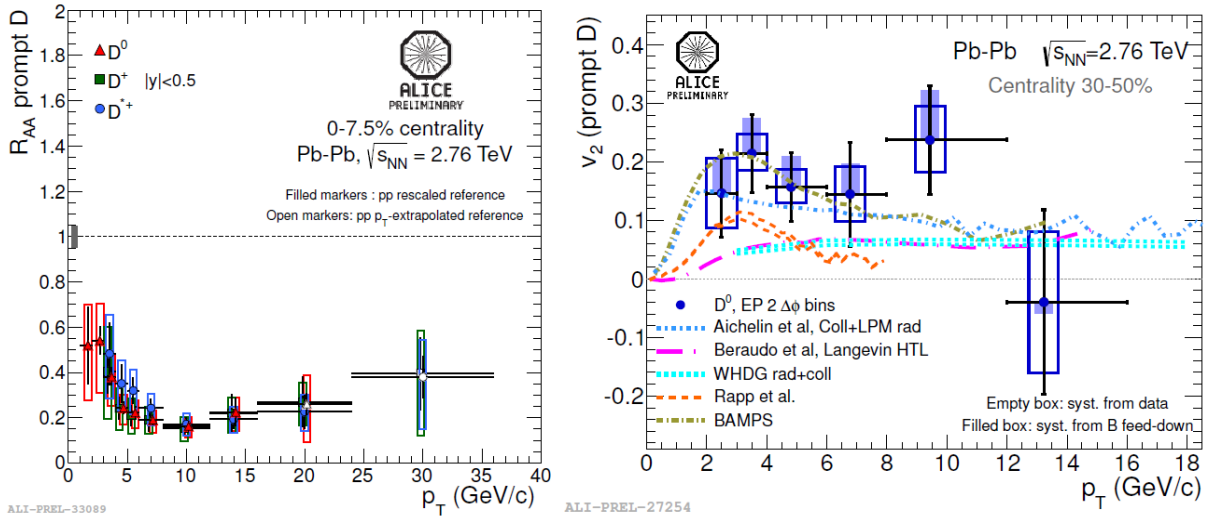

Fig. 7. Nuclear modification factors for D^0, D^+, and D^{*+} mesons in central Pb-Pb collisions (left) and v_2 for prompt D^0 mesons in 30–50 % centrality bin (right) as functions of p_T (from Ref. [8])

6. Charmonium: suppression or regeneration?

30 years ago, the charmonium suppression was proposed as the best signature of the deconfined phase since the deconfined hot medium prevents formation of bound $\overline{c}c$ states due to colour screening effects in the QGP. A large suppression was indeed observed at the SPS and RHIC. However, with high multiplicity of heavy quarks at the LHC, one should consider another scenario: an enhancement of the bound $\overline{c}c$ states *via* regeneration in the thermalized QGP medium or during hadronization.

The nuclear modification factor for J/ψ mesons measured by ALICE at the forward rapidity is shown in Fig. 8 (left) as a function of the number of participants $\langle N_{part} \rangle$ [9]. The observed suppression flattens at $\langle N_{part} \rangle \sim 100$ and appears to be much weaker than at RHIC for central collisions. Such a centrality dependence and p_T differential studies suggest that the $\bar{c}c$ regeneration processes indeed play an important role at the LHC energies. The observed hint for a non-zero elliptic flow shown in Fig. 8 (right) is also in favour of this picture [10].

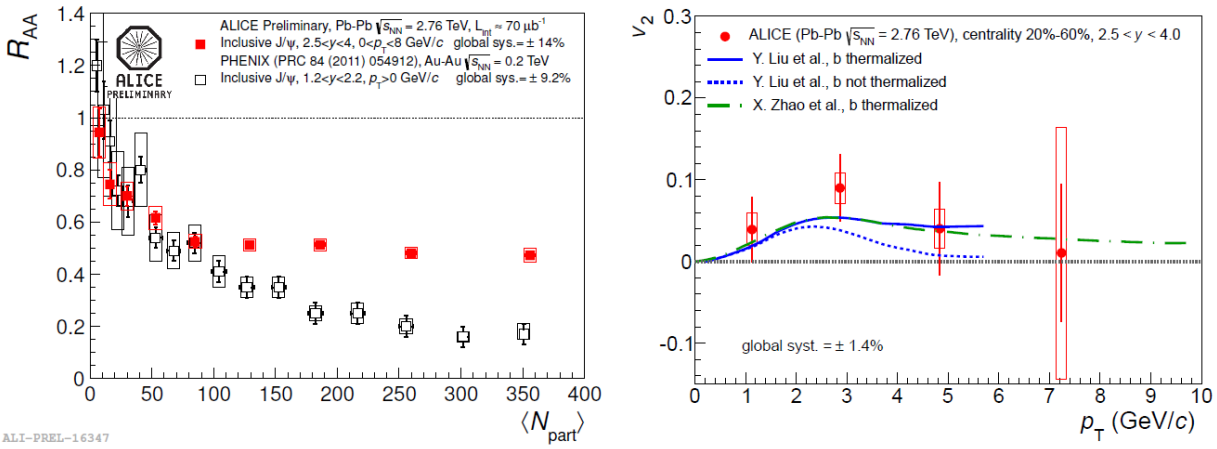

Fig. 8. Inclusive J/ψ R_{AA} as a function of the number of participants (left) and v_2 as a function of p_T (right) at the forward rapidity (from Refs. [9, 10])

7. Proton-lead results

Proton-nucleus collisions are very important for discrimination between the initial state cold nuclear matter effects in heavy ion collisions and the effects of the hot QCD matter dynamics. During a short pilot *p*-Pb run at $s_{NN}^{1/2} = 5.02$ TeV in September 2012, ALICE collected 0.9 μb^{-1} of minimum bias triggers and published first results on these data [11, 12].

Figure 9 (left) shows the pseudorapidity dependence of the charged particle density in non-single-diffractive *p*-Pb events measured by ALICE [11] in comparison with theoretical predictions. The best agreement of theory with experiment is found for the DPMJET model and HIJING2.1 with the shadowing parameter s_g tuned to describe RHIC *d*-Au data, while the gluon saturation models predict a steeper pseudorapidity dependence. The midrapidity particle density was also scaled to the number of participants and compared to few measurements at lower energies showing the trend similar to the *pp* energy dependence.

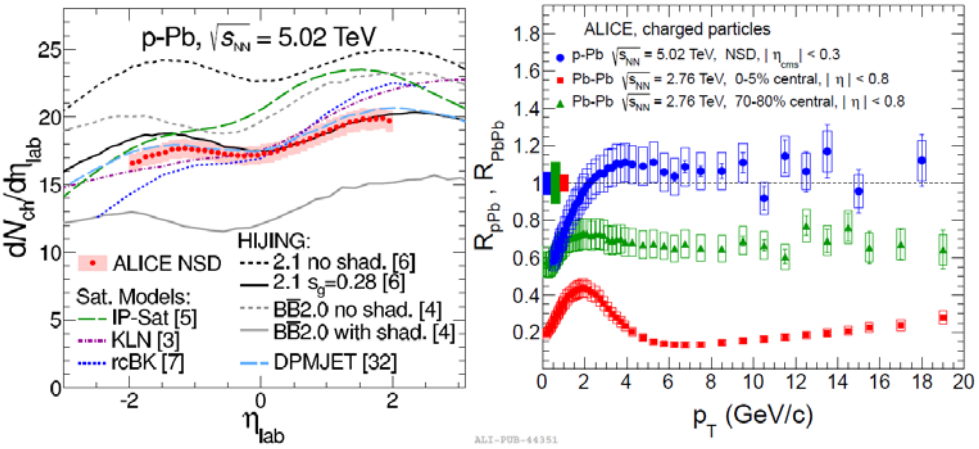

Fig. 9. Pseudorapidity density of charged particles measured in non-single-diffractive *p*-Pb collisions at $s_{NN}^{1/2} = 5.02$ TeV compared to theoretical predictions [11] (left). The nuclear modification factor in *p*-Pb and Pb-Pb collisions at the LHC [12] (right)

ALICE has also measured the nuclear modification factor R_{pPb} of charged particles as a function of the transverse momentum [12]. Figure 9 (right) presents the results in comparison to R_{AA} in central and peripheral Pb-Pb collisions measured with ALICE at $s_{\mathrm{NN}}^{1/2} = 2.76$ TeV. The observed R_{pPb} is consistent with unity at the transverse momentum above 2 GeV/c indicating that the strong suppression of hadron production measured in Pb-Pb collisions at the LHC is not an initial state effect but it is a consequence of jet quenching in the hot QCD matter.

In the beginning of 2013, ALICE collected 12 nb^{-1} of pA data allowing to make further progress in understanding of cold nuclear matter effects.

8. Study of the nuclear modification factor for neutral particles by the PNPI team

The PNPI team participates in an analysis of the data to determine the factors of nuclear modification for neutral hadrons at intermediate and high transverse momenta using the approaches developed in studies performed at RHIC. Standard particle identification techniques like measurements of the particle time-of-flight or ionization losses apparently have a very limited application in this kinematic region. Another problem is a limited statistics available for the analysis.

One of the possible solutions is a measurement of the hadron multi-particle decays with at least one gamma quantum or one neutral meson in the final state. The reconstruction of these decays benefits from the use of the high energy resolution PHOS electromagnetic calorimeter (that provides the means to measure and identify high energy photons, π^0 and eta-mesons) and online trigger selecting only events containing high energy clusters. We analysed minimum bias data samples accumulated by ALICE in 2010 for $p + p$ collisions at $s^{1/2} = 7$ TeV. So far, only a few decay channels for light hadrons such as $\omega \to \pi^0\pi^+\pi^-$, $\eta \to \pi^0\pi^+\pi^-$, $\omega \to \pi^0\gamma$, $K_s \to \pi^0\pi^0$, and $\eta' \to \eta\pi^+\pi^-$ have been considered. The choice of the particles is motivated by their large production rates at intermediate and high transverse momenta: $\omega/\pi^0 \approx 1$, $\eta/\pi^0 \approx K_s/\pi^0 \approx 0.45$, $\eta/\pi^0 \approx 0.25$. The decay modes have relatively large branching ratios: BR($\omega \to \pi^0\pi^+\pi^-$) = (89.2 ± 0.7) %, BR($\eta \to \pi^0\pi^+\pi^-$) = (22.74 ± 0.28) %, BR($\omega \to \pi^0\gamma$) = (8.28 ± 0.28) %, BR($K_s \to \pi^0\pi^0$) = (30.69 ± 0.05) %, BR($\eta' \to \eta\pi^+\pi^-$) = (43.4 ± 0.7) %. These are important considerations for the first ALICE data samples suffering from low integrated luminosities. Later, when all analysis difficulties are resolved and new high-luminosity data samples are accumulated, we will expand this study on the sector of heavy hadrons such as $D^0 \to \pi^0\pi^+K^-$ *etc*., and heavier collision systems.

Another solution is based on reconstruction of peaks in the invariant mass distribution from decay of light hadrons without identification of the daughter particles. So far, we analysed only $\phi \to K^+K^-$ decay in $p + p$ collisions at $s^{1/2} = 2.76$ and 7 TeV, p + Pb collisions at $s^{1/2} = 5.02$ TeV, and Pb + Pb collisions at $s^{1/2} = 2.76$ TeV by combining reconstructed charged tracks of opposite sign in pairs and assigning to all particles in these tracks the mass of a charged kaon. This analysis benefits from a small natural width of the ϕ-meson (Γ = 4.26 ± 0.04 MeV), large branching ratio BR($\phi \to K^+K^-$) = (48.9 ± 0.5) %, and high momentum resolution of the tracking system.

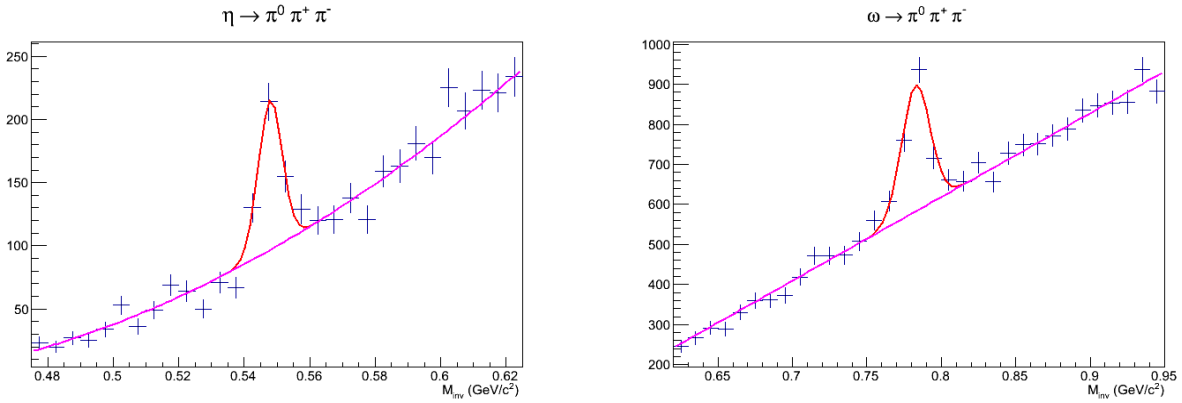

Fig. 10. Invariant mass distributions for ($\pi^0\pi^+\pi^-$) combinations

In this article, we present the results obtained by the PNPI team for light hadrons after about one year of work. The presented results are for $p + p$ collisions; they have been approved by the collaboration and can be shown in public. The remaining $p + p$ and heavy ion results of our analyses are in an advanced state, and they hopefully will be released for public next year.

Figure 10 shows an example of invariant mass distributions obtained for $(\pi^0\pi^+\pi^-)$ combinations. One can clearly see peaks from decay of η and ω mesons. The reconstructed masses of hadrons are in agreement with the PDG values. The widths of the peaks are in agreement with the values expected from simulations and equal to ~ 4 MeV/c^2 and ~ 12 MeV/c^2, respectively. Small values of the peak widths are achieved due to high energy resolution of the PHOS calorimeter and small difference in masses between the original particle and the decay products.

Figure 11a shows the invariant differential production cross section measured for the ω meson in $p + p$ collisions at $s^{1/2}$ = 7 TeV. The particle production was measured in a wide range of the transverse momentum 2–16 GeV/c. This is the first measurement in ALICE that simultaneously utilizes particle reconstruction in the calorimeter and tracking system. Figure 11b shows the ω/π ratio as a function of the transverse momentum measured in $p + p$ collisions at different energies, $s^{1/2}$ = 62–7000 GeV. This plot summarizes world-wide available measurements for the ω meson at high-p_T in $p + p$ collisions. It is interesting to note that the ratio does not depend on the collision energy within the uncertainties.

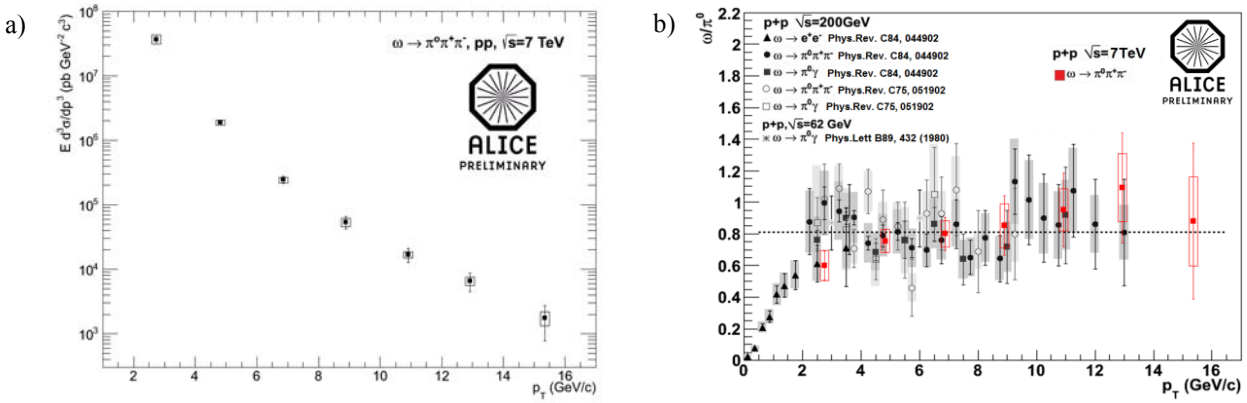

Fig. 11. a) Invariant differential production cross section measured for ω meson in $p + p$ collisions at $s^{1/2}$ = 7 TeV. b) ω/π ratio as a function of the transverse momentum measured in $p + p$ collisions at different energies, $s^{1/2}$ = 62–7000 GeV

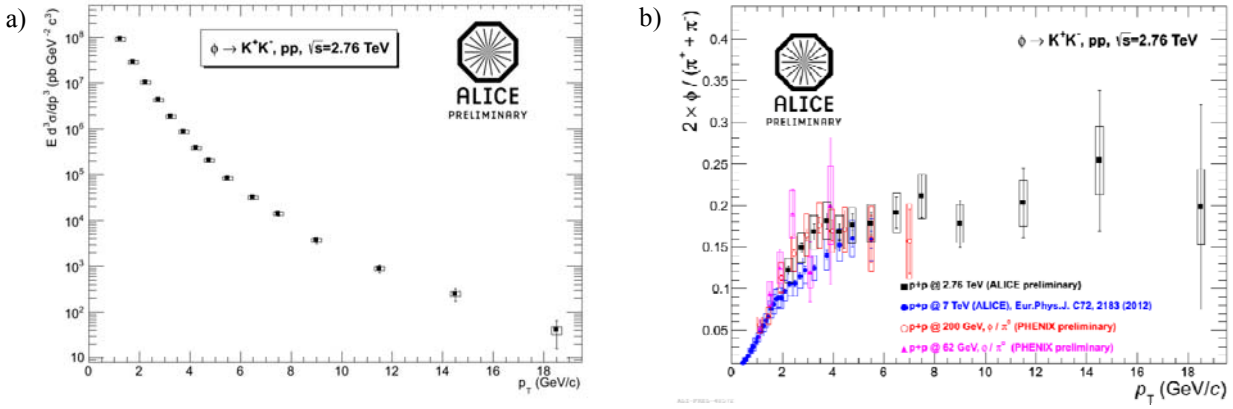

Fig. 12. a) Invariant differential yields measured for the φ meson in $p + p$ collisions at $s^{1/2}$ = 2.76 TeV. b) φ/π ratio as a function of the transverse momentum measured in $p + p$ collisions at different energies, $s^{1/2}$ = 62–7000 GeV

Figure 12a shows the invariant differential yields measured for the φ meson in $p + p$ collisions at $s^{1/2}$ = 2.76 TeV in a range of the transverse momentum 1–20 GeV/c. This is the first measurement for the φ meson at such a high momentum, previous measurements at RHIC spanning over a range

of the transverse momentum up to 7 GeV/c only. Figure 12b shows the ϕ/π ratio as a function of the transverse momentum measured in $p + p$ collisions at different energies, $s^{1/2}$ = 62–7000 GeV. As in the case of the ω meson, this ratio does not depend on the collision energy within the uncertainties.

Measurements of ω and ϕ contribute to precision tests of the pQCD at high p_T, in particular of the currently available parameterizations for fragmentation functions. The ω and ϕ mesons as vector mesons are more directly related to the partonic interactions as compared to pions or kaons, which often emerge as products of decay of more massive particles. The ω and ϕ mesons are also important components of different cocktails crucial for measurements of heavy flavor leptons and direct photons.

The results obtained in $p + p$ collisions were used to estimate the nuclear modification factors for the ϕ meson in Pb + Pb collisions at $s_{NN}^{1/2}$ = 2.76 TeV. Figure 13 shows the nuclear modification factors at different centralities measured as a function of the transverse momentum. The p_T range of the measurements is limited by the available Pb + Pb data and will be extended up to 20 GeV/c in our study. The results for ϕ are also superimposed in these plots with the factors measured for unidentified charged hadrons ($h^{\pm}$). The production of the ϕ meson at intermediate p_T-values is suppressed even in the peripheral (60–80 %) collisions. As for other light hadrons, the suppression gradually increases with the centrality and reaches the maximum in the most central (0–10 %) collisions. The production of the ϕ meson is less suppressed here than that of charged hadrons, which is similar to what was previously observed at RHIC. In the latter case, the observed effect was explained by parton recombination as a dominating particle production mechanism in this kinematic region. For further studies, it is crucial to extent the p_T range of these measurements (coming soon) and to compare the factors obtained for different identified light hadrons.

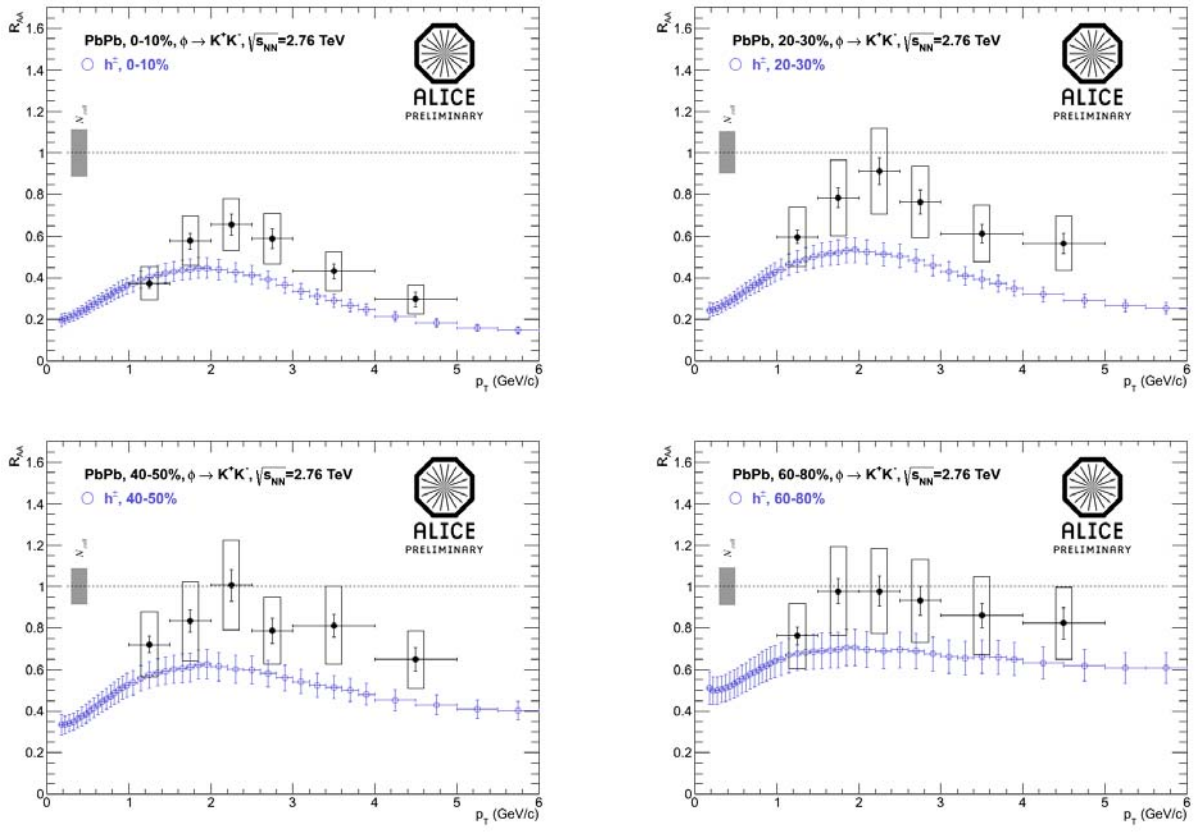

Fig. 13. Nuclear modification factors for the ϕ meson and charged hadrons as a function of the transverse momentum. Panels correspond to different centrality bins from 0–10 % (top-left) to 60–80 % (bottom-right)

9. Study of the heavy ion ultraperipheral collisions in the ALICE kinematics

From the RHIC studies it is well recognized now that the hot dense medium created in the first moment of the central collisions of heavy ions is dominated by the gluons carrying a small fraction x of the momentum of colliding nucleons. In the kinematics of RHIC, the specific values of x are of the order of 10^{-2}, and it is estimated that the nuclear gluon density $G_A(x)$ is suppressed as compared to $G_A(x) = AG_N(x)$ by a factor of about 0.8–0.9. The energy of colliding ions at the LHC is 15 times higher, hence the gluons with x in the range 10^{-3}–10^{-4} will dominate since the nucleon gluon density is known to grow as $x^{-0.2}$ with a decrease of x. The nuclear gluon density in this region of x has not been measured so far, while theoretical calculations of this quantity differ by a factor of about 3–4 due to uncertainties in the estimates of the nuclear gluon shadowing at small x in different approaches. For example, the leading twist gluon shadowing model predicts a much stronger effect than calculations in the higher twist approach. Hence, determination of $G_A(x)$ from independent measurements is a problem of key importance in a study of the properties of the QGP formed in heavy ion central collisions at the LHC.

According to the UltraPeripheral Collision (UPC) group studies, the measurements of the J/ψ photoproduction in ultraperipheral Pb + Pb collisions could be one of the most promising and clean method to obtain information on the behaviour of the nuclear gluon density at small x and to clear up the role of effects of the gluon screening in heavy nuclei since according to the perturbative QCD the cross section for this process is proportional to the squared nuclear gluon density.

During the heavy ion run in 2010–2011, the data on J/ψ coherent photoproduction in Pb + Pb UPC at 2.76 TeV were taken using a special ultraperipheral trigger. To select the ultraperipheral events, no activity other than that with the muon tracks in the TPC, FMD and V0 detectors is required. In order to estimate systematics due to noise in these detectors, a special data sample with an empty trigger was analysed. It appeared that in 0.3 % of these events the multiplicity of the FMD exceeds the threshold. As the TPC is a slow detector integrating events within ~ 0.1 ms, tracks were observed in ~ 6 % of the empty trigger events for $z > 20$ cm. All these effects were taken into account during the analysis.

The final goal of the analysis is determination of the J/ψ photoproduction cross section. So, the measured J/ψ yield should be divided by the efficiency of registration and the integral luminosity. In order to estimate the efficiency of the detector, a special event generator based on the perturbative QCD approach was developed, and simulations within the AliRoot using realistic OCDB data were performed.

The determined experimental values of the cross section for PbPb → PbPb J/ψ production were compared [13] to a number of predictions and appeared to be in better agreement with those which calculated the coherent J/ψ photoproduction on nuclear targets in the leading order (LO) pQCD taking into account the nuclear gluon shadowing. However, it is reasonable to reduce as much as possible the model dependence in comparisons of the experimental cross sections with those of different model calculations. The best strategy to achieve this goal is to analyse the ALICE results in terms of the nuclear suppression factor $S_{exp}(W_{\gamma p})$ defined as the ratio of the coherent photoproduction cross section $\sigma^{exp}{}_{\gamma Pb \to PbJ/\psi}(W_{\gamma p})$ at the given value of the centre-of-mass energy $W_{\gamma p}$ measured in the ultraperipheral ion collisions to the cross section $\sigma^{IA}{}_{\gamma Pb \to PbJ/\psi}(W_{\gamma p})$ calculated in the impulse approximation (IA), which neglects all nuclear effects except those for coherence:

$$S_{exp}(W_{\gamma p}) = [\sigma^{exp}{}_{\gamma Pb \to PbJ/\psi}(W_{\gamma p}) / \sigma^{IA}{}_{\gamma Pb \to PbJ/\psi}(W_{\gamma p})]^{1/2}.$$

Such a definition of S_{exp} $(W_{\gamma p})$ for coherent vector meson photoproduction on a nuclear target corresponds to the standard estimate of the nuclear suppression in terms of A_{eff}/A. Since the nucleus remains intact in the considered process, the transverse momentum distribution of J/ψ is dictated by the elastic nuclear form factor F_A (t). Hence, the cross section in the impulse approximation can be written as

$$\sigma^{IA}{}_{\gamma Pb \to PbJ/\psi}(W_{\gamma p}) = d\sigma_{\gamma p \to pJ/\psi}(W_{\gamma p}, t = 0) / dt \int_{t_{min}}^{\infty} dt\, |F_A(t)|^2.$$

The forward differential cross section for the process $\gamma p \to pJ/\psi$ can be found from the experimental data measured at HERA, FNAL, CERN, while the nuclear form factor of Pb is well known from the studies of *e*Pb and *p*Pb elastic scattering experiments. It is important to point out that the suppression factor determined in this way is practically model independent since the estimate of the cross section in the impulse approximation is based on experimental data. This analysis was realized by the PNPI team participating in the ALICE Collaboration, and the results are compared to calculations of the suppression factors within the framework of the leading order perturbative QCD. In this theoretical approach, the nuclear suppression factor is equal to the ratio of the nuclear gluon density G_A (x, μ^2) to the gluon density in the nucleon (x is the fraction of the nucleon momentum carried by a gluon and μ^2 is the hard scale in J/ψ photoproduction):

$$S(W_{\gamma p}) = GA(x, \mu^2)/AG_N(x, \mu^2).$$

Hence, within the LO pQCD the suppression factor characterizes the nuclear gluon shadowing. The results of this analysis are published in Ref. [14] and are presented in Fig. 14.

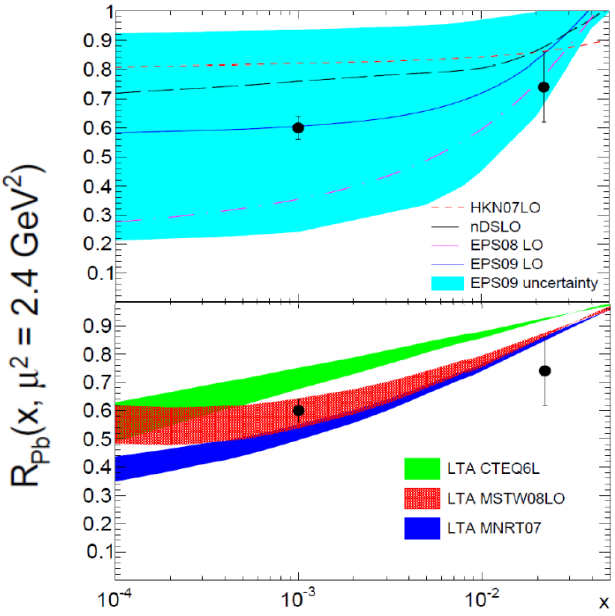

Fig. 14. Comparison of the nuclear suppression factor determined from the ALICE measurement of the coherent J/ψ photoproduction in ultraperipheral PbPb collisions at 2.76 TeV with nuclear gluon shadowing predicted in various theoretical approaches. The top panel presents a comparison with the nuclear gluon shadowing found from the Global nuclear PDF analyses of the DIS and DY processes on nuclear targets. The bottom panel compares the ALICE results to predictions of calculations of the nuclear gluon shadowing in the Leading Twist Approximation with three sets of the gluon distributions in the proton: CTEQ6L, MSTW08, and MNRT07

From a comparison of $S(W_{\gamma p})$ with $S_{exp}(W_{\gamma p})$, one finds that the ALICE measurements give the first direct experimental evidence of a rather strong nuclear gluon shadowing close to that which was obtained from the global fit nuclear parton density distribution analysis EPS09 and was predicted in the Leading Twist approximation (LTA) at small $x \sim 10^{-3}$ and at the scale 2.5–3 GeV^2.

10. Conclusion

Based on the analysis of the data collected during the 2010–2013 runs with proton-proton, proton-ion and ion-ion beams, the ALICE Collaboration has published already more than 50 papers devoted to a study of the produced extreme states of the nuclear matter. The PNPI team actively participates in all stages of this experimental study starting from the data taking during the runs up to the final data analysis. A special attention of the PNPI team in the data analysis is focused on the following two topics: the nuclear modification of the yield of particles with large transverse momenta and the investigation of the heavy quarkonium photoproduction in ultraperipheral ion collisions.

References

1. K. Aamodt *et al.* (the ALICE Collaboration), *The ALICE experiment at the CERN LHC*. JINST **3**, S08002 (2008).
2. K. Oyama for the ALICE Collaboration, *ALICE Detector status and upgrade plans*. EPJ Web Conf. **49**, 02002 (2013).
3. B. Abelev *et al*. (the ALICE Collaboration), *Upgrade of the ALICE Experiment.* The Muon Forward Tracker. CERN-LHCC-2013-**014**.
4. E. Kryshen for the ALICE Collaboration, *ALICE Status and Plans*, PoS IHEP-LHC-2012 (2012) 002.
5. K. Aamodt *et al*. (the ALICE Collaboration), *Charged-particle multiplicity density at mid-rapidity in central Pb-Pb collisions at 2.76 TeV*, Phys. Rev. Lett. **105**, 252301 (2010).
6. K. Aamodt *et al*. (the ALICE Collaboration), *Elliptic flow of charged particles in Pb-Pb collisions at 2.76 TeV*, Phys. Rev. Lett. **105**, 252302 (2010).
7. K. Aamodt *et al*. (the ALICE Collaboration), *Suppression of charged particle production at large transverse momentum in central PbPb Collisions at 2.76 TeV*, Phys. Lett. B **696**, 30 (2011).
8. B. Abelev *et al*. (the ALICE Collaboration), *Suppression of high transverse momentum D mesons in central Pb-Pb collisions at 2.76 TeV*, JHEP **1209**, 112 (2012).
9. B. Abelev *et al*. (the ALICE Collaboration), *J/ψ suppression at forward rapidity in Pb-Pb collisions at 2.76 TeV*. Phys. Rev. Lett. **109**, 072301 (2012).
10. E. Abbas *et al*. (the ALICE Collaboration), *J/ψ elliptic flow in Pb-Pb collisions at 2.76 TeV*. arXiv:1303.5880 [nucl-ex].
11. B. Abelev *et al*. (the ALICE Collaboration), *Pseudorapidity density of charged particles in p-Pb collisions at 5.02 TeV*, Phys. Rev. Lett. **110**, 032301 (2013).
12. B. Abelev *et al*. (the ALICE Collaboration), *Transverse momentum distribution and nuclear modification factor of charged particles in p-Pb collisions at 5.02 TeV*, Phys. Rev. Lett. 110, 082302 (2013).
13. E.Abbas *et.al.* (the ALICE Collaboration), *Charmonium and e^+e^- pair photoproduction at midrapidity in ultraperipheral PbPb collisions at 2.76 TeV*, arXiv:1305.1467 [hep-ex], 2013.
14. V. Guzey, E. Kryshen, M. Strikman, M. Zhalov, *Evidence for nuclear gluon shadowing from the ALICE measurements of PbPb ultraperipheral exclusive J/ψ production*, Phys. Lett. B **726**, 290 (2013).

ON THE WAY TO CRYSTAL COLLIMATION OF THE LHC BEAMS

Yu.M. Ivanov, A.S. Denisov, Yu.A. Gavrikov, L.P. Lapina, L.G. Malyarenko, V.V. Skorobogatov

1. Introduction

In the end of the 90-s, the IHEP and PNPI groups studied short bent silicon crystals with high-energy protons at U-70 and showed that exploiting the multi-pass (or multi-turn) mechanism (experimentally proven at the CERN SPS by H. Akbari *et al*., 1993) one can extract from the accelerator a beam of the intensity up to 6×10^{11} protons per cycle, which is five orders of magnitude higher than that reached in previous experiments, the beam extraction efficiency exceeding 40 % (A.G. Afonin *et al*., 1998). Two approaches to bend short crystals were developed in these studies and realized in strip and O-shaped crystals (Figs. 1 and 2). Improvements of the bent crystal quality in further experiments at IHEP with participation of the BNL, CERN, and INFN groups made possible to enhance the crystal extraction efficiency up to 85 % and to bring the intensity of the beam extracted from U-70 up to 10^{12} protons per cycle (A.G. Afonin *et al*., 2001). As a result, the bent crystals were applied to the main beam and to the halo particles. Thus, the extraction and collimation schemes with many crystals working simultaneously were developed [1].

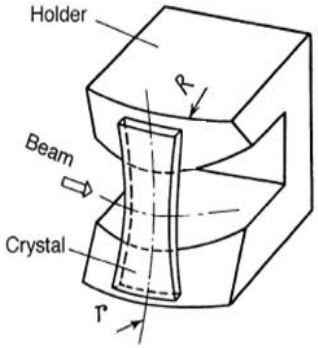

Fig. 1. Strip crystal: the curvature across the strip (in the beam direction) is induced by bending along the strip (the so called anticlastic effect)

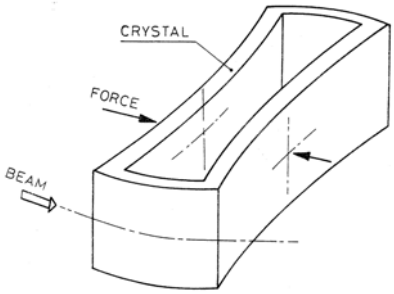

Fig. 2. O-shaped crystal: the curvature in the beam direction is induced by compressing the middle part of the crystal

Then, two crystal collimation experiments using the O-shaped crystals were performed at RHIC and Tevatron. At RHIC, the experimental set-up was mounted at a non-optimal location with high angular divergence of the beam that increased the background rate at the STAR detector (R.P. Fliller *et al*., 2006). Later, the RHIC set-up was moved to FNAL, where an experiment at Tevatron in better conditions showed that replacing a standard 5-mm tungsten target (primary collimator) with a crystal results in reduction of the beam losses in the CDF experiment by a factor of two and in reduction of irradiation of the superconducting magnets by a factor of five. Also, it was shown that the secondary collimator could be placed further away from the beam, thus reducing the machine impedance (R.A. Carrigan *et al*., 2007).

The promising results at IHEP and FNAL encouraged the H8-RD22 program at the CERN SPS, which later became the UA9 experiment and now led to the LUA9 project aiming to improve with crystals the efficiency of the LHC cleaning system. The realization of the project should reduce the background in the collider detectors and avoid quenching of superconducting magnets at the highest luminosities.

Below we describe our recent studies performed at PNPI, IHEP, and CERN with the aim to develop a crystal collimation system for the LHC.

2. Elastic quasi-mosaic effect in silicon and development of bent quasi-mosaic crystals for channeling

A significant advance was reached at PNPI with the development of a new method to produce bent silicon crystals for channeling using the elastic quasi-mosaic effect. This phenomenon was formerly discovered and well studied in quartz (O.I. Sumbaev, 1957 and 1968) and widely used in crystal-diffraction γ- and *X*-ray spectrometry. The effect arises from anisotropic properties of the crystal, which lead to curving

of normal cross sections of the specially cut single crystal quartz plates when they are being bent, thus resulting in broadening diffraction lines as if the single crystal has got a mosaic structure.

In our studies of bent crystals with *X*-rays, the quasi-mosaic effect was observed in silicon [2]. A plate proper cut in respect to the silicon lattice and a bending device with a plate for channeling are shown in Figs. 3 and 4. The measured bending angles of the (111) atomic planes in silicon were found to be in agreement with theoretical estimations and within a range optimal for crystal collimation of high energy charged particle beams (from zero to several hundred μrad).

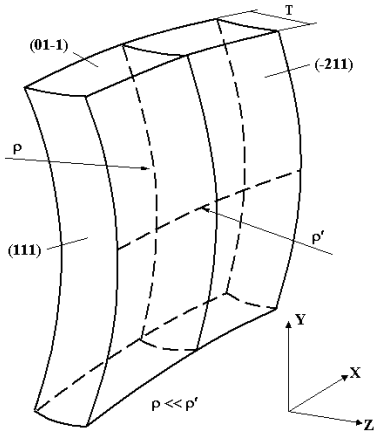

Fig. 3. Elastic quasi-mosaic effect in a bent silicon plate: bending of the plate to a cylinder of a radius ρ results in quasi-mosaic curving of the (111) crystallographic planes along the thickness *T*. The radius ρ' characterizes the curvature induced by anticlastic forces

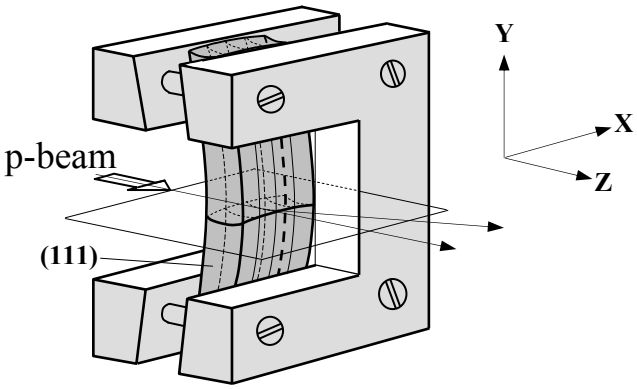

Fig. 4. Quasi-mosaic silicon plate in a bending device. The channeling Si (111) plane coincides with the vertical narrow face of the plate

3. Extraction of a high intensity 70 GeV proton beam with quasi-mosaic silicon crystals at IHEP

The evident advantages of quasi-mosaic crystals are better heat dissipation from the interaction area and a smaller crystal size in the beam direction in respect to the strip and O-shaped crystals. These features were used in the IHEP-PNPI experiment on crystal extraction of a very intensive 70 GeV proton beam at IHEP.

For this experiment, a silicon plate of 2.65(*Z*) × 30(*X*) × 60(*Y*) mm^3 size was prepared and bent to the radius of 1.9 m providing a quasi-mosaic bending of the (111) planes approximately 400 μrad along the plate thickness that was measured with *X*-rays before installation into the accelerator ring. The device was similar to that shown in Fig. 4.

In the proton extraction experiment, the intensity of the extracted beam reached 4×10^{12} protons per cycle and exceeded by a factor of 4 the best previous results. The beam intensity in the ring was equal to 5.5×10^{12} protons per cycle, so the efficiency of the multi-turn crystal extraction with the quasi-mosaic crystal was ~ 73 %. The duration of the extracted beam was ~ 1 second. The heating of the crystal was measured with a thermocouple, and the crystal temperature was found to be ~ 50 °C. So, this experiment has demonstrated a feasibility of extraction of very intense beams from accelerators with crystals and has shown a significant potential to increase the extracted intensity.

4. Observation of the volume reflection effect with quasi-mosaic silicon crystals at IHEP

Details of channeling in quasi-mosaic silicon crystals were studied with the external and internal 70 GeV proton beams at IHEP. For these studies, samples with sub-millimeter thickness were prepared according to simulations, which indicated the advantage of very short (along the beam) crystals. In crystals of small thickness, the multiple Coulomb scattering becomes negligible, and this feature turned out crucial to observe for the first time the volume reflection effect predicted earlier (A.M. Taratin and S.A. Vorobiev, 1987). This effect arises from reflection of protons by a bent atomic plane at the tangency point and results in angular deflection of the reflected particle opposite to the atomic plane bending (Fig. 5a – d). The process

competes with the volume capture effect discovered at PNPI earlier (O.I. Sumbaev and V.M. Samsonov, 1982).

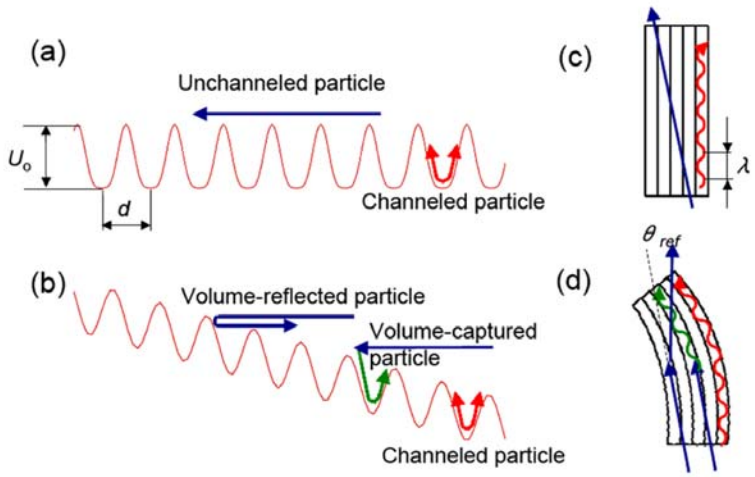

Fig. 5. (a) Periodic planar potential in a straight crystal for positively charged particles. The arrows show a channeled particle with the oscillatory motion in the potential well and a non-channeled particle, whose transverse energy is larger than the depth of the potential well U_0. (c) Schematic representation of the particle trajectories in a straight crystal. (b) Periodic planar potential in a bent crystal for positively charged particles. The arrows show the volume-reflected, volume-captured, and channeled particles. (d) Schematic representation of the particle trajectories in a bent crystal

A scheme of the experiment at IHEP is shown in Fig. 6 [3]. The crystal was mounted on a rotary table providing a 4 mm overlapping in the *X*-direction with a wide parallel beam of 70 GeV protons. The beam had an intensity of 10^5 s^{-1} and a divergence of 15 μrad. The multiple scattering in the crystal was 13 μrad, so both the divergence of the incident beam and the beam scattering in the crystal were small as compared to the critical angle for channeling θ_c equal to 24 μrad. A silicon plate of $20(X) \times 60(Y) \times 0.72(Z)$ mm^3 size was bent to a radius of 0.48 m that induced a quasi-mosaic bending of the (111) planes with a radius of 1.7 m for an angle of 420 μrad. The anticlastic (saddle) radius in the *XZ*-plane was found to be 3.2 m in the middle of the plate, and it was larger near the clamped areas.

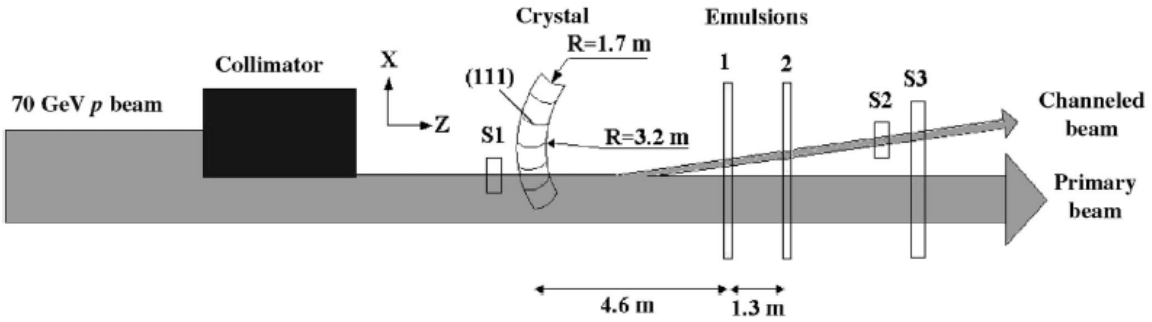

Fig. 6. Layout of the experiment at IHEP.
S1, S2, and S3 – scintillation counters

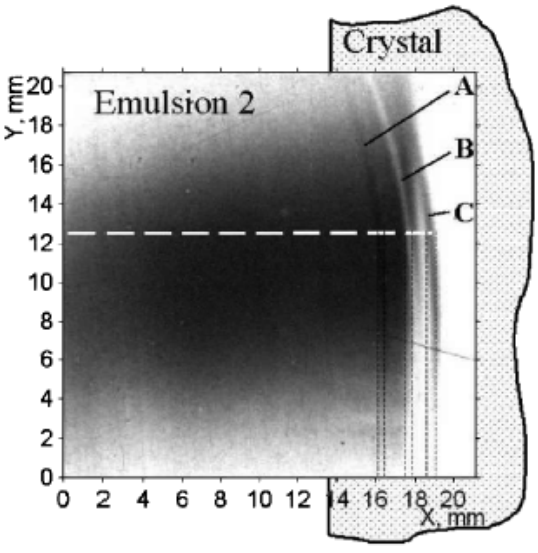

Fig. 7. Image of the proton beam on emulsion 2 (beam goes to the observer). The white dashed line indicates a trace of microscopic measurement. The black dashed lines show *X*-readings corresponding to the borders of lines A, B, and C

Images of the beam transmitted through the oriented crystal were measured with emulsions. They displayed three distinct curved lines A, B, and C (Fig. 7). The lines were well visible near the sharp edge of the primary beam formed by a single jaw collimator in front of the crystal. For both emulsions, the positions and widths of the observed lines were measured with a microscope.

An explanation of the experimental results is given in Fig. 8. Due to anticlastic forces, the (111) planes change their orientation along the *X*-direction. On the entry face in the area where incident protons are tangent to the (111) planes, the main part of protons is captured by channeling (rays between 5 and 6), producing a spot C. For protons tangent to the atomic (111) planes somewhere inside the crystal, a volume reflection takes place (rays in between 1 and 3). Out of the *X*-ranges for the channeling and volume reflection, the incident protons pass through the crystal and experience only multiple scattering (rays above ray 4 and below 2). In this case, there is an area depleted of protons in between the reflected and primary beams, denoted by B, and another area where primary and reflected protons mix, denoted by A. Above and below the mid-plane shown in Fig. 7, the picture is similar except for the shift of the projected spots due to a change of the anticlastic curvature in the vertical direction. As a result, the joint pattern on the emulsions comprises three lines (two black lines A and C and one light line B) of slightly curved shape.

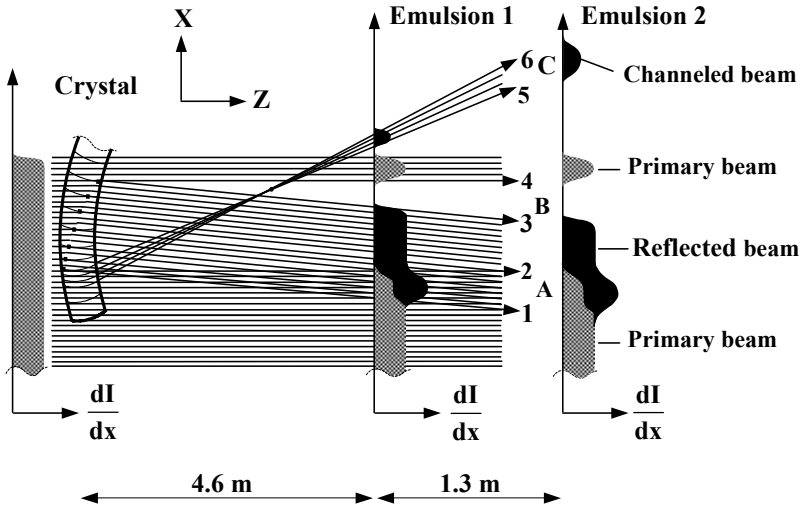

Fig. 8. Channeling and volume reflection in oriented quasi-mosaic crystal: interpretation of beam images on the emulsions (top view, protons go from left to right). The incident beam is shown as parallel and uniform. The dots within the crystal indicate tangency points of proton trajectories with the (111) atomic planes where the volume reflection takes place

The deflection angle of the channeled protons is estimated from the ratio of the distance between lines A and C to the distance between the crystal and the corresponding emulsion. Averaging the results over two emulsions, we find a value of the deflection angle (435 ± 6) μrad that agrees with the bending angle of the (111) planes measured with *X*-rays.

The deflection angle $2\theta_R$ of the reflected protons is estimated from the angular width of lines A and B as the ratio of the line width to the distance from the crystal to each emulsion. Averaging the widths of A and B, we find the deflection angle $2\theta_R$ equal to (39.5 ± 2.0) μrad, or (1.65 ± 0.08) θ_c in terms of the critical angle for channeling. The width of the volume reflected beam shows that the angular acceptance for volume reflection is determined by the bending angle of the atomic planes essentially exceeding the acceptance for channeling ($\approx \theta_c$).

The dark colour of line A demonstrates that the volume reflection is more intense than the channeling, so the volume reflection should play an important role in any application of bent crystals to beam manipulations. In fact, the observation of the volume reflection effect at IHEP resulted in an essential re-interpretation of the crystal collimation experiments at RHIC and Tevatron.

5. Study of the volume reflection effect in quasi-mosaic silicon crystals at PNPI

In the next experiment at PNPI, a bent quasi-mosaic silicon crystal was investigated with a narrow external parallel beam of 1 GeV protons (at IHEP a wide beam was used). This made possible to observe the channeling and volume reflection effects in the measured beam profiles separately, and thus to reveal the volume reflection effect in an evident manner [4].

The experimental layout is shown in Fig. 9. The beam was formed with two collimators distanced by ~ 31 m and with a deflecting magnet between them. In the horizontal plane, the width and divergence of the beam incident on the crystal were ~ 80 μm and ~ 160 μrad, respectively. The vertical size of the beam on the crystal was ~ 1 mm, and the beam intensity was ~ 2×10^4 protons per second.

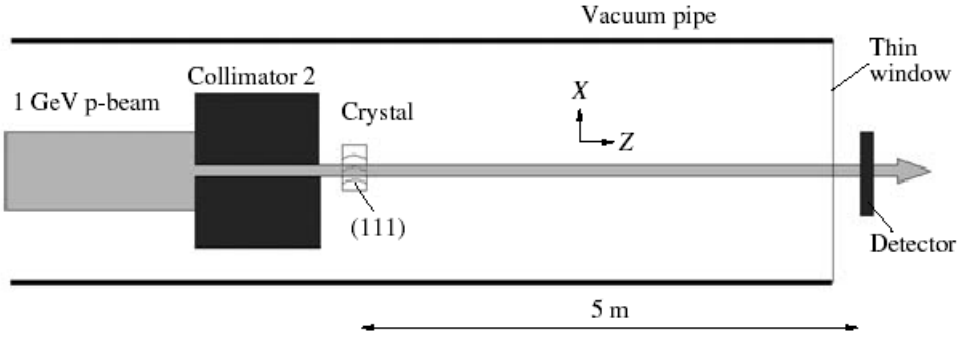

Fig. 9. Layout of the experiment on the observation of volume reflection with the 1 GeV proton beam at PNPI

The silicon plate thickness was 30 μm giving the multiple scattering angle of 105 μrad, which is smaller than the critical angle for channeling equal to 170 μrad for the (111) silicon planes in the case of 1 GeV protons. The plate was bent with a radius of 22 mm in the vertical plane by means of clamping in cylindrical mirrors with a hole of 3 mm in diameter at the centre for passing the proton beam. The quasi-mosaic bending of the (111) planes measured with *X*-rays was found to be ~ 380 μrad. The bent crystal was mounted on a rotary table attached to the exit of the second collimator. Position-sensitive detectors were placed at a distance of 5 m from the crystal outside the vacuum pipe.

Fitting experimental peaks, we found the probabilities of the volume reflection and channeling effects to be (0.71 ± 0.03) and (0.63 ± 0.03), respectively. The mean deflection angle of the protons volume reflected in the crystal was found to be (236 ± 7) μrad. These results confirmed in a clear and evident way the existence of the volume reflection effect in bent crystals.

6. Study of the volume reflection effect in bent silicon crystals with a 400 GeV proton beam at CERN

In 2006–2009, detailed studies of beam-crystal interactions were carried out at the CERN SPS in frames of the H8-RD22 Collaboration. The first experiments in these studies were devoted to measurements of the volume reflection effect with 400 GeV protons [5, 6].

The experimental layout shown in Fig. 10 consisted of a high precision goniometer (G) with crystals and various detectors to track particles [7]. The goniometer consisted of three high precision motion units, two linear and one angular. With the linear motions, the crystals were positioned with respect to the beam centre with an accuracy of several μm. With angular scans, the crystals were aligned with respect to the beam axis with an accuracy of 1.5 μrad. Scintillator counters were used to determine the beam transverse offset with respect to the crystal (S1 and S2), to provide the basic trigger signal for silicon detectors (S3 and S4), and to measure the beam divergence and the beam profile (S5 and S6). High statistics data were taken with a set of silicon micro-strip detectors (SD*n*) with the spatial resolution in the range 10–30 μm.

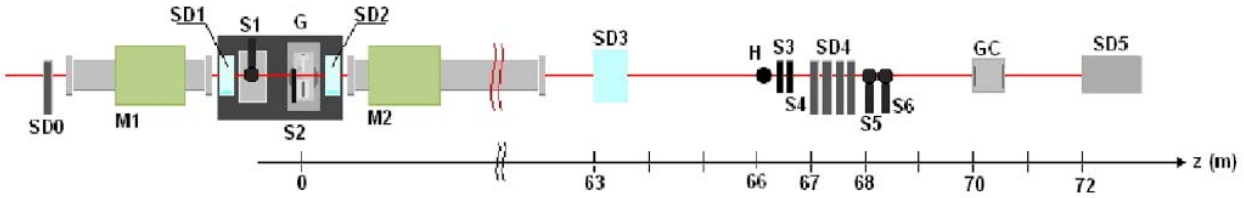

Fig. 10. H8-RD22 experimental set-up in 2006. M1 and M2 are two bending magnets – a part of the H8 beam transport line with no specific function for this experiment. See the text for more details

For the experiment, several quasi-mosaic and strip silicon crystals were prepared. In fact, the results of the measurements with all these crystals turned out to be very similar. A plot of an angular scan made with one of the strip crystals is presented in Fig. 11. This crystal had the (110) channeling planes bent due to anticlastic effect at an angle of 162 μrad along its 3 mm length in the beam direction. The multiple scattering angle of 400 GeV protons in this crystal was equal to 5.3 μrad, which is smaller than the critical angle equal to 10.6 μrad. The proton beam had a divergence of (8 ± 1) μrad and a spot size of about 1 mm.

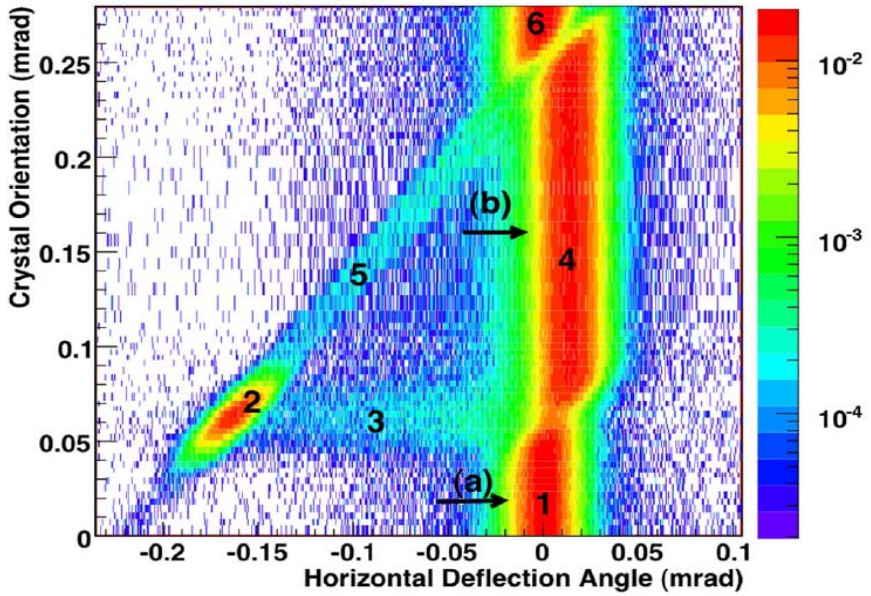

Fig. 11. Beam intensity recorded by the silicon micro-strip detectors as a function of the horizontal deflection angle (*X*-axis) and the crystal orientation (*Y*-axis). Six regions can be distinguished:
1 and 6 – non-channeling mode;
2 – channeling;
3 – dechanneling;
4 – volume reflection;
5 – volume capture.
A wider angular acceptance of the volume reflection as compared to that of channeling is clearly seen

The deflection angle of the channeled beam and the channeling efficiency were found to be (165 ± 2) μrad (in agreement with the value of the bending angle of the crystal) and ~ 55 %, respectively. The deflection angle of the volume reflected beam and the volume reflection efficiency were found to be ($13.9 \pm 0.2_{stat} \pm 1.5_{syst}$) μrad and ~ 98 %, respectively. The latter value is significantly larger than the maximal theoretical single-pass efficiency for channeling.

The trend of the volume reflection parameters (the deflection angle and efficiency) in a bent silicon crystal were investigated as a function of the crystal curvature [8]. The measurements were performed at six different curvatures, the experimental results and simulations are presented in Fig. 12a, b. The agreement between the experimental data, the analytical approach and the MC simulation is fairly good.

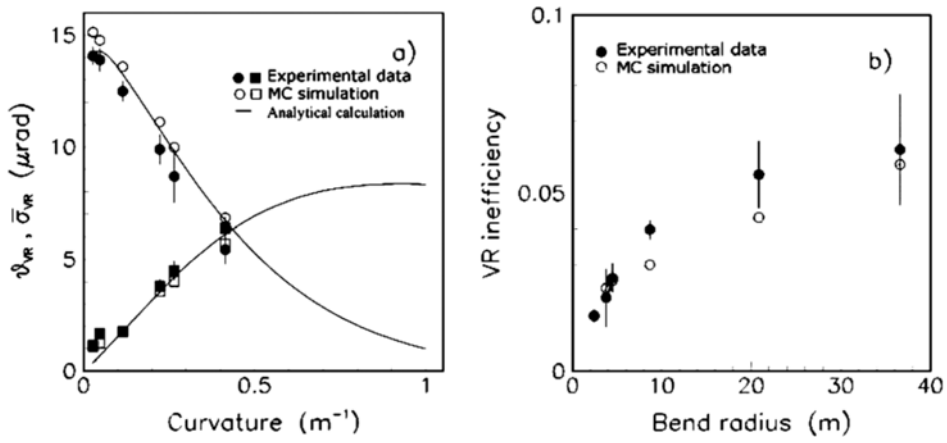

Fig. 12. Dependencies of the volume reflection parameters on the crystal curvature and the bending radius *R*: a – the deflection angle (dots) and its rms deviation due to potential scattering (squares) versus the crystal curvature; b – the volume reflection inefficiency versus the bending radius

Taking into account the observed dependences of the Volume Reflection (VR) parameters on *R*, the optimal bending radius for a short silicon crystal for beam deflection due to VR is found to be about $10R_c$.

The strong potential scattering of particles for *R* close to R_c shows that such a crystal can be used as an effective scatterer. The thickness of the crystal scatterer can be reduced down to the wavelength of the particle oscillations in the planar channel (60 μm for 400 GeV protons and 250 μm for 7 TeV protons). In this way, the inelastic losses of particles in the scatterer can be minimized.

7. Study of multiple volume reflection in bent crystals with a 400 GeV proton beam at CERN

Very high efficiency of volume reflection makes possible to use several crystals to increase the deflection angle of the volume reflected particles. The first experiment was performed with two aligned quasi-mosaic crystals [9]. Then, the multiple volume reflection of the proton beam was studied in detail with a five-crystal deflector [10]. A scheme of this experiment is shown in Fig. 13a, b.

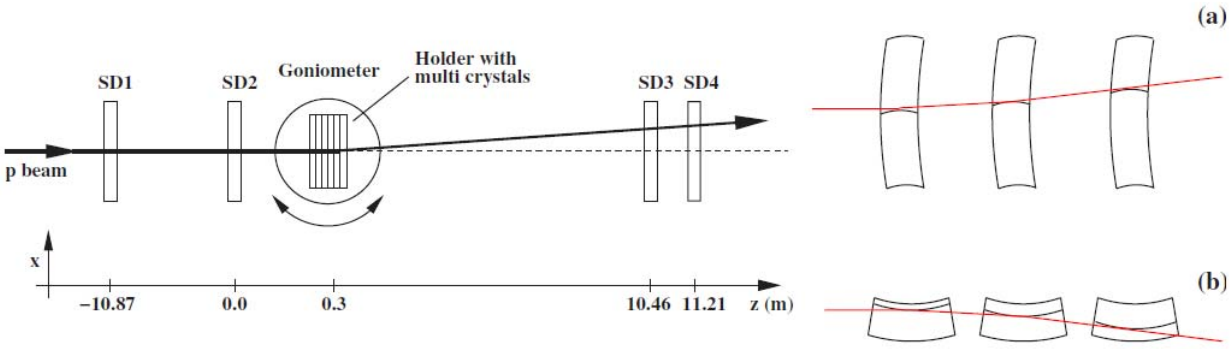

Fig. 13. Schematic layout of the experimental set-up used to study multiple volume reflection at the H8 beam line of the CERN SPS. The trajectory of a particle undergoing a sequence of volume reflections in a series of aligned crystals is schematically represented on the right for quasi-mosaic (a) and strip (b) crystals

In the aligned positions of five bent quasi-mosaic crystals (Figs. 13, 14), the deflection angle was determined to be (52.96 ± 0.14) μrad and the efficiency was found higher than 80 % for the angular acceptance at the deflector entrance of 70 μrad, the maximal efficiency value being (90 ± 1 ± 3) %.

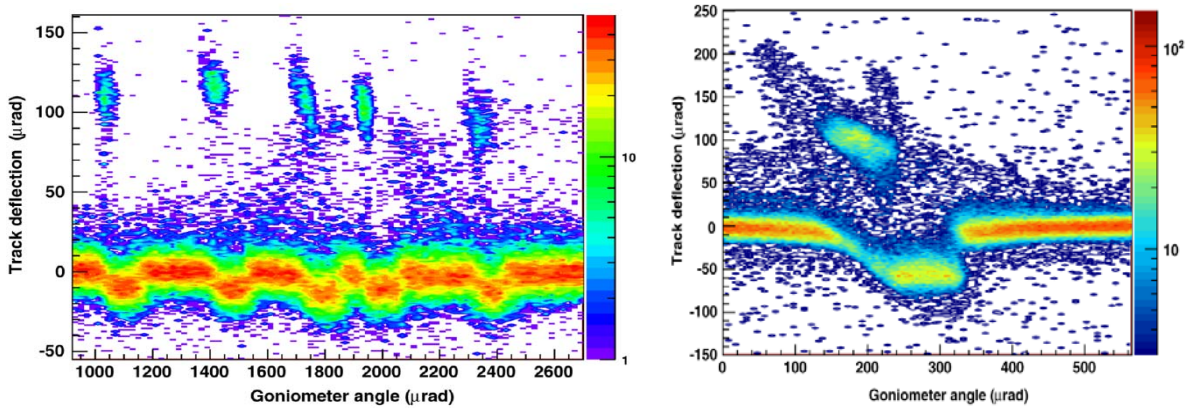

Fig. 14. Beam intensity distributions observed in the angular scans performed before (left) and after (right) the relative alignment of the five crystals. The beam intensity is reported as a function of the track deflection angle (vertical axis) in different goniometer angular positions (horizontal axis)

The experiments demonstrated that the mean deflection angle grows proportionally to the number of reflections, but the deflection efficiency is decreasing with the number of reflections due to volume capture of protons in each of the crystals. The volume-captured beam fraction was typically about $\varepsilon \approx 1.9$ % per reflection.

In the following experiments, we found that under a certain alignment the deflection efficiency can reach 88 % for eleven crystals [11]. Multiple volume reflection in single crystals was also observed [12].

In the whole, the studies of multiple-volume reflections in bent crystals resulted in the development of beam deflectors which have an efficiency exceeding the channeling efficiency and provide a much wider angular acceptance and the deflection angles sufficient for beam collimation.

8. Study of crystal collimation with proton and heavy ion beams at the SPS: the experiment UA9

The idea of crystal collimation in comparison with the traditional one is shown in Fig. 15a, b, where it is easy to see that the crystal deflects halo particles onto the absorber far from the absorber edge, thus decreasing scattering of halo particles back to the main beam.

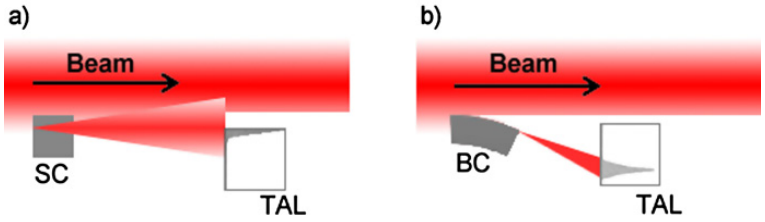

Fig. 15. (a) Collimation scheme using a solid state primary collimator scatterer (SC). (b) Collimation scheme with a bent crystal (BC) as a primary collimator. Halo particles are deflected and directed onto the absorber (TAL – Target Aperture Limitation) far from its edge

After extensive investigations of the beam-crystal interaction at the SPS H8 and H4 external beam lines in frames of the H8-RD22 Collaboration, the UA9 crystal collimation experiment in the SPS ring was proposed. It was approved in September 2008 and started its operation in 2009 [13].

The UA9 set-up consists of two stations [14]. The first station contains four goniometers with crystals of different types, which can be used alternately as a primary collimator. The second station contains a 60-cm-long tungsten absorber used as a secondary collimator. Between the two stations, there are: a Medipix pixel detector to observe the spatial distribution of the deflected particles and a two-sided LHC collimator to align the UA9 elements relative to the beam orbit and to scan the beam halo.

In the first dispersive area downstream the absorber, a TAL station with targets limiting the accelerator aperture is installed to detect the off-momentum halo fraction. Such particles, which have lost some momentum in the crystal or in the absorber, may escape from the collimation area. At the high dispersion area, they undergo an additional displacement from the orbit and may be detected.

The test beam was formed with 120 GeV or 270 GeV protons, typically in a single bunch with 10^9–10^{12} particles. Lead ion beams were used in the same range of energy per nucleon and with ten times less particles. In the storage mode, the beam lifetime ranged from a few minutes to 10 hours. The number of particles hitting the crystal was in the range of 10–10^3 protons per bunch with the duration of a few ns. To increase the total intensity and the loss rate, four, eight or 52 bunches were used.

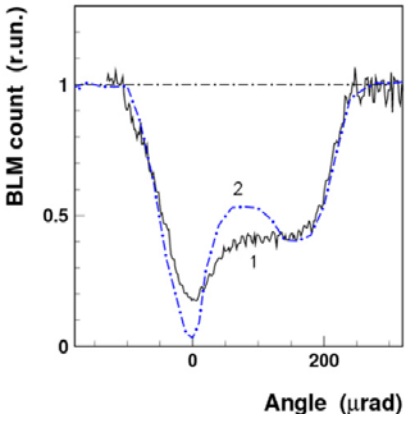

Fig. 16. 1 – dependence of the detector counts on the angular position of the crystal; 2 – the dependence of the number of protons inelastically scattered in the crystal on its orientation angle, as was obtained by simulation

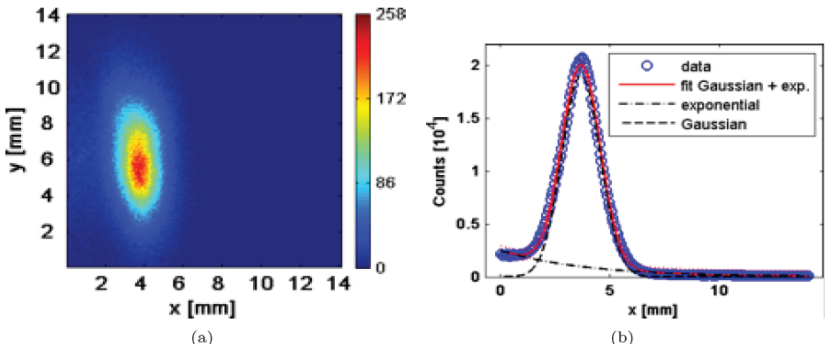

Fig. 17. Image of the beam deflected with the crystal (a) and its horizontal projection (b) obtained with the Medipix detector

A typical response of the beam loss counters to the angular scan of the crystal is shown in Fig. 16 [13, 15]. In the minimum of the loss count, the fraction of the beam halo channeled by the crystal is maximal. With the best crystals, the reduction of beam losses in the channeling state reached a factor of ~ 25.

A wide angular range of decreased beam losses to the right of the minimum is due to volume reflection of halo particles in the crystal.

Images of the deflected beam obtained with the Medipix detector [13] are shown in Fig. 17a, b. The channeling parameters of the crystals in the collimation position were studied by means of collimator scans. For two tested silicon crystals, the channeling efficiencies were found to be (75 ± 4) % and (85 ± 5) % [13].

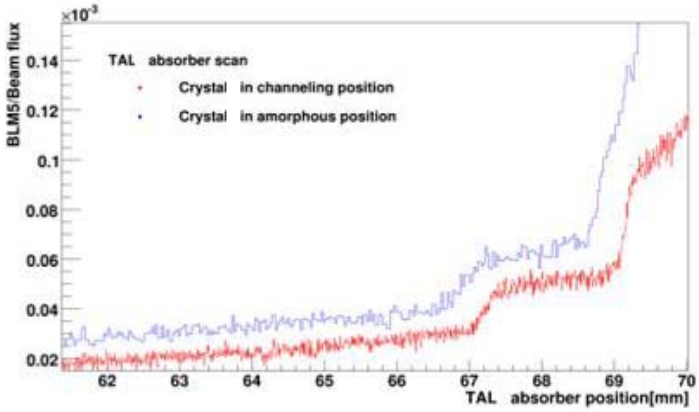

Fig. 18. Off-momentum collimation leakage for the crystal in channeling (red) and in amorphous (blue) positions. See the explanation in the text

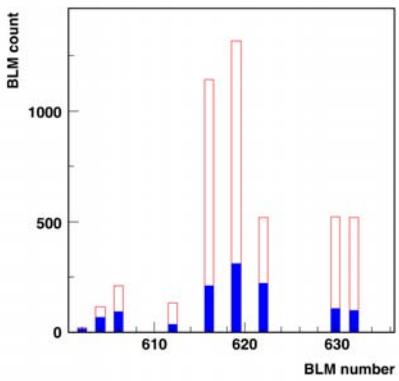

Fig. 19. Beam loss map in the SPS for the amorphous (red) and channeling (blue) orientations of the crystal

The fraction of beam halo particles escaping from the collimation devices was estimated by using the target of the TAL station [16]. Fig. 18 shows the dependence of the loss count (BLM) on the horizontal position of the target (absorber). The off-momentum collimation leakage for the crystal in the channeling mode was found to be reduced by a factor of about 5.

The stored multi-bunched beam was used to measure beam losses in regions of the SPS ring far from the crystal. Fig. 19 shows the beam losses detected 1 km downstream of the crystal [16]. It is seen that the losses for the channeling orientation are few times smaller than those for the amorphous one.

Summarizing, we can conclude that the UA9 results provide a solid demonstration of the potential advantage of the crystal-assisted collimation in colliders.

9. Study of crystal collimation with a 7 TeV proton beam at the CERN LHC: the LUA9 project

In 2011, to extend crystal collimation technology at the LHC, the LUA9 project was proposed [17]. In the project, it is supposed to install crystals close to the existing LHC primary collimators to provide a usage of the secondary collimators as halo absorbers. Beam crystal collimation is planned to test for all degrees of freedom: horizontal, vertical, skew and longitudinal. The crystal orientations are planned to control with an accuracy better than 1 μrad. The optimal channeling angle for the LHC is estimated to be ~ 50 μrad, the optimal crystal length along the beam being ~ 4 mm. It is proposed to carry out all necessary R&Ds during 2012–2014, to install first crystals at the LHC in 2014, and to start experimental studies in 2015.

We thank Yu.A. Chesnokov and his team for joint studies of channeling phenomena at IHEP, the HEPD PNPI leaders, especially A.A. Vorobyev, D.M. Seliverstov, and E.M. Ivanov, for advices and support of our studies at PNPI and CERN, our colleagues N.F. Bondar, B.A. Chunin, O.P. Fedorova, V.A. Gorbunov, A.V. Jelamkov, V.G. Ivochkin, S.V. Kosyanenko, M.A. Koznov, P.M. Levchenko, A.A. Petrunin, V.M. Suvorov, A.I. Schetkovsky, L.A. Schipunov, L.A. Vaishnene, S.A. Vavilov, E.P. Volkov, and N.P. Volkov for assistance, and the participants of the H8-RD22, UA9, and LUA9 Projects for fruitful cooperation. We acknowledge funding of our studies from INTAS, Russian Academy of Sciences, Russian Foundation for Basic Researches, and the National Research Centre “Kurchatov Institute”.

References

1. A.G. Afonin, V.T. Baranov, V.M. Biryukov *et al.*, *Proton beam extraction by a short silicon crystal from the IHEP accelerator,* IHEP Preprint 2003–**33**, Physics of Elementary Particles and Atomic Nuclei **36**, 43 (2005).
2. Yu.M. Ivanov, A.A. Petrunin and V.V. Skorobogatov, *Observation of the elastic quasi-mosaicity effect in a bent silicon single crystal*, Pis'ma v ZhETF **81**, 129 (2005) [JETP Letters **81**, 99 (2005)].
3. Yu.M. Ivanov, A.A. Petrunin and V.V. Skorobogatov *et al*., *Volume reflection of a proton beam in a bent crystal*, Phys. Rev. Lett. **97**, 144801 (2006).
4. Yu.M. Ivanov, N.F. Bondar, Yu.A. Gavrikov *et al*., *Volume reflection of 1 GeV protons by a bent silicon crystal*, Pis'ma v ZhETF **84**, 445 (2006) [JETP Letters **84**, 372 (2006)].
5. W. Scandale, D.A. Still, A. Carnera, *et al*., *High-efficiency volume reflection of an ultrarelativistic proton beam with a bent silicon crystal*, Phys. Rev. Lett. **98**, 154801 (2007).
6. W. Scandale, A. Carnera, G. Della Mea *et al*., *Deflection of a 400 GeV/c proton beam with bent silicon crystals at the CERN Super Proton Synchrotron*, Phys. Rev. ST AB **11**, 063501 (2008).
7. W. Scandale, I. Efthymiopoulos, D.A. Still *et al., Apparatus to study crystal channeling and volume reflection phenomena at the SPS H8 beam line*, Rev. Sc. Instr. **79**, 023303 (2008).
8. W. Scandale, A. Vomiero, S. Baricordi *et al., Volume reflection dependence of 400 GeV/c protons on the bent crystal curvature*, Phys. Rev. Lett. **101**, 234801 (2008).
9. W. Scandale, A. Carnera, G. Della Mea *et al*., *Double volume reflection of a proton beam by a sequence of two bent crystals*, Phys. Lett. B **658**, 109 (2008), Erratum in Phys. Lett. B **660**, 610 (2008).
10. W. Scandale, A. Vomiero, S. Baricordi *et al., Observation of multiple volume reflection of ultrarelativistic protons by a sequence of several bent silicon crystals*, Phys. Rev. Lett. **102**, 084801 (2009).
11. W. Scandale, A. Vomiero, E. Bagli *et al., Multiple volume reflections of high-energy protons in a sequence of bent silicon crystals assisted by volume capture*, Phys. Lett. B **688**, 284 (2010).
12. W. Scandale, A. Vomiero, E. Bagli *et al., First observation of multiple volume reflection by different planes in one bent silicon crystal for high-energy protons*, Phys. Lett. B **682**, 274 (2009).
13. W. Scandale, G. Arduini, R. Assmann *et al.*, *First results on the SPS beam collimation with bent crystals*, Phys. Lett. B **692**, 78 (2010).
14. W. Scandale, G. Arduini, R. Assmann *et al., The UA9 experimental layout*, JINST **6**, T10002 (2011).
15. W. Scandale, G. Arduini, R. Assmann *et al., Comparative results on collimation of the SPS beam of protons and Pb ions with bent crystals*, Phys. Lett. B **703**, 547 (2011).
16. W. Scandale, G. Arduini, R. Assmann *et al., Strong reduction of the off-momentum halo in crystal assisted collimation of the SPS beam*, Phys. Lett. B **714**, 231 (2012).
17. The LUA9 Collaboration (CERN–IHEP–Imperial College–INFN–JINR–LAL–PNPI–SLAC), *LHC collimation with bent crystals* – LUA9, CERN-LHCC-2011-**007**/LHCC-**I-019** 10/06/2011.

EXPERIMENT PHENIX AT RHIC

PNPI participants of the PHENIX Collaboration:
V.V. Baublis, D.A. Ivanishchev, A.V. Khanzadeev, B.G. Komkov, D.O. Kotov, V.G. Riabov, Yu.G. Riabov, V.M. Samsonov, E.A. Vznuzdaev

1. Introduction

PHENIX is one of two active experiments at Relativistic Heavy Ion Collider (RHIC) [1]. The experiment is conducted by a collaboration consisting of more than a thousand scientists from 70 institutions from 13 countries. The main goal of the PHENIX experiment, as well as relativistic heavy ion physics in general, is to study the nature and properties of the QCD matter under extreme conditions of high temperature and/or high baryonic density. One of the lodestars of the experimental program is an expected discovery of the Quark-Gluon Plasma (QGP), a new state of matter with dominance of the partonic degrees of freedom for essentially all momentum scales and over nuclear size distances.

Extensive study of heavy ion collisions at RHIC in 2000–2005 has indeed resulted in a discovery of a new state of matter – strongly coupled QGP (sQGP) [2]. Most of recent experimental efforts at RHIC were directed towards better understanding of the properties of the produced medium.

PNPI was involved in the PHENIX experiment from the very beginning. PNPI was responsible for the design and construction of the main detector of the central tracking system – multiwire focusing Drift Chambers (DCs) [3]. The DCs were successfully operated for last twelve years contributing to about 80 % of all scientific results of the collaboration. It is planned that the DCs will operate at least till 2015 with very vague plans for their replacement. Besides the hardware maintenance, PNPI experts take part in data taking, various physical analyses and interpretation of the results.

Last five years, the PHENIX Collaboration accumulated enormous amount of new experimental results. This paper presents mainly results obtained with participation of PNPI specialists and related to production of light hadrons in $p + p$, d + Au, Cu + Cu, and Au + Au collisions at $\sqrt{s_{NN}}$ = 39–200 GeV.

2. Elementary $p + p$ collisions

Left panel in Fig. 1 presents a compilation of experimental invariant differential cross sections for production of different hadrons in $p + p$ collisions at $\sqrt{s}$ = 200 GeV [4]. These results provide precision tests for pQCD calculations at high transverse momenta and serve as a reference for heavier collision systems.

Measurements at low p_T were performed using the ToF subsystem [5] or in di-electron decay channel. Intermediate and high p_T results are based on measurements of photonic and hadronic decay channels for hadrons. Measurements in different decay modes agree with each other within uncertainties and extend over a wide range of transverse momenta up to 20 GeV/c. The plot on the right shows a comparison of the measured invariant differential cross section for π^0 production with that calculated in the NLO pQCD [6]. Within the uncertainties, the calculations reproduce the experimental results, indicating good understanding of the basic particle production mechanisms at $p_T > 2$ GeV/c in elementary hadronic interactions.

It is interesting to note that invariant differential production cross sections measured for all hadrons in $p + p$ collisions at $\sqrt{s}$ = 200 GeV can be well described over the entire momentum range by the Tsallis distribution [7]. It has only two parameters, and it describes the particle p_T spectra both at low and high transverse momenta. The values of the two parameters extracted from the fits were found to be approximately the same for all mesons with a very weak mass dependence. The ability to describe all particle spectra with a common functional form allows one to estimate particle integrated yields on the basis of measurements performed even in a limited p_T range. The extracted values of the integrated yields were found to be in good agreement with previous PHENIX measurements [4].

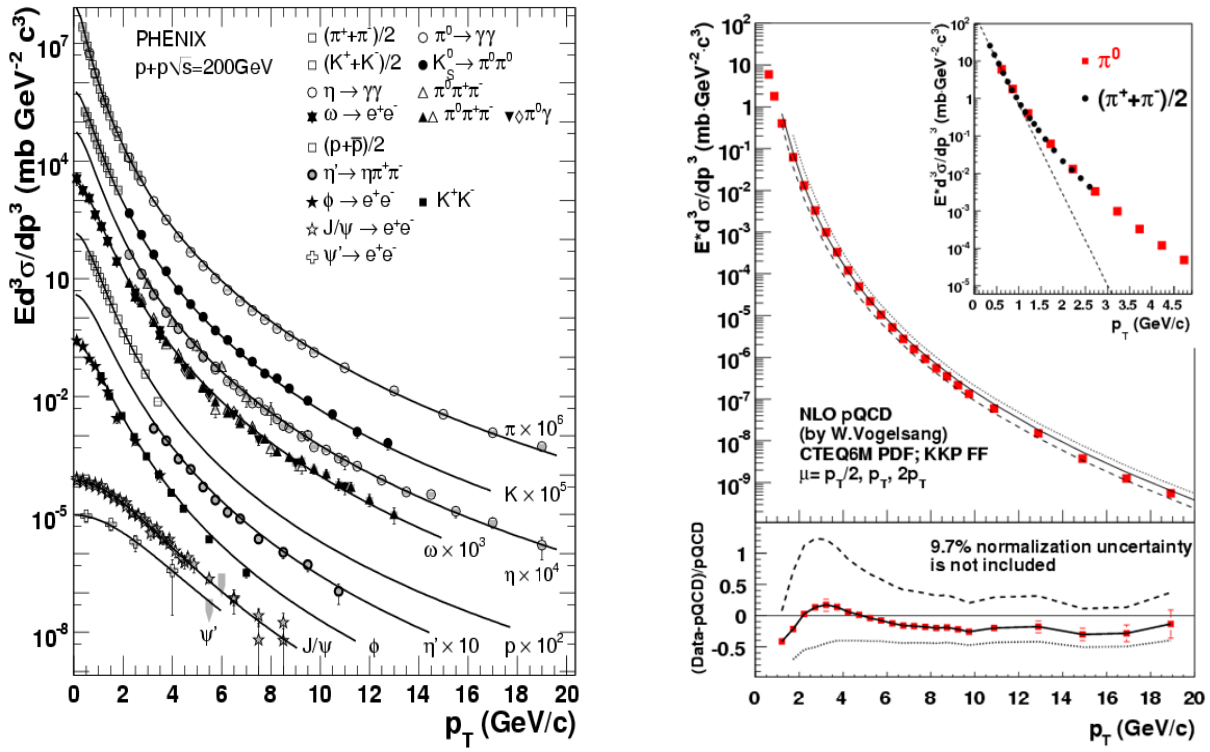

Fig. 1. Invariant differential cross sections for production of hadrons in $p + p$ collisions at $\sqrt{s}$ = 200 GeV (left). Comparison of the measured cross section for π^0 mesons production with that calculated in the NLO pQCD (right)

3. Collisions of light and heavy nuclei

Invariant differential transverse momentum spectra for production of different hadrons were also measured in d + Au collisions at $\sqrt{s_{NN}}$ = 200 GeV. Figure 2 presents nuclear modification factors R_{dA}, which are the ratios of yields measured for particles in d + Au and p + p collisions and scaled by the corresponding numbers of binary nucleon-nucleon collisions estimated within the Glauber model [8]. The plots on the top and bottom correspond to the most central and peripheral d + Au collisions, respectively. The results are shown for production of protons, π^0, η, ω, φ, and η′-mesons [9–11].

For the rare hard scattering processes which are expected to scale with the number of binary collisions, the corresponding ratios should be equal to one in the absence of any collective nuclear effects. And indeed, in the most peripheral collisions the measured ratios at $p_T > 2$ GeV/c are consistent with unity within uncertainties, except probably for protons. At the same time, in central d + Au collisions production of all hadrons is enhanced at intermediate p_T-values. Such an enhancement is not a new effect, it was previously observed in experiments at lower energies and was usually attributed to the Cronin effect [12]. It is interesting to note that the enhancement is about the same for all mesons, and it is on the level of 15 %, while for baryons it is much larger, on the level of 50 %. This observation is hard to reconcile with the explanation of the Cronin effect as appearing from soft multiple recapturing of partons in the initial state. At higher p_T-values ($p_T > 8$ GeV/c), the production of all hadrons is similarly suppressed by ~ 20 %, which could be attributed to modification of the parton distribution functions in heavy nuclei (shadowing effect). However, a quantitative description of this effect for light and heavy ion collisions is still missing.

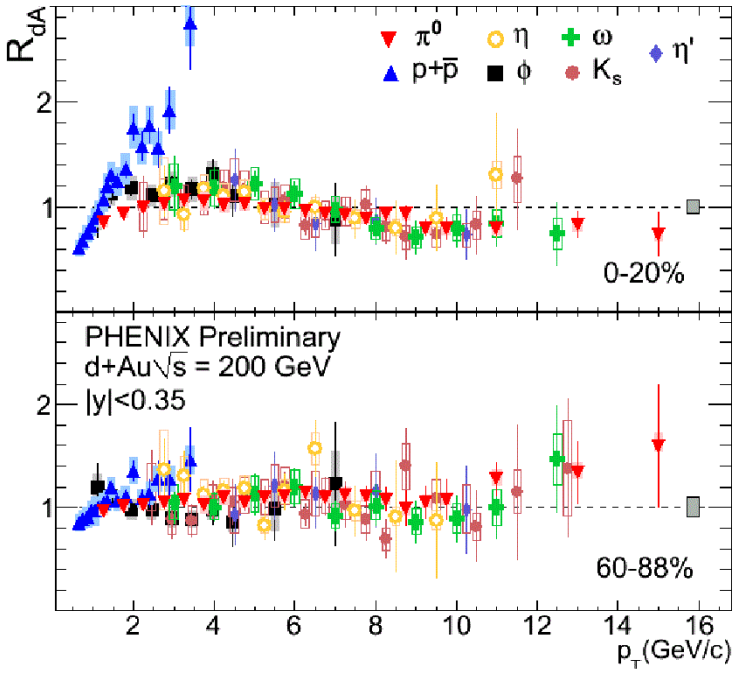

Fig. 2. Nuclear modification factors R_{dAu} for light hadrons in central (top) and peripheral (bottom) d + Au collisions at $\sqrt{s_{NN}}$ = 200 GeV

4. Heavy ion collisions at $\sqrt{s_{NN}}$ = 200 GeV

Suppression of hadron production in Au + Au collisions at high p_{T}-values at RHIC and its absence for direct photons in heavy ion collisions and hadrons in d + Au collisions provided the first evidence for formation of extremely dense medium in heavy ion collisions at RHIC [2]. Several models with very different physical assumptions describe the magnitude of the observed suppression, but predict slightly different evolution of R_{AA} with p_{T} [13–17]. Therefore, a precise measurement of R_{AA} at high p_{T}-values can be used to discriminate theoretical models and to put tighter constraints on the model free parameters.

The left panel of Fig. 3 presents nuclear modification factors measured for π^0 and η mesons in the minimum bias Au + Au collisions at $\sqrt{s_{NN}}$ = 200 GeV [18]. The results obtained for π^0 and η mesons are consistent within uncertainties. Suppression of hadron production is now confirmed up to 20 GeV/c. A linear fit to R_{AA} for π^0 mesons at $p_{\mathrm{T}} > 5$ GeV/c results in a slope consistent with zero, as shown in the right panel of Fig. 3. The slopes obtained from R_{AA} for η mesons are consistent with zero with the largest deviation less than two standard deviations for the most central collisions. While the results indicate that R_{AA} for η is consistent with a constant value, a slow rise of R_{AA} with the momentum increasing cannot be ruled out.

The centrality dependence of R_{AA} on p_{T} provides a means for studying the path-length dependence of the partonic energy loss. However, a better way to test the path-length dependence is to vary the particle emission angle at a fixed centrality. Figure 4 shows the dependence of R_{AA} measured for π^0 on the centrality expressed in terms of the number of participants (N_{part}) [19]. Each panel in this figure corresponds to a particular p_{T} bin. Three sets of points in each panel correspond to different emission angles with respect to the reaction plane. New measurements extend previous results up to 10 GeV/c, to the region where hard scattering is the main process for the particle production. For $N_{\mathrm{part}} > 100$, the out-of-plane R_{AA} is nearly independent of the centrality, while the in-plane R_{AA} rapidly decreases with the centrality increasing. The parton path length in the medium in the direction normal to the reaction plane only weakly depends on the centrality resulting in nearly constant R_{AA} for π^0-mesons. A shorter path length of the parent parton in the reaction plane results in smaller suppression of π^0 production. In the most central collisions where

the nuclear overlap region is nearly symmetric, the parton path length in the medium is about the same in all directions, and the in-plane values of R_{AA} start to match the out-of-plane R_{AA}-values.

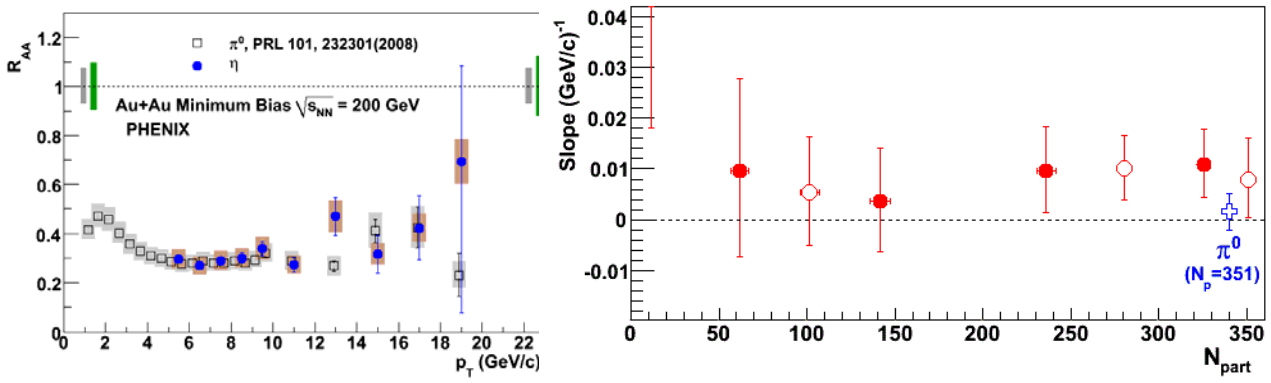

Fig. 3. Nuclear modification factors R_{AA} measured for π^0 and η in minimum bias Au + Au collisions at $\sqrt{s_{NN}}$ = 200 GeV (left). Slopes from linear fits to R_{AA} measured for π^0 and η mesons at $p_T > 5$ GeV/c (right)

The azimuthal distribution of the produced particles can be described by a Fourier expansion, where the angular distribution up to the second order is $dN/d\Delta\varphi \sim 1 + 2v_2 \cdot \cos 2\Delta\varphi$, where v_2 is the elliptic flow coefficient. New v_2 measurements for π^0 and η mesons are shown in Fig. 5. The value of v_2 rapidly increases at low p_T-values, reaches a maximum at 2–3 GeV/c and then starts to decrease. At $p_T > 5$ GeV/c, the momentum dependence of v_2 is weak, although the uncertainties are rather large. Results for π^0 and η mesons are consistent, indicating no mass dependence of v_2 at high p_T. Non-zero value of v_2 at high p_T and similarity of v_2 values for π^0 and η are consistent with the parton energy loss dependence on the path length in the medium and fragmentation of partons in vacuum.

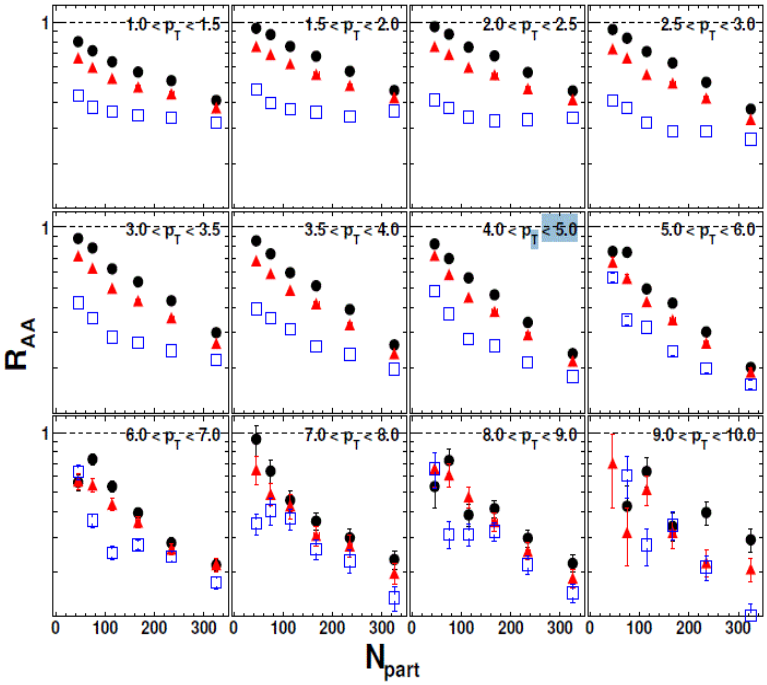

Fig. 4. Dependence of R_{AA} measured for π^0 on the centrality. Three sets of points in each panel correspond to different π^0 emission angles with respect to the reaction plane

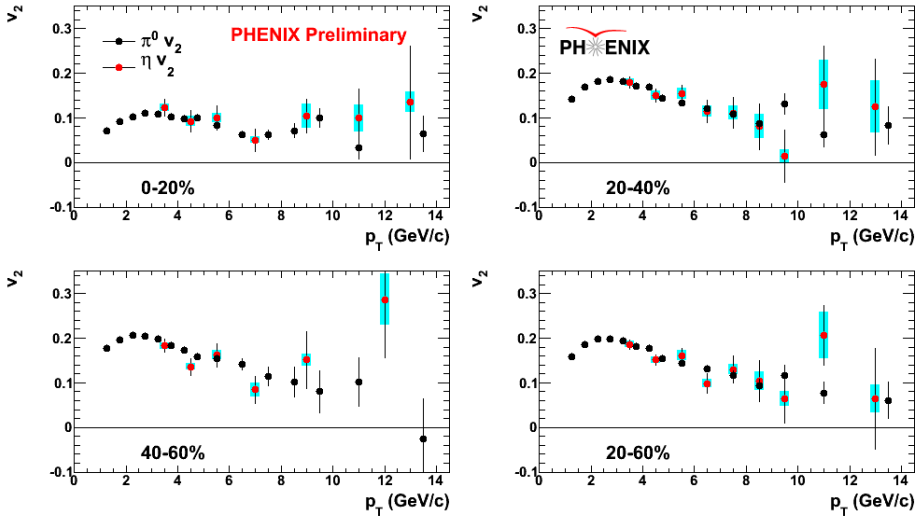

Fig. 5. Elliptic flow for π^0 and η mesons in Au + Au collisions at different centralities

The intermediate p_T region in heavy ion collisions is usually defined in a range of transverse momenta from 2 to 5 GeV/c. In $p + p$ collisions, the hadron production in this p_T range is well described by pQCD calculations [6]. However, in heavy ion collisions the situation is somewhat different. Figure 6 presents nuclear modification factors measured for different hadrons in the most central Au + Au collisions at $\sqrt{s_{NN}}$ = 200 GeV. At p_T > 5–6 GeV/c, production of all hadrons and electrons from semileptonic decays of heavy flavor [20] is similarly suppressed by a factor of 4 to 5. Such behaviour is consistent with the parton energy loss in the dense medium and subsequent fragmentation in vacuum. However, at intermediate p_T-values the production of baryons is enhanced [10]. Although only a half of the sum of protons and antiprotons is shown in the figure, this behaviour takes place for other baryons also, including the strange sector [21, 22]. The production of K^0_s and φ mesons is less suppressed than that of π^0- and η-mesons. Such a difference cannot be explained by the Cronin effect and requires introduction of additional effects and particle production mechanisms to fragmentation of hard scattered partons. For the explanation of this difference, some recombination and radial flow models are usually involved [2]. However, none of the models could explain the whole set of results available in this kinematical region.

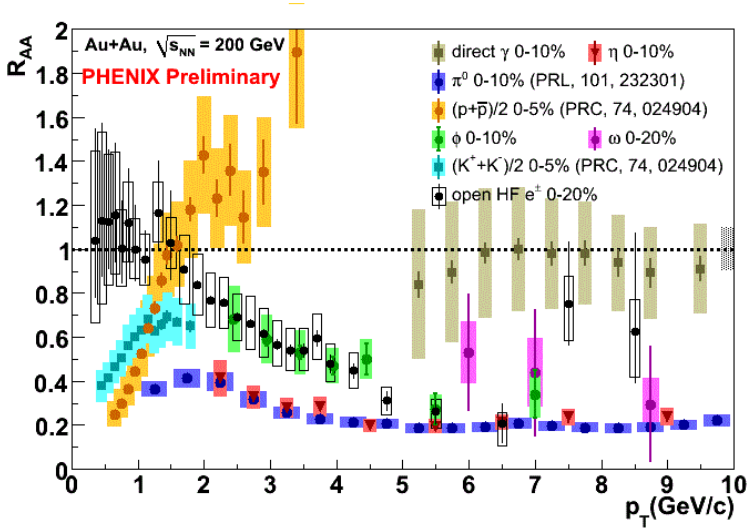

Fig. 6. Nuclear modification factors R_{AA} for different particles in the most central Au + Au collisions at $\sqrt{s_{NN}}$ = 200 GeV

5. Energy scan program

The main goal of the RHIC energy scan program is a detailed study of the QCD phase diagram and a search for the critical point. Low energy runs at RHIC are characterized by relatively low integrated luminosities, thus limiting the number of observables available for an experimental study.

For a systematic study of jet quenching, nuclear modification factors for π^0 mesons were measured in Cu + Cu and Au + Au collisions at different energies: $\sqrt{s_{NN}}$ = 22, 39, 62 and 200 GeV [23]. Such flexibility in collision systems and energies allows to control the size of the interaction region and the amount of energy pumped in this region. Figure 7 presents a summary of all nuclear modification factor measurements for neutral pions. It shows the integrated nuclear modification factors as a function of the total energy stored in the system, which depends both on the number of participating nucleons and on the interaction energy. Different colours in Fig. 7 correspond to different collision energies, boxes and circles correspond to Au + Au and Cu + Cu collision systems, respectively. In Au + Au interactions, the production of π^0 mesons is suppressed in central collisions at all energies. The factors measured at $\sqrt{s_{NN}}$ = 62 and 200 GeV are very similar in absolute values at p_T > 6 GeV/c. In central Cu + Cu collisions, the production of π^0-mesons is suppressed at $\sqrt{s_{NN}}$ = 62 and 200 GeV, while at the energy of $\sqrt{s_{NN}}$ = 22 GeV the opposite effect is observed [24]. The production of π^0-mesons at this energy is enhanced, which is usually associated with the Cronin effect. In Fig. 7 one can see that all measured factors tend to follow the same universal dependence. The green line in the plot corresponds to the maximum energy achieved in Pb + Pb collisions at the SPS. The plot qualitatively explains why suppression of high-p_T hadrons was not observed at the SPS before RHIC.

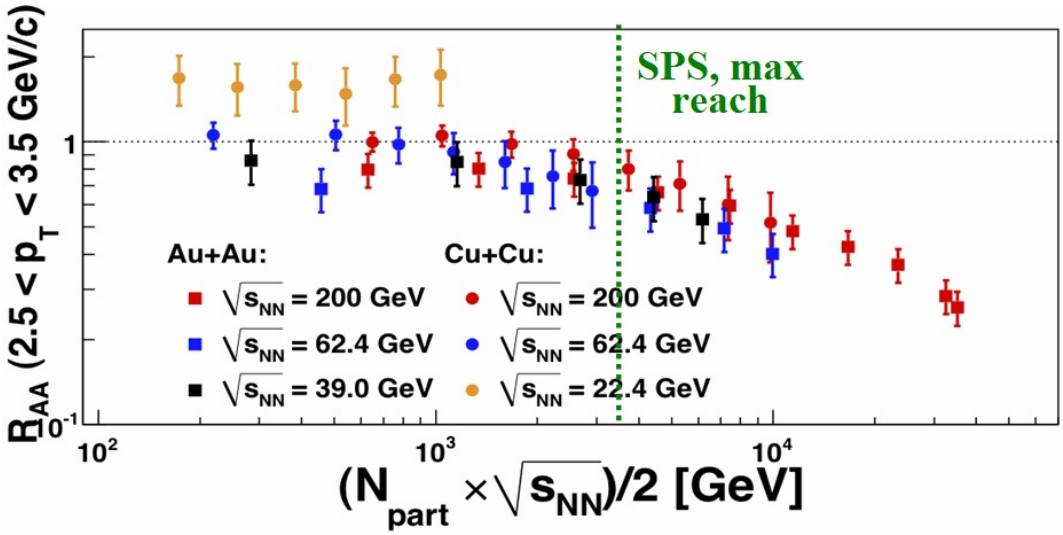

Fig. 7. Integrated nuclear modification factors for π^0-mesons as a function of total energy stored in the system. Different colours correspond to different collision energies, boxes and circles correspond to Au + Au and Cu + Cu collision systems, respectively

Observation of a large azimuthal anisotropy for the particles produced at RHIC became one of the key evidences for creation of dense partonic medium in heavy ion collisions [2]. At sufficiently strong interactions between quanta of the medium, the interaction region can experience local thermalization and hydrodynamic flow. In this case, an initial spatial anisotropy of the nuclear overlap region transforms in the momentum anisotropy of the produced particles.

Different orders of the flow v_2, v_3, and v_4 were measured for unidentified charged hadrons as a function of the transverse momentum in Au + Au collisions at $\sqrt{s_{NN}}$ = 39, 62, and 200 GeV. Within the uncertainties, the flows of the same order perfectly match with each other at these interaction energies. What is even more striking is that the quark number scaling, first observed for identified hadrons in Au + Au collisions at

$\sqrt{s_{NN}}$ = 200 GeV, is also preserved at lower collision energies of $\sqrt{s_{NN}}$ = 39 and 62 GeV. The quark number scaling is usually explained by assuming that the flow is generated at the partonic level, indicating that the produced medium is characterized not only by high temperatures and high densities but also by partonic degrees of freedom. Preservation of the quark number scaling suggests that the quark-like degrees of freedom are still important at interaction energies as low as $\sqrt{s_{NN}}$ = 39 GeV.

Figure 8 shows the flows of different order in dependence on the interaction energy. The left plot shows the elliptic flow for unidentified charged hadrons measured in a range of energies from units of GeV to 2700 GeV at the Large Hadron Collider. The measurements were performed for two values of the transverse momentum – 0.7 and 1.7 GeV/*c*. The elliptic flow is almost independent of the interaction energy at $\sqrt{s_{NN}}$ > > 39 GeV. At lower energies, the elliptic flow rapidly decreases suggesting a change in the basic properties of the produced medium. The plot on the right shows the integrated flows v_2, v_3 and v_4 in dependence on the interaction energy. One can see that like in the previous case, the flows of higher order also do not depend on the interaction energy at $\sqrt{s_{NN}}$ > 39 GeV. These results suggest similarity in the geometry of fluctuations in the nuclear overlap region, and in the properties and evolution of the produced medium at different collision energies of heavy nuclei.

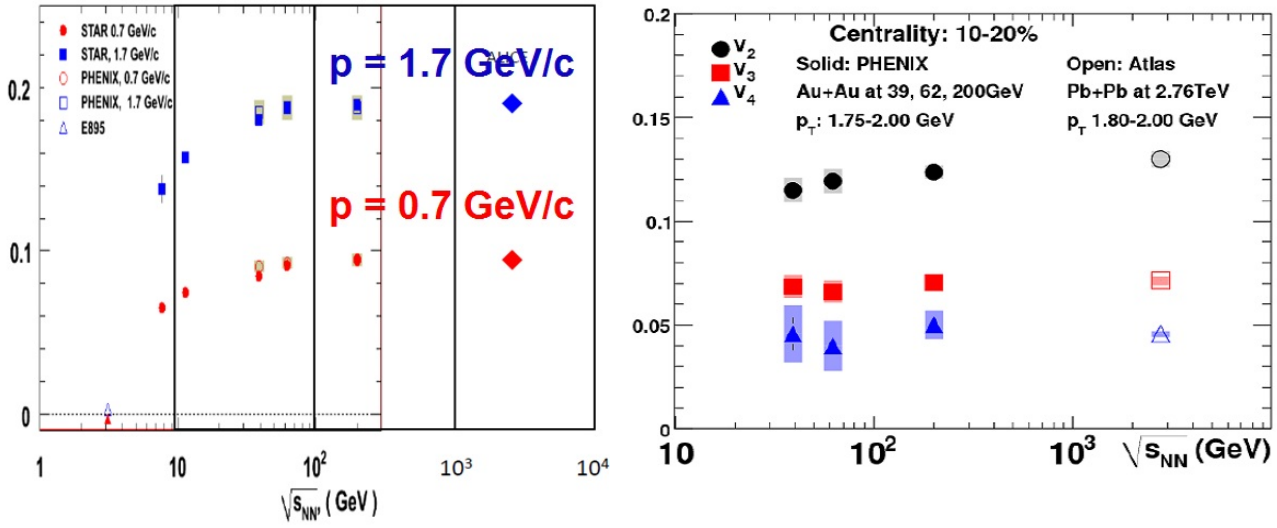

Fig. 8. The elliptic flow for unidentified charged hadrons measured in a range of energies from units of GeV to 2700 GeV at the Large Hadron Collider (left). The integrated flows v_2, v_3 and v_4 in dependence on the interaction energy (right)

6. Conclusion

Last five years, the PHENIX Collaboration produced a wealth of new physical results. Only a few of them related to production of light hadrons were covered in this paper. New measurements of $R_{AA}(p_T, \varphi)$ and $v_2(p_T)$ at high p_T-values are qualitatively consistent with the parton energy loss scenario. Measurements of $R_{AA}(p_T)$ and the p/π production ratio at intermediate momenta are not consistent with hard scattering as the dominating particle production mechanism and require introduction of additional effects, such as the radial flow, recombination, *etc*. New detailed measurements of v_2, v_3 and v_4 allow to test the scaling properties and help to get more accurate estimations for the viscosity to entropy ratio η/s.

Low energy scan results indicate that the jet quenching, development of the flow at partonic level, and strong interaction between the medium quanta are observed not only at full RHIC energy but also at lower collision energies of nuclei at $\sqrt{s_{NN}}$ > 39 GeV. Future low energy program at RHIC will be devoted mostly to a study of lower nuclear interaction energies.

Full understanding and quantitative description of the complicated picture of heavy ion interactions are yet to be achieved.

References

1. K. Adcox *et al.*, Nucl. Instr. Meth. A **499**, 469 (2003).
2. K. Adcox *et al.*, Nucl. Phys. A **757**, 184 (2005).
3. K. Adcox *et al.*, Nucl. Instr. Meth. A **499**, 489 (2003).
4. A. Adare *et al.*, Phys. Rev. D **83**, 052004 (2011).
5. K. Adcox *et al.*, Nucl. Instr. Meth. A **499**, 508 (2003).
6. A. Adare *et al.*, Phys. Rev. D **76**, 051106(R) (2007).
7. C. Tsallis, J. Stat. Phys. **52**, 479 (1988).
8. M.L. Miller *et al.*, Ann. Rev. Nucl. Part. Sci. **57**, 205 (2007).
9. S.S. Adler *et al.*, Phys. Rev. C **74**, 024904 (2006).
10. A. Adare *et al.*, Phys. Rev. C **83**, 024909 (2011).
11. A. Adare *et al.*, Phys. Rev. C **84**, 044902 (2011).
12. D. Antreasyan *et al.*, Phys. Rev. D **19**, 764 (1979).
13. S.A. Bass *et al.*, Phys. Rev. C **79**, 024901 (2009).
14. H. Liu, K. Rajagopal, U.A. Wiedemann, Phys. Rev. Lett. **97**, 182301 (2006).
15. W.A. Horowitz, M. Gyulassy, Phys. Lett. B **666**, 320 (2008).
16. P.M. Chesler, K. Jensen, A. Karch, L.G. Yaffe, Phys. Rev. D **79**, 125015 (2009).
17. S.S. Gubser, D.R. Gulotta, S.S. Pufu, F.D. Rocha, Journ. High Energy Phys. **10**, 052 (2008).
18. A. Adare *et al.*, Phys. Rev. C **82**, 011902(R) (2010).
19. S. Afanasiev *et al.*, Phys. Rev. C **80**, 054907 (2009).
20. A. Adare *et al.*, Phys. Rev. Lett. **98**, 172301 (2007).
21. J. Adams *et al.*, Phys. Rev. Lett. **92**, 052302 (2004).
22. J. Adams *et al.*, Phys. Rev. C **71**, 064902 (2005).
23. A. Adare *et al.*, arXiv:1204.1526 (2012).
24. A. Adare *et al.*, Phys. Rev. Lett. **101**, 162301 (2008).

SELECTED PHYSICS RESULTS FROM THE D0 EXPERIMENT AT THE TEVATRON

PNPI participants of the D0 Collaboration:
G.D. Alkhazov, S.V. Evstyukhin, V.T. Kim, A.A. Lobodenko, P.V. Neustroev, G.Z. Obrant, V.A. Oreshkin, Yu.A. Shcheglov, L.N. Uvarov, S.L. Uvarov

1. Introduction

D0 is an international collaboration of about 670 physicists from 83 institutions, who have designed, built and operated a collider detector at the Fermilab Tevatron.

Main physics goals are precision tests of the Standard Model (SM), the weak bosons physics, top quark physics, Quantum ChromoDynamics (QCD), *B* physics, a search for the Higgs boson, and a search for particles and forces beyond the SM: super-symmetric particles, gravitons, candidates for the cosmic dark matter, and a search for extra dimensions.

During Run II, the Tevatron was operated at an increased $p\bar{p}$ centre-of-mass energy of 1.96 TeV. The luminosity was increased by a factor more than ten, to $\geq 10^{32}$ cm^{-2} s^{-1}. Originally, the Tevatron operation and data taking was planned up to 2009. However, the Tevatron operation was extended to 2011. By the end of September 2011, the data taking was completed, and the Tevatron was shut down. The data, corresponding to about 11 fb^{-1} of an integrated luminosity, have been collected by the D0 experiment. Analyses of the collected data will continue a few more years.

PNPI was involved in the D0 project through the design and programming of the electronic readout for mini drift tubes (50000 channels) and operation of the Forward Muon System [1]. PNPI physicists took part in the data analysis, including QCD, *B* physics, and Electroweak and New phenomena physics studies. Among main D0 physics results are the top-quark mass, B_s mixing frequency, cross section for single top-quark production, discovery of the cascade Ξ_b baryon. This report presents several D0 results obtained in 2007–2012 years.

2. D0 detector

The Run II D0 detector (Fig. 1) [2] consists of a central tracking system, a liquid-argon/uranium sampling calorimeter and an iron toroid muon spectrometer.

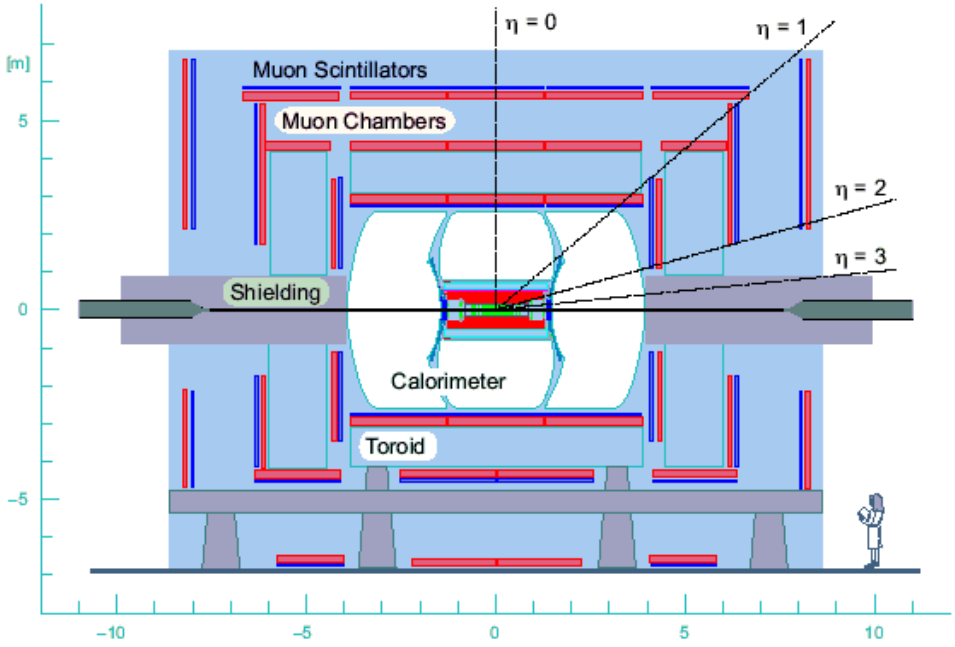

Fig. 1. Schematic view of the D0 detector

The central tracking system is composed of a Silicon Microstrip Tracker (SMT) and a central fiber tracker, both located into a 2 T superconducting solenoidal magnet. The SMT detector has about 800000 individual strips, and its design is optimized for tracking and vertexing capabilities allowing heavy flavour tagging. The calorimeter is longitudinally segmented into electromagnetic and hadronic layers and is housed into three cryostats. The muon system [3] resides beyond the calorimeter and consists of a layer of tracking detectors and scintillation counters before the toroidal magnet, followed by two similar layers after the toroid. Tracking in the muon system relies on wide or mini drift tubes depending on the acceptance. The Run II D0 detector allows to work at the luminosity of $> 10^{32}$ cm^{-2} s^{-1}. The D0 detector is described in detail in [2].

3. Top quark production cross section and mass

The t quark, the heaviest particle known, was discovered at the Tevatron in 1995. Since then, the study of the top quark was one of important directions of investigations at D0. In the triggering and analysis, the event selection was done with high p_T leptons, high E_T multiple jets, a large missing energy E_T and displaced vertices for b-jets. The cross section for the $t\bar{t}$ production was measured by several methods [4]. The determined $t\bar{t}$ production cross section is $\sigma_{t\bar{t}} = = 7.6 \pm 0.6$ pb [5]. Note that within the SM the measured $t\bar{t}$ production cross allows one to predict the top-quark mass: $M_t = 168 \pm 6$ GeV/c^2 [6], which agrees with the results of direct top-quark measurements presented below.

The top-quark mass is a fundamental SM parameter. Together with the W mass, it provides a constraint on the Higgs boson mass. Different methods were used at D0 to derive the top-quark mass. The combined result for the top-quark mass, obtained by the D0 and CDF Collaborations from the data of Run I and Run II, is [7]: $M_t = 173.2 \pm 0.9$ GeV/c^2 (Fig. 2). This is the most accurate measurement of the top-quark mass by now.

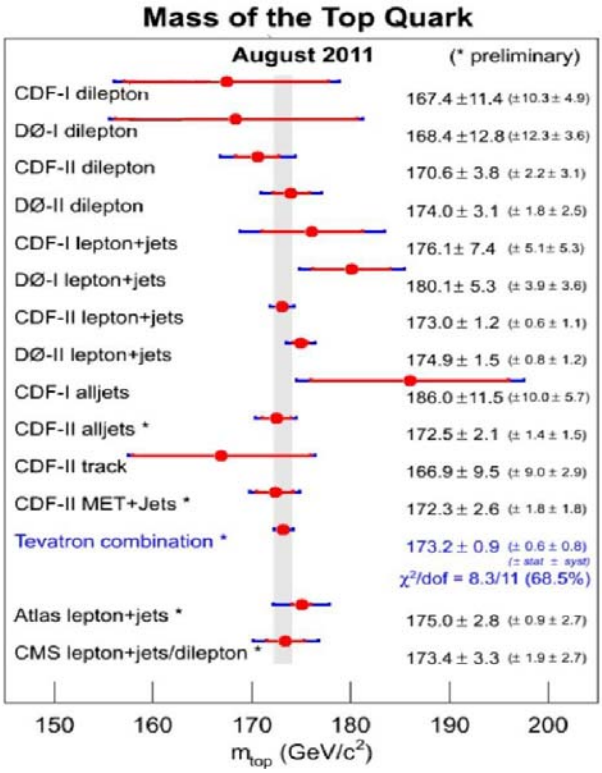

Fig. 2. Results of the t-quark mass measurements in the experiments D0 and CDF

4. Single top-quark production

The top quarks are produced mainly in their $t\bar{t}$ production mode. The single top-quark production with the tb or tqb final states is also possible via the electroweak interaction. However, the cross section for single top-quark production is smaller, while the contribution of background is larger. A measurement of this cross section can be used to constrain the magnitude of the CKM matrix element V_{tb} and to study the Wtb coupling. The event selection in the search for single top quarks is similar to that for the search for top-quark pairs in the l + jets mode.

For the first time, the production of single top quarks was observed by the D0 Collaboration. Using events containing an isolated electron or muon and missing transverse energy, together with jets originating from the fragmentation of b quarks, the cross section for the production of single top quarks in the reactions $p\bar{p} \rightarrow tb + X$, $p\bar{p} \rightarrow tqb + X$ was measured to be 3.43 ± 0.74 pb [8]. The probability to measure a cross section at this value or higher in the absence of signal is about $2.5 \cdot 10^{-7}$, corresponding to a 5.0 standard deviation significance for the observation. The measured cross section was used to determine the CKM matrix element that describes the Wtb coupling. The found value of V_{tb} is $0.79 < |V_{tb}| \leq 1$ at 95% C.L., which agrees with the SM.

5. Mass difference of the top and anti-top quarks

According to the CPT theorem, the mass of an elementary particle should be equal to that of its anti-particle. This is one of the most fundamental principles of the SM, which refers also to the masses of the quarks and antiquarks. The top quark is the only quark which mass can be determined experimentally. Indeed, no bound states are formed before decay of produced top quarks, thereby providing a unique opportunity to measure directly the mass difference between a quark and its antiquark. The difference between the masses of the top and antitop quarks were measured by the D0 experiment with high accuracy, the determined mass difference being $\Delta M = 0.8 \pm 1.8$ (stat) $\pm$ 0.5 (syst) GeV/c^2 [9]. Figure 3 shows the two-dimensional plot for the results of mass measurements for the top and anti-top quarks. The performed measurements are compatible with no mass difference at the level of $\approx$ 1 % of the mass of the top quark.

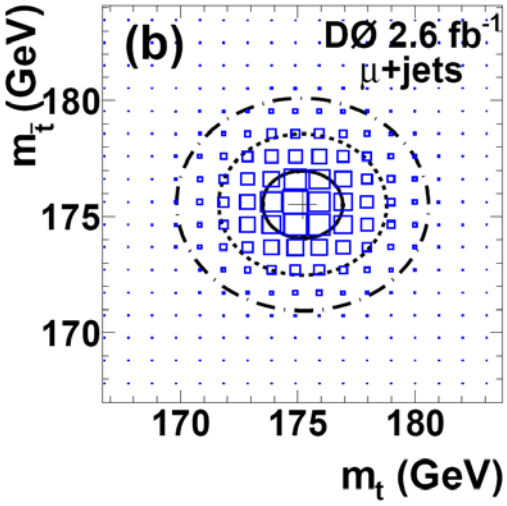

Fig. 3. Two-dimensional plot for the masses of the top and anti-top quarks

6. Top quark pair spin correlation

Although top and antitop quarks are produced unpolarized at hadron colliders, their spins can be correlated, and a significant correlation is expected in the SM. The strength of the spin correlation depends on the production mechanism and differs, for example, for top quark pair production at the Tevatron, where the $q\overline{q}$ production mechanism dominates, and for top quark pair production at the LHC, where the gg production mechanism dominates. The SM predicts that the top quark decays before its spin flips. The spin of the top quark is therefore reflected by its decay products, which allows one to measure the correlation between the spins of pair-produced top and antitop quarks. The D0 Collaboration has measured the top pair quark spin correlation, and for the first time has provided evidence for the presence of spin correlation in $t\overline{t}$ events with a significance of more than three standard deviations. The measured spin correlation coefficient is $A = 0.66 \pm 0.23$ (stat + syst) [10]. This value is consistent with the SM prediction of $A = 0.78$.

7. QCD studies

Motivations of the QCD studies are to use the strong interaction processes for an investigation of the internal proton structure, a search for the quark substructure, a study of the diffractive and heavy flavour production, a study of new objects, like $X(3872)$, and for the understanding of backgrounds to the physics beyond the SM.

The D0 Run II results [11] cover the QCD cross section for inclusive jets production which changes up to 8 orders of magnitude (Fig. 4). The next-to-leading order (NLO) QCD predictions describe the data within the experimental uncertainties for different rapidity $|y|$ intervals in the whole p_T range considered.

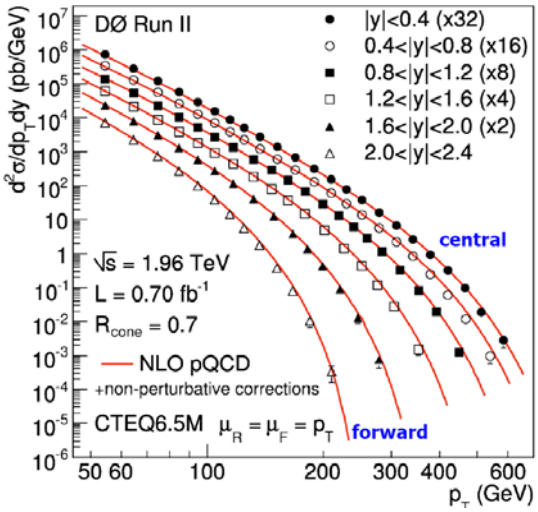

Fig. 4. Cross sections for jet production for different rapidity intervals versus p_t

8. Anomalous like-sign dimuon charge asymmetry

Studies of particle production and decay under the reversal of discrete symmetries (charge, parity and time) have yielded considerable insight into the structure of theories that describe high energy phenomena. Of particular interest is the observation of CP violation, a phenomenon well established in the K^0 and B_d^0 systems, but not in the B_s^0 system, where the effect of the CP-violation is expected to be small in the SM. The violation of CP symmetry is a necessary condition for baryogenesis, the process for the matter-antimatter asymmetry in the universe. However, the observed level of CP violation in the K^0 and B_d^0 systems is not sufficient to accommodate this asymmetry, suggesting the presence of additional sources of CP violation beyond the SM.

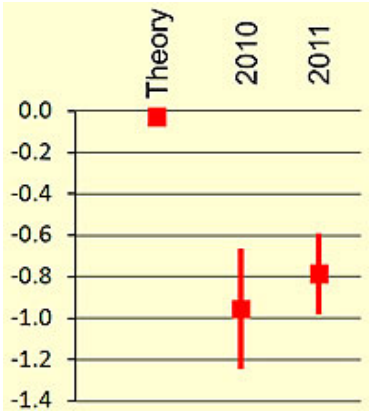

Fig. 5. Asymmetry A_{sl}, measured at D0 in 2010 and 2011, in comparison with theory

The D0 experiment is well suited to the investigation of the small effects of CP violation because the periodic reversal of the D0 solenoid and toroid magnetic field polarities results in a cancellation of most detector-related asymmetries. The charge asymmetry A for like-sign muon pairs was measured by the D0 experiment in 2010 using the data corresponding to an integrated luminosity of 6.1 fb^{-1} [12], and in 2011 using the data of an integrated luminosity of 9 fb^{-1} [13]. The like-sign dimuon charge asymmetry A is defined as $A = (N^{++} - N^{--}) / (N^{++} + N^{--})$, where N^{++} and N^{--} represent the number of events in which the two muons of highest transverse momentum, satisfying the proper kinematic selections, have the same positive or negative charges. After removing contributions from background and from remaining detector effects, any residual asymmetry A_{sl} is assumed to arise solely from the mixing of B_q^0 ($q = d, s$) mesons (via $B_q^0 \leftrightarrow \overline{B}_q^0$ oscillations) that later decay semileptonically. The result of 2010 measurement was $A_{sl} = -(0.96 \pm 0.25\ (\text{stat}) \pm 0.15\ (\text{syst}))\ \%$ (Fig. 5). This asymmetry is significantly larger than that predicted by the SM, and disagrees with the SM prediction $A_{sl} = -0.02\ \%$ by 3.2 standard deviations. The analysis of 2011 has confirmed the result of 2010, the measured asymmetry being equal to $A_{sl} = -(0.79 \pm 0.17 \pm 0.09)\ \%$. This result differs by 3.9 standard deviations from the prediction of the SM and provides evidence for anomalously large CP violation in semileptonic neutral B decay.

9. Forward-backward asymmetry in top quark-antiquark production

At lowest order in QCD, the SM predicts that the kinematic distributions in $p\overline{p} \rightarrow t\overline{t} + X$ production are charge symmetric. However, NLO calculations predict forward-backward asymmetries of (5–10) %, but next-to-next-to leading order calculations predict additional significant corrections for $t\overline{t}$ production. Processes beyond the SM can modify the $t\overline{t}$ production asymmetry. Therefore, the small asymmetries expected in the SM make this a sensitive probe for new physics.

For the first time, the forward-backward production asymmetry defined as $A_{fb} = (N_f - N_b) / (N_f + N_b)$, where N_f (N_b) is the number of events with a positive (negative) rapidity difference between the top and antitop quarks $\Delta y = y_t - y_{\overline{t}}$ was measured in the D0 experiment in 2007 [14]. A relatively small sample of 0.9 fb^{-1} of data, collected at that time by the D0 experiment, was used to determine the asymmetry. The obtained result was consistent within relatively large errors with the SM prediction. In 2010, the forward-backward production asymmetry was measured by the CDF experiment using a larger data sample. A rather large asymmetry, several times larger than that predicted by the SM, was obtained in that new measurement.

In 2011, the D0 experiment presented a new forward-backward asymmetry measurement based on a dataset corresponding to an integrated luminosity of 5.4 fb^{-1}. When corrected for detector acceptance and resolution, the asymmetry in top quark-antiquark production in proton-antiproton collisions was found to be $(19.6 \pm 6.5)\ \%$ [15], to be compared with the SM NLO prediction of $(5.0 \pm 0.1)\ \%$. A forward-backward asymmetry was also determined in an alternative approach that does not depend on a full reconstruction of

the $t\bar{t}$ system – a measurement of a forward-backward asymmetry based only on the rapidity of the lepton in the final state. The determined asymmetry for this case was (15.2 ± 4.0) %, to be compared with the SM NLO prediction of (2.1 ± 0.1) %. The asymmetries measured in D0 data disagree with the SM NLO-based predictions, with the most significant discrepancy above three standard deviations.

10. *W*-boson mass

Since the masses of the *W* boson, top quark, and the Higgs boson are related via radiative corrections, the Higgs mass M_H can be constrained with the precision measurements of the *W*-boson and top-quark masses M_W and M_t. Knowledge of M_W is currently a limiting factor in our ability to tighten the constraints on the Higgs-boson mass. Improving the measurement of M_W is an important contribution to our understanding of the electroweak interaction, and, potentially, of how the electroweak symmetry is broken. The previous world-average measured value was $M_W = 80.399 \pm \pm 0.025$ GeV/c^2 from a combination of measurements from ALEPH, DELPHI, L3, OPAL, D0 and CDF Collaborations.

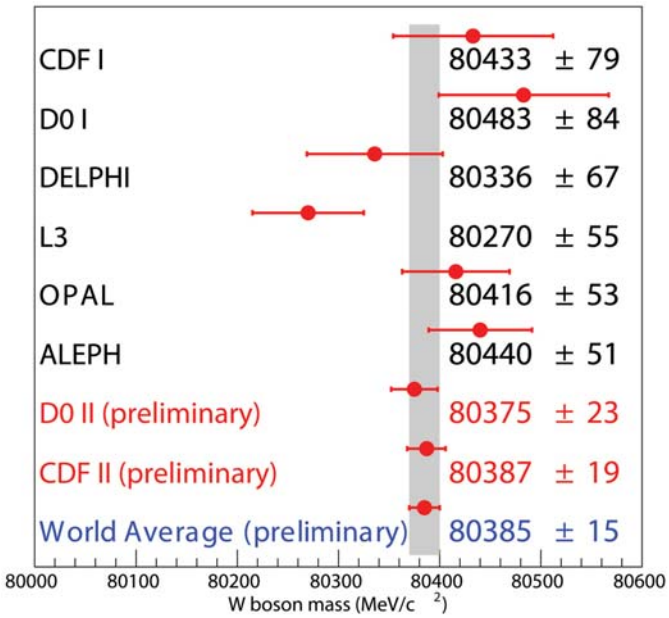

Fig. 6. Previous and new values of the *W* boson mass

The D0 and CDF Collaborations have performed a new measurement of the *W* boson mass. The collaborations measured the particle's mass in six different ways, which all match and combine for a result that is twice as precise as the previous measurement. The D0 Collaboration measured the *W* boson mass to be 80.375 ± 0.023 GeV/c^2 [16], while the CDF Collaboration measured the particle's mass to be 80.387 ± 0.019 GeV/c^2. The two new measurements, along with the addition of previous data from the earliest operation of the Tevatron, combine to produce a measurement of $M_W = 80.387 \pm 0.017$ GeV/c^2, which has a precision of 0.02 percent (Fig. 6). The new *W* mass measurement and the latest precision determination of the mass of the top quark from Fermilab triangulate the location of the Higgs particle and restrict its mass to less than 152 GeV/c^2, this result being in agreement with direct Higgs boson searches.

11. Standard Model Higgs search

In the SM, the Higgs boson is crucial to the understanding of electroweak symmetry breaking and the mass generation of electroweak gauge bosons and fermions. However, this particle has not been observed yet. The mass of the Higgs boson is not predicted in the SM. Precision measurements in particle physics constrain the Higgs mass to $114 < M_H < 152$ GeV/c^2. The low mass region of 120–130 GeV/c^2 is available to a search for the Higgs at the Tevatron. Therefore, a search for the Higgs boson was one of the most important goals of the D0 experiment.

In 2011, new Higgs boson searches including more data, additional channels, and improved analyses techniques compared to previous analyses were performed by both the D0 and CDF Collaborations [17]. All available D0 and CDF results on SM Higgs boson searches, based on luminosities ranging from 4.3 to 10.0 fb^{-1}, were combined. Figure 7 shows (by the solid line) the ratio of the cross section for Higgs production, which is excluded at the confidential level (C.L.) of 95 % by the common data analyses of the D0 and CDF experiments, to that predicted by the SM for different assumed values of the Higgs mass. It is seen that the Higgs masses M_H from 147 to 179 are excluded at the 95% C.L. At the same time, an excess of

the data events with respect to the background estimation is observed in the mass range $115 < M_H < 135$ GeV/c^2. At $M_H = 120$ GeV/c^2, the probability value for a background fluctuation to produce this excess is ~ $3.5 \cdot 10^{-3}$, corresponding to a local significance of 2.7 σ. The global significance for such an excess anywhere in the full mass range is approximately 2.2 σ. The observed excess in the data might be interpreted as coming from a Higgs boson with a mass in the region of 115 to 135 GeV/c^2.

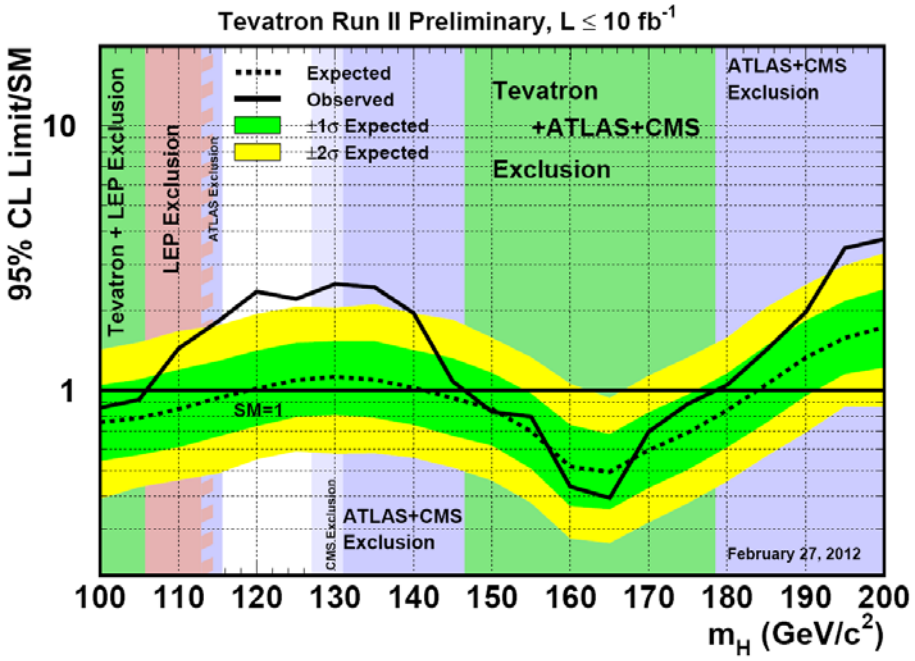

Fig. 7. Ratio of the Higgs production cross section excluded by the data of the D0 and CDF experiments to the cross section predicted by the SM (solid black curve)

In 2012, searches for the Higgs boson by the CDF and D0 Collaborations were continued, in particular, searches for the associated production of a Higgs boson with a W or Z boson and subsequent decay of the Higgs boson to a bottom-antibottom quark pair. The searches were conducted for a Higgs boson with mass in the range 100–150 GeV/c^2. An excess of events in the data compared with the background predictions has been observed, which is most significant in the mass range between 120 and 135 GeV/c^2 [18]. The largest local significance is 3.3 standard deviations, corresponding to a global significance of 3.1 standard deviations. This result is interpreted as evidence for the presence of a new particle consistent with the SM Higgs boson, which is produced in association with a weak vector boson and decays to a bottom-antibottom quark pair.

12. Conclusion

The D0 detector was working well with a high data taking efficiency. A number of physics results have been obtained recent years. Tevatron experiments discovered the top quark, discovered several new elementary particles predicted by the SM, made precision measurements of the top-quark and W boson masses, observed B_s mixing and set many limits on potential new physics theories. In a number of data analyses, only a part of the collected data statistics has been analyzed by now. The data analyses will be continued several forthcoming years.

References

1. G.D. Alkhazov, V.L. Golovtsov, V.T. Kim, A.A. Lobodenko, P.V. Neustroev, G.Z. Obrant, Yu.A. Scheglov, N.K. Terentyev, L.N. Uvarov, S.L. Uvarov and A.A. Vorobyov, in *PNPI XXX, High Energy Physics Division*, *Main Scientific Activities*, *1997–2001*, Gatchina, 2002. p. 124.
2. V.M. Abazov *et al*., Nucl. Instr. Meth. A **565**, 463 (2006).
3. V.M. Abazov *et al*., Nucl. Instr. Meth. A **552**, 372 (2005).
4. V.M. Abazov *et al*., Phys. Rev. D **76**, 072007, 092007, 052006 (2007), Phys. Rev. Lett. **100**, 192004 (2008), Phys. Lett. B **679**, 177 (2009), Phys. Rev. D **82**, 071102 (2010), Phys. Rev. D **84**, 012008 (2011).
5. V.M. Abazov *et al*., Phys. Lett. B **704**, 403 (2011).
6. V.M. Abazov *et al*., Phys. Rev. D **82**, 032002 (2010).
7. T. Aaltonen *et al*., Phys. Rev. D **86**, 092003 (2012).
8. V.M. Abazov *et al*., Phys. Rev. D **84**, 112001 (2011).
9. V.M. Abazov *et al*., Phys. Rev. D **84**, 052005 (2011).
10. V.M. Abazov *et al*., Phys. Rev. Lett. **108**, 032004 (2012).
11. V.M. Abazov *et al*., Phys. Rev. D **85**, 052006 (2010).
12. V.M. Abazov *et al*., Phys. Rev. Lett. **105**, 081801 (2010), Phys. Rev. D **82**, 032001 (2010).
13. V.M. Abazov *et al*., Phys. Rev. D **84**, 052007 (2011).
14. V.M. Abazov *et al*., Phys. Rev. Lett. **100**, 142002 (2008).
15. V.M. Abazov *et al*., Phys. Rev. D **84**, 112005 (2011).
16. V.M. Abazov *et al*., Phys. Rev. Lett. **108**, 151804 (2012).
17. The Tevatron Working Group for the CDF and D0 Collaborations, arXiv:1203.3774[hep-ex].
18. T. Aaltonen *et al*., Phys. Rev. Lett. **109**, 071804 (2012).

PRECISION MEASUREMENT OF THE RATE OF MUON CAPTURE IN HYDROGEN GAS AND DETERMINATION OF THE PROTON'S PSEUDOSCALAR COUPLING g_P

Experiment MuCap

PNPI participants of the MuCAP Collaboration[*]:
V.A. Andreev, V.A. Ganzha, P.A. Kravtsov, A.G. Krivshich, M.P. Levchenko, E.M. Maev, O.E. Maev, G.E. Petrov, G.N. Schapkin, G.G. Semenchuk, M.A. Soroka, A.A. Vasilyev, A.A. Vorobyov, M.E. Vznuzdaev

[*] *Petersburg Nuclear Physics Institute, 188300, Gatchina, Russia;*
Paul Scherrer Institute, CH-5232, Villigen, PSI, Switzerland;
University of California, Berkeley, and LBNL, Berkeley, CA 94720, USA;
University of Illinois at Urbana-Champaign, Urbana, IL 61801, USA;
Universite Catholique de Louvain, B-1348, Louvain-la-Neuve, Belgium;
University of Kentucky, Lexington, KY 40506, USA;
Boston University, Boston, MA 02215, USA

1. Introduction

The goal of the MuCap experiment was a high precision measurement of the ordinary muon capture (OMC) rate Λ_S from the ground singlet state of $p\mu$-atoms:

$$(\mu^- p)_{1S} \rightarrow n + \nu_\mu, \ \text{BR} = 0.16\ \%. \tag{1}$$

The experiment was designed for a 1 % precision measurement, thus improving the existing world data of Λ_S by an order of magnitude. This could provide an evaluation of the proton pseudoscalar form factor g_P, the least known constant in the description of the electroweak structure of nucleons. According to the Standard Model, the electroweak charged-current interaction in reaction (1) is parameterized by four induced form factors g_V, g_M, g_A, and g_P, evaluated at the relevant value of the four-momentum transfer $q_c^2 = -0.88\ m_\mu^2$, where m_μ is the muon mass. Three of them – the vector form factor $g_V(q_c^2)$, the magnetic $g_M(q_c^2)$ and axial $g_A(q_c^2)$ form factors are accurately determined by experimental data and the Standard Model symmetries, and they contribute an uncertainty of only 0.46 % to Λ_S. Process (1) due to its relatively large momentum transfer ($q_c^2 = -0.88\ m_\mu^2$) provides the most direct probe of $g_P(q^2)$. In principle, $g_P(q_c^2)$ could be measured also in the radiative muon capture (RMC) reaction:

$$\mu^- + p \rightarrow n + \nu_\mu + \gamma, \ \text{BR} = 10^{-8}. \tag{2}$$

However, the RMC studies are complicated by the very low branching ratio and some difficulties in interpretation of the experimental data.

The knowledge of the pseudoscalar form factor g_P is important from two points of view. First, for practical applications, as it concludes determination of the amplitude of the electroweak interaction with nucleons, which can be used, for example, for calculations of cross sections for neutrino-nucleon interactions. Second, it gives a possibility to test the validity of a fundamental approach in description of the nucleon structure. The pseudoscalar term in the axial nucleon current has played a significant role in the understanding of weak and strong interactions. Initial theoretical estimates were based on the concept of a *Partially Conserved Axial Current* (PCAC), followed by the recognition of its deeper significance as a consequence of the chiral symmetry and its spontaneous and explicit breaking (Y. Nambu, 1960, Nobel prize 1980). These ideas were foundations for explaining the generation of hadronic masses and the development of Chiral Perturbation Theory (ChPT), the effective field theory of low-energy QCD. Now $g_P(q_c^2)$ can be systematically calculated within the Heavy Baryon Chiral Perturbation Theory (HBChPT) up to two-loop order. The precise QCD result within this approach (V. Bernard *et al.*, 2002) is $g_P(q_c^2) = 8.26 \pm 0.23$. The experimental determination of g_P with a comparable precision could be a critical test of the theory, and studies of the muon capture on hydrogen is the most direct means to determine this form factor.

The MuCap experiment was performed in the muon beam of the "meson factory" of Paul Scherrer Institute (PSI, Switzerland). The proposal of the experiment was presented in 1997 and approved with high priority by the PSI Program Advisory Committee. The first physics run was performed in 2004. Then, measurements were continued in 2006 and 2007 with some essential improvements of the experimental set-up and the muon beam line. In total, the beam time provided for the MuCap experiments was about 10000 hours. The results of an analysis of the 2004 data were published in 2007 [1]. This report contains the final results of this experiment.

2. Status of the μ*p*-capture studies prior to the MuCap experiment

Experimental OMC efforts span a period of more than forty years, and more recently, in 1996, one RMC experiment was performed at TRIUMF. However, the situation prior to the present experiment was inconclusive, as the results lacked sufficient precision due to ambiguities in the interpretation, as well as due to technical challenges. Two experimental methods were applied to measure the OMC rate: detection of neutrons from reaction (1) and lifetime measurements of μ^- in hydrogen by detecting electrons from the muon decay, $\mu^- \rightarrow e^- + \nu_\mu + \nu_e$. A serious limitation of the neutron detection method is an uncertainty in determination of the neutron detector efficiency. Due to this reason, the previous muon capture experiments with neutron detectors obtained a precision in Λ_S only around 10 %. This leads to too high error ($\geq$ 60 %) in determination of $g_P(q_c^2)$. The lifetime method has no such limitations. In this method, the muon capture rate is determined by the difference between the measured μ^- lifetime in hydrogen, τ_{μ^-}, and the known μ^+ lifetime, τ_{μ^+}, assuming that free μ^- and μ^+ mesons decay with identical rates according to the CPT theorem. The contribution of the muon capture rate to the total muon disappearance rate being quite small (0.16 %), this requires very high precision in measurements of τ_{μ^-}. For example, in order to reach ~ 1 % precision in determination of the muon capture rate, one should measure τ_{μ^-} with the precision of $\Delta\tau_{\mu^-}/\tau_{\mu^-} \approx 10^{-5}$. This method was used in a Saclay experiment [2], resulting in the most precise measurement at that time of the OMC rate (4.5 %). However, that experiment was performed with a liquid hydrogen target, where unambiguous derivation of $g_P(q_c^2)$ from the measured τ_{μ^-} was not possible.

The problems of interpretation of the experimental data can be explained by considering the chain of reactions possible for negative muons after stopping them in a hydrogen target of density φ ($1.0 < \varphi \leq 0.01$) relative to that of the liquid hydrogen density (LH_2), as shown in Fig. 1.

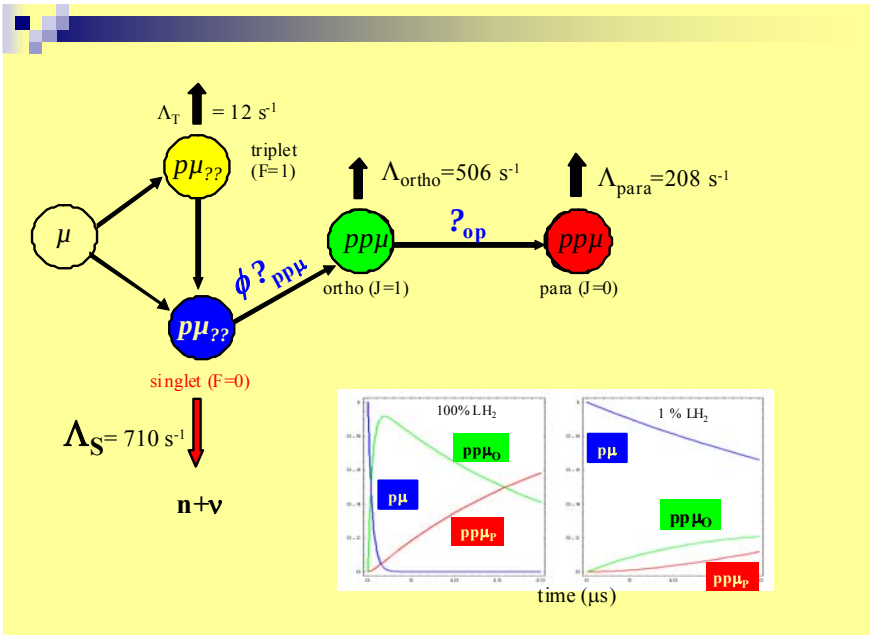

Fig. 1. Scheme of reactions after stopping of negative muons in a hydrogen target. Panels in the right-down corner show percentage of the muon captures from various molecular states for two target densities (LH_2 and 0.01 LH_2) in function of the time after the muon stop

Stopped muons immediately form ground state μ*p* atoms whose hyper-fine states are populated in a statistical manner. The upper triplet spin state is rapidly depopulated in collisions with H_2 molecules, and for densities $\varphi \geq 0.01$ all muons reach the μ*p* singlet state 1*S* well before 100 ns. From there, muons can either decay with a rate close to $\lambda_{\mu}^{+} \equiv 1/\tau_{\mu}^{+} \approx 0.455 \times 10^6$ s^{-1}, or be captured via reaction (1) at the predicted rate $\Lambda_S \approx 710$ s^{-1}. Complications arise at higher densities, however, as the μ*p* atoms increasingly collide with target H_2 molecules to form *pμp* molecules. The *pμp* molecules are initially formed in the ortho state at the density dependent rate $\varphi\lambda_{pp\mu}$, where $\lambda_{pp\mu} \approx 2.0 \times 10^6$ s^{-1}, and then de-excite to the para-state at the rate λ_{op}. The nuclear capture rates from the ortho- and para-states $\Lambda_{ortho} \approx 506$ s^{-1} and $\Lambda_{para} \approx 208$ s^{-1} are quite different from each other and from Λ_S, so the knowledge of the relative populations of the μ*p* and *pμp* states is crucial for correct determination of $g_P(q_c^2)$. Alas, λ_{op} is poorly known. The available experimental and theoretical data are mutually inconsistent. This prevents clear interpretation of the Saclay OMC experiment, which was performed in LH_2, where muon capture occurs predominantly in *pμp* molecules.

The RMC process was studied at TRIUMF [3]. This process is less sensitive to λ_{op}, nevertheless it is difficult to draw firm conclusions from this experiment, whose results suggested a nearly 50 % higher value for $g_P(q_c^2)$ than predicted.

3. Strategy of the MuCap experiment

The MuCap experiment employs a new experimental method, first suggested at PNPI [4], aimed to avoid the described above problems. The main features of this method are as follows.

- The capture rate is determined by measuring the μ^- lifetime in ultra-clean deuterium-depleted hydrogen gas at relatively low density $\varphi \approx 0.01$, where *pμp* formation is slow, and 96 % of all captures proceed from the μ*p* atom singlet state.
- The hydrogen contamination by impurities with $Z > 1$ should be on a level $C_Z \leq 10^{-8}$ to avoid muon disappearance due to capture by these impurities. The concentration of deuterium in hydrogen should be $C_d \leq 10^{-6}$ to prevent formation of *d*μ atoms, which could diffuse far from the muon stopping point.
- Muons are detected in a hydrogen Time-Projection Chamber (TPC), which determines the three coordinates of the muon stopping point. The trajectory and the emission time of the muon decay electrons are measured with an external detector. TPC also provides a self-control for presence of $Z > 1$ impurities on a level of 10^{-8} by detecting recoil nuclei from the μ*Z* capture.
- The high intensity muon beam in combination with fast read out electronics enables collection of the required statistics (~ 10^{10} events) for reasonable running time to provide measurements of the muon lifetime with a precision of 10^{-5} or better.

4. The MuCap experimental set-up

The MuCap experiment was conducted in the πE3 beam line at Paul Scherrer Institute, using a ~ 20 kHz DC muon beam tuned to a central momentum of 32.6 MeV/*c*. Our hydrogen TPC was the key to the experiment. As illustrated in Fig. 2, incident muons first traverse a plastic scintillator (μSC) and a multiwire proportional chamber (μPC) and then pass through a 0.5 mm thick hemispherical beryllium window to enter an aluminum pressure vessel filled with ultra-pure deuterium-depleted hydrogen gas at a pressure of 10 bar and at the ambient room temperature. In the centre of the vessel is the TPC (with the sensitive volume $15 \times 12 \times 28$ cm^3) which tracks incoming muon trajectories and thus enables selection of the muons that stop in the gas at least 15 mm away from the chamber materials.

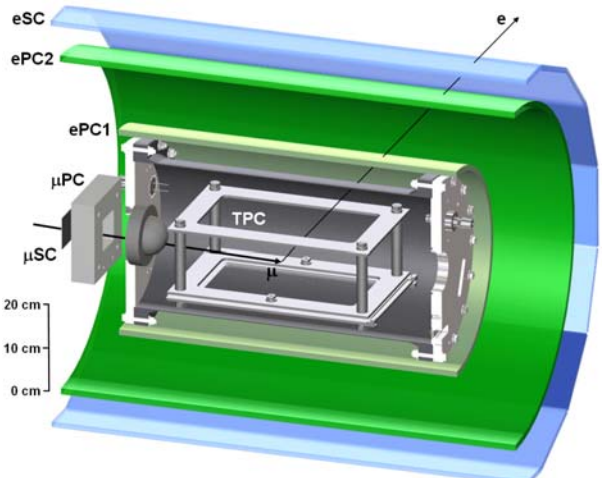

Fig. 2. Simplified scheme of the MuCap detector

Approximately 65 % of the muons passing through the μSC stop within this fiducial volume. The ionization electrons produced by incoming muons drift downwards with the velocity of 5.5 mm/μs at the applied field of 2 kV/cm towards a Multiwire Proportional Chamber (MWPC). The MWPC contains 72 anode wires perpendicular and 36 strip wires parellel to the beam direction. This MWPC unit, with a high voltage of 5.0 kV across the 3.5 mm half-gaps, provides a moderate gas gain of ~ 100 in hydrogen. Anode and cathode signals are discriminated with three energy thresholds and read out by TDCs in 200 ns time intervals providing 3D information on the muon track and the muon stop coordinate. The TPC is surrounded by two cylindrical wire chambers (ePC1 and ePC2), each containing anode wires and inner/outer cathode strips, and by a hodoscope barrel (eSC) consisting of 16 segments with two layers of 5 mm thick plastic scintillator. This tracking system detects trajectories of the outgoing decay electrons with 3π solid angle acceptance. The muon and electron arrival times t_μ and t_e are established by the μSC and eSC detectors, respectively. All data are recorded in a trigger-less, quasi-continuous mode to avoid dead time distortions to the lifetime spectra.

5. High purity hydrogen gas in TPC

Prior to the run, the TPC system was heated up to 115 °C under vacuum for several weeks to remove impurities. Then the TPC vessel was filled with deuterium-depleted hydrogen through a palladium filter. However, these precautions were not sufficient to provide the high gas purity during the run. It was found that, due to outgassing of the TPC materials, the impurity concentration (N_2 and H_2O) increased in time with the rate of $dC_z/dt \approx 10^{-7}$ per day. Therefore, a special gas circulation/purification system (CHUPS) was designed and constructed at PNPI [5], and implemented into the MuCap set-up in 2004. During the data taking, the gas was continuously circulated via an adsorption cryo-pump system and cleaned by cooled Zeolite filters. This system achieved an equilibrium concentration of impurities $C_z < 5 \times 10^{-8}$, as monitored by TPC detection of recoil nuclei from muon capture and by direct measurement target samples in a highly sensitive gas chromatograph. After improving the working conditions of the circulation system in 2006, the N_2 and H_2O contaminations were reduced down to 7 ppb and 18 ppb, respectively. During the 2007 run, the contaminations were further reduced to ~ 5 ppb and ~ 9 ppb for N_2 and H_2O, respectively. A special humidity sensor was located in the hydrogen stream just after the TPC in order to monitor this contaminant. The results indicated that the primary contaminant was H_2O outgassing from the walls of the TPC vessel.

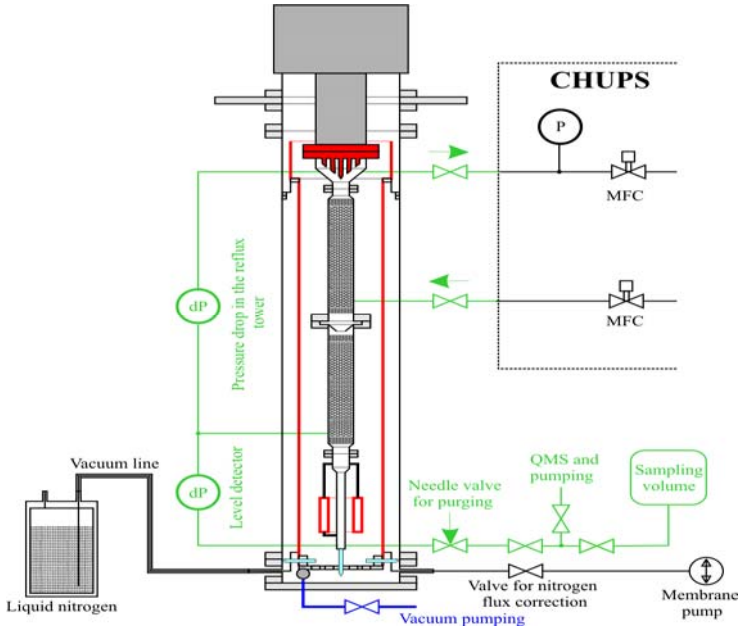

Fig. 3. Cryogenic isotopic exchange column used to prepare deuterium-depleted protium

The isotopic purity of the hydrogen is also critical for high precision measurements of the muon lifetime. Muons preferentially transfer from μ*p* to μ*d* at the rate $\varphi C_d \lambda_{pd}$, where C_d is the deuterium concentration and $\lambda_{pd} \approx 1.4 \times 10^{10}$ s^{-1}. Whereas the μ*p* diffusion is of the order of mm, μ*d* atoms can diffuse cm-scale distances due to the Ramsauer – Townsend minimum in the μ*d* + *p* elastic scattering cross-section. As a result, μ*d* atoms can drift sufficiently far away from the muon's original stopping point, so that the decay event could be rejected by the μ-*e* vertex reconstruction cut in a time-dependent manner. In addition, μ*d* atoms can drift into surrounding materials and be captured there.

Our target gas was produced via electrolysis of deuterium-depleted water provided by Ontario Power Generation Company (Canada). The high sensitive Accelerator Mass Spectrometry (AMS) analysis of this gas determined that $C_d = (1.44 \pm 0.13) \times 10^{-6}$, roughly 100 times below the deuterium's natural abundance. This was the best deuterium-depleted hydrogen available on market, and it was used in our 2004 run. Later, a new cryogenic isotopic exchange column (Fig. 3) was designed and constructed at PNPI [6], which was able to reduce the deuterium concentration in hydrogen down to $C_d < 6 \times 10^{-9}$. The gas of such purity was produced for the first time. This highly deuterium depleted hydrogen was used in the 2006–2007 runs.

6. Muon-on-request facility at PSI

In the MuCap experiment, only muons entering the TPC that are separated in time by ±25 μs from other muons are accepted for registration. But this condition reduces considerably the usable statistics. In the 2006–2007 runs, this pile-up protection was not needed because the so-called "muon-on-request" facility was put into operation in the muon beam at PSI. This facility deflected the muon beam for a requested time as soon as a signal on the muon stop in TPC was registered. Implementation of this method in our experiment allowed us to increase the data taking rate by a factor of three and also helped to reduce the background.

7. Measurements and results

A schematic view of the MuCap set-up is shown in Fig. 4. The measurement procedure started with selection of the muon stops within the $10.4 \times 8.0 \times 20.4$ cm^3 fiducial volume inside the TPC accompanied by outgoing electrons reconstructed in the wire chambers ePC1 and ePC2.

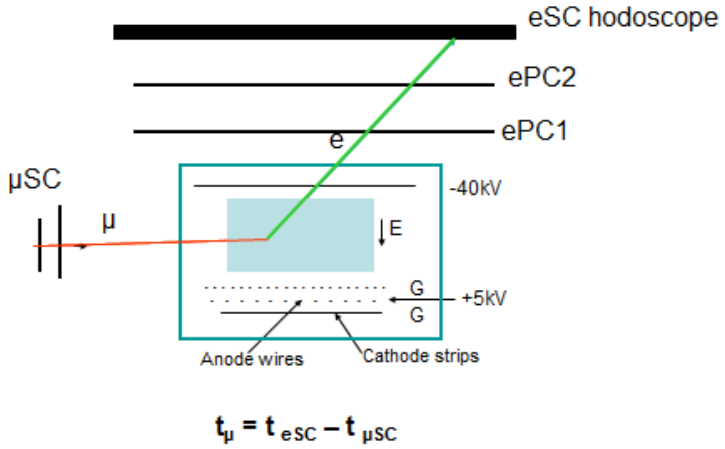

Fig. 4. Schematic view of the MuCap set-up. TPC measures the muon track and determines the 3D coordinate of the muon stop inside the fiducial volume of $10.4 \times 8.0 \times 20.4$ cm^3. The trajectory of the outgoing electron is detemined by the wire chambers ePC1 and ePC2. The muon arrival time t_μ and the electron arrival time t_e are measured with the scintillater counters μSC and eSC, respectively

Special care was taken to select clean muon stops inside the TPC fiducial volume isolated by at least 15 mm from any material in the TPC. The muon pile-ups were eliminated also. Table 1 presents the statistics of fully reconstructed pile-up protected μ–*e* pairs collected during the 2004, 2006, and 2007 runs.

Table 1

Main features of MuCap production runs. Statistics of fully reconstructed μ–*e* pairs, deuterium concentration C_D, water concentration C_{H2O} determined by a humidity sensor (not present in the 2004 run), and the observed impurity capture rate Y_z

	Run 2004	Run 2006	Run 2007
Statistics	1.6×10^9	5.5×10^9	5.0×10^9
C_D (ppb)	1440	< 60	< 10
C_{H2O} (ppb)	Not measured	18	8.7
Y_z (ppm)	12	6.3	3.4

The time differences between the muon arrivals and the decay electron emission, $\Delta t = t_e - t_\mu$, are histogrammed into lifetime spectra, as shown in Fig. 5.

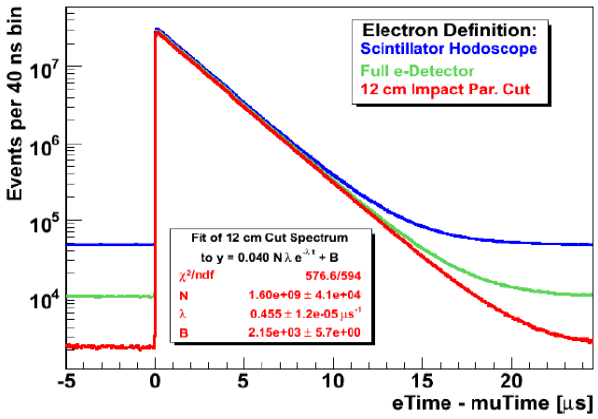

Fig. 5. The muon lifetime spectra $\Delta t = t_e - t_\mu$ for various requirements on muon stop-outgoing electron correlations: blue line – just a signal from eSC after the μ-stop; green line – track reconstructed in the *e*-detector; red line – impact parameter of the electron's trajectory is IP ≤ 12 cm

As shown in Fig. 5, the background suppression is improved by performing a very loose vertex cut IP ≤ 12 cm on the impact parameter between each decay electron's trajectory and its parent muon's stopping point. This cut introduced only a small controllable correction due to diffusion of the μ*p* and μ*d* atoms.

The measured lifetime spectra were fit with the function $N(t) = N_0\omega\lambda\exp(-\lambda t) + B$, over the range $160 < t < 19000$ ns. The bin width ω was fixed at 80 ns, while N_0, B, and λ (in fact, λ_{μ^-}) were free parameters. To thus determined disappearance rate λ_{μ^-} several corrections were applied. The main corrections to λ_{μ^-} were derived directly from the experimental data, with some additional information from external measurements and literature. These corrections are summarized in Table 2.

Table 2

Applied corrections to disappearance rate λ_{μ^-} and systemetics errors (in s^{-1})

	Run 2004	Run 2006	Run 2007
$Z > 1$ impurities	–15.1 ± 5.0	–7.8 ± 1.87	–4.54 ± 0.93
μ-*p* scattering	±3.0	–12.4 ± 3.22	–7.2 ± 1.25
μ*p* diffusion	–2.7 ± 0.5	–3.1 ± 0.10	–3.0 ± 0.10
μ*d* diffusion	–10.2 ± 1.6	±0.74	±0.12
Fiducial volume cut	±3.0	±3.00	±3.00
Total λ_{μ^-} correction	–28.0 ± 8.5	–23.30 ± 5.20	–14.74 ± 3.88

The final result for the μ^- disappearance rate in pure hydrogen, based on $N = 1.2 \times 10^{10}$ fully tracked, pile-up protected decay events from our 2004, 2006, and 2007 data sets, are

$$\lambda_{\mu^-} = 455853.5 \pm 12.5_{stat} \pm 8.5_{syst}\ s^{-1} \quad (2004),$$
$$\lambda_{\mu^-} = 455857.3 \pm 7.7_{stat} \pm 5.1_{syst}\ s^{-1} \quad (2006),$$
$$\lambda_{\mu^-} = 455853.1 \pm 8.3_{stat} \pm 3.9_{syst}\ s^{-1} \quad (2007).$$

The measured disappearance rate λ_{μ^-} is connected with the muon capture rate Λ_S via the following relation:

$$\lambda_{\mu^-} = (\lambda_{\mu^+} + \Delta\lambda_{\mu p}) + \Lambda_S + \Delta\Lambda_{p\mu p} \quad (3)$$

Here, $\Delta\lambda_{\mu p} = -12.30 \pm 0.00\ s^{-1}$ is a precisely calculable correction, which describes a small reduction in the muon decay rate in the bound μ*p* system [7]. The term $\Delta\Lambda_{p\mu p} = -17.73 \pm 1.87\ s^{-1}$ accounts for captures from *pμp* molecules, and is calculated from the full μ^- kinetics in pure hydrogen. Its error terms come from our remeasurement of $\lambda_{pp\mu}$ in a special experiment [8] with doping in hydrogen a small admixture of argon. The new value of $\lambda_{pp\mu}$ is $(1.94 \pm 0.06) \times 10^6\ s^{-1}$. It agrees with the previous world average but is three times more precise. Using also the new world average $\lambda_{\mu^+} = 455170.05 \pm 0.46\ s^{-1}$ (μLAN experiment [9]), we determine the rate of the muon capture by the proton to be

$$\Lambda_S^{MuCap} = 714.9 \pm 5.4_{stat} \pm 5.1_{syst}\ s^{-1}.$$

This result is in close agreement with theoretical calculations [10] of Λ_S where, together with the known parameters $g_V(q_c^2)$, $g_M(q_c^2)$, and $g_A(q_c^2)$, the authors used $g_P^*(q_c^2) = 8.2$. With the latest PDG values for $V_{ud} = 0.97425$ and $g_A(0) = 1.2701$, and using $g_P^*(q_c^2) = 8.2$, we derive from Ref. [10] an updated value of Λ_S^{Calc}:

$$\Lambda_S^{Calc} = 712.7 \pm 3.0 \pm 3.0\ s^{-1}.$$

The difference $(\Lambda_S^{MuCap} - \Lambda_S^{Calc})$ proved to be small, therefore, we can use a linear expansion for $g_P^{MuCap}(q_c^2)$ determination:

$$g_P^{MuCap}(q_c^2) = g_P^*(q_c^2) + (dg_P/d\Lambda_S)(\Lambda_S^{MuCap} - \Lambda_S^{Calc}) = 8.06 \pm 0.48 \pm 0.28, \quad (4)$$

where $dg_P/d\Lambda_S = -0.065$ s (J. Govaerts *et al.*, 2000). The two uncertainties in (4) arise from the error propagation of Λ_S^{MuCap} and Λ_S^{Calc}, respectively.

Figure 6 illustrates excellent agreement of the MuCap result with the prediction of the Heavy Baryon Chiral Perturbation Theory (HB ChPT) and highlights MuCap's reduced sensitivity to the molecular parameter λ_{op}.

This answers the longstanding challenge of unambiguous measurement of g_P. Our result was published in 2013 in Phys. Rev. Lett. [11], and it was selected by the editorial board in the category of "exceptional research".

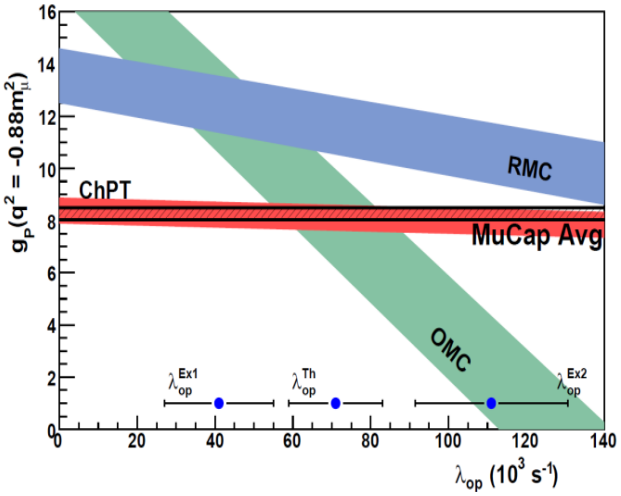

Fig. 6. Experimental and theoretical determinations of $g_P(q_c^2)$, presented versus the ortho-para transition rate λ_{op} in the $p\mu p$ molecule. The most precise previous OMC experiment (Saclay, 1981) and the RMC experiment (TRIUMF, 1998) both depend significantly on the value of λ_{op}, which itself is poorly known due to mutually inconsistent experimental (λ_{op}^{Ex1}, λ_{op}^{Ex2}) and theoretical (λ_{op}^{Th}) results. In contrast, the MuCap result for $g_P(q_c^2)$ is nearly independent of molecular effects

References

1. V.A. Andreev *et al.*, MuCap Collaboration, Phys. Rev. Lett. **99**, 032002 (2007).
2. G. Bardin *et al.*, Nucl. Phys. A **352**, 365 (1981).
3. D.H. Wright *et al.*, Phys. Rev. C **57**, 373 (1998).
4. E.M. Maev *et al.*, Nucl. Instr. Meth. A **478**, 158 (2002).
5. V.A. Ganzha *et al.*, Nucl. Instr. Meth. A **578**, 485 (2007).
6. I.A. Alekseev *et al.*, Preprint PNPI-**2702**, Gatchina (2006).
7. H.C. Von Baeyer and D. Leiter, Phys. Rev. A **19**, 1371 (1979).
8. S. Knaak, Ph. D. Thesis UIUC (2012).
9. D. Webber *et al.*, MuLan Collaboration, Phys. Rev. Lett. **99**, 041803 (2011).
10. A. Czarnecki, W.J. Marciano, A. Sirlin, Phys. Rev. Lett. **99**, 032003 (2007).
11. V.A. Andreev *et al.*, MuCap Collaboration, Phys. Rev. Lett. **110**, 022504 (2013).

PRECISION MEASUREMENT OF THE RATE OF MUON CAPTURE IN DEUTERIUM
Experiment MuSun

PNPI participants of the MuSun Collaboration[*]:
V.A. Ganzha, L.M. Kotchenda, P.A. Kravtsov, A.V. Nadtochy, G.E. Petrov, I.Y. Petrov, V.A. Trofimov, A.A. Vasilyev, A.A. Vorobyov, N.I. Voropaev, M.E. Vznuzdaev

[*] *Petersburg Nuclear Physics Institute, 188300, Gatchina, Russia;*
Paul Scherrer Institute, CH-5232, Villigen, Switzerland;
University of Washington, Seattle, USA;
University of Kentucky, Lexington, KY 40506, USA;
Boston University, Boston, MA 02215, USA;
Regis University, USA;
University of South Carolina, USA;
Universite Catholique de Louvain, B-1348, Louvain-la-Neuve, Belgium

1. Introduction

The weak nuclear interaction plays a crucial role in our Universe. In particular, it starts the *pp* chain of the solar burning. In this chain, the following reactions occur triggered by the weak nuclear interaction:

$$p + p \rightarrow d + e^+ + \nu_e , \quad (1)$$
$$p + p + e^- \rightarrow d + \nu_e , \quad (2)$$
$$p + {}^3\mathrm{He} \rightarrow {}^4\mathrm{He} + e^+ + \nu_e , \quad (3)$$
$${}^7\mathrm{Be} + e^- \rightarrow {}^7\mathrm{Li} + \nu_e , \quad (4)$$
$${}^8\mathrm{B} \rightarrow {}^8\mathrm{Be} + e^+ + \nu_e . \quad (5)$$

The neutrinos produced in these reactions provide valuable information on the star formation. The neutrinos released in reaction (5) have recently been registered in the SNO detector via the reactions

$$\nu_x + d \rightarrow \nu'_x + n + p , \quad (6)$$
$$\nu_e + d \rightarrow e^- + p + p , \quad (7)$$

also induced by the weak nuclear interaction. It is clear that the precise description of reactions (1)–(7) is of fundamental value. However, these reactions cannot be studied experimentally at present with the desired accuracy in terrestrial conditions. In order to perceive them, one should address other weak processes in few-nucleon systems that are feasible in laboratories, such as tritium beta decay and muon capture by ^{3}He and by deuteron:

$${}^3\mathrm{H} \rightarrow {}^3\mathrm{He} + e^- + \bar{\nu}_e , \quad (8)$$
$$\mu^- + {}^3\mathrm{He} \rightarrow {}^3\mathrm{H} + \nu_\mu , \quad (9)$$
$$\mu^- + d \rightarrow n + n + \nu_\mu . \quad (10)$$

Then, relying on the recently developed theoretical principles, one can apply the acquired knowledge on the weak nuclear interaction also to other weak processes, including those occurring in the extraterrestrial conditions. Reactions (8) and (9) have already been studied experimentally in great detail. The lifetime of the triton is known with the accuracy of ~ 0.3 %. The rate of the muon capture by ^{3}He was measured in our previous experiment with high precision: $\Lambda_0 = 1496 \pm 4\ \mathrm{s}^{-1}$ [1]. The situation with reaction (10) is less favorable so far. Indeed, the available measurements of the muon doublet capture rate on deuteron have rather low accuracy: $\Lambda_d = 470 \pm 29\ \mathrm{s}^{-1}$ (J. Martino, 1986) and $\Lambda_d = 409 \pm 40\ \mathrm{s}^{-1}$ (W.H. Breunlich *et al.*, 1987). The goal of the MuSun experiment is to measure the muon capture rate on deuteron with much higher accuracy.

The MuSun experiment is a continuation of our studies of muon capture by light nuclei with sub-percent precision. The experimental method is based on the novel “active target” technique developed at PNPI. Our first experiment in this research [1] was a measurement of the rate of muon capture by ^{3}He in the reaction ${}^3\mathrm{He} + \mu^- \rightarrow t + \nu_\mu$. This experiment has improved the world precision by an order of magnitude. The second

experiment (the MuCap experiment [2], see a special article in this edition) was carried out on muon capture by proton. In that experiment, the muon capture rate from the singlet ground state of the $d\mu$ atom was measured with 1 % precision that allowed for the first time to determine the pseudoscalar coupling of the nucleon g_p, thus completing our knowledge of the nucleon electro-weak interactions. The next step is a high precision study of the muon capture by deuteron. More specifically, the goal of the MuSun experiment is a measurement of the rate Λ_d with a precision better than 1.5 %. Here, Λ_d denotes the capture rate from the doublet hyperfine state of the muonic deuterium atom in its 1*S* ground state.

Following Weinberg's pioneering approach, the Chiral Perturbation Theories have been systematically constructed with the aim to calculate the electro-weak observables in few-body systems. In fact, these are the Effective Field Theories (EFTs) of the QCD at low energies. Such calculations require several "Low Energy Constants" (LECs) to be determined from the experiment. Most of these constants can be determined from the πN scattering experiments. In case of the two-nucleon system, one of the LECs (denoted as d^R) which reflects the short range interaction of the Meson Exchange Currents (MECs) in this system remains undetermined. Up to now, d^R was determined from a fit of the theory to the measured tritium lifetime and to the static properties of the 3*N* system. However, this method suffers from ambiguity as the use of the 3*N* system introduces a second LEC in the 3*N* forces which might correlate with d^R. That is why the calculated values of Λ_d vary from 384 s^{-1} to 419 s^{-1} [3]. The main uncertainty comes from evaluation of d^R, it varies from 1.2 to 5.6. Correspondingly, the MECs contribution to Λ_d varies from 1 % to 9 % in these calculations.

The high precision measurement of Λ_d is a unique method for reliable determination of d^R. The precise knowledge of this constant will allow for consistent calculations of other two-nucleon weak processes, such as proton-proton fusion in the Sun and solar neutrino scattering on deuterons, which is important for astrophysics. Moreover, this will also help to understand better the weak interaction in the 3*N* system. In other words, such a precise knowledge of the rate of the muon capture by deuteron could clarify best the situation in the theory of the reactions triggered by the weak nuclear interaction.

2. Mesoatomic processes in deuterium

The MuSun experiment has much in common with the MuCap experiment. In both cases, the muon capture rate is determined from the measurement of the negative muon lifetime in ultra-clean hydrogen gas (deuterium depleted protium in MuCap, protium depleted deuterium in MuSun) by detecting the electrons from the muon decay reaction

$$\mu^- \rightarrow e^- + \nu_\mu + \text{anti } \nu_e \,. \qquad (11)$$

The muon capture rate is determined by the difference between the measured μ^- and the known μ^+ lifetimes. However, the processes after the negative muon stop in deuterium are quite different from those in protium, and this difference dictated the choice of the experimental conditions. Figure 1 shows the scheme of reactions after stopping of negative muons in deuterium. Two features are of special importance for our measurements. First, a relatively low transition rate from the $(d\mu)_{3/2}$ state to the $(d\mu)_{1/2}$ state. Note that the goal of our experiment is to measure the muon capture rate from the $(d\mu)_{1/2}$ state. This enforced us to increase the gas density in MuSun by a factor of five as compared to MuCap. But even at this gas density the spin-flip rate is only $2 \cdot 10^6$ s^{-1}. Therefore, the fit of the μ^- lifetime could be started only after 1 μs or even later after the muon stop. The second complication comes from the $dd\mu$ molecule formation followed by the muon catalyzed *dd* fusion. This leads to two corrections to Λ_d. The first one is due to ^{3}Heμ molecule formation, resulting in overestimation of the measured value of Λ_d because the muon capture by ^{3}He is about 5 times faster than that by deuteron. The second correction is due to the pile-up of the muon and $t + p$ signals, incurring rejection of such events if the proton reaches the veto pad. This also distorts (increases) the measured value of Λ_d. In order to reduce the effects of the *dd* fusion, it was decided to perform the experiment at 30 K, where the $dd\mu$ molecule formation rate is relatively low.

Note that the kinetic scheme shown in Fig. 1 is well understood now due to our previous studies of the muon catalyzed *dd* fusion [4] and the muon capture by ^{3}He [1]. In addition, it could be controlled in the course of the experiment. Therefore, both above mentioned corrections could be obtained directly from our experimental data. So, we expect that the uncertainties in Λ_d due to mesoatomic processes could be reduced

to an acceptable level at the optimized target conditions: the gas temperature T = 30 K and the gas density φ = 6 % of the LHD (Liquid Hydrogen Density).

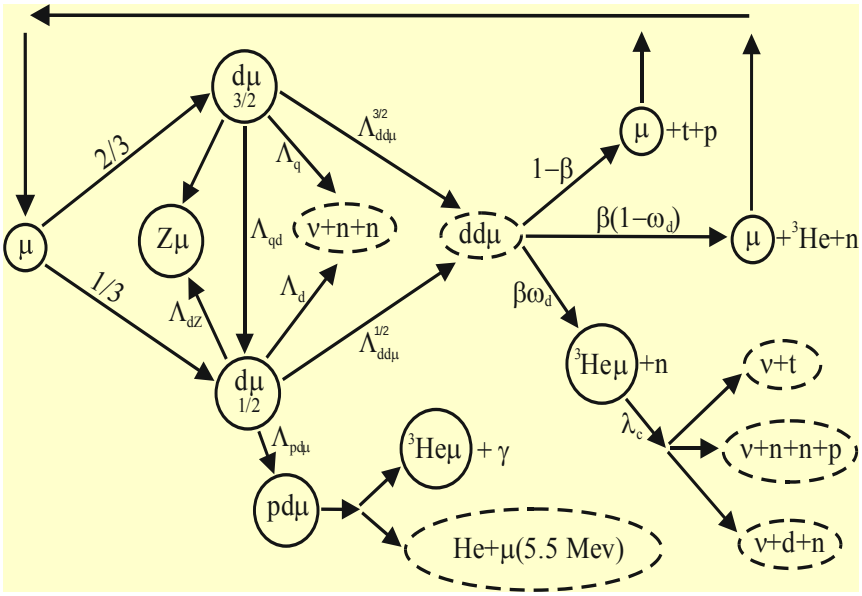

Fig. 1. Kinetic scheme of reactions after stopping of negative muons in deuterium.
Due to ultra high purity of deuterium in this experiment, the transfer rate to impurities Λ_{dZ}, as well as the $pd\mu$ formation rate $\Lambda_{pd\mu}$, are negligible. All other constants in the scheme, $\Lambda^{3/2}_{dd\mu}$, $\Lambda^{1/2}_{dd\mu}$, Λ_{qt}, β, ω_d, and λ_c were measured with high precision in our studies of the muon catalyzed dd fusion [4] and the rate of the muon capture by ^{3}He [1]

3. Strategy of the MuSun experiment

The MuSun experiment employs the experimental method first suggested at PNPI, similar to that used in the MuCap experiment. The main features of this method are as follows.

- A specially designed high-density cryogenic ionization chamber filled with ultra-pure deuterium (operating as a Time Projection Chamber, CryoTPC) determines the muon trajectory and the 3D muon stop point in the fiducial volume of the CryoTPC well isolated from the chamber materials. Also, it detects the muon catalyzed fusion reactions. The deuterium gas density in the CryoTPC is φ = 0.06 LHD, and the gas temperature is $T \approx 30$ K.
- The arrival time of the incoming muons (t_μ), as well as the trajectory and the arrival time of the muon decay electrons (t_e), are measured by external MWPCs and scintillator counters.
- The μ^- lifetime is measured from the distribution of the difference $\Delta t = t_e - t_\mu$. The muon capture rate is determined by the difference between the μ^+ and μ^- lifetimes.
- The deuterium contamination by impurities with $Z > 1$ should be on a level of $C_Z \leq 10^{-9}$ to avoid muon disappearance due to capture by these impurities.
- The concentration of hydrogen in deuterium should be $C_P \leq 10^{-4}$ to prevent formation of the $pd\mu$ molecules followed by the fusion reaction $pd\mu \rightarrow {}^3\mathrm{He} + \mu$ (5.5 MeV).
- The high intensity muon beam in combination with fast readout electronics enables collection of the required statistics (~ 10^{10} events) for reasonable running time to provide measurements of the μ^- lifetime with the precision of 10^{-5}, or better.

4. The MuSun experimental set-up

The MuSun principal scheme is shown in Fig. 2. The incoming muons are detected first by a thin scintillator counter μSC and by a wire proportional chamber μPC. Then they pass through a 0.4 mm thick hemispheric berillium window and stop in the sensitive volume of the CryoTPC. The CryoTPC is the key element of the experimental set-up. It is filled with ultra-pure protium-depleted deuterium gas at the temperature $T \approx 30$ K and pressure $P \approx 5$ bar. Its main goal is to detect the muon stop point within the fiducial volume of the CryoTPC well isolated from the chamber materials (Fig. 3). The trajectory and the

arrival time of the muon decay electrons are detected by two cylindrical proportional wire chambers ePC1, ePC2 and by a scintillator hodoscope eSC, as it was in the MuCap experiment.

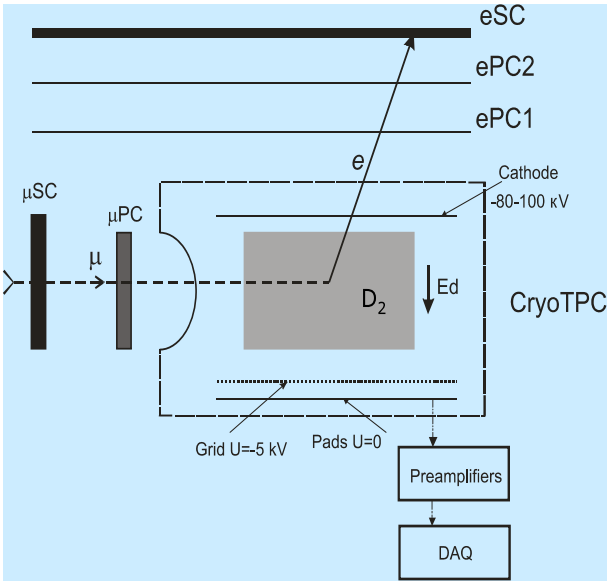

Fig. 2. Simplified scheme of the MuSun set-up

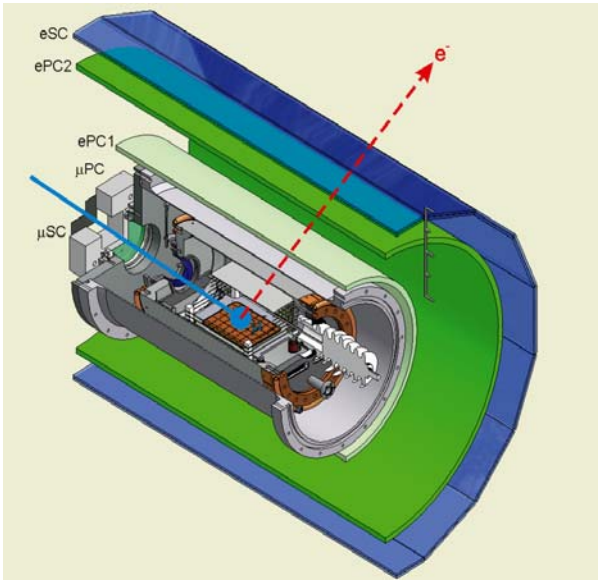

Fig. 3. 3D view of main MuSun set-up elements in cut

The total sensitive volume of the CryoTPC is 7.2 × 7.0 × 9.5 cm^3 in the horizontal (X), vertical (Y), and beam (Z) directions, respectively. Its anode plane is divided into 48 pads (making up a pad matrix 6(X) by 8(Z)). About 50 % of the muons passing through the μSC stop within the fiducial volume above the 24 central pads (with a pad size of 18.0(X) × 15.7(Z) mm^2) at the distance of ≥ 1 cm from the cathode and from the grid. The ionization electrons produced by muons drift downwards with the velocity of 5 mm/μs at the applied field of 11 kV/cm towards the grid, and after passing it they arrive at the anode pads. At such high gas density and relatively low electric field, the electron-ion recombination of the initial ionization becomes essential, especially for doubly charged particles. For example, the recombination is almost 60 % for the ^{3}He peak produced in *dd* fusions. To provide the desired resolution for the ^{3}He peak at such high recombination, the electric field in the chamber should be uniform within 3 %. This is achieved by mounting a set of copper wires along the boundary of the sensitive volume with gradually decreasing potentials on them, from the cathode to the grid. The grid was constructed with 30 micron wires interspaced by 250 microns. The anode-grid distance was 1.3 mm. The anode pads are at the ground potential. The voltage on the grid and the cathode is –3 kV and –80 kV, respectively. All data are recorded in a trigger-less, quasi-continuous mode to avoid the dead time distortions to the lifetime spectra.

The cooling system of the CryoTPC is based on a cryogenerator with a neon coolant. The complete cooling time of the chamber from the room temperature to 30 K is 12 hours. The temperature is stabilized on a level of ± 0.02 K. Like in the MuCap experiment, before filling the CryoTPC, deuterium was purified from hydrogen starting from the factory level $C_P = 2 \cdot 10^{-4}$ to less than 10^{-6} using a special cryogenic isotopic exchange column designed and constructed at PNPI [5]. To preserve the pure deuterium from $Z > 1$ impurities inside the CryoTPC, we use a special gas circulation/purification system, also designed and constructed at PNPI [6] and implemented previously in the MuCap set-up. Besides, the low temperature ($T \approx 30$ K) in the chamber is an additional guarantee of the gas purity due to low vapor pressure of any high Z gas at this temperature, as it is shown in Fig. 4 for the case of nitrogen and oxygen.

Each pad has an independent read out channel equipped with FADCs. The duration of the signals for muons parallel to the chamber planes is determined mostly by the electron drift time between the grid and the pads, and it is about 200 ns. Due to a finite formation time of the preamplifier (~ 600 ns), the final duration of such pulses is approximately 1.2 μs.

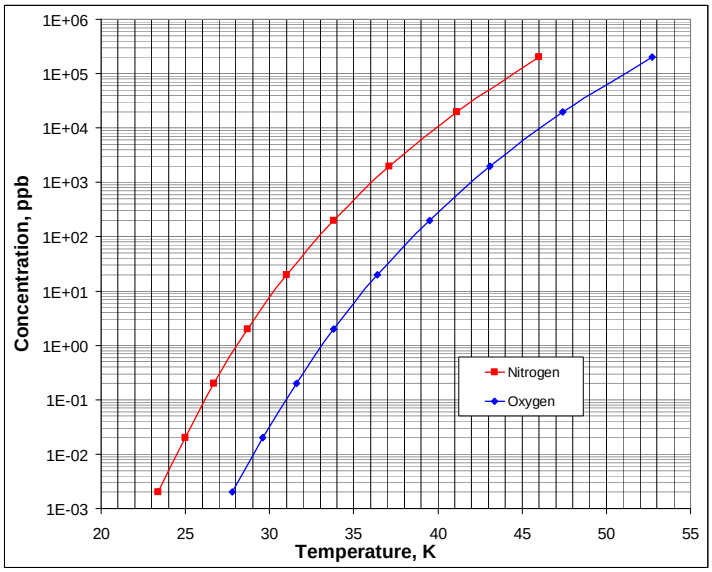

Fig. 4. Vapor pressures of nitrogen (blue) and oxygen (red) versus temperature, recalculated in ppb to 50 bar deuterium pressure

5. First results from test runs at PSI

Preparations for the MuSun experiment were started in 2008. During 2009, the CryoTPC was designed and constructed at PNPI. Then it was transported to PSI and tested in an experimental hall without a beam. At the end of 2010, the whole MuSun set-up was assembled in the πE3 beam line, and the first physics test run was performed in 2011. In total, more than 10^9 muon stops accompanied by outgoing electrons were registered during that run. The analysis of those events allowed us to understand the performance of the experimental set-up and to formulate possible modifications to be implemented before the main physics runs planned for 2013–2014. In 2012, a new muon beam line πE1 was prepared specially for the MuSun experiment. The MuSun set-up was installed in this line, and a technical run was performed aimed for studies of the experimental conditions in the new beam line. These tests have shown that the quality of the new muon beam is even better than that in the previous beam line. An important advantage of the new beam line is that the MuSun set-up may stay in the beam area permanently till the end of the experiment without dismounting it between the runs.

Below we present some results from an analysis of the data collected during the first physics test run in 2011. The procedure of the data analysis started with selection of the muon stops within the $72 \times 50 \times 94$ mm^3 fiducial volume inside the CryoTPC accompanied by outgoing electrons. These electrons were reconstructed using signals from the wire chambers ePC1 and ePC2 and from the two 5 mm thick layers of plastic scintillators in eSC. To select the muons which had stopped in the fiducial volume of the TPC, we use 24 central pads as the muon stop pads (in the *XZ* plane) and the drift time between 4÷12 μs as the measure of the *Y* coordinate of the muon stop points. Such muon selection guarantees that the selected muons were stopped in deuterium gas and did not reach any construction material in the CryoTPC by diffusion in the gas. Only the muons separated in time by ±25 μs were accepted for the analysis. In total, about $3 \cdot 10^9$ thus selected events were collected in the run. The mass chromatographic analysis of deuterium from the CryoTPC was carried out at the beginning and at the end of the run. It was found that the protium concentration was increasing during the run with the rate around 1 ppm per day, remaining at an acceptable level during the whole two months run period. The chromatographic analysis of chemical impurities in deuterium showed that the concentrations of nitrogen and oxygen were on acceptable levels, $C(N_2) = 1$ ppb and $C(O_2) < 0.4$ ppb.

Table 1

Expected systematical corrections to Λ_d in the MuSun experiment. The last correction in the table is due to muon and $t + p$ pile-ups

Correction to Λ_d, s^{-1}	
$Z > 1$ impurities $C_Z = 10^{-9}$	–2.1
Protium $C_p = 10^{-4}$	–2.0
Fusions $dd \rightarrow {}^3\mathrm{He}\mu + n$	–9.0
Fiducial volume cut	~ –7.0

Using the data of that run, we have estimated some systematic corrections which potentially could be introduced in the measured value of the capture rate Λ_d, see Table 1. The main corrections are due to muon capture on ^{3}He and due to pile-up of the muon and $t + p$ signals. We expect that each of these corrections could be determined directly from the experimental data with a precision of 10 %, or better.

The spatial distributions of the muon stops in the sensitive volume of the CryoTPC are presented in Fig. 5. One can see in this figure that a major part of the muon beam is stopped inside the sensitive volume of the CryoTPC. These distributions were obtained under the condition that every muon stop was followed by a *dd* fusion signal.

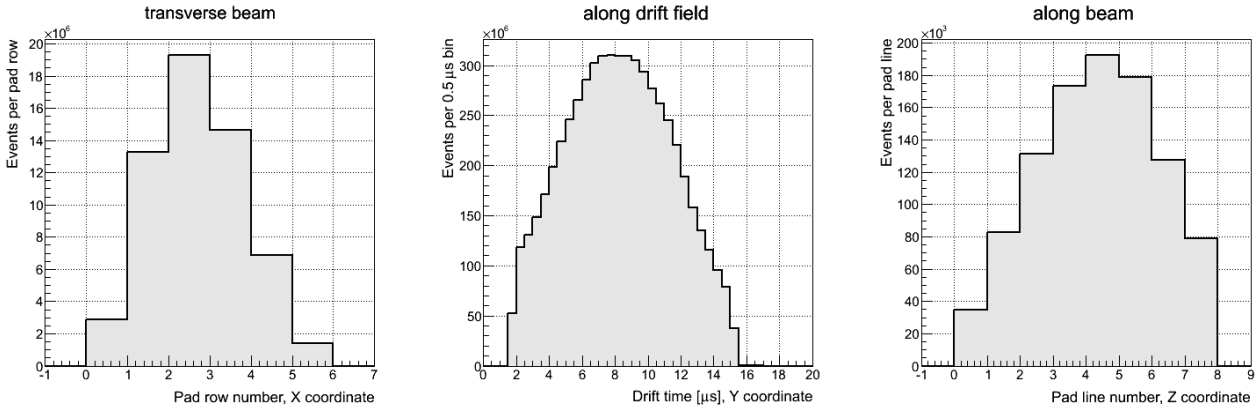

Fig. 5. Spatial distributions of the muon stops in the CryoTPC along the *X*, *Y* and *Z* coordinates, respectively. The *Z* axis is along the beam line

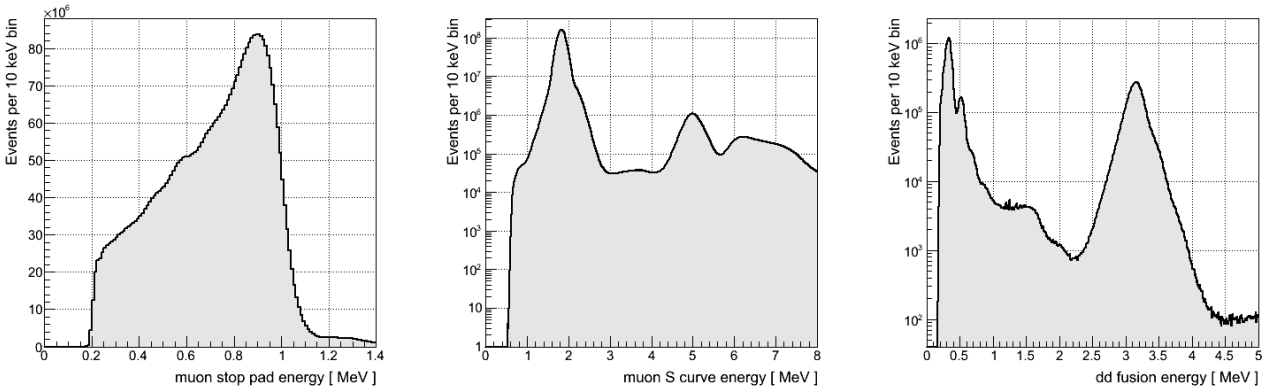

Fig. 6. Energy spectra of muon signals on the muon stop pad (left), the *S* curve (middle), and the *dd* fusion signals (right)

The energy spectrum of the muon signals on the muon stop pad (E_i) and the so called *S* distribution are shown in Fig. 6. The quantity *S* is a combination of the muon energies deposited on the muon stop pad and on the previous one, $S = E_i + 2E_{i-1}$. The peak at 1.8 MeV in the *S* distribution corresponds to the single muons, while the peak at 5 MeV is due to pile-up of the muon and $t + p$ signals. The energy spectrum of the second pulses on the stop pad (mainly the *dd* fusions) is shown in Fig. 6, in the rightmost picture. The peaks

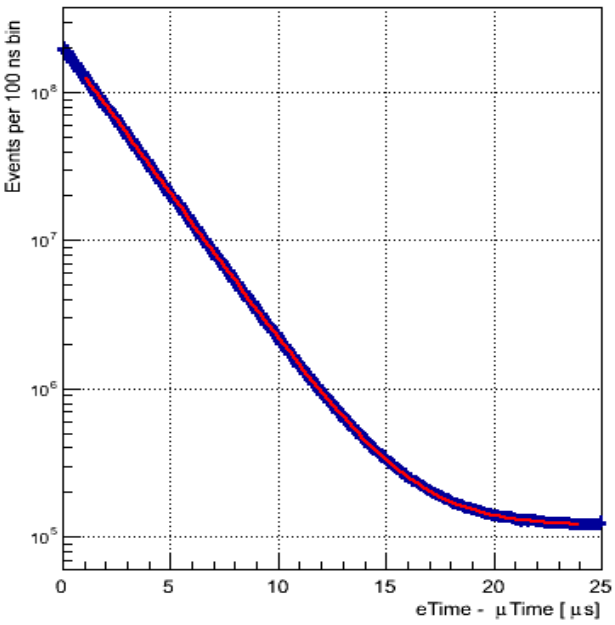

Fig. 7. Muon lifetime spectrum $\Delta t = t_e - t_\mu$

at 0.33, 0.52 and 3.2 MeV correspond to ^{3}He, ^{3}Heμ, and $t + p$ channels of the *dd* fusion, respectively. In this first physics run, the energy resolution for the ^{3}He peak was 40 keV, and it will be improved in the next runs by a factor of 3 due to implementation of new cryogenic preamplifiers recently developed by the MuSun Collaboration.

The time difference between the muon arrival time in μSC and the decay electron arrival time in eSC is presented in Fig. 7. This lifetime spectrum can be fitted with the function $N(t) = N_0 \lambda \exp(-\lambda t) + B$, over the range $1\mu s < t < 24$ μs, where N_0, B, and λ are free parameters. Note that we cannot fit the lifetime spectrum from zero time point like in the MuCap experiment because of the relatively slow spin-flip process in the hyperfine states of the *d*μ atoms. The background B is mostly due to random coincidences with cosmic muons, and it can be further reduced by at least an order of magnitude by applying the space correlation cut (not used in this figure) between the muon stop coordinate and the muon decay electron trajectory. This will be sufficient for the 10^{-5} precision measurement of the μ^- lifetime. The analysis of these data is still in progress, and we expect the first physics results to be evaluated from these data.

6. Plans for the future

The first physics test run in 2011 was quite successful. It has confirmed the capability of the MuSun experiment to reach its goal to measure the muon capture rate Λ_d with the accuracy close to 1 %. On the other hand, some technical problems were identified, and the ways to upgrade the experimental set-up were determined. In particular, it was found that the cryogenerator was malfunctioning. It could provide cooling of the CryoTPC only down to 34 K, instead of 28 K achieved in preliminary tests. A problem was discovered in the cold head. It was sent to the industrial company for repair. In the next run, the gas temperature will be kept at 30 K. Another important improvement will be a replacement of the preamplifiers in the anode pad readout channels operating at the room temperature by the preamplifiers operating at the liquid nitrogen temperature. Preliminary tests have shown that this will improve the energy resolution by a factor of three. Also, we plan to improve the sensitivity of our gas chromatographic system to the sub-ppb level by calibrating it following the vapor-pressure curve.

We plan to perform as minimum two full scale physics runs in 2013 and 2014 to collect the statistics of more than 10^{10} good selected muon stops. These measurements will be performed in the new beam line πE1, specially prepared for the MuSun experiment. This beam line is equipped with the "muon on request" facility (as it was in the π*E*3 beam line), which will allow to increase essentially the data rate in the experiment. Meanwhile, theorists are already considering possibilities to implement new results expected from the MuSun experiment for validation of the Effective Field Theory of weak processes in the few-nucleon systems [3].

References

1. P. Ackerbauer *et al.*, Phys. Lett. B **417**, 224 (1998).
2. V.A. Andreev *et al*., MuCap Collaboration, Phys. Rev. Lett. **110**, 022504 (2013).
3. J. Adam, Jr. *et al.*, Phys. Lett. B **709**, 93 (2012).
4. D.V. Balin *et al*., Elementary Particles and Atomic Nuclei **42**, 361 (2011).
5. L.A. Alekseev *et al*., Preprint PNPI-**2702**, Gatchina (2006).
6. V.A. Ganzha *et al*., Nucl. Instr. Meth. A **578**, 485 (2007).

SELECTED PHYSICS RESULTS FROM THE HERMES EXPERIMENT

S.L. Belostotski, S.I. Manaenkov, Yu.G. Naryshkin and D.O. Veretennikov

1. Introduction

The HERMES experiment stopped data taking in 2007. Most of the data were collected using the 27.6 GeV longitudinally polarized positron beam scattered off a hydrogen or deuterium target. A typical beam polarization was about 50 %. The targets were longitudinally or transversely polarized with the polarization close to 90 %. The whole HERMES data set was accumulated at an integrated luminosity of 1505 pb^{-1}.

The HERMES Collaboration studied sum rules for the nucleon spin, quark helicity distributions, polarization of gluons, transverse spin effects, exclusive reactions and GPDs, hyperon polarization, nuclear medium effects. These studies play a key role in better comprehension of the QCD dynamics and spin structure of hadrons.

The PNPI group was involved in the HERMES experiment since its design phase with significant contributions both to the experiment and data analysis. In the data analysis, PNPI takes an active part in several analysis topics such as quark helicity distribution, vector meson electroproduction, polarization of Λ hyperons. Here we present most important results obtained in 2007–2011 years for two analysis topics where the PNPI group plays the leading role.

2. Exclusive electroproduction of vector mesons in deep-inelastic scattering

A study of exclusive electroproduction of vector mesons on nucleons allows for verification of perturbative QCD (pQCD) predictions and gives access to the Generalized Parton Distributions (GPDs) of nucleons. In the one-photon-exchange approximation, the angular distribution of exclusively produced vector-mesons and their decay into final hadrons can be described with the help of the Spin Density Matrix Elements (SDMEs) or, alternatively, in terms of the helicity amplitudes related to the beam/target spin states. The SDME analysis of the ρ^0 meson production studied by the HERMES Collaboration with the help of the HERA polarized positron beam and an unpolarized proton or deuteron target is presented in [1]. The kinematics of the reaction under study was as follows: the photon virtuality $1 < Q^2 < 7$ GeV^2, the centre-of-mass energy of the photon-nucleon scattering $3.0 < W < 6.3$ GeV, the square of the four-momentum transferred to the nucleon $-t < 0.4$ GeV^2. In this experiment, in addition to fifteen unpolarized SDMEs, eight polarized SDMEs were obtained for the first time. The theoretically predicted hierarchy of the SDMEs was observed. The phase difference between the helicity-conserving amplitudes T_{11} and T_{00} was found to be significantly non-zero and Q^2 dependent. It should be noted that the latter observation is in contradiction with the theoretical calculations [2] based on the pQCD with the GPDs of the nucleon well describing the HERA collider data. The kinematic dependences of all 23 SDMEs are measured for both hydrogen and deuterium targets. No significant difference between the proton and deuteron results is seen, which shows that the ρ^0 meson production is dominated by the two-gluon exchange diagrams. On the other hand, the evaluation of certain linear combinations of SDMEs provides an indication that contributions of Unnatural-Parity-Exchange (UPE) amplitudes at not very high energy of the HERMES experiment can be measured. The violation of the *s*-channel helicity is established with high experimental accuracy for the transition of the transverse virtual photon to the longitudinal ρ^0 meson. Contributions of the transitions of the longitudinal photon to the transverse meson and the double spin-flip transition of the transverse photon to the transverse ρ^0 meson also violating the *s*-channel helicity are shown to be small in accordance with theoretical predictions [3, 4].

Any SDME may be expressed through bilinear products of the helicity amplitudes in its numerator and denominator. The numerator contains typically more than one bilinear product. Due to this SDME property it is not easy to understand which amplitude is not well described with theory when the calculated and measured SDMEs disagree. It is not trivial also to interpret the kinematic dependences of SDMEs in terms of the kinematic dependences of the amplitudes and confirm the hierarchy among the amplitudes predicted in [3, 4]. A direct extraction of the amplitude ratios (the measured angular distributions depend on the ampli-

tude ratios rather than on the amplitudes themselves) excludes these shortcomings. This "amplitude" approach allows for a direct comparison of the pQCD predictions and experimental results and for better specification of the reaction mechanism than that using the SDME method. The most important amplitudes are those without the nucleon spin flip when the data on unpolarized targets are studied. They are denoted $T_{\lambda\mu}$ where λ and μ are helicities of the ρ^0 meson and the virtual photon. The results of the amplitude analysis of the same HERMES data sample as in [1] are published in [5, 6]. The ratios of the helicity amplitudes to T_{00} are determined by fitting the measured angular distributions of the final state pions. Given the electron / positron beam is longitudinally polarized, the extraction of both the real and imaginary parts of the ratios of the natural parity exchange amplitudes $T_{\lambda\mu}$ is possible. The modulus of the ratio $|U_{11}/T_{00}|$, where U_{11} denotes the UPE amplitude, can now be directly found. The ratios T_{11}/T_{00}, T_{01}/T_{00}, and $|U_{11}/T_{00}|$ are found to be sizable and their kinematic dependences are parameterized, while all other similar ratios are proved to be small. The real part of T_{11}/T_{00} is found to follow the asymptotic $1/Q$ behaviour predicted by the pQCD [3, 4].

The HERMES data are in agreement with those of the H1 Collaboration [7] as seen in Fig. 1. The imaginary part of T_{11}/T_{00} grows with Q in contradiction with the large-Q asymptotic behaviour expected in the pQCD. The phase difference between T_{11} and T_{00} grows with Q and has a mean value of about 30 degrees in the HERMES kinematic region, which is in agreement with the SDME method [1] but at sharp variance with pQCD based calculations [2]. The behaviour of $\mathrm{Im}(T_{01}/T_{00})$ does not contradict to the asymptotic pQCD behaviour, while $\mathrm{Re}(T_{01}/T_{00})$ is independent of Q, which disagrees with the pQCD. The HERMES result for $\mathrm{Re}(T_{01}/T_{00})$ is close to that of the H1 Collaboration obtained for higher values of Q as can be seen in Fig. 2 where the dependence of the amplitude ratio on the Mandelstam variable t is presented. This comparison shows also that $\mathrm{Re}(T_{01}/T_{00})$ does not depend on Q for the measured values of the photon virtuality. The UPE signal (the non-zero ratio $|U_{11}/T_{00}|$) is seen with a very high significance for both the proton and deuteron data, confirming the existence of the UPE contribution with a higher precision than that obtained with the SDME method. Finally, we would like to stress that the amplitude method permits to study the kinematic dependences and contributions of small amplitudes better than the SDME method with typically smaller statistical uncertainties. This allows for more definite physical conclusions on the QCD dynamics and vector meson production mechanisms.

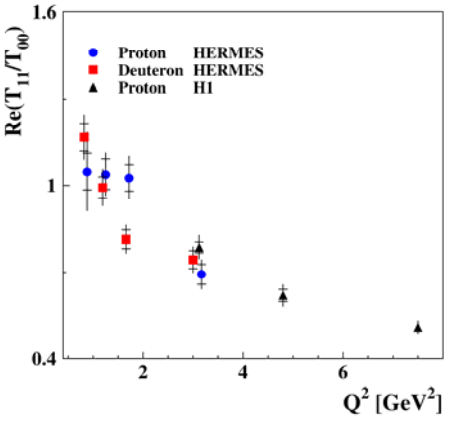

Fig. 1. Q^2 dependence of the helicity amplitude ratio

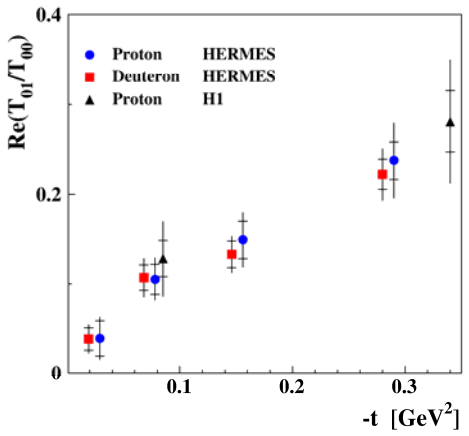

Fig. 2. t dependence of the helicity amplitude ratio

3. Spin transfer to the Λ and $\bar{\Lambda}$ hyperons in semi-inclusive deep-inelastic positron scattering

According to the latest measurements by the HERMES and COMPASS Collaborations, the total quark contribution to the proton spin is found to be $\Delta\Sigma = 0.33 \pm 0.03$ [8]. Using this number and two well-known hyperon β-decay constants ($F = 0.464 \pm 0.008$, $D = 0.806 \pm 0.008$) one can calculate the first moment of the polarized quark distribution $\Delta q_f = q_f^{\uparrow} - q_f^{\downarrow}$ for any SU(6) spin ½ baryon octet state. Here, $f = u, d, s$ is the quark flavour, $q_f^{\uparrow}$, $q_f^{\downarrow}$ is the integrated number density of the quark aligned parallel or anti parallel to the baryon spin, respectively. Thus, for the Λ hyperon one obtains $\Delta q_u^{\Lambda} = \Delta q_d^{\Lambda} = 1/3\ (\Delta\Sigma - D) = -0.16 \pm 0.01$ and $\Delta q_s^{\Lambda} = 1/2\ (\Delta\Sigma + D) = 0.57 \pm 0.01$. It is commonly agreed that the Λ spin is preferentially carried by the

strange quark, while the contribution from the light quarks, even the sign of this contribution, is still debatable. Thus, in the naïve constituent quark model $\Delta q_u^{\Lambda} = \Delta q_d^{\Lambda} = 0$ and $\Delta q_s^{\Lambda} = 1$ ($\Delta\Sigma = 1$ and $D = 1$ should be taken), *i.e.* the Λ hyperon spin is entirely carried by the *s*-quark, while the light quarks are not polarized. A similar conclusion follows from the lattice-QCD calculations [9]: $\Delta q_u^{\Lambda} = \Delta q_d^{\Lambda} = -0.02 \pm 0.04$ and $\Delta q_s^{\Lambda} = 0.68 \pm 0.04$. Alternatively, it was shown in [10] that the hyperfine interaction responsible for $\Delta - N$ and $\Sigma^0 - \Lambda$ mass splitting results in significantly positive polarized non-strange quark distributions.

Experimental information on the hyperon spin structure can be obtained by measuring the spin transfer to the hyperon produced in the process of polarized quark fragmentation. In the case of $\Lambda(\bar{\Lambda})$, the hyperon polarization (spin transfer) can be measured via the weak decay channel $\Lambda \to p + \pi^-$ ($\bar{\Lambda} \to \bar{p} + \pi^+$) through the angular distribution of the final state particle. It is important that, as compared to other hyperons, the yield of the Λ hyperons is typically high enough to obtain satisfactory statistical precision of the polarization measurements. In the LEP experiments OPAL and ALEPH [11, 12], Λ hyperons were predominantly produced via $Z^0 \to s\bar{s}$ decay, both strange quarks being strongly polarized. The measurements indicate a significant $\Lambda(\bar{\Lambda})$ polarization and positive spin transfer from the strange quark. These experiments confirm high positive polarization of the *s* quark in the Λ hyperon with Δq_s^{Λ} in the range of 0.6 to 1. In Deep Inelastic Scattering (DIS) of polarized leptons from nucleons, in contrast to Z^0 decay experiments, Λ hyperons are mostly produced due to fragmentation of non-strange polarized *u* and *d* quarks. In the case of Λ hyperons, non-strange quarks also dominate with somewhat larger contributions from $\bar{u}$ and $\bar{s}$ antiquarks.

Here we present the final HERMES results on the spin transfer to the Λ and $\bar{\Lambda}$ hyperons in DIS. They surpass substantially the data sample in [13, 14] in statistical precision. Unlike previous publication, the spin transfer is treated as a vector in the Λ rest frame. Correspondently, a three dimension analysis formalism has been developed in order to reconstruct all three components of this vector.

In the quark parton model, the process of fragmentation of a polarized struck quark to the polarized Λ (or $\bar{\Lambda}$) hyperon can be quantified in terms of the spin dependent (polarized) $\Delta F_f^{\Lambda}(z)$ and spin independent (unpolarized) $F_f^{\Lambda}(z)$ fragmentation functions. The partial (for a given flavour *f*) spin transfer $D_f^{\Lambda}(z)$ can be defined as

$$D_f^{\Lambda}(z) = \frac{\Delta F_f^{\Lambda}(z)}{F_f^{\Lambda}(z)} = \frac{F_{f\uparrow}^{\Lambda\uparrow}(z) - F_{f\uparrow}^{\Lambda\downarrow}(z)}{F_{f\uparrow}^{\Lambda\uparrow}(z) + F_{f\uparrow}^{\Lambda\downarrow}(z)}. \tag{1}$$

Here, $F_{f\uparrow}^{\Lambda\uparrow\downarrow}(z)$ stands for the fragmentation function of a quark (antiquark) of flavour *f* with the positive helicity fragmenting into the Λ hyperon with the positive or negative helicity, $z = E^{\Lambda}/\nu$ is the fractional energy of the emitted Λ hyperon, ν is the photon energy totally transferred to the struck quark, and E^{Λ} is the Λ hyperon energy. If the target is unpolarized, the observed Λ polarization reads:

$$P^{\Lambda}(x, y, z, Q^2) = D^{\Lambda}(x, z, Q^2) P_b D(y) = \left(\sum_f \omega_f^{\Lambda}(x, z, Q^2) D_f^{\Lambda}(z, Q^2) \right) P_b D(y). \tag{2}$$

Here, $D^{\Lambda}(x, z, Q^2)$ is the total spin transfer, P_b is the beam polarization, $D(y) = [1-(1-y)^2]/[1+(1-y)^2]$ represents the spin transfer from the incident positron to the struck quark (or the depolarization factor of the virtual photon), $y = \nu / E_{\text{beam}}$ is the fractional energy carried by the photon. The Bjorken scaling variable *x* in the target rest frame is given by $x = Q^2 / 2M_p\nu$, where M_p is the target proton mass and Q^2 is the negative four-momentum transfer squared. It is easy to see that the value $P_b D(y)$ stands for the polarization of the struck quark, $\omega_f^{\Lambda}(x, z, Q^2)$ represents the purity (fractional probability) for a quark (antiquark) of flavour f to fragment to the Λ hyperon ($\sum_f \omega_f^{\Lambda}(x, z, Q^2) = 1$). If one assumes that the struck quark f fragmenting to Λ ($\bar{\Lambda}$) preserves its polarization, the partial spin transfer integrated over *z* can be expressed through the first moments of the polarized and unpolarized quark density distributions in the Λ ($\bar{\Lambda}$) hyperon [15]:

$$D_f^{\Lambda}(Q^2) = \frac{\Delta q_f^{\Lambda}(Q^2)}{q_f^{\Lambda}(Q^2)}, \tag{3}$$

i.e. the partial spin transfer of a quark *f* to the Λ ($\bar{\Lambda}$) hyperon is given by the average polarization of this quark in Λ ($\bar{\Lambda}$). Despite a number of simplifying assumptions that have been made in deriving Eq. 3, this equation is a useful starting point for qualitative understanding of the spin transfer. Due to the valence quark dominance ($\omega_u^{\Lambda} + \omega_d^{\Lambda} \approx 1$), the measurement of D^{Λ} can provide a realistic measure of the non-strange quark polarization in the Λ hyperon.

The experiment and event selection were described in detail in [13]. The Λ ($\bar{\Lambda}$) hyperons produced in semi-inclusive reactions were detected via $p\pi^-$ ($\bar{p}\pi^+$) weak decay channel. In order to control false asymmetry, a K_s data sample was also accumulated detecting $K_s \to \pi^+\pi^-$ decay. Invariant mass distributions for Λ, $\bar{\Lambda}$ and K_s events are shown in Fig. 3. N_{Λ}, $N_{\bar{\Lambda}}$, N_{K_s} in Fig. 3 are the total number of events after background subtraction, σ is the Λ and $\bar{\Lambda}$ peak resolutions, and (1 – η) is the background contributions.

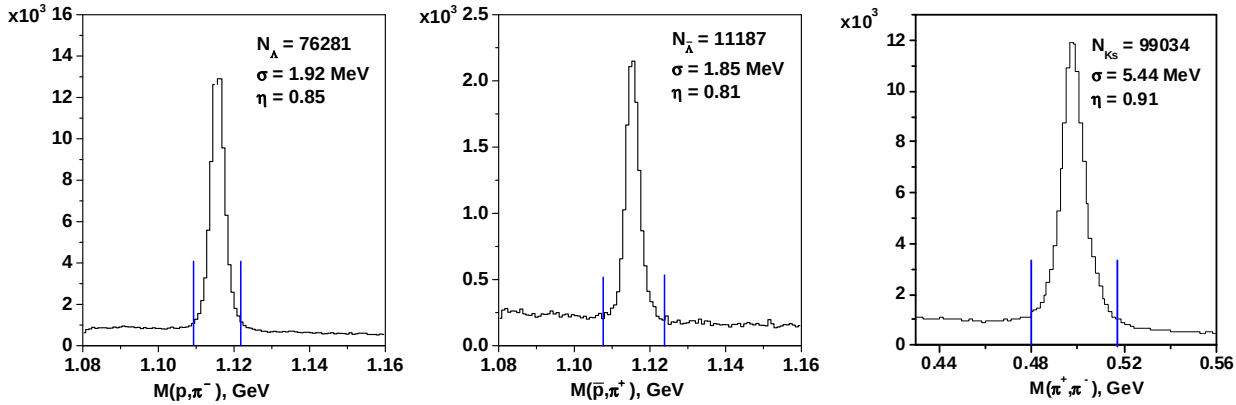

Fig. 3. Invariant mass distributions for Λ, $\bar{\Lambda}$ and K_s events

The spin transfer can be defined in the Λ rest frame as a vector with longitudinal and transverse components both belonging to the production plane formed by the virtual photon momentum $\vec{p}_{\gamma}$ and the Λ momentum $\vec{p}_{\Lambda}$. As the virtual photon is longitudinally polarized (its spin is assumed to direct along the $\vec{p}_{\gamma}$ vector), the component perpendicular to the Λ production plane must be equal to zero because of parity conservation. The coordinate system is defined as follows: the *Z*-axis is taken along the virtual photon momentum $\vec{p}_{\gamma}$ boosted to the Λ rest frame, the *Y*-axis is perpendicular to the production plane, and the *X*-axis is perpendicular to the *YZ* plane.

During the data taking period, the beam polarization was reversed on a month basis such that for the selected data sample the condition $[\![P_b]\!] \approx 0$ was fulfilled. Here, $[\![P_b]\!]$ is the luminosity weighted beam polarization. The extraction of the D_{Li} components is essentially facilitated in this case as no Monte Carlo simulation of the spectrometer acceptance function is needed [13]. Here, the subscript *L* indicates the direction of the virtual photon spin, *i* = *x*, *y*, *z*. The spin transfer components for Λ and $\bar{\Lambda}$, integrated over the whole data sample, are presented below:

$$D_{Lx}^{\Lambda} = -0.016 \pm 0.042_{\text{stat}} \pm 0.02_{\text{syst}} \qquad D_{Lx}^{\bar{\Lambda}} = -0.14 \pm 0.11_{\text{stat}} \pm 0.02_{\text{syst}}$$

$$D_{Ly}^{\Lambda} = 0.004 \pm 0.037_{\text{stat}} \pm 0.02_{\text{syst}} \qquad D_{Ly}^{\bar{\Lambda}} = 0.05 \pm 0.10_{\text{stat}} \pm 0.02_{\text{syst}}$$

$$D_{Lz}^{\Lambda} = 0.186 \pm 0.040_{\text{stat}} \pm 0.02_{\text{syst}} \qquad D_{Lz}^{\bar{\Lambda}} = 0.05 \pm 0.10_{\text{stat}} \pm 0.02_{\text{syst}}$$

$$\left|D_{LL'}^{\Lambda}\right| = 0.187 \pm 0.040_{\text{stat}} \pm 0.02_{\text{syst}} \qquad \left|D_{LL'}^{\bar{\Lambda}}\right| = 0.15 \pm 0.11_{\text{stat}} \pm 0.02_{\text{syst}}$$

For both Λ and $\bar{\Lambda}$ hyperons, the D_{Ly} component is found compatible with zero as it should be. For Λ hyperons, the quantization axis is directed practically along the virtual photon momentum (along the *Z*-axis), the transverse component being correspondently small (compatible with zero), *i.e.* the Λ polarization preserve the spin orientation of the struck quark and $L' = L$, L' being the Λ spin direction. For $\bar{\Lambda}$, the statistical accuracy is not sufficient to come to a similar conclusion.

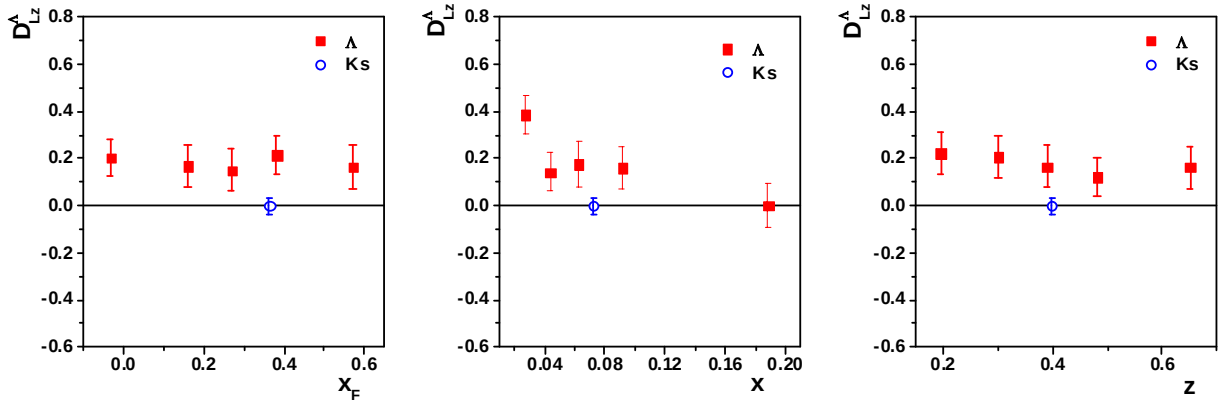

Fig. 4. Dependences of the longitudinal spin transfer to the Λ hyperon on DIS kinematic variables

In Fig. 4, dependences of D_{Lz}^{Λ} on DIS kinematic variables are presented. As seen in Fig. 4, false asymmetries estimated with the K_s data sample are found to be negligibly small and compatible with zero. Comparisons with world data are presented in Fig. 5.

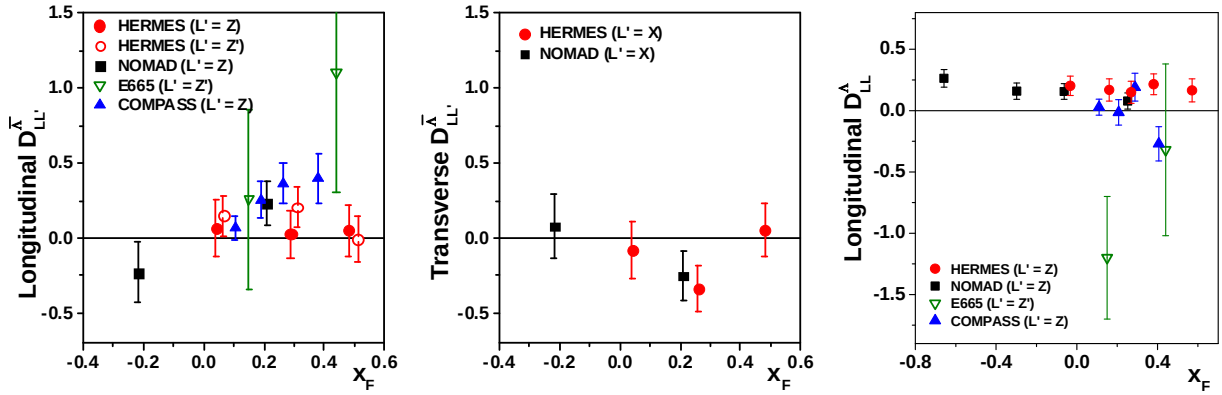

Fig. 5. World data on the longitudinal and transverse spin transfer to the $\bar{\Lambda}$ hyperon and the longitudinal spin transfer to Λ

For Λ hyperons, the obtained results on the longitudinal spin transfer are in good agreement with the NOMAD [16] and recent COMPASS [17] experiments at moderate values of the Feynman scaling variable x_F, while the HERMES and COMPASS results disagree with each other at x_F larger than 0.4. For $\bar{\Lambda}$ hyperons, all D_{Li} components are compatible with zero within statistical error bars of ± 0.1. Open circles in Fig. 5 (left panel) are the HERMES data with the *Z*-axis chosen along the momentum of the $\bar{\Lambda}$ hyperon in the laboratory frame.

To conclude, the longitudinal component of the spin transfer to the Λ hyperon is found to be $D_{LL}^{\Lambda} = 0.19 \pm 0.04_{\text{stat}} \pm 0.02_{\text{syst}}$. It is directed along the virtual photon momentum in the Λ rest frame while two other (transverse) components are compatible with zero. A positive and statistically significant value of D_{LL}^{Λ} can be interpreted in favour of a noticeable positive contribution of the light *u* and *d* quarks to the Λ spin suggesting $\Delta q_u^{\Lambda} = \Delta q_d^{\Lambda} \approx 0.2$ in contradiction to the SU(6) prediction based on the value of $\Delta\Sigma = 0.33$,

well-established for the proton. A possibility of sizeable SU(6) symmetry breaking in the quark distributions of the Λ hyperon and positive non-strange quark polarization in Λ is discussed in [10, 18].

References

1. A. Airapetian *et al*., Eur. Phys. J. C **62**, 659 (2009).
2. S.V. Goloskokov and P. Kroll, Eur. Phys. J. C **53**, 367 (2008).
3. D.Yu. Ivanov and R. Kirschner, Phys. Rev. D **58**, 114026 (1998).
4. E.V. Kuraev, N.N. Nikolaev, and B.G. Zakharov, Pis'ma ZhETF **68**, 667 (1998).
5. A. Airapetian *et al*., Eur. Phys. J. C **71**, 1609 (2011).
6. S. Manaenkov, Proceedings of XYIII International Workshop on Deep-Inelastic Scattering and Related Subjects, April 19-23, 2010, Firenze, Italy; http:/pos/sissa.it: Pos (DIS2010) 079.
7. F.D. Aaron *et al.,* JHEP **1005**, 32 (2010).
8. A. Airapetian *et al.,* Phys. Rev. D **75**, 012007 (2007).
9. M. Gockeler *et al.*, Phys. Lett. B **545**, 112 (2002).
10. C. Boros, J.T. Londergan, and A.W. Thomas, Phys. Rev. D **61**, 014007 (2000).
11. K. Ackerstaf *et al.*, Eur. Phys. J. C **2**, 49 (1998).
12. D. Buskulic *et al.*, Phys. Lett. B **374**, 319 (1996).
13. A. Airapetian *et al.,* Phys. Rev. D **74**, 072004 (2006).
14. A. Airapetian *et al.,* Phys. Rev. D **64**, 112005 (2001).
15. D. Ashery and H.J. Lipkin, Phys. Lett. B **469**, 263 (1999).
16. P. Astier *et al.*, Nucl. Phys. B **588**, 3 (2000).
17. M. Alekseev *et al.*, Eur. Phys. J. C **64**, 171 (2009).
18. B.-Q. Ma, J.-J. Yang, I. Schmidt, Phys. Lett. B **477**, 107 (2000).

OLYMPUS EXPERIMENT AT DORIS, DESY

PNPI participants of the OLYMPUS Collaboration: S.L. Belostotski, G.G. Gavrilov, A.A. Izotov, A.Yu. Kiselev, A.G. Krivshich, O.V. Miklukho, Yu.G. Naryshkin, and D.O. Veretennikov

1. Introduction

Following R. Hofstadter's pioneering work at Stanford, the nucleon Form Factors (FFs) are measured in elastic electron scattering at moderate energies. By 1990's, it was established in unpolarized *ep* elastic scattering experiments that the ratio of the electric $G_E(Q^2)$ to the magnetic $G_M(Q^2)$ FFs are approximately independent of Q^2, *i.e.*, $G_E(Q^2)/\mu_p G_M(Q^2) \approx 1$, where μ_p is the proton magnetic moment. It was generally believed that the dependence on Q^2 of the proton electric and magnetic FFs and the neutron magnetic FF are satisfactorily described by the dipole formula $G_D(Q^2) = \left(1 + Q^2/\Lambda^2\right)^{-2}$ with Λ = 0.84 GeV (0.165 fm^{-1}) in a wide Q^2 range up to 30 GeV.

An unexpected behaviour of the ratio $G_E(Q^2)/\mu_p G_M(Q^2)$ has been recently observed in polarization experiments at JLAB [1]: this ratio is dropping down rapidly, practically linear with Q^2, in sharp disagreement with previously obtained unpolarized data (Fig. 1).

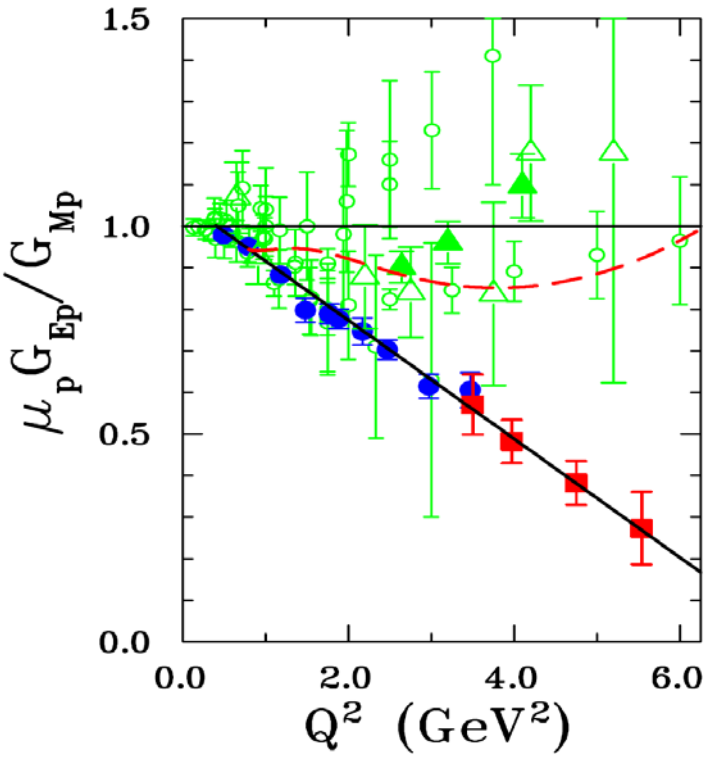

Fig. 1. The ratio $G_E(Q^2)/\mu_p G_M(Q^2)$ extracted from two sets of data obtained in JLAB using the recoil proton polarization technique [1, 2]: blue and red points, respectively, green points are a compilation of unpolarized experiment data

Presently, it is agreed that this large discrepancy might be due to corrections beyond the Born approximation, which include both pure QCD corrections and a "hard" Two Photon Exchange (TPE) mechanism with baryon intermediate states [3, 4]. According to theoretical estimations [4], these corrections to the $G_E(Q^2)/\mu_p G_M(Q^2)$ ratio are small for polarized data, while they are essential and Q^2 dependent for

unpolarized experiments. Therefore, after inserting the second order corrections the discrepancy might be sorted out. The difficulty is that, unlike QED corrections, the TPE correction cannot be calculated in a model independent way as it contains diagrams with various baryon intermediate states, the photo-coupling constants for most of these states being unknown (see, *e.g.*, [5]). In addition, an alternative explanation of the observed discrepancy not related to the TPE mechanism [6] has been recently suggested, which makes theoretical interpretations of the discrepancy even more ambiguous.

The goal of the OLYMPUS experiment is to verify experimentally this TPE theoretical *ansatz* in a definitive way. In addition, there are experiments underway in Novosibirsk (VEPP-3) and at JLAB (EG5 CLAS) with a similar goal.

2. Beam charge asymmetry and two photon exchange mechanism

Feynman diagrams representing the Born approximation, the first order bremsstrahlung and the second order radiative corrections including hard TPE exchange graphs are shown in Fig. 2.

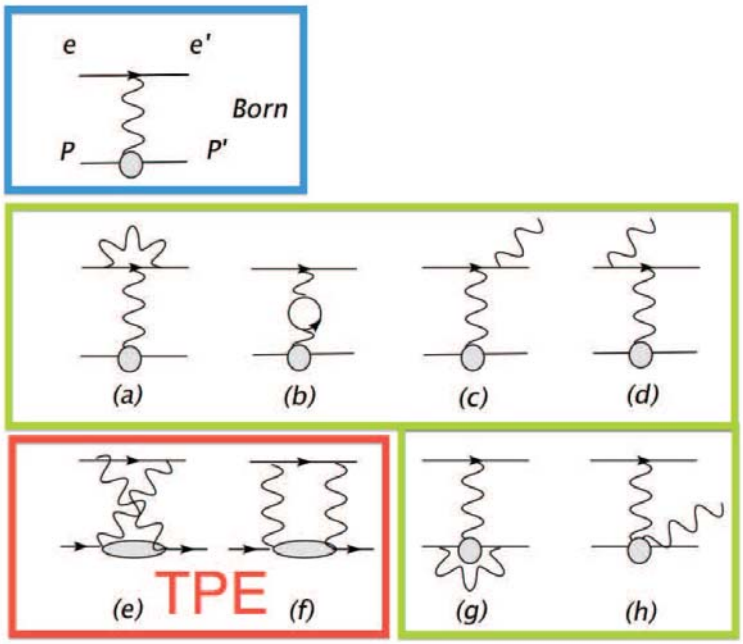

Fig. 2. Feynman diagrams: the Born amplitude, the first order bremsstrahlung and the second order radiative corrections (*a*, *b*, *c*, *d*, *g*, *h*) and TPE graphs (*e*, *f*)

It can be easily shown that the ratio of the positron-proton (σ^+) to electron-proton (σ^-) elastic scattering cross sections at a given Q^2-value, due to interference of the Born amplitude and the hard TPE amplitudes, is sensitive to the hard TPE correction:

$$\chi(\theta_e) = \frac{\sigma^+(\theta_e)}{\sigma^-(\theta_e)} - 1 = \frac{4M_{\text{Born}}(\theta_e)\,\text{Re}(M^*_{2\gamma}(\theta_e))}{\left|M_{\text{Born}}(\theta_e)\right|^2} + QED_{\text{cor}}\,. \tag{1}$$

Here, χ is the beam charge asymmetry, M_{Born} is the Born amplitude, $M_{2\gamma}$ stands for the hard TPE, and QED_{cor} are the pure second order QED corrections.

All three mentioned above experiments are studying the beam charge asymmetry as a function of Q^2 with the precision about 1 % in order to extract a possible contribution from the hard TPE mechanism.

3. OLYMPYS experiment

The layout of the OLYMPUS experiment is shown in Fig. 3. The positron or electron 2 GeV beam of the DORIS accelerator circulates through a hydrogen gas target of the OLYMPUS spectrometer. The detector is based upon an eight-sector toroidal magnetic field.

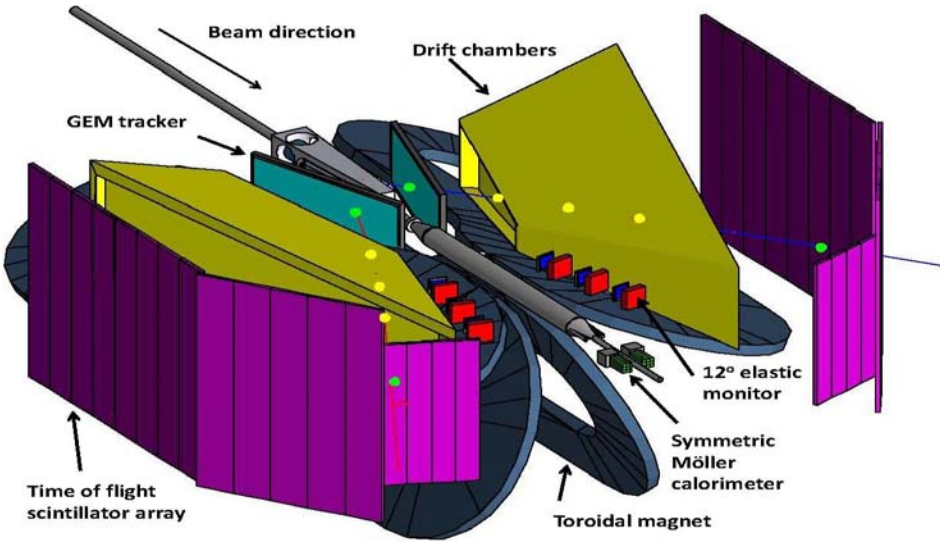

Fig. 3. The OLYMPUS set-up at the DORIS accelerator

Two horizontal sectors are instrumented with detector components: wire drift chambers, two luminosity monitors and time of flight scintillators. The detector is left/right symmetric. Two vertical sectors are used by the internal targets and the vacuum system for the beam line. The toroid, the Drift Chambers (DC) and the Time Of Flight scintillators (TOF) were the main components of the BLAST detector successfully operated at the MIT-Bates Linear Accelerator Centre.

In addition to this system, two luminosity monitors have been designed and built:

- A two arm (left/right) luminosity monitor instrumented with multi-wire proportional chambers (MWPC), GEM detectors and scintillation counters equipped with silicon photo multipliers SiPMs. The SiPMs are used because of hard limitation in space and as they are not sensitive to magnetic fields. This monitor detects elastic e^+p and e^-p scattering at $\theta_e = 12°$, *i.e.* at low Q^2-values ($Q^2 = 0.16$ GeV^2), where the TPE correction is negligibly small. Note that the 12° monitor was proposed by the PNPI group. The MWPCs, readout electronics, scintillation counters with SiPMs and details of the mechanical structure were also designed and fabricated at PNPI.
- A Moeller – Baba luminosity monitor consisting of two lead fluoride Cherenkov calorimeters located in the horizontal plane left/right symmetrically at a very forward scattering angle of 1.29°.

The horizontal/vertical beam positions and slopes in the region of the gas target are monitored with a precision of 0.1 mm and 0.3 mrd, respectively. A possible beam energy instability of the DORIS machine is under control at the level of 0.1 MeV.

The elastic scattering events are selected with the help of the track information provided by the DCs, MWPCs and GEM detectors, the time correlation between the scattered e^+ or e^- and the recoil proton, and the energy deposited in the scintillation bars of the TOF detector. Due to the combined criteria of the scattering angle and momentum correlations, the co-planarity, and the time of flight correlation, the two body kinematics is strongly overdetermined, which allows us to suppress effectively the pion production and soft photon

emission (bremsstrahlung) background. This is important, in particular, in the domain of interest, *i.e.*, at high Q^2-values and low photon polarization ε, where $\varepsilon = \left[1 + 2(1 + Q^2 / 4M_{prot}^2)\tan^2(\theta_e / 2)\right]^{-1}$.

In order to minimize systematic uncertainties, the toroid polarity B^+ and B^-, as well as the beam species e^+ and e^- are changed every 8 hours. This allows us to calculate the cross section ratio in a given θ_e bin as the 4-fold ratio:

$$R(\theta_e) = \frac{\sigma^{e^+p}(\theta_e)}{\sigma^{e^-p}(\theta_e)} = \left[\frac{N_{e+B+}(\theta_e)\cdot N_{e+B-}(\theta_e)}{N_{e-B+}(\theta_e)\cdot N_{e-B-}(\theta_e)}\right]^{\frac{1}{2}} + \delta(\theta_e). \qquad (2)$$

Here, $N_{e+B+}, N_{e-B+}, N_{e+B-}, N_{e-B-}$ are the normalized to the luminosity numbers of the selected *ep* elastic scattering events at the scattering angle θ_e measured for two beam species (e^+ and e^-) and two toroid polarity combinations (B^+ and B^-). The geometrical acceptances of the scattered leptons (positrons or electrons) and the recoil protons in each polarity of the toroid are cancelled out in the 4-fold ratio, the latter being equal to unity provided there is no contribution from the TPE. A small correction δ appears due to slightly different interactions of the scattered positron and electron in the detector materials. It is well determined with the help of Monte Carlo simulations.

4. Outlook and competing experiments

It was planned that the OLYMPUS experiment would collect data in 2012 during two periods: RUN I (4 weeks) in February and RUN II (10 weeks) in October – December. RUN I was mostly dedicated to tuning the sub-detectors and optimization of the beam conditions. The data taking has actually been started in RUN II. The experiment cannot be prolonged after 2012 because of the DORIS accelerator shutdown. The projected statistical precision of the OLYMPUS experiment is plotted in Fig. 4. These estimations have been done for 500 hours of data taking for each (e^+ and e^-) beam species at an integrated luminosity of 3.6 fb^{-1} (the instant luminosity being $2 \cdot 10^{33}\,\text{cm}^{-2}\text{s}^{-1}$). At the lowest value of ε, the statistical uncertainty is expected to be 1.1 %, while the systematic uncertainty is assumed to be not larger than 1 %.

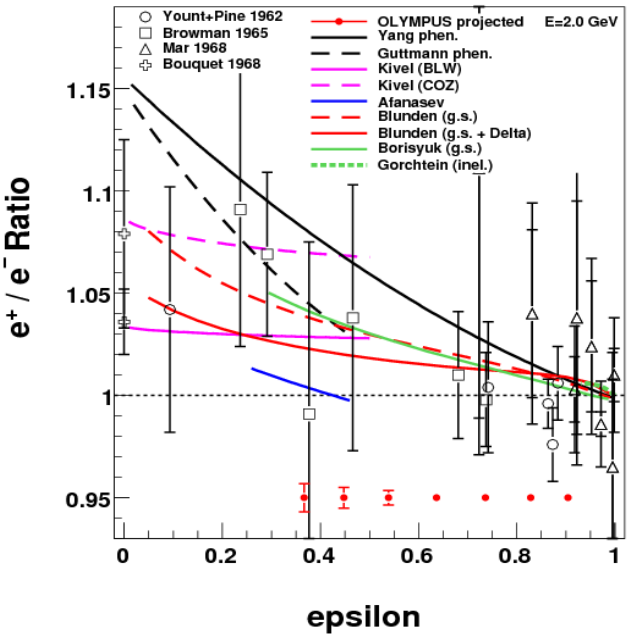

Fig. 4. Projected statistical precision (red points) together with a compilation of previous measurements and theoretical predictions

Preliminary results of the VEPP3 experiment at the primary beam energy of 1.6 GeV are presented in [7]. Having radiative corrections applied, for Q^2 = 1.43 GeV^2 and ε = 0.5 the following value of R has been found: $R = 1.016 \pm 0.011_{\text{stat}} \pm 0.003_{\text{syst}}$. Note that before applying the radiative corrections, this ratio was equal to 1.053. At small Q^2 (Q^2 = 0.23 GeV^2 and ε = 0.5) with a radiative correction, the R-value was $R = 0.9976 \pm 0.0009_{\text{stat}} \pm 0.003_{\text{syst}}$.

The second run of the experiment at 1 GeV is underway in Novosibirsk. It is planned to investigate the region of $\varepsilon = 0.2–0.5$ with the total uncertainty of $6 \cdot 10^{-3}$. A positive feature of the VEPP-3 experiment is that the topologies of e^+ and e^- events are identical as there is no magnetic field in the set-up. On the other hand, the momenta of the scattered particles are not analyzed, which results in somewhat larger background contamination and higher sensitivity to the bremsstrahlung correction.

Preliminary results have been recently reported also by the EG5 CLAS experiment [8]. The beam charge asymmetry not corrected for the bremsstrahlung is found to be positive and close to the VEPP-3 result.

References

1. V. Punjabi *et al.*, Phys. Rev. C **71**, 055202 (2005) [Erratum-ibid. C **71**, 069902 (2005)].
2. O. Gayou *et al.*, Phys. Rev. Lett. **88**, 092301 (2002).
3. C.F. Perdrisat, V. Punjabi, M. Vanderhaeghen, Prog. Part. Nucl. Phys. **59**, 694 (2007).
4. P.G. Blunden, W. Melnitchouk and J.A. Tjon, Phys. Rev. Lett. **91**, 142304 (2003); Phys. Rev. C **72**, 034612 (2005).
5. P.A.M. Guichon and M. Vanderhaeghen, Phys. Rev. Lett. **91**, 142303 (2003).
6. E.A. Kuraev and M.V. Galynskii, JETP Letters **96**, 6 (2012).
7. A.V. Gramolin *et. al.*, Nucl. Phys. Proc. Suppl. **216**, 225 (2012).
8. R.P. Bennet, talk at *Symposium Experimental and Theoretical Aspects of the Proton Form Factors*, July 9–11, 2012, St. Petersburg, PNPI (http://hepd.pnpi.spb.ru/hepd/olympus_2012/program.html), to be published.

EXPERIMENTS WITH THE CRYSTAL BALL AT THE TAGGED PHOTON BEAM OF THE ELECTRON MICROTRON MAMI-C IN MAINZ

PNPI participants of the Collaboration A2:
V.S. Bekrenev, S.P. Kruglov, A.A. Kulbardis, A.B. Starostin

For a number of years, physicists of the Laboratory of the Meson Physics (LMP) of the High Energy Physics Division, PNPI, actively participate in experiments on the tagged photon beam of the electron accelerator MAMI (Mainz, Germany) with the electron energy $E_e = 1500$ MeV [1]. These experiments develop in two basic directions:

1. research of neutral mesons and strange particles photoproduction;
2. studies of rare decays of η and η′ mesons formed in reactions $\gamma p \to \eta p$ and $\gamma p \to \eta' p$.

The basic detector in Mainz is the multicrystal spectrometer of photons, the Crystal Ball, designed for registration of multiphoton final states. It consists of 672 NaI (Tl) crystals. Parallel with measurements, a continuous modernization of the spectrometer is carried out. It aims to increase the efficiency of registration of photons and charged particles produced in a target under small angles, by installation of additional forward detectors and also by placing drift chambers into the internal cavity of the spectrometer (Fig. 1).

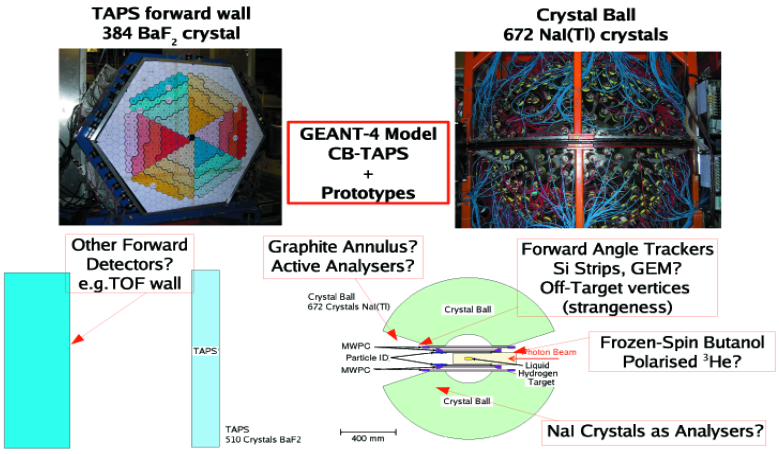

Fig. 1. Schematic image of the installation Crystal Ball and TAPS

Experimental programs of the MAMI accelerator are discussed and accepted by the joint program committee. The existing experimental facilities at the MAMI accelerator make possible to carry out precision experiments due to high intensity and high energy resolution of the photon beam.

The basic advantages of the experimental set-up of the A2 Collaboration are a high intensity of the tagged photon beam and a high energy resolution up to 1 MeV. These features of the experimental facilities substantially define the experimental program of the collaboration and supplement programs of others collaborations that use photon beams. In particular, the high energy resolution allows to carry out a number of precision experiments on photoproduction of mesons on nuclei, including coherent meson production [2, 3].

To improve the Crystal Ball spectrometer parameters and to make possible registration not only of photons, but also of charged products of reactions, the installation is permanently upgraded. A cylindrical multilayered drift chamber was placed in the internal cavity of the Crystal Ball. It allows to trace the trajectories of charged particles in a wide solid angle. Later, a polarized hydrogen / deuterium target was installed inside of the Crystal Ball (Fig. 2). It opened an opportunity to carry out experiments for measurements of double polarizing parameters in reactions of neutral mesons photoproduction, similar to those carried out on the accelerator ELSA in Bonn, but in another range of “tagged” photon energies.

In the initial stage of modernization, the Crystal Ball was supplied with the forward detector TAPS, which is a "wall" of BaF_2 crystals. Now, two alternative upgrade projects are being considered to improve the spatial and time resolutions of the forward detector, either to replace BaF_2 crystals in TAPS by $PbWO_4$ crystals, with smaller sizes and better timing parameters, or to install instead of TAPS a hodoscope with scintillating counters for a time-of-flight analysis of particles emitted from the target under small angles.

Among the physical tasks which were planned for the tagged photon beam of the accelerator MAMI, we should mention studies of rare decays of η- and η′-mesons. These mesons are produced in significant quantities in the reactions $\gamma p \to \eta p$ and $\gamma p \to \eta' p$, and the multiphoton spectrometer Crystal Ball with the almost full solid angle of photon detection is a very suitable device for this task [4].

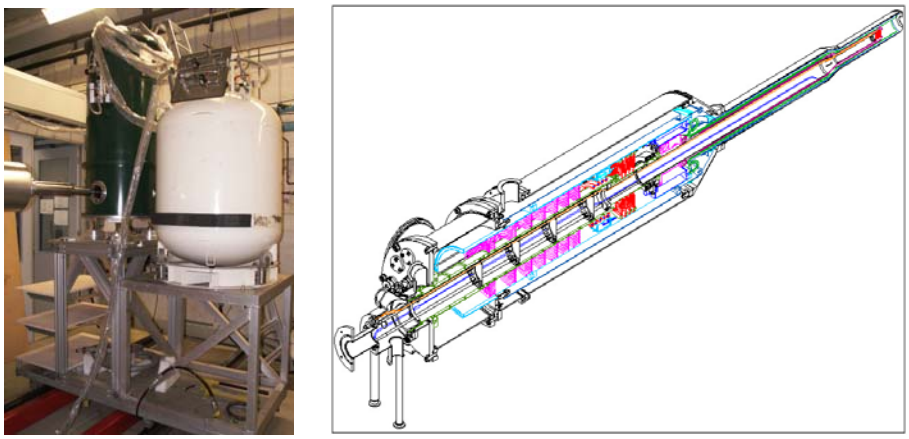

Fig. 2. General view (left) and the schematic image (right) of the polarized target used at the MAMI accelerator

Systematic studies of these decays open a way to understand the symmetries and the effects of symmetries violations in strong interactions. In other words, these studies can test the Chiral theory. Now, the A2 Collaboration is building an additional spectrometer to measure photon energies in the range of η′-meson production that will essentially increase the accuracy of experiments on their rare decays.

The experiments on measurements of the double polarizing parameters *E* and *G* will be carried out also at the MAMI accelerator within the programs accepted by the joint program committee of ELSA and MAMI. These proposals include "Studying of the spiral dependence of the cross-section for mesons photoproduction reactions in the region of resonances D_{13} (1520) and F_{15} (1680)", "Measurement of the asymmetry *G* for the reactions $\gamma p \to \pi^0 p$ and $\gamma p \to \pi^+ n$ in the energy range from 250 to 800 MeV", "Studying of the dependence on the spirality of the cross-section for photoproduction of one and two π^0 mesons on neutrons (at the energies of photons from 400 up to 1400 MeV)", "Measurement of the double polarizing parameter *E* for the reaction of photoproduction of η-mesons on neutrons at photon energies about 1 GeV", "Measurement of the double polarizing parameters *E* and *G* for reactions of photoproduction of pseudo-scalar mesons on neutrons", "Measurement of polarizing parameters for the reaction of coherent photoproduction of π^0 mesons on deuterons". Results of these experiments will supply additional information to the data received in experiments on the accelerator ELSA in Bonn.

A program of studies of rare decays of η- *a*nd η′-mesons was earlier carried out by the Crystal Ball Collaboration on the accelerator of the Brookhaven National Laboratory in the USA [5] and now proceeds in Germany on the photon beam of the accelerator MAMI. The reactions $\gamma p \to \eta p$ and $\gamma p \to \eta' p$ will be used as a source of these mesons. The decay $\eta \to 3\pi^0$ breaks the *G*-parity and, if one ignores a small electromagnetic correction, it can occur only due to the presence of a difference of masses between the *u* and *d* quarks. This difference gives a base to check the Chiral theory, the low energy version of the QCD, based on the Chiral symmetry, which breaks if one takes into account the quark masses. The amplitude of the decay can be expanded with respect to the centre of the Dalitz-plot. For neutral final states, the Dalitz-plot is usually expressed by a linear parametrization with one tilt parameter *a*. Theoretical calculations in which the parameter *a* correlates with the probability of the decay demand practically zero value of *a*. Last

experimental results give the value of a with the correct sign, but it is too large to be considered in agreement with theoretical calculations. New and more precise (and statistically better supported) experimental data will help to solve this problem. The rare decay $\eta \to \pi^0\gamma\gamma$ attracts much attention because of ambiguities both in experimental and theoretical values of this decay width. At present, there is disagreement between the values $BR(\eta \to \pi^0\gamma\gamma) = (2.7–3.5) \times 10^{-4}$, measured by the Crystal Ball Collaboration at the Brookhaven National Laboratory and published in 2002–2005, and the value $BR(\eta \to \pi^0\gamma\gamma) = 0.84 \times 10^{-4}$, published in 2006 by the KLOE Collaboration. The last value of BR exceeds 5 times the result of theoretical calculations. New reliable experimental data are necessary to clarify this unsatisfactory situation. A measurement of the probability of $\pi^0 \to \gamma\gamma$ decay is planned to be carried out on the accelerator MAMI with the spectrometer Crystal Ball. The decays $\eta \to 3\gamma$, $\eta \to 2\pi^0\gamma$, and $\eta \to 3\pi^0\gamma$ will be studied on the accelerator MAMI with the purpose to check the charge conjugation invariance also. Estimations show that the expected statistics will exceed by 10–20 times the statistics obtained earlier in experiments with the Crystal Ball detector in BNL. This will allow to increase considerably the top limit for BR in the above mentioned reactions [3, 6].

Extensive studies of rare and forbidden decays of η' mesons are also planned. For example, a priority task on the accelerator MAMI is the measurement of BR of decays $\eta \to \eta\pi^0\pi^0$ and $\eta' \to 3\pi^0$, to check the perturbation theory. The ratio of these two decays makes possible to determine directly the difference of masses of the u and d quarks, induced by $\pi^0 - \eta$ mixing. The expected statistics is about 10^5 decays of $\eta' \to \eta\pi^0\pi^0$ in 500 hours, 10 times larger than the current world data [6].

The experimental results on photoproduction reactions on non-polarized targets obtained with statistical accuracy 10 times better than the previous world data have allowed to essentially clarify the mechanism of the studied reactions [3, 7–9]. The first results of precision measurements of the differential cross section for the reaction $\gamma p \to \eta p$ discovered sharp energy dependencies of the observables in the region of the so-called "neutron anomaly" (W = 1680 MeV). This is one of the most intriguing problems of modern physics of intermediate energies (Fig. 3) [10]. Studies of this problem will be continued in experiments with a polarized target. The LMP–ITEP Collaboration is carrying out now the experiment EPECUR, which is closely connected to this problem and is supplementary to the experiments with photon beams.

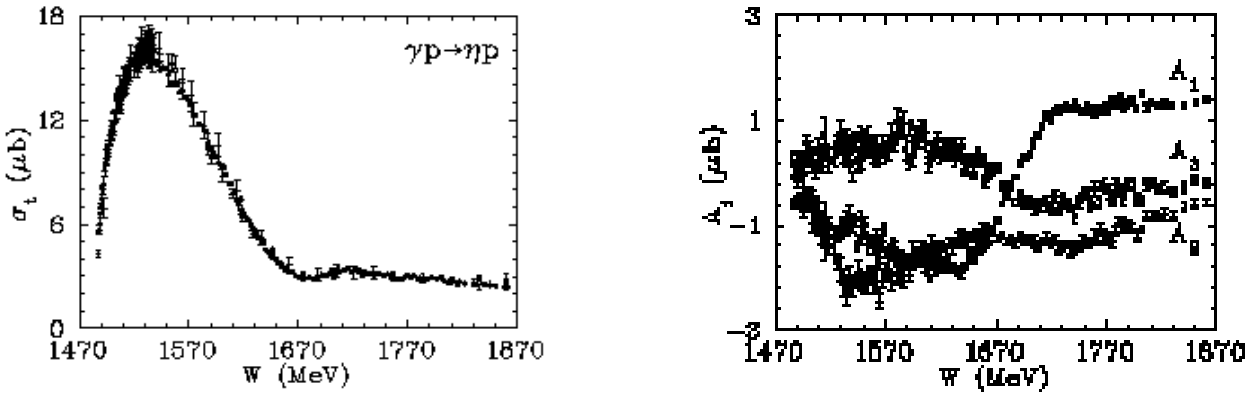

Fig. 3. Results of the $\gamma p \to \eta p$ reaction study. Energy dependence of the total cross section (left). Energy dependence of the decomposition factors (right)

PNPI physicists of the LMP participate in the international Collaboration A2 (MAMI, Mainz) since 1998. They took an active part in the development, construction and commissioning of new detectors and equipment for modernization and improvement of the Crystal Ball detector. PNPI employees have contributed considerably to the upgrade of the tagger, aimed to expand the energy range of the tagged photons, in accordance with the increase of energy of the accelerated electrons from 850 to 1500 MeV, and to improve the energy resolution. For the detecting part of the tagger, the LMP constructed and produced 370 scintillating detectors of various sizes and configurations. These detectors were tuned and commissioned

with participation of LMP scientists. After setting into operation in 2006 of the upgraded tagger, a new series of experiments was started. Scientists of LMP take part in data taking and in data processing.

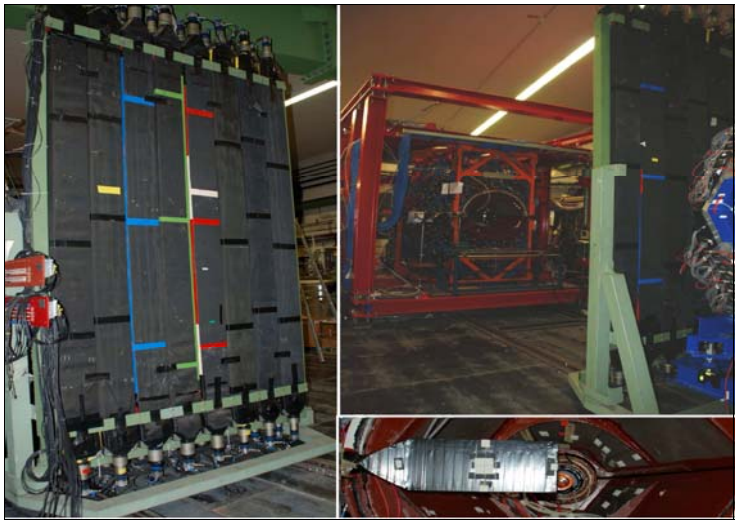

Fig. 4. The time-of-flight **"**wall**"**

The plan for modernization of the Crystal Ball for the accelerator MAMI includes, in particular, building of Time-Of-Flight (TOF) "walls" on the base of hodoscopes of scintillating counters. Its purpose is to measure the energy of charged particles emitted in the forward direction by the time-of-flight method. The hodoscope consists of 112 detectors with scintillators of 50 × 3000 × 200 mm^3 size. They are to be mounted vertically in groups of 8 pieces called "farms", and up to 4 such "farms" can be mounted on each rack. Besides, a set of 32 veto counters are to be installed. The layout of the TOF-wall is shown in Fig. 4.

Physicists of the LMP are supposed to take part in the final assembly and commissioning of the time-of-flight "wall", of its elements and of the entire detector.

References

1. A.B. Starostin, in *Proc. of the Jubilee scientific session-conference of Nuclear Physics section, High Energy Division of RAS "Physics of fundamental interactions"*, ITEP, Moscow, 5–9 Sep. 2005; Yad. Fiz. **70**, 1242 (2007); Phys. Atom. Nucl. **70**, 1203 (2007).
2. C.M. Tarbert… V. Bekrenev *et al.,* Phys. Rev. Lett. **100**, 132301 (2008).
3. S. Schumann… V. Bekrenev *et al.,* Eur. Phys. J. A **43**, 269 (2010).
4. M. Unverzagt… V. Bekrenev *et al.,* Eur. Phys. J. A **39**, 169 (2009).
5. S. Prakhov… V. Bekrenev *et al.,* Phys. Rev. C **79**, 035204 (2009).
6. A. Starostin… V. Bekrenev *et al.,* Phys. Rev. C **79**, 065201 (2009).
7. D. Kreambrich… V. Bekrenev *et al*., Phys. Rev. Lett. **103**, 05200 (2009).
8. V.L. Kashevarov… V. Bekrenev *et al.,* Eur. Phys. J. A **42**, 141 (2009).
9. V.L. Kashevarov… V. Bekrenev *et al.,* Phys. Lett. B **693**, 551 (2010).
10. E.F. McNicoll… V.S. Bekrenev *et al.,* Phys. Rev. C **82**, 035208 (2010).

STUDY OF PHOTOPRODUCTION OF NEUTRAL MESONS USING THE CRYSTAL BARREL AT ELSA

PNPI participants of the CBELSA / TAPS Collaboration:
D.E. Bayadilov, Yu.A. Beloglazov, A.B. Gridnev, I.V. Lopatin, D.V. Novinsky, A.K. Radkov, V.V. Sumachev

The problem of baryon spectroscopy which has not been solved fully yet is the nature and origin of the so called "missing resonances". As a matter of fact, till now the number of the excited states of baryons observed experimentally is significantly less than that predicted by different theoretical models. The reason of such non-consistence may be two-fold. One possibility – such resonance states non-observed in experiments do not exist in reality as a consequence of a "hidden" symmetry. The quark-diquark structure of baryons might be considered as an example of such a "hidden" symmetry. Such a structure could freeze one of the internal degrees of freedom and, hence, would decrease the number of expected resonances. Another possibility with less dramatic consequences – some of observables simply have not been found in experiments. Till recently, practically all information on characteristics of baryon resonances were extracted from experimental data on elastic πN scattering using a partial-wave analysis. However, if some of resonances have anomaly weak coupling with the πN channel, it is impossible to find such resonances in these experiments. On the other hand, the information on resonances coupling weakly with the πN channel may be obtained from experiments on photoproduction of neutral mesons. Thus, the photoproduction of baryon resonances provides an alternative tool to study nucleon states.

The main component of the experimental set-up which is used for studying photoproduction of neutral mesons at the tagged photon beam of the electron accelerator ELSA in Bonn is the multi-crystal photon detector Crystal Barrel (CB). The CB at ELSA is an ideal tool to study nucleon resonances. In particular, it provides a wide angular coverage, which is needed to separate the resonant from non-resonant contributions.

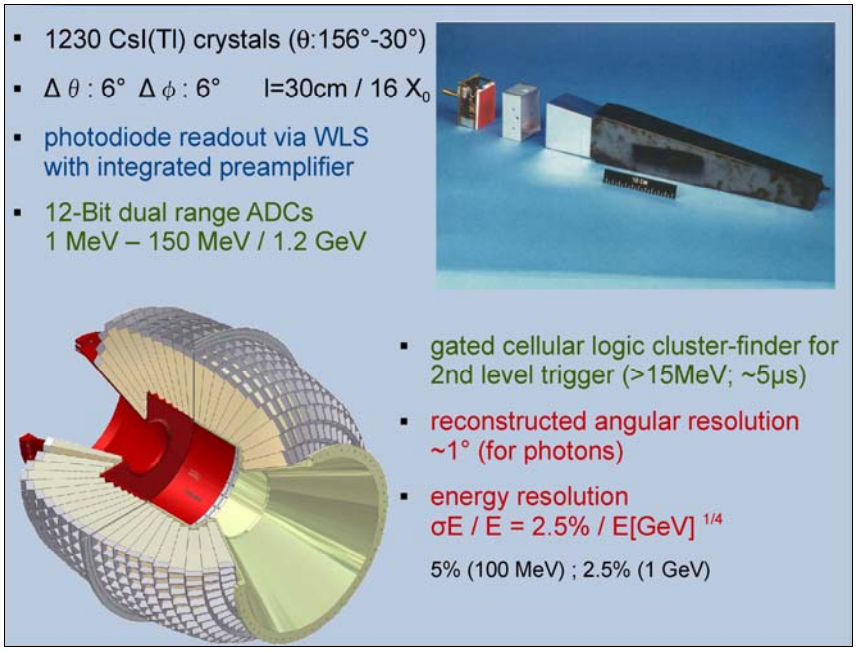

Fig. 1. Schematic view of the multi-crystal photon spectrometer Crystal Barrel

The experiment was carried out at the electron accelerator ELSA with the maximal available electron energy of 3.2 GeV. Electrons hit a radiator target, where they produced Bremsstrahlung. The energy of photons, in the range between 25 and 85 % of the primary electron energy, was measured by detection of the corresponding scattered electrons in the tagging system ("tagger"). It consisted of a dipole bending magnet

and two detecting parts – an array of fourteen scintillation counters providing fast timing information and two Multiwire Proportional Chambers (MWPCs) with a total of 348 channels to provide information about trajectories of the scattered electrons. Each scintillator of the array was observed by two photomultiplier tubes attached to both sides. A logical OR of the left-right coincidence from all the scintillators was required in the first-level trigger.

The tagger was calibrated by direct injection of a very low intensity e^--beam of 600 or 800 MeV, after removing the radiator. Variations of the magnetic field of the tagging dipole magnet enabled us to execute a scan of several spatial positions over the MWPCs. For a given wire, the electron momentum is proportional to the magnetic field strength. The calibration was checked by a Monte Carlo simulation of electron trajectories through the tagger. The set-up geometry, dimensions of the electron beam, angular divergences, multiple and Møller scattering in the radiator foil and air were taken into account. From these simulations, the energy corresponding to each MWPC wire was obtained by a polynomial fit. The uncertainty in the simulation was estimated to be of the same order of magnitude as the "energy width" of the respective wire.

The CB is the central component of the experiment. It consists of 1230 CsI(Tl) crystals of 30 cm length (16 X_0) and has an excellent photon-detection efficiency. Large solid-angle coverage (excluding the 12° openings on both sides of the barrel necessary for technical reasons) and high granularity allow to reconstruct multi-photon final states. The spatial resolution determined by the size of individual crystals is about 20 mrad (≈ 1.1°); it allows separation of two photons stemming from a decay of π^0 mesons with the maximum momentum 1 GeV/c corresponding to a minimum opening angle of 16.6°. The energy resolution of the calorimeter was empirically described as $\sigma_E / E = 2.5\ \% / [E(\mathrm{GeV})]^{0.25}$.

The three-layer scintillating fiber (scifi) detector was inserted into the inner cavity of the CB to identify charged particles leaving the target and to determine their intersection point with the detector. The fibers were 2 mm in diameter; one of the layers was flat, the fibers of other two layers encircled the target over ± 25° with respect to the first layer. The innermost layer covered the solid angle of 92.6 % of 4π.

A coincidence between the tagger and the scifi detector provided the first-level trigger of the experiment. From the hit pattern in the CB, the fast cluster logic determined the number of "particles" defined by the clusters of contiguous crystals with individual energy deposits above 15 MeV. The second-level trigger was generated for events with two or more particles determined by the cluster logic. In the data analysis, the clusters with two local maxima were split into two particles sharing the total energy deposit. The offline threshold for the accepted particles was set to 20 MeV. The proton kinetic energy had to exceed 35 MeV to traverse two inner scifi layers and to produce a trigger. A proton of 90 MeV was needed to reach the barrel calorimeter and to deposit the minimum cluster energy of 20 MeV. The CB acceptance was determined by a Monte Carlo simulation. It vanished for forward protons leaving the CB through the forward outlet and for protons with very low energies.

At the first stage of experiments, the CB was used for measuring the total cross sections and the differential cross sections (angular distributions) for photoproduction reactions $\gamma p \to p\pi^0$, $\gamma p \to p\eta$ and $\gamma p \to p\pi^0\pi^0$. The experiments were carried out with primary electron energies 1.4, 2.6 and 3.2 GeV, providing a total range of photon energies from 0.3 to 3 GeV. Introducing into the partial-wave analysis new cross sections, measured for the above mentioned photoproduction reactions, one can search baryon resonances which were not known earlier and improve our knowledge of properties of the known resonances. Just this way was chosen by the group of physicists from Bonn and Gatchina (group Bn-Ga) for processing new data on the cross sections for photoproduction of neutral mesons.

The next logical step of experiments which are carried out with the CB spectrometer (in combination with the TAPS) is to use beams of linearly (or circularly) polarized tagged photons produced at the electron accelerator ELSA. Linearly polarized photons are produced by coherent bremsstrahlung from a thin (100 μm) diamond radiator which is mounted on a goniometer where its orientation with respect to the beam can be adjusted precisely. The degree of polarization is then deduced from the coherent peak which is measured in the tagging system. The maximal value of the linearly beam polarization is about 50 %. Circularly polarized photons are produced *via* incoherent bremsstrahlung of longitudinally polarized electrons off an amorphous radiator.

In order to have a possibility to detect photons and charged particles emitted from the target with high angular and energy resolution, the main detector of the set-up – the multi-crystal photon spectrometer Crystal

Barrel – was equipped in addition with two forward detectors (see Figs. 2, 3) built specially for this purpose. One of them (the so called Forward Plug) assembled of 90 CsI(Tl) crystals was inserted into the open forward cone of the Crystal Barrel for registering particles emitted at angles from 10 to 30° and, thus, for increasing the total covered solid angle. 180 overlapping veto-counters made of thin scintillators were placed in front of the CsI(Tl) crystals in order to determine the kind of a particle (photon or proton) entering each crystal. Another forward detector (see the right part of Fig. 3) is a "wall" consisting of 216 BaF_2 crystals and 216 veto-counters located in front of the crystals. The central crystal was removed to make a hole for the photon beam. The Mini-TAPS registers particles (photons and protons) emitted at angles from 1° to 10°.

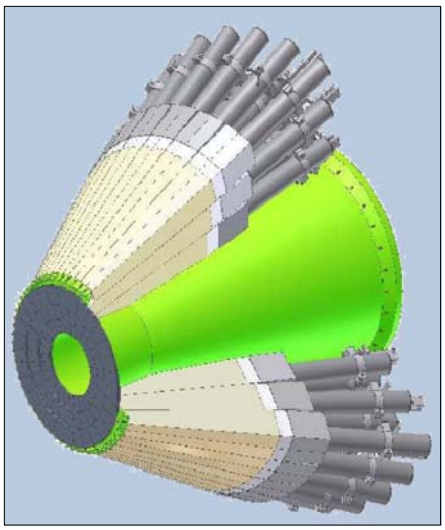

Fig. 2. Forward Plug

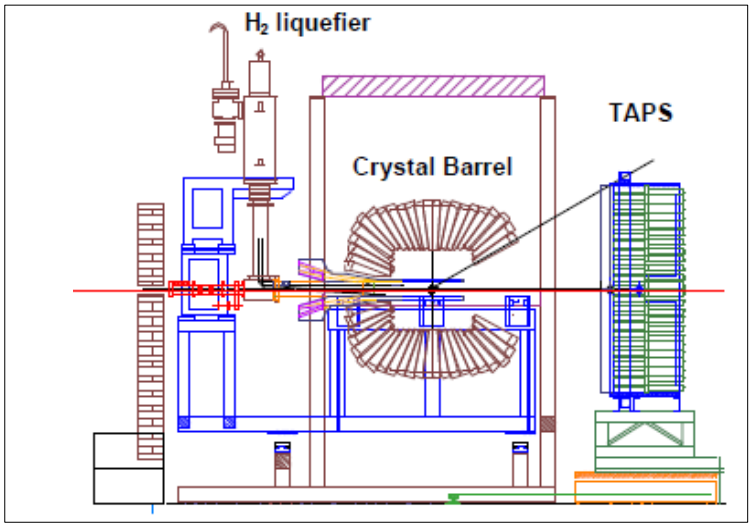

Fig. 3. Schematic view of the experimental set-up for measuring the beam asymmetry

With the use of the linearly-polarized photon beam and the experimental set-up CB (Crystal Barrel with the Forward Plug + TAPS), measurements of the beam asymmetry Σ were performed for π^0, η, and $\pi^0\eta$ photoproduction [1–6]. A combination of the polarized photon beam and the above mentioned set-up enabled high-resolution detection of multiple photons, important for clean detection of 2γ and $3\pi^0$ decays of π^0 and η mesons. As an illustration, we present in Fig. 4 (taken from Ref. [1]) the angular dependence of the beam asymmetry Σ measured for the reaction $\gamma p \to p\eta$. A continuous 3.2 GeV ELSA electron beam was used to produce a linearly polarized tagged photon beam by means of coherent bremsstrahlung off a diamond crystal, covering a photon energy range E = 800–1400 MeV with the maximal achievable polarization up to 49 % at the energy of 1305 MeV. Both dominant decay modes of η meson $\eta \to 2\gamma$ and $\eta \to 3\pi^0$ were used to extract the beam asymmetries from the azimuthal modulation of the cross section. The measurements cover the angular range from 50° to 150°.

In Fig. 4, our new data are compared to two standard calculations, the Mainz isobar model eta-MAID and the Bn-Ga partial-wave analysis. In contrast to eta-MAID, the Bn-Ga analysis in addition to πN also takes the ηN, $K\Lambda$, and $K\Sigma$ coupled channels into account. To calculate the photon asymmetry, the preliminary high energy GRAAL data have already been used in the Bn-Ga fit. This might be the reason for a slightly better description of our data. The overall agreement between the data and both models seems quite satisfactory at first glance. However, a closer examination reveals distinct inconsistencies. While the full model results agree with each other, the individual resonance contributions differ substantially, as is illustrated in Fig. 4.

This unsatisfactory situation cannot be resolved using the measurements of the photon asymmetry alone. Yet, such data provide the necessary basis to be extended with double polarization observables in order to get closer to, or even to accomplish the complete experiment in terms of an introductory discussion. Such an extended program is underway now at ELSA within the Collaborative Research Project SFB/TR-16.

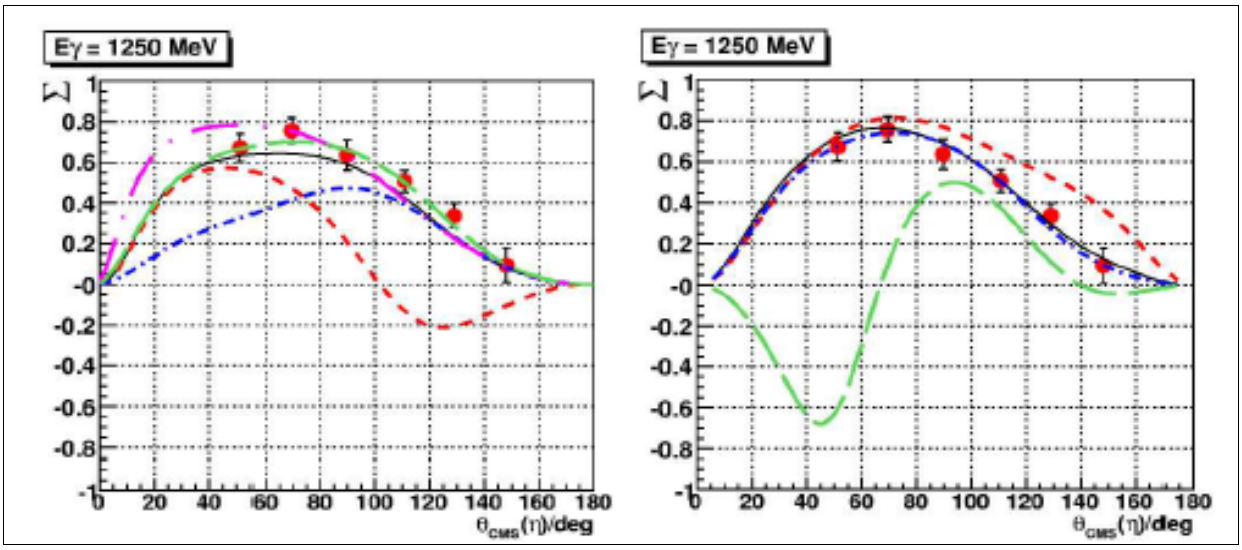

Fig. 4. Angular dependence of the beam asymmetry Σ for the reaction $\gamma p \to p\eta$ at $E = (1250 \pm 50)$ MeV. Comparison of calculations with the experimental data. Left: the eta-MAID result is shown. Right: the result of the BnGa analysis. The full lines represent the respective full calculations. The broken curves illustrate the impact of "turning-off" individual resonances: Long dashed – without P_{13} (1720), long dash-dotted – without P_{11} (1710) (no difference to full calculation in the BnGa analysis), short dashed – without D_{31} (1520), and short dash-dotted – without D_{15} (1675)

After completing the above described stage of the experiments on photoproduction of neutral mesons, measurements of the double polarization observables were started. Such kind of measurements provide physicists with a unique information for identification of different baryonic states, especially in the region of overlapping resonances where "missing" baryonic states could be found.

These complicated experiments need both a beam of polarized photons and a polarized proton target. To realize this, an upgrade of the experimental set-up was performed. First of all, the Crystal Barrel was moved to another beam-line – Fig. 5. The tagging system installed earlier at this line was equipped with 96 new scintillation counters (with overlapping scintillators of varying width) and with an array of 480 scintillating fibers (two layers of 2 mm diameter fibers). This allowed to tag photons with 18 to 95 % of the incoming electron energy with an energy resolution between 0.2 and 2.2 %.

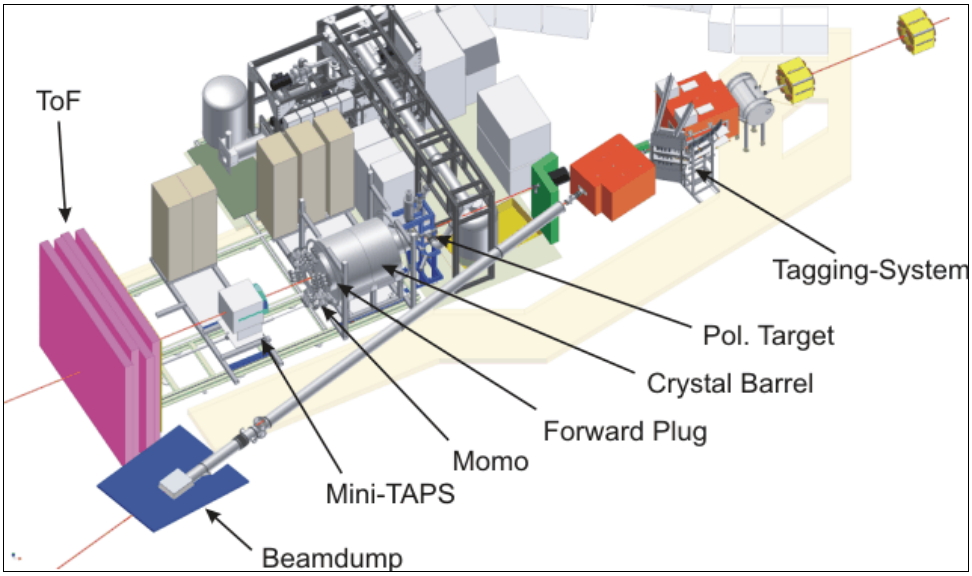

Fig. 5. Disposition of the experimental set-up after its upgrading and replacing to another beam-line

The displacement of the Crystal Barrel to another beam-line allowed to insert a longitudinally polarized proton target into the Crystal Barrel inner cavity and to arrange its operation in the "frozen spin" mode by locating a system of polarization "pumping" outside the Crystal Barrel. This system consists of a horizontal dilution refrigerator and a 5 T superconducting polarization magnet, which will be used in the polarization phase together with a microwave system for dynamical nuclear polarization. The polarization will be preserved in the "frozen spin" mode at the temperature of about 50 mK by a very thin superconducting solenoid located within the target cryostat, which will produce a 0.5 T longitudinal holding magnetic field. In general, the maximal polarization of 90 % is possible. The relaxation time of the target is about 200 h.

Firstly, it was proposed to measure the double polarization observables for π^0, η and ω photoproduction on the longitudinally polarized proton target. When using linearly polarized photons, we can measure the double polarization asymmetry G. This asymmetry, for which scarce data exist, plays an important role to disentangle contributions of various nucleon resonances by the imaginary part of the interference between different partial waves. The asymmetry G has high sensitivity to the Roper resonance $P_{11}(1440)$ in π^0 production at photon excitation energies around 600 MeV, to the resonances $P_{11}(1710)$ and $P_{13}(1720)$ in η photoproduction around 1100 MeV, and to the recently found resonance $D_{15}(2070)$ at 1600 MeV. In an experiment with circularly polarized photons, we were specially interested in measuring the helicity difference of the cross sections $d\sigma/d\Omega_{1/2}$ and $d\sigma/d\Omega_{3/2}$ (and, correspondingly, the helicity asymmetry $E = [d\sigma/d\Omega_{1/2} - d\sigma/d\Omega_{3/2}] / [d\sigma/d\Omega_{1/2} + d\sigma/d\Omega_{3/2}]$) for π^0 and η photoproduction off the proton. These measurements give possibility to distinguish different model predictions of double polarization observables. Furthermore, they allow to fix the quantum numbers of the newly discovered nucleon resonance at $W = 2070$ MeV.

It should be stressed that first measurements of the polarization observable G have been performed already for the reaction $\gamma p \to p\pi^0$ with linearly polarized photons at the energy from 800 to 1100 MeV using the CB with the longitudinally polarized proton target. The first obtained results are published in Ref. [7].

To complete the series of experiments on measurements of the double polarization observables it was necessary to make one more modernization of the set-up by changing the construction of the polarized target. The cryostat of the Bonn frozen spin target was equipped with a saddle type superconducting holding coil producing a transverse magnetic field. The coil is very thin in order to allow particles to pass the coil virtually unaffected. The target material is butanol C_4H_9OH, which has an effective density of 0.57 g/cm^3 and dilution factor $D = 0.1335$. In general, in this target modification the vector of its polarization is directed transversally in respect to the direction of the incident photon beam. The maximal value of the target polarization can reach 90 %. The relaxation time of the target is about 250 hours.

A possibility of inserting the transversally polarized target into the Crystal Barrel allows to measure the double polarization observables for π^0, η and π^0 η photoproduction using both the circularly polarized and the linearly polarized photon beams. In particular, the objects of further measurements are the double polarization observables H, P, and T.

References

1. D. Elsner… D.E. Bayadilov, Yu.A. Beloglazov *et al.*, Eur. Phys. J. A **33**, 147 (2007).
2. E. Gutz… D.E. Bayadilov, Yu.A. Beloglazov *et al.*, Eur. Phys. J. A **35**, 291 (2008).
3. Frank Klein… D.E. Bayadilov, Yu.A. Beloglazov *et al.*, Phys. Rev. D **78**, 117101 (2008).
4. D. Elsner… D.E. Bayadilov, Yu.A. Beloglazov *et al.*, Eur. Phys. J. A **39**, 373 (2009).
5. M. Sparks… D.E. Bayadilov, Yu.A. Beloglazov *et al.*, Phys. Rev. C **81**, 065210 (2010).
6. E. Gutz… D.E. Bayadilov, Yu.A. Beloglazov *et al.*, Phys. Lett. B **687**, 11 (2010).
7. A. Thiel… D.E. Bayadilov, Yu.A. Beloglazov *et al.*, Phys. Rev. Lett. **109**, 102001 (2012).

HIGH PRECISION MEASUREMENTS OF THE PION-PROTON DIFFERENTIAL CROSS SECTION

PNPI participants of the PNPI–ITEP Collaboration:
V.A. Andreev, Ye.A. Filimonov, A.B. Gridnev, V.V. Golubev, E.A. Konovalova, N.G. Kozlenko, V.S. Kozlov, A.G. Krivshich, D.V. Novinsky, V.V. Sumachev, V.I. Tarakanov, V.Yu. Trautman

1. Introduction

The study of elastic scattering can produce a lot of information on the dynamics of strong interaction. The EPECURE Collaboration is aimed at the research of baryon resonances in the second resonance region by measuring the pion-proton elastic scattering and kaon-lambda production. The experiment features high statistics and better than 1 MeV resolution in the invariant mass scale, thus allowing a search for narrow resonances with coupling to the πp channel as low as 5 %. The experiment is of "formation" type, *i.e.* the resonances are produced in the *s*-channel, and a scan over the invariant mass is done by variation of the incident pion momentum, which is measured with an accuracy of 0.1 % with a set of 1 mm pitch proportional chambers located in the first focus of the beam line. The reaction is identified by a magnetless spectrometer based on wire drift chambers with hexagonal structure. The background suppression in this case depends on the angular resolution, so the amount of matter in the chambers and in the whole set-up was minimized to reduce multiple scattering. The measurements started in 2009 with the set-up optimized for elastic pion-proton scattering. With 3 billions of triggers already recorded, the differential cross section for elastic πp-scattering on a liquid hydrogen target in the region of the diffraction minimum was measured with a statistical accuracy about 1 % in 1 MeV steps over the invariant mass. The present article covers the experimental set-up, the current status, and some preliminary results.

An interest to this experiment originated with the discovery in 2003 by two experiments LEPS [1] and DIANA [2] of a new baryonic state Θ^+ with positive strangeness and a very small width. Later, several new results appeared where this state was not seen [3], but recent results from LEPS [4] and DIANA [5] still insist on evidence for this resonance. The quantum numbers of Θ^+ have not been measured yet, but it is believed to belong to the pentaquark antidecuplet predicted in 1997 by D. Diakonov, V. Petrov and M. Polyakov [6]. In such a case, there should also exist a non-strange neutral resonance P_{11} with the mass near 1700 MeV. Certain hints in favour of its presence were found in a modified PWA of the GWU group [7] at the masses 1680 and 1730 MeV [8]. Recently, an indication for this narrow state was found in η photoproduction off neutrons in GRAAL [9, 10]. The observed structure had the mass of 1685 MeV with the width less than 30 MeV, which was screened by the detector resolution. No counterpart was found in the measurement off protons. A similar peak-like structure was also observed in the experiments Tohoku-LNS [11], CB-ELSA [12], and CB-MAMI [13].

Our idea was to search for the $P_{11}(1700)$ resonance in a formation-type experiment on a pion beam [14]. Precise measurements of the beam momentum and high statistics allow us to do a scan with an unprecedented invariant mass resolution. We plan to measure the differential cross sections for the reactions $\pi^- p \to \pi^- p$ and $\pi^- p \to K_s^0 \Lambda^0$ with high statistics and better than 1 MeV invariant mass resolution. If the resonance does exist, our experiment will provide a statistically significant result, and we will measure its width with a precision better than 0.7 MeV.

2. Experimental conditions

The layout of the apparatus for measurements of differential cross sections for the pion-proton elastic scattering is shown in Fig. 1. The main parts are proportional chambers in the first (PC1–3) and the second (PC4–6) focuses of the magneto-optic channel, 8 planes of drift chambers, forming the left (DC1–4) and right (DC5–8) arms of the symmetric two-arm spectrometer, a liquid hydrogen target (LqH2) and scintillation counters (S1, S2 and A1).

Each proportional chamber (PC1–3 and PC4–6) consists of two identical halves with mutually orthogonal sensitive wires providing *x* and *y* coordinates. The chambers have square sensitive regions of

200×200 mm^2, with 1 mm signal wire pitch, 40 micron aluminum foil cathode electrodes and 6 mm distance between the cathodes. We used the "magic" gas mixture (argon-isobutane-freon) to feed the proportional chambers. Beam tests showed the efficiency better than 99 %. The chambers in the first focus measure the momentum of each pion going to the target. Strong dipole magnets between the internal accelerator target and the first focus provide the horizontal distribution of particles with different momenta with the dispersion of 57 mm/%. The distribution over the horizontal coordinate in the first focus is shown in Fig. 2 for protons scattered on the internal beryllium target.

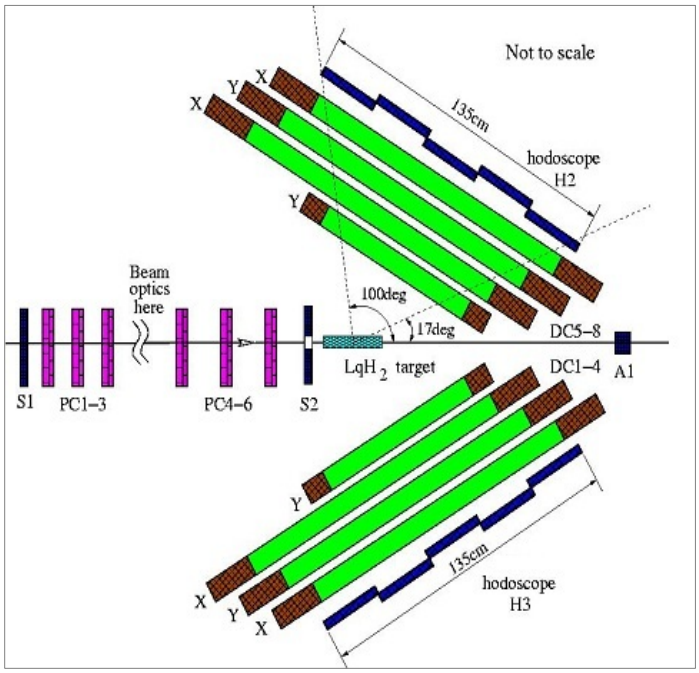

Fig. 1. Layout of the experimental set-up for investigation of $\pi^- p$ elastic scattering

The peaks observed in the picture correspond (from right to left) to the elastic scattering, to the first excitation of the beryllium nucleus, and to the second and third excitations, seen as one peak. This scattering was also used to obtain an absolute calibration of the central beam momentum from the precise knowledge of the accelerator internal beam momenta at three points 1057, 1195, and 1297 MeV/*c*. To ensure stability of the beam momentum, an NMR monitoring of the magnetic field of the last dipole was used. This provided us with the knowledge of each incident particle momentum with a precision of ~ 0.1 %.

The liquid hydrogen target has a cylindric container of mylar with the diameter 40 mm and length about 250 mm, placed in high vacuum inside of 1 mm thick beryllium outer shell. It is connected by two pipes to the liquefier system. One pipe is used for the liquid hydrogen inflow, and through the other the evaporated gas gets back to the liquefier. This design provides minimum of matter on the way of the scattered particles. The refrigeration is provided by liquid helium, its flow is controlled by the feedback supporting constant pressure of hydrogen in the volume. This pressure corresponds to the proper ratio between liquid and gas fractions of hydrogen and thus ensures that the liquid occupies the whole target volume, and that hydrogen is not frozen. The pressure and temperature in the target system are monitored and logged.

There are 8 one-coordinate drift chambers (DC1–4 and DC5–8) in the experimental set-up. The sensitive region in 6 chambers is 1200×800 mm^2, and in 2 chambers closest to the target it is 600×400 mm^2. The chambers have double sensitive layers of hexagonal structure shown in Fig. 3. Compared to conventional drift tubes, this structure has much more complex field, but it provides significantly less amount of matter on the particle path. The potential wires form nearly regular hexagon with the side dimension of 10 mm. The drift chambers are fed with Ar(70 %) + CO_2(30 %) gas mixture. Beam tests showed better than 99 % single layer efficiency and about 0.2 mm coordinate resolution for perpendicular tracks.

A unique distributed DAQ system based on commercial 480 Mbit/s USB 2.0 interface was designed for our experiment [15]. It consisted of 100-channel boards for proportional chambers and 24-channel boards for drift chambers, placed on the chambers frames. Each board was connected by two cables (USB 2.0 and power) to the communication box, placed near the chamber. The data were transferred to the main DAQ computer by the standard TCP/IP connection. The trigger logic was capable of processing several trigger conditions firing different sets of detectors. The following soft trigger condition was used to acquire physics events:

$$T = S_1 \times S_2 \times M_{1\mathrm{FCH}} \times M_{2\mathrm{FCH}} \times A_1,$$

where S_1, S_2 and A_1 are the signals from the corresponding scintillation counters, and $M_{1\mathrm{FCH}}$ and $M_{2\mathrm{FCH}}$ are the subtriggers produced by the trigger logic of proportional chamber planes placed in the 1st and 2nd focuses. Other trigger conditions with large prescaling factors were used for beam positioning and luminosity monitoring. The total statistics of nearly 3 billion triggers was collected. Figure 4 shows the distributions of the collected triggers over runs and beam momentum intervals.

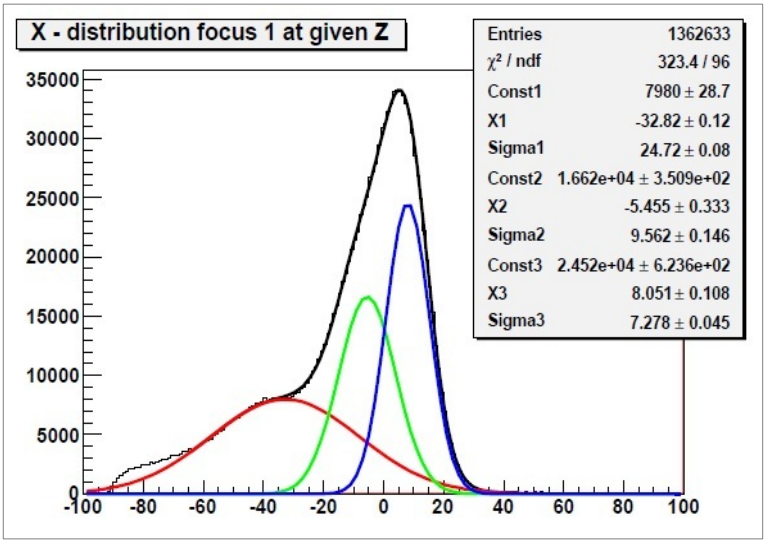

Fig. 2. Horizontal distribution in the first focus of the accelerator beam proton scattered on the internal beryllium target

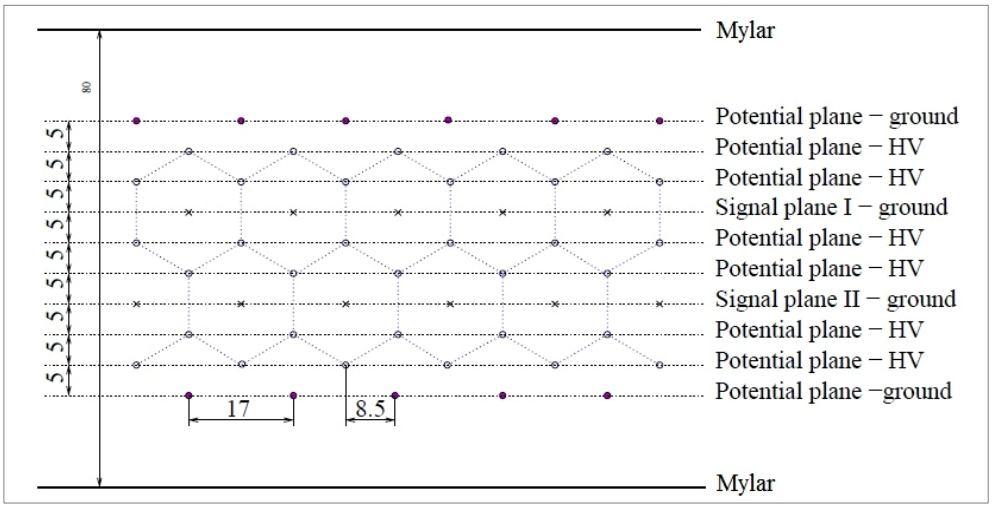

Fig. 3. Drift chamber cross section. View along the wires

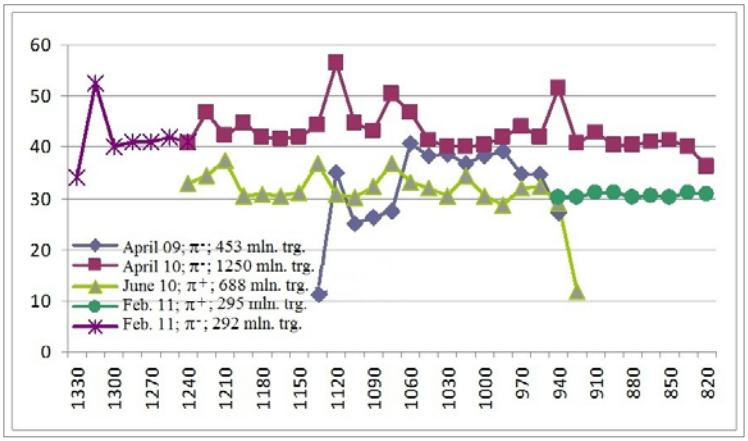

Fig. 4. Distribution of the collected triggers (in millions) over runs and beam momentum intervals

3. Data analysis

Selection of elastic events in this experiment is based on the angular correlation of pion and proton tracks. A single track is required to be present in the beam chambers and in both scattering arms in each projection, and these tracks must form a common vertex inside the target and they must lay within a plane. A centre of mass scattering angle θ_{CM} was calculated for both scattered particles under an assumption that the pion is scattered to the left. The 2-dimensional distribution of events over the difference between the reconstructed scattering angles $\Delta\theta_{CM}$ and the scattering angle θ_{CM} is shown at Fig. 5 (left) for a particular momentum. Two clusters of events are clearly seen. One of them corresponds to pions scattered to the left (this assumption is correct) and the other corresponds to pions scattered to the right (this assumption is wrong). A slice of the distribution for one degree θ_{CM} interval at $\theta_{CM} = 84°$ is shown in Fig. 5 (right).

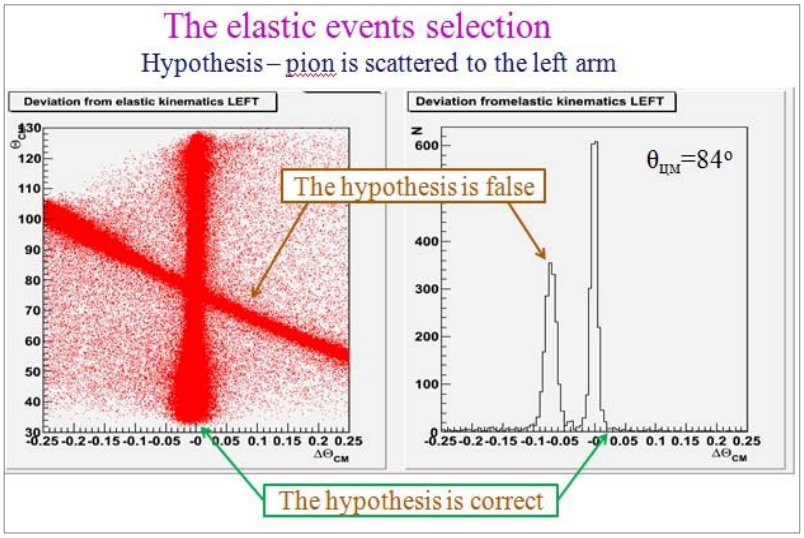

Fig. 5. 2-dimensional distribution of the events over the difference between the reconstructed scattering angles $\Delta\theta_{CM}$ and the scattering angle θ_{CM} (left) and its slice at $\theta_{CM} = 84^0$ (right)

Preliminary results on the differential cross section as a function of the incident momentum for 5-degree θ_{CM} intervals are shown in Fig. 6a, b. These data points correspond to the analysis of about 15 % of the statistics already collected. Some irregularity is manifested at $p_{beam} = 1020–1040$ MeV/c. The nature of this irregularity could be either a narrow resonance with the mass around 1690 MeV and width

of 5–10 MeV, or a threshold effect [16], caused by opening of the channels $\pi^- p \to K^0\Sigma^0$ ($\sqrt{s}$ = 1690.2 MeV) and $\pi^- p \to K^+\Sigma^{--}$ ($\sqrt{s}$ = 1691.1 MeV).

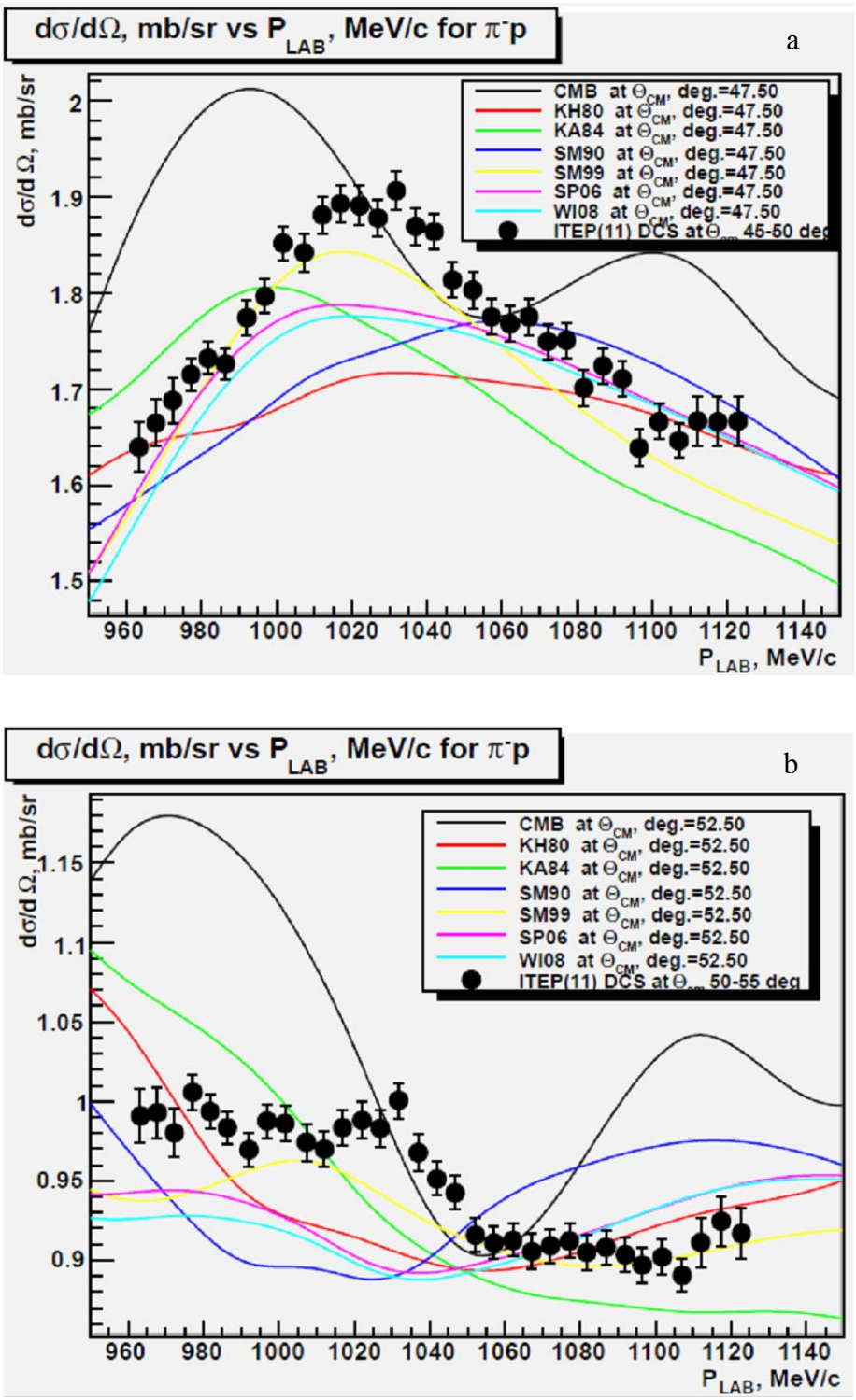

Fig. 6. Preliminary differential cross sections for elastic $\pi^- p$ scattering as a function of the incident pion momentum at θ_{CM} = 47.5°(a). Preliminary differential cross sections for elastic $\pi^- p$ scattering as a function of the incident pion momentum at θ_{CM} = 52.5° (b)

The resonance, if it is a member of the pentaquark antidecouplet, has to be in the *P*-wave, while the threshold effect should manifest itself in the *S*-wave. The structure observed in the differential cross section is a result of interference of a fast change in some partial wave with a slow changing non-resonant background. We plan to collect large statistics in a narrow region $p_{\mathrm{beam}} = 1000–1070$ MeV/c, which will allow us to plot the data in a fine angle and energy binning in order to find out which wave is affected. Further analysis of the data already collected is also under way.

References

1. T. Nakano *et al*., Phys. Rev. Lett. **91**, 012002 (2003).
2. V.V. Barmin *et al*., Phys. Atom. Nucl. **66**, 1715 (2003).
3. R. De Vita *et al*., Phys. Rev. D **74**, 032001 (2006).
4. T. Nakano *et al*., Phys. Rev. C **79**, 025210 (2009).
5. V.V. Barmin *et al*., Phys. Atom. Nucl. **70**, 35 (2007).
6. D. Diakonov, V. Petrov and M. Polyakov, Z. Phys. A **359**, 305 (1997).
7. R. Arndt *et al*., Phys. Rev. C **69**, 035213 (2004).
8. R. Arndt *et al*., Phys. Rev. C **69**, 035208 (2004).
9. V. Kuznetsov *et al*., Phys. Lett. B **647**, 23 (2007).
10. V. Kuznetsov *et al.*, http://2009physicsevents.org/pages/Speaker_KuznetsovNNR_1.pdf
11. F. Miyahara *et al*., Prog. Theor. Phys. Suppl. **168**, 90 (2007).
12. I. Jaegle *et al*., Eur. Phys. J. A **47**, 89 (2011).
13. D. Werthmuller, Chin. Phys. C **33**, 1345 (2009).
14. I.G. Alekseev *et al*., arXiv: hep-ex/0509032.
15. I.G. Alekseev *et al*., Nucl. Instr. Meth. A **578**, 289 (2007).
16. A.I. Baz, JETP **33**, 923 (1957).

BACKWARD ASYMMETRY MEASUREMENTS
IN ELASTIC PION-PROTON SCATTERING AT RESONANCE ENERGIES

PNPI participants of the PNPI–ITEP Collaboration:
Yu.A. Beloglazov, E.A. Filimonov, A.I. Kovalev, D.V. Novinsky, V.V. Sumachev, V.Yu. Trautman

1. Introduction

The aim of the described experiment was to measure the asymmetry parameter *P* for elastic pion-proton scattering in the very backward angular region of $\Theta_{cm} = 150–170°$ at several pion beam energies in the invariant mass range that contains most of the pion-proton resonances. The general goal of the experimental program was to provide new data for partial-wave analyses in order to resolve their uncertainties in the baryon resonance region to allow an unambiguous baryon spectrum reconstruction. Until recently, the parameter *P* has not been measured in the examined domain. This can be explained by the extremely low cross sections. At the same time, predictions of various partial wave analyses are far from agreement in some kinematic areas, and specifically those areas were chosen for the measurements where the disagreement is most pronouncing. The experiment was performed at the ITEP U-10 proton synchrotron, Moscow, by the PNPI–ITEP Collaboration in 2008.

The history of investigations of pion-nucleon interaction is about 40 years old. A systematic set of data in the resonance region was obtained during that period. These days three Partial Wave Analyses (PWA) are known which are the main source of information on baryon resonance parameters: the basic PWA of the Karlsruhe – Helsinki group KH80 [1, 2] in the beam momentum range 0.02−10 GeV/*c*, the analysis of the Carnegie – Mellon – Lawrence – Berkeley – Laboratory group CMB80 [3] up to 2.5 GeV/*c*, and a series of solutions by the George Washington University (GWU) group, formerly located at VPI, below 2.1 GeV/*c* [4, 5]. A detailed presentation of all mentioned PWA results can be found at the CNS DAC web page with the SAID program [6].

But even up to now, there are some kinematics regions where predictions of different PWAs are in evident contradiction with one another. In most cases, this is due to very small cross section values of the order of 0.1 mb/sr (Fig. 1).

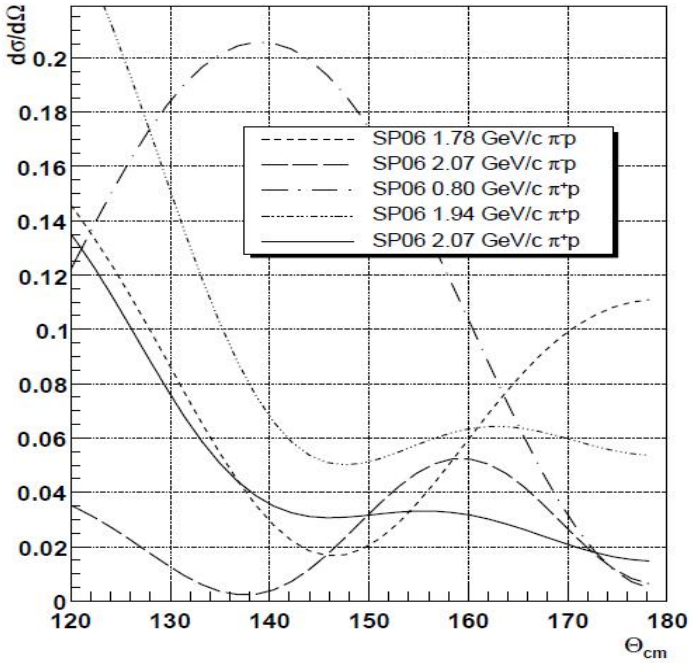

Fig. 1. Cross sections (in mb/sr) for elastic $\pi^- p$ scattering in the backward region *vs* the centre-of-mass scattering angle (in degrees). The data are taken from SP06 PWA [5]

Low quality or absence of experimental data in such regions leads to continuous uncertainties in partial amplitudes, as well as to unresolved discrete ambiguities and consequent wrong choices of solution branches [7]. Some observed minima in the differential cross section are caused by specific behaviour of the pion-nucleon amplitude or, rather, of the Barrelet zero trajectories, and that is why measurements in such areas are particularly important for correct reconstruction of the pion-nucleon amplitude. The main goal of this work was to provide new experimental information for the partial-wave analyses specifically in such kinematic areas where it may best help to resolve the existing PWA uncertainties and thus allow reliable extraction of the non-strange baryon resonance spectrum and baryon properties.

This paper presents the latest results of the PNPI–ITEP Collaboration on measurements of the asymmetry P both for π^+p and π^-p elastic scattering to the backward angles at several energy points.

2. Experimental conditions

The polarization parameter P in elastic scattering is determined by direct measurements of the azimuthal asymmetry of the reaction produced by incident pions on a proton target polarized normally to the scattering plane.

The differential cross section in this case has the following form:

$$d\sigma / d\Omega = (d\sigma / d\Omega)_0 \, [1 + P \cdot (\mathbf{P_T} \cdot \mathbf{n})],$$

where $(d\sigma / d\Omega)_0$ is the differential cross section for πp elastic scattering on an unpolarized target, P is the polarization parameter, $\mathbf{P_T}$ is the vector of the target polarization and $\mathbf{n}$ is the unit vector normal to the scattering plane.

The experimental set-up SPIN-P02 is schematically shown in Fig. 2. The polarized target with vertical orientation of the polarization vector $\mathbf{P_T}$ is located at the focus of the secondary pion beam line of the ITEP proton synchrotron. The scattered pion and the recoiled proton are tracked with blocks of multi-wire chambers, and the full event reconstruction is performed allowing good selection of elastic events. The asymmetry is determined by measuring the normalized event counts for two opposite directions of the target polarization vector. Such configuration corresponds to direct measurements of the polarization parameter P by means of the scattering asymmetry, rather than to determination of the recoil proton polarization vector with the help of a proton polarimeter.

Main parts of the SPIN-P02 set-up [8] are described below. The polarized Proton Target (PT) was located in a cryostat with a superconducting magnet. The container with the polarized target material (propanediole $C_3H_8O_2$ doped with Cr^V complexes) was placed into the magnetic field of 2.35 T formed by a Helmholtz pair of superconducting coils. The relative free proton density was close to 10 % [9]. The container had a cylindrical form with the height and diameter of 30 mm. The cooling of the target material to 0.5 K was provided by an evaporation-type ^{3}He cryostat. The target protons were polarized by the dynamic nuclear orientation method. The polarization was 70–80 % with the measurement uncertainty about 1.5 %. The polarization sign was reversed once a day.

There were three blocks of two-coordinate multi-wire chambers with the spatial measurement accuracy of about 0.5 mm for tracking of the incident pions (CH1-CH6), recoiled protons (CH7-CH10) and scattered pions (CH11-CH14). In some configurations of the set-up one more block was added, adjacent to CH11-CH14 to achieve a wider pion acceptance.

The trigger logic used the signals of the scintillation counters C1-C12. The readout of the chamber data was initiated on the following condition: $C1 \cdot C2 \cdot \overline{C3} \cdot C4 \cdot \overline{C5} \cdot C6 \cdot C7 \cdot [C8 \cdot (C9 + C10)]$. In the case of a positive beam, the TOF technique was used to separate pions from protons at low beam energies, while at beam momenta above 1.8 GeV/c the aerogel Cherenkov counter AGCC [10] was additionally introduced into the beam to tag the pions.

The secondary pion beam was formed by a universal magneto-optical channel based on a two-stage achromatic scheme and provided an intensity of up to $2 \cdot 10^5$ pions per accelerator spill (t = 0.6 s every 4 s). The 46.5 m long beam line was equipped with two vertical correctors, allowing to change the position of the beam intersection with the polarized target with the accuracy about 4 mm. The beam dimensions in the target plane were 32×27 mm^2 (FWHM). The momentum spread of the beam was about ± 2 %.

To achieve the acceptance coverage of the very backward pion angles about 170° at the beam momentum 0.8 GeV/*c*, two configurations of the set-up were used with opposite directions of the target magnetic field and with correspondingly different positions of the proton arm.

The CAMAC based readout system allowed to record up to 40 events per accelerator cycle. The data storage, as well as its on-line processing and the set-up monitoring, were provided by a single PC.

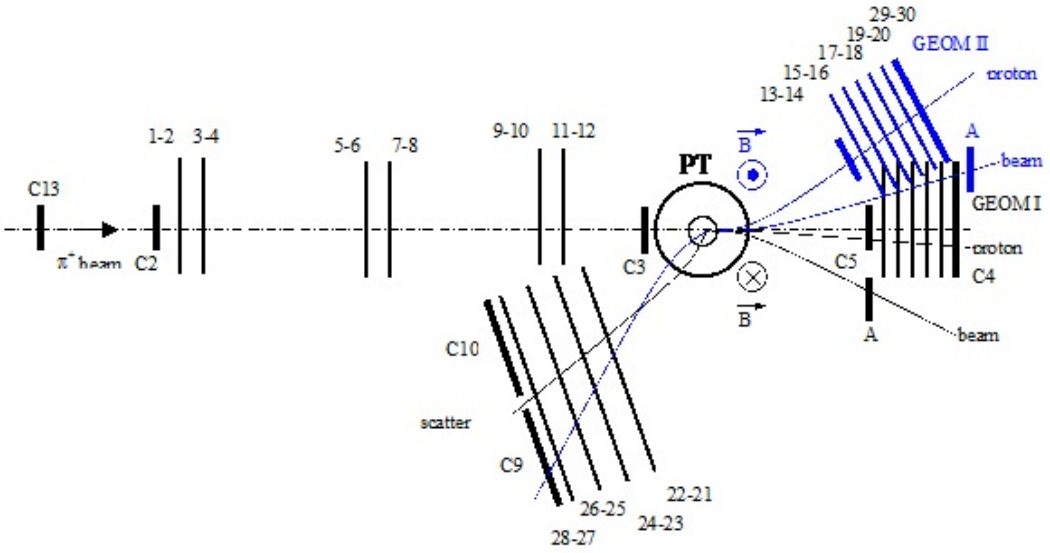

Fig. 2. Schematic top view of the SPIN-P02 set-up

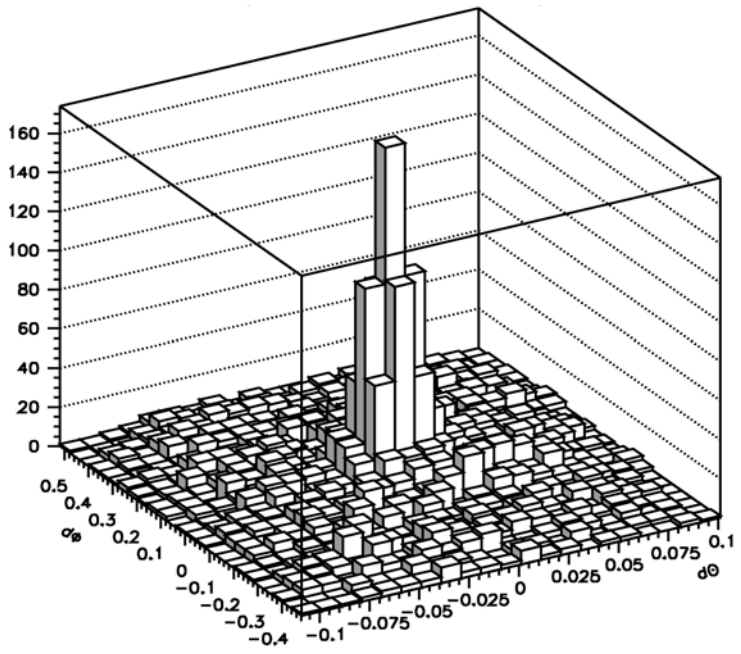

Fig. 3. Two-dimensional distribution $\Delta\theta - \Delta\phi$ illustrating deviations from the elastic kinematics in $\pi^+ p$ scattering at 0.80 GeV/*c*

3. Data processing

The processing of the data was performed in the following steps. Straight trajectories of the beam pion, of the scattered pion and of the recoiled proton were reconstructed by processing the data of the corresponding chamber blocks outside the magnetic field of the target by the least square method. The tracks

obtained for each event were then extrapolated to the target region through the magnetic field, and the interaction vertex was found. The polar and azimuthal angles were separately determined for both scattered particles, and their values were used for event selection. The procedure of the elastic event selection is illustrated by Fig. 3. For each event, the deviation from the elastic kinematics was calculated in terms of two variables: $\Delta\theta$ – the difference in the c.m. scattering angle for the pion and for the proton, and $\Delta\phi$ – the sum of their azimuthal deviations from the scattering plane, and then two-dimensional distributions of these variables were filled. For the best background estimation, these distributions were fit with a 2-dimensional 12-parameter polynomial, excluding the area of the elastic peak, and the error matrix was calculated for these obtained fit parameters. The number of elastic events was determined as the distribution excess over the background, interpolated to the area under the peak. To account for different statistics with opposite target polarizations, the intensity normalization was done based on the quasi elastic event counts, which are believed to be unpolarized and represent the main content of the background. A comparison of results with various cuts around the elastic peak provided additional systematic error checks. The statistical error accounts for the elastic event number, the background error matrix and the uncertainty in the intensity normalization.

The selected events were divided into several angular intervals in Θ_{cm}, and average angles were calculated for each interval, according to the individual values for each event.

4. Results

The asymmetry P in the πp elastic scattering was determined in the very backward angular region of (150–170)° in the c.m. frame at several beam momenta. The values of the momentum were intentionally chosen so that disagreement in the PWA predictions is most pronounced in the backward hemisphere at these momenta. It is worth mentioning that the differential cross sections in the regions of the experiment are very small, though they are significantly different. Thus, the experimental conditions in terms of the event rate and signal to background ratio are also essentially different.

Table 1

Summary of the obtained statistics and experimental conditions

Reaction	P beam, GeV/c	$d\sigma/d\Omega$, mb/sr	N_{el}	N_{BG}/N_{el}
$\pi^- p$	1.78	0.02–0.10	3252	0.45
$\pi^- p$	2.07	0.03–0.05	2047	0.43
$\pi^+ p$	0.80	0.03–0.17	3128	0.19
$\pi^+ p$	1.94	0.05–0.07	1066	1.01
$\pi^+ p$	2.07	0.02–0.03	701	1.56

Table 2

Asymmetry in $\pi^- p$ elastic scattering at 1.78 GeV/c

Mean angle, degrees	Interval of angles, degrees	Asymmetry	Error
153.6	149.2–156.2	–1.012	0.094
157.8	156.2–159.2	–0.794	0.061
153.6	149.2–156.2	–0.594	0.059
153.6	149.2–156.2	–0.537	0.067
153.6	149.2–156.2	–0.199	0.070
153.6	149.2–156.2	–0.276	0.076

Table 3

Asymmetry in $\pi^- p$ elastic scattering at 2.07 GeV/c

Mean angle, degrees	Interval of angles, degrees	Asymmetry	Error
154.4	151.0–156.7	0.125	0.071
158.4	156.7–158.4	–0.023	0.061
161.8	161.1–164.0	0.172	0.062
167.1	164.0–168.5	0.146	0.107
169.9	168.5–172.0	0.099	0.109

Table 4

Asymmetry in $\pi^+ p$ elastic scattering at 0.80 GeV/c

Mean angle, degrees	Interval of angles, degrees	Asymmetry	Error
143.2	137.4–144.9	0.310	0.060
148.7	144.9–152.4	0.400	0.060
155.8	152.4–159.9	0.430	0.060
161.3	159.9–167.4	0.440	0.060
169.3	167.4–172.3	0.760	0.160

Table 5

Asymmetry in $\pi^+ p$ elastic scattering at 1.94 GeV/c

Mean angle, degrees	Interval of angles, degrees	Asymmetry	Error
154.0	148.0–157.9	–0.230	0.129
160.3	157.9–165.0	–0.687	0.139
166.4	165.0–168.0	–0.774	0.145
169.8	168.0–176.0	–0.434	0.154

Table 6

Asymmetry in $\pi^+ p$ elastic scattering at 2.07 GeV/c

Mean angle, degrees	Interval of angles, degrees	Asymmetry	Error
155.3	148.0–158.5	–0.441	0.163
161.0	158.5–164.0	0.037	0.223
167.1	164.0–168.7	0.238	0.286
170.0	168.7–176.0	–0.012	0.260

Table 1 summarizes the statistical material obtained for all data regions. The third column together with Fig. 1 presents the cross section values in the angular domain under study, giving the explanation to the number of elastic events obtained in approximately equal running periods (column 4) and the background levels (column 5).

Tables 2–6, together with Figs. 4 and 5, present the results of the asymmetry measurements as functions of the c.m. scattering angle. The errors are statistical only, while the systematic errors due to uncertainties in the target polarization measurements were below 3 % (typically 1.5 %). The lines in the figures show PWA predictions for comparison: the "classic" analyses CMB80 [3] (dotted) and KH80 [1] (dashed), the latest solution of the GWU group SP06 [5] (solid) and their earlier solution SM95 [4] (dash-dotted). The older experimental data at smaller angles and in the overlapping regions are also shown with open markers.

The points at 1.78 GeV/c in $\pi^- p$ (Fig. 4a) were measured to check the set-up performance. The partial-wave analyses do not show large variations from each other. The data show the best agreement with CMB80,

while the deviation of KH80 from the data points is obviously statistically significant. The point at 153.6° coincides with that from [13] and supports even deeper and saturated minimum than any of the analyses show. Such minima indicate that a branching point of the PWA solution may be present close to this kinematic point. The next point at 157.8° overlaps with the previous ITEP measurement [11] performed using a different set-up, supporting good quality of that result.

The data points at 2.07 GeV/c with negative pions (Fig. 4b) are not followed exactly by any of the PWA solutions. Yet, the closest two are SM95 and CMB80, while SP06 and KH80 do not even resemble the data behaviour. Again, good agreement with the earlier ITEP data in the overlapping region is observed.

A narrow local minimum at 157° confirmed by two independent measurements draws additional attention and indicates a significant presence of a partial wave with a high orbital momentum of the order of L = 8–9. Similarly, a sharp step at 167° in the data at 1.78 GeV/c may point out a large value of the same partial amplitude.

In both cases with $\pi^- p$ scattering, the latest solution – SP06 of the GWU group is not the closest to the new data. On the other hand, in the lower energy domain and the pure I = 3/2 isospin state, the data points are best described just by this solution (see Fig. 5a for $\pi^+ p$ at 0.80 GeV/c). CMB80 does not show the sharp and high peak at 175° implied by the data, while SM95 gives much smaller values of the asymmetry in the whole angular range of measurements. It is worth mentioning that our data are in obvious contradiction to 3 rightmost points from [14] at two adjacent energies.

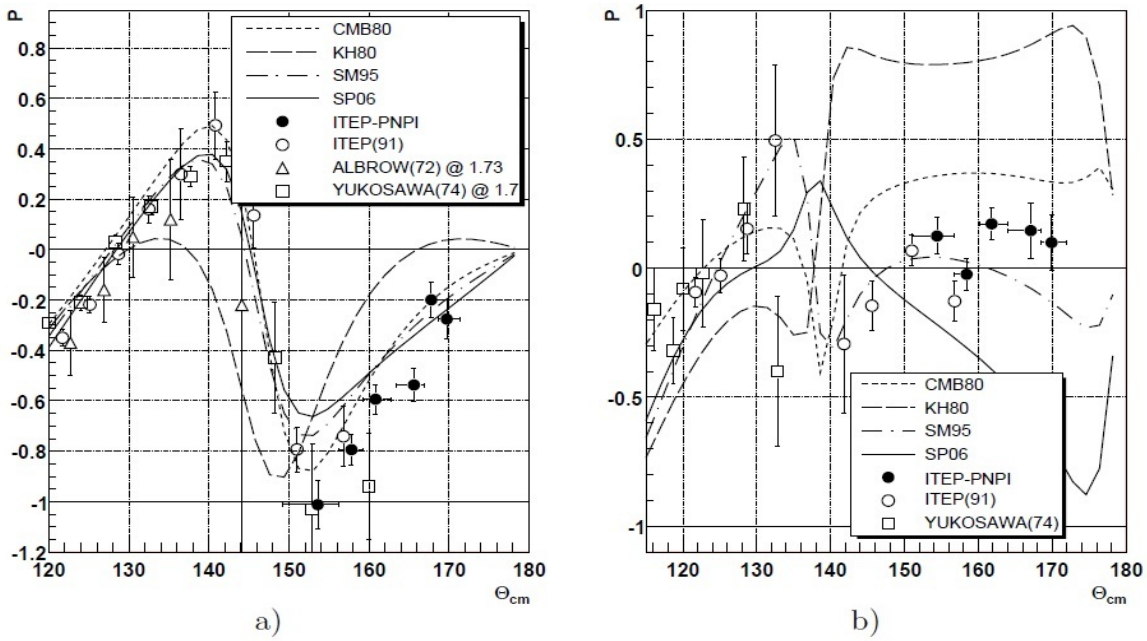

Fig. 4. Asymmetry in $\pi^- p$ elastic scattering at 1.78 GeV/c (a) and at 2.07 GeV/c (b). Earlier data are from [11] (open circles), [12] (triangles), and [13] (squares)

The authors claim very small errors for 4 of these 6 points, while the GWU group has already excluded some of them from their analysis database. The asymmetry of $\pi^+ p$ at 1.94 GeV/c shows large negative values around 165° (Fig. 5b). Neither of the solutions manifest a deep minimum, though all but CMB80 have qualitatively similar behaviour. The closest prediction in this case is from KH80.

The cross section for backward angles at 2.07 GeV/c is extremely low for positive pions (Fig. 5c). That is why the quality of all data points in this region is very poor, and it hardly allows to trace any particular angular behaviour of the asymmetry. The newly obtained results are not much better statistically and they feature the background levels higher than the numbers of useful elastic events (Table 1). Yet, they allow to make some conclusions about their correspondence to various PWA solutions. The angular dependence of the data most resemble the curve from the CMB80 analysis. All other solutions show qualitatively different behaviour, though KH80 and SM95 are not beyond 3σ boundary of the data.

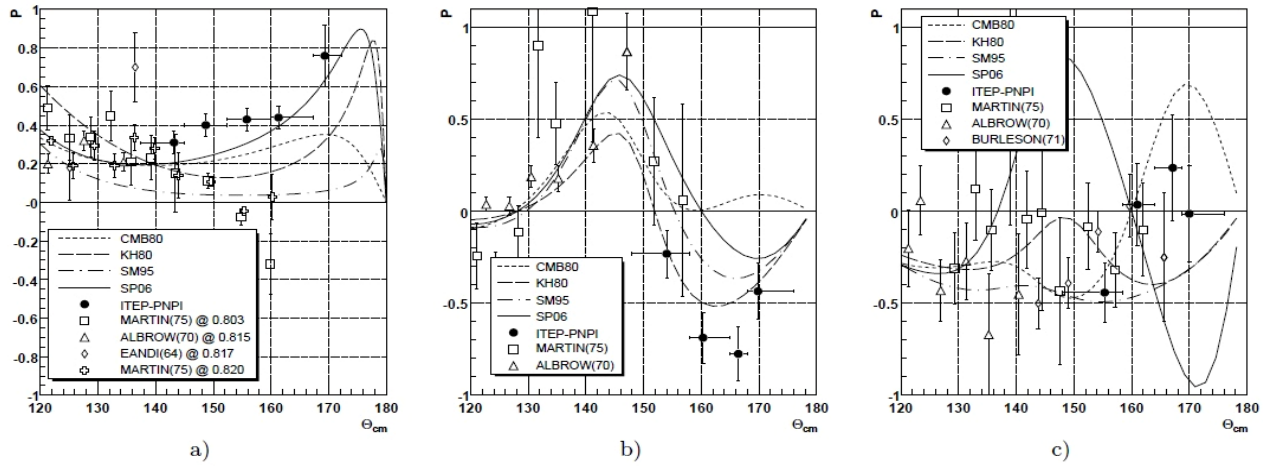

Fig. 5. Asymmetry in π^+p elastic scattering at 0.80 GeV/*c* (a), 1.94 GeV/*c* (b) and 2.07 GeV/*c* (c). Earlier data are from [14] (squares and crosses), [15] (triangles), and [16], [17] (diamonds)

5. Conclusion

The obtained results show that in some kinematic areas one or both of the "classic" partial-wave analyses CMB80 and KH80 are in disagreement with the new data. In several shown cases even the qualitative behaviour of these PWAs does not correspond to that of the data, which may indicate a wrong choice of the solution branch by these analyses and, consequently, a wrong extraction of baryon properties. The latest solution SP06 of the GWU group seems to be consistent with the data in the lower energy domain, while its behaviour looks unstable in the region around 2 GeV/*c* of the beam momentum.

The PNPI-ITEP experimental team believes that their new data on the backward asymmetry in the elastic pion-proton scattering notably improve the database for partial-wave analyses and help to make another step on the way of elimination of PWA ambiguities of various kinds and thus to obtain a reliable light baryon spectrum.

References

1. G. Hoehler, Handbook of Pion Nucleon Scattering, Physics Data **12-1** (Fachinformationzentrum, Karlsruhe, 1979).
2. G. Hoehler *et al.*, πN-Newsletter **9**, 1 (1993).
3. R.E. Cutcosky *et al.*, Phys. Rev. D **20**, 2839 (1979).
4. R.A. Arndt *et al.*, Phys. Rev. C **52**, 2120 (1995).
5. R.A. Arndt *et al.*, Phys. Rev. C **69**, 035213 (2004).
   R.A. Arndt *et al.*, Phys. Rev. C **74**, 045205 (2006).
6. R.A. Arndt *et al.*, Int. J. Mod. Phys. A **18**, 449 (2003);
   http://gwdac.phys.gwu.edu/analysis/pin_analysis.html
7. I.G. Alekseev *et al.*, Phys. Rev. C **55**, 2049 (1997).
8. Yu.A. Beloglazov *et al.*, Instr. Exp. Tech. **47**, 744 (2005).
9. E.I. Bunyatova *et al.*, Preprint LNPI-**1191**, Gatchina (1986).
10. Yu.K. Akimov *et.al.*, Instr. Exp. Tech. **45**, 634 (2005).
11. I.G. Alekseev *et al.*, Nucl. Phys. B **348**, 257 (1991).
12. M.G. Albrow *et al.*, Nucl. Phys. B **37**, 594 (1972).
13. D. Hill *et al.*, Phys. Rev. Lett. **27**, 1241 (1971).
14. J.E. Martin *et al.*, Nucl. Phys. B **89**, 253 (1975).
15. M.G. Albrow *et al.*, Nucl. Phys. B **25**, 9 (1970).
16. R.D. Eandi *et al.*, Phys. Rev. B **136**, 536 (1964).
17. G. Burleson *et al.*, Phys. Rev. Lett. **26**, 338 (1971).

STUDY OF NEAR-THRESHOLD η-MESON PRODUCTION IN THE REACTION $\pi^- p \to \eta n$

D.E. Bayadilov, Yu.A. Beloglazov, E.A. Filimonov, A.B. Gridnev, N.G. Kozlenko, S.P. Kruglov, A.A. Kulbardis, I.V. Lopatin, D.V. Novinsky, A.K. Radkov, A.V. Shvedchikov, V.V. Sumachev

During several years, the Meson Physics Laboratory performed a series of experiments on near-threshold production of η mesons in the reaction $\pi^- p \to \eta n$ at the pion channel of the PNPI synchrocyclotron. These experiments were carried out using the Neutral Meson Spectrometer (NMS) designed and built at PNPI.

In the experiments on near-threshold η-meson production in the reaction $\pi^- p \to \eta n$, we determined the total energy E_η of η mesons and the angle θ_η at which these mesons were produced, by measuring the energies E_{γ_1} and E_{γ_2} of two γ quanta from the decay $\eta \to 2\gamma$, and the angles θ_{γ_1} and θ_{γ_2} of their emission with the NMS (all variables are in the laboratory frame):

$$E_\eta = \left[\frac{2M_\eta^2}{\left(1-\cos\Psi_{\gamma\gamma}\right)\cdot\left(1-X^2\right)} \right]^{1/2} , \qquad (1)$$

where $X = (E_{\gamma_1} - E_{\gamma_2}) / (E_{\gamma_1} + E_{\gamma_2})$ is the parameter which characterizes the sharing of the η-meson energy between two γ quanta, $\Psi_{\gamma\gamma}$ is the angle between the directions of the emitted γ quanta,

$$\cos\theta_\eta = \frac{E_{\gamma_1}\cos\theta_{\gamma_1} + E_{\gamma_2}\cos\theta_{\gamma_2}}{\left(E_{\gamma_1}^2 + E_{\gamma_2}^2 + 2E_{\gamma_1}E_{\gamma_2}\cos\Psi_{\gamma\gamma}\right)^{1/2}} . \qquad (2)$$

A schematic drawing of the NMS is shown in Fig. 1, and the photo of its disposition at the experimental hall of the PNPI synchrocyclotron is presented in Fig. 2. The NMS consists of two total absorption electromagnetic calorimeters, each being an array of 24 CsI(Na) crystals. The size of each crystal was $6 \times 6 \times 30$ cm^3; the largest dimension is the crystal length, it makes 16.2 radiation lengths. Also shown in Fig. 1 are a liquid hydrogen target, it is a vertical cylinder with the height and diameter of 10 cm, and two veto counters for rejection of events with a charged particle entering the calorimeter.

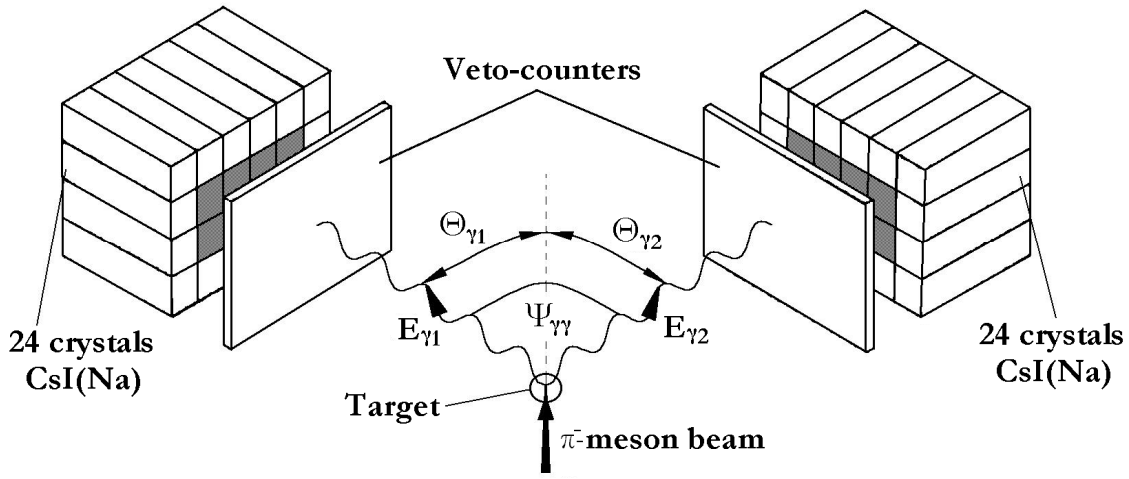

Fig. 1. Schematic drawing of the NMS

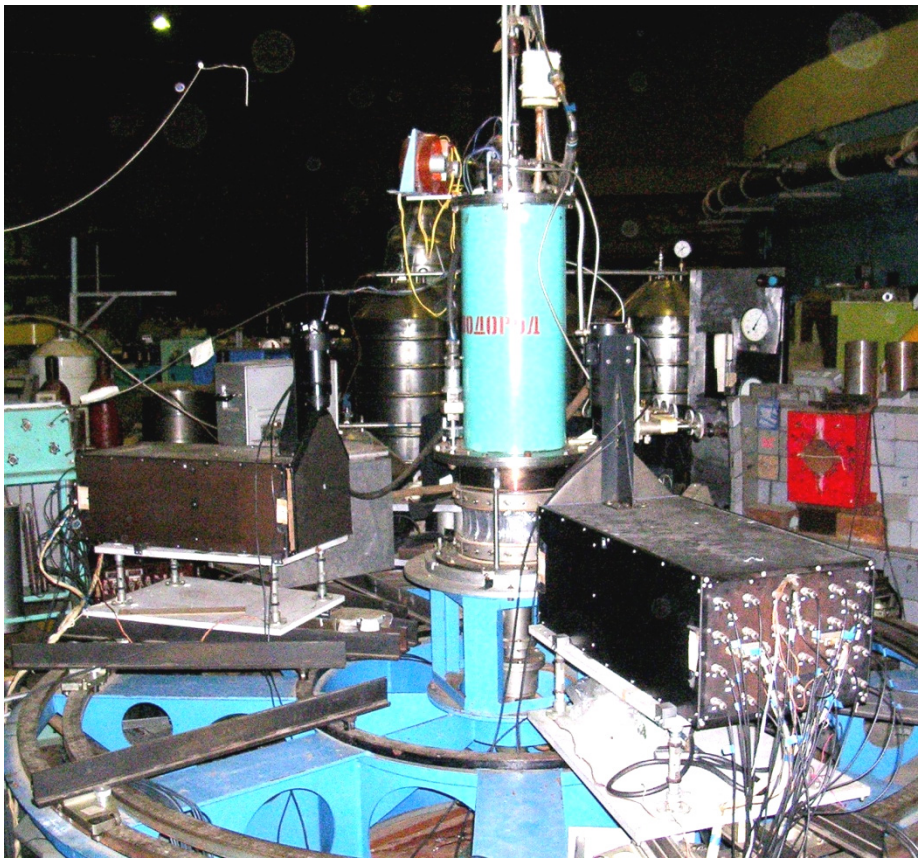

Fig. 2. General view of the experimental set-up including the NMS and the liquid hydrogen target

For detection of light from each crystal, PhotoMultiplier Tubes (PMT) of the FEU-97 type were used. For each of the 48 PMTs a voltage-multiplying stabilized HV source was built; each was mounted directly on the PMT base. Signals from the output of each PMT were split, the anode signal was fed to a Charge-to-Digital Converter (CDC) and provided information about the energy deposited in the crystal, and the signal from the last dynode was used to form a fast trigger. To minimize the uncertainty in determination of the γ quantum energy due to the transverse leakage of the shower energy, the trigger was formed only in the case when the energy deposited in eight inner crystals of each calorimeter exceeded some fixed threshold. For this purpose, the dynode signals from 8 inner crystals were summed up and fed to a shaper with the threshold set to the minimal required energy deposit. The peripheral 16 crystals played a role of a "guard ring", in which the shower energy escaping the central part of the calorimeter was registered. A more detailed description of the NMS and its characteristics are given in [1].

A typical trigger to initiate the set-up was formed as a coincidence of fast logical signals from the two calorimeters and from the monitor counters, if there was no signal from the veto counters placed in front of the calorimeters.

Using the NMS, we have measured the differential cross sections for the reaction $\pi^- p \to \eta n$ at the momenta of incident pions close to the threshold of this reaction (685 MeV/c). Preliminary results of this experiment were presented in [2]. Since the total cross section for this reaction rises sharply with the momentum in the near-threshold region, the momentum spread of particles in the beam was decreased to $\Delta p / p$ = 1.5 % (FWHM), compared to the value $\Delta p / p$ = 6 % for the standard version of the pion channel, by inserting a narrow vertical collimator in that part of the pion channel where the momentum dispersion was maximal.

The angular dispositions of the NMS calorimeters and the distances from the front surface of the calorimeters to the target centre were chosen taking into account the specific kinematics of η production near the reaction threshold. The main peculiarity is that η mesons produced in the centre-of-mass (c.m.s.)

system in a wide angular range from $\theta_\eta = 0°$ to $\theta_\eta = 180°$ are emitted within a narrow cone when transformed to the laboratory frame. For example, at the momentum of incident pions of 710 MeV/*c,* the opening angle of this cone is only ± 23.5°. At the subsequent decay $\eta \to \gamma\gamma$, the γ quanta are emitted in a wide angular range from 0° to 180° with respect to the direction of the *η*-meson momentum, but the most probable is the symmetric decay ($\theta_{\gamma_1} \approx \theta_{\gamma_2}$). These kinematical peculiarities allow to measure the differential cross section for the reaction $\pi^- p \to \eta n$ in the full angular range from $\theta_\eta = 0°$ to $\theta_\eta = 180°$ using the NMS with a rather restricted angular acceptance.

In order to choose the most optimal disposition of the NMS calorimeters, we have performed a Monte Carlo simulation of the experiment. The simulation included the exact geometry of the set-up, the mutual position of the calorimeters, the liquid hydrogen target and the monitor counters, the construction elements of the calorimeters and of the target. Performing the simulation, we have taken into account the momentum distribution, the geometrical size and the angular divergence of the pion beam, as well as the momentum dependence of the total cross section for the reaction $\pi^- p \to \eta n$ obtained by an analysis of rather scarce experimental data existing by now. In the Monte Carlo simulation, we used also the values of the energy resolution of the calorimeters which were obtained in the experiments carried out earlier using the electron component of the PNPI pion channel. The minimal possible distance from the NMS calorimeters to the target centre ($L = 65$ cm) was determined by the requirement that the γ quanta, emitted from the hydrogen container, entered the eight central crystals of the calorimeters without any rescattering on the elements of the target construction. The aim of the simulation was to choose at $L = 65$ cm the angles of the calorimeters disposition with respect to the direction of the incident pion beam in such a manner that the values of the acceptance A calculated for different angular intervals $\Delta\theta_\eta^{\,\mathrm{CM}}$ were diverse in the full scale of angles by a factor not more than 2–3. The Monte Carlo simulation has shown that for the momenta of incident pions 700, 710, 720 and 730 MeV/*c* the most optimal position of the NMS calorimeters was at the angles ± 66° with respect to the beam axis.

The algorithm of processing those events for which at least one γ quantum is registered in each NMS calorimeter, is briefly described below.

1. For each event, the matrices showing the energy deposition in different crystals were formed for both calorimeters, and the crystal with the maximum energy deposition was determined in each calorimeter.

2. The energies E_{γ_1} and E_{γ_2} deposited in both calorimeters were determined as the sum of energies deposited in all nine crystals of those clusters, the central crystal of which was determined at the previous stage.

3. To reconstruct the coordinates of the point at which the γ quantum enters the corresponding calorimeter, the coordinates "*x*" and "*y*" of the shower centre-of-gravity were calculated by weighting the energies deposited in each of the nine-crystal clusters. A comparison was made of different "weighting" functions: E, $\sqrt{E}$, $\ln E$, the maximal accuracy being achieved with the $\ln E$ as a "weight":

$$x(y) = \frac{\sum_{i=1}^{9} \ln E^i \cdot x^i(y^i)}{\sum_{i=1}^{9} \ln E^i}. \qquad (3)$$

4. After the coordinates of the points at which the γ quanta entered both calorimeters are calculated with Eq. (3), it is possible to determine in the first approximation the angles θ_{γ_1} and θ_{γ_2} at which the γ quanta entered the calorimeters, in the assumption that the point in which the η meson was produced in the target (and the point from which the two γ quanta of the η-meson decay were emitted) is the target centre.

5. After the values of E_{γ_1}, E_{γ_2}, θ_{γ_1}, and θ_{γ_2} are determined for all registered events, the angle of η-meson emission may be calculated for each event using Eq. (3).

6. The next stage of processing is to select from all data accumulated in the experiment the events with two γ quanta from the decay of η mesons. For such a selection we used the two-dimension distribution in which the energies of γ quanta deposited in the two calorimeters were plotted along the coordinate axes, as shown in Fig. 3. Two black areas clearly visible at the energies of γ quanta from 200 to 400 MeV are due to

γ quanta from the decay → η 2γ. The cuts which were used for selection of "useful" events (in which the γ quanta from η-meson decay entered the NMS calorimeter) were determined according to the Monte Carlo simulation. These cuts are shown as the elliptic curve in Fig. 3.

7. All "useful" events inside of the ellipse were split into several angular intervals. When choosing the values of these intervals, the NMS angular resolution obtained in the Monte Carlo simulation was taken into account. For each simulated event, the difference between the c.m.s. angle at which the η meson was produced in the target in the reaction $\pi^- p \to \eta n$ and the angle obtained in the event reconstruction were calculated. The resulting distribution looks like a Gaussian curve with $\sigma_\theta \approx 15°$. This corresponds to $\sigma_{\cos\theta} \approx 0.05$ for the angular ranges $\theta_\eta^{CM} \approx -1$ and $\theta_\eta^{CM} \approx +1$, and to $\sigma_{\cos\theta} \approx 0.3$ for $\theta_\eta^{CM} \approx 0$. Since these non-equal $\Delta\theta_\eta^{CM}$ intervals are not convenient for plotting the angular distributions of the differential cross sections, the whole accepted angular spread from $\theta_\eta^{CM} = -1$ to $\theta_\eta^{CM} = +1$ was split into ten equal intervals of $\Delta\theta_\eta^{CM} = 0.2$.

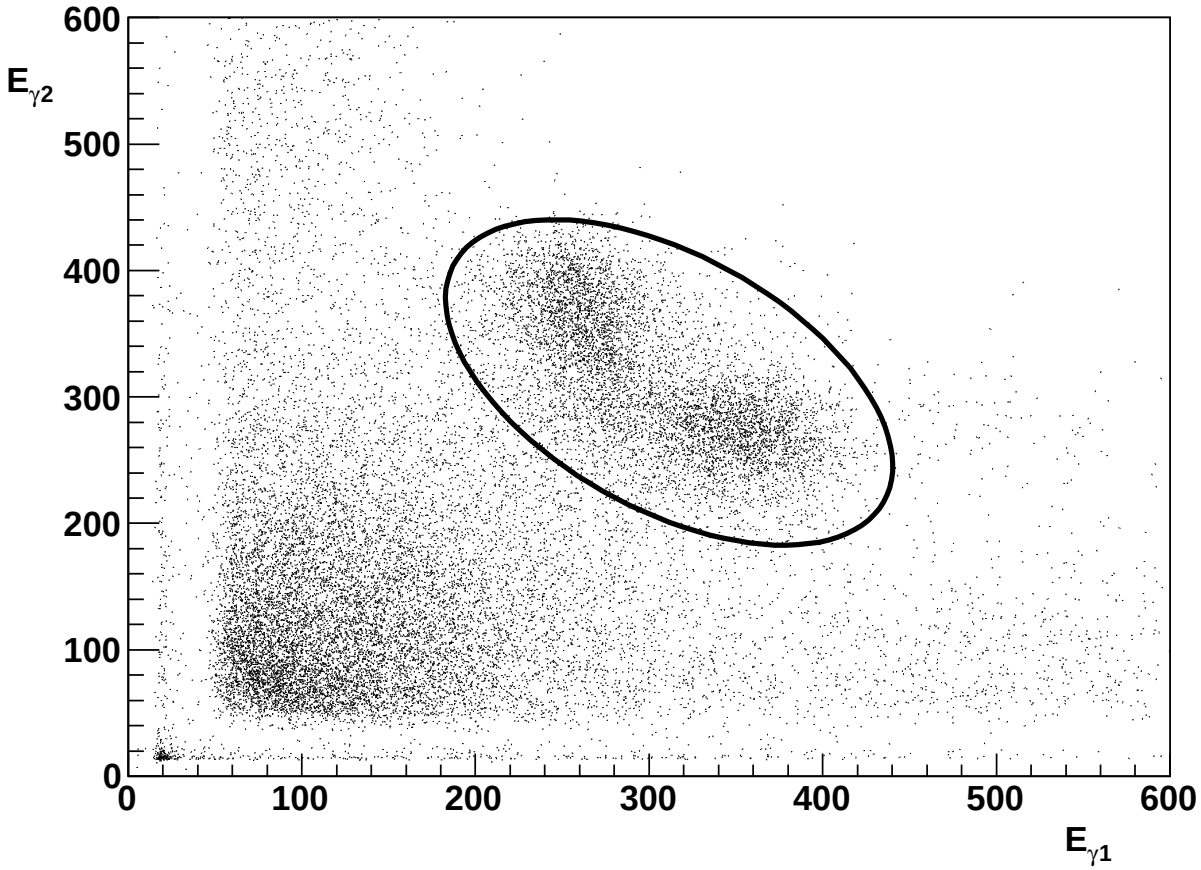

Fig. 3. Two-dimensional distribution $E_{\gamma 1}$ *vs* $E_{\gamma 2}$

Prior to using the above described procedure for calculations of the cross sections for the reaction $\pi^- p \to \eta n$, it is necessary to estimate possible sources of physical background. The first one is the decay of η meson $\eta \to 3\pi^0 \to 6\gamma$, *the* probability of such decay being comparable to that of the decay $\eta \to 2\gamma$. In principle, if one of the six γ quanta enters one of the calorimeters and one more γ quantum hits the second calorimeter, this process can imitate the decay $\eta \to 2\gamma$. However, the Monte Carlo simulation shows that the probability of such events inside the ellipse of the two-dimensional plot E_{γ_2} *vs* E_{γ_1} is negligibly small.

Another possible source of physical background is the production of two π^0 mesons with their subsequent decay into four γ quanta $\pi^- p \to 2\pi^0 n \to 4\gamma n$. A simulation of this reaction shows that the event with one of the four emitted γ quanta entering one calorimeter and another γ quantum entering the second calorimeter has

a considerable probability to be inside of the above-mentioned ellipse. However, it is difficult to estimate this effect quantitatively because of the absence of reliable experimental data on double differential cross sections for the reaction $\pi^- p \to 2\pi^0 n$. For this reason, it was decided to carry out an additional experiment at the incident pion momentum 655 MeV/*c*, below the threshold of the reaction $\pi^- p \to \eta n$. Results of this experiment were processed using the same algorithm as was used for processing the data on η-meson production. The obtained number of events (split into ten angular bins $\Delta\theta_\eta^{CM} = 0.2$) were extrapolated to the momenta of the incident pions 700, 710, 720 and 730 MeV/*c* at which the experiment on the η-meson production in the reaction $\pi^- p \to \eta n$ was carried out. Performing the above-mentioned extrapolation, we used the momentum dependence of the total cross section for the reaction $\pi^- p \to \pi^0 n$ measured earlier at the BNL. The correction obtained by calculations is about 2.5 %.

As to a pair of γ quanta from the decay of π^0 mesons produced in the reaction $\pi^- p \to \pi^0 n$, they practically are not registered in the geometry of the described set-up. This is confirmed by our Monte Carlo simulation.

At last, one more background source is the rescattering of γ quanta, produced in the reactions $\pi^- p \to \eta n \to 2\gamma n$ and $\pi^- p \to \pi^0 n \to 4\gamma n$, on the walls of the target hydrogen container, on the massive steel flanges and steel supports of the target. To estimate this background, an additional experiment with the empty target was carried out at each momentum of the incident pions, after completion of data taking with the hydrogen-filled target. The processing of the data obtained in such control measurements was performed with the same algorithm as in the experiment with the filled target.

The differential cross sections were determined with the formula

$$\frac{\mathrm{d}\sigma^{\mathrm{cm}}}{\mathrm{d}\Omega} = \frac{N_{\eta\to 2\gamma}}{N_{\pi^-} \cdot A \cdot N_p \cdot 2\pi \cdot \Delta\cos\theta_\eta^{\mathrm{cm}} \cdot BR(\eta \to 2\gamma)}. \qquad (4)$$

Here, $N_{\eta\to 2\gamma}$ is the number of η mesons produced in the reaction $\pi^- p \to \eta n$ and decayed by the channel $\eta \to 2\gamma$ (the background of events being subtracted), which are detected in a given c.m.s. angular interval of the solid angle; N_π- is the number of pions that had crossed the monitoring counter C2 during the experiment (obtained after subtraction of the muon and electron admixtures in the pion beam); N_p is the number of protons in the target per cm^2; A is the value of the acceptance obtained by Monte Carlo simulations for a particular angular interval; $2\pi \cdot \Delta\theta_\eta^{CM}$ is the covered solid angle; $BR(\eta \to 2\gamma) = (39.43 \pm 0.26)$ % is the branching ratio of the decay $\eta \to 2\gamma$. The values of the differential cross sections for the reaction $\pi^- p \to \eta n$ obtained in this experiment at the momenta of incident pions of 700 MeV/*c* (a), 710 MeV/*c* (b), 720 MeV/*c* (c), and 730 MeV/*c* (d) are shown in Fig. 4 by black squares. Only the statistical errors are given. Also shown by open circles are the cross sections measured at the BNL pion channel using the Crystal Ball [3] at the momenta of incident pions 718 MeV/*c* (c) and 735 MeV/*c* (d).

The main source of systematic errors is the uncertainty in calculations of the acceptance caused by not sufficient knowledge of the central momentum of the pion beam. Measurements of this momentum were made by several different methods in [4], and the standard deviation for the momentum distribution was estimated as ± 0.2 % (± 1.5 MeV/*c*). The acceptance values obtained as the result of straggling at the central momentum of 710 MeV/*c* was ± 12 % for $\theta_\eta^{CM} = -0.9$, ± 20 % for $\theta_\eta^{CM} = +0.9$, and ± 5 % for $\theta_\eta^{CM} \approx 0$.

Other sources of systematic errors are:

– inaccuracy in determination of the liquid hydrogen density, ± 0.7 %;

– inaccuracy in measurements of muon and electron admixtures in the beam, ± 1.0 %;

– inaccuracy in geometric parameters of the beam;

– inaccuracy in the alignment of the calorimeters relative to the beam axis, ± 1.0 %.

The differential cross sections obtained at the momenta of the incident pions 700, 710, 720, and 730 MeV/*c* varied in shape very essentially. At 700 MeV/*c*, the cross section was practically isotropic in the c.m.s. This means that the process $\pi^- p \to \eta n$ near the threshold goes preferably through the formation of the $S_{11}(1535)$ resonance with its subsequent decay by the η*N* channel. A contribution of the *P* wave is negligible. At higher momenta the angular dependence becomes anisotropic, but symmetric relative to $\theta_\eta^{CM} = 0$.

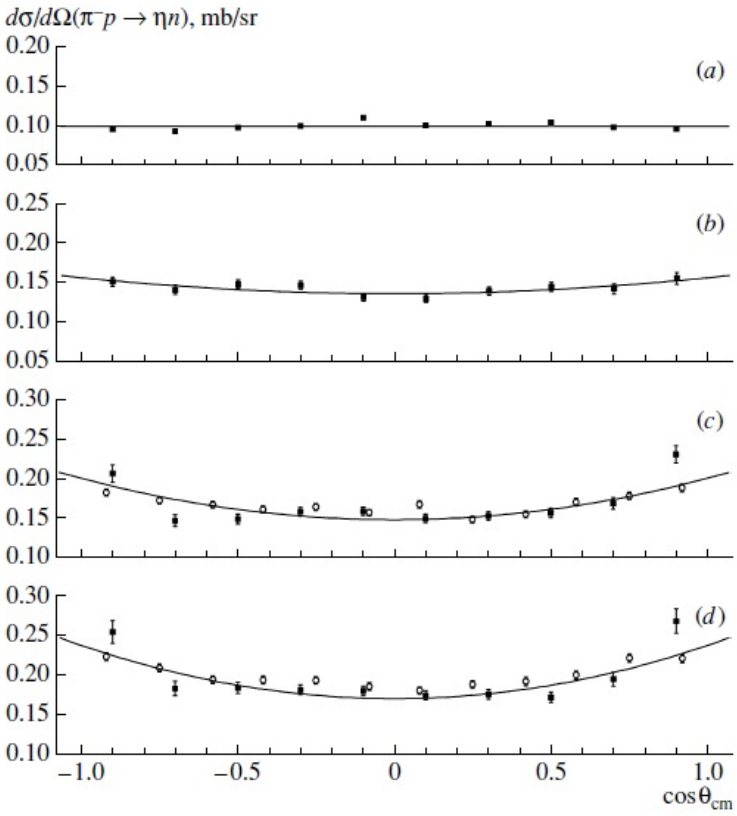

Fig. 4. Differential cross sections for the reaction $\pi^- p \to \eta n$ obtained in this work (black squares) and in the experiment carried out at the BNL using the Crystal Ball (open circles)

Near the threshold, the values of partial amplitudes are proportional to p_η^{CM} (p_η^{CM} is the momentum of η meson in the c.m.s.), so the contributions of the *P*- and *D*-amplitudes are small compared to the *S*-amplitudes. That is why we can use the Legendre polynomial expansion of the differential cross sections for estimation of partial amplitudes:

$$d\sigma / d\Omega = a_0 + a_1 P_1(\cos\,{}_\eta\theta^{CM}) + a_2 P_2(\cos\,{}_\eta\theta^{CM}). \quad (5)$$

The results of fitting of the differential cross sections with Eq. (5) are shown in Fig. 4.

The ratios of coefficients a_1 / a_0 and a_2 / a_0 are presented in Fig. 5 as functions of the momentum of incident pions. The ratio a_1 / a_0 is close to zero, which may be considered as evidence of small contribution of the *P*-wave. At the same time, the ratio a_2 / a_0 grows rapidly from the threshold confirming the existence of a rather large *D*-wave component. Possibly, this effect is due to a contribution of the $D_{13}(1520)$ resonance.

The probability of decay of this resonance by the η*N* channel is very small (0.24 % in the last publication of the Particle Data Group), and the observed effect can be explained by the interference of the $D_{13}(1520)$ resonance and the $S_{11}(1535)$ resonance dominating in the process. To check this hypothesis, the obtained experimental data were fitted with a simple theoretical model for the amplitude of the reaction $\pi^- p \to \eta n$, which contains only the $S_{11}(1535)$ and $D_{13}(1520)$ resonances in the Breit-Wigner form. In this model, the parameters of the $S_{11}(1535)$ resonance were determined, principally, on the base of the total cross sections, since in this case the interference of the *S*- and *D*-waves is absent. The obtained results show that with this fit it is possible to reach good description of the measured experimental data.

The parameters of the resonances determined with the above-mentioned approach are as follows.

For the S_{11} resonance: $\Gamma_\pi = 25$ MeV, $\Gamma_\eta = 61$ MeV, $\Gamma_{tot} = 91$ MeV;

for the D_{13} resonance: $\Gamma_\pi = 60$ MeV, $\Gamma_\eta = 0.08$ MeV, $\Gamma_{tot} = 120$ MeV.

So, the value of $\Gamma_\eta / \Gamma_{tot} = 0.08 / 120 = 0.0007$ (0.07 %) for the D_{13} resonance is good enough for successful description of the experimental data.

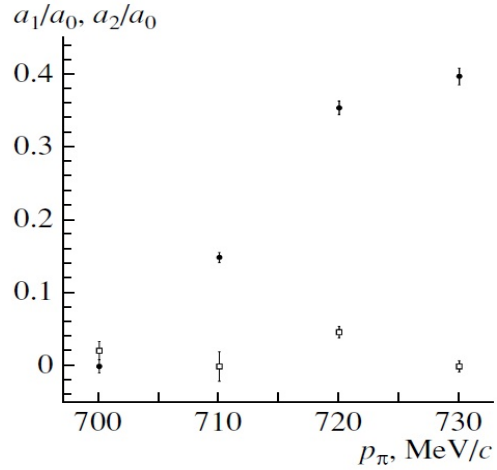

Fig. 5. Ratios of coefficients a_1/a_0 (open points) and a_2/a_0 (solid points) *vs* the momentum of incident pions

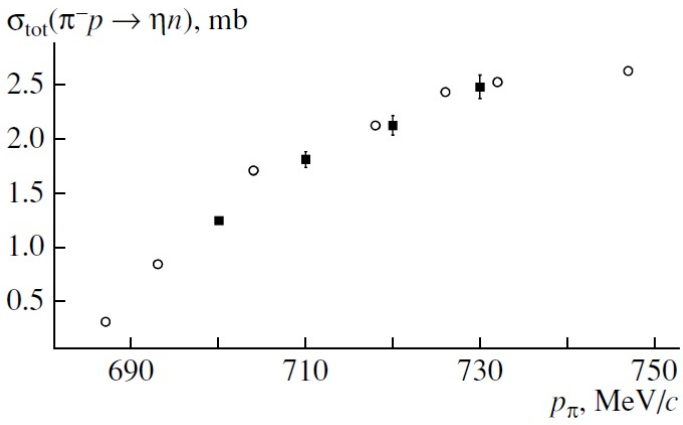

Fig. 6. Dependence of the total cross sections for the reaction $\pi^- p \to \eta n$ on the momentum of incident pions; the black squares are the results of this work, the open circles are the results of the experiment with the Crystal Ball at the BNL

In Fig. 6, the measured total cross sections for the reaction $\pi^- p \to \eta n$ are presented as a function of the incident pion momentum (black squares). For comparison, the data obtained recently in the experiment at the meson channel of the accelerator AGS of the Brookhaven National Laboratory (USA) using the Crystal Ball set-up are also shown (open circles). Evident agreement of these results of the experiments carried out at different accelerators on the experimental set-ups with different values of the angular acceptance may be considered as evidence for reliability of the obtained data.

References

1. D.E. Bayadilov *et al*., in *Proc. of the Workshop on Physics of Excited Nucleons* (Bonn, Germany, 5–8 Sept. 2007), ed. Hans-Verner Hammer, Vera Kleber, U. Thoma and Hartmut, Bonn, 2008, p. 208.
2. D.E. Bayadilov *et al*., Eur. Phys. J. A **35**, 287 (2008).
3 S. Prakhov *et al.,* Phys. Rev. C **72**, 015203 (2005).
4. V.P. Koptev *et al.,* Preprint PNPI-**196**, Leningrad (1975).

STRANGENESS PRODUCTION IN HADRON-INDUCED REACTIONS

S.G. Barsov, A.A. Dzyuba, V.P. Koptev, S.M. Mikirtytchiants, E.N. Shikov, Yu.V. Valdau

The investigation of reactions with a K^+-meson in the final state near the reaction threshold delivers essential information on interactions between strange and non-strange hadrons. Extensive studies of the reactions is in progress at the Cooller Synchrotron COSY-Juelich – a storage ring for a proton or deuteron beam of the varying momentum up to 3.76 GeV/*c*. The ANKE experimental installation built up by the international collaboration between FZ-Juelich, PNPI and JINR is successfully exploited for such measurements.

ANKE is a magnetic spectrometer placed at an internal target position of COSY (Fig. 1) [1]. It is equipped with a detection system, which consists of scintillator counters and multiwire chambers for registration of positive and negative charged particles. It allows detection of $\pi^{\pm}$, $K^{\pm}$, *p*, *d*, *t* and ^{3,4}He in the momentum range 200–2500 MeV/*c* with the resolution about 1.5 % (FWHM). The missing-mass resolution is better than 10 MeV/c^2 (FWHM), and the resolution for the K^+K^- invariant-mass spectrum is about 3 MeV/c^2. A special structure of the detection system for positive charged ejectiles (Pd in Fig. 1) provides reliable K^+-meson identification using the so-called delayed-veto signal technique.

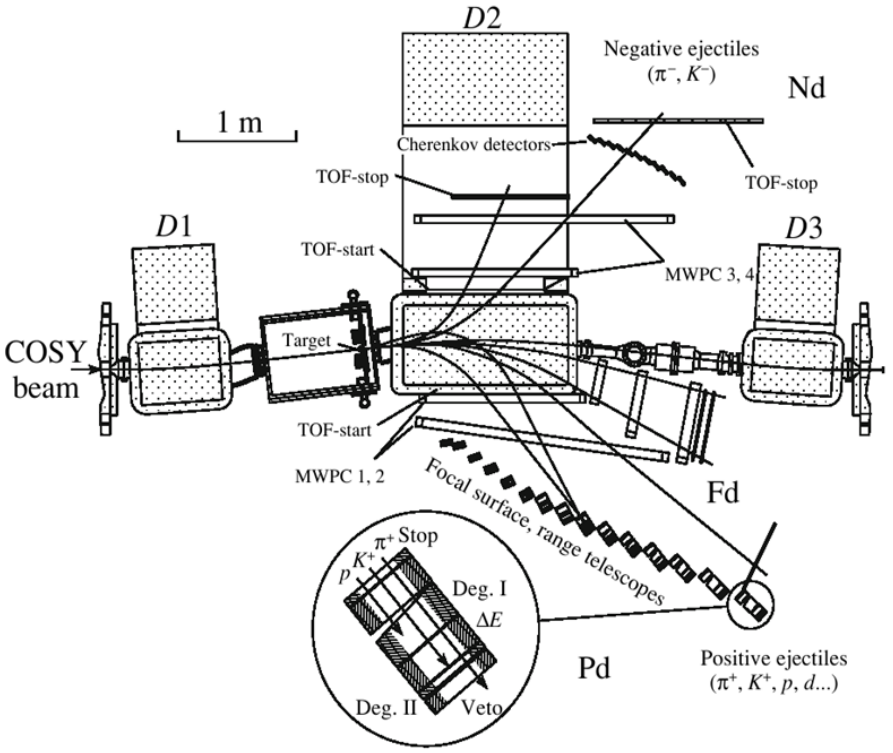

Fig. 1. Spectrometer ANKE

The main activities of the PNPI group in the ANKE Collaboration in 2008–2012 concerned:

- investigations of the $K\overline{K}$ -pair production in *pp*-, *pn*- and *dd*-interactions [2–7];
- measurements of the ϕ-meson properties in the nuclear matter [8];
- studies of the $pN \rightarrow NKY(\pi)$ reactions, where *Y* is (Λ, Σ) [9–12].

1. Kaon-pair production

The investigation of the kaon-antikaon pair production was the main goal to clarify the situation in the scalar meson sector ($J^P = 0^+$), where more states have been observed than needed for the scalar nonet. This

situation initiated a debate about the nature of the $a_0/f_0(980)$ resonances, which both have masses around two masses of the *K*-meson and can decay to $K\overline{K}$. Besides a quark-antiquark state, the $K\overline{K}$ molecule, as well as the tetraquark state, were discussed. A possible observation of the a_0/f_0-mixing violating isospin conservation is very interesting because this symmetry plays an important role in QCD, and such measurements can provide a new observable, which should be sensitive to the structure of light scalar mesons. Indeed, $K\overline{K}$ pairs can be produced in different isospin states. Due to selection rules, the *s*-wave kaon-pair produced in the reaction $pp \to dK^+\overline{K}^0$ is in the $I = 1$ state, while the pair resulting from the $pn \to dK^+K^-$ or $pp \to ppK^+K^-$ reactions may be in both the $I = 0$ and $I = 1$ states, and the one from $dd \to {}^4\mathrm{He}K^+K^-$ is in the $I = 0$ state.

However, kaon pairs can be also formed in the reaction $pN \to NKY^*$, where the excited hyperon decays *via* $Y^* \to N\overline{K}$. A final-state interaction between the proton and neutron can then lead to formation of a deuteron. There are, of course, several excited hyperons that could contribute to such a process, but Λ(1405) and Σ(1385) are of particular interest at low energies. Although the central values of their masses are below the $N\overline{K}$ threshold, their widths extend well above, and these hyperons can certainly influence the spectra through the $N\overline{K}$ final state interaction (FSI).

The differential and total cross sections for kaon pair production in the $pp \to ppK^+K^-$ reaction were measured at three beam energies 2650, 2700, and 2830 MeV, which correspond to 51, 67, and 108 MeV excess energies, respectively [2]. This reaction was identified by direct detection of both charged kaons and one of the two protons, selecting the second proton from the missing-mass spectrum. The near threshold data were decomposed into parts arising from the decay of a $\phi(1020)$ meson and a non-resonant background (see Fig. 2).

In those ranges of the K^+K^- invariant-mass spectra where the ϕ meson production is small, a difference between the K^-p and K^+p interactions has been found. The ratio

$$R_{Kp} = [\mathrm{d}\sigma / \mathrm{d}M(K^-p)] / [\mathrm{d}\sigma / \mathrm{d}M(K^+p)] \tag{1}$$

was strongly peaked close to the *Kp* threshold in both the COSY-11 [13] and in our data [2] (Fig. 3). This clearly indicates that the $pp \to ppK^+K^-$ reaction cannot be dominated by an undistorted production of the a_0 (or f_0) resonance. It has been shown that these data can be explained by introduction of a simple ppK^- interaction model based on the assumption that the overall enhancement factor is the product of enhancements in *pp* and two K^-p systems, all evaluated at the appropriate relative momenta *q*:

$$F = F_{pp}(q_{pp}) \cdot F_{Kp}(q_{Kp1}) \cdot F_{kp}(q_{Kp2}). \tag{2}$$

A similar approach was also proposed for description of the *pp*η final state at low energies [14]. The K^-p enhancement factor was taken in the scattering length approximation

$$F_{kp}(q) = (1 - \mathrm{i}qa)^{-1}. \tag{3}$$

The *pp* enhancement factor is very well known. Using this factor, the effective K^-p scattering length was found ($|a| \approx 1.5$ fm). However, the presented data are primarily sensitive to the module of *a* rather than to its phase, and do not establish the relative strengths for production of the isospin $I = 0$ and $I = 1$ states of K^-p pairs. On the other hand, the proposed model gives a very good description of the differential distributions, as well as the energy dependence of the total cross section in the full measured range of the excess energy.

Besides the K^-pp FSI, the shape of the K^+K^- spectrum at low invariant masses also indicates the importance of the $K\overline{K}$ FSI. It was shown in Ref. [3] that these data can be understood in terms of elastic K^+K^- rescattering plus a contribution coming from the production of neutral kaon-antikaon pair followed by a charge-exchange rescattering. Although the data were not sufficient to establish the size of the cusp at the $K^0\overline{K}^0$ threshold, the low mass behaviour suggests that the isospin-zero production is dominant.

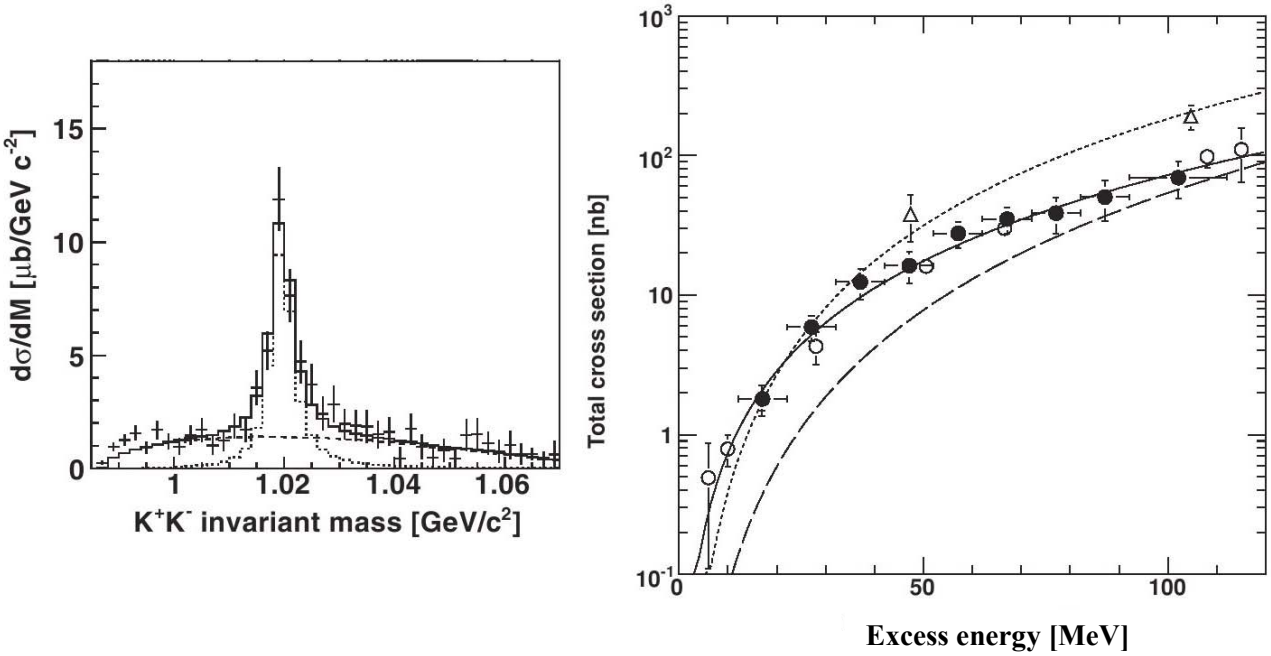

Fig. 2. Left: Differential cross section for the $pp \to ppK^+K^-$ reaction with respect to the K^+K^- invariant-mass at 2830 MeV. The dotted histogram and the dashed curve represent simulations for the ϕ and non-ϕ contributions to the spectrum, with their sum being shown by the solid histogram. **Right:** Total cross section for non-ϕ kaon-pair production in nucleon-nucleon collisions near threshold. The closed circles denote the $pn \to dK^+K^-$ data, and the solid curve shows its energy dependence. Open triangles demonstrate the $pp \to dK^+K^0$ data, and the dotted curve represents its best description. Open triangles show the results for $pp \to ppK^+K^-$. The dashed curve represents the prediction for the $pn \to \{pn\}_{I=0}K^+K^-$ total cross section

The $pp \to dK^+\bar{K}^0$ reaction was investigated at two proton beam kinetic energies, $T_p = 2650$ MeV and 2830 MeV, corresponding to the excess energies of 47.4 MeV and 104.7 MeV, respectively. In both cases, the K^+-meson and the deuteron were observed directly, and $\bar{K}^0$ was identified by a missing-mass technique. The total cross section, angular and invariant-mass distributions were obtained. An interpretation of this kaon-pair production is presented in Ref. [4].

Since the data were taken quite close to the reaction threshold, the analysis was performed in terms of the lowest allowed partial waves. The application of the angular momentum and parity conservation together with the Pauli principle in the initial state shows that all the final particles cannot be in relative *s*-states. Therefore, the permitted final states are *Sp* and *Ps*, where the first letter denotes the orbital angular momentum between two chosen particles and the second label is for the pair orbital momentum relative to the third particle. An interaction in the final state, such as influence of a broad resonance like $a_0^+(980)$ or the $d\bar{K}$ FSI, should distort the corresponding *s*-wave part of the amplitude.

The obtained data clearly demonstrate that both the $K^+\bar{K}^0$ and the $\bar{K}^0 d$ systems are dominantly in the *s*-wave, while the *p*-wave dominates the K^+d channel. A big difference between the kaon and antikaon interactions with deuterons is most clearly seen in the ratio of the differential cross sections in terms of the *Kd* invariant mass:

$$R_{Kd} = [d\sigma / dM(K^0 d)] / [d\sigma / dM(K^+ d)]. \quad (4)$$

This ratio seems to depend primarily on the $d\bar{K}$ interaction, which is described by the scattering length approximation with $a = (-1.0 + i1.2)$ fm. The rapid variation of R_{Kd} observed there is similar to that found in the K^-pp / K^+pp ratio, as described above for the $pp \to ppK^+K^-$ reaction (Fig. 3).

The effect of the $a_0^+(980)$ scalar resonance is more subtle, though its influence is strongly indicated by the fact that the kaon-antikaon pair is almost entirely in the *s*-wave. The shapes of the differential

distributions are very slightly changed from those obtained with the constant parameter solution, provided that both the $K^+\bar{K}^0$ and $\bar{K}^0 d$ FSIs are taken into account. The two FSIs taken together enhance the ratio of the total cross sections σ(47.4 MeV) / σ(104.7 MeV) and lead to better description of the data.

The energy dependence of the K^+K^- production on a neutron target was studied with the $pd \to p_{sp}dK^+K^-$ reaction [5]. By identifying the final deuteron and the kaon pair and measuring their momenta, it was possible to reconstruct the momentum of the recoiled proton p_{sp}. The momentum distribution of the p_{sp} was found to be consistent with that predicted using the Bonn potential. Assuming the proton to be a "spectator" particle, the quasi-free $pn \to dK^+K^-$ cross section was extracted. Despite the experiment was carried out at one fixed beam energy, the intrinsic movement of the target neutron enabled extraction of the data over the wide range of the excess energy $\varepsilon = s^{1/2} - m_d - 2m_K$ on event-by-event basis. The excess energy is typically determined with the uncertainty of 2 MeV, which is small compared to the 10 MeV bin used in the subsequent data analysis. The shape of the K^+K^- invariant-mass distribution was used to separate the ϕ component from the non-ϕ one. The non-ϕ contribution to the total rate was much smaller than that in the case of $pp \to ppK^+K^-$ reaction.

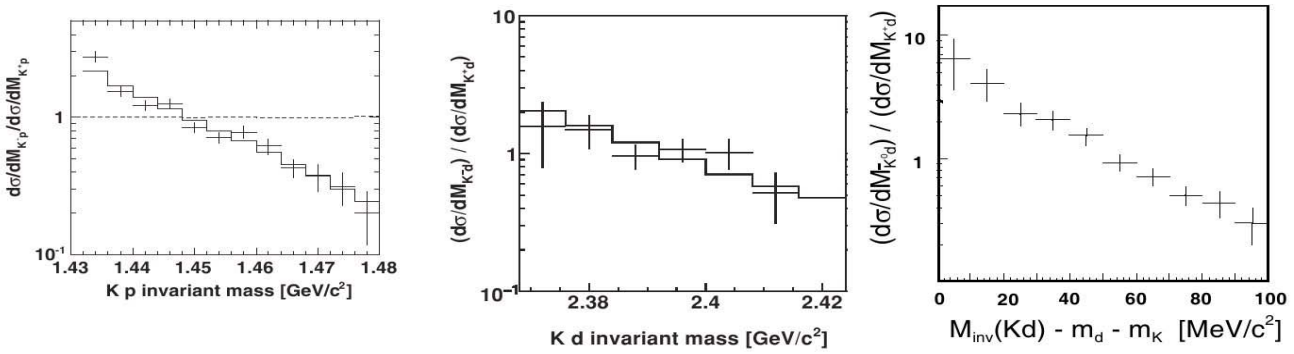

Fig. 3. Left: Ratio of the differential cross sections for the $pp \to ppK^+K^-$ reaction (1) *vs.* the *Kp* invariant-mass at 2650 MeV. The dotted histogram represents results of four-body phase-space simulations, where only the distortion by the *pp* FSI is accounted for. The solid histogram includes also the K^-p FSI described by Eq. (2). **Central:** Ratio of the differential cross sections for the $pn \to dK^+K^-$ reaction, Eq. (4). The solid histogram represents results of three-body phase-space simulations with the K^-d FSI included. **Right:** Ratio of the differential cross sections for the $pp \to dK^+K^0$ reaction, Eq. (4)

The total cross section for the $pd \to p_{sp}dK^+K^-$ reaction and the invariant-mass distributions were measured over a wide range of the excess energy between 20 and 100 MeV. The experimental distribution of the ratio similar to (4) demonstrates the presence of the K^-d FSI (Fig. 3, central panel), which can be described using the scattering length approximation (3) with the same parameter a as in the reaction $pp \to dK^+\bar{K}^0$.

2. The width of the ϕ-meson in the nuclear matter

Modifications of hadron properties inside the strongly interacting medium was extensively studied in connection with the subject of partial restoration of chiral symmetry in the hot or (and) dense nuclear matter. Due to its narrow width of 4.3 MeV/c^2, a small change in the $\phi(1020)$ meson properties is expected to be experimentally observable. The hadronic model suggests an increase of the width of the low-momentum ϕ-meson in the cold nuclear matter at the nuclear saturation density up to a factor of ten, as compared to the free ϕ-meson value (see reviews in Refs. [15, 16]).

Our measurements were carried out at the ANKE spectrometer, where a ϕ meson can be registered *via* its K^+K^- decay. The main goal of these experiments was to obtain the value of the so-called transparency ratio:

$$R = (12\ \sigma(p\mathrm{A} \to \phi X)) / (A\ \sigma(p\mathrm{C} \to \phi X)), \qquad (5)$$

where $\sigma(p\mathrm{A} \to \phi X)$ and $\sigma(p\mathrm{C} \to \phi X)$ are the inclusive cross sections for ϕ-meson production in *p*A and *p*C collisions, respectively, A being the atomic number of the nucleus A.

The experiment was performed with C, Cu, Ag and Au targets at the $T_p = 2830$ MeV beam kinetic energy, which roughly corresponds to the 100 MeV excess energy for elementary $pN \to \phi X$ reactions. A signal from the ϕ meson was identified as a clear peak in the K^+K^- invariant-mass spectra. The transparency ratio was determined for the cross sections within the acceptance of the ANKE spectrometer: $600 < p_\phi < 1600$ MeV/c and $\vartheta_\phi < 8°$. The relative luminosity for normalization at each target was derived by simultaneous detection of π^+ count rate in the 500 ± 25 MeV/c momentum range at $\vartheta_\pi < 8°$.

The A-dependence of the transparency ratio is well fitted with the power function $A^{0.56 \pm 0.03}$. The interpretation of this result has to rely on a detailed theoretical treatment, so the values of the ϕ meson width in the nuclear matter were obtained using two available models ([17] and [18]). The obtained result suggests a substantial increase of the total ϕ width in the nuclear environment by about an order of magnitude, as compared with its free value.

3. Reactions with Λ- or Σ-hyperon production

Other channels of K^+ production at intermediate energies are reactions of the type $pN \to NKY$, where Y stands for the Λ or Σ hyperon. However, the information on the $pp \to nK^+\Sigma^+$ reaction is very inconsistent. A model-independent estimation of the Σ^+ to Σ^0 production cross section ratio might be obtained from the isospin relation, linking different Σ production channels. The amplitudes f for Σ production satisfy the equation:

$$f(pp \to nK^+\Sigma^+) + f(pp \to pK^0\Sigma^-) + 2f(pp \to pK^+\Sigma^0) = 0. \quad (6)$$

This leads to the so-called triangle inequality between the total cross sections. But recent experiments [19] in the close-to-threshold regime have given a surprisingly high total cross section for the $pp \to nK^+\Sigma^+$ process, breaking Eq. (6).

In order to obtain the value of the $pp \to nK^+\Sigma^+$ reaction cross section, measurements were performed at five beam kinetic energies: 1775 MeV (below the threshold of Σ^+ production), 1826, 1920, 1958, and 2020 MeV [9]. The information on Σ^+ production was obtained in four different ways of the data analysis:

1. Evaluation of the momentum dependence of the ratio of the double differential cross sections $d^2\sigma / (dp d\Omega)$ for K^+ production at beam energies above and below the $pp \to nK^+\Sigma^+$ threshold. A significant value of $R(\Sigma^+/\Sigma^0)$ should produce a bump in this spectrum, because almost all K^+ mesons produced together with Σ hyperons at this beam energy are within the ANKE acceptance. However, the experimental data suggest that $\sigma(\Sigma^+) \approx \sigma(\Sigma^0)$ at $T_p = 1826$ MeV.

2. An analysis of inclusive K^+ production was performed in the framework of the model which includes phase-space dependence of the $pp \to pK^+\Lambda$ production cross section (corrected for the $p\Lambda$ final state interaction and for the presence of the $N^*(1650)$ resonance) and the pure three-body phase-space dependence of the $pp \to pK^+\Sigma^0$ reaction. The analysis does not demonstrate any abnormally high contribution from the $pp \to nK^+\Sigma^+$ reaction. This method puts a conservative upper limit on the total cross section.

3. The values of the total cross section for the $pp \to nK^+\Sigma^+$ reaction were obtained from decomposition of the K^+p invariant-mass spectrum using the model described above and a Monte-Carlo simulation.

4. The most reliable values of $\sigma_{tot}(pp \to nK^+\Sigma^+)$ were obtained by detection of $K^+\pi^+$ correlations. Such a coincidence arising from the hyperon decay $\Sigma^+ \to n\pi^+$ is a unique signature of the $pp \to nK^+\Sigma^+$ reaction. The background from the channel $nK^+\Lambda\pi^+$ remains negligible at 2020 MeV because of a very small phase space. At the higher energy of 2880 MeV, it comprises only 4 % of the Σ^+ production cross section.

The measured total cross sections can be reasonably described by the three-body phase-space dependence (see Fig. 4). In parallel, the total cross sections for the $pp \to pK^+\Lambda$ and $pp \to pK^+\Sigma^0$ reactions were obtained at several excess energies.

It should be also mentioned that after the ANKE publication [9], the HIRES collaboration presented its result on $R(\Sigma^+/\Sigma^0) \approx 5 \pm 1$ [20]. However, as it has been shown in Ref. [10], this result is in conflict with the experimental data on the exclusive $pp \to pK^+\Lambda$ reaction.

The crucial constituents for any theoretical interpretation of kaon production in pA- and AA-interactions must be the cross sections for strangeness production in pp and pn reactions. In contrast to the case of pp

interaction, very little is known experimentally about K^+ production on neutrons. Since the proton-neutron bond in the deuteron is weak, the simplest way to determine the $\sigma^{K^+}(pn)/\sigma^{K^+}(pp)$ ratio is the comparison of the K^+ production cross sections in *pp*- and *pd*-interactions. Such measurements were performed at four beam kinetic energies: 1826, 1920, 2020, and 2650 MeV, using the ANKE spectrometer in the 200–600 MeV/*c* momentum range at $\vartheta < 4°$ [11].

In order to describe the momentum spectra of K^+ mesons, a model has been developed, which includes production mechanisms, as well as the Fermi-motion of nucleons in the deuteron. At these beam energies, K^+ mesons are produced only in association with Λ, Σ^0 and Σ^+ hyperons. A contribution from Λ was described by three-body phase-space modified by the $p\Lambda$ final state interaction and the $N^*(1650)$ resonance. For Σ channels, simple phase-space was used. In the framework of the developed model, the shape of the $\sigma^{K^+}(pd)4/\sigma^{K^+}(pp)$ ratio was predicted.

The obtained results clearly indicate that the inclusive K^+ production on neutrons is smaller than that on protons at the four investigated energies. Reasonable agreement between the data and the proposed model can be obtained if the ratio of the total cross sections for proton and deuteron targets has the value of $\sigma^{K^+}(pd)/4\sigma^{K^+}(pp) = 1.4 \pm 0.2$ (see Fig. 4). After taking the Glauber shadowing into account, it means that this ratio for K^+ production in *pp* and *pn* collisions is equal to

$$\sigma^{K^+}(pn) / \sigma^{K^+}(pp) = 0.5 \pm 0.2.$$

However, such a difference could happen due to an unobserved contribution of K^0 production in *pn* collisions.

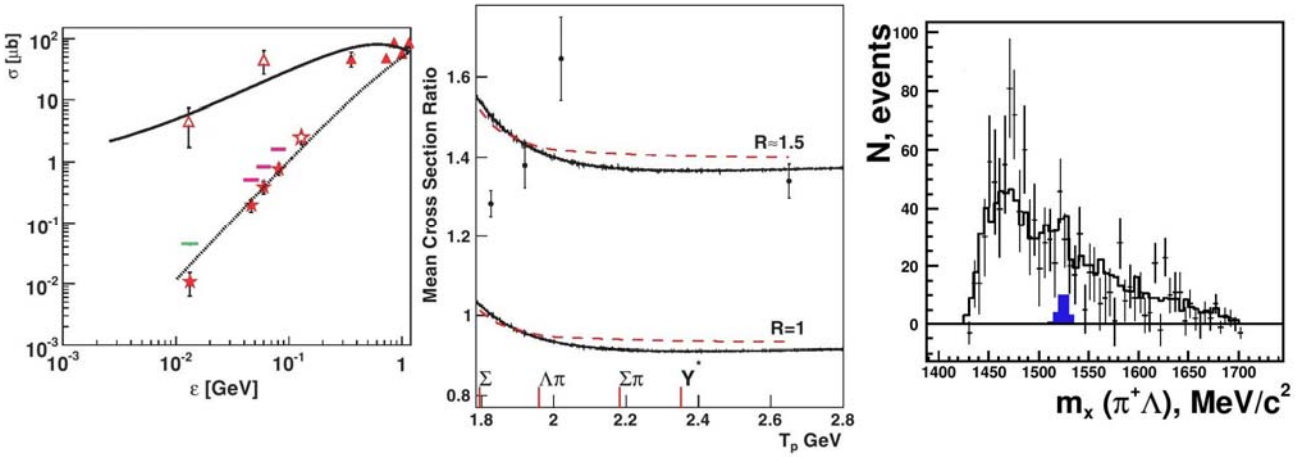

Fig. 4. Left panel: Total cross section for the $pp \to nK^+\Sigma^+$ reaction. Stars represent the ANKE data (the conservative upper limits are shown by four short horizontal lines), and open triangles are the data from Ref. [19]. The dotted line represents the pure three-body phase space simulation, and the solid line represents a parametrization that includes strong $n\Sigma^+$ FSI and an energy-dependent matrix element [21]. **Central panel:** Ratio of the K^+ production cross section on deuterium and hydrogen, averaged over the ANKE acceptance for kaons (see text). Black solid lines represent the ratio of the Fermi-smeared $pp \to K^+p\Lambda$ and $pp \to K^+N\Sigma$ total cross sections to the free hydrogen ones. The ratio is multiplied by the indicated factor *R*. Red dashed lines depict the same ratio, but evaluated from the differential spectra. **Right panel:** Invariant-mass spectrum of the $\pi^+\Lambda$ system in the reaction $pp \to pK^0\pi^+\Lambda$. The solid line denotes the sum of all contributions. The blue region corresponds to the maximum permissible $\Theta^+(1540)$ signal.

The *KN* systems can be also investigated in the hyperon production. They are especially interesting due to a possibility of coupling to the pentaquark baryon $\Theta^+(1540)$, the existence of which was proposed by D. Diakonov, V. Petrov and M. Polyakov [22]. In order to determine the strength of such coupling, the cross section for the reaction $pp \to pK^0\pi^+\Lambda$ was measured at the 3650 MeV/*c* beam momentum [12]. The reaction was identified by observation of four particles (π^+ and π^- mesons and two protons), with subsequent selection of Λ-hyperons in the π^-p invariant-mass spectrum and K^0-mesons in the spectrum of the missing-mass of the $\pi^+\pi^-pp$ system. A physical background remaining in the π^-p invariant-mass distribution after a cut on the K^0-mass range was smooth, and its contribution to the Λ-peak was determined by an interpolation procedure. In addition, the events populating π^-p invariant-mass ranges neighboring to the Λ-peak were used to

reproduce the most probable shape of the background in the $\pi^+\Lambda$ invariant-mass distribution. Figure 4 (right panel) represents the final $\pi^+\Lambda$ invariant-mass spectrum obtained after subtraction of such a background.

Since the acceptances of the four-body phase space production and of the production with an intermediate $\Delta^{++}(1232)$ resonance are very similar, the total cross section for the $pK^0\pi^+\Lambda$ final state was considered to be independent of the decomposition into separate channels. It was deduced as

$$\sigma_{tot} = 1.41 \pm 0.05_{stat} \pm 0.21_{syst}\ \mu b.$$

The $\pi^+\Lambda$ invariant-mass distribution can be described by non-resonant and $\Delta^{++}(1232)$-channels (see Fig. 4). Taking into account the estimated maximum number of 44 events for $\Theta^+(1540)$, an upper limit of 58 nb (at 95% CL) was evaluated for the $pp \rightarrow \Theta^+\pi^+\Lambda$ cross section at $p_{beam} = 3650$ MeV/c.

References

1. S. Barsov *et al*., NIM A **462**, 364 (2001).
2. Y. Maeda *et al.*, Phys. Rev. C **77**, 015204 (2008).
3. A. Dzyuba *et al*., Phys. Lett. B **668**, 315 (2008).
4. A. Dzyuba *et al*., Eur. Phys. J. A **38**, 1 (2008).
5. Y. Maeda *et al.*, Phys. Rev. C **79**, 018201 (2009).
6. X. Yuan, A. Dzyuba, M. Büscher, Chin. Phys. C **33**, 20 (2009).
7. X. Yuan *et al.*, Eur. Phys. J. A **42**, 1 (2009).
8. A. Polyanskiy *et al.*, Phys. Lett. B **696**, 23 (2011).
9. Yu. Valdau *et al*., Phys. Rev. C **81**, 045208 (2010).
10. Yu. Valdau, C. Wilkin *et al*., Phys. Lett. B **696**, 23 (2011).
11. Yu. Valdau *et al*., Phys. Rev. C **84**, 055207 (2011).
12. M. Nekipelov *et al.*, J. Phys. G **34**, 627 (2007).
13. P. Winter *et al*., Phys. Lett. B **635**, 23 (2006).
14. V. Bernard *et al.*, Eur. Phys. J. A **4**, 259 (1998).
15. R. Hayano *et al.*, Rev. Mod. Phys. **82**, 2949 (2010).
16. S. Leupold, V. Metag, U. Mosel, IJMPE **19**, 147 (2010).
17. V.K. Magas *et al.*, Phys. Rev. C **71**, 065202 (2005).
18. E.Ya. Paryev, J. Phys. G: Nucl. Part. Phys. **36**, 015103 (2009).
19. T. Rozek *et al.*, Phys. Lett. B **643**, 251 (2006).
20. A. Budzanowski *et al.*, Phys. Lett. B **692**, 10 (2010).
21. Cao Xu *et al.,* Chinese Phys. Lett. **25**, 888 (2008).
22. D. Diakonov *et al.*, Z. Phys. A **359**, 305 (1997).

STUDY OF PROTON-PROTON COLLISIONS AT THE BEAM MOMENTUM OF 1628 MeV/*c*

K.N. Ermakov, V.I. Medvedev, V.A. Nikonov, O.V. Rogachevsky, A.V. Sarantsev, V.V. Sarantsev, and S.G. Sherman

1. Introduction

The Nucleon-Nucleon (*NN*) interaction is one of the most important processes in nuclear and particle physics that has been extensively studied over a wide energy range. In its turn, the single pion production in *NN* interactions is the main inelastic process at the energies below 1 GeV. Our understanding of the nucleon-nucleon interaction cannot be based on the description of elastic reactions only: any relevant model should also explain inelastic reactions. In this respect, there is an important question of the pion production mechanism: what fraction of the cross section is determined by production of the $\Delta_{33}(1232)$ isobar and what fraction is due to non-resonant transitions. Another important question is the issue of the isoscalar ($I = 0$) channel contribution to inelastic neutron-proton collisions. A detailed investigation of the single pion production in *pp* collisions provides the most accurate information on the isovector channel. When included in the analysis of the neutron-proton data, this information will allow us to correctly extract the contribution of the isoscalar channels.

Various theoretical models, more or less successful, were put forward while the data on the pion production in *NN* collisions were accumulated. For the energy range of up to about 1 GeV, there was proposed the One-Pion Exchange (OPE) model [1–3] assuming the dominance of the one-pion exchange contribution to the inelastic amplitude. In this approach, pole diagram matrix elements are calculated using a certain form factor obtained by fitting to the experimental data. Thus, the OPE model is a semi-phenomenological approach. In addition, only the P_{33} partial wave is taken into account in the intermediate πN-channel [2]. Nevertheless, this model predicts with reasonable accuracy (up to normalization factors) the differential spectra of the $pp \to pn\pi^+$ and $pp \to pp\pi^0$ reactions in the 600–1300 MeV energy range [4, 5]. At the same time, the discrepancies between the measured total cross sections for these reactions and the model predictions are rather sizeable (see Ref. [5]).

It should be noted that the experimental data on the differential spectra of pion production reactions around 1 GeV are rather scarce. In this contribution, we present results of our investigation of the $pp \to pn\pi^+$ and $pp \to pp\pi^0$ reactions at 1628 MeV/*c* and determine the contributions of various partial waves to the process of single pion production.

2. Experiment

The experiment was performed at the PNPI 1 GeV synchrocyclotron. The events were registered by a 35 cm hydrogen bubble chamber placed in the 1.48 T magnetic field. A proton beam (after the corresponding degrader for the momentum of 1628 MeV/*c*) was formed by three bending magnets and by eight quadrupole lenses. The value of the mean incident proton momentum was checked by the kinematics of elastic scattering events. The accuracy of this value and the momentum spread were about 0.5 MeV/*c* and 20 MeV/*c* (FWHM), respectively. The admixture of other particles in the proton beam was measured by the time-of-flight technique and proved to be negligible (less than 0.1 %). A total of 4.6×10^5 stereoframes was obtained. The frames were scanned twice to search for the events due to interaction of the incident beam. The efficiency of double scanning was determined to be 99.95 %. Approximately 8×10^3 two-prong events were used in the subsequent analysis.

The 2-prong events selected in the fiducial volume of the chamber were measured and geometrically reconstructed. The reconstructed events were kinematically fitted to the following reaction hypotheses:

$$p + p \to p + p, \quad (1)$$
$$p + p \to p + n + \pi^+, \quad (2)$$
$$p + p \to p + p + \pi^0, \quad (3)$$
$$p + p \to d + \pi^+, \quad (4)$$
$$p + p \to p + \pi^+ + \pi^0. \quad (5)$$

The identification of the events was performed using the χ^2 criteria with the confidence level of more than 1 %. If an event had a good χ^2 for the elastic kinematics (4C-fit), it was considered as elastic one. The pull, or stretch, functions for the three kinematic variables of a track (the inverse of the momentum, the azimuthal and dip angles) were examined for elastic scattering events to make sure that their errors, as well as the error of the bubble chamber magnetic field, were properly given. If there was only one acceptable fit for an event, it was identified as belonging to this hypothesis (with a check on the tracks of the stopping π^+-mesons in the presence of the $\pi^+ \rightarrow \mu^+ \rightarrow e^+$ decay). If several inelastic versions revealed a good χ^2 value, we used the visual estimation of the bubble density of the track to distinguish between a proton (deuteron) and a pion. For few events, even after repeated measurements, the fit revealed only one acceptable hypothesis, but with large χ^2. If such an event had the χ^2 less than 50 for the 4-constraint fit or less than 20 for the 1-constraint fit, it was taken into account in the calculation of the cross section value of the process corresponding to this hypothesis but was not included in the differential spectra.

There were events that failed to fit any hypothesis. These no-fit events were investigated on the scanning table and most of them appeared to be the events with a secondary track undergoing one more scattering near the primary vertex.

There were also events unfit for the measurements, *e.g.*, the events with a bad vertex or superimposed tracks. The number of such events was counted to be approximately 7 %. The total number of 2-prong events that had not passed the measurement and fitting procedures was counted to be less than 10 %. These unidentified events were apportioned to the fraction of the fitted hypotheses for the total cross section measurements.

The standard bubble chamber procedure was used to obtain absolute cross sections [5] for the elastic and single pion production reactions. These values – together with the statistics of the events selected by the fit – are listed in Table 1.

Table 1

Number of events and the values of the corresponding cross sections at the beam momentum of 1628 MeV/*c*

$pp \rightarrow$	number of events	σ, mb
elastic	3442	21.2 ± 0.7
$pn\pi^+$	3014	17.6 ± 0.6
$pp\pi^0$	696	4.48 ± 0.20
$d\pi^+$	80	0.47 ± 0.05
$d\pi^+\pi^0$	5	0.029 ± 0.013

3. Elastic scattering: experimental results and discussion

The measured differential cross section for elastic *pp* scattering in the centre-of-mass system (c.m.s.) of the reaction is shown in Fig. 1. The value of the total elastic cross section given in Table 1 was calculated as $4\pi A_0$, where A_0 is the coefficient in front of the $P_0(z)$ Legendre polynomial in our fit of the angular distribution using the Legendre expansion over the $-0.95 \leq \cos\theta \leq 0.95$ angular range. This range was chosen in order to take into account a loss of the events due to forward elastic scattering, when a slow proton had a short recoil path and could not be seen in the bubble chamber (at the momentum less than 80 MeV/*c*) or was missed during the scanning. This interval was determined by examining the stability of the Legendre coefficients with decreasing the fitted range of the angular distribution. Our value of the total elastic cross section obtained this way is smaller than that given in Ref. [6] by approximately 13 %. This discrepancy could arise due to i) insufficient control of the loss of the events with small scattering angles or ii) incorrect calculation of the millibarn-equivalent in the chamber. To control the loss of events in the forward angle scattering, we use a reduced range ($-0.95 \leq \cos\theta \leq 0.95$) for fitting the differential cross section by the Legendre expansion, which could repair this shortcoming. We found that already a sum of first three even polynomials provides an excellent fit to the data. Of course, it is possible that we miss a contribution of

higher order polynomials which cannot be determined from the fitted angular region. In this case, our value of the elastic cross section given in Table 1 should be taken as a simple estimate of this magnitude.

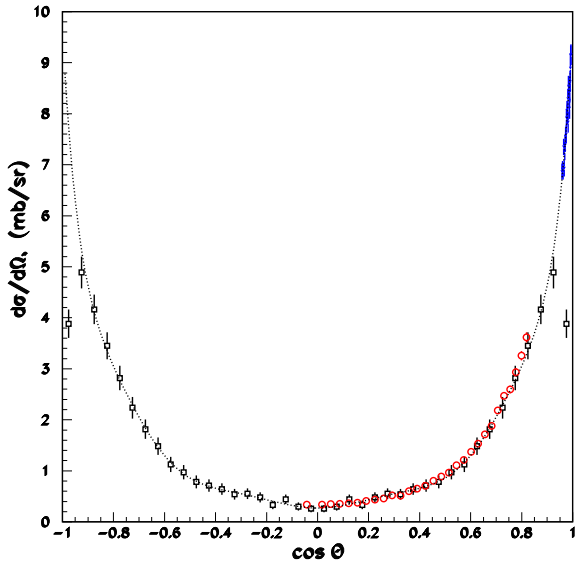

Fig. 1. Elastic differential cross section. The dotted curve is the result of the Legendre polynomial fit over the $-0.95 \leq \cos\theta \leq 0.95$ angular range of our data (open squares) and the data of Ref. [7] (blue triangles). The open red circles show the measurements of the EDDA experiment [8]

In order to take into account the contributions of higher order polynomials, we included in our fit the data of Ref. [7] taken at small forward angles at the energy of 942 MeV. As a result, we obtain 22.7 ± 0.7 mb for the elastic cross section, which is still lower than the value given in Ref. [6] by approximately 7 %.

In Fig. 1, we compare our elastic differential cross section with the data of the EDDA experiment [8] taken at the incident momentum of 1639 MeV/*c*. One can see that there is excellent agreement between our points and the EDDA data, which supports the correctness of our definition of the millibarn-equivalent.

4. Single pion production reactions: comparison with the OPE model

The OPE model [1–4] describes the single pion production reactions by four pole diagrams with π^0 or π^+ exchanges. The main evidence for the pole diagram contributions would be the observation of a peak in the distribution over the momentum transfer from the target particle to the secondary proton in the $pp \to pp\pi^0$ process or, for example, to the secondary neutron in the $pp \to pn\pi^+$ process.

Figures 2 and 3 show the distributions over the momentum transfer squared, $\Delta^2 = -(p_t - p_f)^2$, where p_t is the four-momentum of the target proton and p_f is the four-momentum of the final neutron in $pp \to pn\pi^+$ or of the final protons (two entries) in $pp \to pp\pi^0$, correspondingly. The OPE model calculations normalized to the total number of the experimental events are shown by the dashed lines; the phase space distribution – by the dotted lines. One can see in the figures that the OPE model describes qualitatively well the Δ^2 distribution for both the studied reactions. This is remarkable because only the P_{33} wave is taken into account in the intermediate πN scattering. It could be that the distributions in Figs. 2 and 3 are mainly sensitive to the pole diagram propagator and that a more complicated structure of the amplitude manifests itself in other distributions.

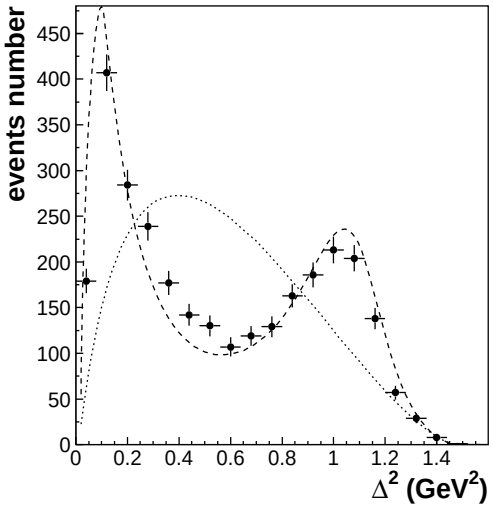

Fig. 2. Four-momentum transfer Δ^2 distribution for the $pp \to pn\pi^+$ reaction. The dashed curve is the OPE calculation, and the dotted one shows the phase space

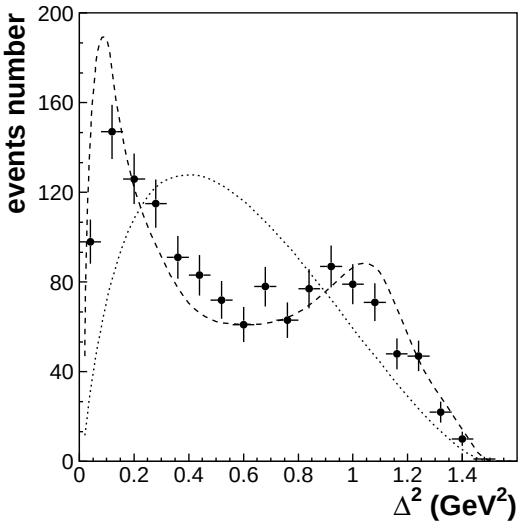

Fig. 3. Four-momentum transfer Δ^2 distribution for the $pp \to pp\pi^0$ reaction. The meaning of the curves is the same as in Fig. 2

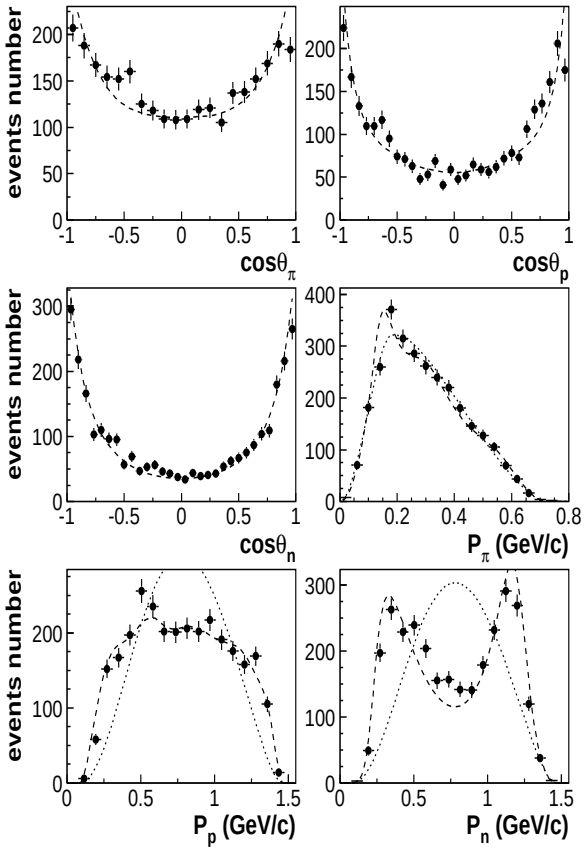

Fig. 4. C.m.s. angular distributions and the laboratory momentum spectra of final particles of the $pp \to pp\pi^0$ reaction. The dashed curves are the predictions of the OPE model; the dotted curves represent the phase space

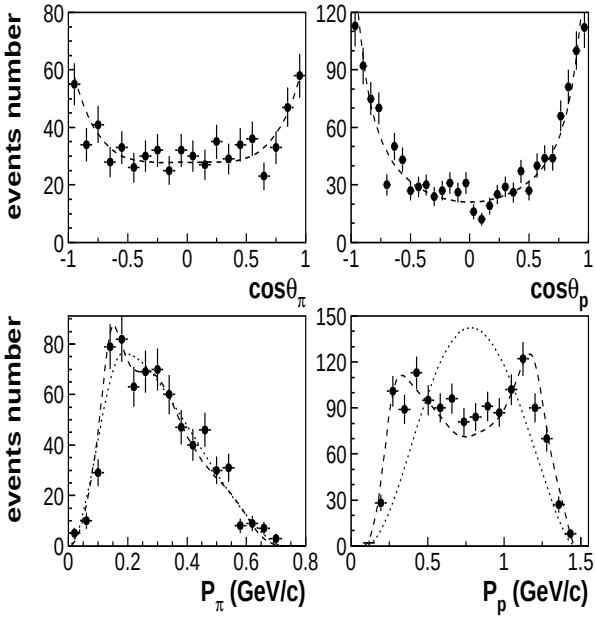

Fig. 5. C.m.s. angular distributions and the laboratory momentum spectra of final particles of the $pp \to pn\pi^+$ reaction. The meaning of the curves is the same as in Fig. 4

Figures 4 and 5 present the angular distributions of the final particles in the c.m.s. of the reactions and the particle momentum distributions in the laboratory frame for the $pp \to pp\pi^0$ and $np \to pp\pi^+$ reactions, respectively. One can see in the figures again that the agreement of the OPE calculations with the experimental data is fairly good. The qualitative agreement is also observed for other spectra, except for the angular distributions of the final particles in the helicity system.

As noted earlier in Ref. [5], although the OPE model provides a qualitative description of most differential spectra, it disagrees with the value of the total cross section for the $pp \to pn\pi^0$ and $pp \to pp\pi^+$ reactions. This means that taking into account only the P_{33} ($\Delta(1232)$ isobar) intermediate state is not enough for an adequate description of these reactions and, thus, a comprehensive partial-wave analysis is needed.

5. Partial-wave analysis, results and discussion

To extract the contributions of different partial waves, we apply [9] an event-by-event partial-wave analysis based on the maximum likelihood method. In the spin-orbital momentum decomposition, we follow the formalism given in Refs. [10–12]. The exact form of the operators for the initial and final states can be found in Ref. [11]. Following this decomposition, we use the spectroscopic notation $^{2S+1}L_J$ for the description of the initial state, the system of two final particles and the system "spectator and two-particle final state". For the initial pp system, the states with the total angular momenta $J \le 2$ and the angular momenta $L = 0$–3 between the two protons are taken into account. In the fitting procedure, for the final three-particle system we restrict ourselves to the angular momenta $L = 0$–2 in the system consisting of a two-body subsystem plus a spectator and to the angular momenta $L' = 0$–2 in the two-particles systems.

For the πN system in the intermediate state, we introduce two resonances, $\Delta(1232)P_{33}$ and the Roper resonance $N(1440)P_{11}$. For $\Delta(1232)$, we use the relativistic Breit-Wigner formula with the mass and width taken from the Particle Data Group. The Roper state was parameterized in agreement with the Breit – Wigner couplings found in the analysis of Ref. [13]. We would like to note that the present analysis is not sensitive to the exact parameterization of the Roper resonance: only the low-energy tail of this state can influence the data. For the description of the final pp interaction, we use the modified scattering-length approximation formula.

We minimized the log-likelihood value by a simultaneous fit of the present data on the $pp \to pn\pi^+$ and $pp \to pp\pi^0$ reactions taken at the proton momentum of 1628 MeV/c and the data on $pp \to pp\pi^0$ obtained earlier [5, 14, 15]. The data [5, 14] were taken at PNPI and measured at nine energies covering the energy interval from 600 to 1000 MeV. The high statistics data at the momentum of 950 MeV/c taken by the Tuebingen group [15] was included to fix the low energy region.

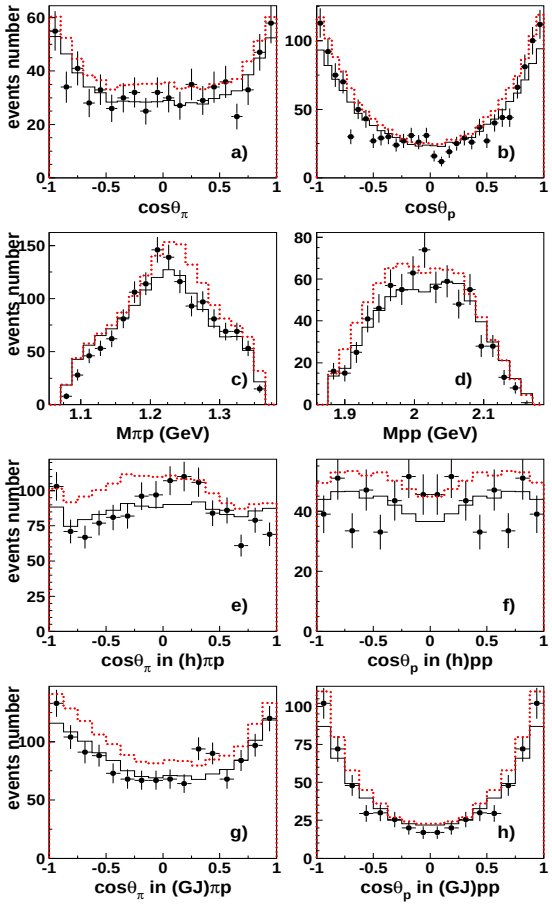

Fig. 6. The $pp \to pp\pi^0$ data taken at the incident proton momentum of 1628 MeV/c. (a, b) Angular distributions of final particles in the reaction rest frame; (c, d) effective two-particle mass spectra; (e, f) angular distributions of final particles in the helicity frames: (e) pion in the πp rest frame, (f) proton in the pp rest frame; (g, h) the corresponding distributions in the Godfrey-Jackson frames. The solid histograms show the result of our partial-wave analysis; the dotted histogram is the contribution of the amplitudes with the $\Delta(1232)$ intermediate state

The experimental data (the points with error bars) and the results of our partial-wave analysis (histograms) for the momentum of 1628 MeV/*c* are shown in Figs. 6 and 7. The first row shows the angular distributions of the final particles in the rest frame of the reaction; the second row shows the effective two-body mass spectra. One can see in the figures that our partial-wave analysis describes these distributions fairly well.

The quality of the partial-wave analysis is also demonstrated by the angular distributions in the helicity (third row) and the Godfrey – Jackson (fourth row) frames. The reduced χ^2 for the shown distributions is 1.70 for the $pp \to pp\pi^0$ data and 2.37 for the $pp \to pn\pi^+$ data, respectively. At this point, we would like to remind that we use the event-by-event maximum likelihood analysis and do not fit directly these distributions.

The initial $^1S_0$ partial wave provides only a small contribution to the $pp \to pp\pi^0$ reaction at the incident proton momentum of 1628 MeV/*c*. The largest contributions come from two *P*-wave initial states: $^3P_2$ and $^3P_1$ (see Table 2). The $^3P_0$ initial state contributes about 10 % to the total cross section. We also see noticeable contributions from the $^1D_2$ and $^3F_2$ partial waves. The $^3F_2$ partial wave interferes rather strongly with the strongest $^3P_2$ wave and, thus, its contribution is determined with a sizeable error.

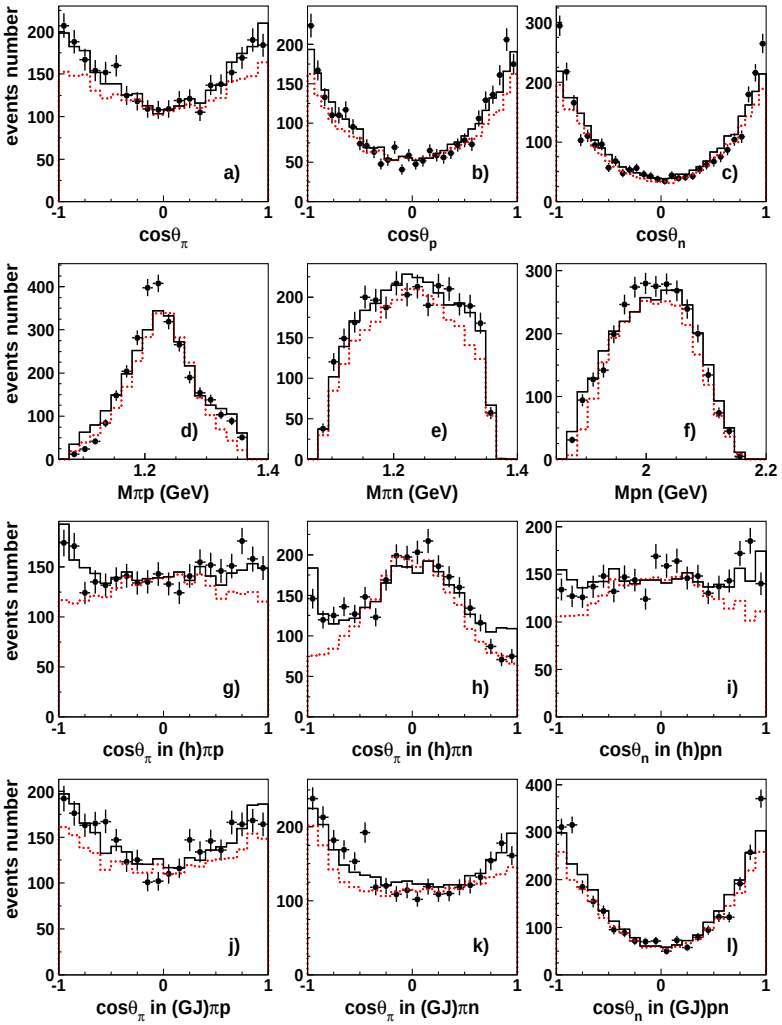

Fig. 7. The $pp \to pn\pi^+$ data taken at the proton momentum of 1628 MeV/*c*. (a, b, c) Angular distributions of the final particles in the reaction rest frame; (d, e, f) effective two-particle mass spectra; (g, h, i) angular distributions of the final particles in the helicity frames: (g) the pion in the πp rest frame, (h) the pion in the $\pi^+ n$ rest frame, and (i) the proton in the *pn* rest frame; (j, k, l) the corresponding distributions in the Godfrey – Jackson frame. The solid histograms show the result of our partial-wave analysis; the dotted histograms are the contributions of the amplitudes with the Δ(1232) intermediate state

Table 2

Contributions of main partial waves to the single pion production reactions at 1628 MeV/*c*

$pp \to pp\pi^0$		$pp \to pn\pi^+$	
$^1S_0$	1.0 ± 0.5 %	$^1S_0$	5.8 ± 2.8 %
$^3P_0$	10.0 ± 0.9 %	$^3P_0$	11.5 ± 0.9 %
$^3P_1$	26.0 ± 7.7 %	$^3P_1$	32.7 ± 0.8 %
$^3P_2$	44.0 ± 1.6 %	$^3P_2$	34.0 ± 1.6 %
$^1D_2$	8.0 ± 1.1 %	$^1D_2$	8.5 ± 1.0 %
$^3F_2$	11.4 ± 7.7 %	$^3F_2$	6.3 ± 1.5 %

All initial partial waves decay predominantly into the Δ(1232)*p* intermediate state. For different partial waves, the contribution of channels with Δ(1232) production varies from 65 to 90 %. The strongest non-resonant contribution is observed from the $^3P_2$ initial state, where the $^3P_2 \to (^3P_2)_{pp}\pi$ transition contributes from 20 to 35 % (of the contribution of the $^3P_2$ partial wave), depending on the fit. This instability appears due to noticeable destructive interference between the $^3P_2 \to (^3P_2)_{pp}\pi$ and Δ(1232)*p* intermediate states in this channel. The contributions of the amplitudes with the Δ(1232) resonance in the intermediate state are shown in Figs. 6 and 7 by the dotted histograms.

In the $pp \to pn\pi^+$ reaction at 1628 MeV/*c*, the non-resonant *pn* partial waves with the isospin 1 contribute much less to the total cross section than the corresponding waves in the $pp \to pp\pi^0$ reaction. For example, the $^3P_2 \to (^3P_2)_{pn}\pi$ transition is found to be less than 10 % of the contribution of the $^3P_2$ initial state leading to a much smaller interference effect for the amplitudes with Δ(1232) in the intermediate state. We also observe a sizeable $^1S_0 \to (^3S_1)_{pn}\pi$ transition, which is dominant for the $^1S_0$ initial state, and an appreciable contribution of the $^3P_1 \to (^1P_1)_{pn}\pi$ transition.

Our partial-wave analysis determines the relative contributions of the isovector waves to the total cross section for the single pion production processes in the energy interval of 400–1000 MeV. Figure 8 shows the experimental behaviour of the $pp \to pp\pi^0$ cross section together with the result of our partial-wave analysis and contributions of the dominant partial waves.

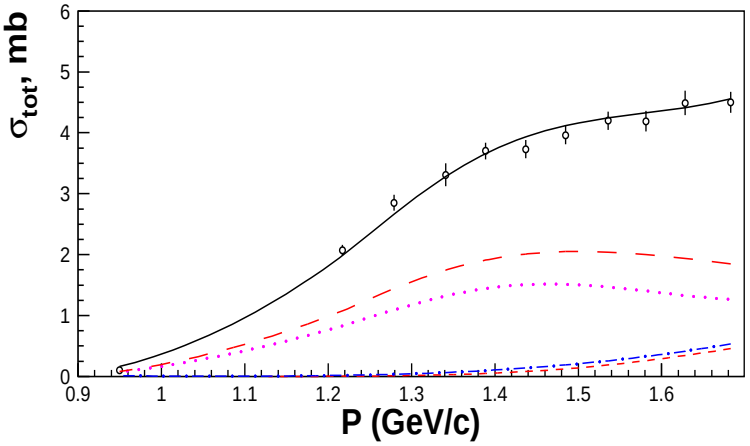

Fig. 8. Energy dependence of the total cross section for the $pp \to pp\pi^0$ reaction. The experimental points are taken from Refs. [5, 14, 15]. The solid curve is the result of our analysis; the long-dashed curve shows the contribution of the $^3P_2$ wave; the dotted curve – $^3P_1$; the dot-dashed curve – $^3P_0$; the short dashed curve – the $^1D_2$ wave

It should be noted that although we use the data on the $pp \to pn\pi^+$ reaction at 1628 MeV/*c* only, our partial waves predict the total cross section at lower energies in good agreement with the values given in Ref. [6].

6. Conclusion

A detailed study of the differential cross section for the $pp \to pp\pi^0$ and $pp \to pn\pi^+$ reactions has been performed [9] at the incident proton momentum of 1628 MeV/*c*. While the shape of most distributions is described qualitatively well by the OPE model, it fails to simultaneously describe the total cross sections for the $pp \to pp\pi^0$ and $pp \to pn\pi^+$ reactions.

The partial-wave analysis of the single pion production reactions reveals that the dominant contribution comes from the $\Delta(1232)p$ intermediate state, which explains the success of the OPE model. In addition, our analysis also allows us to achieve the combined description of all the analysed reactions and to extract the contributions of various transition amplitudes.

References

1. E. Ferrary, F. Sellery, Nuovo Cim. **27**, 1450 (1963).
2. E. Ferrary, F. Sellery, Nuovo Cim. **21**, 1028 (1961).
3. F. Sellery, Nuovo Cim. A **40**, 236 (1965).
4. V.K. Suslenko, I.I. Gaisak, Yad. Fiz. **43**, 392 (1986).
5. V.P. Andreev *et al.*, Phys. Rev. C **50**, 15 (1994).
6. F. Shimizu *et al*., Nucl. Phys. A **386**, 571 (1982).
7. A. Dobrovolsky *et al.*, Nucl. Phys. B **214**, 1 (83).
8. D. Albers *et al.,* Eur. Phys. J. A **22**, 125 (2004), arXiv:nucl-ex/0403045.
9. K.N. Ermakov *et al*., Eur. Phys. J. A **47**, 159 (2011).
10. A.V. Anisovich *et al.*, Eur. Phys. J. A **24**, 111 (2005).
11. A.V. Anisovich and A.V. Sarantsev, Eur. Phys. J. A **30**, 427 (2006).
12. A.V. Anisovich *et al*., Eur. Phys. J. A **34**, 129 (2007).
13. A.V. Sarantsev *et al.,* Phys. Lett. B **659**, 94 (2008).
14. V.V. Sarantsev *et al.*, Eur. Phys. J. A **21**, 303 (2004).
15. S. Abd El-Samad *et al.,* Eur. Phys. J. A **30**, 443 (2006).

STUDY OF NEGATIVE PION PRODUCTION IN NEUTRON-PROTON COLLISIONS AT BEAM MOMENTA BELOW 1.8 GeV/*c*

V.V. Sarantsev, K.N. Ermakov, L.M. Kochenda, V.I. Medvedev, V.A. Nikonov, O.V. Rogachevsky, A.V. Sarantsev, S.G. Sherman, V.A.Trofimov, and A.A. Vasiliev

1. Introduction

Single pion production in nucleon-nucleon (*NN*) collisions is the main inelastic process at the kinetic energies below 1 GeV. Despite the fact that numerous experiments have been performed in this region, many questions related to this process are still far from being satisfactory answered. One of them is the question of the contribution of isoscalar ($I = 0$) partial waves to the amplitude of inelastic neutron-proton scattering. Indeed, the neutron-proton scattering amplitude contains both the isoscalar ($I = 0$) and isovector ($I = 1$) parts, and, while the isovector part is known fairly well, even the order of magnitude of the total isoscalar cross section is badly determined. Usually, this cross section is extracted from the difference of the total cross sections for the $np \to pp\pi^-$ and $pp \to pp\pi^0$ pion production reactions. However, the values obtained in different experiments are significantly dispersed and do not give us the whole picture of the behaviour of the isoscalar cross section at the energies below 1 GeV. The only conclusion that can be drawn from these values is that the contribution of the isoscalar cross section to the $np \to pp\pi^-$ reaction is smaller by about one order of magnitude than that of the isovector one.

It should be noted that the experimental data on the $np \to pp\pi^-$ reaction below 1 GeV are much poorer than those on the *pp* collisions. The main reason for this is the difficulty to produce a pure monoenergetic neutron beam. Therefore, most previous experiments used either a continuous neutron beam with its energy spread in a fairly wide energy range [1], or investigated the *pn* interaction with a proton beam and a deuteron target as a source of neutrons [2–4]. Of course, one should also mention the works where the energy of neutrons was determined using the time-of-flight technique [5–7].

In the present study, we use a continuous neutron beam produced in *pd* interactions, where deuterium serves as a target. To determine the contributions of the isoscalar cross section, we perform the partial-wave analysis of the *np* data in the whole region of the incident neutron momenta combined with the $pp \to pp\pi^0$ data. In such an approach, the isoscalar channel contribution can be determined, for example, from the asymmetry of the pion distribution in the centre-of-mass system (c.m.s.) of the reaction, which is defined by interference of the isoscalar and isovector amplitudes. Thus, small isoscalar amplitudes can be determined with good accuracy.

2. Experiment and data selection

The $np \to pp\pi^-$ data were taken at the PNPI synchrocyclotron with a 35 cm hydrogen bubble chamber placed in the 1.48 T magnetic field. Neutrons were produced in collisions of the 1 GeV proton beam with a thin-walled liquid deuterium target. Charged particles are swept away from the formed neutron beam by a system of additional magnets and lenses situated behind the deuteron target. The neutron beam passes through a collimator with the size of $100 \times 2 \times 1$ cm^3 and then enters the bubble chamber located at a 5 m distance. The produced neutrons have the momentum spread in the range of 1−2 GeV/*c*. The values of the neutron momentum that are larger than that of the incident protons are due to Fermi motion of the neutron in the deuteron. A detailed description of the neutron beam and its energy distribution can be found in Ref. [8].

A total of 10^5 stereofilms have been obtained with this beam. The films were scanned twice with the goal to select events with two positive-curvature tracks and one with a negative curvature. The efficiency of such a selection is nearly 100 % due to small density of tracks in the frames. As a result, 10835 three-prong events were found. These events can belong either to the single pion production reaction,

$$np \to pp\pi^-, \tag{1}$$

or to the double pion production reactions:

$$np \rightarrow pp\pi^-\pi^0,$$
$$np \rightarrow pn\pi^+\pi^-, \quad (2)$$
$$np \rightarrow d\pi^+\pi^-.$$

To separate the former process from the latter ones, the tracks of events disposed in the fiducial volume of the chamber were measured and geometrically reconstructed; the momenta of the assumed particles were determined according to their masses. Event identification was performed by a kinematic fit demanding that the confidence level of the accepted events was more than 1 %. The direction of the incident neutron beam is known from the collimating system providing the direction with the angular spread of 0.3° [8]. However, since nothing is known about the value of the neutron momentum, it had to be defined by a 3C-constrained fit. Three-prong events were constrained by the kinematic fits to all the reactions in Eqs. 1 and 2. A visual scan of the bubble density on the tracks was carried out for the events fitted to several hypotheses to distinguish between a pion, a proton and a deuteron.

The angular resolution of the direction of the incident neutron beam in both azimuthal and polar angles was first estimated to be 1°, which turned out to be more than three times larger than that obtained after the fit. After repeated fits with the corrected errors, we selected 8251 events assigned to reaction (1). In the present experiment we did not monitor the neutron beam and, therefore, the momentum distribution is given in terms of the number of events (but not in millibarns). To determine the absolute isoscalar cross section, in our partial-wave analysis, we included the $pp \rightarrow pp\pi^0$ data for which the total cross section was measured in our previous experiments.

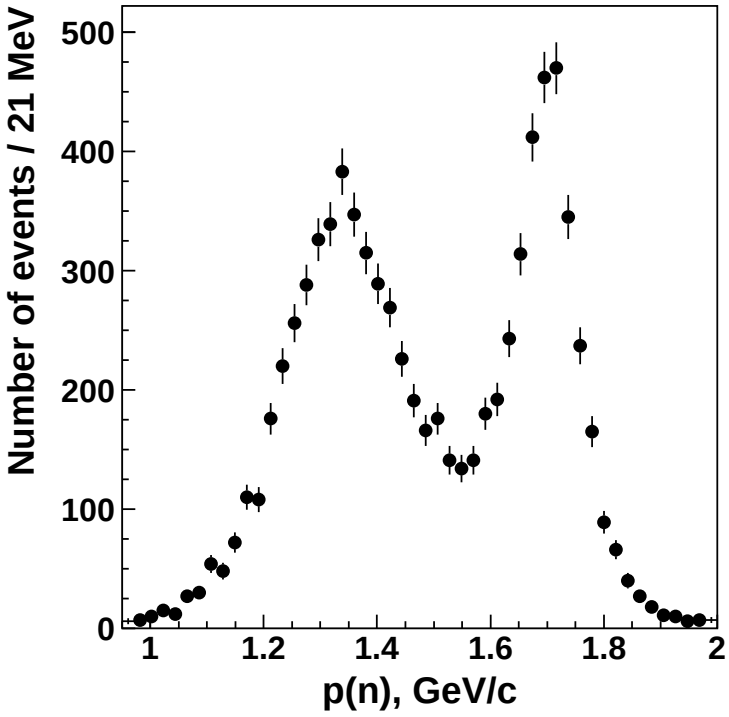

Fig. 1. Neutron beam distribution for events of the $np \rightarrow pp\pi^-$ reaction

Figure 1 shows the neutron beam distribution for the selected $np \rightarrow pp\pi^-$ events. The distribution has a peak (on the right) located approximately at the momentum of the incident protons interacting with the deuterium target. The width of this peak is defined by the Fermi motion of the neutron in the deuteron. The second peak (on the left) corresponds to less energetic neutrons and is formed by inelastic processes.

The angular distributions of the produced pions and protons in the reaction c.m.s. for the chosen intervals of the initial neutron momenta are shown in Fig. 2.

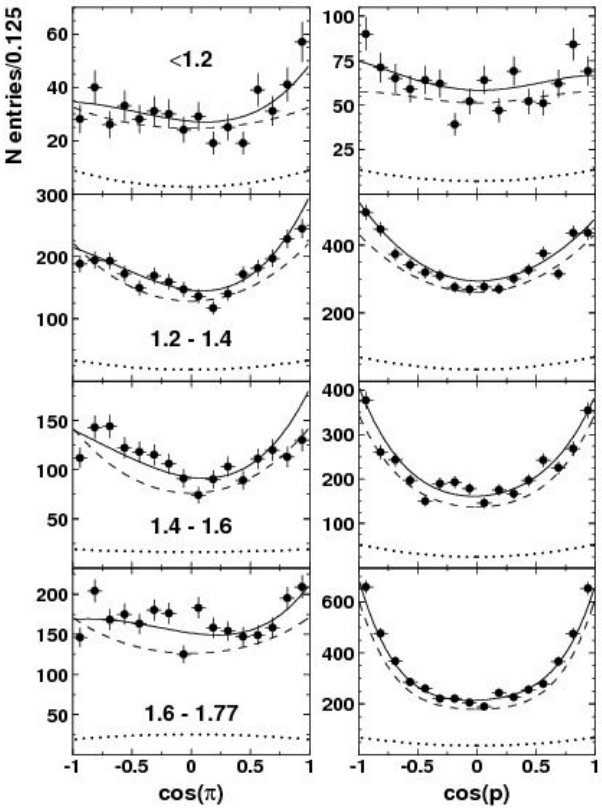

Fig. 2. Angular distribution of pions (left column) and final protons (right column) in the c.m.s. of the $np \to pp\pi^-$ reaction for 4 intervals of the neutron momentum (in GeV/c). The full curves are the result of our partial-wave analysis; the dashed curves are the contributions of the isovector amplitudes; the dotted curves are those of the isoscalar amplitudes

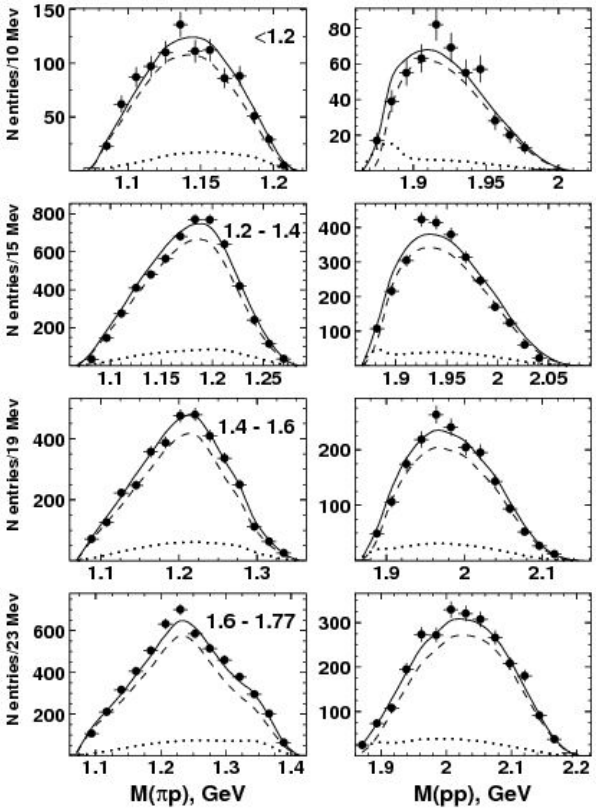

Fig. 3. The πp and pp mass distributions of final particles for 4 intervals of the neutron momentum (in Gev/c). The meaning of the curves is the same as in Fig. 2

The proton angular distributions are almost symmetric due to permutation of the protons, while the pion angular distributions show clear asymmetry (especially for the low momenta of the incident neutrons). While the isovector amplitudes are symmetric with respect to the direction of the produced pion, the isoscalar amplitudes are antisymmetric. Therefore, the asymmetry in the differential cross section is determined by the interference of these amplitudes providing a sensitive tool for determination of the weak isoscalar partial waves.

The two-body invariant mass distributions of final particles are shown in Fig. 3. The πp invariant mass at high energies of the neutrons has a peak determined by production of $\Delta(1232)$. As our partial-wave analysis indicates, the $\Delta(1232)p$ channel is indeed one of the dominant final states of this reaction. The pp invariant mass distributions are smooth and do not reveal any peculiarities.

3. Partial-wave analysis, its results and discussion

To extract the contributions of different partial waves, we apply [9] an event-by-event partial-wave analysis based on the maximum likelihood method. In the spin-orbital momentum decomposition, we follow the formalism of Refs. [10–12]. Following this decomposition, we use the spectroscopic notation $^{2S+1}L_J$ for the description of the initial state, the system of two final particles, and the system "spectator and two-particle final state". For the initial np system, the states with the total angular momenta $J \leq 2$ and the angular momenta $L = 0$–3 between the two nucleons are taken into account. For the final three-particle system, in the fitting procedure, we restrict ourselves to the angular momenta $L' = 0$–2 in the two-body subsystem plus a spectator and to $L_2 = 0$–2 in the two-particle subsystems. For the πN system in the intermediate state, we

introduce two resonances, $\Delta(1232)P_{33}$ and the Roper $N(1440)P_{11}$. For $\Delta(1232)$, we use the relativistic Breit-Wigner formula with the mass and width taken from the Particle Data Group. The Roper state was parameterized in agreement with the Breit – Wigner couplings found in the analysis in Ref. [13]. We would like to note that the present analysis is not sensitive to the exact parameterization of the Roper resonance: only the low-energy tail of this state could influence the data. For the description of the final *pp* interaction, we use the modified scattering-length approximation formula.

We minimized the log-likelihood value by a simultaneous fit to the present *np* data taken in the whole range of the neutron momenta and the $pp \to pp\pi^0$ data [14, 15] obtained earlier and measured at nine energies covering the same energy interval as the *np* data. To fix the low energy region, a sample of the high statistics $pp \to pp\pi^0$ data taken by the Tuebingen group [16] was also included in the fit. The *pp* collision events are produced in the isovector channel ($I = 1$) only and, therefore, the contribution of isovector states to the $np \to pp\pi^-$ reaction (which differs by the Clebsch – Gordan coefficient only) is strongly constrained. This appreciably improves the accuracy of the extraction of the isoscalar contribution from the data.

The results of our partial-wave analysis are shown in Figs. 2 and 3 by the solid curves. The contributions of the isovector channel are given by the dashed curves; the contributions of the isoscalar channel – by the dotted curves. One can see that the fit reproduces well the asymmetry of the pion angular distribution in the c.m.s. (see Fig. 2). Moreover, the angular distribution of the isoscalar channel changes noticeably with the energy demonstrating the contribution of different partial waves.

Table 1

Largest contributions of initial partial waves $^{2S+1}L_J$ to the $np \to pp\pi^-$ reaction. The values are given for the best fit, the errors being extracted from a large number of solutions (see the text)

$I = 1$		$I = 0$	
$^3P_0$	3.7 ± 1.3 %	$^3S_1$	0.9 ± 0.2 %
$^3P_1$	21.6 ± 3.0 %	$^1P_1$	10.9 ± 1.2 %
$^3P_2$	46.1 ± 5.0 %	$^3D_1$	1.8 ± 0.3 %
$^1D_2$	4.7 ± 1.5 %		
$^3F_2$	10.3 ± 2.5 %		

The largest contributions from isovector initial states to the pion production process stem from the $^3P_2$ and $^3P_1$ waves (see Table 1). For large neutron momenta, the $^3F_2$ contribution is significant. As for the $^1S_0$ wave, it gives a negligible contribution. The $^3P_2$ state decays almost equally into the $\Delta(1232)p$, $P_{11}(1440)p$ and $(^3P_2)_{pp}\pi$ states. The $^3P_1$ initial state decays also almost equally into $\Delta(1232)p$ and $(^3P_2)_{pp}\pi$, while $^3F_2$ decays predominantly into the $\Delta(1232)p$ and $P_{11}(1440)p$ final states. The isoscalar $^1P_1$ state decays mainly via $(^3P_1)_{pp}\pi$ and $P_{11}(1440)p$, while the $^3S_1$ and $^3D_1$ states decay almost completely into the $(^1S_0)_{pp}\pi$ channel. The errors in Table 1 are mostly systematic and cover a large number of solutions which we considered to be acceptable. These solutions were obtained with different amplitude parameterizations [9] and/or have slightly different contributions of final-state partial waves.

The quality of our partial-wave analysis is also demonstrated in Fig. 4 where the angular distributions of the pion and the final proton are compared to the fit in the helicity and Godfrey – Jackson frames for the entire range of the incident neutron momentum. The helicity frame is the rest frame of two final particles where the angle is calculated between one of the constituent particles and the spectator. This frame is mostly suitable for investigations of the processes when two initial particles form a system (*e.g.*, resonance) which decays into a final two-body system and a spectator. The Godfrey – Jackson frame is defined as the rest frame of two final particles where the angle is defined between one of the constituent particles and the beam. This system is mostly suitable for studies of two-particle systems in the final state produced by a *t*-channel exchange. We would like to mention that the description of these distributions over the momentum intervals given in Figs. 2 and 3 is of the same quality as for the full range of the incident neutron momentum.

Figure 5 shows a comparison of the isoscalar cross section determined in our partial-wave analysis with the isoscalar cross section extracted from other experimental data using the following expression:

$$\sigma(I = 0) = 3\left[2\sigma(np \to pp\pi^-) - \sigma(pp \to pp\pi^0)\right]. \quad (3)$$

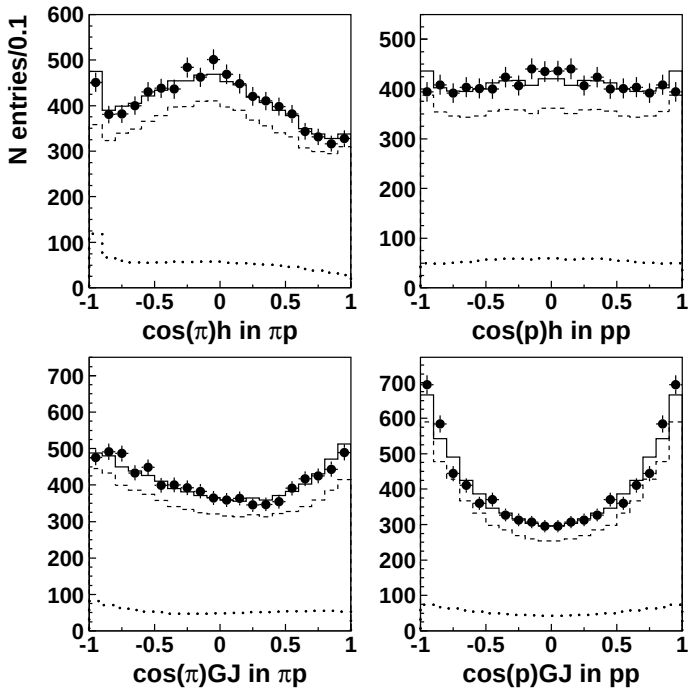

Fig. 4. Angular distributions of the final pion and proton in the helicity and Godfrey – Jackson systems for the entire interval of the neutron momentum. The full histograms are the result of our partial-wave analysis; the dashed histograms are the contributions of the isovector amplitudes; the dotted histograms are the contributions of the isoscalar amplitudes

The points inside the band correspond to our best solution. The band itself corresponds to the systematic errors obtained from a large set of solutions with different parameterizations of the partial-wave amplitudes. One can see in the figure that our cross section systematically exceeds those of previous works. The isoscalar cross section increases smoothly from 1.1 GeV/*c* up to 1.6 GeV/*c*, where it reaches the value of ~ 2.5 mb and then drops sharply down to ~ 1.5 mb. It is possible that this falloff is connected to opening of double pion production channels where the isoscalar *np* states could decay, for example, into two Δ states.

The isoscalar initial channel provides a good tool for determination of the scattering length of the final *pp* system in pion production reactions. In the first fits, we fixed the scattering length and the effective range of the $^1S_0$ final *pp* state to be $a_{pp} = -7.83$ fm and $r = 2.8$ fm [18], respectively. For other partial waves, the effective ranges were also fixed to be $r = 2.8$ fm, while the parameters a_{pp} were free.

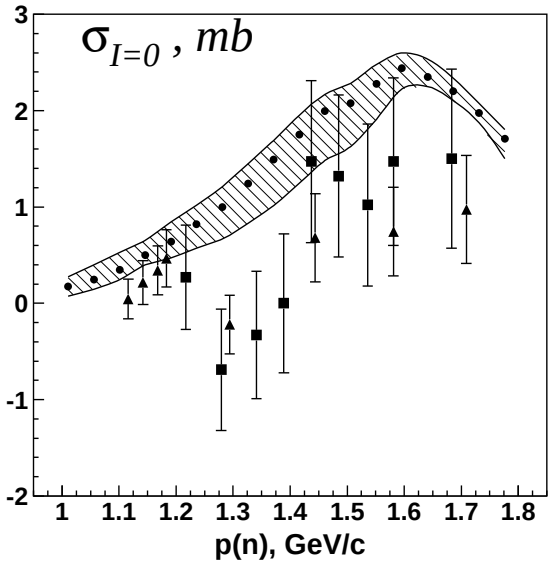

Fig. 5. Isoscalar total cross section. The band represents the systematical errors obtained from a large number of fits. The experimental points are taken from Refs. [15] (squares) and [17] (triangles)

An appreciable fraction of the isoscalar channel decays into the system consisting of a pion and a *pp* pair in the $^1S_0$ state. The $^1S_0$ state produces a sharp peak at the pion backward angle in the helicity frame. This angle corresponds to the lowest *pp* invariant mass and – due to kinematical conditions (the suppression of other partial waves) – this peak is clearly seen in the data.

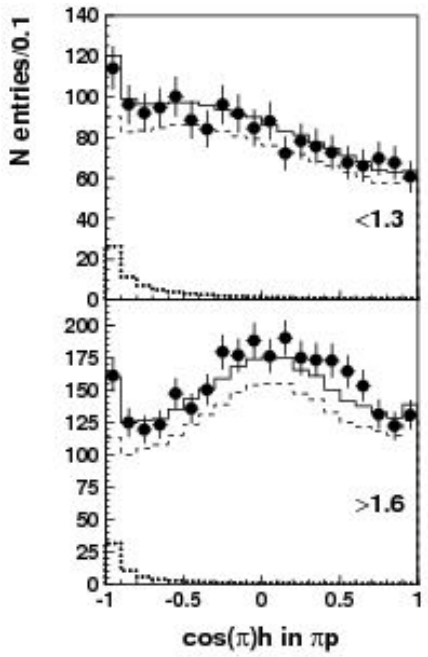

Fig. 6. Angular distribution of the final pion in the helicity frame for two intervals of the incident neutron momentum (in GeV/*c*). The full histograms (close to the data points) are the result of our partial-wave analysis; the dashed histograms show the contributions of the isovector channel; the dotted histograms are the contributions of the isoscalar channel decaying into the $(^1S_0)_{pp}\pi$ final state

The pion angular distributions in the helicity frame for two intervals of the incident neutron momentum are shown in Fig. 6. One can see in the figure that the isoscalar channel dominates for the both considered momentum intervals of the incident neutron. For the effective range *r* fixed to 2.8 fm, we find the scattering length to be $a_{pp} = -7.5 \pm 0.3$ fm.

For the *P*- and *D*-waves, the scattering lengths are determined much worse due large correlations of these parameters with the parameters of the transition amplitudes.

4. Conclusion

We have performed a detailed study of the $np \to pp\pi^-$ reaction [9]. The data were analysed by a maximum-likelihood partial-wave analysis. Our analysis has provided us with the trustworthy values of the weak isoscalar amplitudes from their interference with strong isovector amplitudes. The dominant decay of the initial $^3S_1$ and $^3D_1$ isoscalar states into the $(^1S_0)_{pp}\pi$ final state has allowed us to achieve good determination of the *pp* scattering length in the final state of the pion production reactions.

References

1. J.G. Rushbrooke *et al*., Nuovo Cim. **33**, 1509 (1964).
2. D.C. Brunt *et al*., Phys. Rev. **187**, 1856 (1969).
3. L.G. Dakhno *et al*., Phys. Lett. B **114**, 409 (1982).
4. T. Tsuboyama *et al*., Nucl. Phys. A **486**, 669 (1988).
5. M. Kleinschmidt *et al*., Z. Phys. A **298**, 253 (1980).
6. W. Thomas *et al*., Phys. Rev. D **24**, 1736 (1981).
7. A. Bannwarth *et al*., Nucl. Phys. A **567**, 761 (1994).
8. V.I. Medvedev *et al*., Phys. Atom. Nucl. **72**, 1475 (2009).
9. V.V. Sarantsev *et al*., Eur. Phys. J. A **43**, 11 (2010).
10. A.V. Anisovich *et al*., Eur. Phys. J. A **24**, 111 (2005).

11. A.V. Anisovich and A.V. Sarantsev, Eur. Phys. J. A **30**, 427 (2006).
12. A.V. Anisovich *et al*., Eur. Phys. J. A **34**, 129 (2007).
13. A.V. Sarantsev *et al.,* Phys. Lett. B **659**, 94 (2008).
14. V.P. Andreev *et al*., Phys. Rev. C **50**, 15 (1994).
15. V.V. Sarantsev *et al*., Eur. Phys. J. A **21**, 303 (2004).
16. S. Abd El-Samad *et al*., Eur. Phys. J. A **30**, 443 (2006).
17. G. Rappenecker *et al*., Nucl. Phys. A **590**, 763 (1995).
18. M.L. Gursky and L. Heller, Phys. Rev. **136**, B 1693 (1964).

ANALYSIS OF DATA ON PROTON-PROTON SCATTERING IN THE ENERGY RANGE OF 100–1300 MeV

V.G. Vovchenko, V.V. Polyakov, and O.Ya. Fedorov

1. Introduction

We perform a continuous partial-wave analysis of the data on proton-proton interaction in the energy range of 100–1300 MeV. The advantage of a continuous partial-wave analysis as compared to that at fixed energy consists in better relation between the number of data points and the number of free parameters. In the case of a large number of degrees of freedom, solutions obtained in the former type of the analysis predict the values of the parameters that lie within narrower error bands. Also, the energy region, where the elastic interaction reflects the onset and stabilization of inelastic interactions associated with single π-meson production [1], is of interest for investigation of special features of *pp* interactions.

The aim of our partial-wave analysis is to evaluate the scattering matrix amplitudes more accurately than in other approaches by means of:

a) taking into account all PNPI experimental *pp* data;

b) accurate calculations of the amplitudes of inelastic interaction for each state of the *pp* system;

c) more accurate determination of the inelastic interaction thresholds for each state of the *pp* system;

d) model-independent parameterization of the phase shifts.

These factors constitute the main difference between our analysis and that of Arndt *et al*. [2].

2. Formalism for description of the interaction

In order to describe the interaction, we use the representation of the S matrix in the form proposed by Stapp *et al.* [3]. For singlet states and unmixed triplet states ($J = L$), we have $S_L = \exp(2i\delta_J)$, where δ_J is the phase shift for the transition from the state characterized by the total angular momentum $J = L$. For mixed triplet states characterized by the orbital angular momenta $L_\pm = J \pm 1$, we have

$$S_{L,J} = \begin{pmatrix} \cos(2\varepsilon_J)\exp(2i\delta_{J-1,J}) & i\sin(2\varepsilon_J)\exp(i(\delta_{J-1,J} + \delta_{J+1,J} + \varphi_J)) \\ i\sin(2\varepsilon_J)\exp(i(\delta_{J-1,J} + \delta_{J+1,J} + \varphi_J)) & \cos(2\varepsilon_J)\exp(2i\delta_{J+1,J}) \end{pmatrix}, \tag{1}$$

where ε_J is the mixing parameter and φ_J is the additional ("sixth") parameter. The parameters ε_J and φ_J are assumed to be real. The phase shift becomes complex-valued above the pion production threshold, and its imaginary part δ^{i}_{LJ} reflects the intensity of the inelastic channel. We use the inelasticity parameter $\eta_{LJ} = \exp(-2\mathrm{Im}\delta^{i}_{LJ})$.

To describe the elastic *pp* interaction, we use the following form of the scattering matrix in the spin space:

$$M(\sigma_1, \sigma_2) = a + b\sigma_{1n}\sigma_{2n} + c(\sigma_{1n} + \sigma_{2n}) + e\sigma_{1m}\sigma_{2m} + f\sigma_{1l}\sigma_{2l}, \tag{2}$$

where the amplitudes a, b, c, e, and f are functions of the energy E and the centre of mass system (c.m.s.) scattering angle θ; σ_i are the spin operators (Pauli matrices) of the first (second) proton in the orthonormalized basis made of the vectors $\mathbf{n} \sim \mathbf{k} \times \mathbf{k}'$, $\mathbf{l} \sim \mathbf{k} + \mathbf{k}'$, and $\mathbf{m} \sim \mathbf{k} - \mathbf{k}'$, where $\mathbf{k}$ and $\mathbf{k}'$ are the incident and scattered proton momenta in the c.m.s., respectively.

We represent the differential and total cross sections for *pp* interaction in terms of the parameters of the S matrix in Eq. (1) and the scattering matrix amplitudes in Eq. (2). The formulae given below relate the total cross sections to the zero-angle scattering amplitudes:

$$I_0 = |a|^2 + |b|^2 + 2|c|^2 + |e|^2 + |f|^2, \tag{3}$$

$$\sigma_{\mathrm{tot}} = \frac{4\pi}{k}\mathrm{Im}\,a(0) = \frac{\pi}{k^2}\sum_{LJ}(2J+1)(1 - \eta_{LJ}\cos(2\varepsilon_J)\cos(2\,\mathrm{Re}\,\delta_{LJ})), \tag{4}$$

$$\sigma_{\text{in}} = \frac{\pi}{2k^2}\sum_{LJ}(2J+1)(1-\cos^2(2\varepsilon_J)\eta_{LJ}{}^2 - \sin^2(2\varepsilon_J)\eta_{L+1J}\eta_{L-1J}). \quad (5)$$

The phase shifts $\delta_{L,J}$ and $\delta^{\,i}_{L,,J}$, the mixing parameters ε_J, and the parameters φ_J are found by minimizing the functional $\chi^2(\{\delta\})$ describing the experimental data. Thus, the resulting solution is the energy dependence of the phase shifts describing the experimental data in the best possible way. To seek a solution, we applied a consistent method described below. This made it possible, first, to construct a general solution using the algorithm of searches for particular solutions featuring a smaller number of sought parameters and, second, to ensure a convenient investigation of details of the behaviour of the individual phase shifts as functions of energy.

We employed the data on elastic and total *pp* cross sections, including the data for pure spin states, in the proton energy range of 100–1300 MeV. The sources of the data that we used include the compilation from Refs. [4, 5], the database of Arndt *et al*. [2], and the original publications quoted in Refs. [6–11]. In total, $N = 12841$ experimental points were included in our analysis.

In our analysis, the number of orbital states described by the sought real parts of the phase shifts was up to $L_{\max} = 9$, and the total angular momentum was as high as $J = 10$. It was assumed that only the states with $L \leq 5$ had nonzero imaginary parts. The real parts of the phase shifts were parameterized in the form $\delta_{LJ}(E) = \Sigma_k \delta_{L,Jk} \sin(kz)$, $k = 1\ldots k_{\max}$, $k_{\max} = 3...6$, where $z = \pi P / P_{\max}$, P is the laboratory proton momentum in units of MeV/c, and $P_{\max} = 2200$ MeV/c. The imaginary parts of the phase shifts (and the parameters $\varphi_{2,4}$) were determined by the relation $\delta^{\,i}_{L,J}(E) = \Sigma_k \delta^{\,i}_{LJk} \sin(k z_i)$, $k = 1...k_{\max}$, $k_{\max} = 2\ldots 4$, where $z_i = \pi Q / Q_{\max}$, Q and $Q_{\max}$ are the c.m. pion momenta in the deuteron-production reaction, $pp \to \pi^+ d$, when the proton has the momentum P and $P_{\max}$, respectively.

We have employed $n_{i,p} = 169$ sought (free) parameters. The solution was constructed by successively implementing the following steps:

a) searches for particular minima with respect to the free parameters of the real parts of the phase shifts (parameters $\delta_{L,Jk}$);

b) similar searches with respect to the free parameters of the imaginary parts (parameters $\delta^{\,i}_{L,Jk}$);

c) correction of the normalization factors for the differential cross section, and

d) the same for polarization.

In total, there were 42 normalization factors for the differential cross sections and 55 normalization factors for the polarization. An individual procedure was used to refine the inelastic interaction thresholds [12] which were found from a fit to the data. A distinct minimum in χ^2 was observed for the states in which the inelasticity parameter was large (for example, for the $^3P_2$-wave state), and the position of this minimum on the energy scale was taken to be the threshold. In the case of weak inelastic interaction, where the functional χ^2 may have no minimum, a boundary of the growth of χ^2 was observed – and this boundary was considered to be the threshold. The uncertainty in the thresholds was 0.01 GeV for intensely inelastic states, reaching the value of 0.05 GeV for weakly inelastic states. Since $N >> n_{i,p}$, we have set $\langle\chi^2\rangle = \chi^2 / N$. The quality of the data description by the obtained solution was characterized by the value of $\chi^2 = 14\ 835$, or $\langle\chi^2\rangle = 1.155$.

3. Real parts of the phase shifts and the mixing parameters

Our analysis leads to a more complicated pattern of the energy dependence of the phase shifts than the solution of Arndt [2]. However, up to the energy of 0.6 GeV, there are no significant discrepancies between the predictions for the phase shifts and the mixing parameters in all the analyses. At higher energies, there is a considerable scattering of the predicted values. At the edge of the energy range, according to our predictions, the behaviour of the phase shifts for the $^3P_2$- and $^3F_2$-wave states deviates considerably from the results of other analyses. It is noteworthy that our results for the higher lying $^1K_8$- and $^3L_{8,9}$-wave states agree with those obtained in the framework of a potential model reported in Ref. [13].

The values of the mixing parameters $\varepsilon_{2,4,6}$ fall within the range of the scattered predictions of phase shift analyses at fixed energies. The parameter ε_8 also agrees with the values calculated in Ref. [13]. The large

values of the parameters $\varphi_{2,\,4}$ (in contrast to the generally accepted opinion that they are small, see, *e.g.* Ref. [13]) is a peculiar feature of our analysis.

4. Imaginary values of the phase shifts

Allowing for a small contribution to χ^2, the inelastic parts of the phase shifts for the $^1S_0$- and $^3P_0$-wave states can be treated as uncertainties in their values. This estimate can be extended to the values of the imaginary parts of the phase shifts for the $^3H_{4\,,6}$-wave states . These imaginary parts are 1° and 0.5° for the $^3H_4$- and $^3H_6$-wave states, respectively. For the $^3P_2$ -, $^1D_2$ -, and $^3F_3$-wave states, similarly to the case of the $^1G_4$- and $^3H_5$-wave states giving a dominant contribution to the inelastic cross section, there are no significant discrepancies between the predictions of all the analyses at the energy of up to 1 GeV. At the edge of the energy interval, our solution gives a large value of the imaginary part of the phase shift for the $^3P_2$-wave state.

Low values of the imaginary parts of the phase shifts in the $^3(L = J+1)_J$ mixed triplet states, as well as of the ratios of the imaginary parts of the $^3(L = J+1)_J$ and $^3(L = J-1)_J$ states – is a noteworthy feature of these imaginary parts. As an example, we note that at the energy of 1 GeV, $\delta(^3P_0)$ and $\delta(^3H_4)$ are equal to zero, while $\delta(^3F_2)/\delta(^3P_2) = 0.24 \pm 0.01$ (the partial-wave analysis reported in Ref. [2] yields 0.015). Yet, this feature is not unquestionable. It is possible that another special feature manifests itself here: all mixed triplet states, with the exception of the $^3P_2$-wave and, perhaps, the $^3F_2$-wave state, have low intensity. In either case, the answer to the question should be sought in an adequate theory of pion production.

5. Contribution to the total elastic scattering cross section

Introducing five integrated amplitudes corresponding to the scattering matrix amplitudes in Eq. (2), we obtain

$$\begin{aligned}
&\langle a(E)\rangle = \int |\, a(E,\theta)\,|^2\, d\Omega\ ,\ \langle b(E)\rangle = \int |\, b(E,\theta)\,|^2\, d\Omega,\\
&\langle c(E)\rangle = \int |\, c(E,\theta)\,|^2\, d\Omega,\\
&\langle e(E)\rangle = \int |\, e(E,\theta)\,|^2\, d\Omega,\ \langle f(E)\rangle = \int |\, f(E,\theta)\,|^2\, d\Omega.
\end{aligned} \tag{6}$$

Then, the total elastic scattering cross section will be given by the sum of the amplitudes in Eq. (6):

$$\sigma_{\rm el} = < a > + < b > + \ 2 < c > + < e > + < f > .$$

At the same time, these amplitudes describe the contributions to $\sigma_{\rm el}$ in the specific spin states. In the text, they are denoted as the interaction intensities: the central interaction ‹*a*›, the spin-orbit interaction ‹*c*›, and the spin-spin interactions (for various spin orientations) ‹*b*›, ‹*e*›, and ‹*f*›. We show the energy dependence of the integrated amplitudes in Fig. 1a and of the total and inelastic cross sections in Fig. 1b.

In order to calculate $\sigma_{\rm tot}$, we used Eq. (4). The quantities calculated as the ($\sigma_{\rm el} + \sigma_{\rm in}$) sum deviate from those quoted above by no more than 0.2 mb – this is an indicative of correctness of the individual calculations of $\sigma_{\rm tot}$, $\sigma_{\rm el}$ and $\sigma_{\rm in}$. For $\sigma_{\rm tot}$ and $\sigma_{\rm in}$, we present the experimental values from the used database, which are faithfully reproduced by the results of our analysis. The uncertainties in the integrated amplitudes do not exceed 0.06 mb for all of these amplitudes, while the uncertainties in $\sigma_{\rm tot}$ and $\sigma_{\rm in}$ do not exceed 0.6 mb everywhere, with the exception of the edges of the energy range.

The behaviour of the integrated amplitudes at low energies is determined by the behaviour of the phase shifts, which (all of them, with the exception of the phase shift for the $^1S_0$-wave state) tend to zero as the energy goes to zero. This is provided by the factor k in the numerator of the definition of the partial-wave amplitudes. From the data in Fig. 1a, b, one can draw the following conclusions:

a) above 0.4 GeV, both the sum of the spin-spin interactions and the sum of the central and spin-orbit interactions change only slightly;

b) as the energy grows in the range of 0.4–1.2 GeV, the intensity of the central interaction increases by a factor of 4.5, the intensity of the spin-orbit interaction decreases by a factor of 5, and the sum of the spin-spin interactions increases by ~ 20 %.

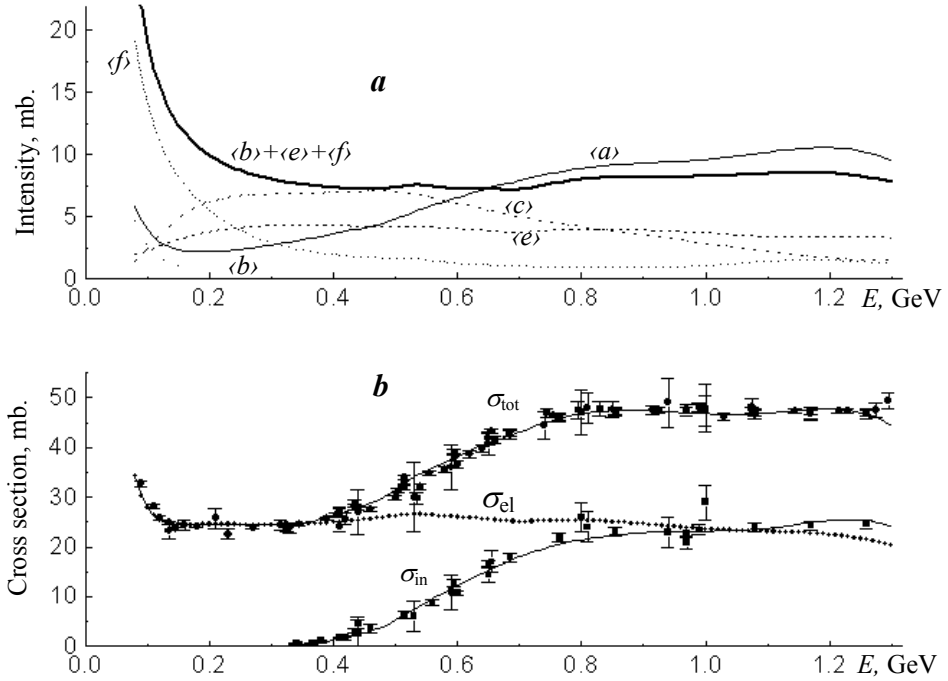

Fig. 1. Energy dependence of (a) the integrated amplitudes and (b) the total cross sections. The points represent the experimental data from the used database (the filled circles and boxes stand for the total and inelastic cross sections, respectively)

6. Behaviour of the *S* matrix amplitudes at zero scattering angles

Our predictions for the *S* matrix amplitudes at the zero scattering angle, along with the corridor of errors, are shown in Fig. 2. They are compared with the results obtained in the calculations of Grein and Kroll [14] for the F_1, F_2, and F_3 amplitudes. Also, the respective imaginary parts are compared with the experimental data on σ_{tot}, $\Delta\sigma_T$, and $\Delta\sigma_L$, redefined as the imaginary parts of the amplitudes *a*, *b*, and *f*, correspondingly. In addition, in this figure, we present predictions of the partial-wave analysis [13], whose amplitudes are redefined according to the *S* matrix form in Eq. (2).

One can see in Fig. 2 that, for the imaginary parts of the amplitudes, σ_{tot} is described quite well (see the discussion of the total cross sections above). The description of $\Delta\sigma_T$ and $\Delta\sigma_L$ can be considered satisfactory. Indeed, there is a discrepancy in the description of small values of $\Delta\sigma_T$ by 0.02 $(\text{mb/sr})^{1/2}$ in the energy range of 0.2–0.3 GeV, but, due to absence of substantial distinctions between the phase shifts in our solution and those in the solutions of other analyses, we consider this discrepancy to be uncertainty in the description of the data.

For the real parts, there are significant distinctions. For Re[*b*(0)], the deviation from the results of other analyses is considerable for low energies and for the energies above 1 GeV. At low energies, a substantial difference is seen at the edge of the energy range and beyond its boundary. The discrepancy at high energies may be attributed to boundary effects in our analysis. It is noteworthy that the agreement between the prediction for Re[*a*(0)] in Ref. [13] and the results of the calculations by Grein and Kroll [14] is due to implementation of the parameter ρ = Re[*a*(0)] / Im[*a*(0)] from Ref. [14] for the quasi-experimental point in Ref. [13]. For Re[*b*(0)] and Re[*f*(0)], the partial-wave analysis of Ref. [12] yielded widely scattered predictions. Compared to the calculations of Grein and Kroll, our calculations exhibit regions of agreement, as well as regions of discrepancies, especially for Re[*f*(0)], where the deviations range from 0.2 to 0.3 $(\text{mb/sr})^{1/2}$. This can be taken as a measure of disagreement between the results of calculations of the real parts of the amplitudes in Ref. [14] and the experimental data.

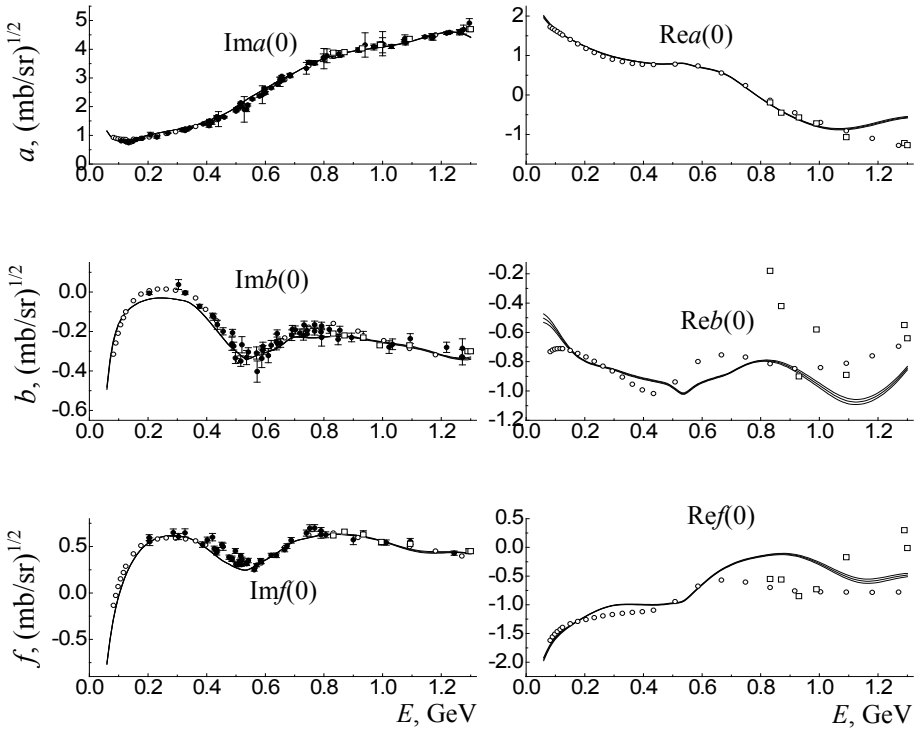

Fig. 2. Energy dependence of the scattering matrix amplitudes at the zero scattering angle. The curve, along with the corridor of errors, represents the predictions of Ref. [1]. The displayed points stand for the results of the calculations of Grein and Croll [14] (open circles), the results of the partial-wave analysis of Ref. [13] (open boxes), and the experimental values from the used database (filled circles)

7. Conclusions

We have found that in the 0.4–1.3 GeV energy range, the proton-proton interaction is characterized by the following special features.

1) The inelastic interaction thresholds depend on the individual angular momentum states.

2) With respect to the orbital angular momentum, the interaction is localised for up to $L = 5$. The lowest states with $L = 0$, 1 are similar in intensity; for higher orbital angular momenta, only the singlet and the unmixed triplet states are intense.

3) The intensity of the central (spinless) interaction becomes stronger by a factor of 4.5, the spin-orbital interaction becomes weaker by a factor of 5, and the spin-spin interaction shows a weak growth.

4) Predictions of our analysis for the imaginary parts of the scattering matrix amplitudes at zero angles agree with the experimental data and with the results of the calculations of Grein and Kroll [14]. For the real parts, there are discrepancies ranging from 0.2 to 0.3 $(\text{mb/sr})^{1/2}$; we can take the magnitude of these discrepancies as a measure of inconsistency between the calculations [14] and the experimental data.

References

1. V.G. Vovchenko *et al*., Yad. Fiz. **73**, 446 (2010) [Sov. J. Nucl. Phys. **73**, 420 (2010)].
2. R.A. Arndt *et al*., Phys. Rev. C **62**, 034005 (2000), http://gwdac.phys.gwu.edu
3. H.P. Stapp, T.J. Ypsilantis, and N. Metropolis, Phys. Rev. **105**, 302 (1957).
4. J. Bystricky and F. Lehar, *Nucleon-Nucleon Data.* Part II (Karlsruhe, 1978).
5. CTU Reports *Proton-Proton Data Measured by the Nucleon-Nucleon Collaboration at Saturne II* (Czech Technical University, Prague, 2000), vol. **4**.
6. V.G. Vovchenko *et al*., in *Proc. of the 3rd Int. Symp. on Pion–Nucleon and Nucleon–Nucleon Interactions* (LNPI, Gatchina, 1989), vol. **2**, p. 13.
7. N.S. Borisov *et al.*, Pisma Zh. Eksp. Teor. Fiz. **43**, 559 (1986) [JETP Lett. **43**, 722 (1986)].
8. V.G. Vovchenko *et al*., Yad. Fiz. **50**, 1005 (1989) [Sov. J. Nucl. Phys. **50**, 625 (1989)].
9. G.N. Velichko *et al*., Yad. Fiz. **35**, 1457 (1982) [Sov. J. Nucl. Phys. **35**, 852 (1982)].
10. A.V. Dobrovolsky *et al*., Nucl. Phys. B **214**, 1 (1983).
11. G.D. Alkhazov *et al.*, Preprint LNPI-**531**, Gatchina (1979).
12. V.G. Vovchenko, V.V. Polyakov, O.Ya. Fedorov, Preprint PNPI-**2800**, Gatchina (2009).
13. J. Bystricky *et al.*, J. Phys. (Paris) **51**, 2747 (1990).
14. W. Grein and P. Kroll, Nucl. Phys. A **377**, 505 (1982).

RATIOS OF THE REAL TO IMAGINARY PART OF THE p^4He AND pn ELASTIC SCATTERING AMPLITUDES AT 0.7 GeV

G.A. Korolev, G.D. Alkhazov, A.V. Dobrovolsky, A.V. Khanzadeev, A.A. Lobodenko, A.A. Vorobyov

A method to study hadron-proton elastic scattering at small angles was proposed and developed at PNPI. The hydrogen-filled ionization chamber IKAR [1−3], which simultaneously served as a target and a detector of recoil protons, was used to measure the differential cross-sections $d\sigma/dt$ for elastic hadron scattering in the interference region of Coulomb and nuclear interactions. The interference Bethe formula was used to obtain the ratio of the real to imaginary part of the spin independent forward scattering amplitude $\rho = \mathrm{Re}\, f_{ns}(0) / \mathrm{Im}\, f_{ns}(0)$ at the proton energy in the range of 500–1000 MeV [4, 5]. The energy dependence of the ratio ρ (at $t = 0$) for $\pi^- p$ and pp elastic scattering was determined also at high energies in experiments at IHEP (Serpukhov) [6] and CERN [7].

Later, the recoil detector IKAR was used for a study of the nuclear spatial structure of neutron-rich He and Li isotopes in experiments performed at GSI (Darmstadt) [8, 9]. The differential cross sections for small-angle proton elastic scattering from the ^{4}He, ^{6}He, and ^{8}He nuclei were measured at 0.7 GeV in inverse kinematics. The obtained cross sections were used to determine the matter density distributions in ^{6}He and ^{8}He [8]. The differential p^4He cross section was measured as a consistency check of the method. The p^4He cross section [10] measured in inverse kinematics is in perfect agreement with that [11, 12] measured in direct kinematics. At the same time, a part of the data of the new experiment [10] was obtained for smaller momentum transfers as compared to the experiment [11, 12] performed in direct kinematics. The data of [10], in combination with those of [11, 12], allow us to extract information on the ratio of the real to imaginary part of the elastic p^4He scattering amplitude $\rho_{p\mathrm{He}} = \mathrm{Re}\, f_s(0) / \mathrm{Im}\, f_s(0)$, where $f_s(0)$ is the forward nuclear strong-interaction amplitude of the proton-helium elastic scattering.

The ratio ρ is an important parameter of the proton-nucleus scattering amplitude. In particular, it is needed to introduce a correction on the Coulomb-nuclear interference when measuring the total proton-nucleus cross section by the conventional transmission method. For determination of ρ from the p^4He elastic scattering cross section $d\sigma/dt$ measured in the Coulomb-nuclear interference region, the interference Bethe formula was used:

$$d\sigma/dt = N\,|f_C(t)\exp(i\varphi) + f_s(t)|^2, \qquad (1)$$

where $f_s(t)$ is the nuclear strong-interaction amplitude, $f_C(t)$ is the Coulomb amplitude, φ is the Bethe phase, N is the normalization factor ($N \approx 1.0$), and t is the four-momentum transfer squared. We have deduced the value of $\rho_{p\mathrm{He}}$ with the help of Eq. (1) analysing the data [10] on the differential cross section for p^4He elastic scattering measured in inverse kinematics in the t-range $0.002 \le |t| \le 0.020$ $(\mathrm{GeV}/c)^2$ at the corresponding proton energy E_p = 702 MeV, and the data [11, 12] obtained in direct kinematics in the t-range $0.013 \le |t| \le 0.060$ $(\mathrm{GeV}/c)^2$ at the proton energy E_p = 695 MeV (Fig. 1). The accuracy in the absolute normalization of the data of both experiments is better than 3 %. From the fit to the data, the value of $\rho_{p\mathrm{He}} = -0.06 \pm 0.06$ was deduced. The details of the fitting procedure are presented in [13]. Figure 1 shows the data and the fitted cross section.

Previously, the ratio ρ_{pp} of the real to imaginary part of the forward amplitude of proton-proton (pp) scattering was determined with good accuracy from differential cross sections for pp-scattering at small momentum transfers (in the t-range of the Coulomb-nuclear interference). Numerous experimental ρ_{pp} data up to very high energies have been compiled by the Particle Data Group. On the other hand, the existing experimental data on the ratio ρ_{pn} of the forward amplitude of proton-neutron (pn) scattering are rather sparse, being evaluated only from the data on proton-deutron (pd) scattering in the framework of the Glauber model with the fixed ρ_{pp} values. Note that experimental information on ρ_{pn} is missing at energies below 1 GeV. We have determined the value of ρ_{pn} at E_p = 0.7 GeV from our data on p^4He scattering. The differential cross-section for p^4He elastic scattering was calculated using the Glauber theory as in [8]. The calculated cross-section was fitted to the data, the free parameters being the value of ρ_{pn} and the parameters of the ^{4}He nucleon distribution. The value of ρ_{pp} was fixed to be $\rho_{pp} = 0.095$. The deduced value of ρ_{pn} is

$\rho_{pn} = -0.28 \pm 0.12$. This value is presented in Fig. 2. Other experimental data on ρ_{pn} obtained from experiments on small-angle elastic *pd*-scattering are also shown in this figure.

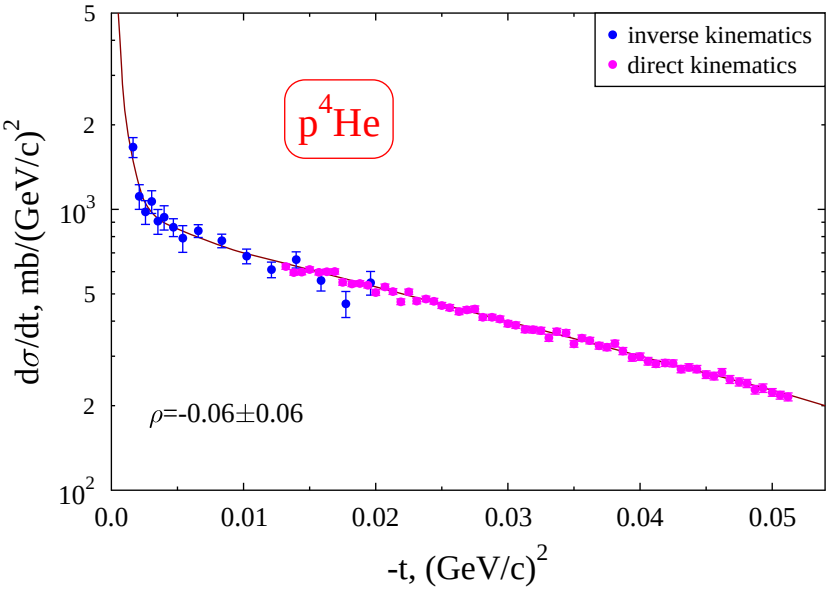

Fig. 1. Absolute differential cross sections $d\sigma/dt$ for p^4He elastic scattering used in the present analysis. The data are from the experiment in direct kinematics [11, 12] and from the experiment in inverse kinematics [10]. The shown errors are statistical only. The solid line represents the results of the fit with interference formula (1) to the measured cross section

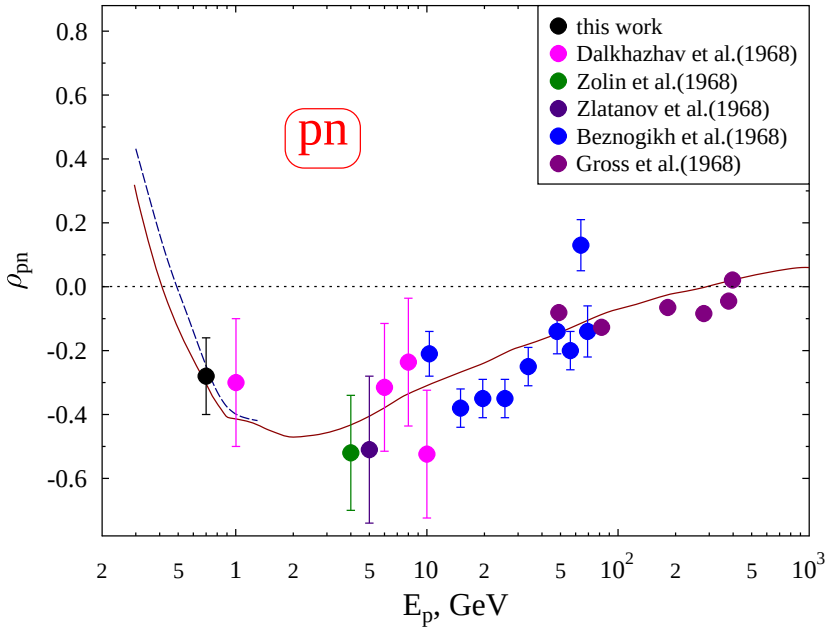

Fig. 2. Energy dependence of the ratio ρ_{pn} = Re $f_{pn}(0)$ / Im $f_{pn}(0)$ for *pn* elastic scattering. Experimental points are the value of ρ_{pn} obtained in this work and the values from experiments on small-angle elastic *pd*-scattering. The solid curve is obtained with calculations based on the FDR, the dashed curve represents the PWA predictions

As is known, the values of ρ_{pp} and ρ_{pn} can be evaluated in a wide energy range with the help of the Forward Dispersion Relations (FDR), which connect the real part of the amplitude of elastic scattering in the forward direction with the energy-integrated total cross sections for interaction of the particles and antiparticles with the target. The validity of such evaluation of ρ for *pp*-scattering was confirmed by experiment [7, 14]. The energy dependence of ρ_{pn} obtained with FDR calculations is shown in Fig. 2 by the

solid curve, whereas the dashed curve correspondes to results of the partial-wave analysis (PWA) of R. Arndt with coauthors. The value of ρ_{pn} determined in the present work at E_p = 0.7 GeV is in good agreement with that evaluated with the FDR: $\rho_{pn} = -0.30$ (see also [8]). Other experimental data on ρ_{pn} (Fig. 2) are also in accordance with the FDR predictions. We see that ρ_{pn} values calculated with the FDR describe the experimental results quite satisfactorily in a wide range of energies.

Attempts to find the intermediate-energy real parts of the forward proton-nucleus elastic scattering amplitude from the dispersion relations were not successful, particularly in the case of nucleon scattering from ^{4}He. At the same time, the values of ρ for proton-nucleus scattering can be evaluated by calculations within the framework of the Glauber theory [11, 12, 15]. It is well known that the Glauber model of multiple scattering has proved to be very successful in describing scattering of high-energy particles on composite targets. The input parameters of the nucleon-nucleon (*NN*) scattering amplitudes to be used in these calculations, namely, σ_{pp} and σ_{pn}, the total *NN* interaction cross sections, and b_{pp} and b_{pn}, the slope parameters of the corresponding differential cross sections for elastic scattering, are taken from experimental data, while the values of ρ_{pp} and ρ_{pn}, the ratios of the real to imaginary part of the *NN* elastic scattering amplitudes, can be taken from calculations based on the FDR. Figure 3 shows the value of $\rho_{p\mathrm{He}}$ obtained in the present work with the interference formula at E_p = 0.7 GeV together with the values of $\rho_{p\mathrm{He}}$ determined in other experiments at proton energies from ~ 0.2 to ~ 400 GeV. The dependence of $\rho_{p\mathrm{He}}$ on the proton energy, calculated using the Glauber theory, is also shown. It is seen that the value of $\rho_{p\mathrm{He}}$ determined in our work by analysing the cross sections for p^4He elastic scattering at E_p = 0.7 GeV is in perfect agreement with the results of the calculations. The calculated values of $\rho_{p\mathrm{He}}$ are also in satisfactory agreement with other experimental data on $\rho_{p\mathrm{He}}$ in the considered range of energies from ~ 0.2 to ~ 400 GeV.

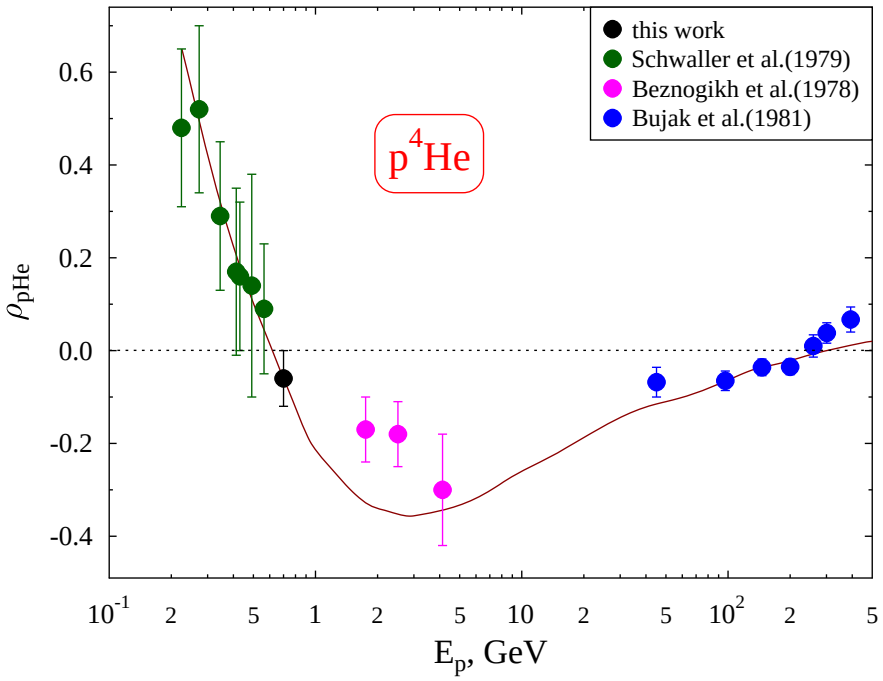

Fig. 3. Energy dependence of the ratio $\rho_{p\mathrm{He}}$ = Re $f_{p\mathrm{He}}(0)$ / Im $f_{p\mathrm{He}}(0)$ for p^4He elastic scattering. Experimental points are the value of $\rho_{p\mathrm{He}}$ obtained in this work and the values determined in other experiments. The solid curve is obtained by calculations with the help of the Glauber theory as explained in the text

To conclude, analysing the differential cross section for p^4He elastic scattering in the Coulomb-nuclear interference region we have determined the ratio of the real to imaginary part of the amplitude of p^4He elastic scattering at E_p = 0.7 GeV: $\rho_{p\mathrm{He}} = -0.06 \pm 0.06$. We have demonstrated that not only the data on the elastic *pd*-scattering but also the p^4He data in the Coulomb-nuclear interference region in combination with the known values of ρ_{pp} permit to evaluate the real-to-imaginary ratio of the *pn*-scattering amplitude. The value of $\rho_{pn} = -0.28 \pm 0.12$ at 0.7 GeV deduced from our data on p^4He elastic scattering is in good agreement with

results of the FDR calculations. The present work also confirms that the FDR for *NN* scattering and the Glauber-type calculations can be effectively used to obtain reliable values of the ratio of the real to imaginary part (at $t = 0$) of the amplitude of proton-nucleus scattering over a rather wide range of energies., The present work is described in more detail in [13].

References

1. A.A. Vorobyov, G.A. Korolev, V.A. Schegelsky *et al.,* Nucl. Instr. Meth. **119**, 509 (1974).
2. A.A. Vorobyov, Yu.S. Grigoriev, Yu.K. Zalite *et al.,* Prib. Tekh. Exp. **5**, 31 (1981).
3. A.A. Vorobyov, G.A. Korolev, A.V. Dobrovolsky *et al.,* Nucl. Instr. Meth. A **240**, 419 (1988).
4. A.A. Vorobyov, A.S. Denisov, Yu.K. Zalite *et al.,* Phys. Lett. **41** B, 639 (1972).
5. G.N. Velichko, A.A. Vorobyov, Yu.K. Zalite *et al.,* Yad. Fiz. **35**, 1457 (1982).
6. V.G. Ableev, V.D. Apokin, A.A. Vorobyov, *et al.,* Yad. Fiz. **28**, 1529 (1978).
7. J.P. Burq, M. Chemarin, M. Chevallier *et al*., Nucl. Phys. B **217**, 285 (1983).
8. G.D. Alkhazov, A.V. Dobrovolsky, P. Egelhof *et al*., Nucl. Phys. A **712**, 269 (2002).
9. A.V. Dobrovolsky, G.D. Alkhazov, M.N. Andronenko *et al*., Nucl. Phys. A **766**, 1 (2006).
10. S.R. Neumaier, G.D. Alkhazov, M.N. Andronenko *et al*., Nucl. Phys. A **712**, 247 (2002).
11. G.N. Velichko, A.A. Vorobyov, A.V. Dobrovolsky *et al.,* Yad. Fiz. **42**, 1325 (1985).
12. O.G. Grebenjuk, A.V. Khanzadeev, G.A. Korolev *et al.,* Nucl. Phys. A **500**, 637 (1989).
13. G.A. Korolev, G.D. Alkhazov, A.V. Dobrovolsky *et al.,* Yad. Fiz. **73**, 11 (2010).
14. G.N. Velichko, A.A. Vorobyov, Yu.K. Zalite *et al.,* Yad. Fiz. **35**, 1457 (1982).
15. B.H. Silverman, J.C. Lugol, J. Saudinos *et al.,* Nucl. Phys. A **499**, 763 (1989).

MECHANISM OF ONE-PION PRODUCTION IN αp-SCATTERING AT 1 GeV/NUCLEON

G.D. Alkhazov, A.N. Prokofiev, I.B. Smirnov

The one-pion and two-pion production in the $p(\alpha, \alpha')X$ reaction was studied at an energy of $E_\alpha = 4.2$ GeV in the SPES4-π experiment performed at the Saturne-II accelerator in Saclay (France) [1]. In this experiment, the scattered α particles and the charged reaction products (protons or pions) were registered with the SPES4-π set-up [2]. A study of inelastic αp scattering at an energy of ~ 1 GeV/nucleon is of significant interest since it is related, in particular, to the problem of the $N(1440)P_{11}$ (Roper) resonance. The Roper resonance is the lowest positive-parity excited state N^* of the nucleon, and in many respects it is a very intriguing and important resonance. Previously, the $p(\alpha, \alpha')X$ reaction at the energy of $E_\alpha = 4.2$ GeV was studied in an inclusive experiment [3], where only the scattered α' particles were registered. The Roper resonance observed in that experiment was interpreted by Morsch *et al*. [3] as the breathing-mode ($L = 0$) monopole excitation of the nucleon. In this interpretation, the $N(1440)$ resonance mass is related to the compressibility of the nuclear matter (on the nucleonic level). This resonance plays an important role in the three-body nuclear forces, in the swelling of nucleons in nuclei, and in many intermediate-energy processes, in particular, in pion production in αp scattering. The investigation of the $N(1440)$ resonance was the goal of a number of theoretical and experimental studies since the nature of this resonance is still not properly understood. An advantage of studying the Roper resonance in an αp scattering experiment, as compared to πN, NN and γN experiments, is that in the case of αp scattering the number of the reaction channels is rather limited. At an energy of ~ 1 GeV/nucleon, the Roper resonance is strongly excited, whereas the contribution of other baryon resonances is expected to be small.

According to theory, only three reaction channels dominate in inelastic αp scattering at $E_\alpha \approx 1$ GeV/nucleon. The first one (Fig. 1a) corresponds to excitation of the Δ resonance in the α-particle projectile, while the second and third ones (Figs. 1b, c) correspond to excitation of the Roper resonance in the target proton mainly through exchange of a neutral "sigma meson". The contribution of other channels is practically negligible. Note that due to isoscalar nature of the α particle and isospin conservation, direct excitation of the Δ resonance in the proton is forbidden. The final-state products from the $p(\alpha, \alpha')X$ reaction may be either a nucleon (a proton or a neutron) and one pion resulting from decay of the Δ or Roper resonances (Fig. 1, diagrams a, b), or a nucleon and two pions resulting from decay of the Roper resonance (Fig. 1, diagram c). The two-pion production in the $p(\alpha, \alpha')X$ reaction studied in the SPES4-π experiment [1] was discussed in [1, 4, 5]. Here, we discuss the one-pion production in this reaction [6, 7].

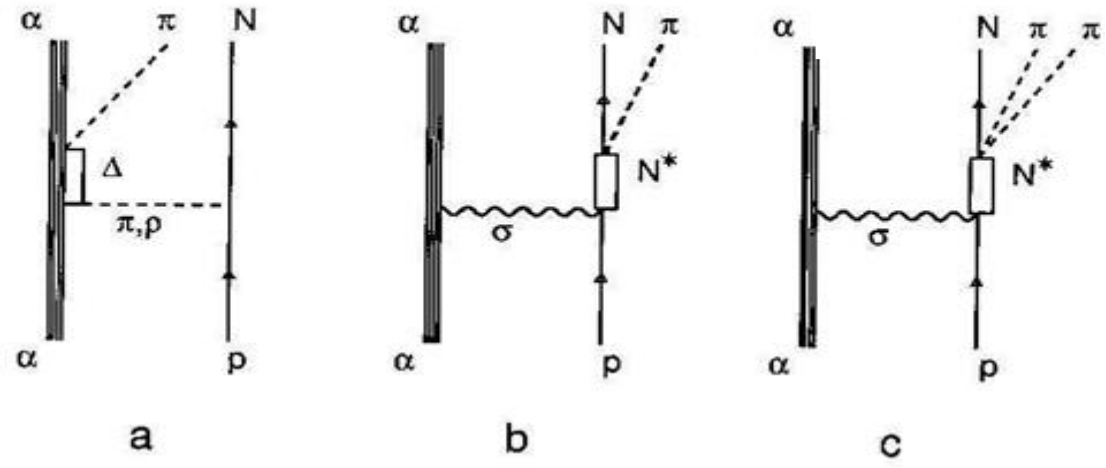

Fig. 1. Main diagrams contributing to the $p(\alpha, \alpha')X$ reaction: a – Δ excitation in the α-particle projectile with the following one-pion decay; b – N^* excitation in the target proton with the following one-pion decay, and c – N^* excitation in the target proton with the following two-pion decay

We remind that in the SPES4-π experiment the α particles scattered on the liquid-hydrogen target at an angle of 0.8 ± 1.0° were registered with the SPES4 spectrometer. The experiment was carried out at four magnetic-rigidity settings of the SPES4 spectrometer with $q_{\alpha'}/Z$ = 3.35, 3.25, 3.15 and 3.06 GeV/c (where $q_{\alpha'}$ is the momentum of the scattered α particles, and $Z = 2$ is the α-particle charge), which gave us an opportunity to study the reaction at an energy transfer from –0.15 to –0.9 GeV. The forward spectrometer (FS), which consisted of an analyzing large-gap dipole magnet and a hodoscope of scintillation counters, allowed to identify the secondary charged particles (protons and pions) and to reconstruct their trajectories and momenta. The identification of the particles in the FS was performed on the basis of the energy-loss and time-of-flight measurements. The SPES4-π set-up and the method of the track reconstruction are described in detail in [2]. The measured momenta $\boldsymbol{q}$ of the scattered α particle and secondary particles were used to determine the missing mass M_{miss} and the invariant masses $M(N\pi)$ and $M(\alpha'\pi)$ for the one-pion production channel, and $M(N\pi\pi)$ and $M(\alpha'\pi\pi)$ for the two-pion production channel. In the case when protons are detected with the FS, the missing mass M_{miss} is the mass of the object X in the $p(\alpha, \alpha')pX$ reaction, the object X consisting of one or two pions. In the case when π^+-pions are detected with the FS, the missing mass M_{miss} is the mass of the object X in the $p(\alpha, \alpha')\pi^+X$ reaction, the object X consisting of a neutron or a neutron and a π^0-pion.

The missing mass spectra obtained at the four SPES4 settings are shown in Fig. 2. The left panel of this figure presents the distributions of events as a function of the missing mass M_{miss} for the case of π^+ registration by the FS. The spectra include the sum of events from the one-pion and two-pion production channels. For the momentum setting 3.35 GeV/c, only one peak at M_{miss} = 0.94 GeV/c^2 corresponding to the mass of the neutron is seen. The width of this peak reflects the experimental resolution of the reconstructed values of M_{miss}. Evidently, this peak contains one-pion events appearing due to decay of Δ excited in the projectile α particle. At the momentum settings 3.15 and 3.06 GeV/c, the contributions of two-pion events

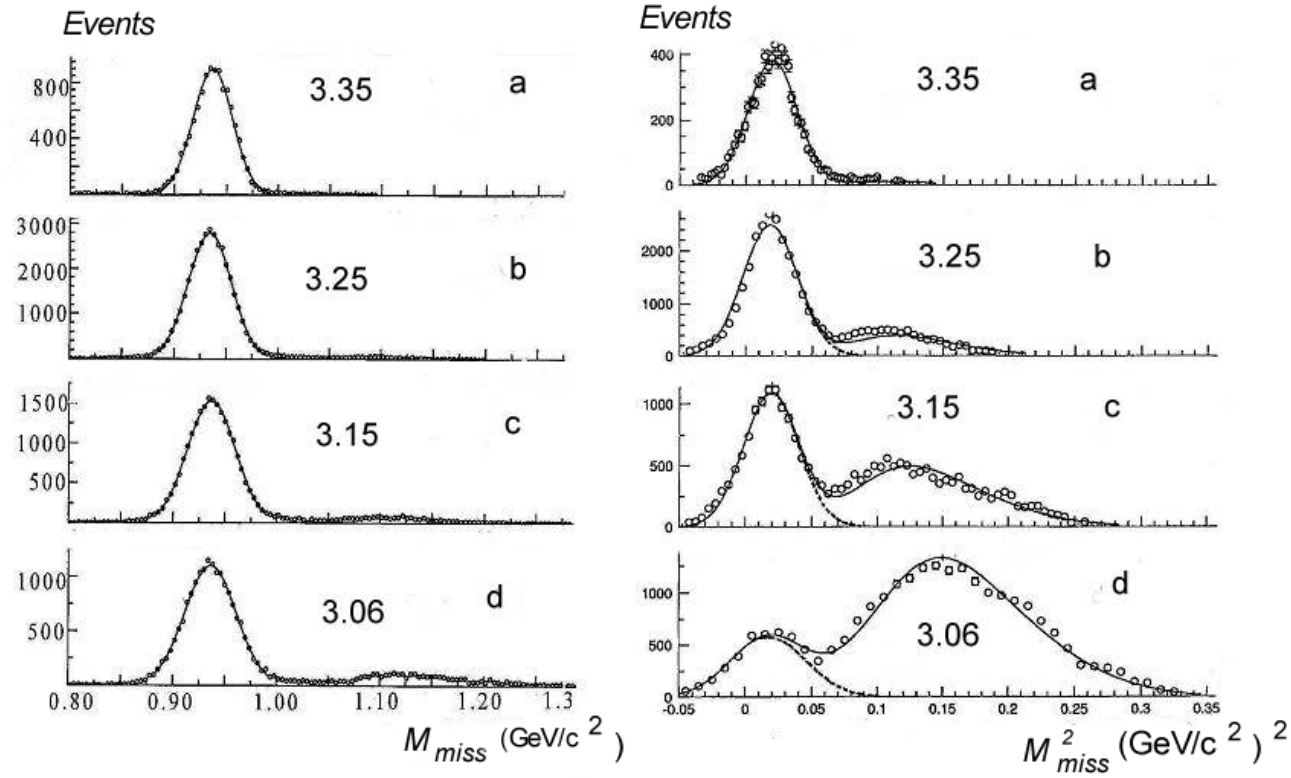

Fig. 2. Missing mass spectra for the $p(\alpha, \alpha')\pi^+X$ (left panel) and $p(\alpha, \alpha')pX$ (right panel) reactions for the SPES4 momentum settings $q_{\alpha'}/Z$ = 3.35 (a), 3.25 (b), 3.15 (c), and 3.06 GeV/c (d). Dots are experimental points. The distributions of the one-pion events are described by Gaussians (solid lines in the left panel and dashed lines in the right panel). The solid lines in the right panel are the sums of the one-pion production and two-pion production simulated distributions, normalized to the experimental data

(at $M_{miss} > M_n + M_\pi$) are observed. The right panel of Fig. 2 presents the distributions of events as a function of M^2_{miss} for the case of proton registration by the FS. It is seen that for the setting 3.35 GeV/c a peak at $M^2_{miss} = 0.02$ (GeV/c^2)^2 (that is at $M_{miss} = M_\pi$) dominates in the spectrum. Evidently, this peak is due to one-pion events mostly produced in the decay of the Δ resonance excited in the scattered α particle, as it was discussed earlier. A slight tail at high masses in the spectrum is presumably due to a small contribution of two-pion events from the low-mass tail of the Roper resonance excited in the proton. By imposing the proper cuts on the values of M_{miss} (or M^2_{miss}) we can select only one-pion or only two-pion events.

The selected one-pion events were qualitatively analyzed by comparing the Dalitz plots of the experimental data for one-pion production with the Dalitz plots of the simulated events for one-pion production via excitation and decay of the Δ and Roper resonances. Figures 3 and 4 present the Dalitz plots of the one-pion events for the cases when pions (Fig. 3) and protons (Fig. 4) are registered by the FS.

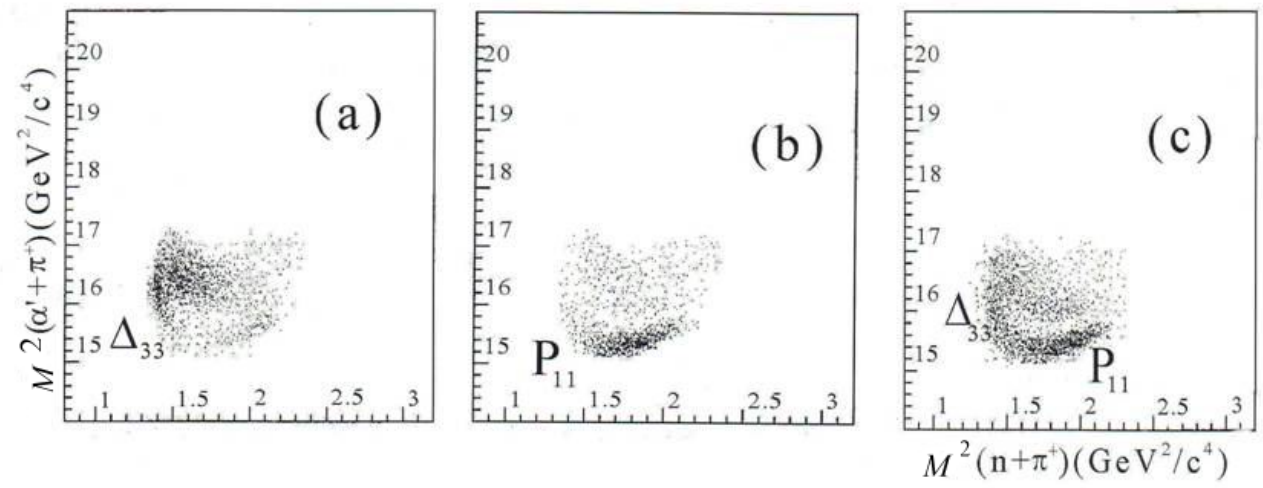

Fig. 3. Dalitz plots for the $p(\alpha, \alpha')n\pi^+$ reaction. a – simulated events of the Δ resonance decay; b – Simulated events of the Roper resonance decay; c – experimental data. Here (and in Fig. 4) the data of all SPES4 momentum settings, properly normalized, are included

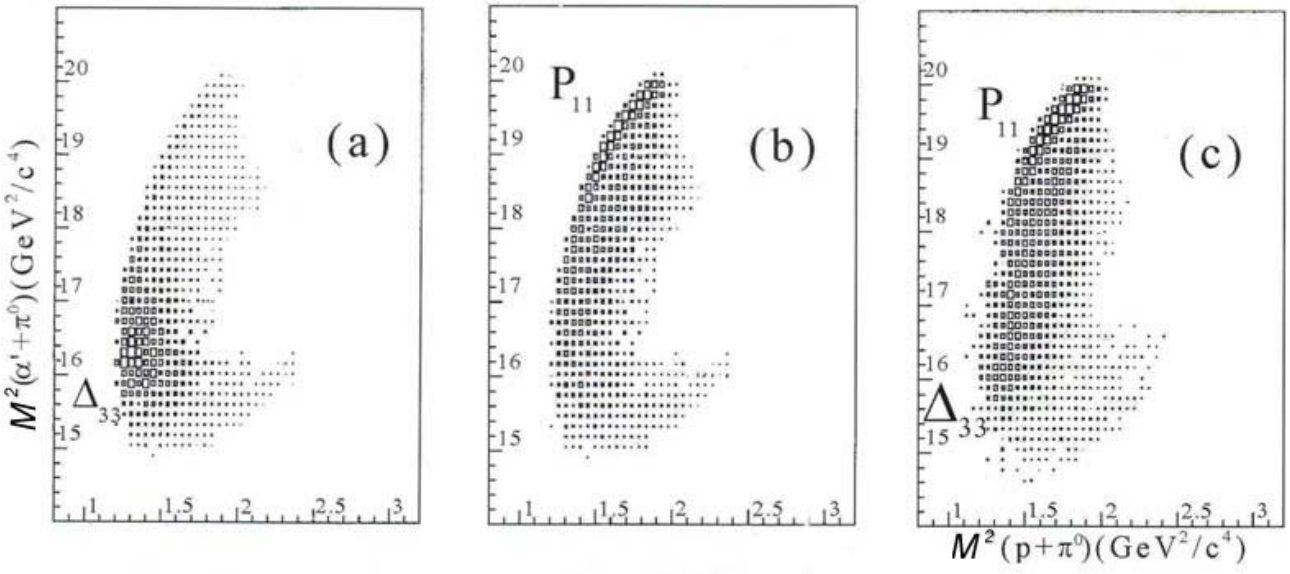

Fig. 4. Dalitz plots for the $p(\alpha, \alpha')p\pi^o$ reaction. a – simulated events of the Δ resonance decay; b – simulated events of the Roper resonance decay; c – experimental data

Comparing the Dalitz plots of the experimental data (Fig. 3c and Fig. 4c) with the Dalitz plots of the simulated events (Figs. 3a, b and Figs. 4a, b) we can conclude that the events in the spots where the experimental data are concentrated in the Dalitz plots correspond to the simulated events from the decay of Δ and Roper resonances. Moreover, the positions of these spots in the Dalitz plots tell us (in agreement with theory) that the Roper resonance is excited really in the target proton, whereas the Δ resonance is excited in the projectile α particle. Indeed, the positions of the maxima in the $M^2(N\pi)$ spectra (as follows from Fig. 3c and Fig. 4c) for the Roper events are approximately the same in both cases when protons and pions are detected, as it should be for the Roper resonance excitation in the target protons. On the other hand, the positions of the maxima in the $M^2(\alpha'\pi)$ spectra in these two cases are very different, which proves that the Roper resonance is excited not in the projectile α particles, but in the target proton. Some depletion of events in Fig. 4c in the region $M^2(p\pi^0) = 1.3–1.4$ $(\mathrm{GeV}/c^2)^2$ and $M^2(\alpha'\pi) = 17–18$ $(\mathrm{GeV}/c^2)^2$ can be interpreted as an indication of destructive interference between the processes of one-pion production through excitation and decay of the Delta and Roper resonances. Note that according to theoretical considerations this interference gives a negative contribution to the cross section for the considered reaction.

To conclude, the experimental Dalitz plot spectra obtained in the SPES4-π experiment were qualitatively compared with the simulated Dalitz plot spectra based on the theoretical predictions of the Valencia university group. The experimental data are in full agreement with theoretical predictions that the main processes of one-pion production in the $p(\alpha, \alpha')X$ reaction are excitation and decay of the Δ resonance in the α-particle projectile and excitation and decay of the Roper resonance in the target proton. Moreover, the data are in agreement with the prediction that these two processes abear destructive interference.

The experimental data discussed in this report were obtained by the SPES4-π Collaboration. The PNPI participants of the SPES4-π experiment were G.D. Alkhazov, A.V. Kravtsov, V.A. Mylnikov, E.M. Orischin, A.N.Prokofiev, B.V. Razmyslovich, I.B.Smirnov, I.I. Tkach, S.S. Volkov, and A.A. Zhdanov.

References

1. G.D. Alkhazov *et al*., Phys. Rev. C **78**, 025005 (2008).
2. G.D. Alkhazov *et al*., Nucl. Instr. Meth. A **551**, 290 (2005).
3. H.-P. Morsch *et al*., Phys. Rev. Lett. **69**, 1336 (1992).
4. G.D. Alkhazov, A.V. Kravtsov, A.N. Prokofiev, in *PNPI, High Energy Physics Division, Main Scientific Activities, 2002–2006*, Gatchina, 2007, p. 147.
5. G.D. Alkhazov *et al*., Phys. At. Nucl. **71**, 1302 (2008).
6. G.D. Alkhazov *et al*., arXiv 1102 15644v1 [nucl-ex] (2011).
7. G.D. Alkhazov *et al*., Phys. At. Nucl. **75**, 1067 (2012).

RATIO R_{dp} OF QUASI ELASTIC $nd \to pnn$ TO ELASTIC $np \to pn$ EXCHANGE DIFFERENTIAL CROSS SECTIONS AT ZERO PROTON EMISSION ANGLE IN THE ENERGY RANGE 0.55–2.0 GeV

PNPI participants of the Delta-Sigma Collaboration:
A.N. Prokofiev, A.A. Zhdanov

Understanding of the *NN* interaction is fundamental for the whole of nuclear and hadron physics. The database on proton-proton elastic scattering is enormous. It includes the data on scattering cross sections and some different polarization parameters, and allows extraction of the *NN* phase shifts in the $I = 1$ isospin channel up to the beam energy approximately 2.5 GeV. The situation is less favorable for the isoscalar channel. Much poorer neutron-proton scattering data permit only to evaluate the $I = 0$ phase shifts up to 1.3 GeV, at most. It has been recently shown that, even without measuring rather complicated triple-spin dependent observables, some data on this channel can be received in the case if the results of experiments on deuterium are included into general considerations.

Experiments on charge exchange scattering of protons or neutrons on deuterons have a very long history [1]. First theoretical papers that dealt with this subject seem to date from 1950s. It is quite clear, that, except the Coulombs effects, the cross section for the reaction $nd \to pnn$ should be the same as that for $pd \to ppn$. The spectrum of secondary particles in the forward direction in this reaction exhibits a very strong peak at the energy which is only slightly smaller than that of the incident proton. The proton and neutron bound in a deuteron are in a superposition of the $^3S_1$ and $^3D_1$ states, and their spins are parallel. On the other hand, if the four momentum $t = -\mathbf{q}^2$ between the incident neutron and the final proton in the reaction $nd \to p\{nn\}$ is very small, then the Pauli principle demands the neutrons $\{nn\}$ emerging with a rather small relative momentum to be in the spin singlet states $^1S_0$ and $^1D_2$. The peaking observed in the energy spectrum of the outgoing protons is due to a huge neutron-neutron scattering length, which leads to a very strong final-state interaction between the neutrons. A detailed evaluation of the proton spectra from the $nd \to pnn$ reaction evidently depends on the deuteron and *nn* wave functions, *i.e.* upon low energy nuclear physics. According to the major advance (made by N.W. Dean [2]) it has been shown that if one integrates over all proton energies, there is a closure sum rule where all dependences from the *nn* wave function vanish:

$$(\mathrm{d}\sigma/\mathrm{d}t)_{nd\to p\{nn\}} = (1 - F(q))\ (\mathrm{d}\sigma/\mathrm{d}t)^{\mathrm{SI}}_{np\to pn} + (1 - (1/3)F(q))\ (\mathrm{d}\sigma/\mathrm{d}t)^{\mathrm{SF}}_{np\to pn}. \quad (1)$$

Here, $F(q)$ is the deuteron form factor. The differential cross section $(\mathrm{d}\sigma/\mathrm{d}t)_{np\to pn}$ for *np* elastic scattering is split into two parts. The first represents the contribution that is independent of any spin transfer (SI) between the initial neutron and the final proton, and the second one is the spin flip (SF) process. If the beam energy is high, then in the forward direction $\mathbf{q} = 0$, $F(0) = 1$, and Eq. (1) reduces to:

$$(\mathrm{d}\sigma/\mathrm{d}t)_{nd\to p\{nn\}} = (2/3)\ (\mathrm{d}\sigma/\mathrm{d}t)^{\mathrm{SF}}_{np\to pn}. \quad (2)$$

Now, we can determine R_{dp} parameter as the ratio of the quasi elastic $nd \to p\{nn\}$ charge exchange scattering differential cross section at zero degree to the corresponding free $np \to pn$ scattering elastic cross section:

$$R_{dp}(0) = (\mathrm{d}\sigma/\mathrm{d}t)_{nd\to p\{nn\}} / (\mathrm{d}\sigma/\mathrm{d}t)_{np\to pn} = (2/3)(\mathrm{d}\sigma/\mathrm{d}t)^{\mathrm{SF}}_{np\to pn} / (\mathrm{d}\sigma/\mathrm{d}t)_{np\to pn}. \quad (3)$$

As follows from Eq. (2) and (3), the ratio of the two unpolarized cross sections can provide information on the spin dependence of neutron-proton interaction.

Experiment

We have obtained new experimental data on the ratio R_{dp} of the quasi-elastic charge-exchange scattering cross section for the $nd \to p\{nn\}$ reaction with the outgoing proton at the angle $\theta_{p,\mathrm{lab}} = 0^\circ$ to the elastic $np \to pn$ charge exchange scattering cross section. The measurements were carried out at the NUCLOTRON accelerator (JINR, Dubna) at neutron beam kinetic energies 0.55, 0.8, 1.0, 1.2, 1.4, 1.8, and 2.0 GeV. An

intense neutron beam with a small momentum spread was produced by breakup of the accelerated deuterons. In study of both the reactions, the outgoing protons were detected with the momentum $\mathbf{p}_p$ approximately equal to the incident neutron momentum in the direction close to that of the incident neutron beam, *i.e.* in the vicinity of the scattering angle $\theta_{p,\,lab} = 0^o$. The data were obtained with a set-up (Fig. 1) consisting of an analysing magnet SP-94 and two sets of multiwire proportional chambers, located downstream and upstream of the magnet. The time-of-flight measurement system was applied to identify the detected particles. The influence of the inelastic background processes was considerably reduced by an additional detector system surrounding the liquid hydrogen (or deuterium) target. Some calibration measurements were performed with polyethylene CD or CH targets.

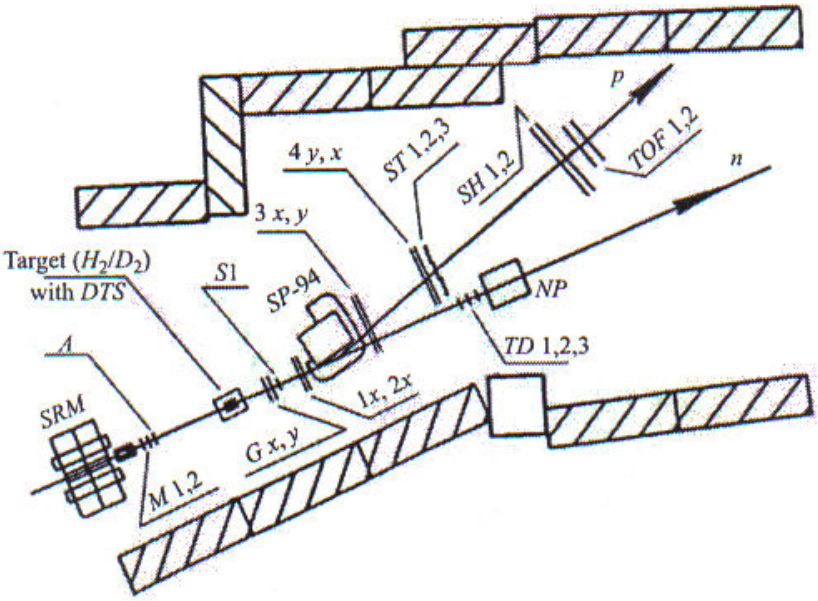

Fig. 1. Magnetic spectrometer for detection of protons scattered at zero degree laboratory angle in the $nd \to pnn$ and $np \to pn$ charge-exchange reactions. SP-94 is the analysing dipole magnet; Gx, y, $1x$, $2x$, $3x, y$, $4y, x$ are multiwire proportional chambers; H_2/D_2 is the liquid hydrogen/deuterium target; S1, TOF1,2, A, and ST1,2,3 are the time-of-flight and trigger counters

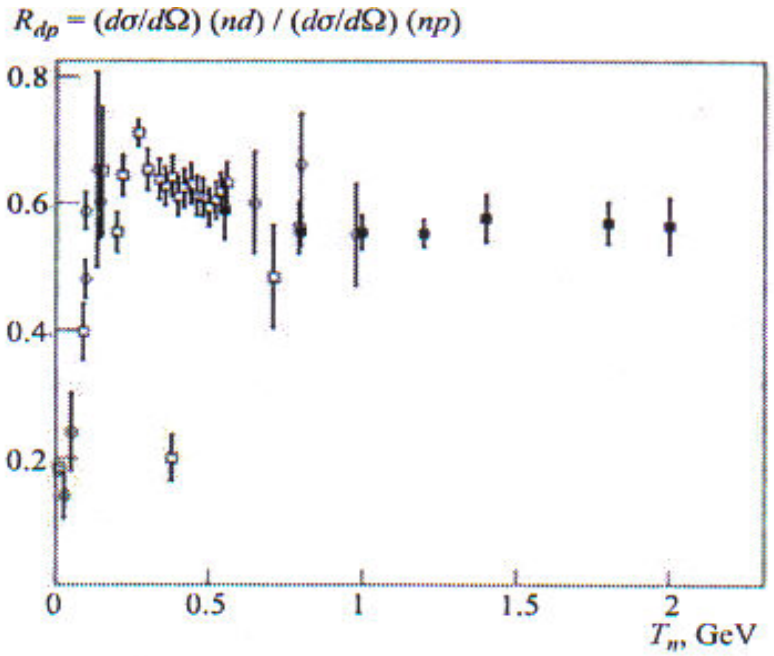

Fig. 2: Energy dependence of R_{dp}. Black squares – this experiment [3–5], open squares and circles – the existing data at energies below 1 Gev [1]. The open squares represent the data obtained in $nd \to p\{nn\}$ reaction measurements and the open circles represent the data obtained in either $pd \to npp$ or $dp \to ppn$ reaction measurements. The point at $T_n = 0.98$ GeV is from the hydrogen bubble chamber experiment carried out at JINR [6]

The obtained results for $R_{dp} = [(d\sigma / d\Omega)\ (nd)] / [(d\sigma / d\Omega)\ (np)]$ are shown in Fig. 2. The ratios of the quasi-elastic $nd \rightarrow p\{nn\}$ charge-exchange yield to the free elastic $np \rightarrow pn$ yield were measured at 0.55, 0.8, 1.0, 1.2, 1.4, 1.8, and 2.0 GeV. The present data are obtained for the first time for the energy above 1 Gev [3–5]. We have found that the R_{dp} values are relatively large (close to 0.56) and almost independent of energy, at least up to 2 GeV. The used experimental method has provided very precise results. The systematic uncertainties are small since both the cross sections were measured with the same set-up. A reasonably quick replacement of the "full' and "empty" targets allowed to suppress possible systematic errors caused by influence of time and temperature drifts of the detector efficiency. The obtained data were compared with the results of different phase shift analyses in the region of confident *np* scattering data (below 1.3 GeV) [7]. It was found that our data are in good agreement in this region with the results of earlier experiments. In general, the data seem to be rather far from the allowed theoretical limit of 0.67. On the other hand, the phase shift analysis (PSA) [7] predicts that the contribution from the spin-independent term should be very small in the region of our investigation. The data of the present work might help to understand this disagreement.

References

1. F. Lehar, C. Wilkin, arxiv:0911.1699v1[nucl-ex] (2009).
2. N.W. Dean, Phys. Rev. D **5**, 1661 (1972); Phys. Rev. D **5**, 2832 (1972).
3. V.I. Sharov *et al.,* Czech. J. Phys. **56**, F117 (2006).
4. V.I. Sharov *et al*., Eur. Phys. J. A **39**, 267 (2009).
5. V.I. Sharov *et al*., Phys. Atom. Nucl. **72**, 1007 (2009).
6. V.V. Glagolev *et al*., JINR Communication P1-2006-**112**, JINR, Dubna (2006).
7. R. Arndt *et al*., Phys. Rev. C **76**, 025209 (2007), http://gwdec.phys.gwu.edu

Nuclear and Atomic Physics

DIRECT PRECISE MASS MEASUREMENT OF NOBELIUM AND LAWRENCIUM ISOTOPES BY THE SHIPTRAP FACILITY

PNPI participants of the SHIPTRAP Collaboration:
S.A. Eliseev, D.A. Nesterenko, Yu.N. Novikov, and G.K. Vorobjev

1. Introduction

One of the intriguing problems of nuclear physics in the second half of the last century was the possible existence of the mysterious island of superheavy stable nuclides with the "magic" proton and neutron numbers $Z = 114$ and $N = 184$, respectively. It was thought that this island was situated far off the last known stable nuclides of the Periodic Table of Elements. Among many open questions, it is interesting to learn whether the physical-chemical properties of the new elements in this island obey the universal law of periodicity. Besides, the unusual nuclear physical properties of very heavy nuclides (ultra-high spin values and large radii) and of heavy nuclear matter ($A \approx 300$), as well as specific nuclear dynamics of their production, engrossed the attention of investigators. Dramatic efforts have been undertaken to reach this enigmatic region by methods of hot and cold complete fusion in heavy ion reactions [1]. In addition, the search for these superheavy elements in nature has also been carried out.

Step-by-step experiments performed over many decades have led to success: a dozen of new elements was discovered by the end of the last century, mainly at the SHIP facility at GSI (Darmstadt) [2]. However, the proton magic number of $Z = 114$ had not yet been reached. Only at the very beginning of the 21-st century, the team from JINR (Dubna) [1, 3] succeeded in discovering nuclides of heavy elements with Z up to $Z = 118$. Although the doubly-magic nuclide was not observed, the performed activity unambiguously showed that superheavies are not fully unstable as the liquid drop model predicts – the measured half-lives of superheavies typically exceed 1 ms.

The position of the maximal stability (the peak of the island) is still unknown. To identify this peak in experiments, one needs to invent new ingenious methods of production. At the same time, the absolute mass mapping of the known region of superheavies can help to make certain predictions of a possible position of the maximal stability. While this mass landscape is so far unknown, it can be determined by direct measurements of masses of superheavy nuclides. Since all known superheavies have been identified by the α-decay chains and α-decay energies have been measured, an independently measured mass value (*i.e.*, the total binding energy) of one of the nuclides in the α-chain will allow one to determine the masses of all the others. In order to fulfill the mass mapping of the known superheavies, about ten mass values of nuclides in different α-chains should be directly measured [4]. This program of direct mass measurements of transfermium nuclides – as a first foray into the region of transuranium – was developed at the SHIPTRAP facility of GSI with participation of PNPI physicists.

The mass mapping can also help to identify new possible semimagic nuclides (*e.g.*, with $N = 152$, *etc.*). The semimagic structure of superheavies may be typical for this region due to strong influence of the shell structure effects, which possibly stabilize these very heavy nuclides. However, to recognize irregularities in the mass landscape, a wide mass mapping is needed. The implementation of this program has started at GSI with the use of the ionic Penning trap – the most precise system for mass measurements presently known [5].

2. The experimental installation

The SHIPTRAP facility is a Penning trap system installed behind the velocity filter SHIP, which was used in the past for identification of new elements of the Periodic Table [2]. Thus, the production conditions for transfermium elements are very well known. A schematic overview of SHIPTRAP is given in Fig. 1, and a picture of SHIPTRAP is shown in Fig. 2.

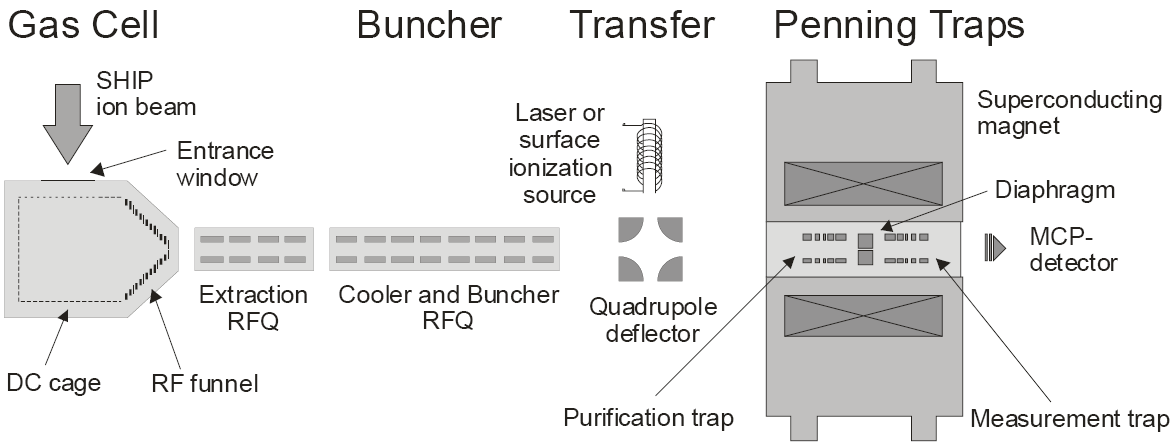

Fig. 1. The scheme of the Penning trap set-up at GSI

Fig. 2. Overview photo of the SHIPTRAP facility

The nobelium and lawrencium isotopes were produced in fusion-evaporation reactions of ^{48}Ca ions accelerated to about 4.5 MeV/u with isotopically enriched ^{206,207,208}Pb and ^{209}Bi target nuclides. They were separated from the primary beam by SHIP and sent to SHIPTRAP with the kinetic energy of about 40 MeV. After slowing down by the mylar degrader foils and the 2 mg/cm^2-thick titanium entrance window of the gas cell, the ions were stopped in ultrahigh-purity helium gas kept at the pressure of 50 mbar. After extraction from the gas cell, they were cooled, bunched, and accumulated by the radiofrequency quadrupole ion trap (see Fig. 1). Afterwards, the ions were transferred to the double Penning trap system hosted by a superconducting 7 T solenoid magnet. In the first purification trap, the isobars can be separated with a mass resolving power of up to 10^5. In the second trap, the ions are excited by the external RF field, and the cyclotron frequency is determined with the time-of-flight ion-cyclotron-resonance method. For a successful fit of the resonance curve, at least about 30 ions must be detected. In the case of ^{256}Lr, a resonance with only

48 ion counts took 93 hours. For such a long measurement, the temporal stability of the magnetic field is critical for the accurate mass measurement. To reduce the drift of the cyclotron frequency, active stabilization was implemented for the pressure in the liquid helium cryostat and also for the temperature in the bore of the superconducting magnet. As a result, the drift of only $2 \cdot 10^{-9}$ per day was obtained [6].

More precisely, the mass is determined by comparing the cyclotron frequency of the ion of interest with that of a reference ion with the well-known mass. In the present case, the ion of $^{133}Cs^{+}$ has the m/q ratio similar to that of doubly-charged nobelium and lawrencium ions. The statistical uncertainty depends on the number of detected ions per resonance and on the Fourier-limit based resolution $\Delta\nu \approx 1/\tau$, where τ is the observation time. In addition, the systematic uncertainties of $4.5 \cdot 10^{-8}$ are taken into account.

The time-of-flight resonance detection technique was used to measure the ion cyclotron frequency,

$$\omega_c = \frac{q}{m} B, \tag{1}$$

where q is the charge and B is the magnetic field strength, thus determining the mass m of the ion. The atomic mass value can be determined from the equation:

$$m_{\text{atom}} = \frac{Z}{Z_{ref}} \cdot (m_{\text{atom,ref}} - Z_{\text{ref}} \cdot m_e) \cdot r + Z \cdot m_e, \tag{2}$$

where m_e is the electron mass; m_{atom} and $m_{\text{atom,ref}}$ denote the atomic masses; r is the ratio of the cyclotron frequencies $r = \nu_{c,\text{ref}} / \nu_c$; Z and Z_{ref} are the charges of the ion under investigation and of the reference ion, respectively. In the present measurement, doubly-charged nobelium and lawrencium ions were investigated ($Z = 2$), which led to a decrease of the relative uncertainty. Furthermore, the observation of doubly-charged ions indicates that helium gas in the cell and in the purification trap is of high purity.

For calibration of the magnetic field, singly-charged ^{133}Cs ions from a surface ion source can be chosen as reference. The obtained weighted mean frequency ratios for $^{252–255}No$ and $^{255,256}Lr$ are presented in Table 1. The uncertainty includes statistical variations, nonlinear magnetic-field changes and the residual systematic uncertainty. For each nobelium isotope, at least three measurements were performed. The atomic mass m_{atom} was determined from the frequency ratios and, thus, the mass excess $ME = m_{\text{atom}} - A$ was found. The nuclear mass can be derived from the atomic mass according to the relation $m_{\text{nucl}}(A, Z) = m_{\text{atom}}(A, Z) - Zm_e - B_e(Z)$, where m_{nucl} is the nuclear mass and $B_e(Z)$ is the electron binding energy for an atom with the atomic number Z.

3. Results

As an example, in Fig. 3 we present the time-of-flight cyclotron resonance curves for ^{254}No and ^{256}Lr. Details of all the ions produced and investigated in this work [7, 8] are summarized in Table 1.

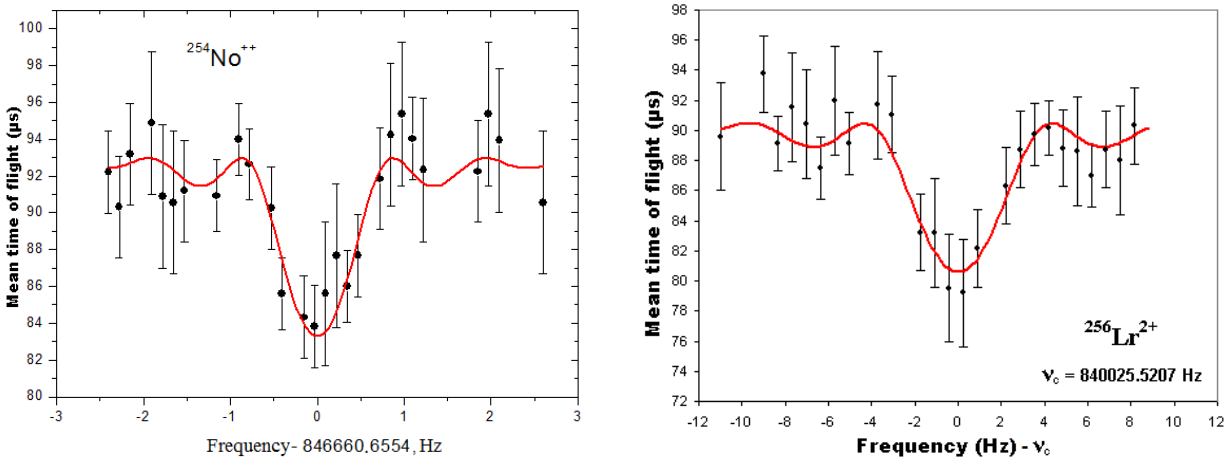

Fig. 3. The time-of-flight resonance curves for ^{254}No and ^{256}Lr ions measured by SHIPTRAP

All of our measurements have improved the accuracy of the mass values. Indeed, the earlier uncertainties in the mass of ^{252}No and ^{254}No were decreased by a factor of 1.4 and the masses of ^{255}No, ^{255}Lr and ^{256}Lr were measured for the first time [9].

For even-even nuclides, the α-decay occurs predominantly from the ground-state to the ground-state. In this case, the directly measured new mass values can be combined with the results of decay spectroscopy to reach higher-Z nuclides in a straightforward way. In particular, a recent study of ^{270}Ds performed at SHIP has discovered the α-decay branch of ^{262}Sg, providing the missing link connecting the decay chain of ^{270}Ds (Z = 110) to ^{254}No. Thus, it will now be possible to determine the mass of ^{270}Ds with an uncertainty of 40 keV and to provide the presently highest-Z anchor point in the SHE region.

Table 1

Properties of investigated nobelium and lawrencium isotopes

Isotope	$T_{1/2}$ (ground state)	$T_{1/2}$ (isomer)	Cross section, nb	Production rate, s	Frequency ratio	Mass-values ($M - A$), keV
^{252}No	2.44(4) s	110(10) ms	400	0.83	0.94837684(5)	82870(16)
^{253}No	1.62(15) min	31 μs	1000	~2	0.95214494(5)	84356(13)
^{254}No	51(10) s	266(2) ms	1800	3.74	0.95590852(4)	84726(14)
^{255}No	3.1(2) min		140	0.29	0.95967902(4)	86808(15)
^{255}Lr	30(4) s	2.5(1) s	300	0.86	0.95969174(5)	89958(16)
^{256}Lr	28(3) s		60	0.17	0.9634610(3)	91746(83)

For other investigated nuclides, the situation is more complex since the strongest α-decays populate the excited states in the daughter nucleus. For many nuclides, detailed decay-spectroscopy data are either lacking or still inconclusive because unambiguous level schemes are not available. In these cases, the new ground-state mass values from direct mass measurements provide important data. For example, the SHIPTRAP mass value of ^{255}No can be used to determine the masses of its daughters linked by the α-decay (^{247}Cf) and electron capture (^{247}Bk). After evaluation of the recent α-spectroscopy data for the nuclides above ^{255}No, the combination with the mass value of ^{255}No will establish the mass of ^{271}Ds (Z = 110).

Mass estimations of superheavy nuclides linked to odd-odd nuclide are even more complicated than in the cases discussed above. The heaviest radionuclide studied so far by Penning trap mass spectrometry, ^{256}Lr, has only recently been studied by α-decay spectroscopy, and it shows a complex spectrum involving several excited states yet unassigned. In the future, the establishment of the relevant states involved in the α-decay chain starting at ^{272}Rg (Z = 111) will allow us to use the mass of ^{256}Lr as an anchor point to fix the mass of ^{272}Rg. The current moderate mass uncertainty results from just a single measurement done at the lower resolution due to beam-time limitations. In future experiments, it will be improved by an order of magnitude similarly to the other studied isotopes.

The nuclides with the directly measured mass values and their links to superheavies *via* α-decay chains are shown on the chart of transuranium nuclides in Fig. 4.

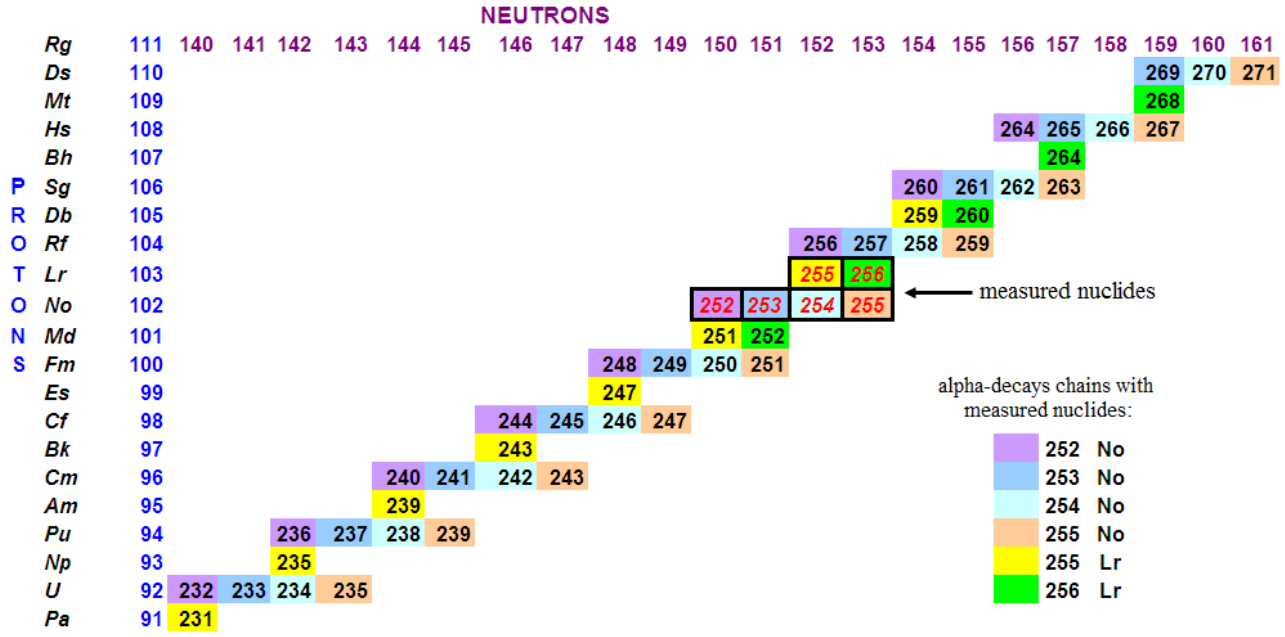

Fig. 4. α-decay chains whose masses can be precisely determined after direct mass measurements of nobelium and lawrencium isotopes (indicated in the squares)

4. Conclusions and outlook

The masses of $^{255}No^{2+}$ and $^{255-256}Lr^{2+}$ nuclides were directly measured with the SHIPTRAP facility for the first time, with the uncertainties ranging down to 15 keV. The masses of ^{254}No and ^{252}No already known from an indirect determination were measured directly, and the previous mass uncertainties were further decreased. The nuclide of ^{256}Lr had the lowest yield (about 10 ions per minute) when investigated at the on-line Penning-trap mass spectrometer. It is the heaviest nuclide of the chart of the nuclides whose mass has ever been measured. Figure 5 shows how much the precision of the measured value is superior to the evaluated one [9]. A combination of the present results with spectrometric data allows one to fix the masses of the nuclides as heavy as ^{270}Ds ($Z = 110$). Thus, experiments with SHIPTRAP pave the way for investigation of superheavy elements and other very exotic nuclides. The performed investigation can be considered as a first step in the long-term program of the precise mass landscape determination of superheavy nuclides by means of the Penning trap mass spectrometry.

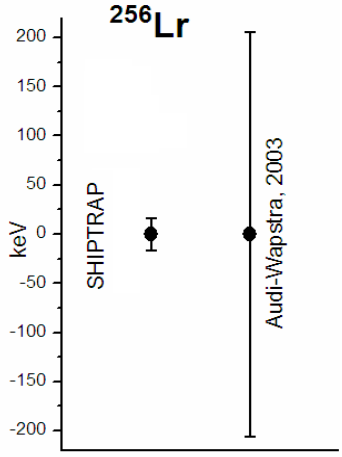

Fig. 5. Comparison of the measured (in this work) and evaluated [10] mass values of ^{256}Lr

Our further plans concern the extension of the region of measurements towards rutherfordium isotopes. This can be done with the titanium beam, which is now under commissioning at the UNILAC linear accelerator at GSI. As the expected yields of rutherfordium are even smaller than those of lawrencium, suppression of the background becomes an important problem. This problem can be solved by replacement of the gas cell with the cryogenic one [11] that is currently under construction. However, a dramatic change in sensitivity of SHIPTRAP is expected when the method of the unperturbed Fourier transformation of the ion cyclotron resonance will be implemented.

The authors would like to thank the SHIPTRAP Collaboration for invaluable contribution to this work, and especially our coauthors K. Blaum, M. Block, C. Droese, M. Dworschak, F. Herfurth, H.-J. Kluge, E. Minaya-Ramirez and L. Schweikhard for their help and support.

References

1. Yu. Oganessian, J. Phys. G **34**, R165 (2007).
2. S. Hofmann and G. Muenzenberg, Rev. Mod. Phys. **72**, 733 (2000).
3. Yu.Ts. Oganessian *et al*., Phys. Rev. Lett. **104**, 142502 (2010).
4. Z. Qin *et al*., Radiochem. Acta **96**, 455 (2008).
5. K. Blaum, Yu. Novikov and G. Werth, Contemporary Physics **51**, 49 (2010).
6. C. Droese *et al*., Nucl. Instrum. Meth. A **632**, 157 (2011).
7. M. Block *et al*., Nature **463**, 785 (2010).
8. M. Dworschak *et al*., Phys. Rev. C **81**, 064312 (2010).
9. E. Minaya-Ramirez *et al*. (in preparation).
10. Atomic Mass Evaluation, Nucl. Phys. A **729**, 1 (2003).
11. S. Eliseev *et al*., Nucl. Instr. Meth. B **266**, 4475 (2008).

SEARCH FOR CANDIDATES FOR RESONANT NEUTRINOLESS DOUBLE-ELECTRON CAPTURE

PNPI participants of the MPIK Collaboration (Heidelberg) – GSI (Darmstadt) – PNPI (Gatchina), Ernst-Moritz-Arndt-Universität (Greifswald), Johannes Gutenberg-Universität (Mainz), ITEP (Moscow), SPbSU (St. Petersburg), Comenius University (Bratislava), TU (Dresden): S.A. Eliseev, D.A. Nesterenko and Yu.N. Novikov

1. Introduction

The discovery of neutrino oscillations, *i.e.* a change of neutrino flavours, has manifested that neutrinos are massive. Although the oscillation experiments are not able to yield the absolute neutrino mass, they raise a question whether neutrinos and antineutrinos are identical (Majorana) or different (Dirac) particles. At present, the only practical way to assess the neutrino-antineutrino duality consists in observation of neutrinoless double-beta transformations: (i) double-beta (negatron) emission $\{\beta^-\beta^-00\}$, (ii) double-positron emission $\{\beta^+\beta^+00\}$, (iii) one-electron capture with an emission of one positron $\{\varepsilon\beta^+00\}$, and (iv) double-electron capture $\{\varepsilon\varepsilon00\}$. These transformations are second-order processes of weak nucleon-lepton interaction, which in the first order drives ordinary single-beta transformations. The neutrinoless double-beta transformations are possible only if neutrinos are Majorana particles. Moreover, an experimental discovery of the neutrinoless mode will certify violation of the conservation of the total lepton number and definitely signalize on new physics beyond the Standard Model.

To date, only two-neutrino double-beta decay $\{\beta^-\beta^-\nu\nu\}$ has unambiguously been observed, and the half-lives for 11 $\{\beta^-\beta^-\nu\nu\}$-nuclides have been measured (the shortest 7.1×10^{18} y for ^{100}Mo and the longest 1.9×10^{24} y for ^{128}Te) [1]. However, only the neutrinoless mode – not yet discovered – can shed light on the mass and type of neutrinos. Presently, the search for the neutrinoless double-beta transformations is focused on neutrinoless double-beta decay $\{\beta^-\beta^-00\}$. The reason for this is its expected higher probability in comparison to the positron emission or double-electron capture. In the steady stream of efforts dedicated to investigations of double-beta decay over many decades, the inverse process, double-electron capture, was in the shade. This process of simultaneous capture of two orbital electrons by a nucleus has much less sensitivity to the decay energy in comparison to double-beta decay.

The theory of double-electron capture was formulated in [2]. It was noted that if the excited state of the daughter atom is energetically degenerate with the state of the initial atom, then the rate of neutrinoless double-electron capture $\{\varepsilon\varepsilon00\}$ can be resonantly enhanced by many orders of magnitude [3]. However, due to a high uncertainty in the atomic mass differences of the promising nuclides, it was impossible to pin down the resonantly enhanced transitions. Only very recently, great progress in Penning-trap mass spectrometry [4] has provided the breakthrough towards higher precision and thus given rise to a search for the resonant enhancement by means of Penning-traps. One of the first nuclide pairs whose mass differences between 0^+-ground states were proposed for measurements were ^{152}Gd–^{152}Sm and ^{164}Er–^{164}Dy [5]. This search has developed into a vigorous hunting for the candidates for the resonant neutrinoless double-electron capture [6] by a collaboration of German-Russian institutions.

2. Double-electron capture

The double capture as a second order process of weak interaction has a very small probability. If stable even-even nuclides are more bound than the neighbouring isobaric odd-odd nuclides, single-electron capture is forbidden. However, double-electron capture between two stable even-even nuclides is possible. The energy diagram of this process is schematically shown in Fig. 1. In the process of capture of two electrons from various atomic orbits, the conservation of the angular momentum of the system should be fulfilled [7]. Neutrinoless double-electron capture starts with "self-absorption" of Majorana neutrinos and generation of an intermediate atomic system with two holes in the atomic shell. The system relaxes towards stable conditions when the holes are occupied by outer electrons with subsequent photon or electron emission. The energy balance is shown in Fig. 1 and in the general case is given by Eq. 1:

$$Q_{\varepsilon\varepsilon} \equiv [M(Z, A) - M(Z-2, A)]c^2 = B_{2h} + E_\gamma, \quad (1)$$

where $Q_{\varepsilon\varepsilon}$ stands for the atomic mass difference between (Z, A) and (Z–2, A) isobaric nuclides, B_{2h} means the (positive) energy of the double-electron hole in the atomic shell in the daughter nucleus, whereas E_γ stands for the gamma-decay energy of the de-excitation of the daughter nucleus. The probability of neutrinoless double-electron capture can be written in the form [3]:

$$\Lambda_{\varepsilon\varepsilon 00} = (\Delta M)^2 \Gamma_{2h} / \{(Q_{\varepsilon\varepsilon} - B_{2h} - E_\gamma)^2 + \Gamma_{2h}^2/4\}, \quad (2)$$

where Γ_{2h} stands for the total width of the intermediate state (see Fig. 1).

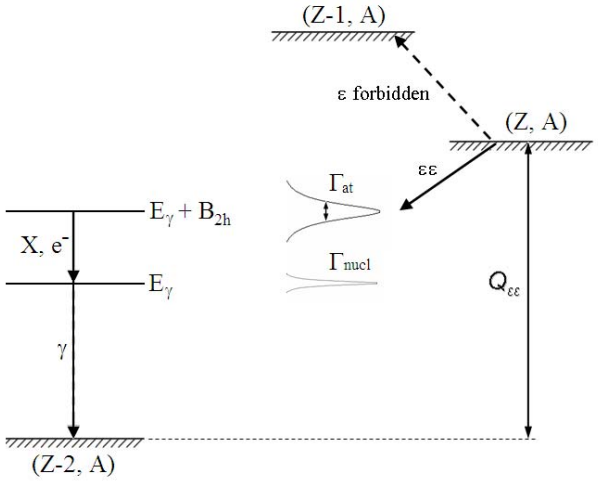

Fig. 1. Energy diagram of double-electron capture between two neutral atoms of isobaric nuclides (with the same mass number A). The intermediate nuclide $(Z-1, A)$ energetically cannot be populated. Both the atomic level de-excitation (by X-rays and Auger and other electrons) and the nuclear de-excitation by gamma-rays are shown. $\Gamma_{at.}$ and Γ_{nucl} are the atomic and nuclear level widths, respectively, and $\Gamma_{at.} >> \Gamma_{nucl}$

For the transition from the ground to ground state (0+→0+ and $E_\gamma = 0$) the neutrinoless process {εε00} dominates since the two-neutrino transition {ενν} is strongly suppressed by phase space: no energy is left for the neutrinos due to Eq. (1), $Q_{\nu\nu} = Q_{\varepsilon\varepsilon} - B_{2h} \leq \Gamma_{2h} \leq 100$ eV. Then observation of low energy gamma-rays with the energy equal to double-electron hole B_{2h} becomes the signature for the {εε00}-transition. No background from the {ενν}-process is expected, unlike the channel {$\beta^-\beta^-$00}, where the peak under interest in the electron-sum spectrum should be retrieved from the dominating continuous physical background caused by {$\beta^-\beta^-\nu\nu$}. Just these ground-to-ground state transitions were noted in [5] for the search of the neutrinoless resonances. This program has been implemented experimentally as it is presented below.

The formalism for writing the amplitude of neutrinoless double-electron capture {εε00} is similar to that of double-beta decay {$\beta^-\beta^-$00}, and differs by the electron wave functions. In the Fermi theory of weak interaction, the lepton and nuclear parts can be factorized. The capture electron part is given by the product of the electron wave function amplitudes of the captured electrons h_1 and h_2 in the nucleus. The neutrino part is given by the effective Majorana neutrino mass and the nuclear part is represented by the nuclear matrix element. The matrix element ΔM can be written as follows [3]:

$$\Delta M = (G_F \cos\theta_C / \sqrt{2})^2 \Psi_{h1} \Psi_{h2} m_{\varepsilon\varepsilon} (g_A^2/2\pi) M_{\varepsilon\varepsilon}. \quad (3)$$

In Eq. (3), G_F stands for the Fermi weak interaction constant, θ_C is the Cabibbo angle, g_A is the axial-vector nucleon coupling constant, $M_{\varepsilon\varepsilon}$ is the nuclear matrix element which connects the nuclear states of the mother and daughter nuclei. This experimentally unknown value specific for each pair of nuclides should be calculated. The electron part of Eq. (3) can be calculated quite precisely. It can be approximated by ~ $(\alpha Z m_e)^3$ for K-electron captures, thus favouring heavy nuclides.

The neutrino part of the matrix element for {εε00} includes the so called effective Majorana neutrino mass:

$$m_{\varepsilon\varepsilon} = |\sum_k U_{ek}^2 m_k|, \quad (4)$$

where m_k means the neutrino eigenstates mass values and U_{ek} stand for the elements of the mixing matrix [8].

The probability of the {εε00}-transformation given by Eq. (2) can be finally expressed in the form of Eq. (5) by inserting Eqs. (3) and (4):

$$\Lambda_{\varepsilon\varepsilon 00} = \ln 2 \,/ T_{1/2} = (g_A G_F \cos\theta_C)^4 / (4\pi R)^2 \; P_{\varepsilon\varepsilon} \langle m_{\varepsilon\varepsilon}\rangle^2 \, |M_{\varepsilon\varepsilon}|^2 \, F, \tag{5}$$

where

$$F = \Gamma_{2h} / \{(Q_{\varepsilon\varepsilon} - B_{2h} - E_\gamma)^2 + (\Gamma_{2h})^2/4\} \tag{6}$$

is the resonance enhancement factor, and

$$P_{\varepsilon\varepsilon} = |\Psi_{h1}|^2 \, |\Psi_{h2}|^2 \tag{7}$$

is the product of the electron wave functions of the captured electrons h_1 and h_2 in the nucleus.

The full resonance conditions of Eq. (6) are fulfilled when the degeneracy factor Δ is close to zero:

$$\Delta \equiv Q_{\varepsilon\varepsilon} - B_{2h} - E_\gamma \approx 0. \tag{8}$$

Then the value of F becomes maximal. The double-electron hole binding energy B_{2h} and the width Γ_{2h} of the intermediate state can be precisely calculated, *e.g.*, with the Dirac – Fock method including the electron correlations and quantum electrodynamics corrections [9].

Equation (5) can be turned for the determination of the effective Majorana neutrino mass:

$$\langle m_{\varepsilon\varepsilon}\rangle^2 = C \,/\, T_{1/2} \, |M_{\varepsilon\varepsilon}|^2 \, F, \tag{9}$$

where C includes all constants and well-defined parameters. Thus, the effective Majorana neutrino mass can be determined if both the rate of $\{\varepsilon\varepsilon 00\}$ and the enhancement factor F are measured and the nuclear matrix element is reliably calculated. The most favourable case for the exploration seems double *s*-electron capture with the $0^+ \rightarrow 0^+$ transition between the nuclear ground states [5]. For this specific case the values of $P_{\varepsilon\varepsilon}$, $M_{\varepsilon\varepsilon}$ and, consequently, $\Lambda_{\varepsilon\varepsilon 00}$ are maximal.

The consideration of $\{\varepsilon\varepsilon 00\}$ as an alternative process to $\{\beta^-\beta^- 00\}$ in the neutrino exploration has a practical sense only if the resonance conditions are fulfilled for double-electron capture, *i.e.* when the energy degeneration between the initial and intermediate atomic states takes place as it is depicted in Fig. 1 and presented by a factor F in Eq. (6). This rate enhancement for $\{\varepsilon\varepsilon 00\}$, which can reach many orders of magnitude, depends only on the Δ-value in Eq. (8) and does not depend on the energy of the excited level of the daughter nucleus or on the binding energy of the captured electrons. This enhancement can be dominant and can prevail over a decrease in $P_{\varepsilon\varepsilon}$ if "unfavourable" orbits participate in the capture, and/or corresponding nuclear matrix elements are suppressed due to the angular momentum or any other reasons.

One can shortly summarize merits and demerits of neutrinoless double-electron capture $\{\varepsilon\varepsilon 00\}$ in comparison to neutrinoless double-beta decay $\{\beta^-\beta^- 00\}$ [9] for the neutrino exploration.

Advantages in the investigation of the resonant process $\{\varepsilon\varepsilon 00\}$ are as follows:

- a variety of states with different low spin values and different parities in one nuclide, which in principle can provide the complete or partial resonance conditions and strongly enhance the decay rates for $\{\varepsilon\varepsilon 00\}$;
- a possibility to establish the existence of the right-hand leptonic current if, *e.g.*, the negative parity resonant states occur [10];
- no meaningful internal physics background from the two-neutrino mode $\{\varepsilon\varepsilon\nu\nu\}$ in the monochromatic spectrum of $\{\varepsilon\varepsilon 00\}$, unlike the $\beta^-\beta^-$ branch where the electron sum peak of $\{\beta^-\beta^- 00\}$ should be retrieved from the dominating continues background caused by $\{\beta\beta\nu\nu\}$. Very clean conditions are fulfilled for the $\{\varepsilon\varepsilon 00\}$ resonant transition $0^+ \rightarrow 0^+$ between the ground states.

Disadvantages in exploration of the process $\{\varepsilon\varepsilon 00\}$ can be:

- typically small abundances of neutron-deficient stable nuclides, which are the sources of double-electron capture under interest, and which can be used for the large scale long term exposition;
- appearance of the α-decay channel in heavy nuclides, which can create a significant background. This issue is not acute though if cryogenic calorimetry for the signal detection is used.

3. Experimental method and installation

Penning-trap mass spectrometry is widely utilized for absolute mass measurements of radioactive nuclides with a precision superior to all other methods used in mass spectrometry. The accuracy of this

method is mainly limited by a systematic uncertainty caused by the time/temperature instability of the magnetic field. The measurements of the mass differences of stable nuclides developed in this work have a big advantage in decreasing a systematic uncertainty due to its partial cancellation. Moreover, the magnet stabilization system has been implemented, and all changes of the magnetic field were under control [11]. The measurements of the reference nuclide with a very well known precise mass value have steadily been done.

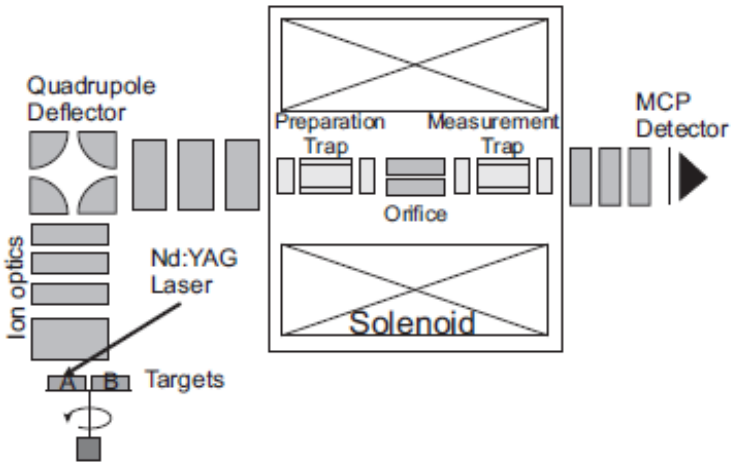

Fig. 2. A sketch of the Penning-trap device used for mass difference measurements

We used the Penning-trap part of the SHIPTRAP facility [12]. The atoms of the isobaric stable nuclides of interest were ionized in turn by a laser (or plasma) ion source and forwarded to the double Penning-trap system (see Fig. 2). There, a few ions were trapped in the homogeneous magnetic and crossed electric fields. The trapped ions could be excited by external rf-fields.

The cyclotron frequency f_c of an ion with the mass m and charge q stored in a magnetic field B is given by

$$f_c = qB / m. \tag{10}$$

Samples of $\{Z, N\}$ and $\{Z-2, N+2\}$ stable nuclides with the same mass number A were deposited onto two stainless steel plates serving as targets. They were fixed to a rotary mechanical feedthrough with a stepper. This allowed an alternate laser irradiation of the samples. Ions created in the ion source were guided into the preparation trap for cooling and centering. A cooled bunch of singly charged ions was then injected into the measurement trap. Here, a precise measurement of the cyclotron frequency f_c was carried out. The cyclotron frequency could be determined by the resonance in the ToF curve of the outlet ions detected by a micro plate channel. The cyclotron resonance frequencies for both samples were measured alternately for a few days/weeks with a Ramsey-type excitation with two 250 ms fringes separated by a waiting time of 1.5 s (Fig. 3a, inset).

For the measurements of the pair ^{164}Er–^{164}Dy with the smallest mass difference, a new method of an octupolar excitation was implemented [13] for the first time. With the octupolar technique, we obtained a resolving power of about $2 \cdot 10^7$ [14], which exceeds that of the quadrupolar technique by more than a factor of 10. With the ordinary quadrupolar technique such a resolving power would require an excitation time of 30 s, which is beyond the present capability.

In the measurement trap, equal starting conditions were ensured for ions of both samples by the same ion production mechanism, their similar masses, abundances in the samples and for some of them by similar chemical properties. Along with the identical f_c-measurement procedure applied to both samples, this led to equal shifts of the measured frequencies due to static imperfections of the measurement trap, and thus did not affect the frequencies ratio. We tried to keep on average a constant mean ion production rate, though temporal fluctuations of this rate from measurement to measurement could not be avoided. To investigate the possibility of a systematic frequency shift due to ion-ion interactions, the data were typically divided into 5 sets according to the number of the detected ions. The data with more than 5 ions per cycle were not used in the analysis. A thorough analysis of the sets did not reveal any correlations between the frequency ratios

and the number of ions. Usually, the drift of the cyclotron frequency in time did not exceed a few tens of mHz over 1 day due to stabilization of the temperature in the magnet bore, as well as of the pressure in the liquid-helium cryostat [11]. The data analysis was performed along the lines of [4].

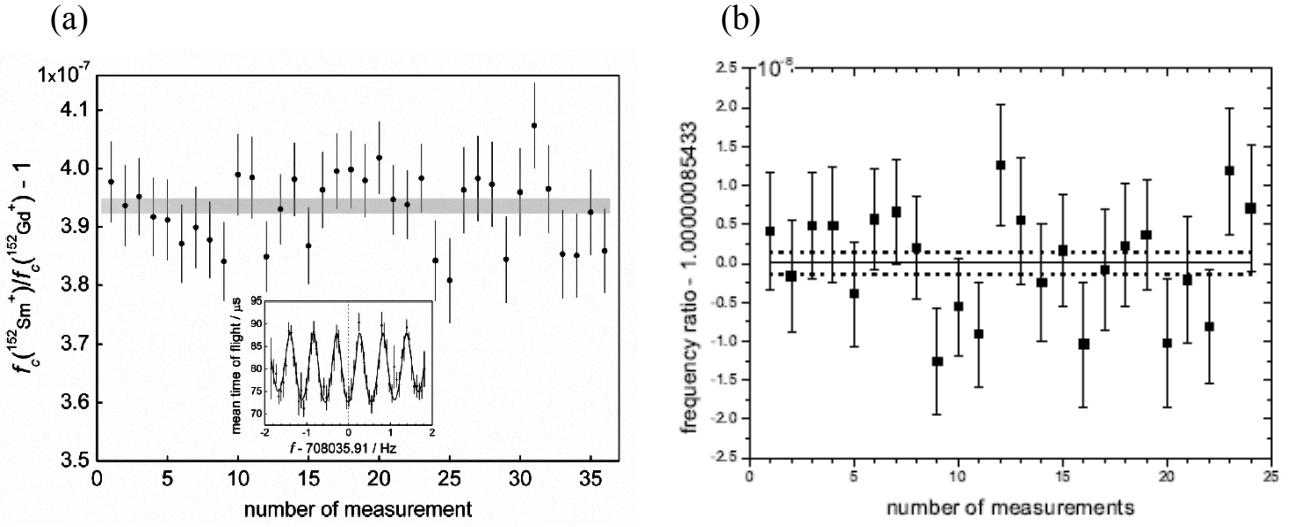

Fig. 3. a – cyclotron-frequency ratios $f_c(^{152}\mathrm{Sm}) / f_c(^{152}\mathrm{Gd})$ measured over three days with up to 5 detected ions [15]. The error bars of the individual measurements are the statistical uncertainties taking into account magnetic field fluctuations. The grey shaded band represents the total uncertainty of the averaged frequency ratio. The inset displays a typical time-of-flight ion cyclotron resonance of ^{152}Sm with a Ramsey excitation pattern 250 ms – 1.5 s – 250 ms. The solid line is a fit of the expected line shape to the data points. b – frequency ratios $f_c(^{180}\mathrm{Hf}^+) / f_c(^{180}\mathrm{W}^+)$ with the average value (solid line) and one sigma statistical uncertainty (dotted lines) [16]

4. Analysis of the data and the results

The $Q_{\varepsilon\varepsilon}$-value of the transition can be derived from the cyclotron-frequency ratio of two nuclides:

$$Q_{\varepsilon\varepsilon} / c^2 \equiv M\{Z, N\} - M\{Z-2, N+2\} = [M\{Z-2, N+2\} - m_e] \cdot [f_c\ \{Z-2, N+2\}^+ / f_c\ \{Z, N\}^+ - 1], \quad (11)$$

where $M\{Z, N\}$ and m_e are the masses of the neutral atom $\{Z, N\}$ and the electron, respectively. The difference in the ionization energies of the nuclides $\{Z, N\}$ and $\{Z-2, N+2\}$ due to its smallness was neglected in Eq. (11). The measured frequency ratios for some pairs of nuclides in double-electron capture are shown in Figs. 3a, b and 4a, b. They were obtained in the campaign of 2010–2012.

Equation (5) clearly shows what values are needed to estimate the probability of neutrinoless double-electron capture. They are as follows:

- the product of the electron wave functions $P_{\varepsilon\varepsilon}$ in the nucleus, which can be precisely calculated by using the one-configuration Dirac – Fock method. These routine calculations have been done for the pair of the investigated nuclides (see details in [15]);
- the effective Majorana neutrino mass $m_{\varepsilon\varepsilon}$, which is a subject of interest. However, in order to estimate the half-life of the process, we parametrized it as $|m_{\varepsilon\varepsilon}| = 1$ eV;
- the nuclear matrix element $M_{\varepsilon\varepsilon}$, which is one of the sensitive part of the transition probability. Unfortunately, it can be only calculated. It was calculated for different nuclear pairs in the quasiparticle random phase approximation (see details in [18]);
- the very sensitive resonance factor F in Eq. (6), which value depends on the measured $Q_{\varepsilon\varepsilon}$ and precisely calculated double-electron-hole binding energy B_{2h} and virtual level width Γ_{2h}. These atomic energy parts were calculated with the Dirac – Fock method including the Breit (electron-correlation) and quantum electrodynamics corrections (see [14, 15, 17]).

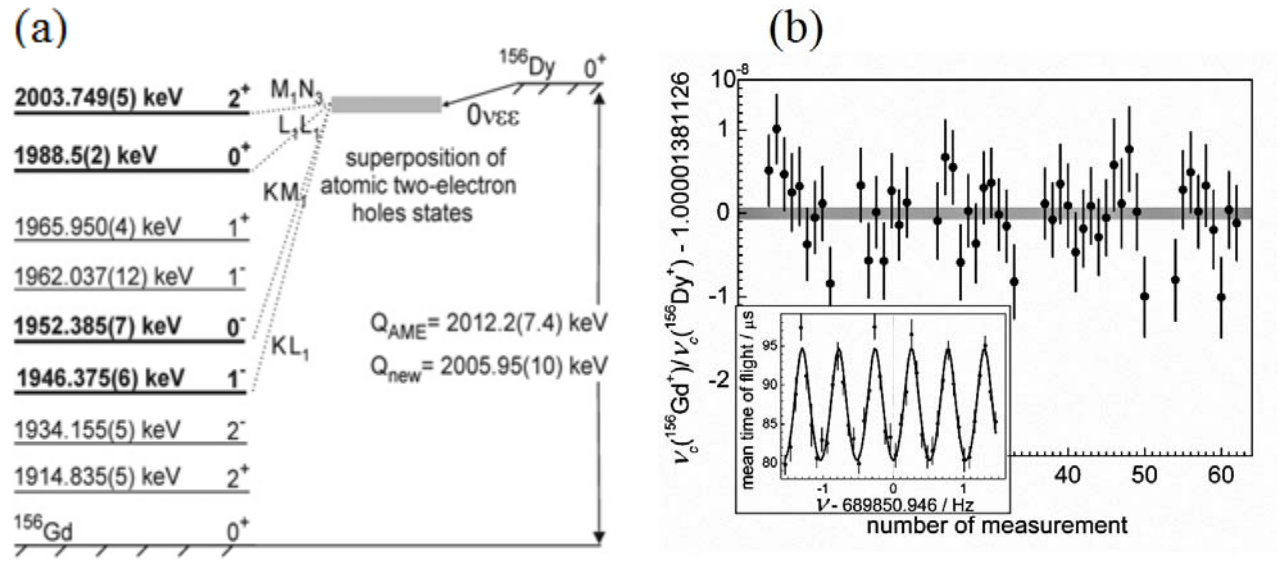

Fig. 4. a – scheme of neutrinoless double-electron capture in ^{156}Dy. Shown are only the nuclear excited states in ^{156}Gd with spin $I_f \leq 2$, to which a resonantly enhanced 0ν transition can result in the half-life which is short enough for a realistic search for neutrinoless double electron capture. The 0ν transitions to the nuclear excited states marked with thick lines are resonantly enhanced, as has been found in this work. b – cyclotron frequency ratio $R = f_c(^{156}Gd^+) / f_c(^{156}Dy^+)$ measured over five days with up to 5 detected ions. The error bars are the statistical uncertainties taking into account magnetic field fluctuations. The grey shaded band represents the total uncertainty of the averaged frequency ratio. The inset displays a typical time-of-flight ion cyclotron resonance of $^{156}Dy^+$ with a Ramsey excitation pattern of 100–1800–100 ms. The solid line is a fit of the expected line shape to the data [17]

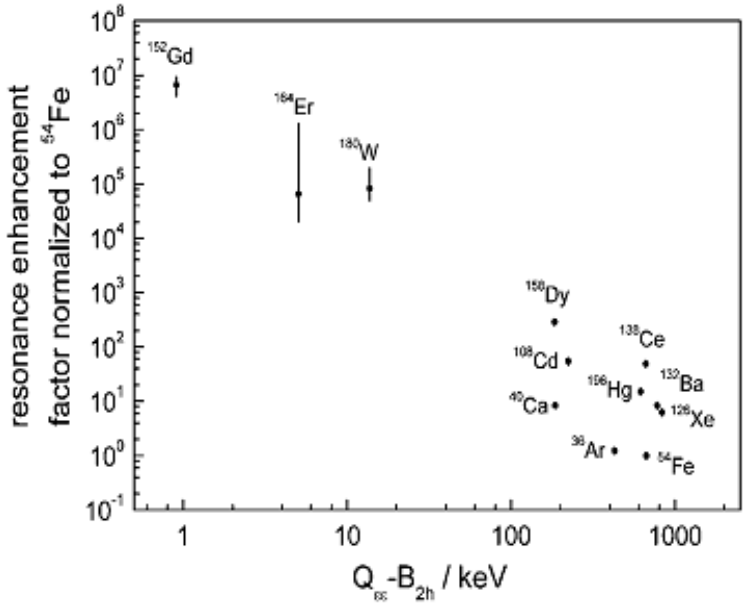

Fig. 5. Resonance enhancement factors F for pure double-electron-capture transitions between the ground states of the mother and daughter nuclides relative to the F value of ^{54}Fe

The data for the ground-to-ground state double-electron-capture transitions are collected in Table 1, whereas the data for transitions to the excited states of the daughter nuclides are presented in Table 2. In Table 1, the old data for Δ from the mass evaluation [19] are also given. As can be seen, the new values are much more precise (by a factor of 20–30) and allow an assessment of the resonance conditions. These conditions appear for the pair ^{152}Gd → ^{152}Sm. Table 2 shows that there are other cases with a resonance degeneracy in the pairs ^{106}Cd → ^{106}Pd, ^{124}Xe → ^{124}Te, ^{156}Dy → ^{156}Gd, and ^{168}Yb → ^{168}Er. The resonance enhancement factors for these states are very high. For the ground-to-ground state transitions they are shown in Fig. 5. This figure shows a comparison of the resonance enhancement factor F [see Eq. (6)] for all known pure εε-capture transitions between the ground states of the mother and daughter nuclides relative to the

nuclide ^{54}Fe with the smallest F value. As can be seen from Fig. 5, the resonance enhancement for ^{152}Gd is by a factor of $6 \cdot 10^6$ larger than that of the definitely non-resonant case of ^{54}Fe, and thus the largest one ever determined. Meanwhile, the transition probability to the resonant states could be small for a reason of the far capture orbitals and/or the small nuclear matrix elements due to a forbidden type of decay. And vice versa, only partly resonance conditions can be attributed to the transitions with favorite capture orbits (*KK*-type with high $P_{\varepsilon\varepsilon}$-values) and allowed nuclear matrix elements. An example is ^{180}W → ^{180}Hf (see Table 1) and may be ^{124}Xe → ^{124}Te (if the spin value for the relevant excited state is 0^+).

We have observed a very rare phenomenon of a multiple resonance appearance in the pair ^{156}Dy → ^{156}Gd [17]. Figure 4 shows this case. However, all resonant states in this transition are unfavored for capture, and thus the total transition probability is not high.

An estimation of the half-lives of the nuclides relative to neutrinoless double-electron capture (Eq. (5)) shows that the most attractive candidate for a large scale long-term exposition is ^{152}Gd. The expected half-life of 10^{26}–10^{27} y is on the upper level of the current capabilities of the search for the neutrinoless process in the capture sector.

Table 1

Double-electron-capture transitions to nuclear ground states ($0^+_I \rightarrow 0^+_f$)

εε-Transition	^{152}Gd →^{152}Sm [15]	^{164}Er →^{164}Dy [14]	^{180}W →^{180}Hf [16]
electron orbitals	KL_1	L_1L_1	KK
$Q_{\varepsilon\varepsilon}$ (old) / keV	54.6(35)	23.3(39)	144.4(45)
Δ (old) / keV	–0.27(350)	5.05(390)	12.4(45)
$Q_{\varepsilon\varepsilon}$ (new) / keV	55.70(18)	25.07(12)	143.20(27)
Δ (new) / keV	0.83(18)	6.82(12)	11.24(27)
nuclear matrix element $M_{\varepsilon\varepsilon}$	2.7–3.2	2.7–2.6	1.8–2.0
min half-life / y	$1.2 \cdot 10^{26}$	$1.9 \cdot 10^{30}$	$3.3 \cdot 10^{28}$
max half-life / y	$1.2 \cdot 10^{27}$	$2.1 \cdot 10^{30}$	$4.5 \cdot 10^{28}$

Table 2

Double-electron-capture transitions to nuclear excited states ($0^+_i \rightarrow I^+_f$)

Transition	E_γ / keV	I^+_f	Electron orbitals	$Q_{\varepsilon\varepsilon}$ / keV	Δ / keV	Ref.
^{96}Ru → ^{96}Mo	2700.21(6)	2^+	L_2L_2	2714.51(13)	9.05(14)	[20]
^{74}Se → ^{74}Ge	1204.205(7)	2^+	L_2L_3	1209.169(49) 1209.240(7)	2.50(5) 2.57(1)	[21] [22]
^{102}Pd →^{102}Ru	1103.047(13)	2^+	KL_3	1203.27(36)	75.26(36)	[23]
^{106}Cd → ^{106}Pd	2748.2(4)	$(2, 3)^-$	KL_3	2775.39(10)	–0.33(41)	[23]
^{112}Sn → ^{112}Cd	1871.00(19)	0^+	KK	1919.82(16)	–4.50(25)	[24]
^{124}Xe → ^{124}Te	2790.41(9)	0^+– 4^+	KK	2856.82(13)	1.96(16)	[25]
^{130}Ba → ^{130}Xe	2544.43(8)	0^+	KK	2623.71(26)	10.15(26)	[25]
^{136}Ce → ^{136}Ba	2315.32(7)	0^+	KK	2378.53(27)	–11.67(28)	[26]
^{156}Dy → ^{156}Gd	1946.375(6) 1952.385(7) 1988.5(2) 2003.749(5)	1^- 0^- 0^+ 2^+	KL_1 KM_1 L_1L_1 M_1N_3	2005.95(10)	0.75(10) 1.37(10) 0.54(24) 0.04(10)	[17]
^{162}Er → ^{162}Dy	1782.68(9)	2^+	KL_3	1846.95(30)	2.69(30)	[20]
^{168}Yb → ^{168}Er	1403.7357(23)	2^-	M_2M_2	1409.27(25)	1.52(25)	[20]
^{184}Os → ^{184}W	1322.152(22)	0^+	KK	1453.68(58)	–8.89(58)	[27]

5. Conclusion

Desperate experimental attempts to observe the neutrinoless mode of double-beta decay have been unsuccessful so far. The inverse, double-electron-capture process, was not even considered because of a smaller expected probability. Meanwhile, the resonance enhancement of neutrinoless double-electron capture was predicted if the mother and daughter atomic states are degenerate. To check such a possibility we have measured the mass differences for 13 pairs of stable nuclides with Penning-trap mass spectrometry. The typical achieved precision in the mass differences is about a few hundred of eV. In addition, precise calculations of the double-electron binding energies in atoms and the electron densities in the nuclei have been performed. Reliable calculations of the nuclear matrix elements of the nuclides have also been carried out.

We have discovered a set of partially resonance states in different pairs of nuclides, which can considerably contribute to the transition rate of neutrinoless double-electron capture. The best case concerns the transition ^{152}Gd $\rightarrow$ ^{152}Sm with the optimistic half-life of 10^{26}–10^{27} y, which is on the limit of the current experimental possibilities. Meanwhile, a hunt on the search for other candidates is still under progress. The question whether the double-electron-capture sector can be a new strong player in the fascinating neutrino world is still open.

We would like to thank our colleagues and coauthors who contributed to this work: K. Blaum, M. Block, M. Goncharov, C. Droese, F. Herfurth, H.-J. Kluge, M. Kretzschmar, M. Krivoruchenko, E. Minaya Ramirez, C. Roux, V. Shabaev, F. Šimkovic, L. Schweihard, I. Tupitsyn, S. Wycech, K. Zuber and N. Zubova.

References

1. A.S. Barabash, arXiv:1101.4502[nucl-ex] (2011).
2. R.G. Winter, Phys. Rev. **100**, 142 (1955).
3. J. Bernabeu, A. De Rujula and C. Jarlskog, Nucl. Phys. B **223**, 15 (1983).
4. K. Blaum, Phys. Rep. **425**, 1 (2006).
5. K. Blaum, Yu. Novikov and G. Werth, Contemp. Phys. **51**, 149 (2010).
6. S. Eliseev, Yu. Novikov, and K. Blaum, J. Phys. G (in press).
7. M. Doi and T. Kotani, Progr. Theor. Phys. **89**, 139 (1993).
8. F.T. Avignon, S.R. Elliot, and J. Engel, Rev. Mod. Phys. **80**, 481 (2008).
9. I. Tupitsyn *et al*., Phys. Chem. Solids **59**, 809 (1998).
10. J.D. Vergados, Nucl. Phys. B (in press).
11. C. Droese *et al*., Nucl. Instr. Meth. A **632**, 157 (2011).
12. M. Block *et al*., Nature **463**, 785 (2010).
13. S. Eliseev *et al*., Int. J. Mass Spectrom. **262**, 45 (2007).
14. S. Eliseev *et al*., Phys. Rev. Lett. **107**, 152501 (2011).
15. S. Eliseev *et al*., Phys. Rev. Lett. **106**, 052504 (2011).
16. C. Droeze *et al*., Nucl. Phys. A **875**, 1 (2012).
17. S. Eliseev *et al*., Phys. Rev. C **84**, 012501(R) (2011).
18. M. Krivoruchenko *et al*., Nucl. Phys. A **859**, 140 (2011).
19. Atomic Mass Evaluation, Nucl. Phys. A **729**, 1 (2003).
20. S. Eliseev *et al*., Phys. Rev. C **83**, 038501 (2011).
21. V.S. Kolhinen *et al*., Phys. Lett. B **684**, 17 (2010).
22. B.J. Mount *et al*., Phys. Rev. C **81**, 032501 (2010).
23. M. Goncharov *et al*., Phys. Rev. C **84**, 028501 (2011).
24. S. Rahaman *et al*., Phys. Rev. Lett. **103**, 042501 (2009).
25. D. Nesterenko *et al*., submitted to Phys. Rev. C.
26. V.S. Kolhinen *et al*., Phys. Lett. B **697**, 116 (2011).
27. C. Smorra *et al*., submitted to Eur. J. Phys.

STUDY OF THE NUCLEAR MATTER DISTRIBUTION IN THE ^{12,14}Be NUCLEI

G.D. Alkhazov, A.V. Dobrovolsky, A.G. Inglessi, A.V. Khanzadeev, G.A. Korolev, D.M. Seliverstov, L.O. Sergeev, A.A. Vorobyov, V.I. Yatsoura, A.A. Zhdanov

1. Introduction

The proton-nucleus elastic scattering at intermediate energies is a well-established method for investigation of the nuclear matter distribution in stable nuclei [1]. When used in inverse kinematics it can be also applied for nuclei far from stability. An interesting phenomenon which appears in some light exotic nuclei is a halo structure, characterized with a long low-density tail in the matter distribution. The nuclear halo is a quantum effect, that appears in nuclei where the valence nucleon(s) have very low separation energy and low angular momentum (l = 0, 1).

The experimental methods applied for studying halo nuclei were mainly measurements of the total interaction cross sections and investigations of the momentum distributions of the reaction products after fragmentation. An alternative method was proposed at PNPI for studying nuclear matter densities of exotic nuclei. It is based on measurements of the differential cross sections dσ/dt for intermediate-energy proton-nucleus elastic scattering in inverse kinematics using an active target IKAR.

The method has already been successfully applied to study the isotopes ^{6,8}He [2, 3] and ^{8,9,11}Li [4]. In the present experiment, the neutron-rich isotopes from the beryllium isotopic chain were investigated employing the same method [5].

2. Experimental procedure

The experiment was performed at GSI, Darmstadt. A primary beam of ^{18}O, accelerated in the UNILAC and SIS accelerators, interacted with the Be target placed at the entrance of the FRagment Separator (FRS). The produced beryllium ions were separated according to their magnetic rigidity, and the secondary beams with an energy of ~ 700 MeV/u and an energy spread of 1.2 % (σ) were focused at the center of the hydrogen target IKAR. The mean energies of the beam particles were determined with an accuracy of ~ 0.1 %. The intensities were about 6000 and 3000 ions/s for ^{12}Be and ^{14}Be, respectively. The contaminations from other isotopes in the secondary beam were of the order of 1 % for ^{12}Be and 25 % (most of which were ^{11}Li nuclei) for ^{14}Be. Such a high level of contamination for ^{14}Be was kept consciously to have a cross-check possibility with the previously measured p-^{11}Li cross section.

A schematic view of the experimental setup is shown in Fig. 1. The central part of the set-up was the ionization chamber IKAR [6, 7] developed at PNPI, which was simultaneously used as a hydrogen target and a detector for the recoil protons. During the experiment it was filled with hydrogen gas (with the purity better than 1 ppm) at a pressure of 10 bar. The chamber contains six identical modules. Each module is an axial ionization chamber, which consists of an anode, subdivided into a central circular electrode A and a concentric ring electrode B, a cathode, and a grid (see insert in Fig. 1). All modules were placed perpendicularly to the beam direction. The signals from these modules provide the recoil energy T_R, the recoil angle θ_R of the scattered protons, and the interaction vertex z-coordinate Z_V (in the direction of the beam). To reduce the interaction of the beam with other matter, the central parts of all electrodes are made of thin aluminum foils. In addition, the entrance and exit windows of IKAR are made of thin beryllium foils of 0.5 mm thickness and 7 cm diameter, having a special semi-spherical shape in order to sustain the high gas pressure. ^{241}Am sources, placed on the anodes and cathodes, were used for energy calibration and determination of the correction coefficients for the measured energy, which take into account the limited transparency of the grid and the loss of the drifting electrons through adhesion to electronegative impurities in the gas. A set of scintillation detectors S1–S3 was used for triggering and beam identification via time-of-flight and ΔE measurements. A VETO detector (scintillator with an aperture of 2 cm in diameter) was used to reject projectiles passing far from the central axis of IKAR. The scattering angle θ_S of the projectiles was determined with a set of multi-wire proportional chambers MWPC1–MWPC4, measuring x and y coordinates each. Cylinder bags filled with He gas were placed in between each pair of multi-wire chambers

in order to reduce the multiple Coulomb scattering of the projectiles. The ALADIN magnet (A Large Acceptance DIpole magNet) and the position sensitive scintillation wall behind it were used to discriminate against break-up reaction channels using different magnetic rigidity and energy loss of the reaction products.

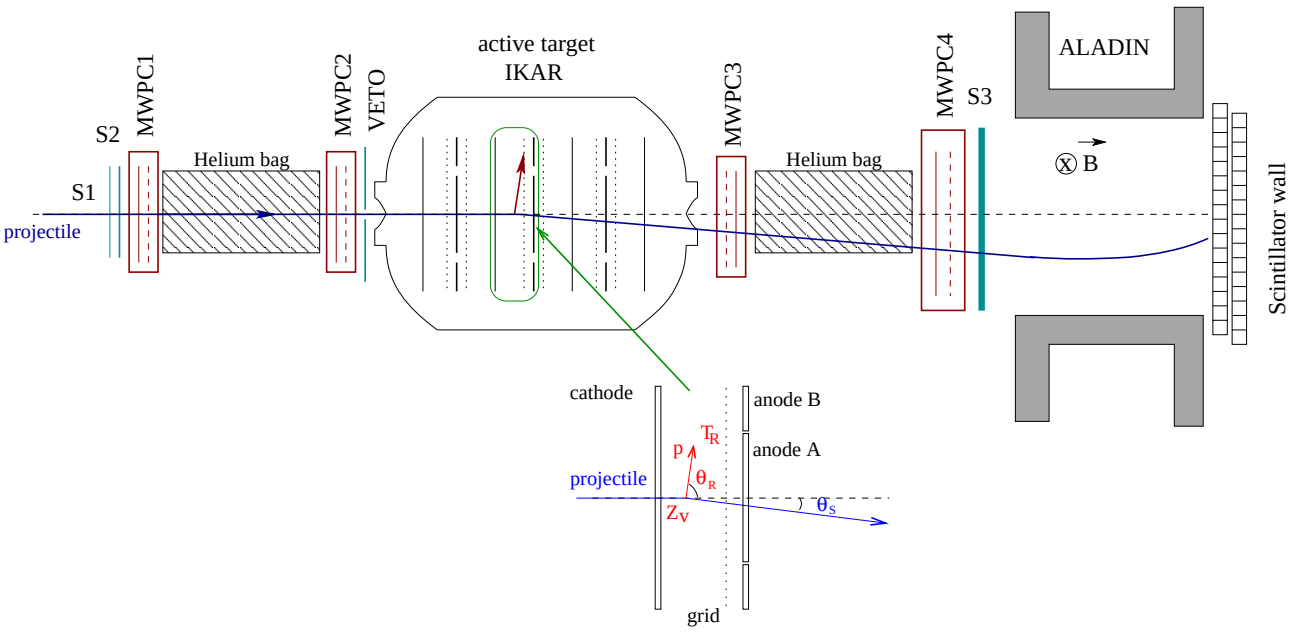

Fig. 1. Schematic view of the experimental set-up for small-angle proton elastic scattering in inverse kinematics. The ionization chamber IKAR serves simultaneously as a hydrogen target and a detector for the recoil protons. In six identical modules, the recoil energy T_R, the recoil angle θ_R, and the vertex point Z_V of the interaction are determined (see insert). The scattering angle θ_S of the projectile is determined with four multi-wire proportional chambers MWPC1–MWPC4. The scintillation detectors S1–S3 and VETO are used for beam identification and triggering. The scattered projectiles are identified with the ALADIN magnet and the position sensitive scintillation wall, thus separating the break-up reaction products

The major steps in the analysis of the raw IKAR data, such as the energy and active volume calibration, are the same as in the previous experiments described in detail in [2]. The tracking of the projectiles was accomplished with a different type of multi-wire chambers, as compared to the previous experiments. The MWPCs used in the discussed experiment had a strip readout. The position resolution of the MWPCs was determined to be about $\sigma = 150$ μm.

The total energy of the recoil protons can be measured with the IKAR detector only up to 5 MeV. Faster protons leave the active volume of the detector, and in this case only the energy loss is measured. For these events the recoil energy is calculated from the scattering angle of the projectile using the two-body kinematics for elastic scattering:

$$T_R = T_p(T_p + 2M)\frac{m + (T_p + M)\sin^2\theta_S - \cos\theta_S\sqrt{m^2 - M^2\sin^2\theta_S}}{(T_p + m + M)^2 - T_p(T_p + 2M)\cos^2\theta_S}, \quad (1)$$

where T_R is the recoil energy of the target particle, T_p is the energy of the projectile, M is the mass of the projectile, m is the mass of the target particle, and θ_S is the scattering angle of the projectile.

The parameters of the proton signals in IKAR (*e.g.*, width, amplitude, rise time, *etc.*) were used to eliminate background events. The background appeared mainly from interactions of the beam particles with the IKAR windows and electrodes (anodes, cathodes and grids), and partly from reactions other than elastic scattering, namely inelastic and quasi-elastic scattering, Coulomb dissociation, nuclear fragmentation and pion production.

The differential cross section for proton elastic scattering was deduced after the event selection as

$$\frac{\mathrm{d}\sigma}{\mathrm{d}t} = \frac{\mathrm{d}N}{\mathrm{d}tBn\Delta L}, \quad (2)$$

where the four-momentum transfer squared is calculated via

$$-t = 2mT_R\,, \tag{3}$$

dN is the event rate of elastic p-nucleus scattering in the interval dt of the four-momentum transfer squared, B is the number of beam particles impinging on the target, n is the volume density of the target calculated from the measured pressure and temperature of the H_2 gas, and ΔL is the effective target length.

The obtained cross section includes, due to the limited energy and angular resolution of the set-up, events of inelastic scattering to the first excited state of the projectile, for the cases where no break-up followed. The cross sections for inelastic p-^{12}Be and p-^{14}Be scattering were calculated using the Glauber multiple-scattering theory, and the measured elastic scattering cross sections were corrected for the contribution of the inelastic events. In the calculations, the deformation lengths of 1.93 fm for ^{12}Be and 1.18 fm for ^{14}Be, respectively, were used.

The differential cross sections dσ/dt obtained in this experiment are plotted in Fig. 2 as a function of $-t$. The energies indicated in Fig. 2 correspond to the equivalent proton energies in direct kinematics. The error in the absolute normalization of the cross sections is estimated to be 4 %, and the uncertainty in the four-momentum transfer squared $-t$ is $\approx$ 1.5 %. The uncertainty in the deformation lengths, used in the calculations and corrections for the contribution of the inelastic scattering to the cross section, results in an additional error of $\leq$ 0.01 fm to the determined matter radius.

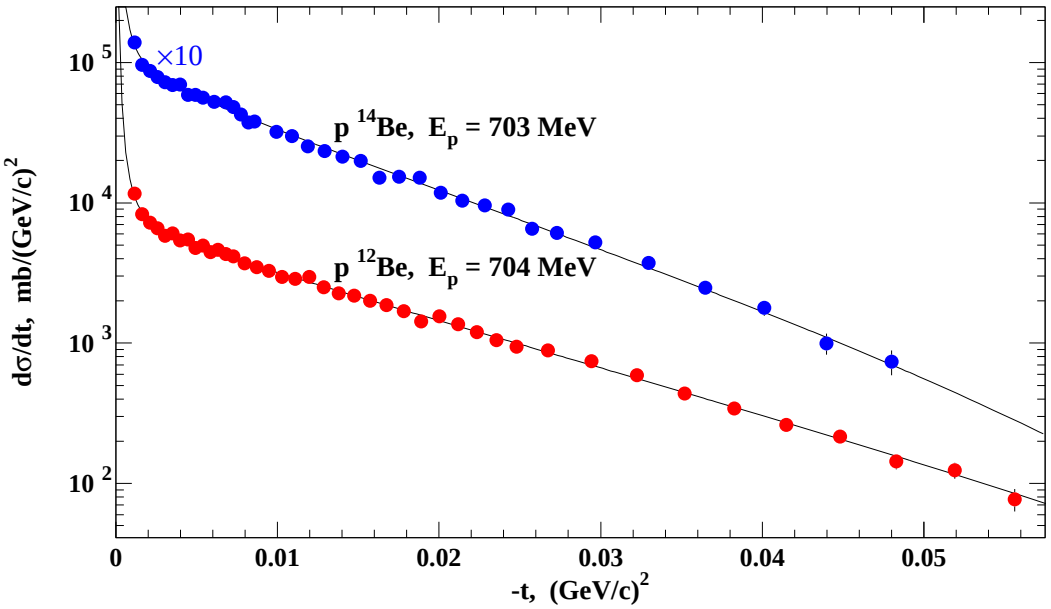

Fig. 2. Differential cross sections dσ/dt for the p-nucleus elastic scattering as a function of the four-momentum transfer squared $-t$. The indicated energies correspond to the equivalent proton energies in direct kinematics. The indicated error-bars are statistical only. Fits to the cross sections using the Gauss-Oscillator parameterization within the Glauber multiple-scattering theory are shown with solid lines (for details about the fits see next section)

3. Theoretical interpretation and results

For establishing the nuclear density distributions from the measured cross sections, the Glauber multiple scattering theory was applied. Calculations were performed using the basic Glauber formalism for proton-nucleus elastic scattering and taking experimental data on the elementary proton-proton and proton-neutron scattering amplitudes as input [5].

In the analysis of the experimental data, the nuclear many-body density ρ_A was taken as a product of the one-body densities, which were parameterized with different functions. The parameters of these functions were found by fitting the calculated cross sections to the experimental data. The fitting procedure is described in detail in [3].

For the model nuclear-matter density distributions, several phenomenological distributions, as well as a sum of Gaussian (SOG) parameterization were used in the present analysis. The following phenomenological density parameterizations were used: the Single Gaussian (SG), Gaussian-Gaussian (GG), Gaussian-Halo (GH), Gaussian-Oscillator (GO) and Symmetrized Fermi (SF). For the explicit expressions of these parameterizations see [3]. Each of these parameterizations has two free parameters. While the SG, SF and GH parameterizations do not make any difference between the neutron and proton distributions, the GG and GO parameterizations assume that the nuclei consist of core nucleons and valence nucleons with different spatial distributions. The core distribution is assumed to be a Gaussian one in both the GG and GO parameterizations. The valence nucleon density is described by a Gaussian or a 1*p* shell harmonic oscillator-type distribution within the GG or GO parameterization, respectively. The free parameters in the GG and GO parameterizations are the r.m.s. radii R_c and R_h of the core and valence nucleon ("halo") distributions.

In an attempt to perform a more model independent analysis, the SOG parameterization was used. The SOG method was previously used in data analyses of experiments on electron scattering, and is considered to give very good results for determination of charge densities. In contrast to the above listed phenomenological densities, this method is in principle model independent as no constraint on the shape of the nucleus is made a priori, rather the density is expanded on a basis of Gaussian functions. One should note, however, that the SOG analysis gives most accurate results when the cross section data are available for the entire range of the momentum transfer which is never the case in real experiments where only limited data sets are available.

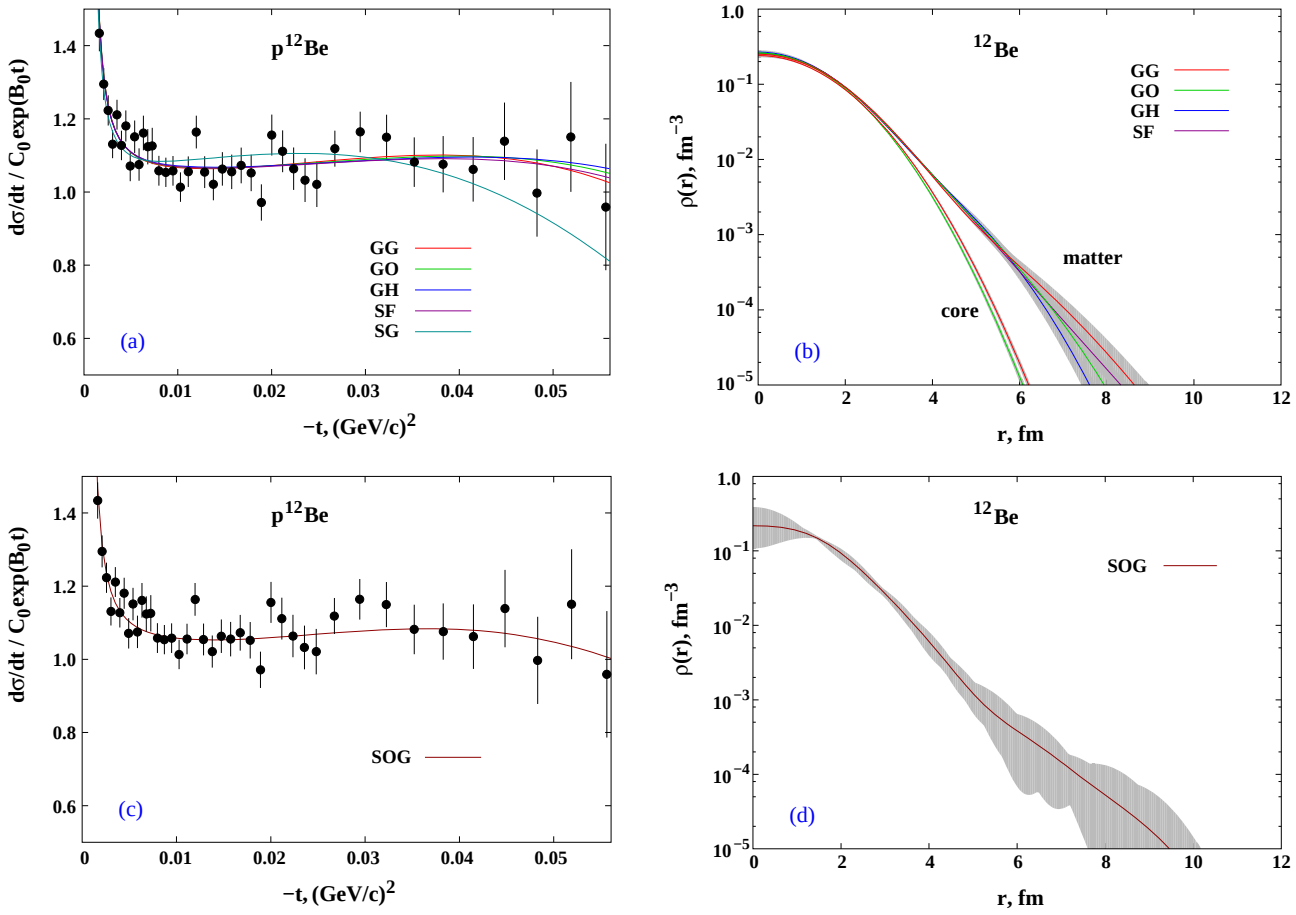

Fig. 3. a, c – fits to the experimental cross section with different parameterizations of the one-body nuclear density for the case of the ^{12}Be isotope. To enhance the visibility of the effect of the halo structure, the cross sections are divided by an exponential function. b – deduced nuclear matter and core density distributions obtained with the SF, GG, GO, GH parameterizations. The error-band represents the envelopes of the density variation within the model parameterization applied, superimposed by the statistical errors. d – nuclear-matter density distribution deduced with the SOG parameterization

The experimental data and the corresponding fits using different model density functions are plotted in Figs. 3a–d and 4a–f for the ^{12}Be and ^{14}Be isotopes, respectively. In these plots, the cross section is divided by an exponential function $C_0 \exp(B_0 t)$ for a better visibility of the effect of the halo on the cross section shape. The B_0 and C_0 coefficients represent the slope and the absolute value of the nuclear part of the differential cross section, calculated with the GO parameterization, at $-t = 0.01$ (GeV/c)^2.

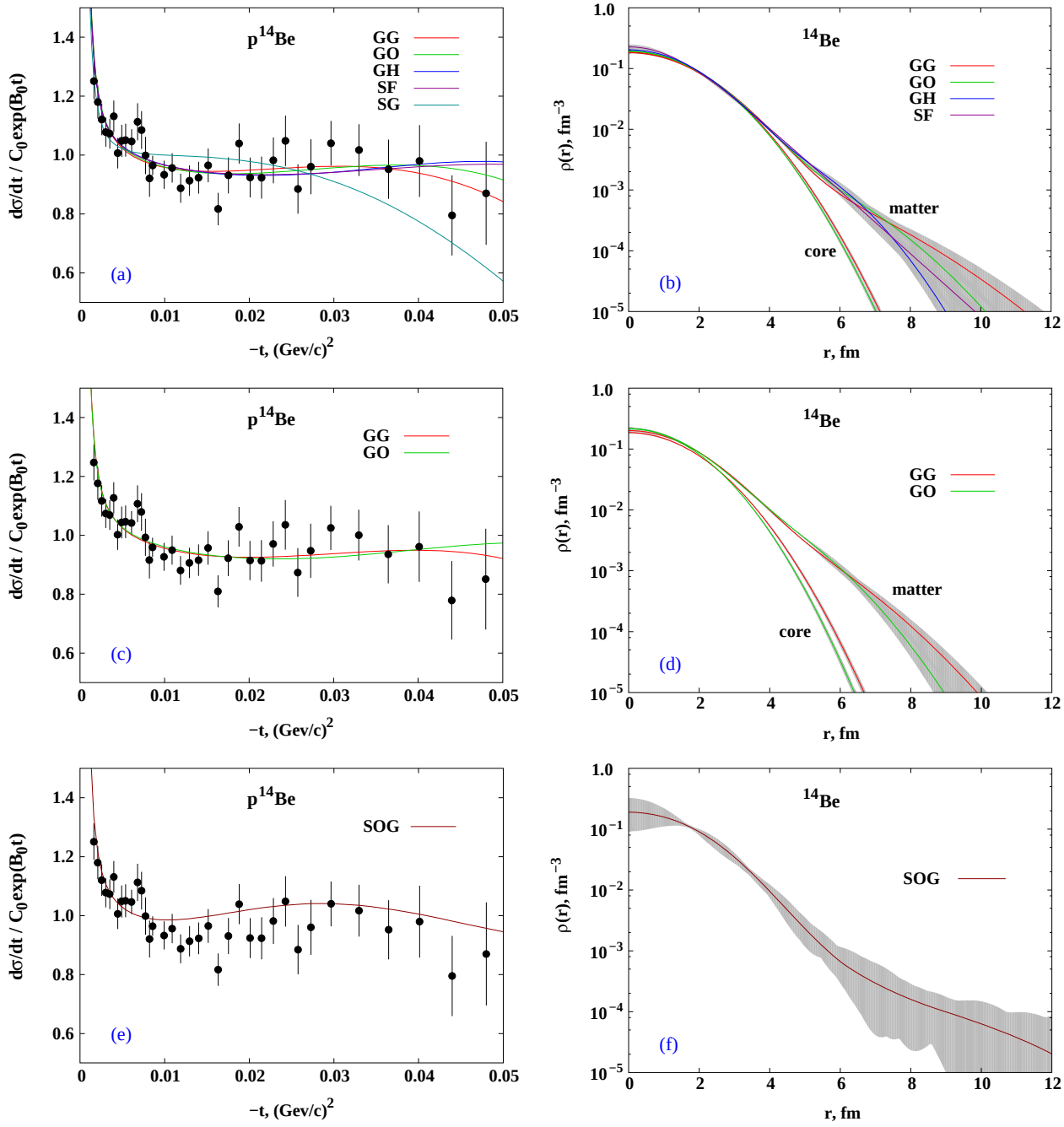

Fig. 4. a, c, e – fits to the experimental cross section with different parameterizations of the one-body nuclear density for the case of the ^{14}Be isotope. To enhance the visibility of the effect of the halo structure, the cross sections are divided by an exponential function. In Figs. a and c, the GG and GO fits were performed assuming two and four neutrons in the halo, respectively. b – deduced nuclear-matter and core density distributions obtained with the SF, GG, GO and GH ($2n$ halo) parameterizations. d – deduced nuclear-matter and core density distributions for a $4n$ halo structure. The error-band in both b and d represents the envelopes of the density variation within the model parameterization applied, superimposed by the statistical errors. f – deduced nuclear-matter density distribution from the SOG analysis

For the ^{12}Be isotope, the GG and GO analyses were performed adopting a ^{10}Be core plus two valence neutrons structure of the nucleus. Based on the χ^2 values of the fits, all parameterizations except SG give good description of the data for ^{12}Be and consistent results for the matter, core and halo radii. The weighted mean radius calculated from the values obtained with the SF, GG, GO and GH parameterizations is

$$R_m = 2.71 \pm 0.06 \text{ fm},$$

where the error includes statistical and systematic uncertainties. The systematic errors are due to uncertainties in the absolute normalization of the experimental cross section (4 %), the errors introduced to the analysis from the free *pp* and *pn* scattering amplitudes (with an estimated contribution of 0.04 fm [3]), correction for inelastic scattering contribution ($\leq$ 0.01 fm), and the error in the *t*-scale (1.5 %). The nuclear matter and core densities with their combined error-band, obtained with different model parameterizations, are shown in Fig. 3a–d. The obtained densities are consistent with each other. The mean values for the core and the halo deduced in the present analysis are $R_c = 2.36(6)$ fm and $R_h = 4.00(28)$ fm, respectively (the errors include statistical and systematic uncertainties). The core radius is slightly bigger than the matter radius of the free ^{10}Be nucleus, $R_m = 2.30(2)$ fm, which can be attributed to the centre-of-mass motion of the nucleus.

The present analysis suggests that the last two neutrons in ^{12}Be form an extended distribution. Even though the ^{12}Be isotope does not have a low neutron separation energy typical for a halo nucleus, and ^{11}Be is bound, the determined matter distribution agrees with the non-Borromean halo structure of ^{12}Be proposed by some authors. This extended matter distribution is consistent with an $N = 8$ neutron magic number disappearance in the ^{12}Be isotope.

For the analysis of the ^{14}Be data, two different assumptions on the core-halo structure of the nucleus were made for the density parameterization within the GG and GO models. In the first case, a structure of a ^{12}Be core plus two valence neutrons, and in the second one, a ^{10}Be core plus four valence neutrons were assumed. Also, the SG parameterization for this isotope gives a poor fit to the experimental data, while all other densities fit the experimental data well and give consistent results. Independent of the assumed core-halo structure, consistent results on the matter radius were obtained. The weighted mean r.m.s. radius of ^{14}Be, deduced from the SF, GG(2*n*,4*n*), GO(2*n*,4*n*) and GH parameterizations is

$$R_m = 3.25 \pm 0.11 \text{ fm}$$

including the statistical and systematic errors. For the core radius, the mean values of R_c (^{10}Be) = 2.54(11) fm and R_c (^{12}Be) = 2.77(6) fm were determined, and for the halo radius R_h (4*n*) = 4.55(19) fm and R_h (2*n*) = 5.28(43) fm, respectively, again with both statistical and systematic errors included. The deduced nuclear-matter densities with the combined error-band are plotted in Fig. 4b and Fig. 4d for two- and four-neutron halo structure, respectively, and the SOG density is shown in Fig. 4f.

The analysis of the data has given consistent results for all extended matter density parametrizations used (SF, GG, GO, GH and SOG). However, the analysis could not discriminate between these parameterizations, showing limitations of the obtained data. Also, proton elastic scattering at low momentum transfer has weak sensitivity to halo density tails at the nuclear far periphery ($r > 6$ fm), which contain nuclear matter with very low densities. In the present analysis such tails were not included. Taking such tails into account can result in some increase of the deduced nuclear-matter radii. This is the case in the SOG analysis where the density parameterization gives a possibility for a longer tail, and this parameterization gives larger radii for both ^{12}Be and ^{14}Be nuclei:

$$R_m = 2.78 \pm 0.02 \text{ fm for } ^{12}\text{Be},$$
$$R_m = 3.36 \pm 0.06 \text{ fm for } ^{14}\text{Be}.$$

4. Conclusion

The proton-nucleus elastic scattering at intermediate energies is a well-established method for investigation of the nuclear-matter density distribution in stable nuclei. Recently, this method was applied in inverse kinematics for investigation of radioactive nuclei. In the present experiment, the absolute differential cross sections $d\sigma/dt$ as a function of the four-momentum transfer squared $-t$ for small values of t ($|t| \leq 0.05$ (GeV/c)^2) at intermediate incident energies ($\approx$ 700 MeV/u) were measured for the cases of elastic p-^{12}Be and p-^{14}Be scattering. An analysis of the experimental data was performed using the Glauber

multiple-scattering theory. The results of the analysis show that for ^{14}Be a good description of the experimental cross section is obtained when density distributions SF, GG, GO, GH and SOG are used. Two possible assumptions on the halo structure of the ^{14}Be nucleus were made, a ^{12}Be core plus two valence neutrons or a ^{10}Be core plus four valence neutrons. Both of them give similar results for the r.m.s. nuclear-matter radius of the nucleus. The weighted mean value of the nuclear-matter radius was determined to be R_m = 3.25(11) fm. One can note that the quality of the p-^{14}Be cross section description is slightly better when the ^{14}Be nucleus is supposed to consist of a ^{12}Be core and two halo neutrons.

In the case of the ^{12}Be nucleus, again a good description of the experimental data was obtained with the SF, GG, GO, GH and SOG parameterizations. The results show an extended matter distribution for this nucleus, as well. The "halo" consists of two valence neutrons around a ^{10}Be core. For ^{12}Be, the r.m.s. nuclear-matter radius of 2.71(6) fm was determined.

The data presented in this article were obtained and analysed by the IKAR Collaboration:

G.D. Alkhazov, A.V. Dobrovolsky, A.G. Inglessi, A.V. Khanzadeev, G.A. Korolev, D.M. Seliverstov, L.O. Sergeev, A.A. Vorobyov, V.I. Yatsoura, A.A. Zhdanov – Petersburg Nuclear Physics Institute, Gatchina;

S. Ilieva – Extreme Matter Institute, GSI, Darmstadt;

L. Chulkov, V.A. Volkov – Kurchatov Institute, Moscow;

P. Egelhof, H. Geissel, M. Gorska, X.C. Le, Yu.A. Litvinov, C. Nociforo, H. Simon, H. Weick, – GSI Helmholtzzentrum, Darmstadt;

O.A. Kiselev – Institut für Kernchemie, Johannes Gutenberg-Universität, Mainz;

R. Kanungo – Saint Mary's University, Halifax.

References

1. G.D. Alkhazov, S.L. Belostotsky, A.A. Vorobyov, Phys. Rep. **42**, 89 (1978).
2. S.R. Neumaier, G.D. Alkhazov, M.N. Andronenko *et al*., Nucl. Phys. A **712**, 247 (2002).
3. G.D. Alkhazov, A.V. Dobrovolsky, P. Egelhof *et al*., Nucl. Phys. A **712**, 269 (2002).
4. A.V. Dobrovolsky, G.D. Alkhazov, M.N. Andronenko *et al*., Nucl. Phys. A **766**, 1 (2006).
5. S. Ilieva, F. Aksouh, G.D. Alkhazov *et al.*, Nucl. Phys. A **875**, 8 (2012).
6. A.A. Vorobyov, G.A. Korolev, V.A. Schegelsky *et al*., Nucl. Instrum. Meth. **119**, 509 (1974).
7. A.A. Vorobyov, Yu.S. Grigoriev, Yu.K. Zalite *et al*., Instrum. Exp. Tech. **24**, 1127 (1982).

SEARCH FOR THE MUON CATALYZED d^3He-FUSION

PNPI participants of the MuCF Collaboration[*]:
D.V. Balin, V.A. Ganzha, E.M. Maev, O.E. Maev, G.E. Petrov, G.G. Semenchuk, G.N. Schapkin, A.A. Vasiliev, A.A. Vorobyov, N.I. Voropaev

[*] *Austrian Academy of Sciences, A-1090 Vienna, Austria;*
Institut de Physique de l'Université, Perolles, 1700 Friburg, Switzerland;
Technical University of Munich (TUM), D-85747 Garching, Germany;
Paul Scherrer Institut (PSI), CH-5232 Villigen, Switzerland;
University of California and LBNL, Berkeley CA 94720, USA

1. Introduction

The nuclear fusion reaction

$$d + {}^3\mathrm{He} \rightarrow {}^4\mathrm{He}\ (3.66\ \mathrm{MeV}) + p\ (14.64\ \mathrm{MeV}) \tag{1}$$

is interesting for various reasons: as a mirror reaction of the $d(t, {}^4\mathrm{He})n$ fusion process and as a perspective source of thermonuclear energy. This fusion process was involved in the primordial nucleosynthesis of light elements in the early universe. For these reasons, it is important to know the cross section for this reaction at low collision energies, $E < 10$ keV. The phenomenon of the muon catalysis opens an opportunity to study this reaction at practically zero collision energy, when fusion occurs in the ${}^3\mathrm{He}d\mu$ mesomolecule:

$${}^3\mathrm{He}d\mu \rightarrow {}^4\mathrm{He}\ (3.66\ \mathrm{MeV}) + p\ (14.64\ \mathrm{MeV}) + \mu. \tag{2}$$

Formation of the ${}^3\mathrm{He}d\mu$ molecule occurs in collisions of slow $d\mu$ atoms with ${}^3\mathrm{He}$ atoms:

$$d\mu + {}^3\mathrm{He} \rightarrow [({}^3\mathrm{He}d\mu)e]^+ + e. \tag{3}$$

This process was first predicted theoretically [1] as an intermediate step in the muon transfer from the deuterium mesoatom to helium. This prediction was confirmed in our experiments at PNPI [2] where the $d\mu + {}^3\mathrm{He} \rightarrow {}^3\mathrm{He}\mu + d$ transfer rate was measured at the room temperature for the first time: $\lambda_{d^3\mathrm{He}}\ (300\ \mathrm{K}) = (1.24 \pm 0.05) \cdot 10^8\ \mathrm{s}^{-1}$, in close agreement with the predicted rate. The discovered formation of the ${}^3\mathrm{He}d\mu$ molecules allowed to search for the muon catalyzed d^3He-fusion reaction, similar to the $dd\mu$- and $dt\mu$-fusions. However, a serious complication arises from competition of this fusion reaction with very fast decay of the ${}^3\mathrm{He}d\mu$ molecule:

$$[({}^3\mathrm{He}d\mu)e]^+ \rightarrow \begin{cases} [({}^3\mathrm{He}\mu)e] + d + \gamma \\ [({}^3\mathrm{He}\mu)e] + d \\ {}^3\mathrm{He}\mu + d + e. \end{cases} \tag{4}$$

According to the theoretical calculations [3], the decay rate is $\lambda_{\mathrm{dec}} \approx 7 \cdot 10^{11}\ \mathrm{s}^{-1}$. The nuclear fusion rates $\lambda_f(J)$ in the ${}^3\mathrm{He}d\mu$ molecule depend on the value of the molecular angular momentum J. The theoretical predictions are: $\lambda_f(0) = (1.9 - 2.1) \cdot 10^5\ \mathrm{s}^{-1}$ and $\lambda_f(1) = 6.5 \cdot 10^2\ \mathrm{s}^{-1}$ [4]. About 99 % of the initially produced ${}^3\mathrm{He}d\mu$ molecules are in the $J = 1$ state. However, as Men'shikov noted [5], the transition $({}^3\mathrm{He}d\mu)_{J=1} \rightarrow ({}^3\mathrm{He}d\mu)_{J=0}$ is possible in ion-molecular reactions between the ${}^3\mathrm{He}d\mu$ and D_2 molecules *via* formation of the muonic molecular complex $[({}^3\mathrm{He}d\mu)eD_2]^+$ [6]:

$$[({}^3\mathrm{He}d\mu)_{J=1}\ e]^+ + D_2 \rightarrow [({}^3\mathrm{He}d\mu)_{J=1}\ eD_2]^+ \rightarrow [({}^3\mathrm{He}d\mu)_{J=0}\ e]^+ + D_2^+ + e. \tag{5}$$

According to theoretical estimates [6], the formation rate of the complex $[({}^3\mathrm{He}d\mu)_{J=1}eD_2]^+$ is $\lambda_1 \approx 3 \cdot 10^{13}\varphi\ \mathrm{s}^{-1}$ (where φ is the D_2 density normalized to the Liquid Hydrogen Density (LHD)), and the decay rate of this complex is $\lambda_2 \approx 5 \cdot 10^{11}\ \mathrm{s}^{-1}$. Such estimates show that one can expect quite efficient transfer $({}^3\mathrm{He}d\mu)_{J=1} \rightarrow ({}^3\mathrm{He}d\mu)_{J=0}$ and, as a consequence, a detectable ${}^3\mathrm{He}d\mu$-fusion process.

The first experimental limit on the ${}^3\mathrm{He}d\mu$-fusion rate $\lambda_f < 4 \cdot 10^8\ \mathrm{s}^{-1}$ was set at PNPI in 1990 [7]. In 1996, the MuCF Collaboration performed a short test run in the intense muon beam at PSI [8] and reduced the upper limit for the ${}^3\mathrm{He}d\mu$-fusion rate: $\lambda_f < 1.6 \cdot 10^6\ \mathrm{s}^{-1}$. Later in 1997, there was a special physics run

dedicated to the ^{3}He$d\mu$-fusion search [9]. Below we present a brief description of that experiment and the final results of the data analysis.

2. Experimental method and data analysis

The experiment was performed in the μE4 beam of the meson factory at PSI with the experimental set-up used at that time by the MuCF Collaboration for studies of the muon catalyzed *dd*-fusion [10]. The basic element of the set-up was a high-pressure cryogenic hydrogen ionization chamber (HIC) operating as an active target in the time-projection mode to detect both the proton and ^{4}He from reaction (1). The chamber was filled with the gas mixture HD + ^{3}He (5.6 %) at 50 K and 13.2 bar pressure (φ = 9.21 % of the LHD). The pure HD gas with a minimal D_2 content (0.52 %) was obtained using a special technology developed at PNPI [11]. These conditions were chosen to optimize the formation of the ^{3}He$d\mu$ molecules and to minimize background from the $dd\mu$-fusion. The chamber was exposed to an intense negative muon beam of PSI, and $9.7 \cdot 10^8$ muon stops were selected during three weeks of data taking.

The muons were stopped in the sensitive volume of the HIC which was defined by the 12 mm drift distance (from the cathode to the grid) and the anode area of 10 cm^2 subdivided into 13 pads (Fig. 1a, b). The HIC operated at –35 kV on the cathode and –4 kV on the grid. The maximum drift time of electrons was 2 μ*s*. For detection of signals from the anodes, a fast (100 MHz, 8 bit) Flash ADC based electronics was used. It allowed to receive full information about the signals (amplitude, duration, time and energy) from all the charged particles which were detected inside the HIC. The energy resolution (rms) and the energy threshold were 30 and 120 keV, respectively.

The strategy of the measurements was to select a clean sample of muon stops (N_μ) in the fiducial volume inside the HIC. The muon signals had to satisfy a set of amplitude, duration and energy criteria that provided reliable selection of such muon stops avoiding completely (on a level of 0.01 %) any wall effects in the measurements. Then we had to look for events with a large signal on the muon-stop anode, separated in time from the muon signal. Such events correspond to detection of ^{4}He with the energy of 3.66 MeV. Then it was required that the ^{4}He signal was accompanied by signals on at least two neighbouring anodes, that constitute a continuous track, with the energy deposit corresponding to the track of a 14.64 MeV proton. This combined registration of the ^{4}He and proton signals drastically suppressed most of the background, where one of the reaction products was the long-range charged particle, *e.g*., from μ-capture on the wall materials or from the breakup reactions in μ^3He-capture. One candidate for the d^3He-fusion event is presented in Fig. 1a.

According to the kinetics of the processes in the HD + ^{3}He gas mixture, the following reactions can occur after a muon stop: $pd\mu$-, $dd\mu$- and ^{3}He$d\mu$-fusions, as well as muon capture on nuclei (^{3}He and gaseous impurities: O_2, N_2, *etc*.). The HIC detected all the charge products of these reactions with an energy higher than 200 keV. Figure 2 shows the measured amplitude distribution of pulses which follow the muon signals. In this spectrum, one can see the peaks corresponding to the products of the following processes: the $dd\mu$-fusion channels with ^{3}He + *n*, ^{3}Heμ + *n*, *t* + *p*; the channel with ^{3}He + μ from the $pd\mu$-fusion, and the triton peak from the muon capture on ^{3}He. The interpretation of this spectrum requires to take into account the effect of ion-electron recombination in the ionization chamber gas that shifts the observed peaks towards lower amplitudes. The quantitative evaluation of these shifts is known from our previous measurements. The number of the ^{3}He$d\mu$ molecules formed after the muon stops is given by the expression:

$$N_{^3\mathrm{He}d\mu} = N_\mu \cdot C_{d\mu} \cdot \Lambda_{d^3\mathrm{He}} / \lambda_{\mathrm{tot}}, \qquad (6)$$

where λ_{tot} is the disappearance rate of the $d\mu$ atoms, $\Lambda_{d^3\mathrm{He}}$ is the ^{3}He$d\mu$ molecule formation rate, and $C_{d\mu}$ is the fraction of the stopped muons which had reached the $d\mu$-atom ground state. All these three parameters were measured directly in our experiment.

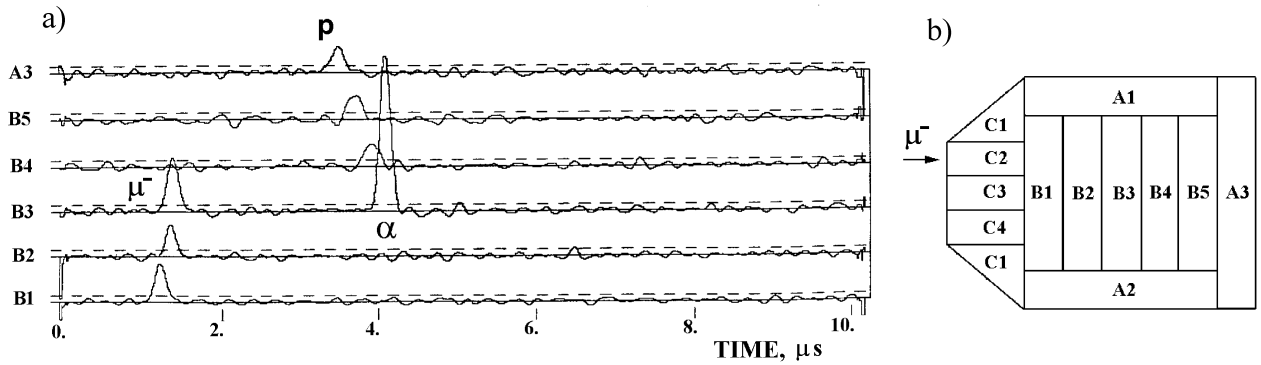

Fig. 1. a – display of the Flash ADCs for a candidate event of d^3He-fusion. The dotted lines show the threshold levels. b – top view of the anode pad plane

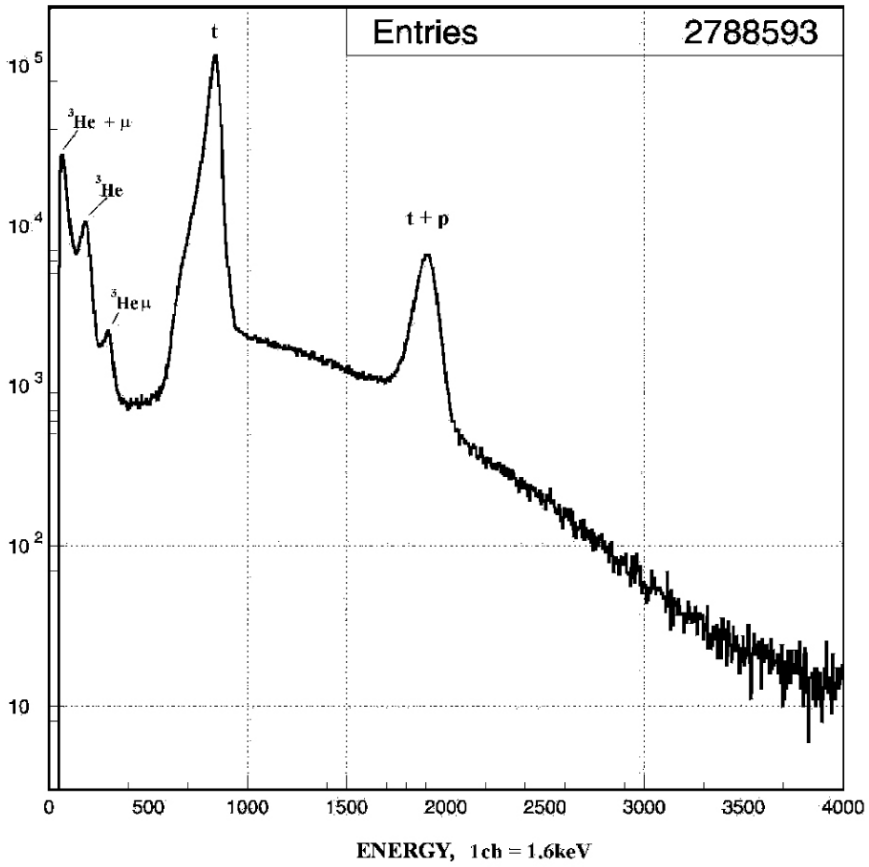

Fig. 2. Amplitude spectrum of pulses after the muon signals

The rates λ_{tot} and Λ_{d^3He} were obtained from the analysis of time distribution of $t+p$ signals from the $dd\mu$-fusion. In order to select such events, we analysed the part of the energy spectrum around the peak in the region 2.8–3.2 MeV (see Fig. 2). The disappearance rate of the $d\mu$ atoms determined from the slope of the time distribution proved to be $\lambda_{tot} = (1.907 \pm 0.037) \cdot 10^6\ s^{-1}$. The rate Λ_{d^3He} was determined by the formula:

$$\Lambda_{d^3He} = \lambda_{tot} - \lambda_0 - \Lambda_{dd\mu} - \Lambda_{pd\mu} - \Lambda_{\mu Z}, \tag{7}$$

where $\lambda_0 = 0.455 \cdot 10^6\ s^{-1}$ is the muon lifetime.

The rates $\Lambda_{dd\mu} = (2.18 \pm 0.046) \cdot 10^3\ s^{-1}$, $\Lambda_{pd\mu} = (2.5 \pm 0.1) \cdot 10^5\ s^{-1}$ and $\Lambda_{\mu Z} \leq 3 \cdot 10^3\ s^{-1}$ were measured in our previous experiments. This gives $\lambda_{d^3He} = (1.197 \pm 0.046) \cdot 10^6\ s^{-1}$. Finally, normalizing to the LHD, we obtain [12]:

$$\lambda_{d^3He}(50\ K) = \Lambda_{d^3He} / (\varphi\, C_{^3He}) = (2.32 \pm 0.09) \cdot 10^8\ s^{-1}, \quad (8)$$

where $\varphi = 9.21$ % is the HD + ^{3}He gas density and $C_{^3He} = 5.6$ % is the ^{3}He concentration.

This result could be compared with the d^3He formation rate measured at the room temperature in our previous experiment [2]: $\lambda_{d^3He}(300\ K) = (1.24 \pm 0.05) \cdot 10^8\ s^{-1}$. Both results are in good agreement with the theoretical predictions based on the resonant exchange mechanism [13]. The value of $C_{d\mu}$ was estimated in the measurement of the triton yield (Y_t) from the reaction of μ^3He-capture. The triton events from the μ^3He-capture correspond to the peak in the region 1.1–1.5 MeV of the amplitude spectrum in Fig. 2. The method of Y_t determination was totally identical to that used in our experiment for precise measurement of the rate of the muon capture on ^{3}He [14]. After an analysis of the amplitude and time distributions of these events, we obtained $Y_t = (1.88 \pm 0.04) \cdot 10^{-3}$. The triton yield Y_t depends directly on the value of $C_{d\mu}$, on the rates of the $pd\mu$ and $dd\mu$ fusions, and on the rate of the μ^3He-capture. All the rates necessary for calculations of Y_t are well known from our previous measurements or have been measured in the present experiment. Finally, from the measured triton yield Y_t we obtain the value of $C_{d\mu} = 0.82 \pm 0.06$. Using the measured values of Λ_{d^3He}, λ_{tot}, and $C_{d\mu}$, we have calculated from Eq. (6) the number of ^{3}He$d\mu$ molecules formed in our experiment by the selected stopped muons:

$$N_{^3Hed\mu} = (4.9 \pm 0.4) \cdot 10^8.$$

The background processes, which can in principle imitate signals from the d^3He-fusion in the HD + ^{3}He gas mixture are: the muon catalyzed *dd*- and *pd*-fusions, the muon capture on ^{3}He, and the muon capture on gas impurities. Also, a possible source of background is the pile-up of signals from these reactions with each other and with muons. The important background reactions are:

a) channel $t + p$ of $dd\mu$-fusion (the energy and the range of the emitted particles are $E_p = 3.02$ MeV, $R_p = 0.9$ cm, $E_t = 1.01$ MeV, $R_t = 0.06$ cm);

b) channel $^3He + n$ of $dd\mu$-fusion ($E_{^3He} = 0.82$ MeV). This channel is dangerous because it produces d^3He-fusions in flight in collisions of ^{3}He with deuterium atoms, especially since the cross section for the d^3He-fusion has a maximum near 0.8 MeV. To suppress these channels of background, we replaced D_2 in the experimental gas mixture by HD and reduced the target temperature to 50 K. By this, we decreased the yield of the $dd\mu$-fusion events by a factor of ~ 50;

c) μ-capture on ^{3}He, namely, the breakup reactions with long-range protons and deuterons. These reactions can imitate the d^3He-fusion only in the case of pile-up with the products of other reactions, *e.g.*, $t + p$. However, the probability of such pile-ups is very low;

d) μ-capture on impurities accompanied by long-range protons.

It turned out that the process *d*) is the main source of background in the experiment (this we understood after special investigations) and really can imitate signals from the products of the ^{3}He$d\mu$-fusion reaction. To study the background from the μ-capture reactions, we performed an additional experiment with high concentration of nitrogen admixture ($H_2 + N_2$, 140 ppm, $\varphi = 0.0872$). Also, in order to estimate the probabilities of background events from $dd\mu$-fusion and μ-capture on ^{3}He, we analysed the data from our experiments with the HD-mixture ($\varphi = 0.0941$) and from the experiment devoted to a study of the μ-capture on ^{3}He ($\varphi = 0.0656$). All these measurements were performed in similar experimental conditions with the same experimental set-up.

No candidates for the ^{3}He$d\mu$-fusion events in either pure HD or pure ^{3}He gas targets were found in our analysis. The background due to the $dd\mu$-fusion and ^{3}Heμ-capture reactions was shown to be negligible. In contrast, the experiment with $H_2 + N_2$ (140 ppm) yielded such candidate events. They imitated the signals which we anticipated from the ^{3}He$d\mu$-fusion events. These signals could appear due to charged products of μ capture on nitrogen: protons, deuterons, α, *etc*. Nitrogen was the main admixture in our case (on a level of ~ 1 ppm).

However, the time distribution of such μ-capture events is very different from that of the d^3He-fusion events. About 95 % of the fusion events should be earlier than 1.8 μs after the stopped muon, however the μN-capture events appear mostly after 1.8 μs. We applied this criterion to three selected candidates for the d^3He-fusion events in the experiment with the HD + ^{3}He gas mixture and found that only one of them was in the (0–1.8) μs interval.

Finally, in the course of our experiment, $4.9 \cdot 10^8$ ^{3}Hedμ-molecules were formed with only one event which passed the selection criteria as a candidate for the ^{3}Hedμ-fusion event. On the other hand, the expected background was also one event. Following the PDG recommendations, we have concluded that the number of the d^3He-fusion events detected in our experiment is $N_f < 3.3$ on the 90 % confidence level. From this, the effective fusion rate λ_f is determined:

$$\lambda_f = N_f \lambda_{dec} / (N_{^3\mathrm{He}d\mu}\, \varepsilon), \tag{9}$$

where N_f is the number of the d^3He-fusion events ($N_f < 3.3$), $N_{^3\mathrm{He}d\mu}$ is the number of the ^{3}Hedμ-molecules ($4.9 \cdot 10^8$), λ_{dec} is the decay rate of the ^{3}Hedμ-molecules ($\lambda_{dec} \approx 7 \cdot 10^{11}$ s^{-1}), and ε is the detection efficiency of the products of the ^{3}Hedμ-fusion reactions. This efficiency was defined as $\varepsilon = \varepsilon_\tau \cdot \varepsilon_S$. The factor ε_S was determined mostly by the efficiency of registration of the ^{3}Hed-fusion protons (their range was 16.4 cm), according to the geometry of the HIC and the selection criteria on the amplitude and duration of signals in a proton track (the detection efficiency of the 3.66 MeV alpha particles was 100 %). The value of ε_S was calculated by Monte-Carlo simulations: $\varepsilon_s = 0.13 \pm 0.01$. The factor ε_τ takes into account the dead time resulting from pile-ups of signals of the fusion products with the muon signals. To define the factor ε_τ, we used the experimental time distribution of the $t + p$ signals of the dd-fusion, which in our experimental conditions was similar to the expected time distribution of the d^3He-fusion events. Besides, we used the results of Monte-Carlo simulations of durations of signals from the products of the d^3He-fusion to take into account the selection criteria which were applied in the search of the candidates for the ^{3}Hedμ-fusion events. In this way, we have evaluated $\varepsilon_\tau = 0.63 \pm 0.05$ and the total efficiency $\varepsilon = \varepsilon_\tau \cdot \varepsilon_S = (8.2 \pm 0.8)$ %.

Finally, from Eq. (9) we obtain the upper limit for the effective fusion rate λ_f :

$$\lambda_f < 6 \cdot 10^4 \text{ s}^{-1} \text{ at 90 \% C.L.}$$

In addition, we can deduce the upper limit of the fusion rate $\lambda_f(0)$ from the $J = 0$ state of the ^{3}Hedμ-molecule using the theoretical value for the population $P(0)$ of this state [4]:

$$\lambda_f(0) < 5 \cdot 10^5 \text{ s}^{-1}.$$

The obtained upper limit is still higher than the theoretical prediction $\lambda_f(0) \approx 2 \cdot 10^5$ s^{-1} [4].

Recently, new results were published [15] from an experiment that was performed with the D_2 + ^{3}He (5 %) gas mixture at two densities (φ = 5.21 % and φ = 16.8 % of the LHD). From an analysis of their data, the authors obtained the following values of the effective fusion rate: $\lambda_f = (4.5 + 2.6 - 2.0) \cdot 10^5$ s^{-1} at φ = 5.21 %, and $\lambda_f = (6.9 + 3.6 - 3.0) \cdot 10^5$ s^{-1} at φ = 16.8 %. In spite of a rather low (~ 40 %) accuracy of these data, the estimated values of λ_f seem to exceed by an order of magnitude the upper limit for λ_f set in our experiment. Assuming this difference is not due to some problems in either of the experiments, but rather due to differences in the experimental conditions, this might be an interesting interpretation of the experimental results indicating a way for further investigations.

3. Conclusion

A new upper limit for the d^3Heμ-fusion rate, $\lambda_f < 6 \cdot 10^4$ s^{-1}, was experimentally set in the experiment performed with the HD + ^{3}He (5.6 %) gas mixture at the 50 K temperature and gas density φ = 9.21 % of the LHD. From this result, we have derived an upper limit for the d^3Heμ-fusion rate λ_f (0) from the $J = 0$ state of the ^{3}Hedμ molecule: $\lambda_f(0) < 5 \cdot 10^5$ s^{-1}. In addition, the $d\mu \rightarrow {}^3$Heμ transfer rate $\lambda_{d^3\mathrm{He}}$ was measured for the first time at 50 K: $\lambda_{d^3\mathrm{He}}(50\text{ K}) = (2.32 \pm 0.09) \cdot 10^8$ s^{-1}. This value could be compared with the result of our previous measurement at the room temperature: $\lambda_{d^3\mathrm{He}}(300\text{ K}) = (1.24 \pm 0.05) \cdot 10^8$ s^{-1} [2]. Both values are in agreement with the theoretical prediction [13] based on the resonant formation of the ^{3}Hedμ molecule.

The measured upper limit $\lambda_f < 6 \cdot 10^4$ s^{-1} for the d^3Heμ-fusion rate looks to be in strike disagreement with the reported in Ref. [15] observation of the d^3Heμ-fusion signals with the rate $\lambda_f \approx 5 \cdot 10^5$ s^{-1}. However, that experiment was performed with another gas mixture, namely with D_2 + ^{3}He(5 %), and we do not exclude that the difference between the results of these two experiments might be due to a possible difference in the formation rates of the $[(^3\text{He}d\mu)_{J=1}\ e\text{HD}]^+$ and $[(^3\text{He}d\mu)_{J=1}\ eD_2]^+$ clusters. To clarify the situation, some new measurements are desirable. For example, using the existing set-up of the MuSun experiment (see the article devoted to the MuSun experiment in this edition), one could increase the sensitivity for the search of the muon catalyzed d^3He-fusion by an order of magnitude with a quite low background.

References

1. Y.A. Aristov *et al*., Yad. Fiz. **33**, 1066 (1981).
2. D.V. Balin *et al*., Preprint LNPI-**964**, Gathina (1984); D.V. Balin *et al*., Pisma ZhETF **42**, 236 (1985).
3. Y. Kino and M. Kamimura, Hyperfine Int. **82**, 195 (1993); A.V. Kravtsov *et al*., Z. Phys. D **29**, 49 (1994); S.S. Gershtein and V.V. Gusev, Hyperfine Int. **82**, 205 (1993).
4. L.N. Bogdanova, V.I. Korobov and L.I. Ponomarev, Hyp. Interact. **118**, 187 (1999); D.I. Abramov, V.V. Gusev and L.I. Ponomarev, Hyp. Interact. **119**, 127 (1999).
5. L.I. Men'shikov, Preprint IAE-**3810/12**, Moscow (1983).
6. M.P. Faifman and L.I. Men'shikov, Hyp. Interact. **118**, 183 (1999).
7. D.V. Balin *et al*., Muon Catalyzed Fusion **7**, 301 (1992).
8. D.V. Balin *et al*., Preprint PNPI-**2221**, Gatchina (1998).
9. E.M. Maev *et al*., Hyp. Interact. **118**, 171 (1999).
10. D.V. Balin *et al.*, Particles & Nuclei **42**, part 2, 361 (2011).
11. G.N. Schapkin *et al*., Preprint PNPI-**2395**, Gatchina (2000).
12. E.M. Maev *et al*., Hyp. Interact. **119**, 121 (1999).
13. V.K. Ivanov *et al*., JETP Lett. **91**, 358 (1986).
14. P. Ackerbauer *et al*., Phys. Lett. B **417**, 224 (1998).
15. V.M. Bystritsky *et al.*, Europ. Phys. J. D **38**, 455 (2006).

NEW LASER SET-UP FOR SELECTIVE ISOTOPE PRODUCTION AND LASER SPECTROSCOPY INVESTIGATIONS IN A LASER ION SOURCE AT THE IRIS FACILITY

A.E. Barzakh, D.V. Fedorov, V.S. Ivanov, K.A. Mezilev, P.L. Molkanov, F.V. Moroz, S.Yu. Orlov, V.N. Panteleev, Yu.M. Volkov

The method of resonance laser photoionization in a Laser Ion Source (LIS), developed and applied for in-source laser spectroscopy at the IRIS facility of PNPI [1], proves to be one of the most efficient tools for isotope shift and hyperfine structure investigations and for isobarically clean radioactive isotope production. The essential point of the experimental method is step-by-step resonant laser excitation from the ground state of an atom, through intermediate states to autoionization states or to continuum.

A new laser installation based on this technique has been built and put into operation at the IRIS facility [2]. This was a significant improvement of the laser-ion source device of the IRIS mass-separator working on-line with a 1 GeV proton beam of the PNPI synchrocyclotron. The new laser set-up provides two- or three-resonance step ionization in the range of wavelengths of 265–850 nm. Two narrowband scanning dye lasers can be applied for laser spectroscopy inside an ion source-target device of the mass-separator.

The laser system designed by Medical Sterilization Systems Company (Moscow region, Russia) consists of Copper Vapor Lasers (CVL), dye lasers, nonlinear crystals and other optical elements for manipulations with light beams (see Fig. 1). The key elements of the LIS laser set-up are pulsed CVL with high repetition rate. The system consisting of a laser oscillator and two parallel amplifiers has been assembled using commercially produced, sealed-off, discharge-heated CVL tubes LT-40Cu. The CVLs run at the pulse repetition rate of 11 kHz, with the pulse duration of 20 ns. All three tubes are triggered simultaneously and produce two beams with an average power of 50 W. The CVL radiation is composed of two spectral lines of 511 and 578 nm. After separation of these components, four beams are available for pumping of dye lasers.

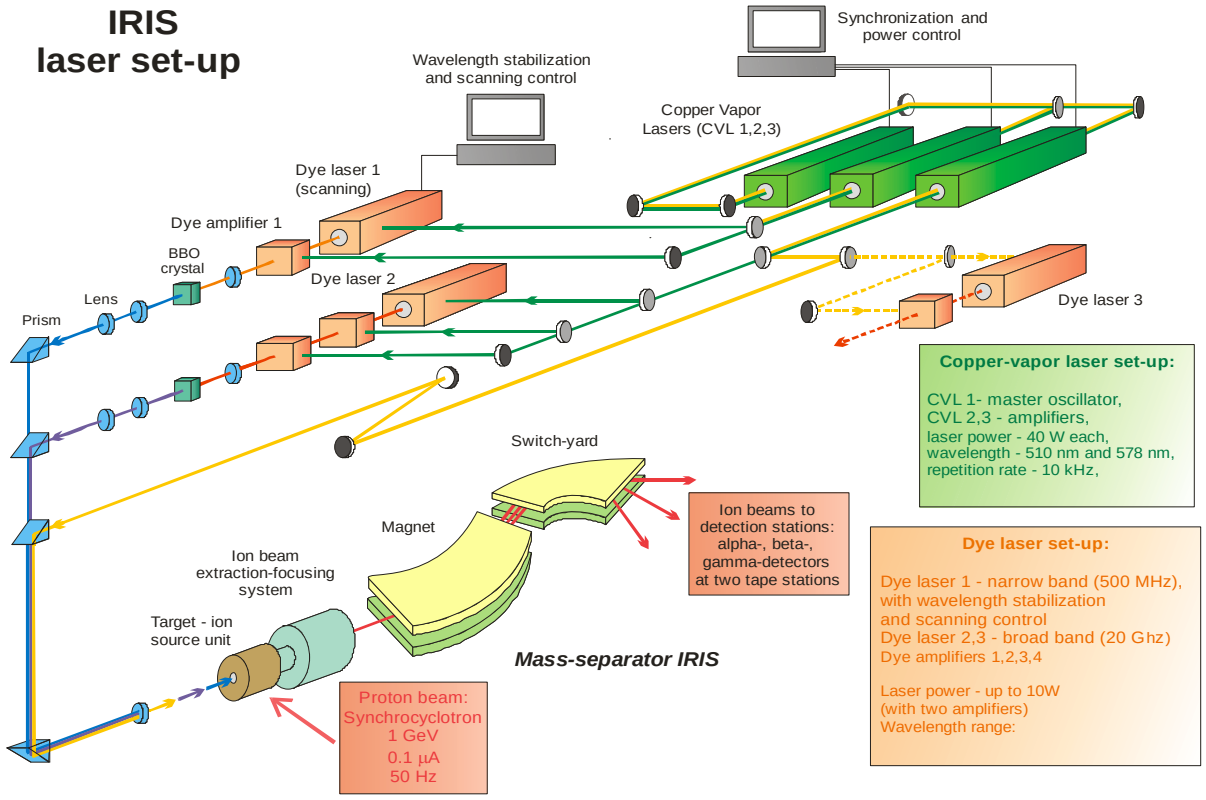

Fig. 1. Scheme of the new laser-nuclear complex of the IRIS facility

Two or three dye lasers and some amplifier dye cells can be pumped by a CVL. As an option, one CVL beam can also be used to ionize atoms from highly excited states into continuum. With various laser dye solutions it is possible to cover the spectral range 530–850 nm, but this range can be extended to the ultraviolet region by doubling and tripling of the light frequencies using nonlinear BBO crystals. The dye laser wavelength is tuned by rotation of the diffraction grating in the dye laser cavity. The lasers tuned to some fixed wavelengths of specific atomic transitions provide selective ionization of the element under investigation.

The new CVL installation is controlled by specific hardware and software to stabilize the electric power consumption and control the synchronization of CVL tube triggering. An electromechanical system for laser frequency scanning has been installed. It incorporates step motors for setting of the narrowband laser etalon and positions of the diffraction gratings, a wavemeter LM-007 for frequency read-out, and also communications to the data acquisition system. The new system provides a smooth narrowband scanning by self-calibration of the etalon and grating positions according to the laser line quality criterion. All parameters of the scanning mode can be set using a LabView-based program.

The nuclides under study are produced in a hot target of the mass separator by 1 GeV protons of the PNPI synchrocyclotron. The atoms are thermally released from the target to the ion source cavity (tungsten tube of 40 mm length and 1.5 mm diameter). The beams from lasers are directed to the same cavity through a quartz window in the front-end back side to provide multi-step resonance ionization of the atoms under study. The distance between the laser set-up and the ion source is about 25 m. The wavelength of the narrow-band laser (NBL; with fundamental bandwidth of 1 GHz) scans the selected transition area. The photo-ion current at the collector of the mass separator increases at the resonance. Thus, the experimental spectra represent the dependence of the ion current on the scanning laser frequency. The detection of the ion current is provided by α-, β-, or γ-counting.

A substantial increase of the ionization efficiency can be achieved by decreasing the inner diameter of the laser ion source tube with corresponding focusing of the laser beam. At the IRIS facility, the laser spot as small as 1 mm in diameter can be formed by a lens, placed at the distance of 2 m from the ion source. The first experiments with isotopes of In and Tl have been carried out at the new laser set-up of the IRIS facility. The radioactive isotopes were produced by 1 GeV protons of the PNPI synchrocyclotron in 91 g/cm^2 thick $^{238}UC_x$ target.

Insertion of a Fabry – Perot etalon in the dye laser resonator results in reduction of the laser bandwidth to nearly 1 GHz. By scanning its frequency over the resonance, together with simultaneous counting of the mass-separated photo-ions, we can measure the Isotope Shift (IS) and hyperfine structure (hfs) constants of the atomic spectral lines. From these data the changes in nuclear mean square charge radii and the electromagnetic moments can be determined according to the well-known formulas:

$$
\begin{aligned}
&\nu^{F,F'} = \nu_0 + \nu_F - \nu_{F'};\\
&\nu_F = a \cdot \frac{K}{2} + b \cdot \frac{3/4 \cdot K \cdot (K+1) - I \cdot (I+1) \cdot J \cdot (J+1)}{2 \cdot (2I-1) \cdot (2J-1) \cdot I \cdot J};\\
&K = F \cdot (F+1) - I \cdot (I+1) - J \cdot (J+1);\\
&\vec{F} = \vec{I} + \vec{J},\ F = | I - J |,\ | I - J | + 1,\ \ldots\ ,\ I + J;\\
&a \propto \mu,\ b \propto Q,
\end{aligned}
\qquad (1)
$$

where $\nu^{F,F'}$ is the position of a component of the hfs in the experimental spectrum, I and J are the nuclear and electronic spins, F is the total atomic spin, a and b are the hfs constants which are proportional to the magnetic and electric quadrupole moments, μ and Q, correspondingly. The displacement of the position of the centre of gravity of the hfs for the isotope with atomic number A, ν_0^A, relative to the position of the centre of gravity of the hfs for the stable isotope A_0 gives the isotope shift $\Delta\nu^{A,A_0}$, $\Delta\nu^{A,A_0} = \nu_0^A - \nu_0^{A_0}$. It depends linearly on the change of the nuclear mean square charge radius:

$$\Delta\nu^{A,A_0} = f\cdot\lambda + \frac{M\cdot(A-A_0)}{A\cdot A_0}; \qquad (2)$$
$$\lambda = K(Z)\cdot\Delta < r^2 >^{A,A_0},$$

here f is the electronic factor and M is the mass shift constant for a particular atomic transition. The constant $K(Z)$ is close to unity and can be reliably calculated with sufficient accuracy. Two-step resonance schemes were used for In and Tl isotopes:

$$\text{In: } 5p^2P_{1/2} \xrightarrow[\text{NBL}]{303.9\text{ nm}} 5d^2D_{3/2} \xrightarrow[\text{CVL}]{511\text{ nm}+578\text{ nm}} \text{continuum;}$$

$$\text{Tl: } 6p^2P_{1/2} \xrightarrow[\text{NBL}]{276.9\text{ nm}} 6d^2D_{3/2} \xrightarrow[\text{CVL}]{511\text{ nm}+578\text{ nm}} \text{continuum.}$$

The optical spectra of stable isotopes were recorded by measuring the Faraday cup current *vs* the scanning frequency of a NBL at the first excitation step. For all but ^{207}Tl radioactive isotopes, the ion current was monitored by the counts under the γ- or α-peaks produced in decays of the corresponding isotopes. For ^{207}Tl, a β-counter was used.

In Table 1, the results of IS and hfs measurements for three Indium isotopes are presented. The magnetic hfs constants a correspond fairly well to those previously measured by collinear spectroscopy. The isotopic shifts of 303.9 nm optical line for radioactive ^{119,121}In isotopes have been measured for the first time. These values are of significance for the King-plot calibration for future measurements of IS for Indium isotopes very far from stability ($A < 104$, $A > 127$). The accuracy of the LIS method is significantly lower than the accuracy of collinear spectroscopy due to lower resolution of LIS method due to Doppler broadening. At the same time, the LIS method has markedly higher efficiency and thus enables one to go further away from stability. This crucial advantage of the LIS method is clearly demonstrated by the results obtained for Tl isotopes.

Table 1

Results of the IS and hfs measurements for In isotopes

A	$T_{1/2}$	IS (λ = 303.9 nm), MHz	$a(5p^2P_{1/2})$, MHz	$a(5p^2P_{1/2})$, MHz (literature)
115	stable	0	2380(80)	2281.9501(4)
119	2,4 m	550(130)	2300(70)	2270.6(1.2)
121	23.1 s	680(160)	2440(120)	2266.0(1.8)

In Fig. 2, some hfs spectra of Tl isotopes and isomers are shown. The hfs of the exited state ($6d^2D_{3/2}$) is extremely narrow (less than 10–50 MHz depending on the magnetic moment) and can not be resolved in LIS experiments. Therefore, in processing of hfs spectra, the ratio of the constants a for the ground and excited atomic states was fixed according to the known a-values for stable Tl isotopes: $a_{6d^2D_{3/2}} / a_{6p^2P_{1/2}} = -0.00201$. Possible variation of this ratio due to hyperfine anomaly is less than 2–3 % and does not affect the results of the fits. The nuclear quadrupole moment does not influence the hfs of the ground states of Tl as its electronic moment J is equal to 1/2.

The isotopic shifts and hyperfine constants for 20 Tl isotopes and isomers have been measured (for A = 207, 203, 197m, 195m, 194g, 194m, 193m, 192g, 192m, 191m, 190g, 190m, 189m, 188m, 187m, 186g, 186m2, 185m, 184, 183). For the optical line of 276.9 nm these values were measured previously for the stable isotopes ^{205,203}Tl only. Previously, the results of the IS and hfs measurements for 535 nm transition by collinear spectroscopy for great variety of the Tl isotopes and isomers with $186 < A < 194$ were reported. The higher efficiency of the LIS method enables us to go further away from stability down to A = 183 and,

besides, to obtain the IS and hfs data for those short-lived low yield isomers with larger A, which remained unattainable for the collinear spectroscopy (^{197m,195m,186m2}Tl).

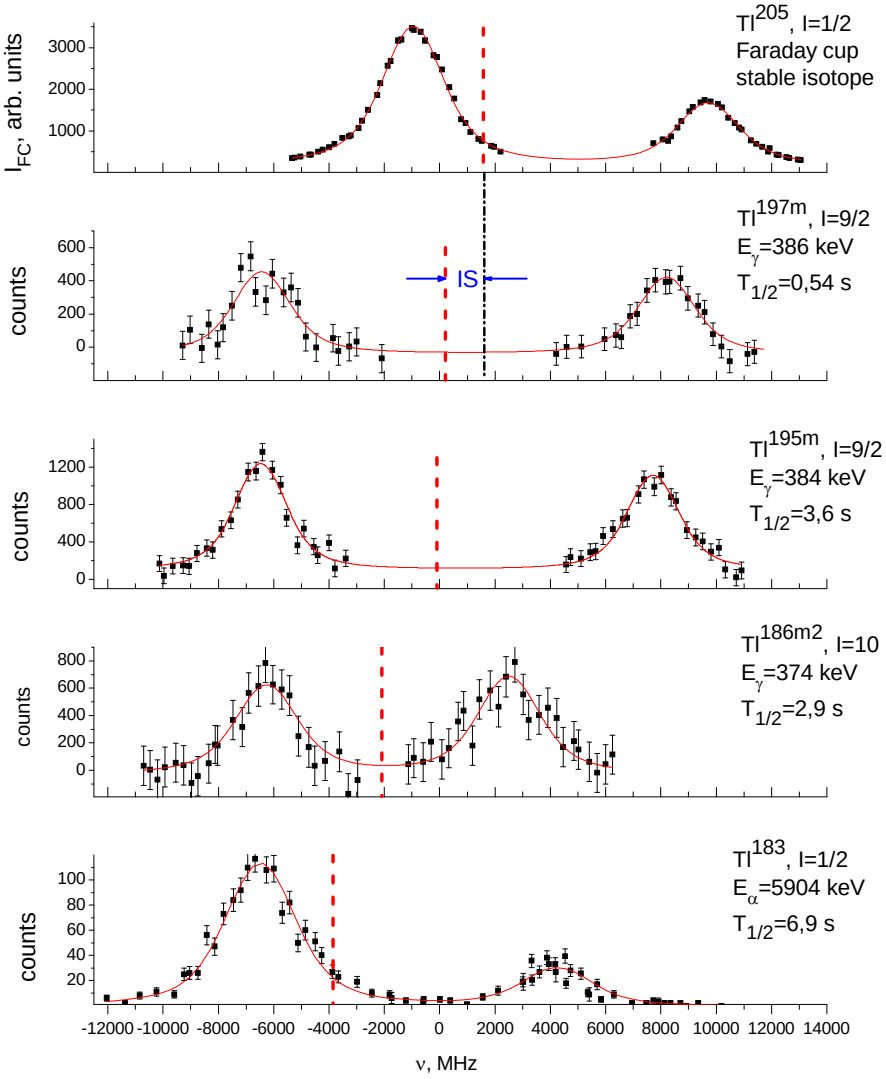

Fig. 2. Hfs spectra of several Tl isotopes. In the inserts, the atomic number, spin, energy of the γ- or α-lines for ion current monitoring and the lifetime of the isotope in question are presented. Full lines are the results of fitting with the Voigt profile. Vertical dash lines mark the centres of gravity of the corresponding hfs. The displacement of each of these lines relative to the centre of gravity of the stable isotope (^{205}Tl) hfs is the value of the isotope shift

The lower limit of the efficiency ε of the new LIS – IRIS installation for investigation of Tl isotopes was determined by comparison of the observed photo-ions yield with the calculated in-target production of the long-living ^{194}Tl. Both the isomer and the ground state yields at the resonance frequency of NBL were taken into account. The in-target production was calculated with the known cross-section for the reaction $(p^{238}\mathrm{U})^{194}$Tl at 1 GeV. The obtained value, $\varepsilon_{\mathrm{IRIS}}(\mathrm{Tl}) \cong 3\,\%$, is quite comparable with the efficiency of the RILIS – ISOLDE installation for Tl: $\varepsilon_{\mathrm{ISOLDE}}(\mathrm{Tl}) \cong 2 \div 4\,\%$. The latter value was estimated in the same way taking into account the yields of ^{190,192,195}Tl with RILIS at 1.4 GeV proton energy and the measured difference in these isotopes productions between 1 and 1.4 GeV proton energies.

According to Eq. (2), in order to extract $\Delta\langle r^2\rangle$ values from the IS data for the atomic transition one should know the electronic factor f and the mass shift constant M. The values of f and M are well established

for the 535 nm transition of the *p*-*s* type. To determine the values of *f* and *M* for the *p*-*d* type 276.9 nm transition, the well-known King-plot procedure was applied. It is clearly seen from the Eq. (2) that the values $\Delta\sigma_{A,A'}(\nu) \equiv \Delta\nu_{A,A'}(\nu) \cdot \frac{A \cdot A'}{A - A'}$ for different atomic transitions ν should lie on a straight line with the slope equal to the ratio of the corresponding *f*-factors, and the point of intersection of this line with the *y*-axis gives *M*-factor for the transition with the unknown electronic constants provided these constants are determined for one of the transitions involved. At the same time, this King-plot procedure enables one to check the consistency of the newly obtained IS data, especially when the IS data for the comparing transition have significantly smaller errors. This is the case for the 535 nm transition. In Fig. 3, the King-plot for the 276.9 and 535 nm transitions is presented. It shows absence of systematic errors in our data and enables us to determine the *f*- and *M*-factors for the 276.9 nm transition.

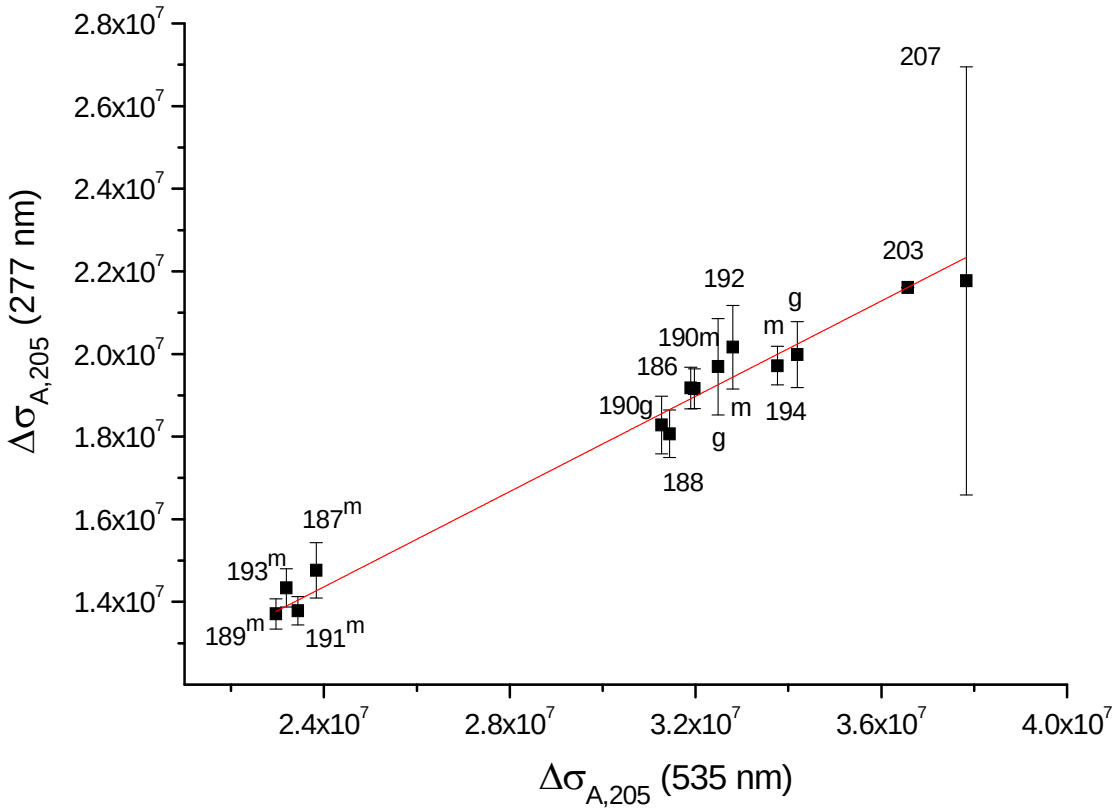

Fig. 3. King-plot for 535 and 277 nm optical transitions in Tl. Data for 535 nm transition and for $\Delta\nu_{203,205}$(276.9 nm) were taken from literature. Other data are from the present work. The atomic numbers *A* for corresponding isotopes and isomers are shown near the experimental points

With these factors one can calculate the values of $\Delta\langle r^2\rangle$ for newly investigated nuclei. These new values together with previously determined ones are presented in Fig. 4. It is generally acknowledged that the isotopic trend of the $\Delta\langle r^2\rangle$ is described by the Droplet Model (DM). Deviations from the DM trend are attributed to a contribution from the mean squared quadrupole deformation:

$$\langle r^2 \rangle = \langle r^2_{DM} \rangle (1 + \frac{5}{4\pi} \langle \beta^2 \rangle). \quad (3)$$

The lines of DM-predicted $\Delta\langle r^2\rangle$ *vs A* with fixed mean squared deformations are shown in Fig. 4 to get an insight into the development of deformation in the chain of Tl isotopes.

A rather large isomer shift between $I = 1/2$ and 9/2 states for odd Tl isotopes is preserved for both sides of previously investigated mass range (for $A < 186$ and $A > 192$). This means that a moderate oblate deformation is favored by the $h_{9/2}$ intruder state already in the comparably close vicinity of the neutron magic

number $N = 126$, and it only slightly increases toward the mid-shell ($N = 104$). For the first time, a similar isomer jump in deformation was found for the odd-odd isomer, ^{186m2}Tl. This, along with the measured magnetic moment value for $I = 10$ isomer, confirms the proposed intruder ($\pi\, h_{9/2}$, $\nu\, i_{13/2}$) configuration of this isomeric state. In contrast with the well-known jump-like behavior of deformation for the adjacent Hg isotopes, Tl ground states preserve their near sphericity even at the mid-shell and beyond ($A \leq 185$).

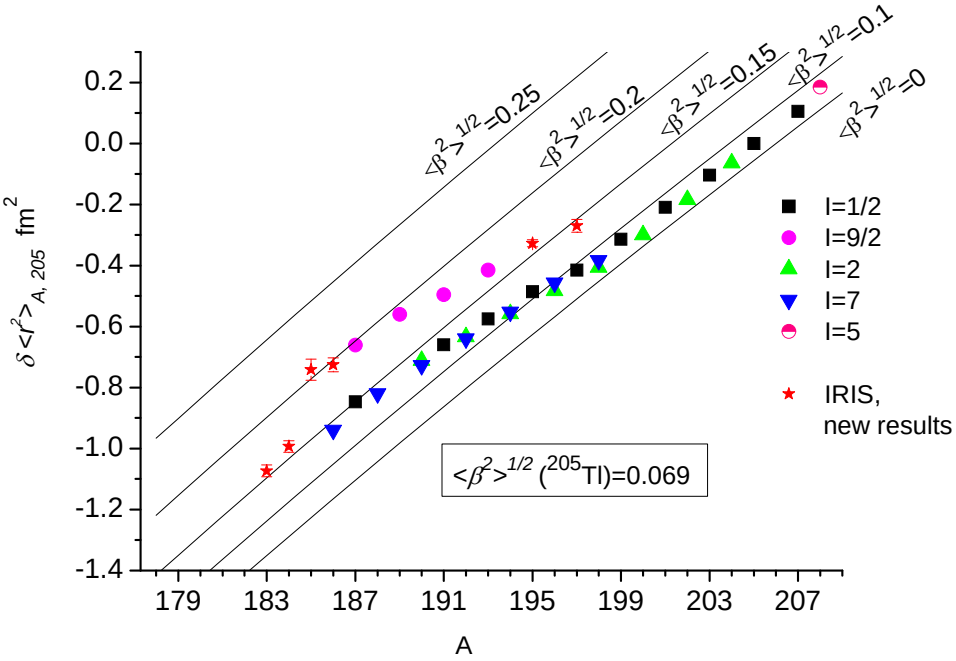

Fig. 4. Isotopic dependence of changes in the mean squared charge radius for Tl isotopes. Red stars show the data of the present paper. Other data were taken from literature. Uncertainties in *f*- and *M*-factors were not taken into account. The straight lines represent the DM prediction with different mean squared deformations

References

1. G.D. Alkhazov, A.E. Barzakh, V.P. Denisov, K.A. Mezilev, Yu.N. Novikov, V.N. Panteleyev, A.N. Popov, E.P. Sudentas, V.S. Letokhov, V.I. Mishin, V.N. Fedoseyev, S.V. Andreey, D.S. Vedeneyev and A.D. Zyuzikov, Nucl. Instr. Meth. B **69**, 517 (1992).
2. A.E. Barzakh, D.V. Fedorov, V.S. Ivanov, P.L. Molkanov, V.N. Panteleev and Yu.M. Volkov, Rev. Sci. Instr. **83**, 02B306 (2012).

GROUND AND ISOMER STATE PROPERTIES OF NEUTRON-DEFICIENT LEAD, POLONIUM AND TALLIUM ISOTOPES INVESTIGATED BY LASER ION SOURCE SPECTROSCOPY AT THE ISOLDE FACILITY

A.E. Barzakh, D.V. Fedorov, V.S. Ivanov, P.L. Molkanov,
V.N. Panteleev, M.D. Seliverstov, Yu.M. Volkov
In collaboration with Institut für Physik, Johannes Gutenberg-Universität; Oliver Lodge Laboratory, University of Liverpool; TRIUMF, Vancouver; Instituut voor Kern-en Stralingsfysica, K.U. Leuven; Institut de Physique Nucléaire, Université Paris-Sud, Orsay; ISOLDE, CERN; Laboratoire de Physique subatomique et de cosmologie, Université Joseph Fourier, Grenoble; Institut Laue – Langevin, Grenoble; Department of Physics, University of Manchester

1. Shape coexistence in Pb region studied by laser spectroscopy

For neutron-deficient nuclides around the closed proton shell at $Z = 82$, subtle interplay between individual and collective behavior of nucleons leads to the appearance of states with different shapes at low excitation energy. These the so-called shape coexisting states can be interpreted as particle-hole excitations across the closed proton shell gap, whereby the interaction of the valence proton particles and holes with the neutrons drives the nucleus to deformation. The phenomenon of shape-coexistence is a subject of intensive experimental and theoretical studies. The excited bands built on top of the 0^+ states were observed in $^{182-190}$Pb, and recent lifetime measurements confirmed the deformed character of these bands. For ^{186,188}Pb, it was concluded that the ground state and the 2_1^+ state have a very different structure, the 0^+ground state is predominantly spherical, while the 2_1^+ state is predominantly prolate. Monopole transition strengths between the 0^+ states were used to estimate the mixing between the normal and intruder configurations and they revealed a limited configuration mixing in the ground-state wave functions of ^{190,192,194}Pb. At the same time, as the excited 0^+ states become lower in energy when approaching $N = 104$, the mixing could increase substantially. All models that provide a consistent picture of the available data suggest that the ground states of lead isotopes are dominated by spherical configurations, even when the prolate and oblate rotational bands come down very low in energy around $N = 104$, and the barrier that separates the corresponding structures in the total energy surface is very small. Most experimental data, however, concern transitions to the ground state, which depend on the structure of the initial state. Note that the observables which give detailed information on the ground-state wave function are the charge radii determined in atomic spectroscopy.

Approaching $N = 104$, the intrusion of a presumed oblate band was seen at low energy in ^{192}Po also. In ^{190}Po, an evidence for a prolate configuration in the polonium isotopes was obtained, which is believed to become the ground state in ^{188}Po. In order to understand the change in the configuration, a direct measurement of ground-state properties independent of nuclear models through the charge radii studies is crucial.

We have measured isotopic shifts in the atomic spectra of the very neutron-deficient $^{182-188}$Pb isotopes [1, 2], neutron-deficient polonium isotopes from ^{210}Po down to ^{191}Po ($T_{1/2}$ = 22 ms) and of the neutron-rich isotopes ^{216,218}Po [3] and deduced the corresponding changes in mean square charge radii. The in-source laser spectroscopy technique was first used at PNPI. By combining the in-source laser spectroscopy technique with efficient alpha detection, the mean square charge radii data were obtained for nuclides, which were detected with a rate of about 1 ion per second. The radioactive isotopes were produced at the PSB – ISOLDE facility at CERN, in a proton-induced (E_p = 1.4 GeV) spallation reaction on a thick (50 g/cm^2) UC_x target. The reaction products diffuse out of the target toward the ion source cavity, heated to around 2050 °C. In this cavity, the isotopes were selectively ionized in a three-step laser ionization process. With copper-vapor pumped tunable dye lasers, atomic electrons were promoted out of the ground state toward the excited state (λ_1 = 283.3 nm for Pb and λ_1 = 255.8 nm for Po). In a second excitation step, the second tunable dye laser was tuned to λ = 600.19 nm for Pb and λ = 843.38 nm for Po. The final ionizing step was supplied by the pumping laser (see Fig. 1).

In order to determine the isotope shift of the optical line, the first excitation step for Pb and the second step for Po were set to a narrow linewidth of 1.2 GHz, and its frequency was scanned over the resonance.

After ionization and extraction, the radioactive ions of interest were accelerated to 60 keV, mass separated and subsequently implanted in one of ten identical 20 μg/cm^2 carbon foils, mounted on a rotating wheel. A Si-detector (area 150 mm^2, thickness 300 μm), placed behind the foil, measured the α-radiation during a fixed implantation time. After this period, a new wavelength was set, and a fresh carbon foil was introduced by turning the wheel. The implanted lead ions were counted via their characteristic α-decay and the intensities of the α lines as functions of the laser frequency revealed the optical isotope shift.

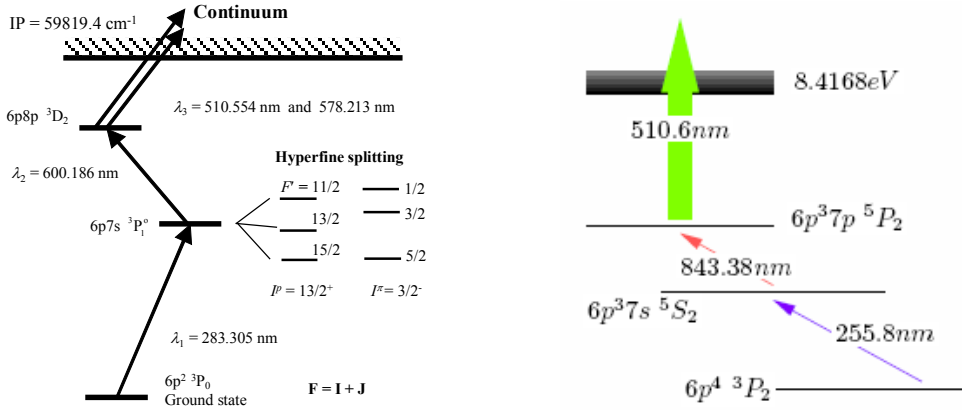

Fig. 1. Ionization schemes used for Pb (left) and for Po (right) laser spectroscopy

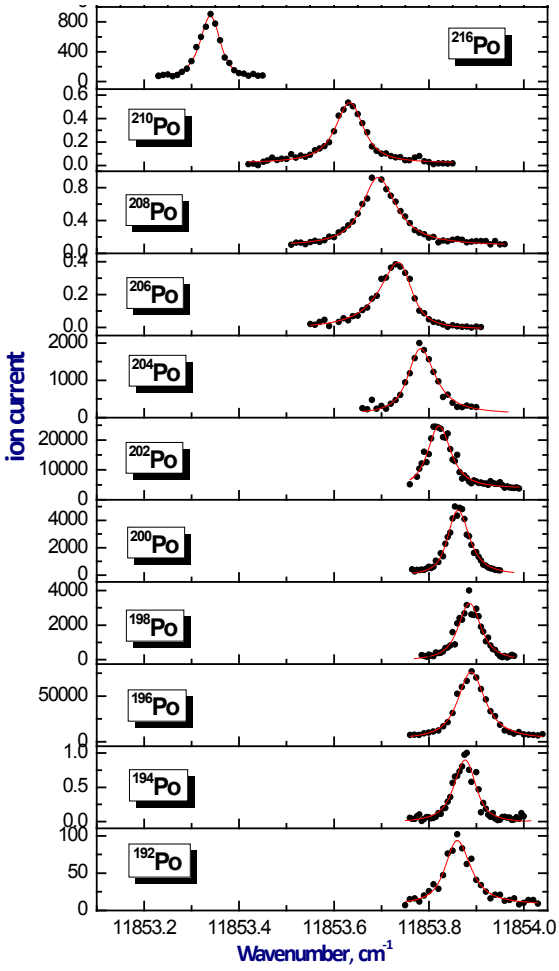

Fig. 2. Examples of optical spectra measured for even Po isotopes

The isotopes $^{199–204}$Po and ^{189,190}Pb were detected via their β-decay and the subsequent characteristic γ-ray emission at the ISOLDE tape station. The polonium isotopes $^{206–210}$Po were measured with a Faraday cup. To determine the absolute wavelength calibration and the shape of the resonance curve, laser scans using the mass separated ion current of the stable isotope ^{208}Pb and the reference isotope ^{202}Po were performed regularly. By scanning the frequency of the narrow band laser over the resonance, together with simultaneous counting of the mass-separated photo-ions, the Isotope Shift (IS) and hyperfine structure (hfs) constants of the atomic spectra lines can be measured. From these data the change in nuclear mean square charge radii ($\delta\langle r^2\rangle$) and the electromagnetic moments can be determined according to the well-known formulas (see Eqs. (1) and (2) in *A.E. Barzakh et al.* in the present volume).

Figure 2 shows examples of the obtained frequency scans for even Po isotopes. In Fig. 3, the mean square charge radii for polonium, bismuth, lead, mercury, thallium, and gold isotopes are displayed. For the sake of clarity, the data for different elements are shifted relative to each other by a vertical offset. In our experiments the data for $^{218,216,211,203,201,199–191}$Po ($N$ = 134, 132, 127, 119, 117, 107–116), $^{182–189}$Pb (N = 100–107) and the corresponding isomers were obtained for the first time.

It is generally acknowledged that the isotopic trend of $\delta\langle r^2\rangle$ is described by the Droplet Model (DM).

Deviations from the DM trend are attributed to the advance of the mean squared quadrupole deformation (see Eq. (3) in *A.E. Barzakh, D.V. Fedorov, V.S. Ivanov et al.* in the present volume). The large deviation observed for the ground state of the odd-mass mercury isotopes and the odd- and even-mass gold isotopes around $N = 104$ has been interpreted as due to the onset of a strong prolate deformation.

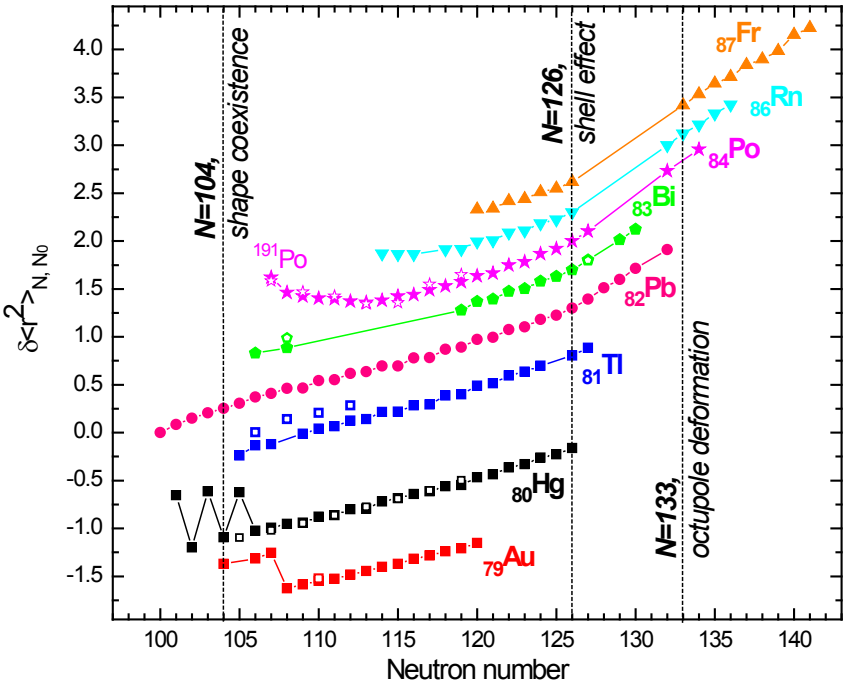

Fig. 3. Changes of the mean square charge radii for polonium, bismuth, lead, mercury, thallium, and gold isotopes. Hollow symbols mark the isomers. For the sake of clarity the data for different elements are shifted relative to each other by a vertical offset

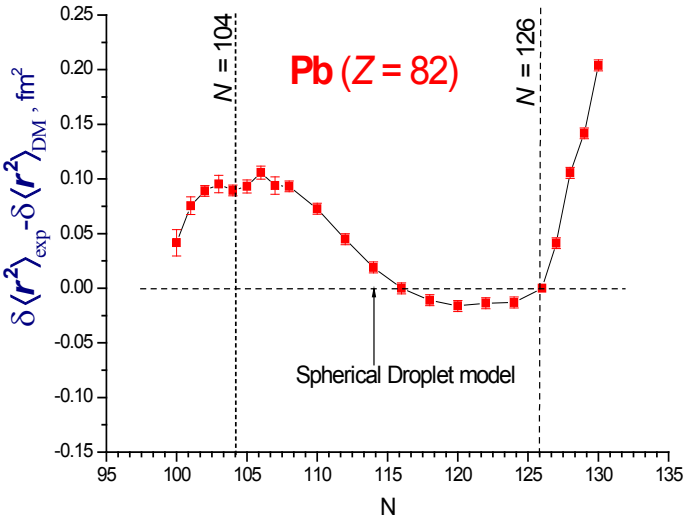

Fig. 4. Difference between the experimental $\delta\langle r^2\rangle$ for Pb isotopes and the DM calculations for spherical nuclei

In the case of lead, a modest deviation is observed, and Fig. 4 shows the difference between the experimental charge radii and the droplet model predictions.

From ^{196}Pb downwards, the spherical droplet model predictions deviate from the data, with an underestimation around 0.1 fm^2 from ^{190}Pb to ^{184}Pb. Introduction of a static deformation into the droplet model with $\beta_2 = 0.1$ improves the agreement with the data for $^{184-190}$Pb, but is inconsistent with spectroscopic properties. A more realistic approach that provides good description of the coexisting bands in the neutron-deficient lead isotopes is beyond the mean-field calculations. This model mixes the mean-field wave functions which all have different axial quadrupole deformations. Around the midshell where lead isotopes are soft, the collective wave function is spread over a large number of configurations, and the notion of a spherical or deformed nucleus becomes ill defined.

Calculations with this model show that isotopic shifts are very sensitive to correlations in the ground-state wave functions of lead. A slight reduction of the pairing strength has a significant effect on precise

balance between the excited prolate and oblate configurations, but leads only to a very small increase in the mean deformation of the ground state.

The values of $\delta\langle r^2\rangle$ for Po isotopes are compared with those predicted also by the spherical DM (see Fig. 5). On the neutron-deficient side, a surprisingly large deviation from sphericity can be seen starting from ^{198}Po that becomes increasingly marked for lighter isotopes.

The deviation is larger in magnitude and occurs for larger neutron numbers than in the $Z \leq 82$ isotones. In order to understand the unexpectedly large and early deviation from sphericity in polonium isotopes, the values of $\delta\langle r^2\rangle$ were calculated using the same beyond mean field method.

The SLy4 Skyrme parametrization was tested together with the effect of reduced pairing strength. The results of these calculations are shown on Fig. 5.

Two main effects that increase the radii of neutron-deficient polonium isotopes, compared to the global trend set by spherical configurations, are the spread of the collective wave function in deformation space and the shift of the dominant configurations from near-spherical to oblate. The increasing softness of the deformation energy surfaces, when going down from ^{210}Po to ^{194}Po, leads to collective ground-state wave functions of increasing spread, but which remain centred in spherical shapes. For ^{192,190}Po, the ground-state wave function becomes centred in an oblate minimum in the deformation energy surface, and the contribution from near-spherical configurations (or smaller radii) becomes suppressed, while from ^{188}Po onwards, the ground-state wave function becomes more localized in a deformed minimum. The calculated values of $\delta\langle r^2\rangle$ are compared with the experimental data in Fig. 5, after subtraction of the DM value. There is a qualitative agreement between theory and experiment, although some discrepancies exist, especially for ^{192,194}Po, where the data indicate a significant deviation from sphericity. The effect of a reduced pairing strength, which clearly improves the agreement between theory and experiment for the lightest nuclei, implies a larger contribution of deformed oblate configurations. From our calculations, it can be concluded that none of the polonium isotopes measured in this work have a static deformation. One still needs to construct more flexible energy functionals to correct the deficiencies of the actual ones.

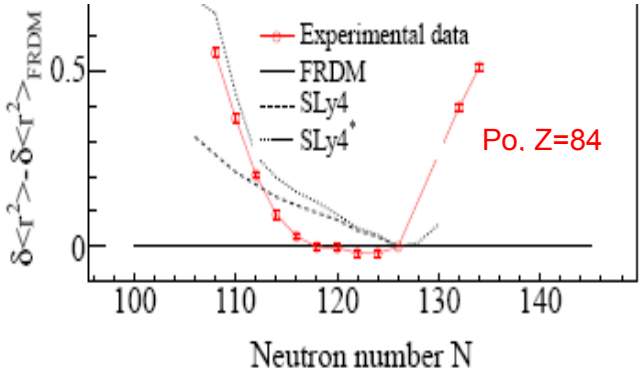

Fig. 5. Difference between the measured values of $\delta\langle r^2\rangle$ and those predicted by the spherical DM. Dotted lines represent the beyond mean field calculations with the SLy4 and SLy4* (with reduced pairing) interactions

In conclusion, the in-source resonant ionization laser spectroscopy has been performed on polonium and lead isotopes. From ^{190}Pb downwards, the $\delta\langle r^2\rangle$ data show a distinct deviation from the spherical DM suggesting ground-state deformation, but comparisons of the data with model calculations show that $\delta\langle r^2\rangle$ is very sensitive to correlations in the ground-state wave functions and that the lead isotopes stay essentially spherical in their ground states even at and beyond the $N = 104$ midshell region. The $\delta\langle r^2\rangle$ values for even-A polonium isotopes have been compared with systematics of this region and recent calculations. An unexpectedly large divergence from sphericity was observed compared with the $Z = 82$ isotones. A comparison to beyond mean field calculations indicates that the coexistence of different shapes at low excitation energies leads to a very soft nature of the most neutron-deficient polonium nuclei. The different trend with respect to the $Z = 82$ nuclei might suggest that high-j orbitals occupied by the protons play a critical role.

2. New type of asymmetric fission in proton-rich nuclei

Usually, the fission process is described by the interplay between the macroscopic (liquid-drop) and microscopic nuclear (shell corrections) degrees of freedom. Only in fission below or slightly above the barrier, the so-called low-energy fission, this interplay can be most fully explored. Until recently, such low-

energy fission studies were limited to nuclei from around thorium (Th) to fermium (Fm) using spontaneous fission, fission induced by thermal neutrons, or by β-Delayed Fission (βDF). These studies have shown the dominance of asymmetric fission over symmetric fission for most isotopes of these elements and suggested that structure effects due to the spherical shell structure of doubly magic ^{132}Sn dominate the mass split. Recently, the low energy fission studied by Coulomb-excited fission of radioactive nuclei demonstrated the transition from mostly asymmetric fission in the actinides towards symmetric fission as the dominant mode in the light thorium to astatine region. Another way to study low-energy fission is through βDF. In this two-step nuclear process, a parent nucleus first undergoes β decay, in this case Electron Capture (EC), populating the states in the daughter nucleus which may be fissile, provided the energy release Q_{EC} of the parent nuclide is comparable to the fission-barrier height B_f of the daughter nucleus. The βDF is of special interest because it allows to study the low-energy fission properties of exotic nuclei possessing unusual neutron to proton ratios, *e.g.*, $N/Z = 1.25$ for ^{180}Hg, in contrast to a typical ratio of $N/Z = 1.55$–1.59 in the U region.

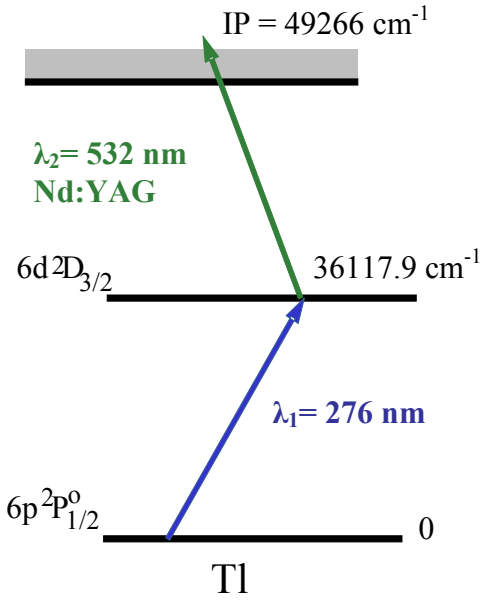

Fig. 6. Scheme of Tl resonance ionization

We have carried out a dedicated βDF study of ^{180}Tl at the ISOLDE mass separator at CERN [4]. A 1.4 GeV proton beam with an average intensity of 1.2 μA impinges on a 50 g/cm^2 UC_x target, producing a large variety of nuclides. To obtain a high-purity source of ^{180}Tl, allowing a precise study of its decay, a combination of resonance laser ionization and mass separation was used, resulting in a unique isotopic selection. The scheme of resonance ionization of Tl atoms is presented in Fig. 6.

After selective ionization, acceleration up to 30 keV and mass separation, a pure ^{180}Tl beam of ~ 150 atoms/s passed through a hole in an annular silicon detector and was implanted into a carbon foil of 20 μg/cm^2 thickness. A second Si detector was placed 3 mm behind the foil. By using the two silicon detectors (both of 300 μm thickness), the single α and fission decays, as well as the double-fold fission-fragment coincidences, could be measured. The total registration efficiency for a single α or fission decay in one of the Si detectors was ~ 66 %, while the coincident fission fragments were registered with an efficiency of ~ 20 %.

A segmented MINIBALL Ge cluster, consisting of three individual germanium crystals, and a planar Ge detector were installed around the detection chamber to allow γ and *K X*-ray measurements in coincidence with particle events. Approximately, $1.4 \cdot 10^6$ α decays of ^{180}Tl were detected in total. All observed α lines originated from ^{180}Tl or its subsequent decays (cf. the decay scheme in Fig. 7) as they were reduced by a factor of ~ 70 when laser light was blocked, preventing laser ionization of Tl. No direct production of ^{180}Hg was possible as it could be ionized neither by surface ionization nor by laser ionization tuned to Tl isotopes. This proved the purity of the ^{180}Tl source, which allowed an accurate determination of different branching ratios. The half-life value of $T_{1/2}(^{180}\text{Tl}) = 1.09(1)$ s was deduced, more precise than the literature value 1.4(3) s. The total of 1111 single fission events in the region 30–90 MeV were observed when the lasers were tuned to Tl ionization.

In total, 346 dual coincidences between fission fragments were observed. Finally, the prompt coincidences between the fission fragments and Hg *K*-line *X*-rays were registered. These observations together unambiguously prove the observation of prompt fission of the excited states in ^{180}Hg fed by the β decay of ^{180}Tl.

The purity of the ^{180}Tl sample allowed the absolute branching ratios of its decay channels to be deduced by comparison of the summed numbers of ^{180}Tl α decays and βDF events to the number of ^{180}Hg α decays using the well-known α branching ratio of ^{180}Hg [48(2) %] and the corrections for the different half-lives due to the implantation-decay cycle. This resulted in the β^+/EC branching ratio of 94(4) % and the βDF probability $P_{\beta DF}(^{180}\text{Tl}) = 3.6(7) \cdot 10^{-3}$ % for ^{180}Tl. A fission-fragment mass distribution from the 346

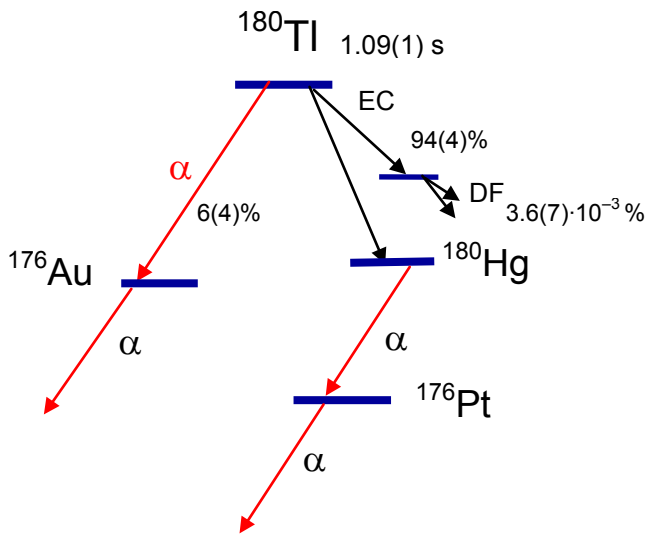

Fig. 7. A simplified decay scheme of ^{180}Tl with the deduced halflife and branching ratios for its various decay modes

coincident fission events of ^{180}Hg, could be obtained through a well-established procedure. The resulting spectrum as a function of the total kinetic energy and the fission-fragment mass is shown in Fig. 8. The mass distribution is clearly asymmetric. The most probable Z values of the heavy and light fission fragments were deduced to be $Z_H = 44(2)$ and $Z_L = 36(2)$, respectively, assuming that the N/Z ratio of the parent nucleus ^{180}Hg is preserved in the fission fragments. Thus, the most abundantly produced fission fragments were ^{100}Ru and ^{80}Kr and their neighbors.

The most surprising result of this study was the asymmetric mass distribution of the fission fragments of ^{180}Hg. Indeed, one might have expected a symmetric fission fragment mass distribution, as this was observed to be the main mode of the low-energy fission in a broad neutron-deficient region below Th. In addition, very common arguments applied, *e.g.*, for fission of heavy actinides that shell effects in fragments (rather than shell effects in the fissioning nucleus in the region near the saddle) determine the mass distributions would also lead to an expectation of symmetry.

This is because there are no strong ground-state shell effects in the measured asymmetric fragments of ^{180}Hg, while a weak shell effect for the nucleus ^{90}Zr, with the magic $N = 50$ and semimagic $Z = 40$ would, if it were determinative, lead to symmetric splitting. A realistic description of the fission process needs the structure of the entire, multidimensional fission potential energy surface based on at least five independent shape parameters. A dynamical model would be required to make a specific prediction of the mass split implied by these potential-energy calculations. In the actinide region, one can identify a connection between the asymmetric fission-fragment distribution and the strong shell effects in the region near the saddle, extending and increasing as one moves towards the scission point.

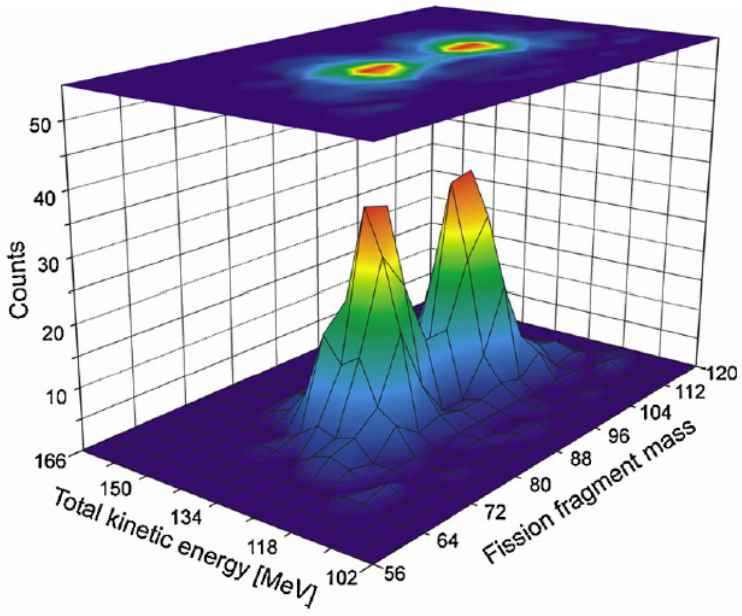

Fig. 8. The derived fission-fragment distribution of ^{180}Hg as a function of the fragment mass and the total kinetic energy

These shell effects are related to the extra binding energy of the doubly magic nucleus ^{132}Sn. In contrast, in the neutron-deficient Hg region such a combined effect of magic proton and neutron shells in the observed fission fragments is completely absent, and the asymmetric splitting is determined by relatively small microscopic effects that do not persist to scission but which cause the fission saddle point and a nearby valley to be mass-asymmetric. This new mode, which should survive only in very low energy fission, arises from the complex interplay between macroscopic and microscopic contributions to the total energy as a function of shape and is observed for the first time. Prediction of this mass asymmetry and related properties comprises a stringent test for any nuclear structure

model. It is a challenge to the experimental approaches as well as current theories to elucidate this new fission mode which gives the opportunity to study the topography and dynamics of the saddle to scission region, the least understood part of the fission process.

References

1. H. De Witte *et al*., Phys. Rev. Lett. **98,** 112502 (2007).
2. M.D. Seliverstov *et al*., Eur. Phys. J. **A** 41, 315 (2009).
3. T.E. Cocolios *et al.*, Phys. Rev. Lett. **106**, 052503 (2011).
4. A.N. Andreyev *et al.*, Phys. Rev. Lett. **105**, 252502 (2010).

INVESTIGATION OF THE NUCLEAR MEDIUM EFFECT ON CHARACTERISTICS OF PROTON-PROTON SCATTERING AT 1 GeV

O.V. Miklukho, A.Yu. Kisselev, V.A. Andreev, O.Ya. Fedorov, A.A. Izotov, L.M. Kotchenda, A.N. Prokofiev, A.V. Shvedchikov, S.I. Trush, and A.A. Zhdanov

1. Introduction

Studies of nuclear structure using the 1 GeV proton beam in high resolution experiments are traditional at the PNPI synchrocyclotron. In the first experiments performed about 40 years ago, the nuclear matter distributions were investigated and the neutron density parameters were extracted using the Glauber diffractive scattering model [1]. Later, there were performed high precision experiments on (p,2p) and (p,pn) reactions studying the proton and neutron shells in detail [2].

The polarization was also measured in high resolution proton diffraction scattering [3]. The deuteron structure at small distances was studied in (p,2p) quasielastic scattering with the polarization measured in the low momentum arm of the spectrometer [4]. The upgrade of the two-arm magnetic spectrometer to equip it with polarimeters in each arm allowed for new experiments to be developed. For instance, an interesting phenomenon of the effective polarization was first studied in Refs. [5, 6].

Later, the goal of these investigations was shifted to an important question of how the free nucleon scattering amplitude is modified in the nuclear matter. The first experiments were performed jointly in collaboration with the group of physicists from the RCNP (Japan) [7, 8]. In the present contribution, we report mainly the results of the experiments done with the help of new fast readout electronics CROS-3 developed at PNPI for the two-arm magnetic spectrometer.

It is theoretically predicted in the framework of QCD and QHD (quantum hadrodynamics) that hadron masses in the nuclear medium are modified as a result of the partial restoration of chiral symmetry and as an enhancement of the lower component of the nucleon Dirac spinor in the strong scalar field [9]. It is one of the challenges of modern nuclear physics to find experimental evidence for such medium effects.

In studies of nucleon elastic scattering, a significant success was achieved in the framework of the relativistic impulse approximation, where the modification of the Dirac spinor is implicitly taken into account. The effect of the meson-mass modification on proton-nucleus scattering was investigated by Brown *et al.*, and they found that theoretical descriptions of the experimental data become better when this effect is taken into account.

Another type of nuclear reactions suitable for studying in-medium nucleon-nucleon (*NN*) interactions is the nucleon quasifree scattering, which, in a simple picture, is the *NN* scattering in the nuclear field. It was first pointed out by Horowitz [9] that the values of the analysing power A_y measured in inclusive experiments at LAMPF are smaller than those predicted using the free *NN* interaction. It was suggested that this decrease in A_y is a signature of the relativistic effect mentioned above.

This decrease was also found to be much more distinct for the (p,2p) reaction studied in the TRIUMF experiment on the proton knockout from the *S*-shell of the ^{16}O target using the incident proton with the energy of 500 MeV. Maxwell and Cooper analysed these data using the relativistic distorted wave impulse approximation (RDWIA) formalism that includes both the dynamic and kinematical recoil effects. Although their formalism includes the relativistic effect exactly, the calculated values of A_y for the knockout from the *S*-shell and the corresponding experimental data are in significant disagreement.

Krein *et al.* investigated influence of the modifications of meson masses and coupling constants on the *NN* interactions in the nuclear field. They found that the effective polarizations of the target nucleons – derived from the TRIUMF data on the ^{16}O(p,2p) reactions at the incident energy of 200 MeV leading to 3/2P and 1/2P hole states – can be consistently accounted for if such modified *NN* interactions are employed.

The (p,2p) experiments were also performed for several types of target nuclei with the beam energy of 392 MeV at RCNP [10]. As in the case of the TRIUMF data mentioned above, the values of A_y for the proton knockout from the *S*-shells of nuclei were found to be smaller than those estimated using the *NN* interactions in the free space. In addition, it was found that the reduction rates are significantly target-dependent. There was defined an effective mean density providing a good measure of sensitivity of the (p,2p) reaction to

the density-dependent term of the *NN* interactions, and it was demonstrated that the observed decrease of A_y monotonically depends on the mean density. It was also shown that this density-dependent reduction cannot be accounted for by such a medium effect in the non-relativistic framework as the Pauli-blocking effect [11]. Miller *et al.* compared the TRIUMF data with results of "the best available DWIA reaction models" and concluded that the existing density-dependent *NN* interactions are not adequate for nucleon knockout reactions, which implied a possibility of a more interesting mechanism, such as a hadron-level medium effect.

At PNPI, the polarization P of both secondary protons in the (p,2p) reaction on the ^{7}Li nucleus was measured with the 1 GeV proton beam. The reduction of the measured polarizations of both protons with respect to the polarization in the free elastic proton-proton scattering was observed, and the value of the reduction was especially significant for the (p,2p) reaction involving *S*-shell protons [6]. It was also shown that this effect cannot be related to depolarization of the secondary protons due to proton-nucleon rescatterings in the nuclear matter since the values of the reduction for these protons are close to each other, in spite of the fact that they have essentially different energies.

In a joint PNPI – RCNP experiment, the polarization in the (p,2p) reaction with almost immovable 1*S*-shell protons of the ^{4}He, ^{6}Li, ^{12}C nuclei and with 2*S*-shell protons of ^{40}Ca was investigated at 1 GeV, that is at the energy higher than that at TRIUMF and RCNP. The density-dependent reduction of the polarization was also obtained.

In this contribution, we present new results obtained recently in the (p,2p) experiment performed after an upgrade of the electronics of the two-arm magnetic spectrometer. As in the joint experiment mentioned above, we have measured the polarization of both secondary protons $P_{1,2}$ in the (p,2p) reaction with 1*S*-shell protons of the ^{4}He, ^{6}Li, ^{12}C nuclei and with 2*S*-shell protons of the ^{40}Ca nucleus, the energy of the incident protons being 1 GeV, however the measurements were performed with much better statistical accuracy. We also present new data on the polarization in the reaction with 1*S*-shell protons of the ^{28}Si nucleus, which has a large value of the binding energy E_S. The data on the spin correlation parameters C_{ij} – obtained for the first time for the (p,2p) reaction with 1*S*-shell protons of the ^{4}He and ^{12}C nuclei – are presented as well. The data on the polarizations $P_{1,2}$ and the spin correlation parameters C_{ij} measured in the same (p,2p) experiment can provide more comprehensive information on the modifications of hadron properties in the nuclear medium.

2. Experimental method

The experimental method is described in detail in Refs. [7, 8]. A general layout of the experimental set-up used to investigate the (p,2p) reaction with nuclei is presented in Fig. 1.

The (p,2p) experiment was performed at non-symmetric scattering angle geometry – $\Theta_1 = 21–26°$ and $\Theta_2 = 53.2°$ of the final protons – under the conditions of the practically coplanar quasi-free scattering geometry and the complete reconstruction of the reaction kinematics.

The external proton beam of the PNPI synchrocyclotron was focused onto a target (denoted by TS) of the two-arm spectrometer (the magnetic spectrometers MAP and NES). In the experiment, the solid targets of CH_2, ^{6}Li, ^{12}C, ^{28}Si, ^{40}Ca, and the liquid helium (^{4}He) target were used [12].

The polarizations P_1 and P_2 of the secondary protons from the reaction and the spin correlation parameters C_{ij} (for the ^{4}He and ^{12}C targets) were measured by polarimeters located in the focal planes of the MAP and NES spectrometers. In the measurement of the target dependence of the polarization, the recoil spectrometer NES was installed at the fixed angle of $\Theta_2 = 53.2°$. For each target, the momentum settings of the NES and MAP spectrometers and the angular position of the latter (given by the angle Θ_1) corresponded to the kinematics of the (p,2p) reaction with a 1*S*-shell proton (and with a 2*S*-shell proton for the ^{40}Ca target), where the nuclear proton momentum K before the interaction has a value close to zero (in the impulse approximation, K is equal to the residual nucleus momentum K_r). This is the condition when the cross section for the *S*-shell knockout process is maximal, and the reaction mechanism is expected to be the simplest.

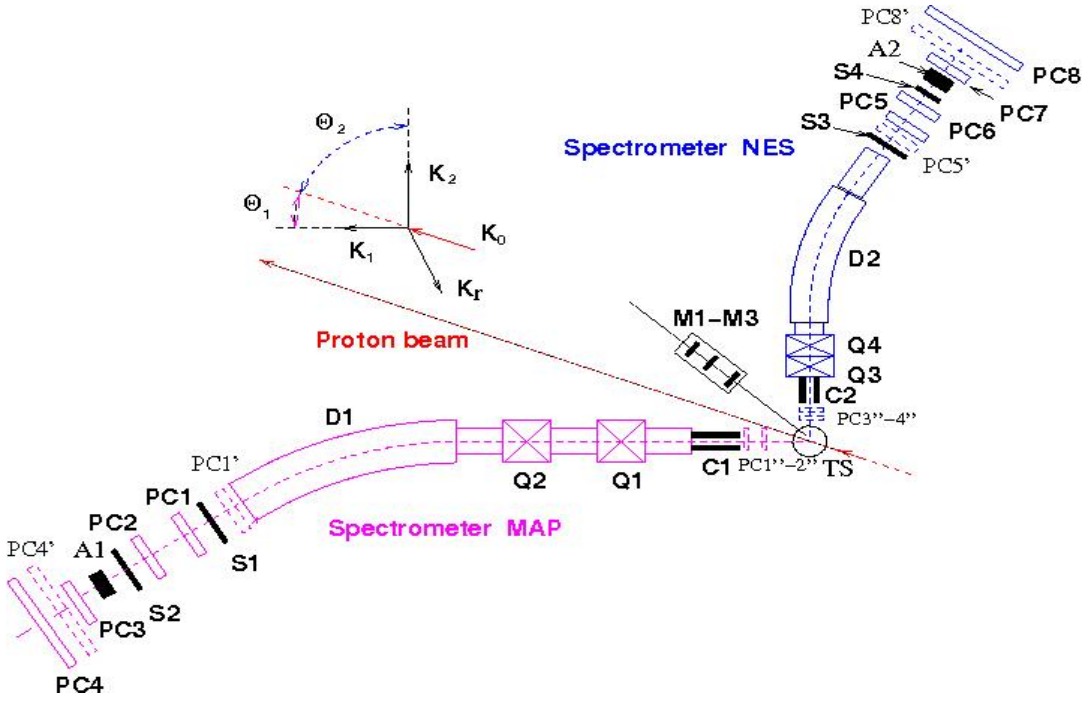

Fig. 1. Experimental set-up. TS is the target of the two-arm spectrometer; Q1–Q4 are the magnetic quadrupoles; D1, D2 are the dipole magnets; C1, C2 are the collimators; S1–S4 and M1–M3 are the scintillation counters; PC1–PC4, PC1', PC4' (PC5–PC8, PC5', PC8'), and A1 (A2) are the proportional chambers and the carbon analyser of the high-momentum (low-momentum) polarimeter, respectively; PC1"–PC4" are the proportional chambers. Shown above is the kinematics of the (p,2p) reaction

In Fig. 2, we show the proton separation energy spectrum for the (p,2p) reaction on the ^{28}Si nucleus obtained in the present work. As one can see in the figure, even in the preferable condition for the S-shell proton knockout process, the contribution of the scattering off the external shell protons is dominant.

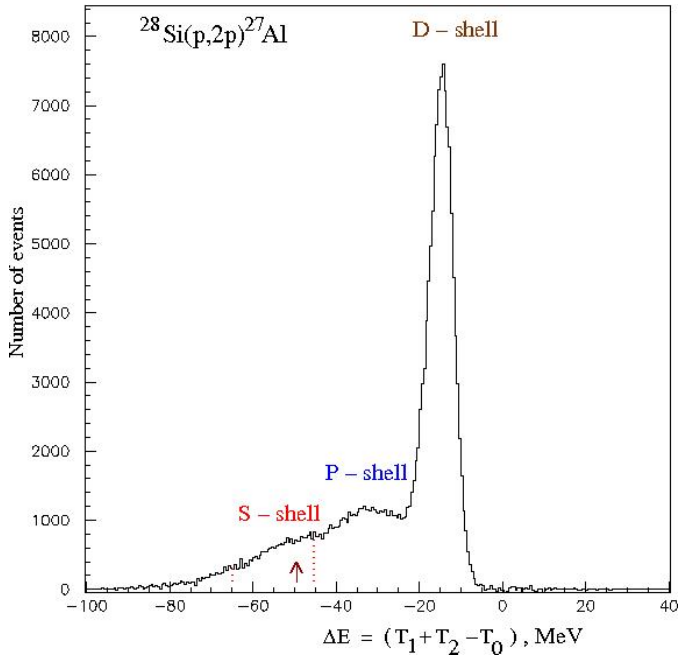

Fig. 2. Proton separation energy spectrum for the ^{28}Si(p,2p)^{27}Al reaction. The area between the vertical dotted (red) lines has been used for the data analysis

3. Experimental results

In Fig. 3, the values of the polarizations P_1 and P_2 in the (p,2p) reaction with S-shell protons of various nuclei averaged over the results obtained in the present work and those obtained earlier [7] are plotted as functions of the S-shell proton binding energy E_S and the effective mean nuclear density ρ normalized to the saturation nuclear density $\rho_0 \approx 0.18$ fm^{-3} [13]. In the figure, the experimental data are compared with various theoretical calculations.

These experimental data were obtained under the kinematical conditions that the nuclear S-shell proton had the momentum close to zero before the interaction and that the momentum transferred to the nucleus, q, depended weakly on the type of the nuclear target. The calculation of the effective mean nuclear density ρ, which is determined by the absorption of the incident and both outgoing protons, was carried out following the procedure described in Ref. [10] using the computer code THREEDEE.

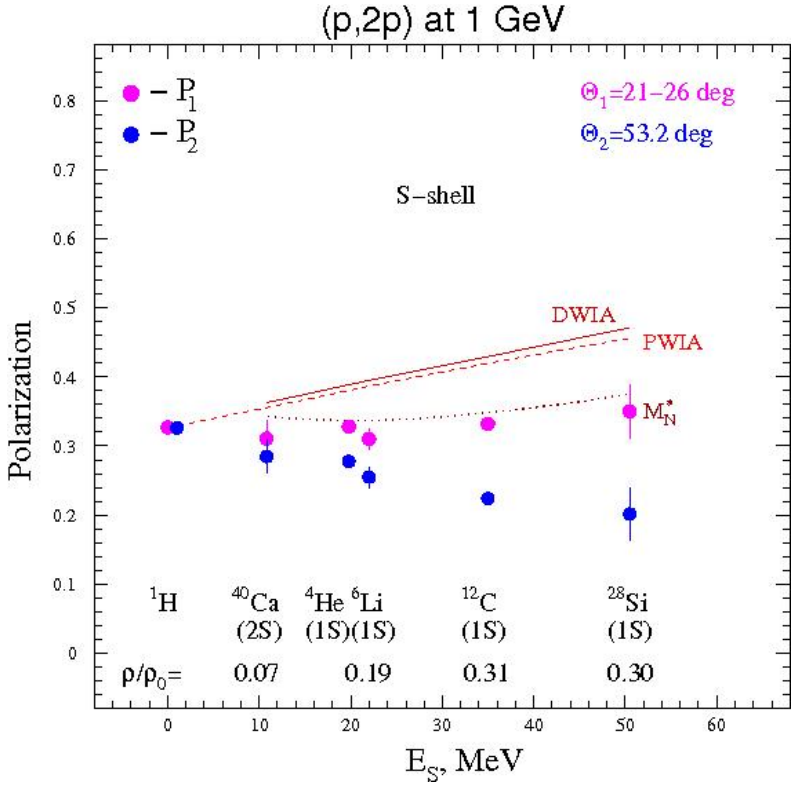

Fig. 3. Target dependence of the polarization data for pp scattering and (p,2p) reactions. The polarizations of the forward and recoil outgoing protons are denoted by P_1 and P_2, respectively. The data points are plotted as functions of the effective mean nuclear density ρ and the average binding energy E_S of the S-shell protons. The dashed and the solid curves represent the results of the PWIA and DWIA calculations using the NN interaction in the free space, respectively. The dotted curve (M_N^*) is the DWIA result, where the relativistic effect is taken into account in the Schroedinger-equivalent form

Figure 4 displays the angular distributions of the polarizations P_1 and P_2 in the (p,2p) reaction with 1S-shell protons of the ^{12}C nucleus and the results of various theoretical calculations. The data corresponding to the NES angle in the $\Theta_2 = 53.2$–$64.0°$ range are plotted as a function of the momentum q transferred to the nucleus. These distributions correspond to the zero momentum of the nuclear proton before the interaction. In this case, the momentum q is equal to the momentum K_2 of the recoil proton scattered into the NES spectrometer. In the present work, we have essentially improved the statistical accuracy of the polarization measurements at $q = 3.4$ fm^{-1}.

The results of the measurement of the spin correlation parameters $C_{i\,j}$ in the elastic pp scattering and in the (p,2p) reaction with S-shell protons of the ^{4}He and ^{12}C nuclei are shown in Fig. 5 [13, 14].

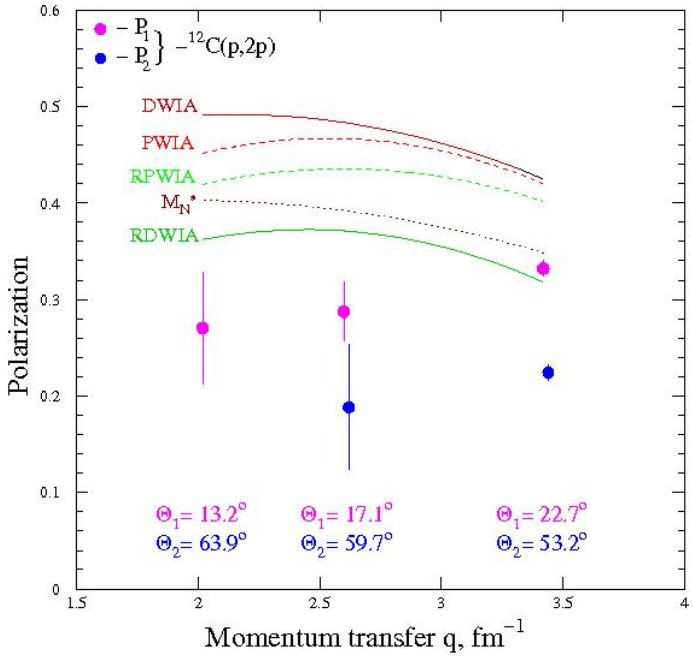

Fig. 4. Angular dependence of the polarization for the (p,2p) reaction with 1S-shell protons of the ^{12}C nucleus. P_1 and P_2 are the polarizations of the forward and recoil outgoing protons, respectively. The data are plotted as a function of the momentum q transferred to the nucleus. The green dashed and solid curves are the results of full relativistic PWIA and DWIA calculations [15], respectively. The identification of other curves is the same as that in Fig. 3

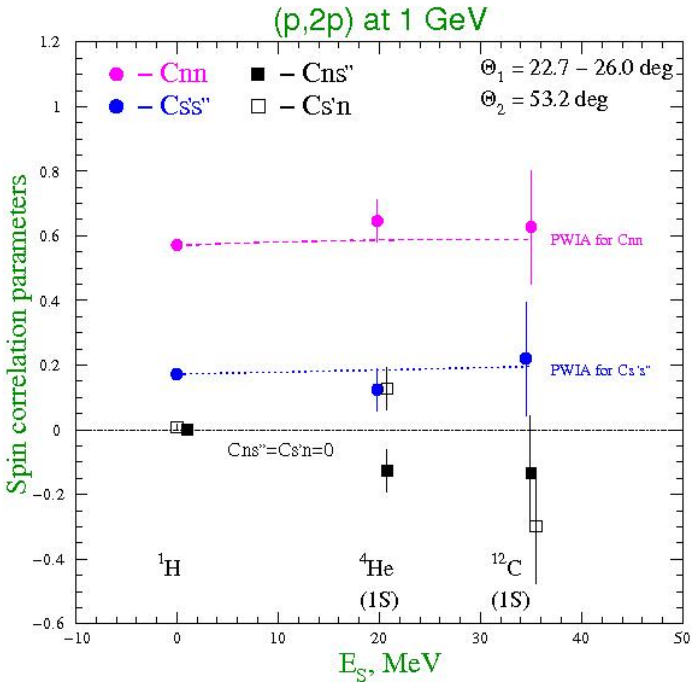

Fig. 5. Spin correlation parameters C_{ij} in the (p,2p) reaction at 1 GeV with S-shell protons of the ^{4}He and ^{12}C nuclei for the secondary proton scattering angles $\Theta_2 = 53.2°$, $\Theta_1 = 24.2°$ and $\Theta_2 = 53.2°$, $\Theta_1 = 22.7°$, respectively. The points at $E_S = 0$ correspond to the free elastic proton-proton scattering ($\Theta_1 = 26.0°$, $\Theta_{cm} = 62.25°$). The dashed and dotted curves are the results of the PWIA calculation of the $C_{n\,n}$ and $C_{s's''}$ spin correlation parameters, respectively

4. Comparison with theoretical predictions and discussion

The experimental data presented in Sect. 3 were compared with the calculations in the framework of the nonrelativistic Plane-Wave Impulse Approximation (PWIA) [8] (see the dashed curves in Figs. 3 and 4) and in the framework of the spin-dependent Distorted-Wave Impulse Approximation (DWIA) employing the on-shell factorized approximation. Note that "the final energy prescription" [6] was used in the calculations.

The solid curves corresponding to the DWIA represent the results of the calculations for the ^{6}Li, ^{12}C, ^{28}Si and ^{40}Ca nuclei obtained using the computer code THREEDEE [7]. In this approach, the global optical potential – parameterized in the relativistic framework and converted to the Schroedinger-equivalent form – was used to calculate the distorted waves of the incident and outgoing protons; the conventional well-depth method was used to construct the bound-state wave functions. Since the difference between the values of the P_1 and P_2 polarizations in the DWIA calculations was found to be small, typically smaller than 0.01 and no more than 0.02, only the P_1 values obtained in the DWIA are plotted in these figures. As one can see in Figs. 3 and 4, the difference between the PWIA and DWIA results is quite small. This suggests that in the conventional non-relativistic framework, the spin-dependent distortion does not play an essential role in the polarization under the kinematical conditions employed in the present work.

The difference between the values of the polarization P_1 obtained in the PWIA calculations (see Fig. 3) and the measured ones for all the investigated nuclei (except for the ^{4}He nucleus) is a monotonically increasing function of the effective mean nuclear density. This result is similar to that obtained at the RCNP at 392 MeV [10] with regards to the analysing power and provides further evidence that there exists an effect of the nuclear medium.

The corresponding difference for the polarization P_2 is most probably determined by the value of the S-shell proton mean binding energy E_S. As for the ^{4}He nucleus, the reduction of both polarizations P_1 and P_2 in the (p,2p) reaction is determined by the value of E_S. According to the studies of elastic nucleon-nucleus scattering, the ^{4}He nucleus has the largest mean nuclear density in comparison with the other investigated nuclei. The calculation of the relative effective mean nuclear density ρ/ρ_0 for the ^{4}He nucleus also gives the large value of 0.6. However, one should note that this result obtained following the procedure described in Ref. [10] and using the computer code THREEDEE is unreliable. It is possible that for light nuclei the value of E_S is a good measure of the influence of the nuclear medium on the pp interaction.

As seen in Fig. 3, there is a systematic negative difference between the P_2 and P_1 values, though they have the same value in the case of free elastic pp scattering. This difference depends on the S-shell proton mean binding energy E_S. Possible origins of the difference include nonrelativistic and relativistic distortions (though the former is excluded, if the present DWIA calculations are valid), multistep processes (contributions, for instance, from (p,2pN) reactions), and even nontrivial modifications of the nucleons in the nuclear field. There may be another explanation of a stronger reduction of the polarization P_2. The recoil S-shell proton with the momentum q and the polarization $P_2 \approx P_1$ sometimes collides with a two-nucleon or three-nucleon dense association in the 1S-state of the nucleus. As a result, the S-shell proton of the association leaves the nucleus with the same momentum and, according to the Pauli exclusion principle, with the opposite sign of the polarization $P_2 \approx -P_1$ [13].

In Figs. 3 and 4, the polarizations P_1 and P_2 observed in the (p,2p) experiment with the ^{6}Li, ^{12}C, ^{28}Si, and ^{40}Ca nuclei are also compared with the theoretical result (the dotted curve) obtained in the framework of the relativistic treatment of proton-nucleus scattering by Horowitz and Iqbal [7]. In this approach, the modification of the NN interaction in the nuclear medium is assumed to be due to the effective nucleon mass, the effective mass being smaller than that of the free nucleon, which affects the Dirac spinors used in the calculations of the NN scattering matrix. Further, a linear dependence of the nucleon effective mass on the nuclear density was assumed in the calculations. As seen in Fig. 3, this relativistic approach gives the results close to the experimental values of the forward scattered proton polarization P_1 in the (p,2p) reactions with nuclei at the large transferred momentum q = 3.2–3.7 fm^{-1}. This fact also confirms that the observed reduction of the polarization P_1 is determined by the effective mean nuclear density.

However, in the case of the (p,2p) reaction with the ^{12}C nucleus, for the values of the momentum transfer smaller than 3.2 fm^{-1}, this relativistic approximation fails to describe the experimental data (see Fig. 4). The full relativistic dynamical consideration of the ^{12}C(p,2p) scattering process in the framework of the DWIA

performed by Hillhouse *et al.* [15] also gives the results noticeably different from our experimental data for $q < 3.4$ fm^{-1} (the green solid curve labeled RDWIA in Fig. 4). This difference can be related to yet another possible medium effect. In the Relativistic Love-Franey (RLF) model, Krein *et al.* have shown that the modifications of the exchanged mesons and meson-nucleon coupling constants in the *NN* interaction cause significant changes in spin observables, which include the suppression of A_y. Such a type of modifications was investigated by Hillhouse *et al.* [15] using our earlier experimental data on polarization in the (p,2p) reaction with *S*-shell protons of the ^{12}C nucleus in a wide range of the momentum transfer q [7].

The results of the spin correlation parameter C_{ij} measurement in the (p,2p) reaction with *S*-shell protons of the ^{4}He and ^{12}C nuclei are given in Fig. 5. In the figure, the dashed and dotted curves correspond to the PWIA calculations for the C_{nn} and $C_{s's''}$ spin correlation parameters, respectively. In these calculations, the current Arndt phase-shift analysis (SP07) was used. The $C_{s's''}$ parameter was determined by taking into account its distortion in the magnetic fields of the MAP and NES spectrometers due to the proton anomalous magnetic moment. The points at the mean binding energy value of $E_S = 0$ correspond to the free elastic *pp* scattering.

As seen in Fig. 5, the differences between the values of C_{nn} and $C_{s's''}$ measured in the (p,2p) experiment with nuclei and those calculated in the PWIA are within the statistical error bars.

The parity conservation in the free elastic proton-proton scattering requires that the spin correlation parameters $C_{ns''}$ and $C_{s'n}$ should be equal to zero. In Fig. 5, this is confirmed by the experimental data at $E_S = 0$. For the (p,2p) reaction with nuclei, parity in the *pp* interaction system can be violated since there exists a residual nucleus in the knockout process. However, in this case, according to the Pauli exclusion principle, there is a relation between the parameters in the centre-of-mass *pp* interaction system: $C_{ns} = -C_{sn}$. This relation can be violated in the laboratory system because of the distortion of the parameters by the magnetic fields of the MAP and NES spectrometers.

5. Conclusion

The observed reduction of the polarization P_1 of forward scattered protons in the (p,2p) reaction with *S*-shell protons of the ^{6}Li, ^{12}C, ^{28}Si and ^{40}Ca nuclei in comparison with that calculated in the framework of the PWIA and DWIA monotonically increases with the effective mean nuclear density. Calculations in the relativistic approximation, where the modification of the nucleon Dirac spinor is taken into account, reproduce well the magnitude of the reduction. This indicates that there really exist modifications of the proton-proton scattering matrix in the nuclear medium.

The experiment with the ^{4}He nucleus has shown that the magnitude of the reduction of P_1 in light nuclei (the nuclei with at least $A \leq 12$) is also determined by the mean binding energy of *S*-shell protons of the nucleus. The second important significance of the ^{4}He experiment is the possibility to observe the medium effect without any contribution from the multi-step processes, which can take place when there are nucleons of the outer shells as is the case with heavier nuclei. The obtained negative difference between the polarizations of the recoil proton P_2 and the forward scattered proton P_1, which depends on the mean binding energy E_S of 1*S*-shell nucleons, may be related to the mentioned above nontrivial mechanism of the recoil proton interaction with the dense nucleon associations in a nucleus. Note that the same mechanism also decreases the C_{nn} parameter. This and the fact that the experimental value of C_{nn} is close to the PWIA prediction could mean that the nuclear medium increases the value of C_{nn} in comparison with the case of free elastic *pp* scattering. Further theoretical investigations of the results of the present work are required.

The authors are grateful to the PNPI 1 GeV proton accelerator staff for stable beam operation and to the members of the PNPI HEP Radio-electronics Laboratory for providing the CROS-3 proportional chamber readout system. The authors would like to express their gratitude to A.A. Vorobyov and S.L. Belostotski for their support and fruitful discussions.

The following physicists participated in the experiment discussed in the present paper: D.A. Aksenov, G.M. Amalsky, V.A. Andreev, S.V. Evstiukhin, A.E. Ezhilov, O.Ya. Fedorov, G.E. Gavrilov, D.S. Ilyin, A.A. Izotov, A.Yu. Kisselev, L.M. Kochenda, P.A. Kravtsov, M.P. Levchenko, D.A. Maysuzenko,

O.V. Miklukho, V.A. Murzin, V.I. Murzin, D.V. Novinsky, V.A. Oreshkin, A.N. Prokofiev, V.Yu. Trautman, A.V. Shvedchikov, S.I. Trush and A.A. Zhdanov.

References

1. G.D. Alkhazov, S.L. Belostotski, A.A. Vorobyov, Phys. Rep. **42**, 89 (1978).
2. A.A. Vorobyov, Yu.V. Dotsenko, PNPI Research Report 1971–1996 (HEPD), 172 (1998).
3. G.D. Alkhazov *et al*., Phys. Lett. B **90**, 364 (1980).
4. N.P. Aleshin *et al*., Nucl. Phys. A **568**, 809 (1994).
5. O.V. Miklukho *et al*., Yad. Fiz. **63**, 894 (2000).
6. O.V. Miklukho *et al*., Nucl. Phys. A **683**, 145 (2001).
7. V.A. Andreev *et al*., Phys. Rev. C **69**, 024604 (2004).
8. O.V. Miklukho *et al*., Phys. Atom. Nucl. **69**, 474 (2006).
9. C.J. Horowitz, M.J Iqbal, Phys. Rev. C **33**, 2059 (1986).
10. K. Hatanaka *et al*., Phys. Rev. Lett. **78**, 1014 (1997).
11. T. Noro *et al.*, Nucl. Phys. A **663–664**, 517 (2000).
12. L. Kotchenda *et al*., Preprint PNPI-**2816**, Gatchina (2009).
13. O.V. Miklukho *et al*., Phys. Atom. Nucl. **76** (7), 871 (2013).
14. O.V. Miklukho *et al*., Phys. Atom. Nucl. **73**, 1 (2010).
15. G.C. Hillhouse, T. Noro, Phys. Rev. C **74**, 064608 (2006).

INELASTIC INTERACTIONS OF FAST NUCLEONS WITH NUCLEI AND FISSION OF NUCLEI

V.G. Vovchenko, V.V. Polyakov, O.Ya. Fedorov, Yu.A. Chestnov

1. Introduction

Investigations of the process of nuclear fission are of interest as a method to study nuclear forces and as a basis for obtaining data for practical applications. A large number of experiments were devoted to measuring cross sections for nucleon-induced fission of nuclei (see the EXFOR database [1]). In some articles, the authors tried to describe the existing experimental data on specific nuclei in the energy range from several MeV to several tens of GeV in terms of the unified energy dependence. Until recently, there has been only a scanty amount of experimental data on the cross sections for proton- and neutron-induced fission of nuclei in the energy range from 200 MeV to 1 GeV. Thus, it was impossible to draw a definite conclusion on the cross section energy dependence in this energy range.

To study this dependence, we have measured the cross sections for proton-induced fission of ^{239}Pu, ^{237}Np, ^{233,235,238}U, ^{232}Th, ^{209}Bi, and ^{nat}Pb nuclei in the energy range from 200 to 1000 MeV with a step of about 100 MeV using the proton beam of the PNPI synchrocyclotron [2]. On the basis of these data, it was concluded that the cross section for proton-induced fission of actinide nuclei is stable in the 400–1000 MeV energy range.

The question of the energy dependence of the cross section for neutron-induced fission of nuclei in this energy region is still open. An answer to this question may be sought by studying the energy dependence of the ratio of the cross sections for proton- and neutron-induced fission of nuclei. It appears that over the energy region extending up to 200 MeV this ratio is larger than unity [3], which corresponds to the well-known facts that in the nucleonic composition of heavy nuclei the number of neutrons is larger than that of protons, and that at energies of up to about 500 MeV the cross section for the proton-neutron (pn) interaction is larger than that of the proton-proton (pp) interaction. Therefore, the investigation of this ratio in the 200–1000 MeV energy range is of value both to obtain a deeper insight into the mechanism of nuclear excitations inducing fission and to plan experiments on neutron-induced fission of nuclei [4, 5].

The interaction of fast nucleons with nuclei manifests itself, first, as the interaction with a nucleus as a whole and, second, as the interaction with individual intranuclear nucleons. The interaction with the intranuclear nucleons occurs either in the kinematics close to that of elastic nucleon-nucleon scattering, or in the kinematics of inelastic scattering accompanied by pion production. The spectra of protons scattered off nuclei (from light to heavy ones) exhibit more or less pronounced peaks associated with the respective channels [6, 7]. In the energy range specified above, where the nucleon can be treated as a fast particle, the total cross section for the nucleon-nucleus interaction is likely to be dominated by the sum of the aforementioned channels.

2. Inelastic cross sections

In this section, we describe the total inelastic cross sections for the interaction of nucleons with nuclei as a result of elementary nucleon-nucleon interactions. A nucleus is characterized by its charge Z and the mass number A. The number of neutrons in the nucleus is ($A - Z$). For nucleons with the kinetic energy E in the laboratory frame (the corresponding momentum and speed are denoted by P and β, respectively), the inelastic cross section for nucleon-nucleus interaction can be represented in the following form:

$$\sigma_{\text{inj}}(E, A, Z) = A^{\nu} \left\langle \sigma_{jZN}(E) \right\rangle d\left(E, A, Z\right), \tag{1}$$

where the A^{ν} factor ($\nu \approx 0.7$) takes into account the dependence on the mass number of the involved nucleus; the index $j = p$ or $j = n$ stands for a proton or a neutron, respectively; the factor in the angular

brackets is the weighted mean of the nucleon-nucleon interaction cross sections in a nucleus characterized by the values of A and Z,

$$\begin{aligned} &< \sigma_{pZN}(E) > = (Z\sigma_{p\langle p\rangle}(E) + N\sigma_{n\langle p\rangle}(E))/A, \\ &< \sigma_{nZN}(E) > = (Z\sigma_{n\langle p\rangle}(E) + N\sigma_{p\langle p\rangle}(E))/A. \end{aligned} \tag{2}$$

The function $d(E, A, Z)$ in Eq. (1) takes into account the suppression of the nucleon-nucleon interaction in nuclei with respect to the interaction of free nucleons. This suppression can be attributed to the cascade character of the nucleon interaction in nuclei. In our calculations, we employed the following parameterization of this function:

$$d(E, A, Z) = a_1 P + a_2 \beta + a_3 \exp(-\varepsilon P^{-4}) + a_4 (A - 2Z). \tag{3}$$

The parameters a_i (i = 1–4) and ε in Eq. (2) are free parameters evaluated by minimization of the functional $\chi^2(a_i)$ characterizing the model description of experimental data in terms of Eq. (1). The first three terms in $d(E, A, Z)$ represent the energy dependence, while the fourth term is responsible for an additional shift proportional to the $A - 2Z$ difference. The parameter ε = 2.2 is found from a fit to the experimental data. Also, for the initial value of the parameter v, we took v = 0.73 and then refined it on the basis of the fit.

There is a vast set of experimental data on interactions of nuclei with incident protons and neutrons with the energy of around several tens of MeV and higher. Below, we describe the experimental data on the total cross sections for inelastic nucleon-nucleus interactions that we used. We employed the data on the interactions with the nuclei ranging from beryllium to uranium in the nucleon energy range of E = 60–2200 MeV. In total, this gave us 558 data points for 48 nuclei, with the range of Z between 4 and 92 and the range of A between 9 and 238, see the databases in Refs. [6, 8, 9].

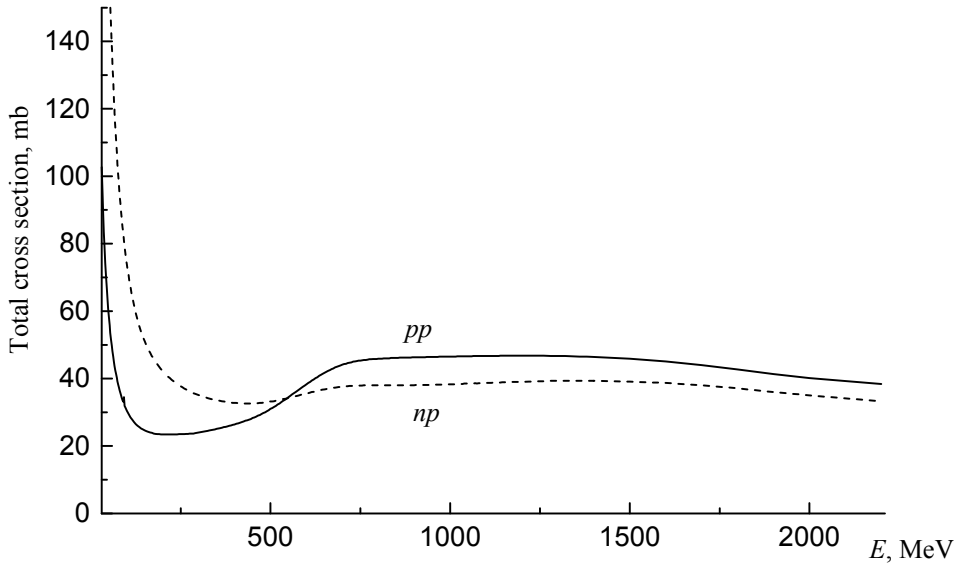

Fig. 1. Energy dependence of the total cross sections for nucleon-nucleon interaction. The solid and dashed curves represent the results for proton-proton and neutron-proton interaction, respectively

The total cross sections for inelastic nucleon-nucleus interaction are described by the expression in Eq. (1). The total cross sections for the nucleon-nucleon interaction were set to be equal to the corresponding cross sections for free nucleons. These cross sections were taken from the partial-wave analysis performed in Ref. [10] and are shown in Fig. 1. One can see in Fig. 1 that because of the special features of the behaviour of the nucleon-nucleon cross sections in the states with the total isospin 1 and 0, the respective cross sections are different. The total cross section for *pp* interaction has a minimum at the energy of about 250 MeV. This minimum is determined by the dynamics of elastic scattering and scattering accompanied by pion production. In the *np* cross section, this minimum manifests itself only very slightly.

Both the cross sections grow as the energy decreases. At low energies, the cross section for *np* interaction exceeds that for *pp*- interaction. In the energy region of $E > 550$ MeV, the *pp* cross section, on the contrary, is larger than the *np* one. Both the cross sections attain their maxima in the energy range of 1000–1200 MeV and then decrease smoothly at higher energies.

The free parameters of the function $d(E, A, Z)$ were found from a fit to the experimental data. For the statistical errors in the data, we took the quantity $(\Delta Y^2 + (\gamma Y)^2)^{1/2}$, where Y is the value of the experimental data point, ΔY is its true statistical error, and $\gamma = 0.05$ (one can take it for the lower limit of the data description uncertainty). The parameter γ takes into account disregarded systematic errors in the data and smoothes the effect of the data having unreasonably small statistical errors, making it possible to attain the values of $\langle\chi^2\rangle$ (the reduced values of χ^2) that are close to unity, and, therefore, permits an estimation of statistical errors of the sought parameters. With four free parameters a_i, the minimum of the functional $\langle\chi^2\rangle$ is 1.034. The values of the parameters are given in Table 1.

Table 1

Parameters of the function $d(E, A, Z)$

a_1	a_2	a_3	$a_4 \times 10^2$
0.219 ± 0.018	1.441 ± 0.020	-0.891 ± 0.025	-0.156 ± 0.015

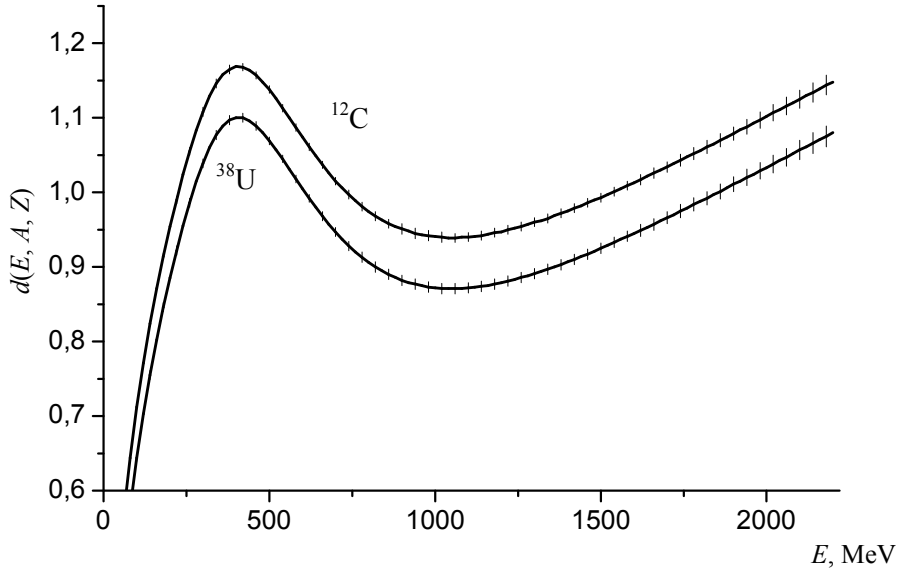

Fig. 2. Energy dependence of the function $d(E, A, Z)$ for the carbon and uranium nuclei

The energy dependence of the function $d(E, A, Z)$ for the carbon and uranium nuclei is shown in Fig. 2, where the errors are also displayed. Since $a_4 < 0$, the values of $d(E, A, Z)$ for carbon exceed those for uranium. The function $d(E, A, Z)$ reaches its maximal values exceeding unity at ~ 410 MeV. As the energy decreases, $d(E, A, Z)$ decreases fast since the probability of the projectile nucleon interaction with the target nucleons decreases, while the probability of the projectile nucleon scattering on the target nucleus as a whole increases. Therefore, the model for the nucleon-nucleus interaction considered here is valid for the energies for which the values of the function $d(E, A, Z)$ are close to unity, for example, 0.8; this is so at the energy of 150 MeV. One can assume that the maximum of $d(E, A, Z)$ is associated with production of pions followed by their absorption in the target nucleus [11]. As the energy grows above that of the maximum, the function decreases, reaches its minimum at ~ 1060 MeV, and then increases smoothly. As we explained above, the decrease stems from suppression of pion absorption in nuclei because of the shorter pion de Broglie wavelength, while the increase is due to production of multiple pions. However, there are also other interaction channels that may contribute in this energy interval, *e.g.*,

the fragmentation reaction. The cross section for fragmentation grows rapidly from the threshold energy (below 1 GeV) to the energy of 5 GeV [12].

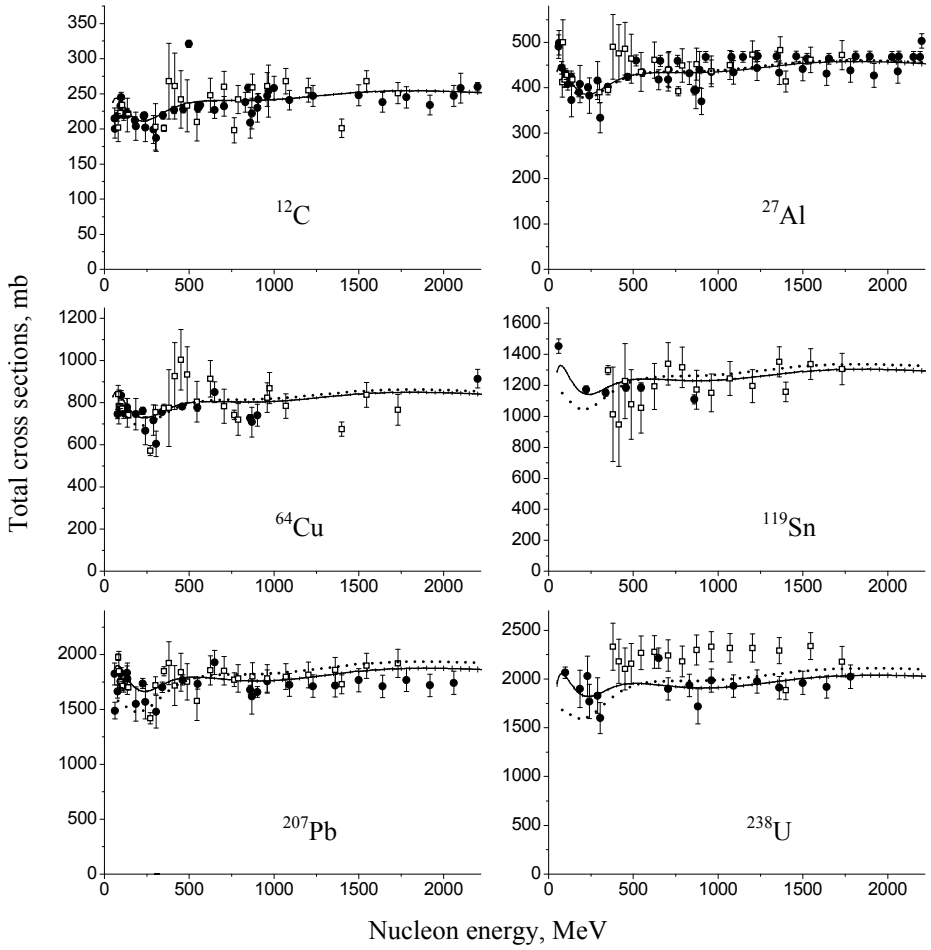

Fig. 3. Total cross sections for inelastic proton (solid curves within the corridor of errors) and neutron (dotted curves) interaction with nuclei. The filled circles and open boxes represent the corresponding experimental data

Figure 3 illustrates the quality of our description of the total cross sections for inelastic proton and neutron interactions with nuclei by the model presented here. We chose the nuclei separated by approximately the double interval of the mass number A (the heaviest considered nucleus is uranium). The energy dependence of the cross sections for nucleon-nucleus interaction has a maximum at 60 MeV and a minimum at 300 MeV. The first maximum arises from the product of the function $d(E, A, Z)$ – which decreases as the energy decreases – and the cross sections for *pp*- and *np*-interactions, which show the opposite behavior. The minimum reflects the minimum in the cross section for nucleon-nucleon interaction in the state with the total isospin 1. For this reason, the cross section for interaction of neutrons with nuclei in the range of $E < 550$ MeV is smaller than that of protons. In the energy region of $E > 550$ MeV, the neutron cross sections are larger than the proton ones.

3. Cross sections for nucleon-induced fission

With the model for inelastic cross sections that we just described, one can determine the energy dependence of the cross sections for nucleon-induced fission of nuclei. In this case, nuclear fission reduces to two independent sequential processes – the excitation of the target nucleus and its subsequent fission:

$$\sigma_{\mathrm{f}}\left(E, A, Z\right) = \sigma_{\mathrm{in}}(E, A, Z)\, f(E, x), \tag{4}$$

where $\sigma_{in}(E, A, Z)$ describes the excitation of the nucleus; $f(E, x)$ describes its fissility, the fissility parameter being $x = Z^2/A$.

Our aim is to describe fission of actinide nuclei with large values of the fissility parameter [4]. The fission of these nuclei can be supposed to be governed by similar mechanisms, and their fission cross sections can be described on the basis of a unified approach. However, an attempt to describe simultaneously six actinide nuclei in Ref. [2] was not successful. At the same time, two groups of four nuclei, ^{239}Pu, ^{237}Np, and ^{235,238}U (group 1) and ^{235,238,233}U and ^{232}Th (group 2) were described well. The reason of the discrepancy in Ref. [2] may be a systematic error in the measurement of the targets thickness – the authors estimated it to be 5 %. A shift of the cross sections by two standard deviations for some nuclei may substantially change the situation. However, the authors of Ref. [2] considered it to be unjustified to give preference to some values over the others on the basis of only one experiment, in which the total experimental error was 8 to 10 %. Accordingly, several groups of nuclei were described individually.

The fission cross sections for group 1 were described in terms of fissility using the following parameterization, referred to below as version 1:

$$f_1(E, x_0) = x_0(a_{10} + a_{11}\exp(-(2P)^2)). \tag{5}$$

For the sake of convenience, we used the fissility parameter normalized to its value for ^{235}U: $x_0 = x/36.02$. The coefficients a_{1i} ($i = 0, 1$) in Eq. (5) were free parameters. They were found from a fit to the data [2] on fission of ^{239}Pu, ^{237}Np, and ^{235,238}U in the energy range of 200–1000 MeV. For χ^2, the minimal value of 18.4 was obtained (the number of data points was 36). This yields $<\chi^2> = 0.559$, the respective parameter values being $a_{10} = 0.829 \pm 0.010$ and $a_{11} = -0.482 \pm 0.140$.

The fission cross sections in the second group of nuclei (^{235,238,233}U and ^{232}Th) were described in terms of fissility as

$$f_2(E, x_0) = (a_{20} + a_{21}x_0) + a_{22}\exp(-(2P)^2), \tag{6}$$

this version is called version 2.

The minimal value of the functional χ^2 proved to be 4.1 for 36 data points ($<\chi^2> = 0.127$), the fitted parameter values being $a_{20} = -5.507 \pm 0.541$, $a_{21} = 6.361 \pm 0.549$, and $a_{22} = -0.173 \pm 0.140$. The small value of the functional $<\chi^2>$ indicates that the values of the total errors in Ref. [2] are evidently overestimated.

The values of the functions f_1 and f_2 tend to a constant equal to x_0a_{10} for the first group, and $(a_{20} + x_0a_{21})$ for the second group, respectively. This regime is reached at the energy higher than 400 MeV. As the energy decreases, the functions also decrease. An explanation of this phenomenon requires a dedicated investigation.

Figure 4 shows the cross sections for proton- and neutron-induced fission of nuclei. The displayed experimental data are from Ref. [2]. Also, for comparison, in this figure we present the data quoted in the EXFOR database and obtained after 1970. The filled and open symbols represent the data for incident protons and neutrons, respectively.

The solid curves with the associated error band stand for the fission cross sections calculated with Eq. (4). The versions of the calculation are indicated in the parentheses. Version 1 was used for ^{239}Pu and ^{237}Np and version 2 – for ^{233}U and ^{232}Th. Both versions 1 and 2 are shown for ^{235,238}U. The dotted curves represent the cross sections predicted for neutron-induced fission. Either version describes well the experimental data of Ref. [2]. The scattered data from EXFOR demonstrate the degree of uncertainty in the normalization of the data from Ref. [2] and EXFOR.

At the energies below 550 MeV, the cross sections for neutron-induced fission are predicted to be smaller than those for proton-induced fission, but at higher energies, neutron-induced fission prevails. This phenomenon reflects the corresponding feature of the energy dependence of the total cross section for the inelastic interaction of nucleons with nuclei and was discussed above. The difference between the cross sections for proton- and neutron-induced fission at 1 GeV is 4 % with respect to the cross section for proton-induced fission.

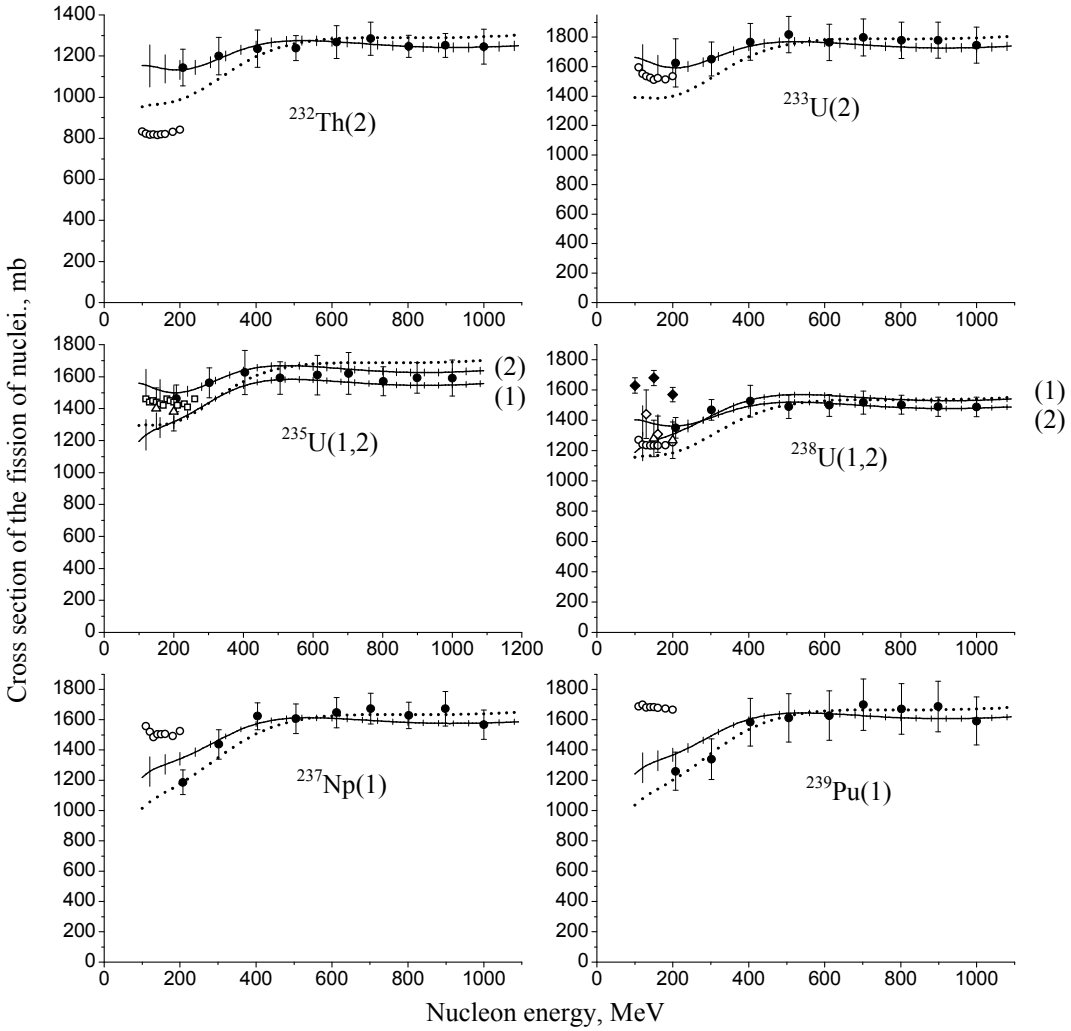

Fig. 4. Predicted cross sections for fission induced by protons (solid curves within the error corridor) and neutrons (dotted curves). The version of the parameterization is indicated in the parentheses. The experimental data are from Ref. [2] (filled circles) and the EXFOR database: the data obtained by Bychenkov *et al.* [13] (filled diamonds), Shcherbakov *et al.* [14] (open circles), Nolte *et al.* [15] (open triangles), Lisowski *et al.* [16] (open boxes), and Eismont *et al.* [17] (open diamonds)

Thus, the description of the cross sections for proton-induced fission of actinides on the basis of the respective inelastic cross sections agrees with the conclusion that in the energy range of 400–1000 MeV these two cross sections are related by an energy-independent factor. It is natural to assume that this relation remains valid presumably for the energies of up to 2 GeV, since, up to this energy, the cross section for inelastic interaction of nucleons with nuclei changes insignificantly because the total nucleon-nucleon cross section behaves the same way. A definite answer will be given by future experiments. In order to refine the behaviour of fissility of nuclei in the $100 < E < 400$ MeV energy range, it is also necessary to perform additional experiments.

As for fission of lighter nuclei, *e.g.*, of bismuth and lead, the special features of the energy dependence of the cross section and its smallness are likely to suggest that their fission involves production of pions in nucleon-nucleon interactions and their absorption within the target nucleus. As a result, the fissility parameter of the residual nucleus may increase considerably. This and other circumstances call for development of a dedicated approach to description of the cross sections for fission of these nuclei. It would be natural to assume that this process contributes in the case of actinides as well, but due to smallness of this contribution in the considered energy interval it does not manifest itself.

4. Conclusions

1. From the model presented in this contribution, it follows that for inelastic interaction of nucleons with nuclei in the energy range of 60–2200 MeV the total cross sections receive contributions predominantly from interactions of the projectile nucleon with target nucleons.

2. The energy dependence of the cross sections for fast-proton-induced fission of actinides replicates the energy dependence of the total cross section for inelastic interaction of nucleons with nuclei, at least in the energy range of 400–1000 MeV.

3. At energies of up to 550 MeV, the cross sections for neutron-induced fission of nuclei are lower than the respective cross sections for proton-induced fission. At higher energies, the cross section for neutron-induced fission exceeds that for proton-induced fission. For actinide nuclei, at the energy of 1 GeV, this excess constitutes 4 % of the cross section for proton-induced fission.

References

1. http://www.nea.fr/html/dbdata/
2. A.A. Kotov *et al.*, Phys. Rev. C **74**, 034605 (2006).
3. A.N. Smirnov *et al.*, J. Nucl. Sci. Techn., Suppl. **2**, 238 (2002).
4. V.G. Vovchenko *et al.*, Preprint PNPI-**2844**, Gatchina (2010).
5. V.G. Vovchenko *et al.*, Yad. Fiz. **75**, 3 (2012); Phys. Atom. Nucl. **75**, 1 (2012).
6. V.S. Barashenkov and V.D. Toneev, *Interactions of High-Energy Particles and Nuclei with Nuclei*, Moscow (1972), p. 27 (in Russian).
7. L.S. Azhgirei *et al.*, Sov. Phys. JETP **9**, 1163 (1959).
8. L. Sihver *et al.*, Phys. Rev. C **47**, 1225 (1993).
9. http://www.rea.fr/html/dbdata/bara.html
10. http://gwdac.phys.gwu.edu
11. E.N. Volnin *et al.*, Preprint LNPI-**847**, Gatchina (1983).
12. E.N. Volnin *et al.*, Preprint LNPI-**101**, Gatchina (1974).
13. V.S. Bychenkov *et al.*, Sov. J. Nucl. Phys. **17**, 496 (1973).
14. O.A. Shcherbakov *et al.*, J. Nucl. Sci. Techn., Suppl. **2**, 230 (2002).
15. R. Nolte *et al.*, J. Nucl. Sci. Eng. **156**, 197 (2007).
16. P.W. Lisowski *et al.*, in *Proc. of the Specialists' Meeting on Neutron Cross Section Standards for the Energy Region above 20 MeV*, Uppsala, Sweden, May 1991, OECD/NIA Report NEANDC-305 “U” (1991), p. 177.
17. V.P. Eismont *et al.*, Phys. Rev. C **53**, 2911 (1996).

STUDY OF ENERGY DEPENDENCE AND ISOTOPIC EFFECT OF TOTAL CROSS SECTIONS FOR FISSION OF Pb, Tl AND Au NUCLEI INDUCED BY PROTONS WITH ENERGIES UP TO 1 GeV

Yu.A. Chestnov, Yu.A. Gavrikov, O.Ya. Fedorov, A.A. Kotov, V.V. Poliakov, A.I. Shchetkovskiy, M.G. Tverskoy, L.A. Vaishnene, V.G. Vovchenko

The need for information concerning fission induced in nuclei by intermediate energy projectiles is obvious. The interest in this process emerges from both fundamental and applied problems of nuclear physics. In spite of extensive experimental efforts, nuclear fission remains insufficiently understood in many aspects. Measurements of the energy dependence of the total cross sections for fission of nuclei by intermediate energy protons will add to our understanding of the fission process in terms of nuclear properties of highly excited nuclei, such as temperature dependence of the level density and fission barriers of excited nuclei. For physics applications, the nuclear data are required for new energy production concepts with the accelerator driven systems (ADS), for nuclear waste transmutation technologies, for accelerator and spacecraft radiation shields. All the above mentioned problems require fission cross section data of high accuracy and reliability. Unfortunately, the majority of experimental fission cross sections, obtained in various experiments with different methods of registration, are dispersed in the range which exceeds the declared accuracy of measurements, not allowing to derive a reliable energy dependence of the fission cross section on the proton energy. High accuracy of fission cross section measurements may be achieved only by modern electronics methods of registration of both fission fragments in coincidence together with high precision monitoring of the proton flux on the studied target. In the present experiment, a method based on the use of gas parallel plate avalanche counters (PPAC) for registration of complementary fission fragments in coincidence and a telescope of scintillation counters for direct counting of incident protons on the target has been applied. This method allowed us to measure the absolute cross sections for proton induced fission of ^{206}Pb, ^{207}Pb, ^{208}Pb, ^{203}Tl and ^{197}Au in the energy range from 200 to 1000 MeV with a step of 100 MeV.

The experiment was performed at the 1 GeV PNPI synchrocyclotron. Since the external proton beam of the PNPI synchrocyclotron has a fixed energy of 1 GeV, a method of energy reduction by beam absorption in a copper degrader was applied in order to obtain proton beams with energies in the range from 200 to 900 MeV [1]. The proton energy was measured by the time-of-flight (TOF) method. The TOF spectra analysis showed that π^+ mesons were practically absent. The beam diameter at the target chamber location for all proton energies did not exceed 40 mm. The beam profile was measured by a thin scintillation counter, which scanned the beam in two orthogonal directions. The beam divergence was determined by monitoring the beam profile at the chamber inlet, outlet and in its centre at each proton energy variation. The beam intensity distribution on the target was a 2-dimensional normal distribution with the FWHM not larger than ~ 18 mm.

In the present experiment, the fission fragment detector comprised an assembly of two identical gas PPACs with the target to be studied between them. The PPACs provide a large solid angle for fragments registration, have a high efficiency for fragments detection, and have good time characteristics (better than 300 ps time resolution for fission fragments). The latter property, together with the PPAC insensitivity to neutrons, photons and light charged particles with minimal energy loss in the matter, makes PPACs extremely favorable tools for accelerator experiments, allowing one to place them in a direct proton beam.

PPAC pulse amplitudes were determined both by the specific energy losses of the detected particles in heptane and by the gas gain value. The latter depends on the voltage between the anode and cathode, so the detection efficiency could be controlled by setting a proper voltage. By appropriate choice of the voltage value, one can introduce a threshold selection criterion. Nevertheless, it is not sufficient to employ only the threshold selection criterion when using a PPAC directly in the proton beam. In fact, the amplitude spectrum of the detected particles contains, together with the pulses of fission fragments, a considerable contribution of low-amplitude background events. These events are caused by various proton-induced nuclear reactions in the matter along the beam line. Such a low-energy component is strongly suppressed by the coincidence criterion switched on. Moreover, an analysis of amplitude correlations of the coinciding fragments allowed us to exclude almost all background events. Thus, in our experiment we used three criteria to select binary

fission events: a threshold criterion, coincidences, and a criterion of the total kinetic energy of the detected coincident particles (the amplitude correlations).

A PPAC is so thin that it does not harm the beam characteristics when located in the beam. For this reason, several assemblies with various targets could be readily placed into the beam. This allowed us to reduce considerably the measurement time. In the real experiment, up to six assemblies were used at the same time. The layout of the set-up including the reaction chamber with the fission event detectors and the proton monitoring system is shown in Fig. 1. The main part of the set-up is a hermetic chamber with six detector assemblies, each assembly comprising two PPACs and a target in between.

Before entering the reaction chamber, the proton beam passed three scintillation counters (S1&S2&S3), combined *via* the coincidence scheme for direct proton counting. Just downstream of the reaction chamber, a polyethylene target $(CH_2)_n$ was placed. Protons elastically scattered from this target were detected by a two-arm scintillation telescope (S4&S5&S6), which served as a secondary beam monitor.

Direct counting of the incident protons with a scintillation counter telescope was used for beam monitoring. This method provides good monitoring accuracy only for low intensity beams, up to $\sim 10^5$ s^{-1}. However, for experiments with lead, thallium and gold nuclei, which have small fissility, one needs much higher beam intensity. For this reason, measurements were performed at two intensity values of the proton beam: $\sim 10^5$ s^{-1} and 10^6–10^7 s^{-1}. In the latter case, the beam monitoring was done by two methods: 1) by detecting fission events from a calibration target of ^{238}U residing in the reaction chamber, and 2) by detecting events of *pp* scattering on an auxiliary $(CH_2)_n$ target with the two-arm scintillation telescope (S4&S5&S6). Both methods were previously calibrated at low intensity ($< 2 \times 10^5$ s^{-1}) with the direct monitoring telescope (S1&S2&S3). A comparison of both methods at high intensity has shown agreement of the results within $\sim$ 3–6 % at all energies from 200 to 1000 MeV. The calibration procedure for secondary monitoring was described in detail in [2]. The target to be investigated was a thin layer of material deposited by vacuum evaporation on one of the electrodes of the PPAC assembly. The thickness of targets was determined by measuring the energy losses of α-particles passing through the target. So, using the methods of detection of the binary fission events and beam monitoring described in [2] we have measured the fission cross sections for each target at nine proton energies.

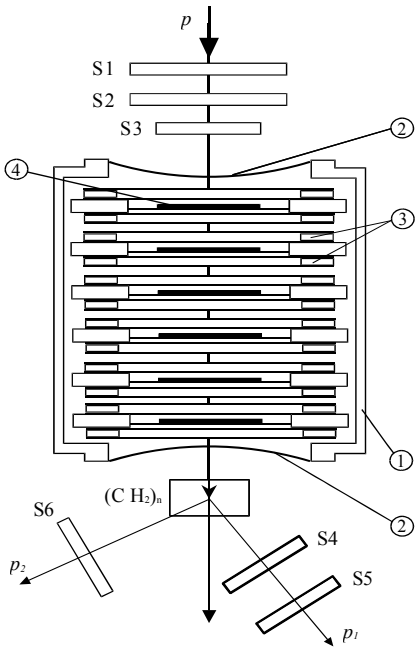

Fig. 1. Experimental set-up: 1 – chamber filled with heptane; 2 – entrance window; 3 – PPACs; 4 – target; S1–S6 – scintillation counters

The cross section calculation procedure comprised the following steps.

1. Background subtraction after analysis of the 2-dimensional amplitude distribution of the detected events. The number of background events amounted to 3–5 % of the total number of the detected events.

2. Determination of the solid angle for fission event detection for each assembly. The calculation was done by Monte Carlo simulations which took into account the proton beam profile on the target, the geometry of the fission fragments detection, the fragments mass and their energy distributions, as well as the anisotropy of the fragments angular distributions in the laboratory system due to the longitudinal momentum component of the fissile nucleus. The statistical accuracy of the solid angle calculations was about 0.1 %.

3. Estimation of the undetectable fraction of the fission events caused by the energy loss of fission fragments in the target, in its supporting foil, and in the PPAC electrodes. The undetectable part of the events depended on the target nucleus and thickness, and was about 4 %.

4. Determination of the integral proton flux through the target, with the account of the scintillation telescope efficiency and the probability of arrival of more than one proton in a microbunch at low intensity.

5. Determination of the normalization factors to calculate the proton flux at high intensity *via* the counting rate of the *pp*-scattering monitor and the fission counting rate from the calibration target.

The measured cross sections for fission of the ^{197}Au, ^{203}Tl, ^{206}Pb, ^{207}Pb, ^{208}Pb and ^{nat}Pb nuclei are shown in Table 1. For most of the nuclei, the presented data were averaged over the results of several measurements, the errors being determined mainly by the monitoring errors and the uncertainties in the target thickness.

Table 1

Proton induced fission cross sections (mb)

Energy, MeV	^{197}Au	^{203}Tl	^{206}Pb	^{207}Pb	^{208}Pb	^{nat}Pb
207	35 ± 2	63 ± 5	104 ± 6	80 ± 9	66 ± 6	60.5 ± 3.5
302	47 ± 2	81 ± 5	127 ± 6	100 ± 10	82 ± 6	84 ± 4.5
404	58 ± 28	104 ± 5	145 ± 6	134 ± 8	100 ± 6	110 ± 6
505	67 ± 2	123 ± 6	164 ± 6	135 ± 7	110 ± 7	118.5 ± 6
612	74 ± 3	116 ± 6	168 ± 6	136 ± 7	120 ± 7	127 ± 6.5
702	81 ± 3	147 ± 8	178 ± 7	143 ± 7	132 ± 8	132.5 ± 9.5
802	85 ± 4	144 ± 8	189 ± 8	144 ± 7	135 ± 8	131 ± 8.5
899	87 ± 4		182 ± 7	146 ± 7	130 ± 8	133.5 ± 7.5
1000	78 ± 5	126 ± 8	180 ± 7	144 ± 7	129 ± 8	129 ± 8.5

The energy dependences of the fission cross sections obtained in the present experiment for ^{197}Au and ^{203}Tl are shown in Figs. 2 and 3 together with the EXFOR data for the energy range 40 MeV < E_p < 1 GeV. The closed circles represent the experimental results that were used to get the parameters of the approximation curve. The open circles represent the data that were rejected due to their large deviations from the average values. For the first approximation, an exponential function was used:

$$\sigma_f = \sigma_1 - C_1 \exp(-E_p / t_1), \quad (1)$$

where σ_1 is the asymptotic value of the fission cross section, C_1 and t_1 are free parameters. The parameter values obtained by the fit are presented in Table 2. The values of χ^2 / ν, where ν is the number of degrees of freedom, are listed in the last column of Table 2. They confirm the reliability of our approximations.

There were no experimental data on cross sections for fission of lead isotopes by protons in the energy range 200–1000 MeV. We have performed measurements to obtain information on the energy dependence of the isotopic effect in this energy range. The isotopic effect consists in the dependence of the total fission cross sections on the fissility parameter (Z^2 / A) of the target nucleus, where Z is its charge number and A is its mass number. As is well known, this parameter reflects the ratio of the Coulomb energy of a charged liquid drop to its surface tension energy. The electric charge tends to break the drop, while the surface tension maintains its integrity. The isotopic effect is relatively weak, but the existing fission models underestimate it even more. Its experimental study is therefore of interest for physics of nuclear fission.

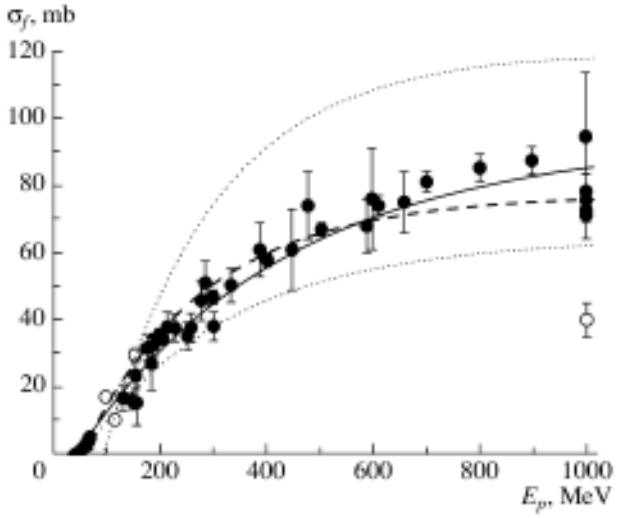

Fig. 2. Energy dependence of the proton induced fission cross sections for ^{197}Au. The closed circles stand for the experimental results used here to derive the approximation by Eq. (1) (solid curve); the open circles are the ignored data. The dashed curve is the approximation from [3], while the lower and upper dotted curves represent the results of model calculations from [4] and [5], respectively

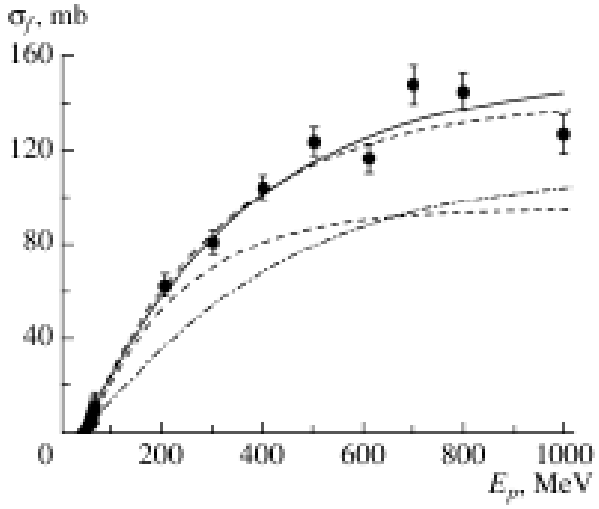

Fig. 3. Energy dependence of the proton induced fission cross sections for ^{203}Tl. The displayed points are the experimental data measured in our experiment and in experiment [6] in the energy region of $E \sim 30$ MeV, and used here for the approximation by Eq. (1) (solid curve). The upper and lower dashed curves represent, respectively, our approximations for ^{208}Pb [7] and Prokofiev's approximation for ^{205}Tl [3]. The dash-dotted curve is our prediction for the energy dependence of the cross section for proton induced fission of ^{205}Tl

Table 2

Parameters for the Eq. (1) approximation for different nuclei

Parameters	σ_1, mb	C_1, mb	t_1, MeV	χ^2 / ν
^{197}Au	93 ± 2	103 ± 2	396 ± 17	0.99
^{203}Tl	152 ± 8	172 ± 6	329 ± 35	0.99
^{206}Pb	179 ± 4	225 ± 5	181 ± 12	0.99
^{207}Pb	144 ± 3	186 ± 5	168 ± 11	0.99
^{208}Pb	140 ±4	163 ± 4	278 ± 13	0.97

We have studied this effect for fission of uranium isotopes by protons with energies E_p = 200–1000 MeV. It has been found that it runs from ~ 30 mb for the difference between ^{235}U and ^{238}U fission cross sections per each missing neutron up to ~ 80 mb for half of the difference between the ^{233}U and ^{235}U fission cross sections. The relative contribution from the isotopic effect in uranium (3 ± 1 %) is almost independent of the proton beam energy [8].

The measurement results contained in the EXFOR database [3] show that the increase in total fission cross sections for lead isotopes at $E_p \approx 50$ MeV is ~ 40 % per each missing neutron. For platinum nuclei, the relative contribution from the isotopic effect is even larger [6]. Its absolute contribution increases with the fissility parameter (Z^2/A).

There were no experimental data on cross sections for fission of lead isotopes by protons in the energy range 200–1000 MeV. We have performed such measurements to obtain information on the energy dependence of the isotopic effect in this energy range.

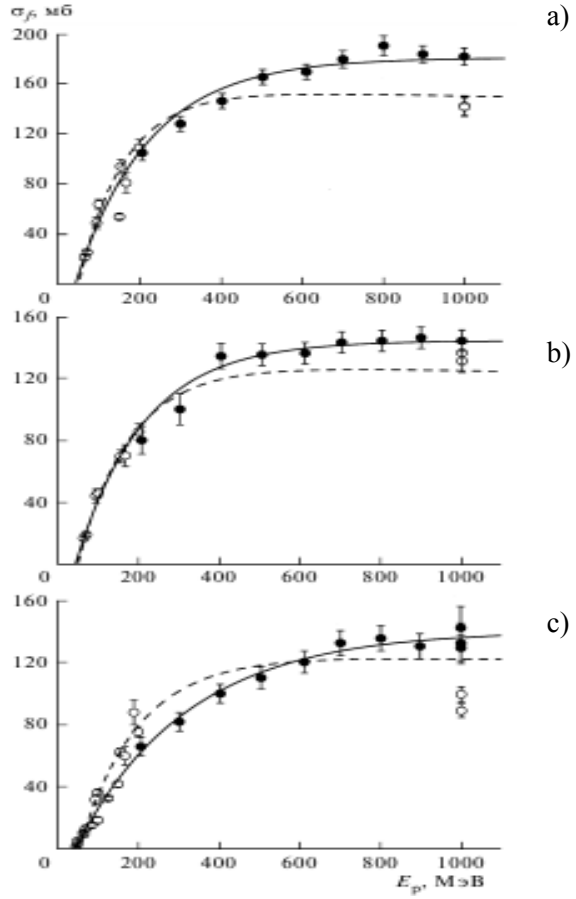

Fig. 4. Energy dependences of the total cross sections for fission of: a – ^{206}Pb; b – ^{207}Pb, and c – ^{208}Pb nuclei by protons. Closed circles are the results of our measurements, open circles are the EXFOR database values [3]. Solid and dashed curves are our approximations and approximations by A.V. Prokofiev [3]

In Table 1, the measured total cross sections for fission of lead isotopes are presented. They are also shown in Fig. 4a–c by closed circles, together with the cross sections for fission by 1 GeV protons that we had published previously [9]. The EXFOR database values [3] are represented by open circles. The absence of error bars means that the authors considered the experimental errors to be equal to 10 % of the corresponding total fission cross section. The data were approximated by the exponential function.

The absolute increase in the total cross sections for fission of ^{208}Pb and ^{238}U nuclei by protons with energies of 200–1000 MeV after a loss of a neutron was almost identical, *i.e.*, 20–30 mb, despite these cross sections are different by more than a factor of 10. As is well known, a decrease in the parameter (Z^2/A) is

accompanied by an increase of the fission barrier of heavy nuclei. The higher the fission barrier, the larger the relative contribution of the isotopic effect should be.

The measured total cross sections for fission of uranium and lead isotopes induced by protons indicate a progressive increase of the isotopic effect as the nucleus mass decreases, approximately in proportion to its fissility parameter (Z^2/A).

References

1. N.K. Abrossimov, V.G. Vovchenko, V.A. Eliseev, E.M. Ivanov, Yu.T. Mironov, G.A. Riabov, M.G. Tverskoy and Yu.A. Chestnov, Preprint PNPI-**2525**, Gatchina (2003).
2. V.G. Vovchenko, L.A. Vaishnene, Yu.A. Gavrikov, A.A. Kotov, V.I. Murzin, V.V. Poliakov, S.I. Trush, O.Ya. Fedorov, Yu.A. Chestnov, A.V. Shvedchikov and A.I. Shchetkovski, Preprint PNPI-**2532**, Gatchina (2003).
3. A.V. Prokofiev, Nucl. Instr. Meth. Phys. Res. A **463**, 557 (2001).
4. V.S. Barashenkov, F.G. Gereghi, A.S. Iljinov *et al*., Nucl. Phys. A **222**, 204 (1974).
5. M.H. Simbel, Z. Phys. A **333**, 177 (1989).
6. O.A. Zhukova, A.V. Ignatyuk, M.G. Itkis *et al*., Yad. Fiz. **26**, 473 (1977).
7. L.A. Vaishnene, V.G. Vovchenko, Yu.A. Gavrikov *et al*., Izv. Akad. Nauk, Ser. Fiz. **74**, 529 (2010).
8. A.A. Kotov, L.A. Vaishnene, V.G. Vovchenko *et al*., Izv. Akad. Nauk, Ser. Fiz. **71**, 837 (2007) [Bull. Russian Acad. Sci. (English Transl.) **71**, 809 (2007)].
9. L.A. Vaishnene, L.N. Andronenko, G.G. Kovshevny *et al*., Z. Phys. A **302**, 143 (1981).

SECONDARY NEUTRONS AS THE MAIN SOURCE OF NEUTRON-RICH FISSION PRODUCTS IN IRRADIATION OF THICK U TARGETS BY 1 GeV PROTONS

PNPI participants of the GANIL (France) and INFN (Italy) Collaborations:
A.E. Barzakh, L.Kh. Batist, D.V. Fedorov, V.S. Ivanov, K.A. Mezilev, P.L. Molkanov, F.V. Moroz, S.Yu. Orlov, V.N. Panteleev, Yu.M. Volkov

1. Introduction

The ISOL (Isotope Separation On-Line) technique is commonly used to produce radioactive ion beams. The design of the next generation ISOL facilities like SPIRAL2 and EURISOL motivates studies of large targets containing up to several kilograms of ^{238}U. For such massive targets the prediction of final radioactive beam intensity is a complex task depending on a variety of physical and chemical processes involved in production, release and transportation of the beam.

In our study of target properties, we take as the starting point the commonly used Diffusion-Effusion Model (DEM). According to this model, the radioactive nuclei produced in the grains of target material escape from the target by diffusion from the grains with subsequent effusion from the target to the ion source. The yield of radioactive isotopes is determined by the diffusion-effusion parameters of the target and the transportation tube. The advantage of this approach is a possibility to describe the production efficiency dependence on the isotope half-life, as well as the time dependence of the release of isotopes from the target by a single set of parameters.

At the IRIS facility of PNPI, exotic nuclei far from stability are formed in interaction of 1 GeV protons with a thick uranium carbide target. In the targets tested at PNPI, besides heavy reaction products of proton induced spallation and fission, a large amount of secondary particles are created. These particles also contribute to production of nuclides inside the target. Therefore, it is important to take into account these processes in calculations of the in-target production rate, which is crucial for accurate predictions of the yields of nuclides far from stability. We present an experimental evidence for a secondary particles contribution and compare these results with FLUKA calculations that take into account such processes.

We have studied $^{238}UC_x$ targets exposed to 1 GeV protons of the PNPI synchrocyclotron. We used the high density uranium carbide (ρ = 11 g/cm^3) with U : C mass ratio 95 : 5. A surface ionization ion source was used for investigation of isotopes of alkaline elements.

2. Yield determination

To determine the yields in question (the ion beam intensities at the exit of the ion source), the intensities of characteristic gamma or alpha lines of the investigated isotopes were measured. For gamma-measurements, the radioactive source, which has been collected on the tape during the time interval t_c, was moved to the detector (during the transportation time t_t). If the measurement time interval is t_m and the area under the chosen gamma peak is S, then the yield can be calculated as follows:

$$Y_\gamma = \frac{S \cdot \lambda}{\exp(-\lambda \cdot t_t) \cdot \left(1 - \exp(-\lambda \cdot t_c)\right) \cdot \left(1 - \exp(-\lambda \cdot t_m)\right)} \cdot \frac{1}{\varepsilon_{\text{tr}} \cdot b(E_\gamma) \cdot \varepsilon_{\text{det}}(E_\gamma)}, \quad (1)$$

where ε_{tr} is the efficiency of the ion beam transmission from the ion source to the measurement station, $b(E_\gamma)$ is the branching (absolute intensity) of the chosen gamma line, $\varepsilon_{\text{det}}(E_\gamma)$ is the gamma-detector efficiency at the energy of the chosen line, λ is the decay constant for the isotope under study.

To determine the yields of the isotopes with life-times in the millisecond region, an alpha detector was placed near the spot of collection. In this configuration, the radioactivity collection and the data acquisition were made at the same time, and Eq. (1) was modified correspondingly.

In some cases, absolute branching ratios for gamma lines are not known or dubious. In these cases, a beta counter was used. To take into account beta counts from the decay chain of the isotope in question, the time dependence of beta counts was measured. The corresponding formulas can be found in [1].

A special procedure was applied for determination of ^{92}Rb branching [2]. For some other Rb and Cs isotopes, the absolute intensities of gamma-lines were determined for the first time or were substantially revised from a comparison of the yield determined by a beta decay curve analysis and using the results of gamma measurements for the same isotope (see Tables 1 and 2).

Table 1

Revised absolute intensity of γ-lines for Rb isotopes

A	E_γ, keV	Intensity, % (literature data [3])	Intensity, % (present work)
91	93.63	33.8(2.0)	20.2(3.2)
92	814.98	33(12)	3.2(0.2)
93	432.61	20.2(1.0)	9.5(1.7)
94	836.90	87.1(0.4)	44.2(6.4)
95	352.02	49(3)	29.3(6.3)

Table 2

Revised absolute intensity of γ-lines for Cs isotopes

A	E_γ, keV	Intensity, % (literature data [3])	Intensity, % (present work)
140	602.35	53.3(2.0)	32.9(5.7)
142	359.60	27.2(2.7)	21.0(3.8)
144	199.33	*only relative intensity*	31.9(7.3)
145	175.40	19.8(2.4)	10.7(2.4)
146	181.02	*only relative intensity*	27.1(6.3)

3. Yields description in the Diffusion-Effusion Model

In the DEM, the observed yield $Y(A)$ of the isotope A with the life-time $T_{1/2}$ can be presented as follows:

$$Y(A) = Y_{\text{in target}}(A) \cdot \varepsilon_{\text{diff}}(T_{1/2}) \cdot \varepsilon_{\text{eff}}(T_{1/2}) \cdot \varepsilon_{\text{ioniz}}, \quad (2)$$

where $Y_{\text{in target}}(A)$ – in-target production of the isotope A; $\varepsilon_{\text{diff}}$, ε_{eff}, $\varepsilon_{\text{ioniz}}$ – diffusion, effusion and ionization efficiencies.

The in-target production can be estimated through the product of the known target thickness x, proton beam intensity I_0, and the cross-section σ_A for the isotope A production in the reaction (p^{238}U) at 1 GeV:

$$Y_{\text{in target}}(A) = \sigma_A \cdot x \cdot I_0 . \quad (3)$$

(For clarity we assume in this formula the reduction of the proton beam in the target to be negligible.)

The diffusion and effusion efficiencies depend on the diffusion and effusion time constants t_d and t_e:

$$\varepsilon_{\text{eff}} = \frac{T_{1/2}}{T_{1/2} + t_e}, \ \varepsilon_{\text{diff}} = 3 \cdot \alpha^{1/2} \left[\coth(\alpha^{-1/2}) - \alpha^{1/2} \right], \quad (4)$$

where $\alpha = \dfrac{T_{1/2}}{\pi^2 \cdot t_d}$.

The ratio of the experimentally observed yield $Y_{\text{exp}}(A)$ of the isotope A to its in-target production, $Y_{\text{exp}}(A) / Y_{\text{in target}}(A)$, will be denoted as the production efficiency $\varepsilon_R(T_{1/2}(A))$.

To obtain the experimental value of $\varepsilon_R(T_{1/2}(A))$, one should know the cross section σ_A. The primary reaction cross-sections were measured for nuclei with A from 15 to 237 at GSI, Darmstadt, in inverse kinematics. In these experiments with thin targets, the influence of secondary neutrons on the isotope yields was negligible. This is not the case for our targets. However for the nuclei with $A > 170$, the fission reactions

contribution to the yield vanishes. One can expect that Darmstadt cross-sections can be reliably used for σ_A in (3) for this spallation region. Therefore, this region gives an opportunity to test the applicability of the DEM. We have made this test with Fr isotopes.

4. Release description in the Diffusion-Effusion Model

There exists another method to determine the diffusion-effusion parameters t_d and t_e. These parameters govern the time dependence of isotopes release from the target. Experimentally, the release process was observed using the following procedure. After exposing the target to the proton beam during t_p seconds, the proton beam was switched off. Radioactive nuclei were collected on the tape during t_c seconds, then the source was moved to the detector (the moving time was t_t) and the gamma-spectrum was collected during t_c seconds. At the same time, the next radioactive source was prepared, and the procedure was repeated. The time dependence of the area under the chosen gamma peak is the so-called release curve.

An experimental release curve is described in the DEM by the infinite series [1]:

$$R(t_j) = n \cdot \frac{2m}{\pi^2} \cdot \exp(-\lambda \cdot t_c) \cdot \exp(-\lambda \cdot t_t) \cdot (1 - \exp(-\lambda \cdot t_c)) \cdot \exp(-\lambda \cdot t_j) \times$$
$$\times \sum_{k=1}^{\infty} \frac{\exp(-c_k \cdot \lambda_D \cdot t_j) \cdot (1 - \exp(-c_k \cdot \lambda_D \cdot t_c))}{c_k \cdot (c_k \cdot \lambda_D + \lambda)} \cdot (1 - \exp(-(c_k \cdot \lambda_D + \lambda) \cdot t_p)), \quad (5)$$

where $\lambda_D = \frac{\ln(2)}{t_d}$, $t_j = j \cdot (t_c + t_t)$, $j = 0,\ 1,\ 2, \ldots$

Under assumption that the target material consists of uniform spherical grains, one has to use in Eq. (5) $m = 3$ and $c_k = k^2$.

It is often impossible to fit the experimental release curve with a single diffusion parameter. In these cases, it is necessary to suppose that there are two different diffusion processes with different λ_D constants. The corresponding generalization of Eq. (5) is straightforward. This approach will be denoted as the double-diffusion model.

5. Description of Fr production efficiencies in the Diffusion-Effusion Model

The target parameters were as follows: the pellets diameter was 11 mm, the uranium density $\rho = 11$ g/cm^3, the thickness $x = 6.3$ g/cm^2. A tantalum container was used. The target temperature was $T = 1850$ °C. It is worth noting that a similar analysis was successfully applied to many other targets with completely different properties. (See some our yield results for Fr isotopes in [4–6].)

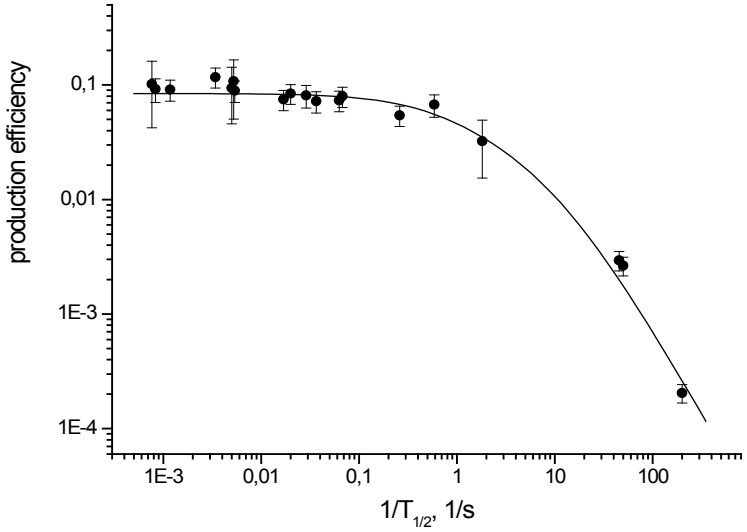

Fig. 1. Fr efficiency curve taking into account the in-target Ac decay. Fitted with t_d (Fr) = 1.4(1.1) s, t_e (Fr) = 85(34) ms, $\varepsilon_{\text{ioniz}} = 0.8(1)$ %

To calculate the in-target production of Fr isotopes, one has to take into account the in-target alpha decay of Ac isotopes. This was done by a special procedure [1].

The experimental production efficiencies of $^{205–214,218–221}$Fr are presented in Fig. 1 along with the fitting curve according to Eqs. (2) and (4), the Ac in-target decay being taken into account.

Note that for ^{214}Fr and ^{218}Fr the production of isomers was taken into account in the calculation of the production efficiency.

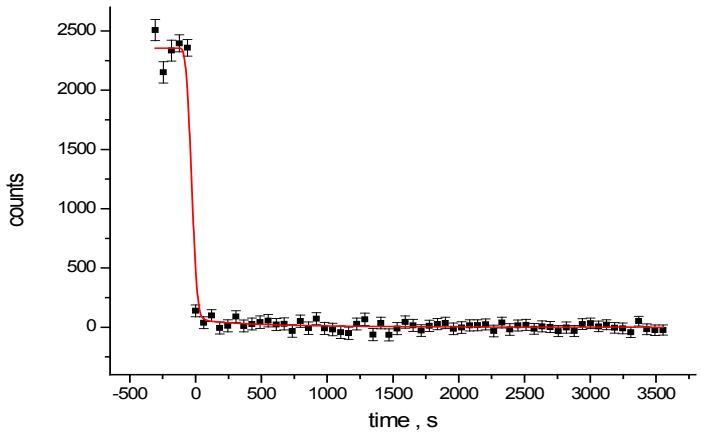

Fig. 2. ^{222}Fr release curve (E_γ = 206 keV), fitted with Eq. (7) and t_d = 1.9(1.5) s

The important point for verification of the applicability of the DEM is the consistency of two different approaches to the determination of the diffusion time, namely, the analysis of the efficiency curve and the release curve. The release curve for ^{222}Fr was analysed using Eq. (5). The fitting curve is shown in Fig. 2. One can see that t_d obtained from the efficiency curve (1.4(1.1) s) agrees well with the t_d value obtained from the release curve (1.9(1.5) s).

6. Production of neutron-rich Cs isotopes by secondary neutrons

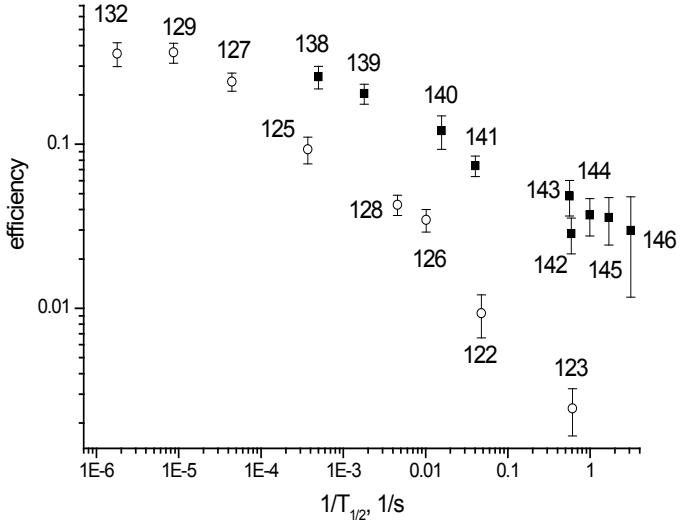

Fig. 3. Production efficiency for Cs isotopes calculated with the GSI-Darmstadt cross-sections for proton-induced fission. The black boxes are the efficiencies for neutron-rich isotopes, empty circles are the efficiencies for neutron-deficient isotopes

Let us consider the efficiency curve for Cs isotopes. We use the experimental data obtained with a uranium target of diameter D = 11 mm with the density ρ = 11 g/cm^3 in a graphite container with the length L = 5.9 mm in the proton beam direction, denoted in the following as the Small Target. The temperature of the target was T = 2000 °C. (A more detailed description of this target can be found in [4, 5].) The production efficiencies for Cs isotopes are presented in Fig. 3. These values were calculated with the Darmstadt cross-sections, *i.e.* the secondary particles contribution was not taken into account.

It is clearly seen that the production efficiency for the neutron-rich isotopes with the mass number A in the range 139–146 is considerably overestimated in comparison with the production efficiency for neutron-deficient isotopes (122 < A < 132) with similar life-times, while they should be comparable according to the DEM. This systematic discrepancy unambiguously points to the necessity to take into account the secondary particles contribution in the analysis of production of neutron-rich isotopes. Yet, this contribution may be neglected for production of neutron-deficient isotopes. Therefore, the diffusion properties of the target can be studied by an analysis of the neutron-deficient isotopes produced with primary reactions only.

7. Diffusion properties of the Small Target studied with Cs isotopes

The release curves were measured for several Cs isotopes without mother nuclei, namely for ^{132}Cs (6.48 d), ^{130m}Cs (207.6 s) and ^{138m}Cs (174.6 s). Their decay curves are thus not distorted by delayed feeding.

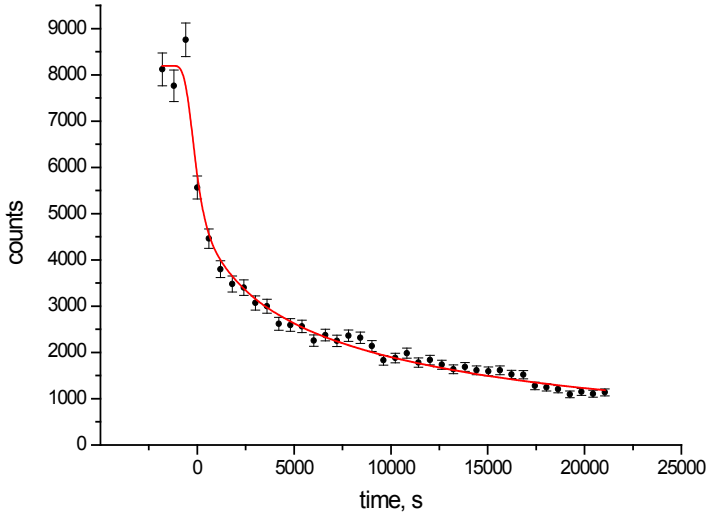

Fig. 4. Release curve for ^{132}Cs (E_γ = 668 keV), fitted using the double-diffusion model

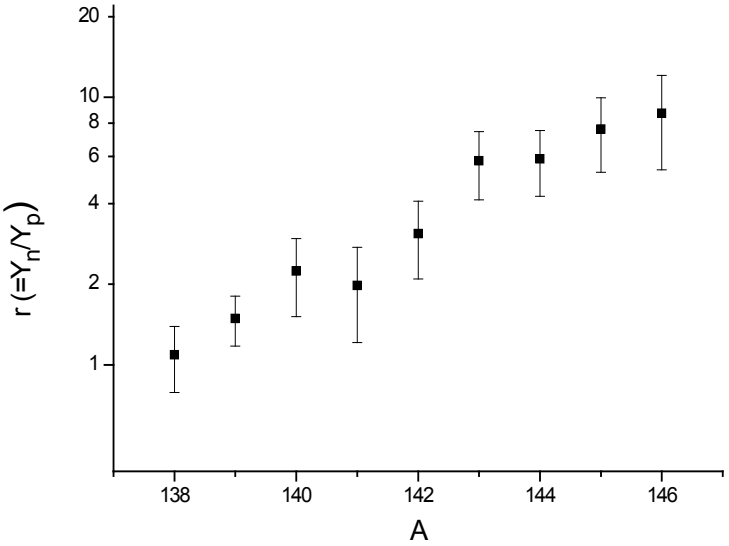

Fig. 5. Ratio of the secondary-neutron contribution to the direct reaction contribution to the yields of neutron-rich Cs isotopes (for the Small Target)

The result of the fits for ^{132}Cs is presented in Fig. 4. The "fast" component constants (t_{d2}), determined in the analysis of three release curves of the three Cs isotopes (t_{d2} = 90(90) s for ^{132}Cs, t_{d2} = 124(40) s for ^{138m}Cs, and t_{d2} = 182(63) s for ^{130m}Cs) are in reasonable mutual agreement. The weighted mean value is t_{d2} = 135(32) s.

The diffusion time from the analysis of the production efficiency of the neutron-deficient Cs isotopes ($t_d = 2.8(8) \cdot 10^4$ s) agrees fairly well with the slow time constant t_{d1} obtained in the analysis of the ^{132}Cs release curve. A self-consistent description of the efficiency curve for neutron-deficient Cs isotopes and Cs release curves in the framework of the double-diffusion model is thus achieved, as it was for Fr isotopes. Secondary particles, *i.e.* neutrons, are responsible for the observed discrepancy between production efficiencies for neutron-rich and neutron-deficient Cs isotopes (see Fig. 3).

With the diffusion parameters determined for Cs isotopes, the direct (p ^{238}U) reaction contribution to the observed yields of Cs neutron-rich isotopes at 1 GeV can be calculated as

$$Y_p^* = \sigma_A \cdot x \cdot I \cdot \varepsilon_{\text{diff}}(T_{1/2}) \cdot \varepsilon_{\text{ioniz}} .$$

Hence, the ratio r of the secondary neutrons contribution to the direct proton reaction contribution is given by

$$r = \frac{Y_A^{\text{exp}} - Y_p^*}{Y_p^*} \equiv \frac{Y_n}{Y_p^*} . \qquad (6)$$

These ratios are displayed in Fig. 5. For ^{138}Cs the secondary neutrons contribution covers nearly 50 % of the total yield, and for ^{145,146}Cs this contribution reaches 90 % of their production in the Small Target.

8. Description of the secondary neutrons contribution

To estimate independently the secondary neutrons contribution to the yield of neutron rich isotopes, the following parameters were used. The neutron multiplicity after absorption of a 1 GeV proton was set to be M_n = 20 (determined from analyses of various experimental data). In the range of energy from 20 to 250 MeV, the total neutron induced fission cross-section $\sigma_{n,\text{fiss}}$ slowly changes between 1.1 b and 1.3 b. So, for our estimation we may adopt the constant value $\sigma_{n,\text{fiss}}$ = 1.2(2) b. To calculate the effective target thickness x_n^{eff} for secondary neutrons, we used the simplest model of a uniform distribution within a solid

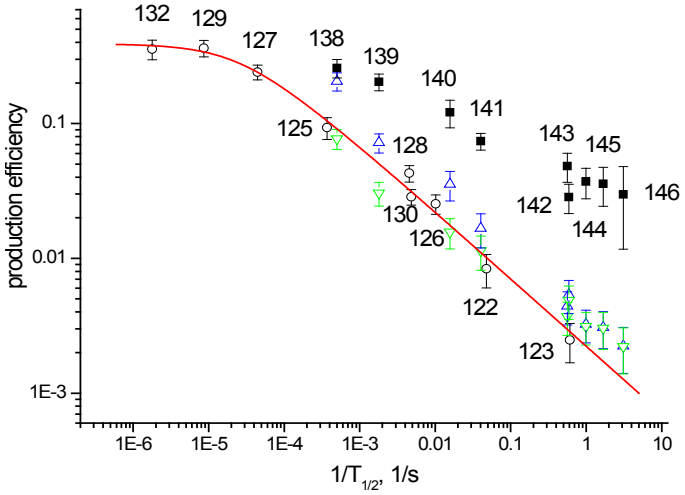

Fig. 6. Efficiency curve for Cs isotopes (Small Target) for neutron-deficient isotopes (empty circles) and for neutron-rich isotopes calculated using Darmstadt cross-sections only (black boxes), with the secondary neutrons contribution (upward triangles) and with both neutrons and Xe in-target decay contributions (downward triangles). The curve is the fit of the neutron-deficient data only by Eq. (4)

angle defined by the parameter θ. Finally, for the yield calculation, the tabulated values of fission product yields per 100 fissions were used for ^{238}U high-energy neutron fission. These values were tabulated for neutron energy 14 MeV. We used these data, though the energy distribution of secondary neutrons is rather wide. In spite of this rough assumption, the experimental data could be described fairly well.

The results of efficiency calculations for Cs isotopes, including the secondary-neutron contribution calculated with the above mentioned parameters, are presented in Fig. 6. The efficiencies calculated for $^{138–141}$Cs are quite sensitive to delayed feeding (by Xe in-target decay), and they agree with the data for neutron-deficient isotopes only after taking into account in-target decay of Xe nuclei (with $t_d(Xe) = 3000$ s). The efficiencies calculated for the more neutron-rich $^{142–146}$Cs isotopes remain stable, whether adding Xe decay or not.

An excellent overall correspondence between the production efficiencies for neutron-deficient and neutron-rich Cs isotopes after taking into account the secondary neutrons and Xe in-target decay is shown in Fig. 6.

It is of importance to verify the applicability of our approach to another target with completely different parameters. The parameters of another target were as follows: the mass of the target $M = 730$ g, the diameter $D = 24.5$ mm, the length along the proton beam $L = 129$ mm, the uranium density $\rho = 11.3$ g/cm^3, the target thickness $x = 148$ g/cm^2, and the target temperature 1900 °C. We shall denote this target in the following as the Large Target, see also [5].

The diffusion parameters for the Large Target were determined from a combined analysis of the efficiency curve for neutron-deficient isotopes and the release curve for ^{130m}Cs by the same procedure as the one applied to the Small Target: $t_{d1} = 5.37(86) \cdot 10^5$ s, $t_{d2} = 200(72)$ s, $\alpha = 0.96(2)$. With these parameters one can calculate the relative secondary neutron contribution for the Large Target $r(LT)$ with Eq. (6) (*cf.* Fig. 5 for the Small Target).

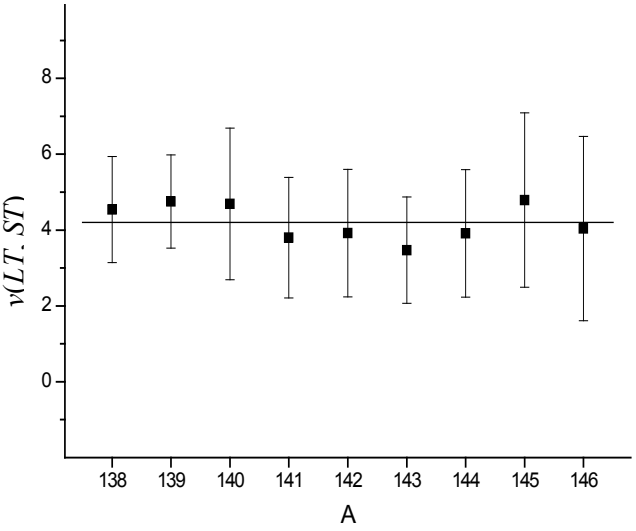

Fig. 7. Ratio of the relative secondary neutron contributions to Cs isotopes production efficiency for the Large and Small Targets. The line is the mean value $\nu(LT, ST) = 4.2(5)$

One can compare the r values for both investigated targets. Their ratio $\nu(LT, ST) = r(LT)/r(ST)$ exhibits a remarkable constancy over the whole mass range (Fig. 7), independently of the large variation of the decay half-lives (from 2004 s for ^{138}Cs to 0.321 s for ^{146}Cs). This confirms the adequacy of our approach. In our model, only the single parameter, the effective thickness, is responsible for the change of the r value:

$$\nu(LT, ST) = \frac{r(LT)}{r(ST)} = \frac{x_n^{\text{eff}}(LT)}{x_n^{\text{eff}}(ST)}.$$

One can estimate x_n^{eff} in model calculations with a uniform angular neutron distribution inside of a revolution cone with the half-angle θ:

$$v(LT, ST)_{\theta=0} = 18.8;$$
$$v(LT, ST)_{\theta=2\pi} = 3.7.$$

The latter value fairly agrees with the mean experimental value: $v(LT, ST)_{exp} = 4.2(5)$. In the following, we assume the angular distribution for secondary neutrons to be isotropic.

The production efficiencies have been calculated with this assumption for all neutron-rich Cs isotopes and are presented in Fig. 8. The curve is drawn according to the DEM description of neutron-deficient Cs isotopes. The production efficiencies for neutron-rich Cs isotopes taking into account very large corrections for the secondary neutrons contribution and the in-target decay of Xe isobars correspond well to this curve.

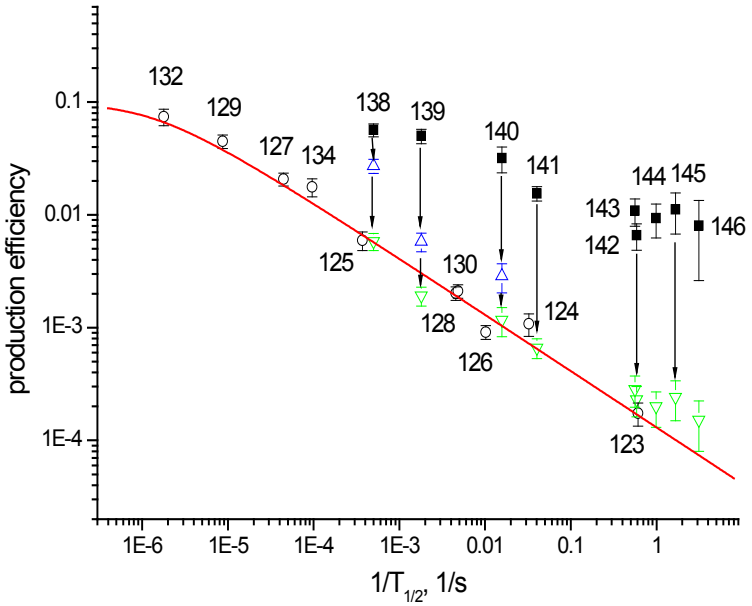

Fig. 8. Efficiency curve for Cs isotopes (Large Target) for neutron-deficient isotopes (empty circles), for neutron-rich isotopes calculated with Darmstadt cross-sections only (black boxes), including the secondary neutrons contribution (upward triangles) and with both neutrons and Xe in-target decay contribution (downward triangles). The curve is a fit of the neutron-deficient data only by Eq. (4)

9. Direct and secondary reaction contribution to Cs isotopes production efficiencies in FLUKA calculations. Comparison with the experiment

The Monte-Carlo code FLUKA was widely used for calculations of various target properties and reactions yields [7, 8]. It is important to test the reliability of this model bearing in mind the task to predict in-target productions of isotopes far from stability in uranium targets of future on-line facilities. It can provide an insight into possible yields of isotopes near the drip lines where the cross-section data are scarce or missing.

We have compared our results with the predictions of the FLUKA model. The ratios of the rest of the total in-target production (after subtraction of the primary reaction contribution) to the primary reaction contribution are compared with the experimental values of $r(ST)$ and $r(LT)$ in Fig. 9.

The agreement of the experimental and FLUKA data after taking into account the decay of mother nuclei in the target is appropriate for both targets. The ratios of the relative secondary reactions contributions for Large and Small targets $v(LT, ST)$ are consequently well reproduced by FLUKA. The mean value of $v(LT, ST) = 4.2(3)$ over the masses of Cs isotopes obtained by FLUKA perfectly corresponds to the mean experimental value 4.2(5).

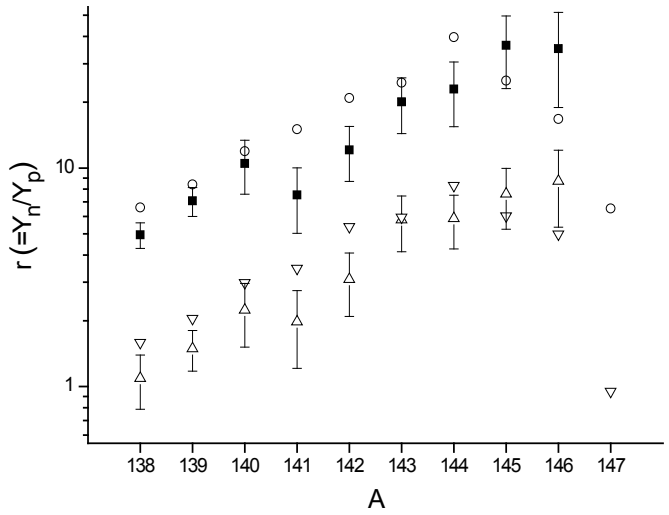

Fig. 9. Relative contribution of secondary reactions to in-target production of Cs isotopes. Large Target: experiment (squares), FLUKA (empty circles). Small Target: experiment (upward triangles), FLUKA (downward triangles)

10. Conclusions

The DEM has been used to analyse the production of Fr and Cs isotopes from uranium carbide targets of very different thicknesses (6.3 and 148 g/cm^2) irradiated by a 1 GeV proton beam. The applicability of this model has been shown first by the analysis of Fr isotopes and then by the analysis of neutron-deficient Cs isotopes. The release curves for several isotopes of the same element and the target efficiency *vs* decay half-life were well fitted with the same set of parameters. Further, a comparison of efficiencies for neutron-rich and neutron-deficient Cs isotopes enabled the separation of contributions from the primary (p + ^{238}U) and secondary (n + ^{238}U) reactions to the production of neutron-rich Cs isotopes.

Neutron-induced fission has been shown to dominate for the most exotic isotopes of Cs. For ^{146}Cs, its contribution is 10 times larger than the primary reaction contribution for the Small Target and 40 times larger for the Large Target. A rather simple calculation of the neutron contribution based on the known secondary neutron multiplicity, the isotope production cross-sections in the reaction (n + ^{238}U) at E_n = 14 MeV and the assumption of isotropic angular distribution of the secondary neutrons describes these data fairly well. The FLUKA code describes the primary and secondary reaction contributions to the Cs isotopes production efficiencies for different targets quite well. The branching ratios (absolute intensities) of γ-lines following β-decay of some Rb and Cs isotopes have been substantially revised or measured for the first time as a by-product of our target studies.

In conclusion, a consistent framework has been presented in which the releases and yields of neutron-deficient and neutron-rich products are well reproduced for very different target thicknesses.

References

1. A.E. Barzakh *et al.*, Eur. Phys. J. A **47**, 70 (2011).
2. G. Lhersonneau *et al*., Phys. Rev. C **74**, 017308 (2006).
3. http://www.nndc.bnl.gov/ensdf/
4. G. Lhersonneau *et al*., Nucl. Instr. Meth. Phys. Res. B **266**, 4326 (2008).
5. V.N. Panteleev *et al.,* Nucl. Instr. Meth. Phys. Res. B **266**, 4326 (2008).
6. V.N. Panteleev *et al.,* Eur. Phys. J. A **42**, 495 (2009).
7. G. Battistoni *et al.*, *Proceedings of the Hadronic Shower Simulation Workshop 2006, Fermilab, 6–8 September 2006*, M. Albrow, R. Raja eds., AIP Conference Proceeding **896**, 31 (2007).
8. A. Fassò *et al.*, CERN-2005-10 (2005), INFN/TC_05/11, SLAC-R-773.

REACTION CROSS SECTIONS FOR EXOTIC NUCLEI IN THE GLAUBER APPROACH

G.D. Alkhazov, A.A. Lobodenko

Reaction cross sections serve as one of the main sources of information on sizes of exotic halo nuclei. The nuclei sizes are determined from the measured reaction cross sections σ_r by comparing the calculated cross sections for nucleus-nucleus scattering with their experimental counterparts. Therefore, it is important to measure and calculate reaction cross sections with rather high accuracy. It is believed that at intermediate energy the scattering cross sections can be calculated with high accuracy by using the Glauber multiple scattering theory. However, a calculation of cross sections by the exact Glauber theory formula in the case of nucleus-nucleus scattering is not a simple task, and previously such calculations for scattering involving exotic nuclei were performed using some approximate approaches, most often an optical limit (OL) approximation to the Glauber theory.

In the present study [1, 2], reaction cross sections for scattering involving halo nuclei have been calculated for the first time by using directly the Glauber formula without any simplifying approximations. The reaction cross sections were calculated for scattering of ^{6}Li and the exotic ^{6}He and ^{11}Li nuclei with the target ^{12}C nuclei at energies of about 0.8 GeV per nucleon. According to the Glauber theory, the reaction cross section for scattering of nuclei A and B may be calculated by the formulas

$$\sigma_r = 2\,\pi \int_0^\infty \{\, 1 - |S_{\mathrm{AB}}(b)|^2 \,\}\; b\; \mathrm{d}b, \tag{1}$$

$$S_{\mathrm{AB}}(b) = < \Psi_{\mathrm{B}}\Psi_{\mathrm{A}} \,|\, \prod_{k,l}^{AB} \,[\, 1 - \gamma(\mathbf{b} - \mathbf{s}_k + \mathbf{s}_l)] \,|\, \Psi_{\mathrm{A}}\Psi_{\mathrm{B}} >, \tag{2}$$

where $S_{\mathrm{AB}}(b)$ is the S matrix for the interaction of nuclei A and B; $\gamma(\mathbf{b} - \mathbf{s}_k + \mathbf{s}_l)$ is the profile function for free nucleon-nucleon (*NN*) interaction; $\mathbf{b}$ is the impact vector parameter; $\mathbf{s}_{\mathrm{k}}$ and $\mathbf{s}_{\mathrm{l}}$ are the nucleon transverse coordinates; Ψ_{A} and Ψ_{B} are the nuclear wave functions, and A and B are the mass numbers of nuclei A and B. In our calculations, the profile function $\gamma(\mathbf{b})$ was parametrized as

$$\gamma(\mathbf{b}) = \sigma(1 - i\varepsilon) / 8\pi\beta \quad \text{for } b \le 2\beta^{1/2}, \quad \text{and} \quad \gamma(\mathbf{b}) = 0 \quad \text{for } b > 2\beta^{1/2}, \tag{3}$$

where σ is the total cross section for *NN* interaction, ε is the ratio of the real to imaginary part of the free *NN* scattering amplitude, and β is the relevant slope parameter. We used the following isospin-averaged values of σ, ε, and β: $\sigma = 4.25$ fm^2, $\varepsilon = -0.18$, and $\beta = 0.2$ fm^2. The nuclei ^{6}Li, ^{6}He and ^{11}Li were supposed to consist of two valence (halo) nucleons and a nuclear core having 4 and 9 nucleons, correspondingly in ^{6}He (^{6}Li) and ^{11}Li. The core and halo nucleon density distributions were described by Gaussian functions. The root mean square (rms) radius of the cores R_{c} in their centre-of-mass systems were taken to be 1.49 fm for ^{6}He (and ^{6}Li) and 2.30 fm for ^{11}Li. The calculations were performed for different assumed values of the rms halo radii R_{h}. More realistic density distributions, corresponding to theoretical few-body calculations were also used. The density distribution of the target nucleus ^{12}C was described by a Gaussian, the rms radius of ^{12}C being set to 2.32 fm. Multidimensional integration in (2) was performed by the Monte Carlo technique.

In calculations of reaction cross sections, the OL approximation was routinely used in the past. More recently, a more accurate "few body" (FB) approximation was applied to deduce nuclear sizes of light halo nuclei (the formulas for calculating σ_r in the OL and FB approximations are presented in [1]). In our study, the reaction cross sections were calculated by the exact Glauber formula, using the OL and FB approximations, and also with the aid of the "rigid target" (RT) approximation [3]. In the last case, one first calculates the S matrix for the interaction of one of the nucleons of the exotic nucleus involved with the target nucleus and then uses this matrix to calculate the total S_{AB} matrix.

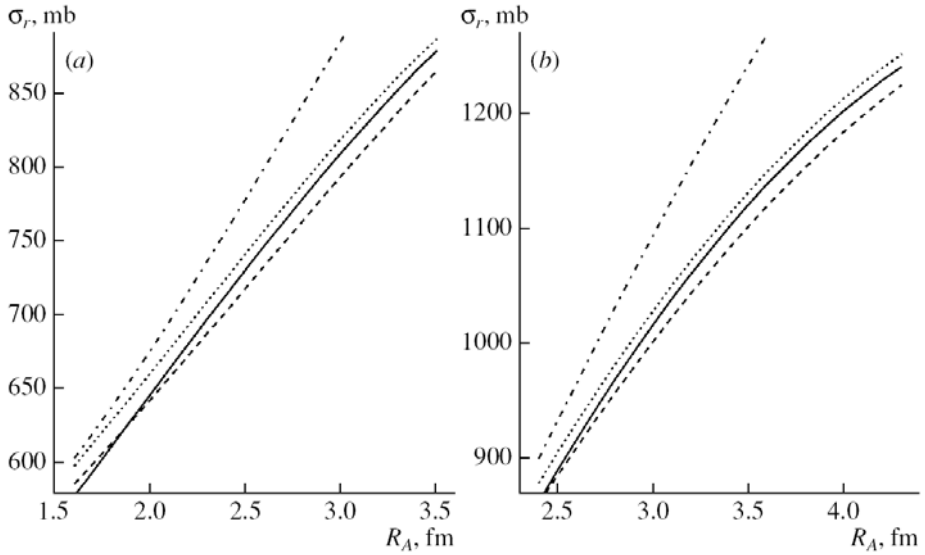

Fig. 1. Calculated reaction cross sections σ_r for the interaction of: a – ^{6}He (^{6}Li) and b – ^{11}Li with the ^{12}C nuclei at the energy of 0.72 GeV per nucleon versus the assumed total rms matter radius R_A of the considered halo nucleus

Figure 1a, b presents the reaction cross sections for different assumed halo radii (and, therefore, for different total matter radii R_A) calculated using the exact Glauber formula (solid curves), and approximate formulas of the OL approximation (dash-dotted curves), RT approximation (dotted curves), and the optical limit for the case of a rigid target (dashed curves). One can see that an approximate calculation in the RT approximation allows us to calculate the reaction cross sections significantly more accurately than that in the OL approximation, which significantly overestimates the reaction cross sections, the difference between the OL and the exact Glauber calculations being especially big for halo nuclei with a large halo radius.

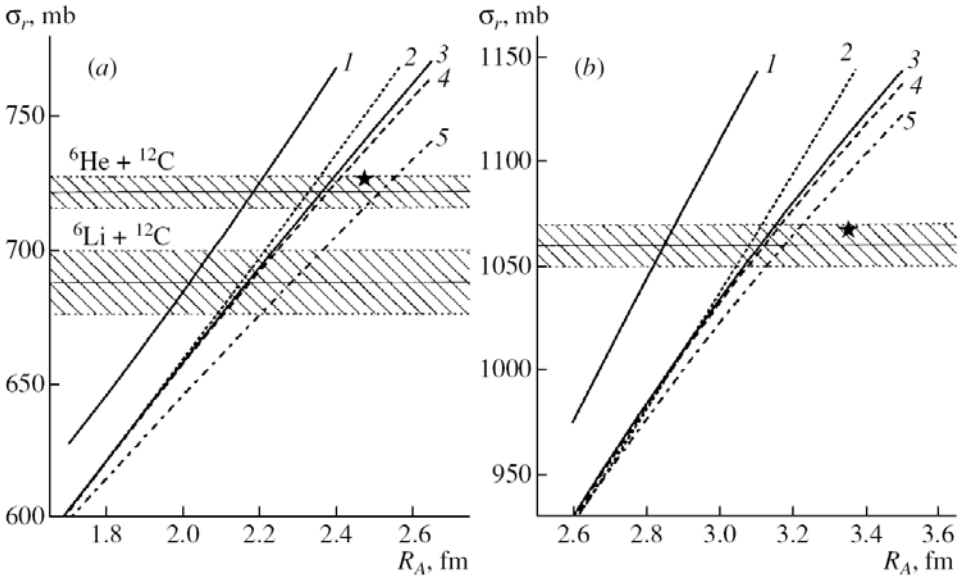

Fig. 2. Calculated reaction cross sections σ_r and their experimental counterparts at the energy of 0.79 GeV per nucleon for the interaction of: a – ^{6}He (and ^{6}Li) and b – ^{11}Li nuclei with the ^{12}C target nuclei for different assumed total matter rms radii R_A. Calculations were performed using the OL approximation (curves 1) and the exact Glauber formula (all other results) with different assumed structures of the considered exotic nuclei (see the text). The horizontal lines and the shaded corridors correspond to the experimental cross sections with their errors

Figure 2a, b displays reaction cross sections σ_r calculated in the OL approximation (curves 1) and using the exact Glauber formula (other results) for different matter radii R_A and different assumed spatial structures of ^{6}He, ^{6}Li and ^{11}Li. Curves 2–5 correspond respectively to calculations for the cases when the considered nuclei have no halo structure ($R_h = R_c = R_A$), when these nuclei have a halo structure ($R_h > R_c$), the halo nucleon motion being not correlated, when the halo nucleons form a di-neutron cluster with the rms matter radius R_d = 3 fm, and when the di-neutron cluster matter radius is R_d = 2 fm. The stars in Fig. 2a, b correspond to calculations with the ^{6}He and ^{11}Li theoretical nuclear matter distributions [4, 5].

The performed calculations have shown that the OL approximation overestimates considerably the reaction cross sections for halo nuclei. At the same time, a rather simple RT approximation allows one to calculate the cross sections σ_r significantly more accurately, the calculated cross sections being very close to those calculated by the exact Glauber formula. The calculations have also shown that the reaction cross sections depend not only on the total rms matter radius of the investigated nuclei, but also on their spatial structure – on nucleon correlations and on the radial shape of the nuclear matter distributions. Therefore, the rms nuclear matter radii R_A deduced from the experimental reaction cross sections σ_r are subject to influence of the spatial structure of the investigated nuclei. In more detail, the obtained results are discussed in [1].

References

1. G.D. Alkhazov, A.A. Lobodenko, Phys. At. Nucl. **70**, 93 (2007); Yad. Fiz. **70**, 98 (2007).
2. G.D. Alkhazov, A.A. Lobodenko, Phys. At. Nucl. **64**, 1898 (2001); Yad. Fiz. **64**, 1981 (2001).
3. G.D. Alkhazov *et al*., Nucl. Phys. A **280**, 365 (1977).
4. J.S. Al-Khalili, J.A. Tostevin, I.J. Thompson, Phys. Rev. C **54**, 1843 (1996).
5. I.J. Thompson, M.V. Zhukov, Phys. Rev. C **49**, 1904 (1994).

μSR INVESTIGATIONS AT PNPI

S.G. Barsov, A.L. Getalov, E.N. Komarov, V.P. Koptev, S.A. Kotov, A.E. Moroslip, I.I. Pavlova, G.V. Shcherbakov, S.I. Vorobyev

1. Introduction

Magnetic properties of $R\mathrm{Mn_2O_5}$ manganites (R = Eu, Gd), of the nano-structured $\mathrm{Fe_3O_4/D_2O}$ ferrofluid and of the EK-181 steel were investigated by the muon spin rotation (μSR) method. The experiments were carried out with the μSR set-up [1] placed at the polarized muon channel of the PNPI synchrocyclotron [2]. Muons of $P = 90$ MeV/c momentum with $\Delta P / P = 0.02$ (FWHM) were stopped inside of a sample under investigation, and positrons resulting from the muon decay were detected within a certain solid angle. The μSR set-up allows us to vary the sample temperature over 10–300 K range and to apply an external magnetic field up to 1.5 kOe.

Since muon decay is asymmetric with respect to the muon spin (magnetic moment) direction, the positron count rate varies in time not only due to finite muon life-time τ_μ, but also due to the muon spin behavior inside of the sample. In general, a decay positron time spectrum can be expressed as

$$N(t) = N_0 \cdot [1 + a_0 \cdot G(t)] \cdot \exp(-t / \tau_\mu) + B, \tag{1}$$

where t is the time interval measured for every detected positron starting from the moment of the muon stop.

Apart from an accidental background B and the normalization factor N_0, the total experimental asymmetry a_0 is proportional to the initial muon polarization. The value of a_0 is independent of the temperature and the magnetic field applied to a sample, while it depends on other experimental conditions (such as the beam momentum, the geometry and efficiency of the set-up, the size and density of the sample), which are fixed during one set of measurements. The specific value of a_0 can be measured for a sample in the paramagnetic state.

The relaxation function $G(t)$ in Eq. (1) originates from the polarization behaviour of the muon ensemble inside of the sample resulting from the interaction of each muon magnetic moment with the local magnetic field h_{loc}. Neglecting effects of the muon-electron bound state (muonium), such interaction leads to the Larmour precession of the muonic magnetic moment with a frequency ω_μ determined by the h_{loc} magnitude. So, evaluation of the function $G(t)$ and its parameters delivers information on the distribution of internal magnetic fields. Note that the μSR-method can be used in the absence of any external magnetic fields.

Taking into account that local fields may be unstable in time due to, *e.g.*, spatial magnetic fluctuations near a phase transition, the $G(t)$ function can be represented as a product of two functions:

$$G(t) = G_d(t) \cdot G_s(t). \tag{2}$$

The dynamic relaxation function $G_d(t)$ describes the influence of the h_{loc} fields with typical correlation times comparable or smaller than the muon precession period. This usually leads to an exponential decrease of polarization, so that the function $G_d(t)$ takes the form:

$$G_d(t) = \exp(-\lambda t). \tag{3}$$

On the other hand, local fields changing in time much slower than $\omega_\mu / 2\pi$ can be considered as static ones. The static relaxation function is defined by the distribution of such local fields over the sample volume. Some specific relaxation functions corresponding to different types of the magnetic phase were obtained in [3]. The explicit forms of $G_s(t)$ used for data analyses are presented and discussed below in the corresponding sections of this paper.

2. Manganites $\mathrm{EuMn_2O_5}$ and $\mathrm{GdMn_2O_5}$

The materials $R\mathrm{Mn_2O_5}$ (R is a rare-earth ion) are considered to be promising materials for production of devices which are able to manipulate with both the electric and magnetic signals due to strong correlation of the magnetic and electric phenomena observed. In particular, a large magnetoelectric effect was

discovered in these substances at low temperatures, where coexistence of AntiFerroMagnetic (AFM) and FerroElectric (FE) ordering takes place [4].

Here, we report results of a comparative study of $EuMn_2O_5$ and $GdMn_2O_5$ manganites by the μSR method. Since magnetic moments of rare-earth ions in these compounds are significantly different (namely, the ground state of Eu^{3+} is nonmagnetic, while the moment of Gd^{3+} is about 3.5 μ_B) such a study allows to clarify effects related to the $R^{3+}(Mn^{4+}, Mn^{3+})$ exchange interaction. In addition, for each of the manganites a ceramic sample and a sample consisting of chaotically oriented macroscopic (2–3 mm) single crystals were investigated. It is also worth mentioning that in the case of $GdMn_2O_5$ the use of neutron scattering technique is practically impossible due to high absorption of neutrons by Gd nuclei.

Figures 1a, b and 2a, b show temperature dependencies of the dynamic relaxation rate λ obtained in the absence of external magnetic fields for $EuMn_2O_5$ and $GdMn_2O_5$, respectively. For all samples, the relaxation rate has a pronounced maximum at nearly the same temperature of about 40–45 K, which corresponds to the paramagnetic – antiferromagnetic (PM – AFM) phase transition caused by the AFM ordering of the Mn^{3+} and Mn^{4+} magnetic moments. Although a large difference in the Eu^{3+} and Gd^{3+} moments does not affect the transition temperature, it manifests itself in the relaxation rate value, which is 10 times larger in $GdMn_2O_5$ than in $EuMn_2O_5$ even in the PM state ($T > T_{N1}$). An unusually large value of λ ($\lambda \approx 1$ μs^{-1}, Fig. 2a, b), was found to be independent of temperature up to 300 K. It may be caused by the presence of short-range magnetic correlations well above T_{N1}, which has been observed in magnetic susceptibility measurements [5].

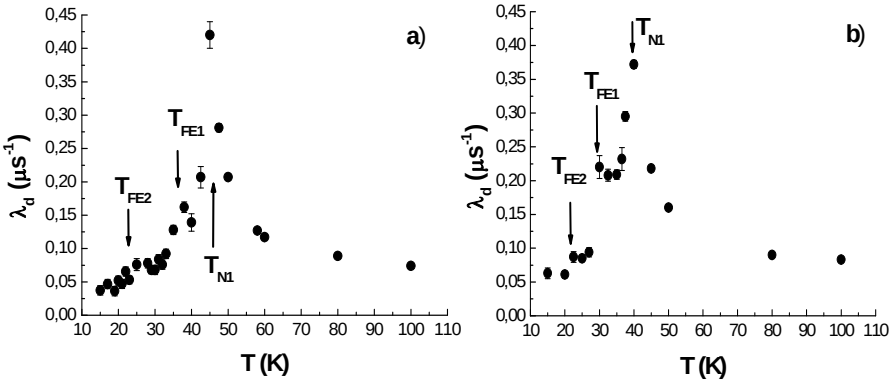

Fig. 1. Temperature dependencies of the dynamic relaxation rate in $EuMn_2O_5$: for a ceramic sample (a) and for a sample consisting of single crystals (b). The phase transitions indicated by arrows are discussed in the text

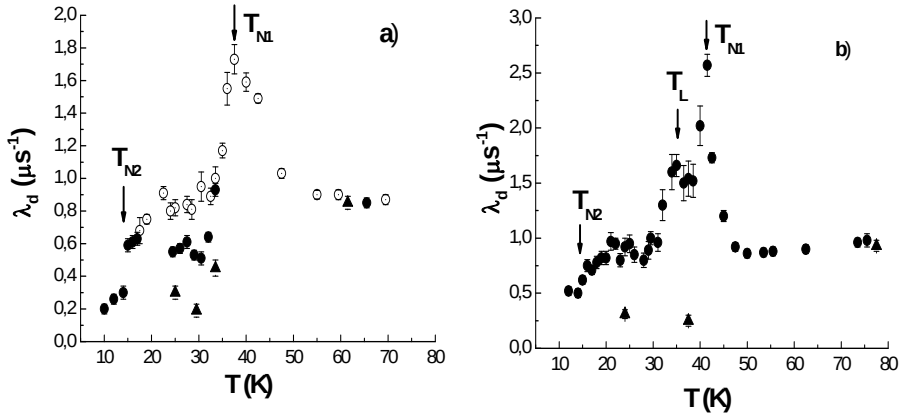

Fig. 2. Temperature dependences of the dynamic relaxation rate in $GdMn_2O_5$: for a ceramic sample (a) and for a sample consisting of single crystals (b). Solid circles represent the data taken during heating of the samples. The data taken during cooling are denoted by open circles. Triangles show the results of measurements in the 280 Oe external magnetic field. The phase transitions indicated by arrows are discussed in the text

The anomalies in the temperature dependencies of λ below T_{N1} correspond to the known ferroelectric phase transitions (T_{FE1} and T_{FE2} in Fig. 1a, b) [3] and the magnetic ordering of Gd^{3+} moments (T_{N2} in Fig. 2a, b) [6]. In contrast to $EuMn_2O_5$, the anomaly at the temperature T_L (Fig. 2b) is related to a lock-in transition (rearrangement) of the AFM order but not to FE phase transitions, which are known [5] to take place in the 22–30 K range. It is interesting to note that the anomaly at T_L was not seen in the ceramic sample of $GdMn_2O_5$.

The best description of the time spectra below the temperature T_{N1} was achieved using the collinear (anti)ferromagnetic state model [3]:

$$dN/dt \sim \{a_1 \cdot [1/3 + 2/3 \cdot \exp(-\Delta_1 \cdot t) \cdot \cos(\Omega_1 \cdot t)] + a_2 \cdot [1/3 + 2/3 \cdot \exp(-\Delta_2 \cdot t) \cdot \cos(\Omega_2 \cdot t)]\} \cdot G_d(t), \quad (4)$$

where the terms in square brackets represent a typical form of the static relaxation function in the case of random orientation of internal magnetic fields. The muon spin precession frequency $\Omega_i = 2\pi F_i$ is determined by the mean value of the fields, while the static relaxation rate Δ_i is defined by their spread. Two different precession frequencies observed below T_{N1} originate from two different sites of muon localization in the lattice cell. The partial asymmetries a_1 and a_2 depend on relative populations of the localization sites, but their sum ($a_1 + a_2$) is expected to be equal to the total asymmetry a_0 determined above the temperature T_{N1}.

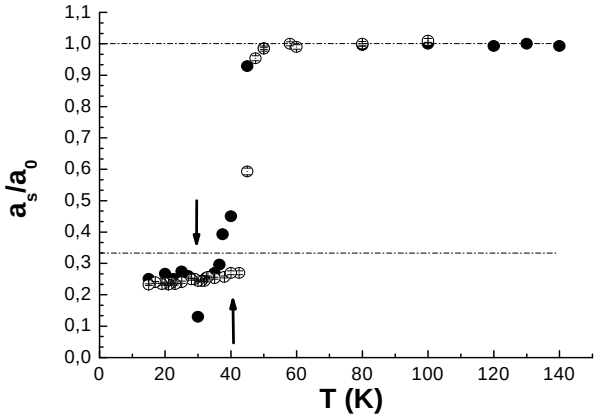

Fig. 3. Temperature dependence of the relative "residual" asymmetry a_s / a_0 for a sample $EuMn_2O_5$ consisting of single crystals (closed circles) and for a ceramic sample (open circles). The arrows mark the transition temperature $T_{FE1} \approx 30$ K for a single crystal sample and the magnetic ordering temperature $T_{N1} \approx 40$ K

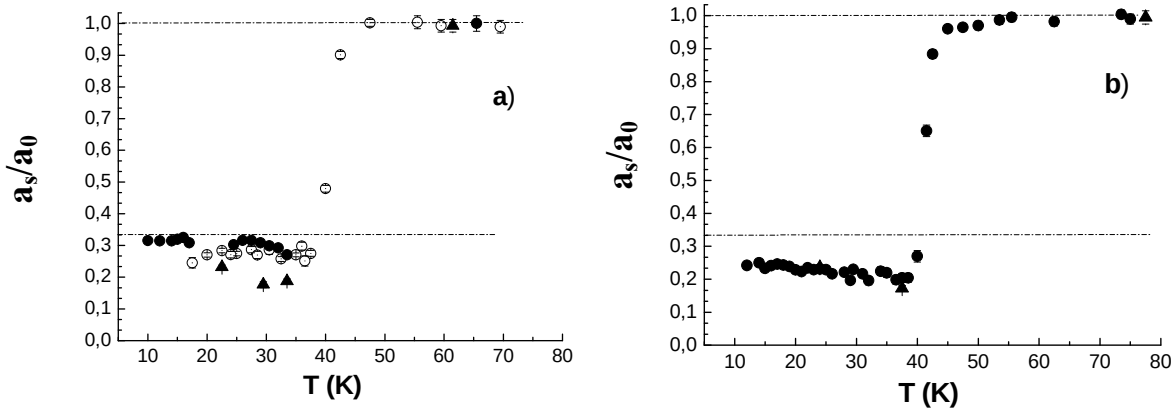

Fig. 4. Temperature dependence of the relative residual asymmetry a_s / a_0 for a sample $GdMn_2O_5$: the levels of the normalized asymmetry $a_s / a_0 = 1/3$ ($T < T_{N1}$) and $a_s / a_0 = 1$ ($T > T_{N1}$) are marked by the dash-dotted lines: a – for a ceramic sample; b – for a sample assembled from small single crystals (solid circles refer to heating, open circles refer to cooling); measurements in the external magnetic field $H = 280$ Oe are shown by triangles

However, it has been found that at $T < T_{N1}$ some part of the initial muon polarization is lost so fast that $(a_1 + a_2) < a_0$. To avoid an uncertainty related to the phase of the muon precession, the total asymmetry of the non-precession terms in (4) is presented in Figs. 3 and 4a, b as a function of temperature. It is clearly seen that the normalized "residual" asymmetry a_s / a_0 is significantly smaller than its expected value 1/3 at $T < T_{N1}$ in all samples excluding $GdMn_2O_5$ ceramics. The lack of a_s / a_0 may be explained by formation of a muonium. Indeed, the magnetic ordering leads to some change of the charge distribution, and, as a result, the probability of muonium production may be increased. An important role of the charge transfer processes was pointed out in a study of the second optical harmonic in $TbMn_2O_5$ [7]. In particular, it was found that the external magnetic field increases the charge transfer probability. In our study, the external magnetic field of 280 Oe decreases the a_s / a_0 value at $T < T_{N1}$ in $EuMn_2O_5$ samples, as well as in $GdMn_2O_5$ ceramics, but does not affect the "residual" asymmetry in the sample consisting of single crystals (Fig. 4b).

Another evidence of modification of magnetic properties due to strong Gd-Mn interaction comes out from the temperature dependencies of Ω_1 and Ω_2, see Eq. (4). In contrast to the dependencies presented in Fig. 5a, b for $GdMn_2O_5$, both precession frequencies in $EuMn_2O_5$ were observed to appear at the same temperature just below T_{N1}, and to follow quite well the Curie – Weiss temperature function which is typical for Heisenberg 3D magnets [3]. Despite the value of Ω_1 (as well as the value of Ω_2) is nearly the same at $T > 30$ K for each of the samples under investigation, in the case of $GdMn_2O_5$ only the frequency Ω_2 follows the Curie – Weiss dependence. In the $(T_{N1} - T_L)$ temperature range, the amplitude of Ω_2 is very small ($a_2 \approx 0$), but the partial asymmetry a_1 is equal to the sum $(a_1 + a_2)$ measured at $T < 30$ K. So, the muon localization site responsible for the frequency Ω_2 is not occupied in this temperature range in $GdMn_2O_5$, while at $T < 30$ K its population becomes about 70–80 %.

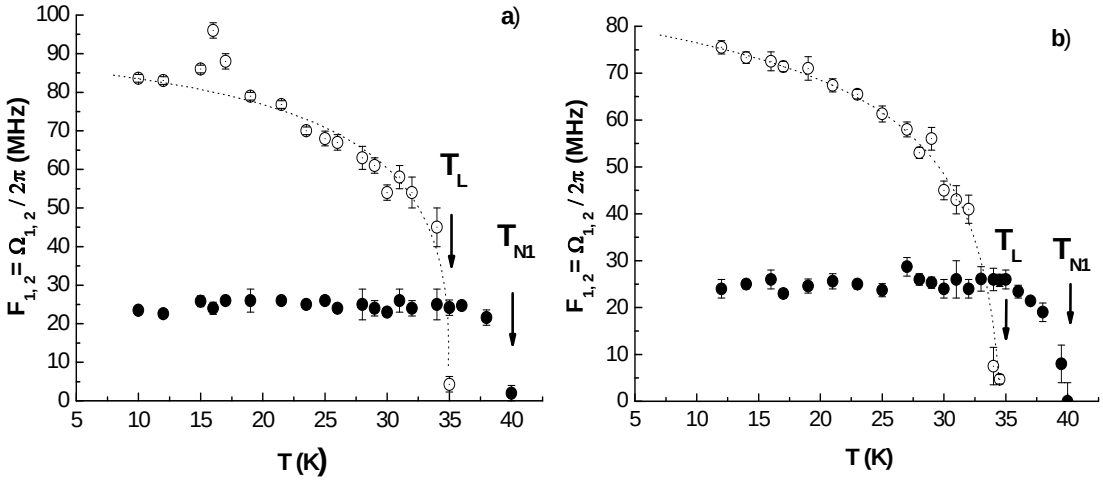

Fig. 5. Temperature dependencies of the muon precession frequencies in internal magnetic fields in $GdMn_2O_5$: a – in a ceramic sample; b – in a sample consisting of single crystals. Solid circles stand for the F_1 frequency, open circles – for the F_2 frequency. Arrows indicate the phase transition temperatures. Dotted curves show the fits of F_2 dependencies by the Curie – Weiss function $(1 - T / T_L)^{\beta}$; $T_L = 35$ K; $\beta = 0.39 \pm 0.02$

3. Fe_3O_4-based nanostructured ferrofluid

A modification of magnetism in the objects with dimensions smaller than a domain size is of great interest from both scientific and practical points of view. Information on the progress in such studies of magnetic nanoparticles can be found in review [8].

Magnetic systems consisting of nanoparticles of magnetite Fe_3O_4 or $MeFe_2O_4$, where Me denotes Mg, Cr, Mn, Fe, Co, or Zn, dispersed in organic or inorganic liquids, allow to vary the concentration of magnetic particles. The stability of magnetic fluids is ensured by the surfactant coating of the magnetic-particle surfaces which prevents their van der Waals and magnetic dipole-dipole conglutination. The magnetic moment of each nanoparticle at temperatures below the Curie temperature for Fe_3O_4 is supposed to be equal to the total magnetic moment of iron ions. Such a system behaves as a (super) paramagnetic material if

nanoparticle concentration in the medium is low (< 5–7 %). The magnetic structure of Fe_3O_4 single crystals is well known [9]. This compound is a ferromagnet at the temperatures below the Curie temperature $T_C = 858$ K. The Verwey (metal – dielectric) structural transition occurs at the temperature $T_V \approx 123$ K.

The studied ferrofluid (Fe_3O_4/2DBS/D_2O) was a suspension of nanodispersed magnetite (Fe_3O_4) in heavy water (D_2O) stabilized by the dodecylbenzenesulfonic acid (2DBS). The volumetric concentration of magnetic particles was 4.7 %. One milliliter of the ferrofluid contained 0.244 g of magnetite, and the ratio was 0.3 g of the surfactant per 1 g of Fe_3O_4.

The temperature dependencies of the relaxation rate and the precession frequency of the muon spin in the ferrofluid Fe_3O_4/2DBS/D_2O were investigated in the temperature range from 26 to 300 K [9]. The muon spin precession in a sample under investigation was compared with that in a Cu sample. For the last one the experimental asymmetry of the decay position was $a = 0.302 \pm 0.002$ at the external magnetic field $H = 280$ Oe.

For the Fe_3O_4/2DBS/D_2O sample, the observed muon polarization fraction was about 30 % smaller than that for the D_2O sample, because the precession frequency of the muon stopped inside of magnetic nanoparticles is very large, and it is integrated due to a limited time resolution of the μSR set-up. Thus, only the precession of the muons stopped outside the particles could be resolved.

The fraction of muons stopped inside of nanoparticles is in agreement with the thickness of Fe_3O_4 along the muon beam, which is about 0.25 g/cm^2 to be compared with 1.2 g/cm^2 thickness of the sample.

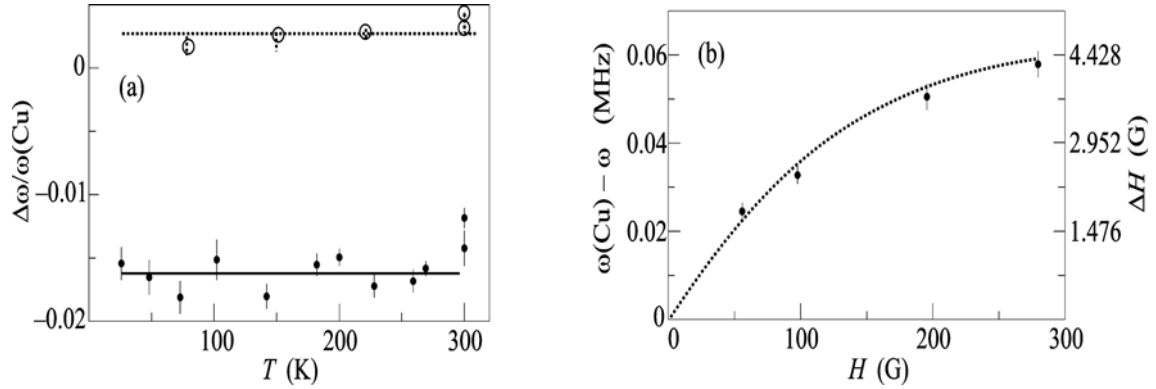

Fig. 6. Shift of the muon-spin precession frequency: a – versus temperature for $H = 280$ Oe and b – versus external magnetic field at $T = 200$ K. The closed and open circles are the data for Fe_3O_4/2DBS/D_2O and D_2O, respectively. The samples were cooled in the magnetic field

In the sample Fe_3O_4/2DBS/D_2O, the muon relaxation rate was much higher than that in the D_2O sample. This effect is completely due to interaction of the magnetic moments of muons and nanoparticles. When the magnetic field is absent, the magnetic moments of nanoparticles are directed arbitrarily. The external magnetic field gives rise to a small polarization of the magnetic moments of nanoparticles. As a result, the magnetic field in a sample is different from the external one. The frequency shift $\Delta\omega = \omega - \omega(\mathrm{Cu})$ in D_2O water and in the Fe_3O_4/2DBS/D_2O sample with respect to the precession frequency in the Cu sample is shown in Fig. 6 a, b. As one can see, in both samples the frequency shift does not depend on temperature. In the ferrofluid, it is about 6 times larger than that in D_2O water and has an opposite sign. This effect is due to the fact that D_2O water is diamagnetic, while the Fe_3O_4/2DBS/D_2O sample is (super) paramagnetic.

The frequency shift $\Delta\omega$ is proportional to the mean magnetic field ΔB generated by the nanoparticle magnetic moments. In one's turn, the last one is proportional to the magnetization M of the sample:

$$\Delta\omega \sim \gamma \cdot \Delta B \sim M,$$

where $\gamma = 13.5544$ kHz/Oe is the gyromagnetic ratio of the muon.

It was found experimentally that at small nanoparticle concentrations (< 6−7 %) the magnetization of paramagnets is described by the Langevin function [10]:

$$M = n \cdot m \cdot (\mathrm{cth}\,\xi - 1/\xi),$$

where n is the number of nanoparticles per volume unit; m is the magnetic moment of the nanoparticle (J / T); $\xi = \mu_0 mH / kT$, $\mu_0 = 4\pi \times 10^{-7}$ is a constant, H is the magnetic field (A / m), $k = 1.38 \times 10^{-23}$ J / K is the Boltzmann constant, T is the absolute temperature.

Finally, one finds that at $T = 200$ K the mean value of the magnetic moment of a nanoparticle is

$$m = \left(\frac{\xi}{H}\right) \cdot \left(\frac{kT}{\mu_0}\right) = 4.68 \times 10^{-19}\,\mathrm{J/T} = 5 \times 10^4\,\mu_B\,,$$

here μ_B is the Bohr magneton.

As the magnetic moment of the molecule Fe_3O_4 is 4.1 μ_B [11], the nanoparticle consists of 1.2×10^4 Fe_3O_4 molecules and, correspondingly, its size is about 12 nm.

This value is in good agreement with the value 11.2 nm derived by fitting the magnetization curves with the Langevin function [12] for the studied sample.

4. Construction steel EK-181

Nuclear and thermonuclear reactors of new generations require radiation-heat-resistant materials with fast deactivation of an induced radioactivity. However, they should withstand high mechanical loads under intensive irradiation, which usually leads to an undesirable increase of the temperature of the brittle-ductile transition.

At present, it is assumed that materials with the desired properties can be obtained by appropriate thermal treatment of chromium ferritic-martensitic steels with formation of nanoscale structures (clusters, nanoscale secondary phases, *etc*.) [13]. The structures like these have been found, for example, in samples of the steel EK-181.

This section reports very preliminary results obtained by the μSR-method for 2 samples of the EK-181 steel produced in different technological ways. The first sample was just annealed at 1070 °C, while the second one was in addition quenched at 1070 °C and then tempered at 720 °C for 3 hours. The samples were investigated in the temperature range 80−300 K. The best description of the time spectra of the muon magnetic moment precession in internal fields was obtained in the framework of the hypothesis suggesting that two phase states (the Collinear FerroMagnetic (CFM) and the Spin Glass (SG)) coexist:

$$\mathrm{d}N/\mathrm{d}t \sim \{a_{CFM} \cdot [1/3 + 2/3 \cdot \exp(-\Delta_{CFM} \cdot t) \cdot \cos(\Omega_{CFM} \cdot t)] + \\ + a_{SG} \cdot [1/3 + 2/3 \cdot (1 - \exp(-\Delta_{SG} \cdot t))]\} \cdot \exp(-\lambda \cdot t). \quad (5)$$

In the area of the brittle-ductile transition, an anomality in the temperature dependence of the dynamic relaxation rate λ (at 180−200 K, Fig. 7) and the redistribution of the partial contributions a_{CFM} and a_{SG} were observed (Fig. 8).

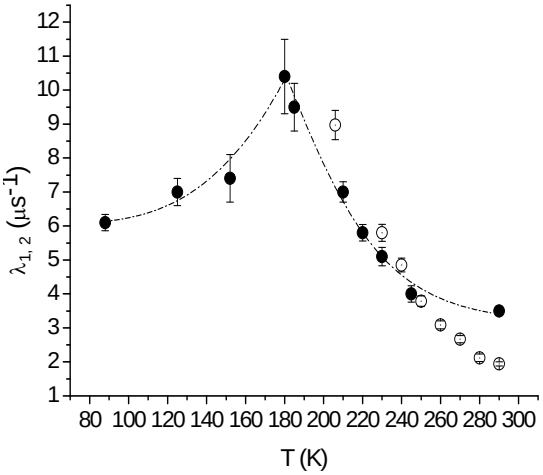

Fig. 7. Temperature dependence of the dynamic relaxation rate λ for the 1-st sample (solid circles) and for the 2-nd sample (open circles)

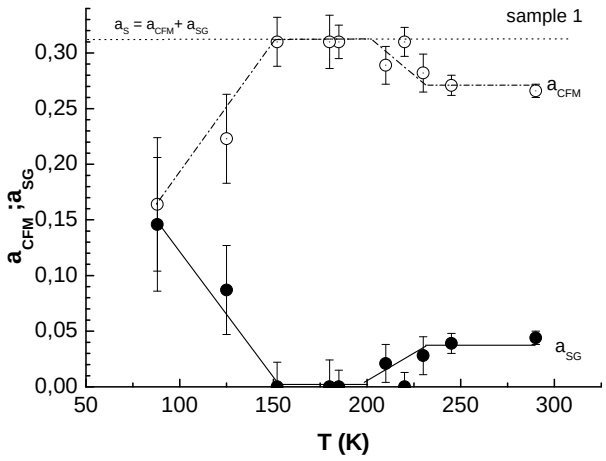

Fig. 8. Temperature dependence of the partial contributions a_{CFM} and a_{SG}

We plan to continue systematic studies of these samples and, furthermore, to investigate the effect of the thermal aging, hardening and thermal cycling in the area of the phase γ-α transition with a subsequent release of stresses near the brittle-ductile transition.

5. Conclusion

Thus, the μSR investigation of multiferroics again demonstrates the efficiency of this method for studying magnetic materials. The μSR investigation of $R\mathrm{Mn_2O_5}$ (R = Eu, Gd) samples (consisting of single crystals and ceramic grains) has revealed a number of interesting features of this compound. The charge density changes locally in both samples at the temperatures $T < T_N$; this change is manifested in additional depolarization of muons. The external magnetic field also leads to the loss of polarization in the samples at $T < T_N$ and likely gives rise to additional redistribution of the charge density in the samples. The phase transitions observed at the temperatures $T < T_N$ are not manifested in the distribution of the internal local magnetic fields. They are seen only in the temperature dependence of the dynamic relaxation rate $\lambda_d(T)$. The electron density is redistributed at the phase transition point at the temperature T_N. The mechanism of multiferroicity is possibly associated with this phenomenon.

The relaxation and shift of the precession frequency of the spin of a positive muon in the D_2O medium, where Fe_3O_4 magnetic nanoparticles are randomly distributed, have been studied in a wide temperature range. The mean magnetic field generated by the magnetic moments of nanoparticles randomly distributed in the medium was determined experimentally. It was shown that the mean-field dependence on the external magnetic field does not contradict the Langevin law. The mean size and magnetic moment of the nanoparticles were estimated.

References

1. S.G. Barsov, S.I. Vorobyev, V.P. Koptev *et al.*, Instr. and Exp. Techn. **50**, 750 (2007).
2. S.G. Barsov, S.I. Vorobyev, V.P. Koptev *et al.*, Preprint PNPI-**2738**, Gatchina (2007).
3. S.I. Vorobyev, E.I. Golovenchits, V.P. Koptev *et al.*, JETP Lett. **91**, 512 (2010).
4. S.I. Vorobyev, A.L. Getalov, E.I. Golovenchits *et al.*, Preprint PNPI-**2845**, Gatchina (2010).
5. E. Golovenchits, and V. Sanina, Journ. Phys. Cond. Matter **16**, 4325 (2004).
6. Yu.F. Popov, A.M. Kadomtseva, G.P. Vorobyev, S.S. Krotov, K.I. Kamilov, and M.M. Lukina, Sov. Phys. Solid State **45**, 205111 (2003).
7. Th. Lottermoser, D. Meier, R. Pisarev and M. Fiebig, Phys. Rev. B **80**, 100101(R) (2009).
8. B.M. Berkovski, V.F. Medvedev, and M.S. Krakov, *Magnetic Fluids* (Oxford Univ. Press, Oxford, 1993; Khimiya, Moscow, 1989).
9. M. Balasoiu, S.G. Barsov, D. Bica *et al.*, JETP Lett. **88**, 243 (2008).
10. D. Bica, L. Vekas, M.V. Andreev *et al.*, J. Magn. Matter **311**, 1721 (2007).
11. Physical Values: The Manual, Eds. by I.S. Grigoriev and E.Z. Meilikhov (Energoatomizdat, Moscow, 1991) (in Russian).
12. D. Bica, L. Vekas, M.V. Avdeev *et al.*, J. Magn. Mater **311**, 1721 (2007).
13. A.G. Yoltukhovsky, M.V. Leontyeva-Smirnova, B.M. Cherna *et al.*, in *Structure Features of the Chrome Steels with the Fast Radioactivity Drop*, VANT **2** (63), 142 (2004).

New Projects

IRIN: INSTALLATION FOR PRODUCTION AND INVESTIGATION OF NEUTRON-RICH NUCLIDES

V.N. Panteleev, A.E. Barzakh, D.V. Fedorov, V.S. Ivanov, V.V. Lukashevich, P.L. Molkanov

1. Introduction

As it is presently very well understood, investigations of neutron-deficient and neutron-rich nuclei at the edge of proton and neutron stability valley with ISOL (Isotope Separator On-Line) methods are of great importance for many goals for:

- low energy nuclear physics studies – so far nearly all information about the nuclear structure and nuclear state characteristics has been obtained in experiments at ISOL facilities;
- astrophysics – the ideas about creation of chemical elements in the Universe and evolution of stars can be tested experimentally by interaction of radioactive nuclear beams with a hydrogen target;
- solid state physics – radioactive ion implantation can be used to investigate properties of materials;
- modern medicine – providing fast and harmless diagnostics of diseases.

The installation IRIS (Investigation of Radioactive Isotopes at the Synchrocyclotron) of the ISOL type has been operating at PNPI since the middle of 1970-s [1, 2]. The Short-Lived Nuclei Laboratory has carried out successful series of systematic investigations of nuclei far from beta-stability. More than 300 nuclides were studied, 17 of them were produced and investigated for the first time. New approaches and methods of production and investigation of short-lived isotopes were developed and applied at the IRIS facility.

Presently, there are more than twenty ISOL facilities operating all over the world, and about ten more are planned to be built in the following decade. Studies of exotic nuclei far from stability using ISOL facilities at beams of various projectiles (protons, thermal neutrons, heavy ions and others) strongly depend on the possibility of production of nuclear beams needed for investigations. A use of high-flux neutron reactors for these purposes looks very promising in this respect. According to preliminary calculations, the yield of the ^{132}Sn reference nuclide (double-magic nucleus far from β-stability) at an ISOL facility at a thermal neutron beam of the reactor PIK (with the neutron flux of 3×10^{13} n/cm^2 s and the target of 4 g of ^{235}U) can be about 10^{11} nuclei per second. Presently, the operating ISOL systems IRIS (PNPI) and ISOLDE (CERN) are able to provide 10^7 and 10^8 of ^{132}Sn nuclides per second, respectively. The maximum yield of this isotope at the perspective ISOL installation SPIRAL-2 (GANIL, France) will not exceed 10^9 nuclides per second.

For efficient investigations of nuclei very close to the neutron stability border, the isobaric purity of an isotope under study becomes a decisive factor. To provide the isotope selective ionization of a range of elements, the resonance laser ionization in a hot cavity can be applied [3]. This method has been developed and successfully used at IRIS. Recently, a new laser installation based on this technique has been built and put into operation at the IRIS facility [4]. This is a significant improvement of the laser ion-source device of the IRIS mass-separator working on-line with the proton beam of the PNPI synchrocyclotron. It makes us able to use isobarically clean radioactive isotope beams of a great variety of chemical elements.

2. Scientific program and IRIN project description

The project IRIN (Investigation of Radioactive Isotopes with Neutrons) is proposed for high intensity exotic neutron-rich isotope production by thermal neutrons of the reactor PIK. In Table 1, the expected production rate of some very neutron-rich isotopes at the IRIN facility is presented.

The data for SPIRAL-2 [4] are given for comparison. As one can see from the table, the production rates of neutron-rich nuclides at IRIN will be considerably higher than those at SPIRAL-2. At the same time, one should take into account additional difficulties in operation with very thick uranium carbide targets (up to 2 kg of ^{238}U) at SPIRAL-2. This kind of targets releases short-lived isotopes slowly due to their poor diffusion-effusion properties.

The following scientific activities of the Short-Lived Nuclei Laboratory are the most interesting and important.

Table 1

Production rate of some very neutron-rich isotopes at the IRIN and SPIRAL-2 facilities

Isotope	Z	$T_{1/2}$, s	Yield (IRIN), at./s	Yield (SPIRAL-2), at./s
^{74}Ni	28	0.9	4.58E+06	2.75E+05
^{78}Cu	29	0.342	1.09E+07	1.15E+06
^{84}Ga	31	0.085	1.11E+10	1.24E+07
^{127}Ag	47	0.109	1.58E+02	1.71E+01
^{130}Cd	48	0.195	8.78E+10	8.03E+08
^{133}In	49	0.18	1.71E+08	1.06E+08
^{134}Sn	50	1.12	1.77E+10	2.62E+09
^{136}Sb	51	0.82	1.15E+10	3.45E+09

The position of the neutron drip-line is very uncertain, and its experimental determination is a problem of intense interest. The neutron drip-line is identified only up to fluorine ($Z = 9$). The predicted positions of the neutron drip-line for heavier elements differ greatly depending on the model used. Beyond its influence on the nuclear structure, understanding the behaviour of very neutron-rich nuclei could help, for instance, to elucidate properties of the neutron matter needed for theory of neutron stars.

Penetrating deep into an unknown area of the nuclear chart quite probably can reveal many new phenomena. One of them is the predicted change of the shell structure. It is possible that the shells which have been identified in the known nuclei are considerably different in very exotic nuclei. Hints that this is indeed the case have already been found in light nuclei, with $N = 20$ and 28, and many other similar cases could occur, which need experimental verifications.

A complete description of the nucleosynthesis requires detailed knowledge of nuclei near the neutron drip-line and of nuclear reactions in which they are involved. A possible path of the rapid neutron-capture process (or *r*-process) goes deep into the region of very exotic neutron-rich nuclei with lifetimes, binding energies and delayed-neutron emission probabilities unknown. Knowledge of these properties is thus a prerequisite for full understanding of the nucleosynthesis of about half of heavy elements between iron and uranium.

Experiments with nuclei very far from stability will undoubtedly provide new possibilities to carry out a research with unexpected results. Thus, high priority should be given to systematic investigations of nuclei covering the whole interval from stability to the neutron drip-line.

Measurements of masses of short-lived nuclei have been of great interest for many years. The atomic mass is the nuclear gross property that absorbs all the effects of the forces that are acting in it. Measurements of masses of a large set of nuclei are required to detect trends in the nuclear binding energy and also to test nuclear models. Masses may reveal vanishing of shell closures and appearance of new magic numbers far from stability. Similar arguments can be given for the half-lives of exotic species. When compared to model calculations, they may open up shell effects and their changes far from stability. In addition, to understand the stellar evolution and the origin of elements in the universe, extensive model calculations are used to describe and simulate different processes occurring in stars. Especially, for violent processes, like supernovae explosions or *X*-ray bursts, properties of unstable nuclei are the most important inputs to the models.

In these investigations of nuclear characteristics of nuclei very far from stability, the isobaric selectivity becomes more and more important to provide the "purity" of the objects under investigation. Due to their extremely low production rate in proton-nucleus collisions, investigations of these nuclides is to be done with the interference of isobars with production rates of several orders of magnitude higher than those for the isotopes under study. Hence, the crucial point is to provide isobarically pure sources of investigated nuclei to enable investigations of life-times, decay modes and other nuclear characteristics.

A possibility of isomer selectivity is also a very important point. There is a range of interesting problems where a source of pure isomers could give an excellent opportunity for investigations (isomer-selective measurements of beta-strength functions, *etc*.).

The next very important direction is measurements of the ground state properties of short-lived nuclei (spins, mean square charge radii, electromagnetic moments, *etc*.). These investigations require, besides a high isobar and isomer selectivity, a high production efficiency of the nuclides to be studied. High efficiency could allow penetration into the region of more exotic nuclei. Such a possibility is of great importance for traditional area of laser-nuclear spectroscopy applications – for isotopic shift and hyperfine splitting measurements. Changes in mean square charge radii, spins and electromagnetic moments can be evaluated from such experimental data.

One of the most interesting objectives of the laser-nuclear spectroscopy is investigation of shell effects in mean square charge radii of nuclides far from beta-stability. An observation of absence of sudden kinks in the slope of the mean square charge radii sequence versus neutron number N at the "magic" numbers can be treated as a "change of magicity".

In this respect, the most interesting nuclei are Sb, Sn, In, Cd, and Ag with neutron numbers close to $N = 82$. Systematic investigations of mean square charge radii for a long isotopic chain are to be done to discover general trends and basic properties of the nuclear matter. There is not enough information about the shell-closure effect near $N = 50$. Here, the most interesting isotope chains are the chains of Ge, Ga, Zn, Cu, and Ni isotopes. These isotopes attract additional interest as unique objects to test the mean square charge radius trend between two neighboring closed sub-shells.

Additionally, there is a plan for a construction of a special ion guide at IRIN for production of high purity sources. It can be used for solid-state physics and nuclear medicine purposes.

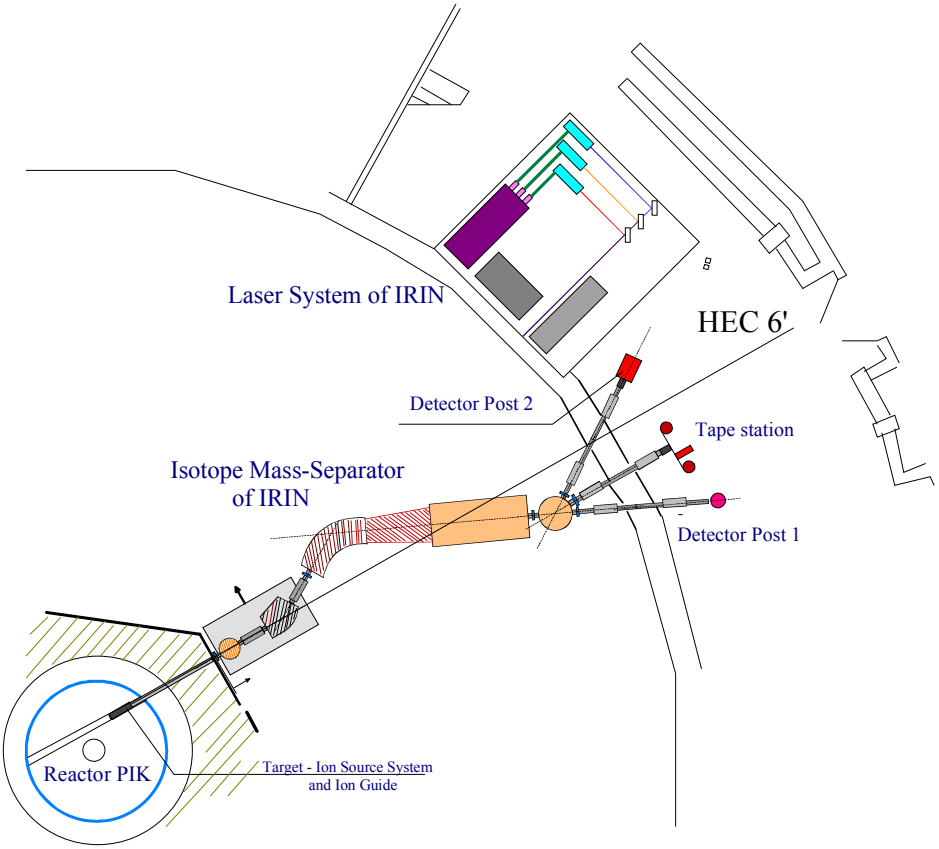

Fig. 1. Schematic view of the IRIN set-up with a laser ionization complex

A schematic view of the IRIN set-up with a laser ionization complex in the reactor PIK hall with horizontal neutron channels is presented in Fig 1. The main part of IRIN is an isotope mass-separator. A target-ion source device of the mass-separator is placed inside of a reactor channel with the thermal

neutron flux of 3×10^{13} n/cm^2/s. This neutron flux irradiates the target material and heats it up to 2000–2400 ºC. The power emission as a result of 10^{14} fissions in 4 g of the ^{235}U (90 % enriched) target is ~ 3 kW.

The fission products are thermally released from the target material due to diffusion and effusion processes, and they penetrate into the ion source cavity. The ions from the ion source are formed with the extraction electrode into a 30 keV beam (with the angular divergence of 2×10^{-2} rad). Then, a parallel beam is formed with a focusing lens, consisting of 3 cylindric electrodes. After the beam shaper system and the steering-filter magnet, the ion beam goes to an analyzing 55º magnet for mass separation. It enters the magnet normally to the magnetic field lines and is focused in the vertical and horizontal planes. The ion beam size in the focal plane of the mass-separator magnet is about 1 mm in the vertical plane and 1.5 mm in the horizontal plane. The central trajectory curvature in the magnetic field is $R = 1500$ mm. It provides a distance between the neighbouring masses $D = R / A$ mm (A is the mass number). For instance, for $A = 150$ the dispersion is $D \approx 10$ mm. The mass range in the focal plane is ± 15 % of the central mass (the mass in the centre of the focal plane). For example, the mass range in the tin region is from 110 to 150. Mass-separated ion beams are transported from the collector chamber to the bending and beam distribution chamber, the vacuum chamber with two cylindric capacitors bending the ion beams to 30 and 60 degrees. The selected ion beams are directed to the experimental hall with the ion guide systems. Focusing triplet electrostatic lenses are installed along the ion beam lines to focus the ion beams to detection posts of the experimental set-up. The ion beam dimensions in the implantation points are about 2×2 mm^2. The vacuum system should provide the residual pressure of about $(2 - 4) \times 10^{-6}$ mbar in all parts of the mass-separator. The ion beam transmission from the ion source to detection posts should be in the range of 60–90 % (depending on the ion source type and focusing quality).

All ion beam lines are connected to the corresponding experimental set-ups. The first ion guide will be supplied with an ion trap for high precision mass measurements (detection post 2 in Fig. 1). With the ion trap, where the Penning trap performs mass measurements, it has already been shown that even for nuclides with half-lives as short as few hundred milliseconds it is possible to reach an accuracy of $\delta m/m \approx 1 \times 10^{-7}$ [5].

A neutron 4π detector for delayed neutron registration will be installed at the first ion guide (detection post 1 in Fig. 1). A fast tape station with α-, β-, and γ-detectors for identification and investigation of rare isotopes will be placed at the second ion guide. All detection posts, tape stations and the mass-separator will be controlled with a mainframe computer.

3. Conclusion

The project IRIN at the reactor PIK opens new possibilities for production and investigation of neutron rich nuclei. It will be able to compete with and in some cases to surpass the existing and projected ISOL installations. In these investigations, the combination of a mass-separator and a laser resonance-ionization facility enables one to overcome inevitable problems which are due to low production rates of the most exotic nuclei. The Penning trap technique will make possible to measure nuclear masses with high precision for a large array of extremely neutron rich nuclei far from the beta-stability region.

References

1. E.Ye. Berlovich *et al.*, Izvestiya Akad. Nauk SSSR, Ser. Fiz. **40**, 2036 (1976).
2. V.N. Panteleev *et al.*, Rev. Sci. Instr. **73** (2), 738 (2002).
3. G.D. Alkhazov *et al.*, Nucl. Instr. Meth. A **306**, 400 (1991).
4. A.E. Barzakh *et al.*, Rev. Sci. Instr. **83**, 02B306 (2012).
5. F. Herfurth *et al.*, Nucl. Phys. A **701**, 516 (2002).

PROJECT OF THE RADIOISOTOPE FACILITY RIC-80 AT PNPI

V.N. Panteleev, A.E. Barzakh, L.Kh. Batist, D.V. Fedorov, A.M. Filatova, V.S. Ivanov, K.A. Mezilev, F.V. Moroz, P.L. Molkanov, S.Yu. Orlov, Yu.M. Volkov

1. Introduction

The main sources of production of radioactive nuclides are thermal-neutron reactors and accelerators of charged particles. Since recent years no new research reactors have been constructed in Russia (the only reactor, which has now basically been completed after a long break and whose physical start was performed in 2011, is the reactor PIK at PNPI in Gatchina), there is a move to the accelerators of charged particles – cyclotrons, as the safest and most reliable accelerators. The list of cyclotron-produced radionuclides is much longer and richer than that of reactor-produced isotopes. Also, much higher specific activity of radionuclides can be reached at cyclotrons in comparison to that produced at reactors. Moreover, cyclotron-produced radionuclides can be used both for diagnostics and therapy. Since the cyclotrons generally used in Russia have the energy of accelerated particles less than 30 MeV, the variety of nuclides produced with these installations is limited. The cyclotron at the RSC "Kurchatov Institute" is currently the only cyclotron with the energy of the extracted proton beams higher than 30 MeV. Only with this cyclotron the isotope ^{123}I can be produced with the high radionuclide purity from a xenon target.

At INR of RAS (in Troitsk near Moscow), a powerful linear accelerator is in operation – the Moscow meson factory. A laboratory, which has the installation for irradiation of targets by the 160 MeV proton beam of the 120 μA current, was organized for production of medical radionuclides. This installation is used full-time; it is one of the largest in the world in terms of the beam energy accumulated in production of radionuclides and provides the possibility to produce practically the whole list of accelerator radionuclides. An essential disadvantage of this facility is that operation of the accelerator of this kind is very expensive and, hence, the production costs of medical radionuclides are vastly higher than the costs of radionuclides which can be produced by means of a cyclotron with the proton energy of up to 80 MeV.

We also have to mention another very important circumstance which concerns production of cyclotron radionuclides for medical purposes. In this case, enriched stable isotopes are often used as target material. Russia is one of not so many countries in the world where production of enriched isotopes is set up by various methods and where enriched stable isotopes of all elements are available. Practically all of them are exported to other countries, where they are used to produce radionuclides for medical purposes. Sometimes, Russian medical institutions import radionuclides prepared on the base of the stable enriched isotopes produced in Russia. The price of such imported product is three orders of magnitude higher than that of the exported enriched isotopes.

2. Design of the RIC-80 (Radioactive Isotopes at the cyclotron C-80) installation

In Fig. 1, the layout of the RIC-80 [1] installation is presented. The installation is intended for production of medical radionuclides in the beam of the C-80 cyclotron, which is under construction at PNPI in Gatchina. The proton beam energy at the target will be 40–80 MeV, and the intensity will be up to 200 μA. This cyclotron is intended for treatment of ophthalmologic diseases by irradiation of malignant eye formations, as well as for production of a wide spectrum of medical radio nuclides for diagnostics and therapy. The cyclotron is located in the right side of the experimental hall (ground floor) of the PNPI synchrocyclotron.

The extracted proton beam is deflected by 15 degrees to the left, then – by 45 degrees downward to the underground floor, and then – by 45 degrees up with respect to the horizontal direction. After that, the beam can be directed to one of the target stations: a) to the isotope mass-separator target by the 25-degree clockwise deflection from the "zero" beam direction, b) to the first target station by the "zero"-deflection, and c) to the second target station by the 25-degree counterclockwise deflection. In the drawing, the deflecting and focusing magnet elements are shown. They are installed on the way of the proton beam to the target stations and to the masses-separator target. Two available target stations allow us to obtain higher efficiency in using the proton beam since during the cooling of the irradiated target, where long-lived

radionuclides are produced, another target with possibly different target material can be irradiated by the proton beam to produce another radionuclide. The mass-separator, with its target as the third target station, will produce high purity separated isotopes of some medical radionuclides, which are implanted into the corresponding collector, from which they can be easily extracted. The target stations will be equipped with manipulating devices to place the highly radioactive targets in protection containers to safely transport them to their storage places or to hot cells for after-treatment and production of preparations for pharmaceutics.

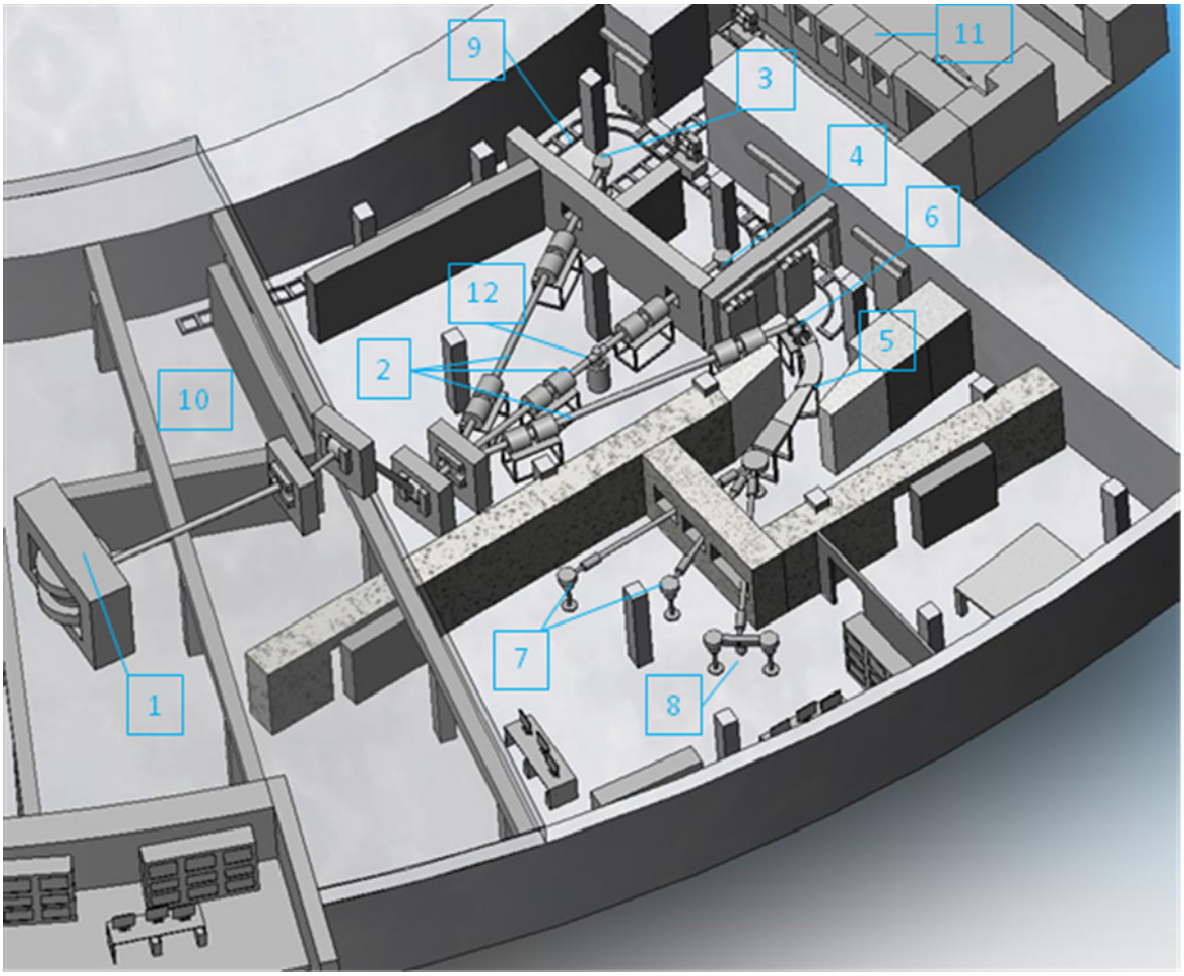

Fig. 1. Layout of the RIC-80 radioisotope complex. 1 – Cyclotron C-80; 2 – proton beam tubes; 3, 4 – target stations for radiochemical production of medical isotopes; 5 – mass-separator for production of medical isotopes of high purity; 6 – target station of the mass-separator; 7 – collecting stations for separated radionuclides; 8 – detector stations for purity measurements of the obtained radionuclides; 9 – transportation system for activated targets to storage or to hot cells; 10 – storage place for irradiated targets; 11 – hot cells; 12 – pneumatic rabbit station

3. Estimated yields of radionuclides expected to be produced at the RIC-80 facility

The RIC-80 facility is unique because it is the largest cyclotron in Russia in terms of the beam energy accumulated in production of radionuclides providing a sufficiently high energy of accelerated protons (80 MeV). It gives the possibility to produce sources of high activity within the entire list of radionuclides produced at accelerators. Table 1 shows estimated yields of the radionuclides planned to be obtained at the RIC-80 facility.

Table 1

Yields of the radionuclides planned to be produced at the RIC-80 facility with the proton beam energy of 40–80 MeV and the current of 100 μA. The calculations correspond to 2 g/cm^2 target thickness

Isotope	Half-life	Target	Irradiation time interval (h)	Target Activity (Ci)
^{68}Ge	270.8 d	Ga	240	2
^{82}Sr	25.55 d	Rb	240	8
^{106}Ru	1.024 y	^{238}U	240	0.6
^{111}In	2.8 d	Cd	25	30
^{123}I	13.27 h	Te	5	34
^{124}I	4.17 d	Te	25	20
^{149}Tb	4.1 h	Gd	20	1
^{201}Tl	3.04 d	Tl	25	30
^{223}Ra	11.4 d	Th	240	1.5

As one can see in Table 1, the RIC-80 facility provides production of almost the entire spectrum of radionuclides produced currently in Russia and abroad. It is necessary to emphasize that the activities of the radioisotopes are shown for production in the target. The actual activities extracted from the target material can be smaller because of incomplete extraction of the produced radioisotopes. For improvement of the extraction efficiencies for the targets under development, test experiments with target prototypes to estimate the effective production of the listed nuclides will be performed at the PNPI synchrocyclotron.

Possibilities of the radionuclide production at the RIC-80 installation are not limited by the list of the isotopes presented in Table 1. The unique parameters of the C-80 cyclotron allow one to produce a broad nomenclature of radioisotopes, which, at present, are under discussion as being perspective for diagnostics and therapy. A comparison of the isotopes used for many years with the new ones – which are under discussion and are subject to clinical tests – brings us to the conclusion that the use of more short-lived radionuclides for diagnostics and therapy significantly reduces radiation hazards for patients.

4. On-line mass-separator at the RIC-80 installation for medical isotope beams of high purity

The production of radioactive isotopes and their study by ISOL systems (Isotope Separator On-Line) is one of the fundamental directions in nuclear physics. The extraction and isotopic separation of the produced radionuclides were successfully performed during last 40 years using ISOL installations at beams of different particles – protons, neutrons and heavy ions. At present, such on-line systems as ISOLDE (CERN, Switzerland), ISAC (TRIUMF, Canada), and IRIS (PNPI, Gatchina, Russia) [2, 3] allow one to obtain more than 2000 species of separated isotopes of almost all elements of the Periodic Table. The produced radioactive isotopes with half-lives ranging from several milliseconds to several thousand years are used in nuclear physics, solid state physics and radiation medicine.

The only ISOL facility in Russia is IRIS (Investigation of Radioactive Isotopes at the Synchrocyclotron) at the PNPI synchrocyclotron. It operates to produce and investigate radioactive isotopes of diverse elements. For more than thirty years, at IRIS, different target-ion devices for production and studies of a very wide variety of radioactive isotopes were developed and used. During the time of the facility operation, more than 300 nuclides were investigated and 17 of them were identified for the first time. A method of the laser ion source for selective production of nuclides has been developed and used at IRIS for the first time. At present, this method is actively used providing the factor of selective separation of isobars as high as up to $\varepsilon_s = 10^5$ [4]. In the period since 2000, new target devices of high efficiency were designed and used for production of more than 50 radionuclides, whose β^+-, β^-- and α-decays were studied. Using the targets made of the high-density uranium monocarbide [5], the radioactive isotopes of Mn, Fe, Co, Ni, Ga, Rh, Pd, Rb, Cd, In, Sn, Sb, Te, I, Cs, Tl, Pb, Bi, Po, and At needed for nuclear physics studies were produced. High temperature targets made of Ta foils were used to produce radioisotopes of alkaline metals – Li, Rb and Cs, and also the isotopes of rare earth elements – Sm, Eu, Gd, Tm and Yb [6]. New developments and 35 years of experience in

operation of the IRIS installation will be used for the new ISOL at the high current C-80 cyclotron for production of intensive beams of medical radionuclides of high purity.

The proton beam of the cyclotron (see Fig. 1), after going through the deflecting and focusing magnetic elements, is directed to the target of the mass-separator, which is located inside the vacuum chamber at high temperature (1800–2000 °C), where radionuclides are produced in nuclear reactions. The radionuclides leave the target container and get into the ion source where the ionization occurs. The ions going out of the ionizer are shaped by the field of the extracting electrode into a beam with the $\sim 2 \times 10^{-2}$-radian divergence. Moving through the focusing lens, the ion beam is converted into a parallel one and gains the energy of 30 keV. Then the beam of monoenergetic ions enters the magnet-analyser, where the mass separation takes place. The dimensions of the beam at the focal plane of the mass-separator magnet are about 1 mm in the vertical direction and 1.5 mm in the horizontal direction. The beams of radioactive ions separated over masses enter the switchyard chamber and go along the vacuum ion guide tubes to the experimental hall, where they are implanted into the corresponding collectors. The sources of radionuclides obtained without any carrier and admixtures are monitored during the accumulation process for determination of their purity and activity by means of α-, β- and γ-detectors installed close to the collectors, where the implantation of radioactive ions occurs. The mass-separator method possesses the following advantages.

- It allows one to obtain very pure beams of medical isotopes of various elements.
- Several mass-separated radionuclides can be accumulated simultaneously.
- The implantation depth of some tens of Ångstroms allows one to use very fine organic substrates significantly simplifying production of medical preparations.
- The method of radioactive ion implantation allows one to produce unique generators of radioactive noble gases.
- The target can be used many times and does not require reconstruction.
- Except for a number of relatively long-lived nuclides, the mass-separator operating on-line with an accelerator or a reactor allows one to produce many new "short-lived" radioactive isotopes for medical diagnostics with $T_{1/2}$ ranging from several minutes to several hours.
- The diagnostics can be realized "on-line" in medical laboratories equipped with the installations producing a variety of short-lived mass-separated radioactive nuclides of high purity.

The estimated activities of radionuclides, which can be obtained with the mass-separator, are shown in Table 2. For many of them, with half-lives longer than several tens of a minute, the efficiency of extraction from the target at the temperature of 1800–2000 °C is close to 100 %.

Table 2

Estimated activities of those radionuclides produced in the mass-separator target which are traditionally used in medical practice. The activity of nuclides at the output may be lower due to losses inside the target and the ion source device. The calculations are for the target thickness of 2 g/cm^2

Isotope	Half-life	Target	Irradiation time (h)	Activity inside of the mass-separator target (Ci)
^{67}Ga	3.2 d	Ge	25	5.4
^{82}Sr	25.55 d	Y	240	1.3
^{99}Mo	16.99 d	^{100}Mo	120	8
^{111}In	2.8 d	Sn	25	1.4
^{123}I	13.27 h	Te	5	34
^{124}I	4.17 d	Te	25	20
^{201}Tl	3.04 d	Pb	25	8.6
^{223}Ra	11.4 d	Th	240	1.5

As one can see from a comparison of the radiochemical and mass-separator methods of the medical radioactive isotopes production, preference for one of them for production of a specific isotope can be made only after preliminary studies of the designed targets, which are the main components for both methods.

5. Conclusion

Studies of target materials and target device prototypes for the RIC-80 facility started at the PNPI synchrocyclotron in 2010. The RIC-80 facility can provide implementations of both the traditional radiochemical method of extraction of produced nuclides and the innovative mass-separator method. The latter will produce radionuclides of high purity directly at the collector of the mass-separator providing a unique possibility to obtain short-lived radioactive nuclides. Advancing into the area of short-lived isotopes, with the half-life from about one minute to several tens of a minute, we can significantly extend the number of radionuclides which can be used.

References

1. V.N. Panteleev *et al*., Abstracts of 7th Intern. Conf. on Isotopes, 4–8 Sept. 2011, Moscow, p. 35.
2. E.Ye. Berlovich *et al*., Izvestiya Akad. Nauk SSSR, Ser. Fiz. **40**, 2036 (1976).
3. V.N. Panteleev *et al*., Rev. Sci. Instr. **73**, 738 (2002).
4. G.D. Alkhazov *et al*., Nucl. Inst. Meth. A **306**, 400 (1991).
5. V.N. Panteleev *et al*., Eur. Phys. **150**, 297 (2007).
6. V.N. Panteleev *et al*., Nucl. Phys. A **701**, 470 (2002).

DOUBLE POLARIZED *dd*-FUSION

N.N. Chernov, K.Yu. Grigoryev, I.Yu. Ivanov, E.N. Komarov, L.M. Kotchenda, P.A. Kravtsov, M.S. Mikirtychyants, S.G. Sherman, S.N. Terekhin, V.A. Trofimov, A.A. Vasilyev, M.E. Vznuzdaev

1. Introduction

A double-polarized *dd*-fusion experiment is under preparation at PNPI, Gatchina. The experimental program includes measurements of the asymmetry in the differential cross-sections for the reactions $d + d \rightarrow$ $\rightarrow {}^3\mathrm{He} + n$ and $d + d \rightarrow t + p$. The total cross section modification for polarized *dd*-fusion will also be investigated. An increase by a factor of 1.5 was already established for the $d + {}^3\mathrm{He}$ and $d + t$ reactions. The spin-correlation coefficients $C_{z,z}$ and $C_{zz,zz}$ will be measured for both reactions to determine the quintet-state suppression factor, which has quite different theoretical predictions and is very important for building a neutron-lean fusion reactor. In addition, more spin-correlation coefficients can be measured at different energies with this experimental set-up in order to get more information about the *dd*-fusion process. The screening effect due to atomic electrons which shows up in the astrophysical *S*-factor may also be investigated in this experiment for different spin combinations of the electron and the nucleus.

The principal aspects of the thermonuclear fusion problem include understanding of the nuclear processes of the fundamental fusion reactions at low energies, confinement of the hot and dense plasma, and energy extraction from the plasma. Standard candidates for the fusion fuel include the hydrogen isotopes (deuterium and tritium) and the light helium isotope – ${}^3\mathrm{He}$. For the practical use of fusion reactors one needs to know the nuclear cross sections for nuclear interactions of light nuclei. These cross sections were extensively studied, but not all of them are well known. This is also true for the spin sector, where spin effects in few-body reactions are very large.

One of the classical examples is the bound state in the nucleon-nucleon system. It exists only in the spin-triplet channel, the spin-singlet scattering length being about four times larger than the spin-triplet one and having an opposite sign. The second example is the broad 0^+ resonance in the ${}^4\mathrm{He}$ nucleus. It causes a gigantic cross section for n-${}^3\mathrm{He}$ scattering in the spin-singlet channel, which leads to an almost 100 % spin filtering of neutrons with an excellent transmission rate of 50 % in the polarized ${}^3\mathrm{He}$ target [1]. This technique is used to generate intense polarized neutron beams [2]. The fact that the amplitudes of important fusion reactions

$$d + {}^3\mathrm{H} \rightarrow n + {}^4\mathrm{He} \text{ and}$$
$$d + {}^3\mathrm{He} \rightarrow p + {}^4\mathrm{He}$$

are dominated by an *S*-wave $J = 3/2^+$ resonance, significantly simplifies handling of the double-polarization effects. Simple counting of the spin states implies that only 2/3 of nuclei can undergo fusion in unpolarized plasma. Alternatively, the full polarization of the deuteron and ${}^3\mathrm{He}$ would enhance the fusion cross section by 50 % [3].

Based on the available experimental data on the deuteron-deuteron interactions, Ad'yasevich and Fomenko suggested in 1969 a possibility of polarization enhancement of the *dd*-fusion rate by a factor of two [4]. The first experimental proposal to study the polarization coefficients in the double-polarized fusion [5] was not realized because the polarized atomic and ion beam technique at that time did not allow to produce beams of enough intensity.

A substantial step forward was made in 1982 in a theoretical study of depolarization of nuclei in magnetically confined plasma [6]. The main conclusion was that the depolarization time significantly exceeds that of the fusion reaction. Presently, it is considered feasible to confine ${}^3\mathrm{He}$ with the nuclear polarization reaching 55 %, and to inject neutral deuterium with the nuclear polarization of about 55 %. The experiment is planned at the DIII-D Tokamak at San Diego [7]. The estimated enhancement of the fusion should be around 15 %. If the retention of the deuterium polarization is confirmed, these measurements will be continued with tritium.

An alternative approach to confirm experimentally the persistence of the nuclear polarization in a fusion process in the plasma generated by a petawatt laser hitting a polarized frozen HD target was suggested at

Orsay [8]. Detecting the final state gamma quanta and neutrons, one would have an experimental access to both reactions $p + d \rightarrow {}^3\mathrm{He} + \gamma$ and $d + d \rightarrow {}^3\mathrm{He} + n$.

2. Measurements of the cross sections for polarized fusion reactions

The reactions $\vec{d} + \vec{t}$ and $\vec{d} + {}^3\vec{\mathrm{He}}$ with the initially polarized particles have been already investigated [3]. As for the basic fusion reaction $\vec{d} + \vec{d}$ in the energy range of 10–100 keV, the spin-correlation components of this reaction have not been measured yet. For the practical use of the polarized fuel in a fusion reactor, only two spin combinations are of importance, when the deuteron spins are parallel or anti-parallel to each other. Theoretical predictions for a change of the reaction cross section are shown in Fig. 1.

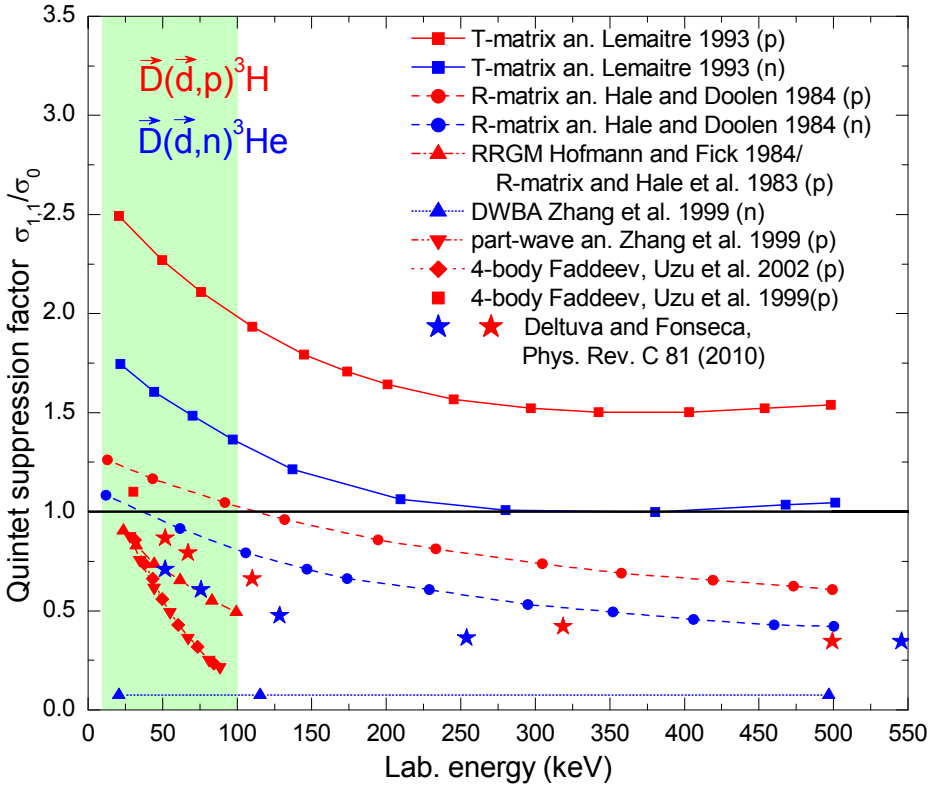

Fig. 1. Theoretical predictions of the quintet suppression factor

Here, the quintet state suppression factor (QSF) is defined as the ratio of the reaction cross section for parallel spins of the initial particles to the total unpolarized reaction cross section. The value of the QSF = 1 means that the polarization of the initial particles does not affect the total reaction cross section. Large discrepancy in predictions illustrates a great demand for direct measurements of this observable to check theoretical models. The experimental plan includes measurements of the asymmetry of the differential cross sections, determination of the total cross section change for polarized initial particles, and measurements of the spin-correlation factors $C_{z,z}$ and $C_{zz,zz}$ for investigation of the quintet suppression factor.

3. Investigations of methods for increasing the intensity of polarized sources

Polarized deuterium is produced at present mainly with the help of atomic beam sources (ABS). These sources are used at accelerator injectors (with subsequent ionization of atoms) or for the internal targets at storage rings of accelerators [9]. Building of a polarized atomic beam source is possible only in the framework of high-expenditure accelerator experiments due to high cost of the ABS equipment. The intensity of the world-best polarized sources do not exceed 10^{17} at/s. At the same time, the feeding flux of polarized deuterons for 100 MW full fledged polarized thermonuclear reactors should be 10^{21}–10^{22} at/s.

An intensity increase by 4–5 orders of magnitude is not feasible with atomic beam sources. Thus, it is necessary to search for a new source of polarized deuterons. One of possible directions in this search is to use nuclear polarized molecular deuterium.

4. Experiment

We propose to investigate at various energies (between 10 and 100 keV) the angular distributions of the products of the reactions

$$\vec{d} + \vec{d} \rightarrow t + p \quad \text{and}$$

$$\vec{d} + \vec{d} \rightarrow {}^3\mathrm{He} + n.$$

The energy of the initial particles is very low, and the penetrating depth is exceedingly small. The solid target experiments would have large uncertainties in the results because of an unknown surface polarization and influence of the multiple scattering on the energy of the reaction products. To reduce these uncertainties, one can investigate direct interaction of a polarized deuteron beam with polarized neutral deuterium atoms in vacuum (Fig. 2).

The ABS for this experiment is constructed on the basis of the Cologne University source which was used in the SAPIS project [10]. It produces a beam of neutral polarized atoms with the given vector or tensor polarization. Polarized atoms in the beam have thermal velocities with the energy of about 0.1 eV. The beam intensity of 10^{15} at/s achieved at the Cologne University is not sufficient for measurements, and there are plans to upgrade the ABS and to increase the beam intensity up to 10^{16} at/s.

Using neutral atoms for the target allows to increase significantly the target density (there is no space charge restriction), but it requires to take into account an impact of the atomic electron on the reaction rate, which does not exist in the ionized plasma of thermonuclear reactors. An electron screening effect (the so-called astrophysical *S*-factor) is well known and measured experimentally [11]. This effect has a considerable influence on the reaction rate at the energies below 10 keV, but is not important at higher energies. Reversing the arguments, direct experimental investigations of this effect with allowance for polarization of both the incident nucleus and the target atomic electron would be very interesting on its own. No experimental data exist, and no theoretical calculations in this field have been performed so far.

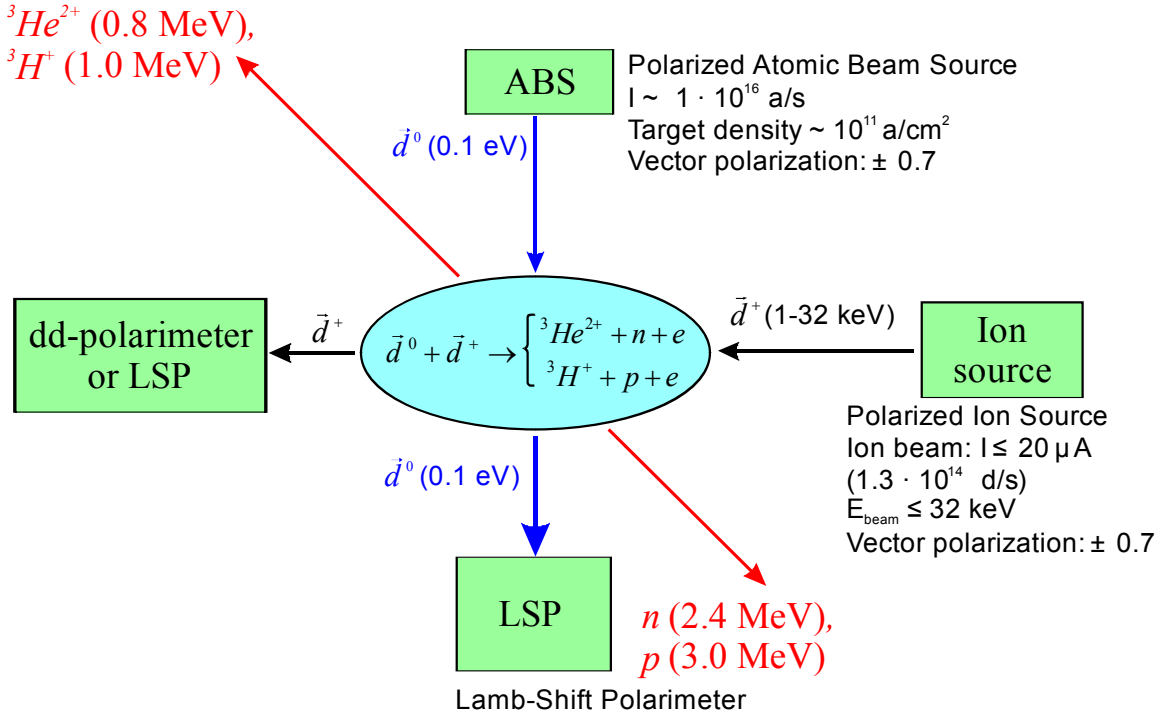

Fig. 2. Layout of the experiment

Neutral atoms of the target will be bombarded by positive deuterium ions (deuterons), which are produced by a polarized ion source (POLIS). This source was utilized as an injector of the cyclotron accelerator at the KVI institute, Groningen, Netherland. The source is producing an ion beam of 20 μA and energies up to 35 keV [12]. A substantial upgrade of this source to increase the beam energy up to 100 keV is required. At this energy one can cross-check the experimental results with the existing data (available for the energies higher than 100 keV). It is planned to use a linear ion accelerator to increase the ion energy from 35 keV up to the desired range of 35–100 keV. This upgrade will change the constant beam into a bunched one with certain intensity losses.

The production and use of polarized ion and atomic beams require accurate measurements of the polarization. It is planned to use three polarimeters in the experiment: two Lamb-shift polarimeters (LSP) for initial tuning of the beams and a nuclear reaction polarimeter for constant monitoring of the ion beam polarization during the production runs.

The LSP has a substantially better precision, and allows measurements of more spin states of the beam, but its operation is more complicated compared to the nuclear reaction polarimeter. Therefore, this polarimeter will be used only for tuning of the beam sources and periodic checking of the polarization. The nuclear reaction polarimeter makes use of the asymmetry of the nuclear fusion reaction products, which can be detected with semiconductor detectors.

One of the main tasks of the experiment is to detect the fusion reaction products – protons, tritium and ^{3}He ions (neutrons cannot be detected in this experiment). The estimated count rate at the energy of 20 keV is about 13 events per hour. Therefore, the detector system should have low background and noise to distinguish these rare events. Problems of the cosmic radiation and the natural radioactivity of the construction materials should be carefully investigated.

5. Detector set-up

The main goal of the experiment is to perform direct measurements of the angular distributions of the reaction products. Therefore, the detector system should cover the maximum solid angle around the interaction point (the ideal case – 4-π solid angle), with typical angular resolution of 10–15°. The prototype of the detector system will consist of two Elementary Detector Cells (EDC) located at 180° to each other, which can be rotated by two step motors in a gimbal suspension (see Fig. 3). This set-up will be used to measure the energy resolution of the detectors, preliminary angular distributions with small statistics, and also to determine the necessary angular resolution for the final detector system. The prototype will also help to investigate technical questions to the detectors: the degradation time of the semiconductors in the vacuum with some traces of atomic deuterium, which is quite an active substance, the lifetime of the detector in the experimental conditions, *etc*. The final detector system should cover 4-π solid angle. It is supposed to be built in a cubic shape construction with 80 % covering of the area around the interaction point (Fig. 4). The detector system will be surrounded with Helmholtz coils to provide constant magnetic field in the interaction region and rotation of the atomic polarization. The EDC will contain 16 surface barrier silicon detectors with the total size of 32 × 32 mm^2.

Fig. 3. Initial prototype of the detector system

The readout electronics for the detector system is under development, including electronic signal conditioning and processing with a dedicated software. All information from the detector system will be acquired, accumulated and analysed off-line to determine the differential cross sections.

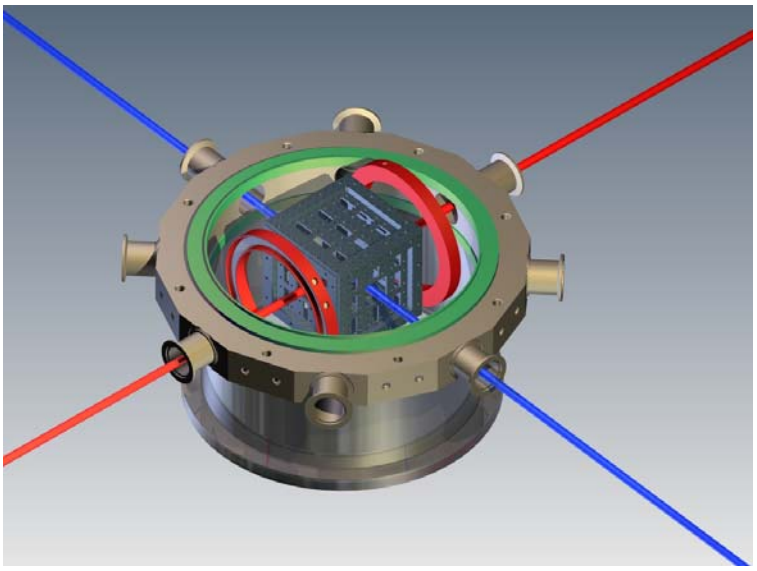

Fig. 4. Detector set-up

6. Conclusion

This experiment to measure the cross sections for the polarized deuterium fusion reaction will provide for the first time direct measurements of the spin-correlation coefficients in the energy range of 10–100 keV, and finally will give a systematic ground for the practical use of polarized deuterons in the thermo-nuclear fusion with estimation of possible benefits from the polarization.

References

1. R.M. Moon, T. Riste, and W.C. Koehler, Phys. Rev. A **181**, 920 (1969).
2. T.E. Chupp *et al*., Nucl. Instr. Meth. A **574**, 500 (2007).
3. H. Paetz gen. Schieck, Eur. Phys. J. A **44**, 321 (2010).
4. B.P. Ad'yasevich, D.E. Fomenko, Sov. J. Nucl. Phys. **9**, 167 (1969).
5. B. Ad'jasevich, V. Antonenko, Preprint IEA-**2704**, Moscow (1976).
6. R.M. Kulsrud *et al*., Phys. Rev. Lett. **49**, 1248 (1982).
7. A. Honig, A. Sandorfi, *Proceedings of the 17th International Spin Physics Symposium*, AIP Conference Proceedings **915**, 1010 (2007).
8. J.-P. Didelez and C. Deutsch, Persistence of Polarization in a Fusion Process, EPJ Web of Conferences **3**, 04018 (2010).
9. M. Mikirtychiants, Design and Investigation of the Polarized Atomic Hydrogen/Deuterium Beam Source for Experiments at the Storage Accelerator Rings, Ph. D. Thesis, PNPI, Gatchina (2002).
10. R. Emmerich and H. Paetz gen. Schieck, Nucl. Instr. Meth. A **586**, 387 (2008).
11. F. Raiola *et al*., Eur. Phys. J. A **13**, 377 (2002).
12. H.R. Kremers *et al*., Nucl. Instr. Meth. A **536**, 329 (2005).

PNPI IN FAIR: INTRODUCTION

The **F**acility for **A**ntiproton and **I**on **R**esearch, **FAIR**, is an International project (Austria, China, Finland, France, Germany, Greece, India, Italy, Poland, Romania, Russia, Slovenia, Slovakia, Spain, Sweden, and the United Kingdom are the partner countries), which is being built now at GSI, Darmstadt, Germany. It will provide unique accelerator and experimental facilities allowing for a large variety of research in physics and applied science. The main thrust of the FAIR research focuses on the structure and evolution of matter on both a microscopic and on a cosmic scale, deepening our understanding of fundamental questions like those:

- how does the complex structure of matter at all levels arise from the basic constituents and the fundamental interactions?
- how can the structure of hadronic matter be deduced from the strong interaction? in particular, what is the origin of hadron masses?
- what is the structure of matter under the extreme conditions of temperature and density found in astrophysical objects?
- what was the evolution and the composition of matter in the early Universe?
- what is the origin of the elements in the Universe?

The FAIR core facility embraces the 14 experiments which have been approved by the International Steering Committee (July 24, 2006, Berlin). These approved experiments form four scientific pillars of the FAIR research program. More than 2500 scientists and engineers are involved in the design and preparation of the FAIR experiments. They are organized in the experimental collaborations listed below.

APPA – **A**tomic, **P**lasma **P**hysics and **A**pplications (atomic and plasma physics, and applied sciences in the bio, medical, and material sciences) including the following research activities:

BIOMAT – BIOlogy and MATerial science;

FLAIR – Facility for Low-energy Antiproton and Heavy Ion Research;

HEDgeHOB/WDM – Plasma physics experimental stations;

SPARC – Stored Particle Atomic Research Collaboration.

CBM/HADES – **C**ompressed **B**aryonic **M**atter (physics of hadrons and quarks in compressed nuclear matter, hypernuclear matter).

PANDA – Anti**P**roton **AN**nihilation in **Da**rmstadt (hadron structure and spectroscopy, strange and charm physics, hypernuclear physics with anti-proton beams).

NuSTAR – **N**uclear **S**tructure, **A**strophysics and **R**eactions (structure of nuclei, physics of nuclear reactions, nuclear astrophysics and radioactive ion beams) including the following experiments:

R3B – Reaction with Relativistic Radioactive Beams;

DESPEC – DEcay SPECtroscopy;

HISPEC – HIgh resolution SPECtroscopy;

MATS – Precision Measurements of very short-lived nuclei with Advanced Trapping System;

LASPEC – LAser SPECtroscopy of short-lived nuclei;

ILIMA – Isomeric beams, LIfetimes and Masses;

ELISE – Electron-Ion ScattEring in a Storage Ring;

EXL – EXotic nuclei studied in Light-ion induced reactions at the NESR storage ring.

In order to enable an expeditious start of the FAIR construction, a proposal was prepared in 2007 for a **start version** while securing the discovery potential of the facility. For this purpose, the start version as agreed upon in 2007 was structured in six modules:

Module 0: Heavy-Ion Synchrotron SIS100 – the basis and core facility of FAIR, which is required for all science programmes;

Module 1: CBM/HADES cave, an experimental hall for APPA and detector calibrations;

Module 2: Super-FRS for NuSTAR;

Module 3: Antiproton facility for PANDA, providing further options also for NuSTAR ring physics;

Module 4: Second cave for NuSTAR, NESR storage ring for NuSTAR and APPA, a building for antimatter programme FLAIR;

Module 5: RESR storage ring for higher beam intensity for PANDA and parallel operation with NuSTAR.

Based on recent cost estimates and the firm commitments on funding of FAIR Member States, the new start version comprised of Modules 0–3 was accepted (see Fig. 1). This Modularized Start Version (MSV) provides for research programs in all four scientific areas. Modules 4 (the low energy physics program) and 5 (intense secondary beams and an improved accelerator operation due to the time-sharing mode bringing FAIR towards its full parallel operation capacity) are scientifically highly desirable, and obviously the MSV will be upgraded in future.

Fig. 1. FAIR MSV. Colouring of modules: 0 – green; 1 – red; 2 – yellow; 3 – orange. Modules 4 and 5 are not marked in colour. Not shown is the additional experimental area above ground, which is a part of Module 1. On the left hand side of the figure, the existing GSI facility is shown

The construction phase of the FAIR MSV is scheduled to be completed in 2017, and the experiments should start in 2018.

PNPI participates in three of the four FAIR scientific pillars – CBM, PANDA, and NUSTAR (experiments R3B and MATS). The plans of PNPI participation in these FAIR projects are described in the following.

PNPI IN THE CBM PROJECT AT FAIR

V.V. Baublis, E.A. Chernysheva, V.V. Dobyrn, V.A. Evseev, V.V. Ivanov, A.V. Khanzadeev, B.G. Komkov, L.M. Kotchenda, P.A. Kravtsov, E.L. Kryshen, L.G. Kudin, N.M. Miftakhov, V.N. Nikulin, V.V. Polyakov, E.V. Roshchin, G.V. Rybakov, V.M. Samsonov, O.P. Tarasenkova, V.G. Tolchin, E.A. Vznuzdaev, M.E. Vznuzdaev, M.B. Zhalov

1. Introduction

The Compressed Baryonic Matter (CBM) project has been accepted for realization at the SIS300 accelerator, a component of the FAIR accelerator complex that is built in GSI, Darmstadt. Unfortunately, because of changing the FAIR construction strategy, the start of the SIS300 construction is expected in 2018, or even later. Due to this, the research on the compressed baryonic matter will start already with beams from SIS100, the pre-accelerator for SIS300, as an integral part of the physics programme of the FAIR modularized start version outlined in the FAIR Green Paper [1]. Investigations of dilepton, strangeness, and charm production over the full range of the SIS100 nuclei beams and energies will be conducted with the basis version of the CBM set-up and will be continued with the full scale set-up at SIS300.

The SIS100 accelerator will deliver ion beams up to 11 (14) A GeV with Au (Ca) nuclei, and proton beams up to 29 GeV. The CBM research program based on these beams will address the following fundamental questions:

- what is the equation-of-state of the nuclear matter at neutron star densities (up to 6 times saturation density ρ_0), and what are the relevant degrees of freedom at these densities? Are there new phases of the QCD matter?
- to what extent are the properties of hadrons modified in the dense baryonic matter, and are there signatures for chiral symmetry restoration?
- how is charm produced at threshold beam energies, how does charm propagate in the nuclear matter, and what are the in-medium properties of charmed particles?
- how far can we extend the chart of nuclei towards the third (strange) dimension by producing single and double hypernuclei? Does the strange matter exist in the form of heavy multi-strange objects?

Heavy-ion collisions in the SIS100 energy range were pioneered at the AGS in Brookhaven with gold beams in the energy range from 2 to 10.7 A GeV. Using several experimental set-ups, global observables such as pion, proton, kaon and lambda yields and phase-space distributions, collective proton flow and particle correlations were studied exhaustively. However, the experiments at AGS were restricted to measurements of hadrons that undergo strong final state interactions, and therefore carry only limited information on the early and dense stage of the collision. New insight will come from investigations of observables that are sensitive to the early and dense phase of the fireball evolution. The start version of the CBM detector system at SIS100 is designed as a large-acceptance high-rate spectrometer to measure lepton pairs, multi-strange particles and charmed hadrons in proton-nucleus and nucleus-nucleus collisions.

The CBM experimental set-up comprises a large-aperture super-conducting magnet (polar angle acceptance 2.5–25° for all azimuthal angles), a Micro-Vertex Detector (MVD) for identifying the decay vertex of particles with open charm, a Silicon Tracking System (STS) to measure the particle trajectories in the magnetic dipole field, a large area detector consisting of Multi-gap Resistive Plate Chambers (TOF – MRPC) for Time-Of-Flight (TOF) measurements, a RICH detector for identification of electron-positron pairs from the decay of low-mass vector mesons, an intermediate tracking station (TRD) between STS and the TOF wall, and a muon detection system (MUCH) to measure J/ψ decays to dimuon pairs. The Projectile-Spectator Detector (PSD) measures the collision centrality and the reaction plane. For photon measurements, an electromagnetic calorimeter (ECAL) is foreseen.

PNPI contributes to the CBM project in several directions:

- simulations to optimize the absorber and detector layout of the muon system (MUCH) aiming at obtaining an acceptable signal-to-background ratio, especially in the case of light vector mesons;
- elaborating the muon tracking system, with special care for the central part, where the highest rate and occupancy is present. For today, the muon tracking system is considered as a combination of

micro-pattern gas detectors (such as GEMs and Micromegas) for the central part, thick GEMs to cover the rest peripheral part of the aperture, and straw tubes for the last two stations. R&D on the choice of the appropriate detectors is on the way;

- mechanical design of the MUCH detector including the superstructure;
- mechanical design of the RICH detector;
- gas systems for both detectors.

2. MUCH related activity

2.1. Simulations to optimize the MUCH layout

MUCH is designed as a sequence of tracking stations sandwiched between a set of absorbers. The starting SIS100 option consists of 3 absorbers and 3 tracking stations, the final SIS300 version consists of 6 absorbers and 6 tracking stations. Each tracking station includes three chambers, measuring X and Y coordinates of the track.

PNPI is responsible for the software development and optimization of MUCH. A full chain of simulation and reconstruction algorithms was developed and extensively used during last 5 years. The simulation chain starts from building of the absorber and detector volumes, with the materials, dimensions and positions calculated automatically using a flexible parameter file. The modules of the tracking detectors are automatically arranged in rows on both sides of each support plane keeping overlaps of the sensitive volumes essential to avoid dead zones. Few years ago, only small rectangular GEM modules with default dimensions of 26 × 26 cm^2 were considered due to limitations of the GEM-foil production technology. However, intensive work on improving the technology gives hopes to produce large area foils in the nearest future. Due to this, the sector arrangement of modules was also considered. Finally, it was proposed to replace GEM modules with straw-tubes for the last two stations. All three types of modules have been implemented in the simulation software (see Fig. 1).

At the next step of the simulation chain, each detector module is logically segmented into pads. Manual and automatic segmentation algorithms have been developed for this purpose. In the automatic algorithm, the module granularity is tuned to keep the channel occupancy below a certain value and to provide a certain spatial resolution. The smallest pad sizes at the first station are mostly determined by the occupancy restrictions, while starting from the 3rd station they are limited by the resolution requirements. 3 × 3 mm pads result in up to 10 % occupancy in the central region of the first station. In addition, one can use the manual segmentation algorithm, tune pad dimensions for different radial regions and reduce the number of channels trying to keep physics performance unchanged.

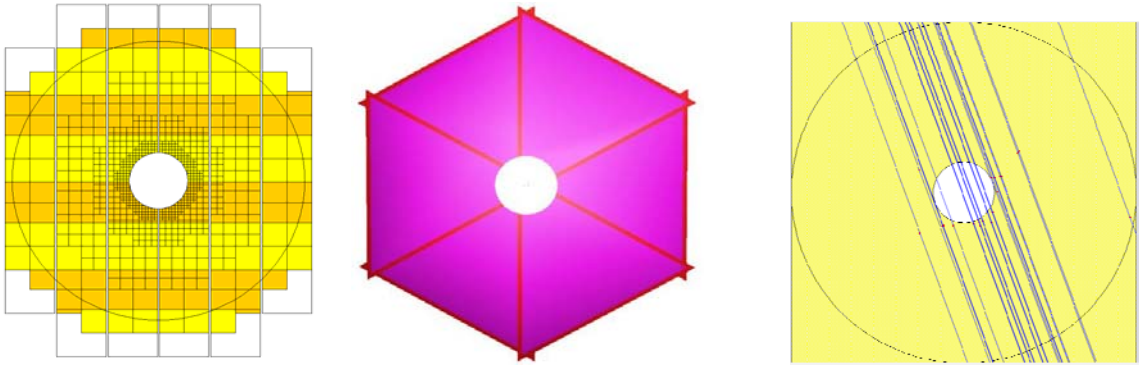

Fig. 1. Three detector concepts implemented in the MUCH simulation software: rectangular GEM modules (left), sector modules (middle), and straw tube modules (right)

Detailed digitization algorithms have been developed for simulation of the realistic detector response. The digitization starts from the simulation of the number of primary electrons per track in accordance with the particle type, energy, track length and corresponding parameters of the Landau distribution. For each primary

electron, the number of secondary electrons is determined with the exponential gas gain distribution. The pad-by-pad response is calculated taking into account the given properties of the readout electronics such as the dynamic range, thresholds and noise parameters. Then, the fired pads are grouped into clusters. Final hit distributions are determined with several cluster deconvolution algorithms. An example of the pad response in the first station is shown in Fig. 2.

Special efforts were devoted to simulations of the timing response since the muon system is foreseen to operate at rates up to 10^7 Hz of Au-Au collisions with the free streaming data acquisition. A typical distribution of busy channels for these rates is shown in Fig. 2, left side.

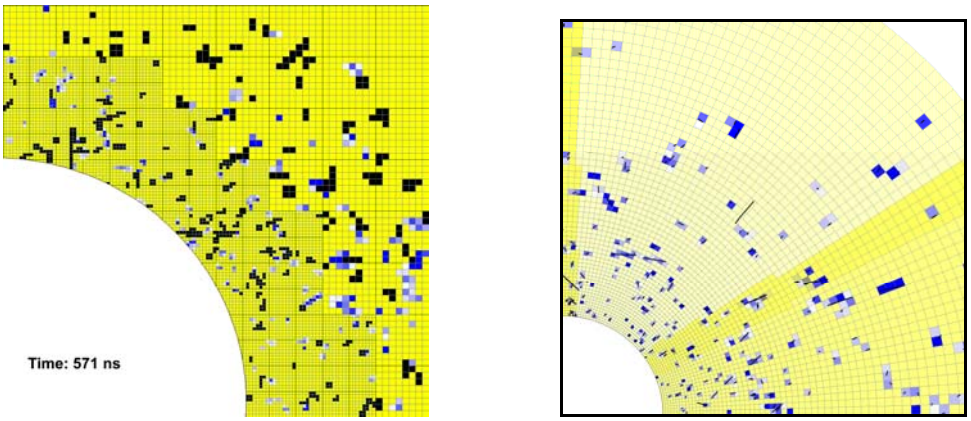

Fig. 2. Typical distributions of fired pads at the first MUCH station in rectangular (left side) and sector (right side) module concepts. The charge distribution is shown with the gradient of blue. Busy channels are shown in black (left side)

In conclusion, we can state that a flexible simulation instrument exceptionally important for the design and optimization of the MUCH detector has been made.

2.2. R&D on choosing the coordinate detectors for the MUCH tracking system

The development of the muon tracking detectors concentrates on the construction and tests of prototype gaseous detectors based on different technologies. The detector layers behind the first and second hadron absorber gaps (with the particle density up to 500 kHz/cm^2) will be based on the GEM technology or on hybrid detectors combining different technologies. In the third and forth absorber gaps (with the particle density up to 5 kHz/cm^2) we foresee double thick GEMs. The multiple-layer straw tubes are considered for the last two stations.

Various prototype detectors were built in PNPI: double and triple thin GEMs (GG and 3G), double thick GEMs (DTG), and hybrids of thin and thick GEMs with Micromegas (MG and MTG). All these prototypes were tested with radioactive sources at a specially made test stand equipped with a gas mixture supply, a HV supply, front-end and readout electronics, and a set of programs for data analysis. During the work in the lab, we got an experience in production technology of all types of the detectors mentioned above, measured the gas gains in dependence on the applied HV, measured the times of charge collection, made estimations of the efficiency and discharge probability, tried different 2- and 3-component gas mixtures with argon and helium as the main gas. This first R&D stage resulted in assembling four prototypes (MG, MTG, GG, and DTG) with the working region of 10 × 10 cm^2 each prepared for tests with accelerator beams. All prototypes had the same pad structure of the readout electrode with every pad size of 1.5 × 3.0 mm^2, and the distance of 0.2 mm between the pads.

In November 2010, the prepared chambers were installed at the CERN test station T-10 (see Fig. 3) to conduct tests with a 5 GeV beam mainly containing protons and π-mesons. For the tests we had only 128 channels of rather slow readout electronics. Therefore, it was possible to equip with the electronics a 5.1 × 1.2 cm^2 region only, all other pads were grounded, and to work with the rate not higher than 1 kHz. A beam spot was formed (see the beam profile obtained with one of the chambers at the right side of Fig. 3)

by the 4-fold coincidence of signals from four scintillation counters, the coincidence signal serving as a trigger one.

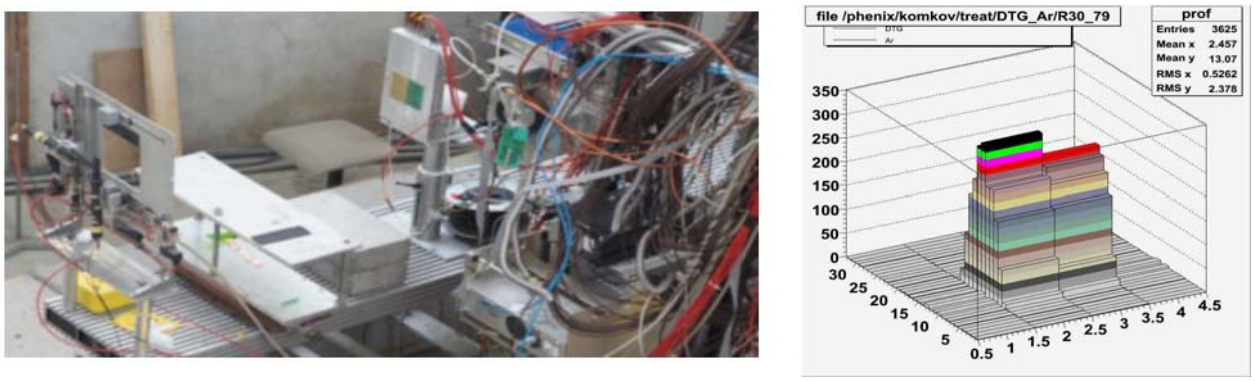

Fig. 3. One of the prepared chambers located at the CERN test station T-10. An example of the beam profile measured with the chamber is also depicted (right side)

Tests were done at different angles relatively the beam direction (0°, 15°, 30° and 45°) and for two gas mixtures $Ar/CO_2/iC_4H_{10}$ (88/8/4) and $He/CF_4/iC_4H_{10}$ (76/22/2).

Main goals of the tests were to measure:

- amplitude spectra;
- gas gains;
- detector efficiency;
- cluster size (number of the fired pads);
- radius of the charge spot induced on the readout electrode.

An example of the measured amplitude spectra for the case of MG detector and two working gases is shown in Fig. 4. For the amplitude spectra we used sums of the signals from all fired neighboring pads. The shapes of the obtained spectra are in good agreement with the Landau distribution.

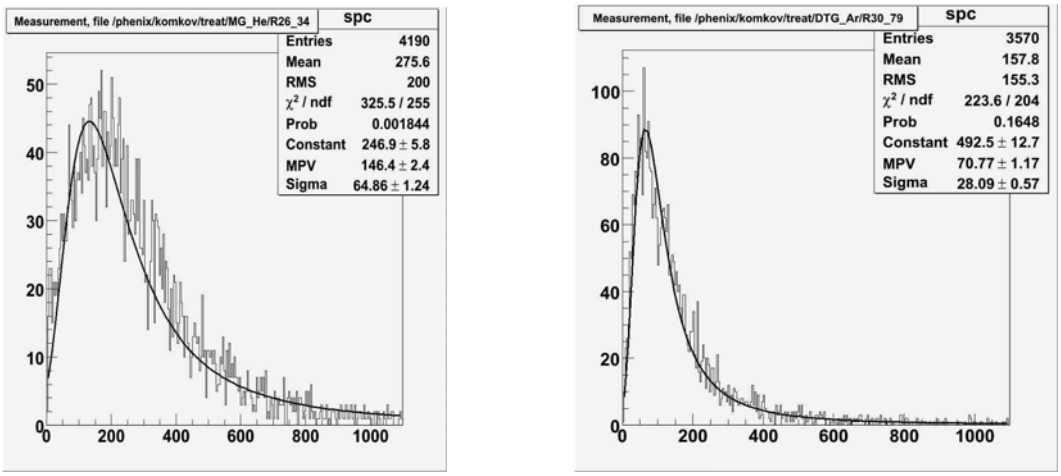

Fig. 4. Amplitude spectra measured by the Micromegas + GEM detector: helium based mixture – left side, argon based mixture – right side. Vertical axis – number of events

The values of the efficiency for all tested detectors, estimated as a ratio of the number of detected events to the number of triggers, are presented in Table 1. An event is considered as detected if at least one of the pads after the pedestal subtraction had the amplitude larger than the threshold of 4 σ, where σ is the width of the electronics noise distribution fitted by a Gaussian. Due to limited beam time we did not measure the dependence of the efficiency from the applied high voltage to get the optimal regime, and used the

working regimes established during the work in the lab with radioactive sources. Table 1 contains also the estimated values of the gas gains. To get the gas gain value we used the following procedure. With the HEED program, the most probable number (MPV_{HEED}) of the produced ion pairs in the drift gap of the known dimension was calculated. By fitting the experimental spectra measured by the charge collecting electrode to the Landau distribution, we know the ADC channel corresponding to the MPV_{LANDAU} multiplied by the gas gain, and using the measured calibration coefficient (0.209 fC/ADC channel or ~ 1250 electrons/ADC channel) we can get the collected charge, or the number of collected electrons corresponding to this MPV_{LANDAU}. The ratio of the measured MPV_{LANDAU} to the calculated MPV_{HEED} gives us the value of the gas gain.

Table 1

GAS GAIN

Detector type	gap (mm)	$He/CF_4/iC_4H_{10}$ (76/22/2)				$Ar/CO_2/iC_4H_{10}$ (88/8/4)			
		MPV_{HEED} (electrons)	MPV_{LANDAU} (channels)	GG $\times 10^3$	eff. (%)	MPV_{HEED} (electrons)	MPV_{LANDAU} (channels)	GG $\times 10^3$	eff. (%)
MG	3.7	7.8	145.6	23.4	98.8	18.2	250.6	17.3	99.9
MTG	4	8.7	96.3	13.9	97.0	20.3	57.4	3.5	99.8
DTG	4	8.7	46.4	6.7	95.0	20.3	73.9	4.6	99.0
GG	4.9	10.8	99.0	11.5	98.2	25.1	41.3	2.1	99.9

The performed tests have shown that for the drift gap of 4 mm, with the used type of electronics and the beam intensity of ~ 1 kHz, we can reach 99–100 % efficiency of the *mip* registration at the gas gain value of $\sim 15 \cdot 10^3$ in the He based gas mixture and $\sim 5 \cdot 10^3$ in the Ar based gas mixture for all types of the detectors under test.

The cluster size distribution and the radius of the charge spot induced on the readout electrode caused by a crossing particle are important characteristics that should be taken into account at the stage of the detector design and optimization. A cluster is defined as a number of the neighboring pads fired (fired means having the amplitude larger than 4 σ, where σ is the width of the noise distribution). The cluster size distributions were measured for the He and Ar based gas mixtures at four angles. An example of the cluster size distributions for a MG detector filled with the He based mixture is presented in Fig. 5.

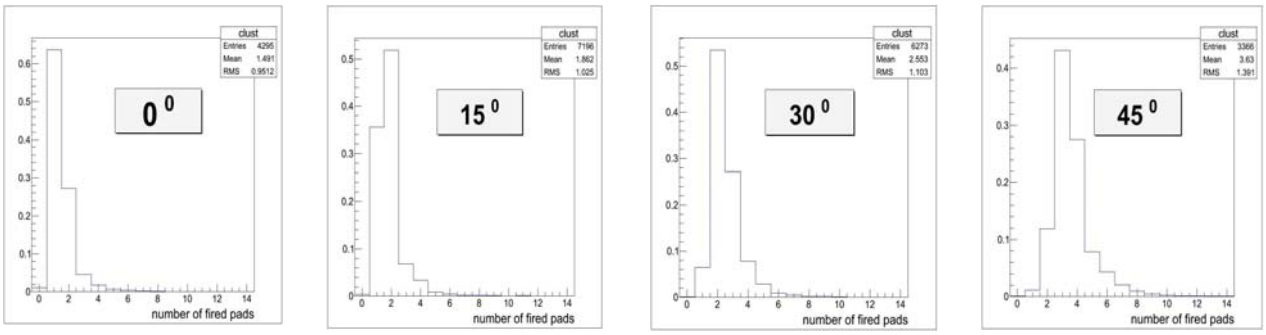

Fig. 5. Cluster size distributions for a MG detector filled with the He based mixture. Horizontal axis – number of fired pads, vertical axis – number of events normalized to 1

It is interesting to compare the cluster sizes for different detectors and gases. Unfortunately, the detectors had different gas gains and different gaps where primary ionization (before gas amplification) was produced. For correct comparisons it was necessary to make some normalization procedure:

- by fitting the measured amplitude spectra to the Landau distribution we get MPV;
- by comparing MPV for different detectors we obtain the coefficients to normalize all MPV to the smallest one that we have for the case of the GG detector with the Ar based gas mixture;
- by changing the signal amplitudes with normalization coefficients and applying then thresholds of 4 σ (where σ is the width of the electronics noise distribution fitted to a Gaussian) we find the corrected cluster distributions.

The corrected sizes of the clusters for the case of 0° are presented in Table 2. For a comparison, Table 2 also shows the efficiency obtained by normalizing the signal amplitudes and applying the threshold at a 4 σ level.

Table 2

Corrected cluster size (for the case of 0°)

Detector type	$He/CF_4/iC_4H_{10}$ (76/22/2)		$Ar/CO_2/iC_4H_{10}$ (88/8/4)	
	mean (number of pads)	eff. (%)	mean (number of pads)	eff. (%)
MG	1.24	97.3	1.72	99.5
MTG	1.31	96.8	1.76	99.6
DTG	1.78	94.5	2.14	98.2
GG	1.63	97.9	2.10	99.9

The radius r_{exp} of the charge spot induced on the readout electrode was estimated in the case of 0° with a simple model (see Fig. 6, left side). A class of events with only one or two neighboring pads fired in the *X* or *Y* row of the pads was separated. For these events, we built the ratio $F = Q_1/(Q_1 + Q_2)$, where Q_1 – maximal amplitude, and $Q_2 \le Q_1$ or $Q_2 = 0$ – amplitude of the signal from the neighboring pad. Considering the *F* distribution (see an example in Fig. 6, right side) along the *X*- or *Y*-coordinate in assumption of the uniform distribution of the beam particles we can get the charge spot radius.

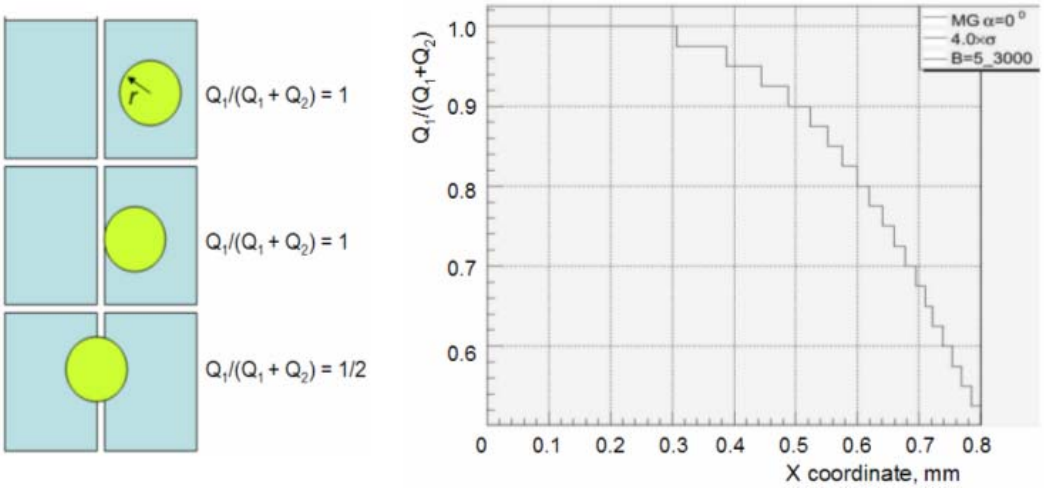

Fig. 6. The model to estimate the charge spot radius *r* (left side). An example of the distribution of the ratio $F = Q_1/(Q_1 + Q_2)$, where Q_1 – maximal amplitude, and $Q_2 \le Q_1$ or $Q_2 = 0$ – amplitude of the signal from the neighboring pad along the *X*-coordinate for a MG detector filled with the Ar based mixture (right side)

The r_{MC} value could be obtained by Monte-Carlo simulation with the following input data:

- geometry of the detector;
- HEED results for pair production in the He and Ar based mixtures;
- Landau distribution of produced ion pairs in the drift gap;
- experimental gas gain.

In the simulation procedure, we varied the spot radius r_{MC} and checked the cluster size distribution obtained by the same manner as was done for the experimental data. The procedure was stopped when the simulated cluster size distribution coincided with the experimental one. The experimental *r* values and those obtained with the simulation for the case of 0° and *X*-direction are presented in Table 3. Practically the same values of *r* were obtained in the consideration of the distribution of the ratio *F* along the *Y*-direction.

Table 3

Experimental (r_{exp}) and simulated (r_{MC}) r values

Detector type	$He/CF_4/iC_4H_{10}$ (76/22/2)		$Ar/CO_2/iC_4H_{10}$ (88/8/4)	
	r_{exp} (mm)	r_{MC} (mm)	r_{exp} (mm)	r_{MC} (mm)
MG	0.18	0.19	0.49	0.48
MTG	0.17	0.16	0.45	0.41
DTG	0.42	0.49	0.65	0.73
GG	0.41	0.44	0.58	0.62

We can see good coincidence of the experimentally obtained and the simulated r values, which means the correctness of the detector model built for the simulation procedure, and right understanding of the detector response on a crossing charge particle. The final choice of the base detectors for the CBM muon tracking system will be made after testing the prototypes in high intensity beams and an environment close to real experimental conditions.

2.3. MUCH mechanics

The CBM project foresees a flexible configuration of the detectors according to the demands of the physics to be studied: after the silicon tracker STS one can put either RICH for electron physics or MUCH to study the decays to muons. The weight of RICH is relatively low, it can be handled with the existing regular bridge crane, while the weight of MUCH is about few hundred ton, and it requires a special displacement system. That is why the MUCH absorbers and superstructure are mounted on a special platform (see Fig. 7) that moves the detector horizontally (from the working position to the parking one and back). The platform is equipped with the mechanisms for displacements and fixation of the detector. In 2008, the PNPI team demonstrated a possibility of RICH and MUCH coexistence in the CBM cavern.

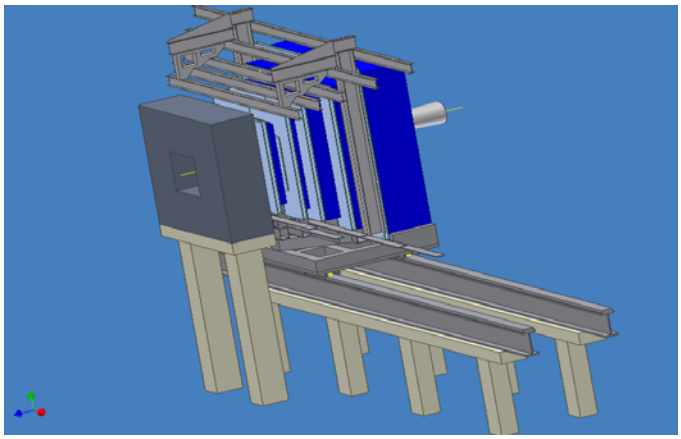

Fig. 7. A version of the general layout for SIS300 configuration of MUCH: blue blocks represent iron absorbers, a grey object at left side of the figure is the dipole magnet. The absorbers and chambers sit on a movable platform that enables MUCH displacements from the working position to the parking one

MUCH consists of tracking stations inserted into the spaces between a set of absorbers. Each tracking station includes three chambers. As there is a beam-pipe in the centre of the detector, the chambers are divided into two halves. Each half-chamber will be equipped with devices that ensure its hanging, displacements, position adjustments, and fixation at the chosen position (for the work at the beam pipe and service apart). The rails for displacements are attached to a space frame, the so called superstructure.

Due to technical difficulties of the large detection elements production, it is proposed to mount a set of the Detection Elements (hereafter DE) of an admissible size onto a rigid support panel. One of the key requirements of MUCH is to reduce its total length in order to minimize the contribution of the muons originated from the in-flight decay of π- and K-mesons. Hence, the tracking stations should be as thin as possible. It is proposed to remove all rigid elements from the DE, even to make DE not self-supporting, and to use the support panel to maintain the shape of the chamber. The exact values of the tolerances of the panel deformation and errors of the DE positioning will be defined during the Monte-Carlo analysis of the set-up.

The design of the support panel is not fixed yet, it could be a composite sandwich (nomex honeycomb with fiberglass skins) or a frame made of standard profiles. In order to reduce the electronic noise and pick-ups, it is recommended to avoid conductive materials. It is also proposed that in order to minimize external mechanical loads to the panel, the distributors of the gas, HV, LV and cooling will be grouped and attached to a separate panel, which will move together with the main one. The service cables should be flexible and sufficiently long to avoid reconnections during displacements of the half-chambers.

The dipole field would cause huge forces applied to the absorbers closest to the dipole and to the superstructure in the case they are made of iron. Most likely these elements will be manufactured of non-ferromagnetic alloys like inox. However, the economic option of using regular steel is not abandoned.

A first version of the integration and assembly scenario has been presented to the collaboration.

3. RICH related activity

The Ring Imaging Cherenkov (RICH) detector is intended to perform an acceptable electron identification and the π-meson suppression in order to provide the feasibility of the low-mass vector meson measurements. The current conceptual layout of the detector is shown in Fig. 8.

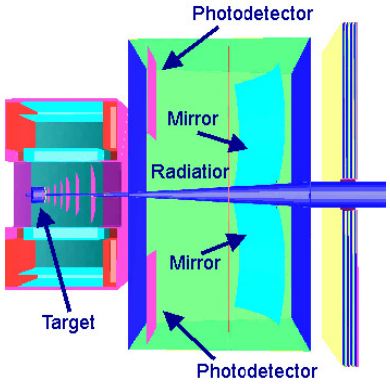

Fig. 8. Conceptual RICH layout

A crucial component of the CBM RICH detector is a mirror system consisting of two parts segmented by a number of tiles with the common surface of about 11.8 m^2. Another essential part of the CBM RICH detector is a gas radiator filled with CO_2 for generation of Cherenkov light. The light is detected by a photodetector consisting, the same way as the mirror system, of two separate units. The efficiency of the electron identification and the π-meson suppression will be defined by the spatial resolution of the RICH detector depending, among other issues, on the precision of the mirror tiles alignment and the stability of the mirror mount system.

3.1. Development of the mirror mount system

One of the main tasks of the segmented RICH mirror design is the development of the mirror tile mount, which is intended to provide a joint between the trapezoid mirror tile and the mirror support structure. Such a connection should not add a noticeable deformation of the mirror tile, but has to provide an independent adjustment of each tile to the common spherical surface with a manual local control or a remote automated one. The precision of the positioning should correspond to the demands of the experiment.

The mount of the trapezoid mirror tile [2] is based on a triangular layout with the acute angles between the lines connecting three support points (see Fig. 9). Each point has the degrees of freedom that allow various movements of the mount legs relatively the mirror tile: three rotations around all space axes (*X*, *Y*, and *Z*) and a shift along the directions showed by arrows in Fig. 9.

The geometry of this 3-point layout is a subject of optimization, the required deformation of the mirror tile under the gravitational force being the purpose function. At the present time, the proposed geometry provides the maximal value of deformation along the radius of the tile of about 5 microns, which

corresponds to 500 microns contribution to the D_0 value – the diameter of the spot with 95 % of the reflected light from the point source at the centre of the mirror curvature.

The mount leg design is shown in Fig. 10. It consists of a Cardan hinge connected to a mirror tile through a ring plate at the mount point. Into another end of the hinge a rotating rod is inserted, which is the base axis of the mount leg. It passes through the mount support and ends with a manual screw. A linear actuator is fixed on the support in parallel to this screw. The actuator plays the same role as the screw but can be operated remotely.

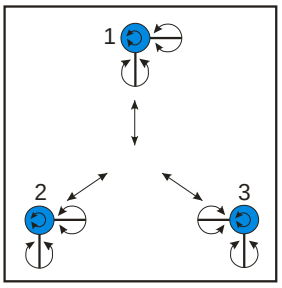

Fig. 9. Layout of the 3-point mount

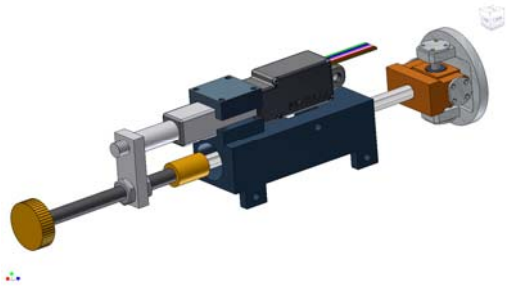

Fig. 10. Mount leg structure (CAD model)

Three mount legs attached to a mirror tile (tripod) represent a complex mechanism with the implicit kinematical properties. Movement of any leg along its axis calls a response of other two legs. Therefore, it is especially important to be sure that no stress arises in this system. A possible method to analyze the kinematical consistency of the proposed mount scheme is to use a 3D model in the frame of CAD systems. The model uses a simplified kinematics, which is adequate to the real hardware design (see Figs. 11, 12). Thus, the number of degrees of freedom of the hinge joints and ranges of the movements correspond to the layout given in Fig. 9. Preliminary tests of the kinematical correctness have shown that the mount assembly in the actual configuration is able to provide the demanded movements.

The first prototype mount of the mirror tile and its study were done for one mirror tile (Fig. 11). The purpose of the tests was mainly to check experimentally the kinematical consistency of the proposed design, as well as the assembling procedure, especially the gluing of the tile to the legs. They showed that in the full range of movements (±15 mm) no mechanical collisions occurred. Hence, the design of the mount based on a Cardan hinge is acceptable.

Preliminary optical tests have demonstrated good optical quality as well. The measured D_o size for this mounted mirror tile is about 1 mm. It correlates with our estimation of the influence of the gravitational force on the D_o value (0.5 mm).

Fig. 11. First prototype of the mirror mount

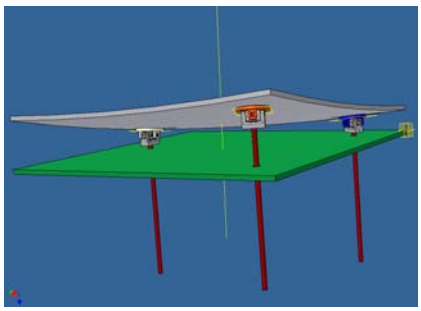

Fig. 12. 3D kinematical model of the mirror mount prototype

The four mount systems (one tile and three actuators in each assembly) were combined into one system on the basis of one overall frame (Figs. 13, 14). This assembly is intended to be integrated into the full-scale RICH prototype and must be operated in the remote mode. The mount legs were assembled on the framework made from the standard aluminum profile. Special wedge attachments were used to connect the

legs to the frame. The tiles were glued by an epoxy composition to the legs afterwards. The initial gap between the tiles was set by spacers (specially prepared calibrated rods).

Tests of the kinematical consistency of the prototype assembly showed the capability of the system to operate the tiles independently without a risk of a mechanical overlap and damaging of the moving parts. A visual optical alignment procedure for the prototype assembly was performed in the horizontal position as well, and was repeated afterwards using an optical procedure with a laser-based system in the working vertical position of the mirror assembly.

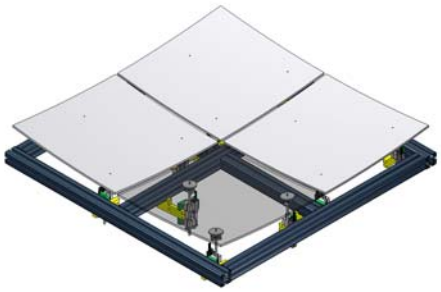

Fig. 13. Preliminary CAD model of the four-mirrors mount

Fig. 14. Real assembly of the four-mirrors mount for the prototype

3.2. Beam tests

Along with other essential components (the photodetector, gas system, high voltage, readout electronics, and software) the described mirror assembly was used to compose the full RICH prototype structure, which was thoroughly and successfully tested during the October 2011 test beam run at CERN. In particular, the level of acceptable mirror misalignment was estimated using a remote control of the mirror positions with the actuators (see Figs. 15, 16).

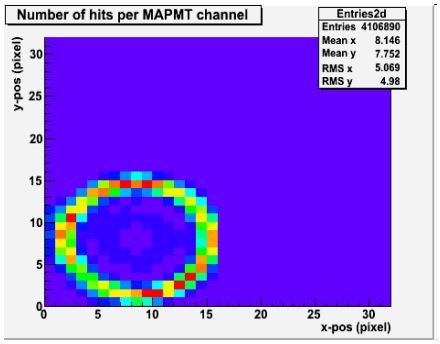

Fig. 15. Cherenkov integrated rings before the mirror position staggering

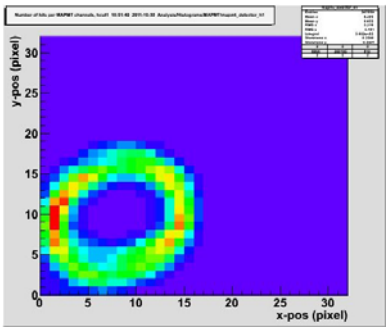

Fig. 16. Cherenkov integrated rings after the mirror position staggering

In conclusion, we can note the following:

- mirror tile mount mechanics was developed with manual and remote control options;
- its mechanical (static and kinematical) properties were studied;
- four mirror tiles were equipped with this mechanics for a full RICH CBM prototype;
- the RICH prototype was thoroughly and successfully tested during the CERN beam test.

3.3. RICH gas system prototype

A CBM – RICH Prototype Gas System [3] has been designed to provide pure CO_2 gas to the RICH prototype at the correct differential pressure. The system operates as a closed-circuit gas system. During normal operations, the system measures and keeps constant differential pressure at the 2 mbar level.

Oxygen and humidity analyzers monitor the purity of the recirculation gas. A fraction (up to 30 %) of the recirculation gas can run through a purifier and a dryer to remove oxygen and moisture. There is a possibility to check the gas purity with analyzers after the purifier and dryer.

A computer driven data acquisition/control system monitors all the process variables, and provides the differential pressure stabilization. The computer system flags quantities which fall outside of predefined limits, initiates corrective actions, and estimates the CO_2 refraction index.

The developed control computer software, successfully used in the STAR and PHENIX experiments at RHIC, provides reliable data acquisition, automated alarm condition handling and manual control. All alarm events and system variables are logged into a database. A special program was designed for visualization of the actual state of the system.

The gas system is assembled in a single 19″ rack (Fig. 17).

Fig. 17. RICH Prototype Gas System

It was a good opportunity to test the gas system during the beam test at CERN in October 2011. The major goal was to check the differential pressure stability in the recirculation mode. The differential pressure of the RICH prototype was stable at 2.0 ± 0.1 mbar although the barometric pressure varied in a range of 22 mbar.

The efficiency of the gas system dryer and purifier was also checked. The inner surface of the RICH prototype vessel did not pass through a special cleaning process, and a lot of water and oxygen was adsorbed by the walls and inner structure elements. Even in these conditions, both the dryer and the purifier were able to remove moisture and oxygen to the required level.

In general, the gas system provided stable operation with stabilization of all required gas parameters in the RICH prototype, and was reliably controlled. This system can be used in the future for the whole RICH detector with minor changes.

References

1. http://www.fair-center.de/fileadmin/fair/publications_FAIR/FAIR_GreenPaper_2009.pdf
2. V. Dobyrn *et al*., Development of a Mirror Mount System for the CBM – RICH Prototype Detector, CBM Progress Report 2011, Darmstadt, p. 39.
3. L. Kochenda *et al*., A Gas System for the CBM – RICH Prototype, CBM Progress Report 2010, Darmstadt, p. 31.

PNPI IN THE PANDA PROJECT AT FAIR

V.A. Andreev, S.L. Belostotski, O.Ya. Fedorov, G.E. Gavrilov, A.A. Izotov, A.Y. Kiselev, N.G. Kozlenko, P.V. Kravchenko, O.V. Miklukho, Y.G. Naryshkin, D.V. Novinsky, M.P. Levchenko, A.V. Shvedchikov, S.I. Trush, V.V. Vikhrov, D.O. Veretennikov, A.A. Zhdanov

1. Introduction: the PANDA experiment at HESR, GSI

The PANDA (AntiProton ANihilation at DArmstadt) experiment [1] is one of the key projects at the future Facility for Antiproton and Ion Research (FAIR), which is currently under construction at GSI, Darmstadt. The FAIR accelerators will deliver primary proton and ion beams, as well as secondary beams of antiprotons or radioactive ions of high intensity and high quality.

The PANDA experiment will perform precise studies of antiproton-proton annihilations and reactions of antiprotons with nucleons of heavier nuclear targets. It will benefit from antiproton beams with unprecedented intensity and quality provided by the High-Energy Storage Ring (HESR) in the momentum range from 1.5 to 15 GeV/*c*. In a High momentum Resolution mode (HR) of HESR defined for a limited momentum range from 1.5 to 8.9 GeV/*c*, the relative momentum spread of the beam is reduced to 10^{-5} with 10^{10} circulating antiprotons and the peak luminosity of 2×10^{31} cm^{-2}s^{-1} (assuming the target density of 4×10^{15} atoms/cm^{-2}). In a High Luminosity mode (HL) available for the full momentum range (from 1.5 to 15 GeV/*c*), the peak luminosity reaches 2×10^{32} cm^{-2}s^{-1} at the same target density. The relative momentum spread in this regime is expected to be about 10^{-4}. The HR and HL modes are established to meet the challenging requirements of the PANDA experimental program.

The PNPI group in the PANDA project is responsible for the Forward Time-Of-Flight (FTOF) detectors described in sections 2 and 3. The process $\bar{p}p \to \bar{Y}Y$, where Y is a strange or charm baryon (*e.g.*, Λ_c), is studied by the PNPI group using the PANDA Monte Carlo package as a benchmark reaction to determine particle identification capabilities provided by the FTOF in combination with other PANDA sub-detectors.

The PANDA experiment exploits an extraordinary physics potential of the projected high quality antiproton beams. Main experimental topics of the hadron physics program are briefly itemized in the following.

Charmonium Spectroscopy. A precise measurement of all states below and above the open charm threshold is of great importance for QCD. All charmonium states can be formed directly in $\bar{p}p$ annihilation in the invariant mass range $2.25 < M(\bar{p}p) < 5.46$ GeV. At full luminosity, PANDA will be able to collect several thousand $\bar{c}c$ states per day. By means of beam momentum scans, it will be possible to measure masses with accuracies of the order of 100 keV and widths to 10 %, or better.

Search for Gluonic Excitations. One of the main challenges of hadron physics is the search for gluonic excitations: *i.e.*, hadrons consisting of pure glue and hybrids, which consist of a $\bar{q}q$ pair and excited glue. Due to additional gluon degrees of freedom, these objects may have exotic quantum numbers J^{PC}, which makes their experimental identification easier. Specifically, further exploration of recently discovered *X*, *Y*, and *Z* ($\bar{c}c$ like) states is assumed, as well as searches for multi-quark (quark molecule) states.

Electromagnetic Processes. It has been shown that a study of proton form factors is feasible in the time-like region by measuring the $\bar{p}p \to e^+e^-$ exclusive channel up to S = 14 (GeV)^2. The statistical precision of these measurements is expected to essentially surpass that of the existing to date world data. In order to access the "unphysical region" $S < (2M_p)^2$, the inelastic $\bar{p}p \to e^+e^-\pi^0$ channel is also planned to study.

Study of Hadrons in Nuclear Matter. So far, experiments have been focused on the light quark sector. The high-intensity antiproton beam of up to 15 GeV/*c* will allow an extension of this program to the charm sector both for hadrons with hidden and open charm.

Hyperon Physics. The antiproton beam at FAIR allows for efficient production of hypernuclei with more than one strange hadron, making PANDA competitive with the planned dedicated experiments. Another aspect of the hyperon (and charm) physics is a measurement of the cross sections and polarization

parameters in exclusive reactions like $\bar{p}p \to \bar{\Lambda}\Lambda$, $\bar{p}p \to \bar{\Xi}\,\Xi$, $\bar{p}p \to \bar{\Omega}\,\Omega$, $\bar{p}p \to \bar{\Lambda}_c\Lambda_c$. Of particular interest is the study of production of multi-strange and charm baryons.

There are also many other important and challenging topics, like, *e.g.*, CP violation in the hyperon sector, which are still under investigation and not presented in the physical program discussed above. The PANDA physics in more details is described in Ref. [2].

2. Forward Time-Of-Flight detectors (FTOF)

The PANDA experiment is designed to achieve 4π solid angle, high resolution for tracking, good particle identification, high precision calorimetry, high rate capabilities and versatile readout and event selection. A detailed description of the PANDA detector can be found in Ref. [3]. The detector is composed of two magnetic spectrometers: the Target Spectrometer (TS), based on a superconducting solenoid magnet and the Forward Spectrometer (FS) based on a dipole magnet (Fig. 1). The TS is designed to have practically 4π solid angle, while the FS is used to measure small angle tracks. The TOF measurements are foreseen both in the TS (Barrel TOF) and FS (FTOF detectors).

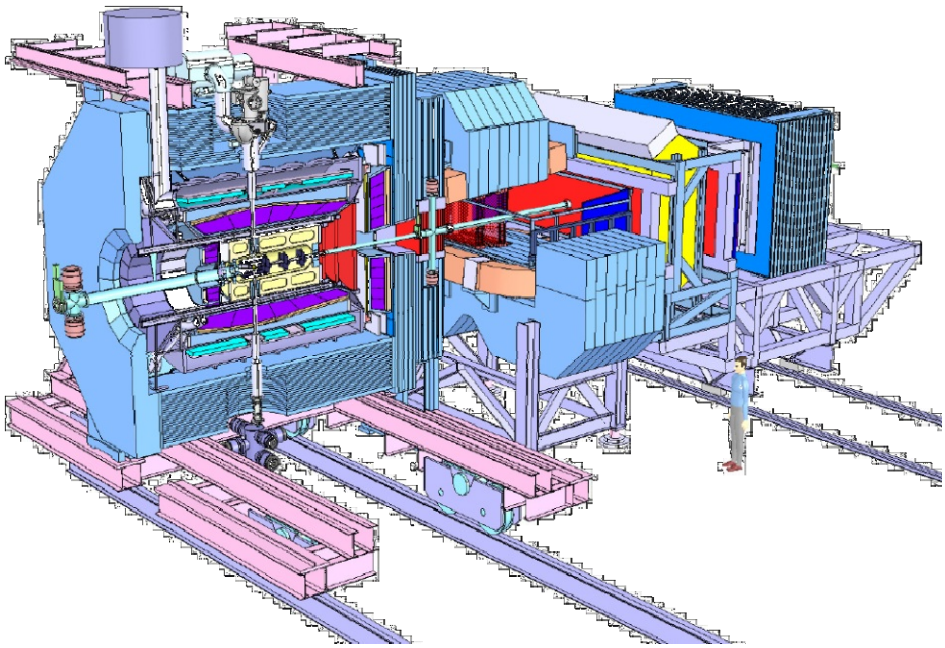

Fig. 1. Overview of the PANDA detector: a detailed description can be found in Ref. [3]

Prototyping and building of the FTOF detectors is a full responsibility of the PNPI group in the PANDA Collaboration. The FTOF is dedicated to measure the TOF of forward particles emitted within the FS acceptance under laboratory angles below 5° and 10° in the vertical and horizontal directions, respectively. The FTOF consists of scintillation counters built of plastic scintillator (Bicron 408) slabs with fast photo-detector readout. The counters are placed as a wall about 7.5 m downstream the target and in the rear part of the dipole magnet inside its opening. Locations of the FTOF wall and the scintillation counters in the dipole gap (dipole TOF detectors) are indicated in Fig. 2.

The FTOF wall depicted in Fig. 3 consists of 66 scintillation counters: 20 counters in the central part and 46 counters in the side parts (23 counters in each side part). The height of all plastic scintillator slabs is 140 cm, and their thickness is 2.5 cm, while the width of the slabs is 5 and 10 cm for the central and side parts, respectively. Each scintillator is viewed from both ends by high time resolution PMTs. It is planned to use Hamamatsu R4998 or R2083, depending on the slab width and light guide configuration. The opening in

the central part of the wall allows for passing the beam vacuum pipe through the wall. It is made asymmetrically because of deflection of the beam by the PANDA dipole.

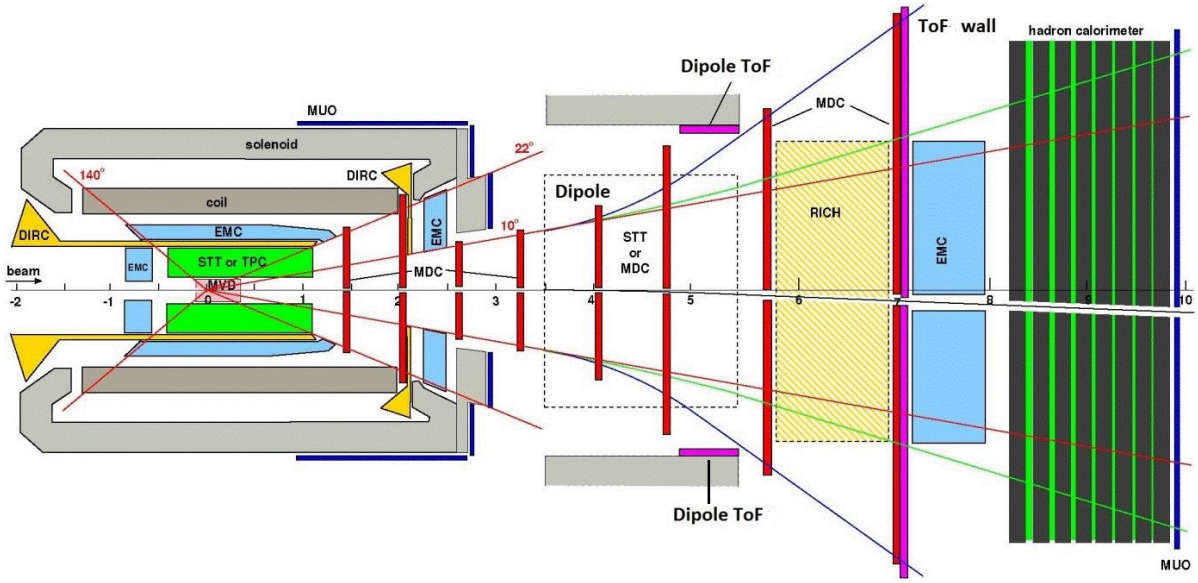

Fig. 2. Schematic top view of the PANDA detector with the FTOF wall and the dipole TOF locations

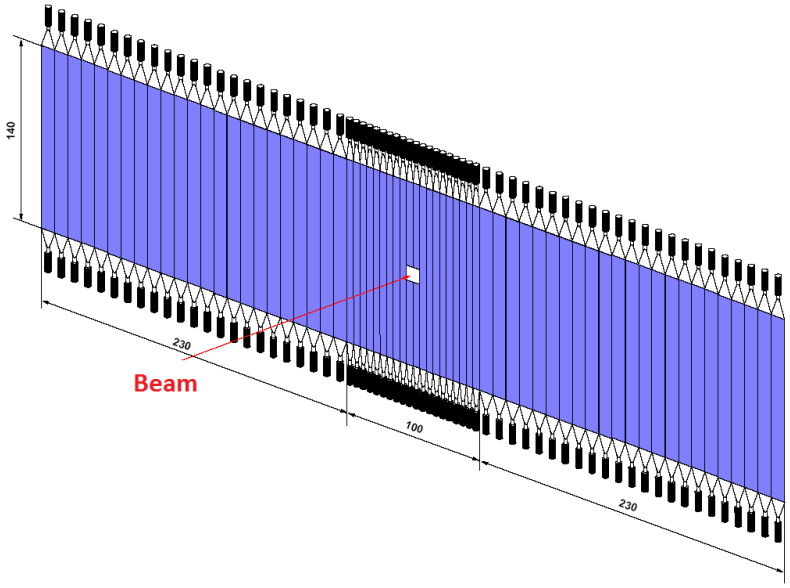

Fig. 3. FTOF wall configuration (described in detail in text)

The dipole TOF detector is designed for detection of low momentum particles strongly deflected by the dipole magnetic field. It consists of two sets of scintillation counters to detect particles of opposite charge deflected by the dipole. Each (left and right) detector is preliminary planned to equip with 10 counters. The height of slabs in the dipole gap is planned to be 100 cm, the width being 10 cm. The slab thickness and the final configuration of the dipole TOF detectors are not finally optimized. This will depend on the results of Monte Carlo simulations of several benchmark reactions according to the PANDA experimental program. It must also comply with the final performance of the PANDA dipole magnet and the forward tracking system.

Given a high level of the magnetic field, magnetic-field-protected photomultipliers (*e.g.*, PMT 187, production of the "Electron" firm in St. Petersburg) or SiPM's (Avalanche Micro-Pixel Photo Diodes with the expected high time resolution) will be used for light collection from the scintillation slabs in the dipole gap.

The performance of the FTOF detectors was investigated using the PANDA Monte Carlo (MC) with the Dual Parton Model generator [4] applied for hadron production on the hydrogen target and the antiproton beam momentum in the range from 2 to 15 GeV/*c*. The integrated rates of hadrons emitted within the FS acceptance are presented in Table 1. The main contribution to the total rate in the $\bar{p}$ beam momentum range under study is related to a sharp forward peak of $\bar{p}p$ elastic scattering. As a source of background, this peak can be essentially supressed by kinematical criteria. Other hadron count rates are found to be substantially lower.

Table 1

Integrated rates of hadrons within the acceptance of the FS at the HESR cycle-averaged luminosity $L = 10^{32}$ cm^{-2}s^{-1}

$\bar{p}$ beam momentum, GeV/*c*	Pion rate, 1/s	Kaon rate, 1/s	Proton rate, 1/s	Antiproton rate, 1/s
2	3.9×10^5	2×10^3	1.2×10^4	1.07×10^6
5	6×10^5	7.8×10^3	3.8×10^4	9.5×10^5
15	9.6×10^5	4.7×10^4	3.2×10^4	8.2×10^5

The rates of individual slabs in the FTOF wall related to various processes versus the *X* axis perpendicular to the beam line in the horizontal plane are shown in Fig. 4. The rates are calculated in bins equal to the slab widths in the side parts of the wall, *i.e.*, 10 cm both for the central and side parts.

One can conclude that even in the central part of the FTOF wall the total rates are below the limit admitted by the technical characteristics of the fast scintillation counters. The individual rates of the scintillation counters in the dipole gap (dipole TOF detectors) are expected to be on the level of a few per cent of those in the FTOF wall.

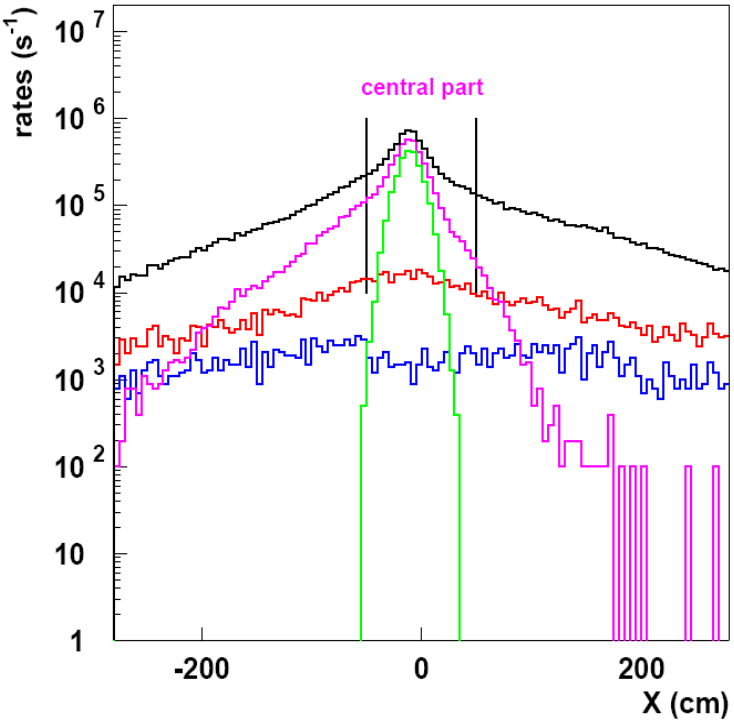

Fig. 4. Forward TOF wall rates versus the *X* axis perpendicular to the beam line at the 15 GeV/*c* antiproton beam. The rates are normalized to 10^7/s interactions in the target. The black curve is the total rate of all charged particles emitted from the target, the purple curve is the rate of antiprotons both from elastic $\bar{p}p$ scattering and inelastic reactions, the green curve shows antiprotons from elastic scattering only, the red curve is all charged particles produced in the beam vacuum pipe, and the blue curve corresponds to e^+e^- pairs produced in the beam vacuum pipe by gammas emitted from the target as products of the $\pi^0 \to 2\gamma$ decay

The FTOF capabilities in hadron identification were simulated assuming that the FS momentum resolution is $\sigma_p / p = 0.01$ and the TOF resolution of an individual scintillation counter is $\sigma_{TOF} = 50$ ps or 100 ps. The results obtained for the case of the maximal antiproton beam momentum (15 GeV/c) are presented in Fig. 5. As can be seen, the TOF information obtained with the help of the FTOF wall provides a reliable pion and kaon identification up to the secondary particle momentum of 2.5 GeV/c (up to 3.5 GeV/c for simulations with $\sigma_{TOF} = 50$ ps) and proton (antiproton) identification up to 4 GeV/c (up to 5.3 GeV/c for $\sigma_{TOF} = 50$ ps). The particle mass is reconstructed using the equation

$$m = p\sqrt{\frac{t^2}{t_c^2} - 1}\,. \tag{1}$$

Here p is the particle momentum, $t_c = L/c$, L is the length of the particle track counted from the interaction point (start point) to a stop TOF counter, c is the speed of light ($c = 1$), t is the measured TOF, *i.e.*, $t/t_c = 1/\mathrm{v}$, where v is the particle velocity. A fractional uncertainty of the calculated mass can be estimated as

$$\frac{\delta m}{m} = \sqrt{\left(\frac{\delta p}{p}\right)^2 + \gamma^4\left(\frac{\sigma_{TOF}}{t}\right)^2}\,, \tag{2}$$

where $\gamma = 1/(1 - \mathrm{v}^2)^{1/2}$. Due to the relativistic γ factor, the TOF resolution of 100 ps gives the main contribution to the mass smearing for the particles with the momenta $p \geq 1$ GeV/c, while the momentum resolution of 1 % has a much smaller effect. The uncertainty in t_c, which comes from the track reconstruction in the magnetic field of the target solenoid and the FS dipole, is estimated to be on the level of a few ps, *i.e.* can be neglected.

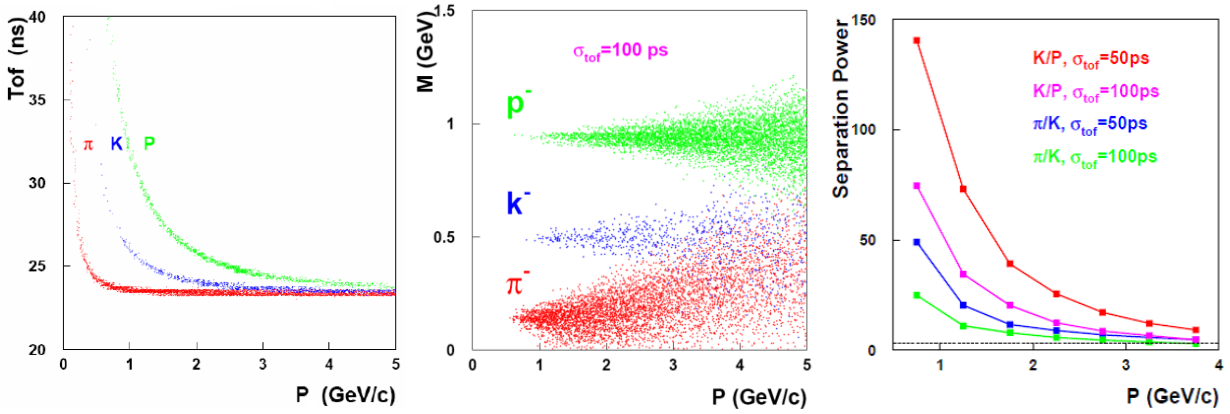

Fig. 5. TOF of hadrons detected by the FTOF for the 15 GeV/c antiproton beam (left panel). Hadron masses reconstructed using the TOF information with the TOF resolution of $\sigma = 100$ ps (middle panel). Proton-kaon and kaon-pion separation powers (red, pink, blue, and green lines); the dash line shows the 3σ separation (right panel)

Construction of a dedicated start counter in the interaction point area is technically not feasible and not foreseen for the PANDA detector. The TOF information is assumed to be obtained using the time correlations between two or more responded scintillation counters of the FTOF and/or Barrel TOF detectors. The TOF is then extracted off-line in combination with other criteria similar to the HADES experiment at GSI. The efficiency of such a procedure will depend on the multiplicity of the particles produced in the reaction under investigation, the event topology and the background situation. It is typically high for many benchmark reactions. A positive feature of this approach is that the overall time resolution in this case is improved with the increase of n, where n is the number of the responded counters.

Hadrons with the momentum in the range 2–4 GeV/c will be identified by combining information from the TOF and the forward RICH detectors. At higher momenta, provided the PID is available with the help of

RICH, the TOF detector is used to establish the start of the TOF of a particle detected by the FS which is important for the PANDA trigger-less data taking procedure.

3. Experimental tests of prototypes of the FTOF detectors

The prototyping of a high time resolution detector for the PANDA experiment was started by selection of appropriate fast photo-detectors. Two types of PMTs were chosen for the FTOF wall: Hamamatsu R4998 for the slabs of 5 cm width and R2083 for those of 10 cm width. Both PMT samples coupled to a small ($2 \times 2 \times 2$ cm^3) plastic scintillator were tested using a ^{90}Sr radioactive source. It was found that the inherent time resolution of an individual PMT was better than 50 ps. For the dipole TOF, a magnetic-field-protected PMT 187 produced by the "Electron" firm in St. Petersburg was preliminary selected. As an alternative, Hamamatsu MPPC S10931-50p were tested. Unfortunately, the time resolution of the tested SiPMs was found to be worse than 160 ps. The final choice between PMTs and SiPMs for the strong magnetic field case has not yet been made having in mind good prospects in investigations of SiPM matrices with much better time resolution and larger light collection area [5].

Prototypes of the FTOF scintillation counters with the projected dimensions of the plastic scintillators were tested using elastically scattered protons with energies 730 [6] and 920 MeV at the PNPI 1 GeV proton syncrocyclotron, and at the 2 GeV proton test beam at the COSY accelerator in Juelich. The COSY test beam intensity could be varied from 10^4 to 10^7 1/s, which allowed for control of high rate capability. At the COSY test beam, the readout was based on the Trigger and Readout Board interface (TRB) formerly developed for the HADES experiment. The TRB, recently upgraded, is presently assumed to be used as a prototype of the versatile readout for the PANDA experiment. Here we briefly summarize the results of these tests mostly focusing on the recent experiment in Gatchina using 920 MeV protons. The tested samples are listed in Table 2.

Table 2

Samples of scintillation counters tested using 920 MeV protons at PNPI

Scintillation slab dimensions	Photo multiplier tube	Comments
140 × 10 × 2.5 cm	Hamamatsu R2083	Accepted as a prototype for the FTOF wall
140 × 5 × 2.5 cm	Hamamatsu R4998	Accepted as a prototype for the FTOF wall
140 × 2.5 × 2.5 cm	Hamamatsu R4998	Variant of a prototype with a smaller scintillator width
140 × 10 × 1.5 cm	Hamamatsu R2083	Projected originally for the FTOF wall
140 × 5 × 1.5 cm	Hamamatsu R4998	Projected originally for the FTOF wall
140 × 5 × 2.5 cm	Electron PMT187	Magnetic field protected, tentatively projected for the dipole TOF
100 × 10 × 2.5 cm	Electron PMT187	Magnetic field protected, tentatively projected for the dipole TOF

The time resolution was calculated using offline corrections on the event basis which took into account raw TDC and QDC information together with proton hit position in the slab measured with the help of multi-wire proportional chambers. The results of these tests are itemized below:

- for samples of the scintilation counters accepted as prototypes for the FTOF wall, the off-line time resolution of 70–80 ps was obtained which meets the requirements of the PANDA experiment. The time resolution is slightly better for the counters based on the slabs of 5 cm width;
- the time resolution of 60 ps was obtained for the slabs of 2.5 cm width. Practical application of such slabs would result in substantial increase of the number of channels which confronts the detector cost limitation;

- samples with slabs of 1.5 cm thickness originally projected for the FTOF wall showed essentially worse time resolution than those of 2.5 cm finally accepted as the TOF wall prototypes;
- the magnetic field protected PMTs 187 coupled with $140 \times 5 \times 2.5$ cm^3 and $100 \times 10 \times 2.5$ cm^3 slabs were also tested. The data are analysed. Further investigations are needed including tests in a strong magnetic field;
- an alternative choice of a SiPM matrix for the dipole TOF is to be investigated. In particular, provided we suppose to use silicon photo-detectors, their radiation hardness must be studied. These measurements have already been started at PNPI using the 1 GeV proton beam of the synchrocyclotron in the frames of the European Union Seventh Framework Program (FP7/2007–2013).

We are grateful to E.M. Ivanov, head of the PNPI synchrocyclotron department, and the management of the COSY accelerator in Juelich for their significant help in carrying out the test experiments. The tests at the COSY beam in Juelich and the SiPM radiation hardness tests at PNPI were partly supported from the funds of the European Union Seventh Framework Program (FP7/2007–2013). We are grateful to M. Palka from the Jagellonian University, Krakow, for his valuable contribution to the experimental set-up and effective participation in test experiments in Juelich.

References

1. PANDA Collaboration, Letter of Intent for PANDA – *Strong Interaction Studies with Antiprotons*, Technical Report FAIR-ESAC (2004).
2. PANDA Collaboration, Physics Performance Report (2009), arXiv:0903.3905v1.
3. PANDA Collaboration, Technical Progress Report for PANDA, FAIR-ESAC (2005).
4. A. Capella, U. Sukhatme, C.I. Tan, and J. Tran Thanh Van, Rhys. Reports **236**, 225 (1994).
5. Gabriela Losa *et al*., IEEE Nuclear Science Symposium Conference Record (2007).
6. S.L. Belostotski *et al*., Preprint PNPI-**2833**, Gatchina (2010).

PNPI IN THE NUSTAR PROJECT AT FAIR: INTRODUCTION

The NUSTAR project is devoted to the study of NUclear STructure, Astrophysics, and Reactions. NUSTAR encompasses all experiments that will be benefiting from the unique possibilities opened up through the new fragment separator Super-FRS, which will deliver an unprecedented range of Radioactive Ion Beams (RIBs). The experiments will exploit beams of different energies and characteristics at three branches; the high-energy branch utilizes the RIBs at relativistic energies (300–1500 MeV/u) as created in the production process, the low-energy branch aims at using beams in the range of 0–300 MeV/u, whereas the ring branch will exploit cooled and stored beams in the storage ring NESR. These projects are gathered within the NUSTAR Collaboration and share development and other synergies across the projects.

The NUSTAR project is based on the following seven subprojects.

1. The HISPEC/DESPEC experiments are intended to address questions in nuclear structure, reactions and nuclear astrophysics by means of high-resolution gamma-ray spectroscopy based on cutting edge germanium detector technology.

2. The aim of the R^3B project is to develop and construct a versatile reaction set-up with high efficiency, acceptance, and resolution for kinematically complete measurements of reactions with high-energy radioactive beams. The set-up will be located at the focal plane of the high-energy branch of the Super-FRS.

3. The aim of the MATS experiment is to perform precision measurements of very short-lived nuclei using an advanced trapping system for highly-charged ions. The experimental set-up MATS is a unique combination of an electron beam ion trap for charge breeding, ion traps for beam preparation, and a high precision Penning trap system for mass measurements and decay studies.

4. The aim of the LaSpec experiment is to perform laser spectroscopy of radioactive isotopes and isomers, which is an efficient and model-independent approach for determination of nuclear ground and excited state properties. Hyperfine structures, isotope and isomer shifts in electronic transitions exhibit readily accessible information on the nuclear spin, magnetic dipole and electric quadrupole moments, as well as root-mean-square charge radii. The obtained results will provide fundamental information on the structure of nuclei at the limits of stability.

5. The ILIMA experimental program is based on the combination of the in-flight separator Super-FRS and a system of storage rings CR – RESR – NESR. The Super-FRS will be an ideal tool to provide short-lived nuclides of all elements for precise mass and half-life measurements in the new storage rings. Unique investigations of decay modes and half-lives of stored bare and highly charged nuclides are possible. Another important feature of the new facility will be the access to pure isomeric beams. Two methods will be used for accurate mass measurements of stored exotic nuclei: “Schottky Mass Spectrometry for electron-cooled beams of longer-lived isotopes” and “Isochronous Mass Spectrometry” for short-lived fragments.

6. In the ELISE project, scattering experiments at internal targets are planned in the New Experimental Storage Ring (NESR) with radioactive ions at energies up to 740 MeV/u. Additionally, an intersecting electron-ion ring (*e*A collider) will allow to scatter electrons with an energy of 125–500 MeV off exotic nuclei. The *e*A collider will enable for the first time to perform elastic, inelastic and quasielastic electron scattering off shortlived radioactive isotopes. Charge distributions, transition form factors in giant resonance or electro-fission experiments and spectral functions can be measured with a clean electromagnetic probe.

7. The aim of the EXL experiment is to study the structure of unstable exotic nuclei in light-ion scattering experiments at intermediate energies. The objective is to capitalize on light-ion reactions in inverse kinematics by using novel storage-ring techniques and a universal detector system providing high resolution and large solid angle coverage in kinematically complete measurements.

PNPI physicists plan to participate in the project NUSTAR in the experimental programs MATS and R3B.

PNPI IN THE MATS PROJECT AT FAIR

PNPI participants of the MATS Collaboration:
S.A. Eliseev, Yu.I. Gusev, P.A. Kravtsov, A.Kh. Khusainov, D.A. Nesterenko, Yu.N. Novikov, A.V. Popov, A.K. Pustovoit, D.M. Seliverstov, M.D. Seliverstov, S.V. Tchenmarev, V.A. Trofimov, A.A. Vasiliev, G.K. Vorobjev, and M.E. Vznuzdaev

1. Introduction

Ion traps occupy a weighty place among methods of modern physics experiments. These traps make it possible to study the problems of physics in a wide range: from the cosmological scale to atomic and nuclear dimensions and from astrophysics to nuclear, atomic, and molecular physics, working with particles in a wide range of mass from the atoms of superheavy elements to elementary particles, including a tiny neutrino [1]. The Penning Trap Mass Spectrometry (PTMS) relates to the low energy region and complements ultra-high energy experiments performed with particle colliders. Both ultra-low and ultra-high energy approaches may provide a complete picture of the properties of matter in Nature.

Ion traps have come into use in nuclear physics recently. Ions can be confined for a long time in traps, making it possible to study their atomic and nuclear structure. Traps can be installed directly in beams of short-lived nuclides in the on-line regime, thus investigating exotic nuclides. The MATS project (precision Measurements of very short-lived nuclides using an Advanced Trapping System for highly-charged ions) [2] is one of the projects combined by the association of scientists NUSTAR (NUclear STructure, Astrophysics, and Reactions). The objective of this scientific collaboration is to study the structure of nuclei under extreme conditions, nuclear reactions, and nuclear astrophysics. The MATS project presupposes PTMS of very short-lived nuclides in a wide range of mass numbers with the use of the FAIR accelerator complex, which can produce nuclides in the "inverse fragmentation" reaction, almost completely covering the Periodic Table of elements. The expected intensity of the FAIR radioactive beams can be many orders of magnitude higher than that in the currently functioning facilities. Thus, FAIR can provide an unprecedented variety of radioactive samples for investigations by means of PTMS with the proposed MATS facility. The MATS project incorporates about 20 laboratories from 10 countries.

This paper has a goal to present the MATS project at FAIR (Darmstadt) with the emphasis on the PNPI contribution.

2. MATS tasks

Precision measurements of nuclear masses (*i.e.*, the total binding energy) that are basic characteristics of nuclei pose the following problems of physics:

- construction of a precise mass surface (landscape) of the nuclear chart;
- determination of the limits of proton and neutron stability of nuclei;
- construction of the isomeric states landscape;
- determination of the pathway of the astrophysical processes (*r* and *rp*) under high temperature conditions in stars;
- checking the hypothesis of the vector current conservation and the unitarity of the Cabibbo – Kobayashi – Maskawa matrix.

The PTMS at MATS can solve each of these problems by precise measurements of a large number of nuclides, including exotic ones whose masses are still unknown. Indeed:

- the mass landscape for ground and isomeric states of nuclides can be determined only after the masses of a large number of nuclides have been measured;
- the determination of the boundaries of the nucleon stability (the so called "drip-lines") presupposes the knowledge of the separation energy of nucleons (*i.e.*, the corresponding mass differences) along the expected boundary;
- the pathways of the astrophysical explosive processes (rapid proton capture "*rp*", and rapid neutron capture "*r*") fully depend on the proton and neutron separation energies, respectively, that is,

on the corresponding mass differences, which should be known along the expected lengthy process paths on the chart of the nuclides. Such a pathway for the *r* process is shown in Fig. 1, which represents the nuclear chart of interest. As can be seen in Fig. 1, the *r*-process pathway largely passes along the regions of extremely neutron-rich nuclides which have yet to be discovered. For this reason, the task of the MATS project will be not only to measure the mass of these nuclides but at first to discover them. The knowledge of the right position of the *r*-process pathway in combination with the known solar element abundances, shown in Fig. 1 [3], paves the way for determination of the astrophysical temperature and neutron density giving rise to the fast multipole capture. It is expected that the masses of the most nuclides participating in the *r* process can be determined with MATS. There are also a plenty of nuclides from the valley of stability towards the *r*-process path whose masses also should be determined.

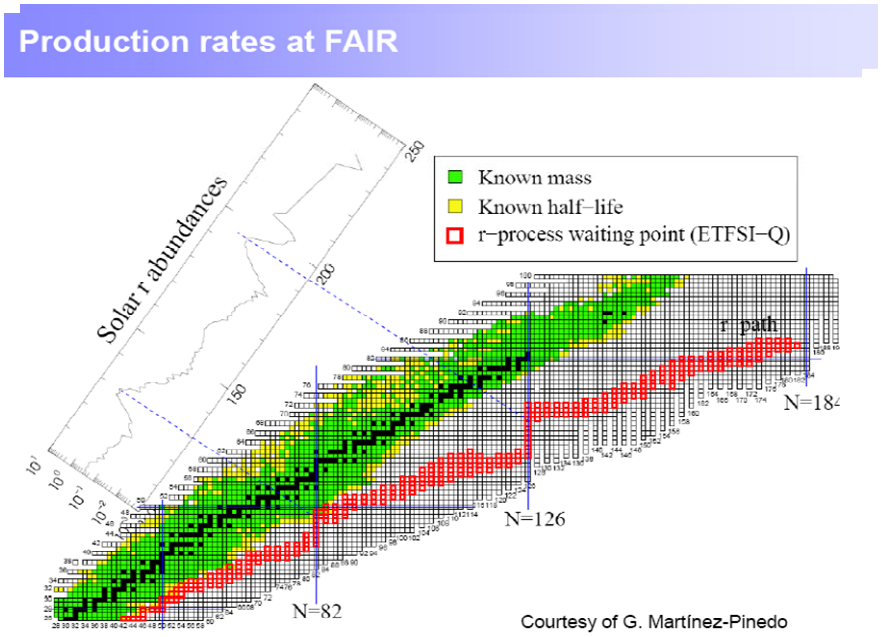

Fig. 1. Chart of nuclides. The expected pathway for the astrophysical rapid neutron capture process (*r*-process) is shown by red colour [3]. The valley of stability is shown by black colour. The known solar abundances for the *r*-process nuclides are also shown in relative units

Aside from direct measurements of nuclear masses, the MATS project is also tasked with a precision spectroscopic exploration. Since the ion trap is a precision mass spectrometer, it makes possible to have ions of definite nuclide at the exit of the system and to perform measurements under ideal background conditions by means of in- and post-trap spectroscopy [2].

3. MATS experimental complex

The main measuring instrument is a series of Penning ion traps in tandem. Therefore, the ions directed into the traps should have low energy. However, the primary ion beam of the SIS-100 synchrotron bombarding the target will have an energy of about 2*A* GeV. The products of the inverse fragmentation reaction which pass through the SuperFRS separator will also have a relativistic energy. For spectrometry with traps, these products should be moderated to an acceptable energy less than 1 keV. This is supposed to be done using a solid state moderator, which is followed by a large cryogenic He-gas cell where the ions are stopped. This absorber should make it possible to obtain thermolysed singly charged ions and after their extraction to form the Low-Energy Branch (LEB) of beams of radioactive products which should be used in different NUSTAR experiments including MATS. The ion-optical channel for transporting ions into

the measurement apparatus was calculated and designed by Russian specialists. The part A3 of this channel, bending the beam in the required direction, is shown schematically in Fig. 2. The MATS facility consists of an electronic source of highly charged ions EBIT (Electron Beam Ion Trap) indicated as B1 in Fig. 2, a mass calibrator B2 using ion sources of different types, and Penning ion traps themselves: a preparatory trap B3 and a precise one B4.

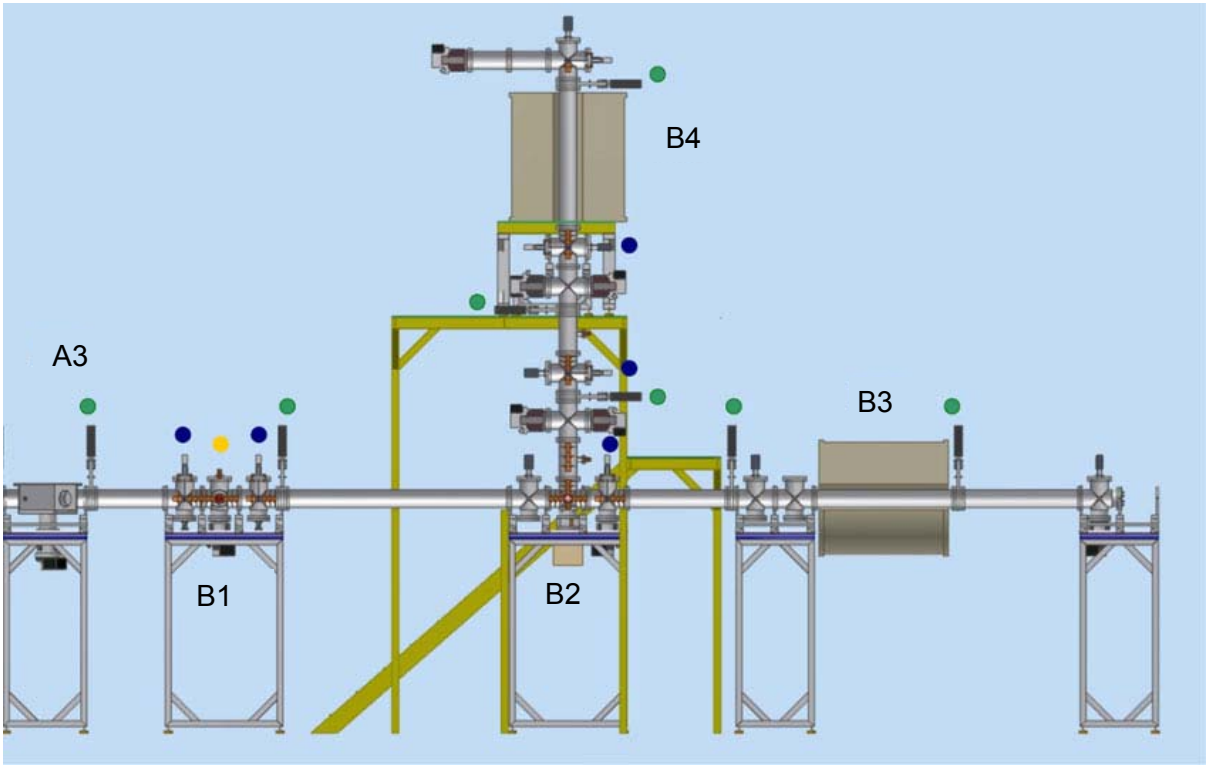

Fig. 2. Schematics of the principal units of the MATS complex [2]: A3 – electrostatic system for bending the ion beam towards the set-up; B1 – EBIT system to produce highly charged ions; B2 – mass calibration unit; B3 – preparatory trap; B4 – measuring trap for precise mass measurements performed in the second stage

An ion in a Penning trap is confined by a combination of magnetic and electric fields in a very small volume with the radius $r < 100$ μm. The ion motion is limited in three spatial dimensions with a certain combination of a strong uniform magnetic and week electrostatic fields. A confined particle with the charge-to-mass ratio q/m circulates in a plane perpendicular to the magnetic field B with the cyclotron frequency $\omega_c = q/mB$. A magnetic field directed along the Z axis confines the ion to the radial plane. If a quadrupole electrostatic field is added, then the ion motion in the radial plane will consist of two harmonic motions: a fast modified cyclotron motion and a slow magnetron one. The two motions are coupled by the relation of the angular frequencies $\omega_+ + \omega_- \approx \omega_c$. An axial harmonic motion along the Z axis will also be present. Thus, the motion of the charged particle in the trap is a superposition of three independent harmonic motions – one axial motion and two radial ones [4]. An additional *rf* field applied between the segments of an annular electrode gives rise to a quadrupole excitation which couples the motion in the radial plane.

This excitation applied at a frequency ω_c couples two radial motions. It makes possible to determine the cyclotron frequency ω_c and, therefore, the desired ratio q/m if the applied field is under conditions of a resonance. The resonance frequency can be determined more accurately with the octupole excitation, as it was accomplished in Ref. [5]. In order to achieve high precision in the mass measurement, the magnetic field should have high homogeneity of $\delta B/B < 10^{-7}/\text{cm}^3$. It is necessary also to provide vacuum of $\sim 10^{-8}$ Pa and to cool ions to the liquid-helium temperature [1]. Before entering the precision measuring trap, the ions are directed into the preparatory trap B3 (see Fig. 2). This trap should be used to separate ions by mass using the buffer gas and to prepare the cooled ions for the precision trap B4 or for a detector trap placed in

the second uniform part of the same magnet as the preparatory trap. The task of the detector trap should be in-trap spectroscopy. In order to increase considerably the precision of measurements, a use of highly charged ions was proposed. Increasing the value of q/m, and hence of ω_c, makes it possible to decrease $\delta\omega_c/\omega_c$ by the same factor. Since after the He gas chamber of LEB the ions fly out predominantly singly charged and enter the MATS system with the same charge, it is proposed to use the electron gun EBIT to produce high-charge ions right up to completely ionized atoms (bare nuclei). This unit is presented schematically by the block B1 in Fig. 2. The schematic of the precision measurement Penning trap proposed for the MATS project is presented in Fig. 3 [2]. Since it is the frequency that is measured in the trap system, and it can be measured much more accurately than, for example, the potentials, it makes PTMS unprecedented with respect to the precision with which the nuclear masses can be determined. Thus, the expected precision of PTMS in MATS will exceed all other known methods of measuring nuclear masses by factors of 10–100.

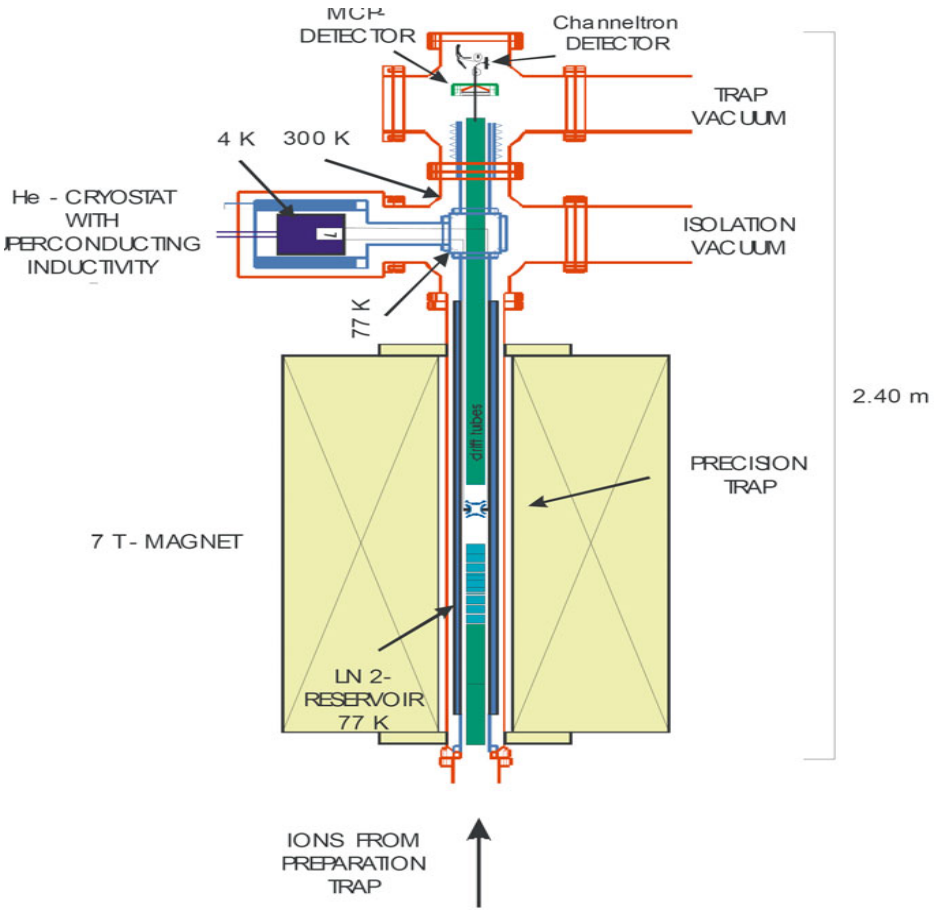

Fig. 3. Scheme of the precision Penning trap proposed for the MATS system. The measurement trap is placed in a magnetic field of 7 T produced by a superconducting solenoid. The Micro Channel Plate (MCP) and the channeltron detector are shown

The cyclotron frequency will be determined by two methods: using the Time-Of-Flight Ion Cyclotron Resonance (TOF – ICR) and the Fourier frequency Transformation method (FT – ICR). In the TOF – ICR method, the cyclotron frequency is determined from the resonance in the TOF curve for the ions releasing the trap and detected by the MCP. If the scanned external *rf* coincides with the characteristic cyclotron frequency, dependent on the ratio q/m, the ions will have the maximal energy and therefore will reach the detector (MCP) ahead of those at the non-resonance frequency. A typical experimental resonance TOF curve for this destructive method, in which ions are lost, is shown in Fig. 4a [6]. Recently, a novel approach based on the projection of the Penning trap ion motion onto a position-sensitive MCP detector has been proposed and checked at the SHIPTRAP system at GSI [7]. This new approach opens the door to very precise mass measurements on the sub-ppb level even for short-lived nuclides with half-lives well below a second. In

addition to increasing the precision in the mass determination, the new method provides a superior resolving power by which low-lying isomeric states with the excitation energy on the 10-keV level can be easily separated from the ground state. All these advantages just suit the MATS requirements. The precision of the mass determination will reach in the absolute values a level of 100 eV, or even better for light nuclides.

In the nondestructive method, the ion moves inside the trap with the oscillation frequency and produces an induced charge in the resonance circuit. A single ion induces a very weak current (less than one picoampere), which is amplified. The Fourier transformation permits identification of the resonance frequency (see Fig. 4b). This method is appropriate for nuclides whose production yields are very small and thus is relevant for the MATS project. However, the FT – ICR requires strict fulfilment of several conditions, among which is the presence of ideal mechanical and thermal characteristics of the material of the trap and the magnetic field, whose homogeneity should be as high as possible. Moreover, the trap should be cooled to the liquid-helium temperature. Note that the FT – ICR method has not yet been implemented in any existing trap systems for radioactive nuclides.

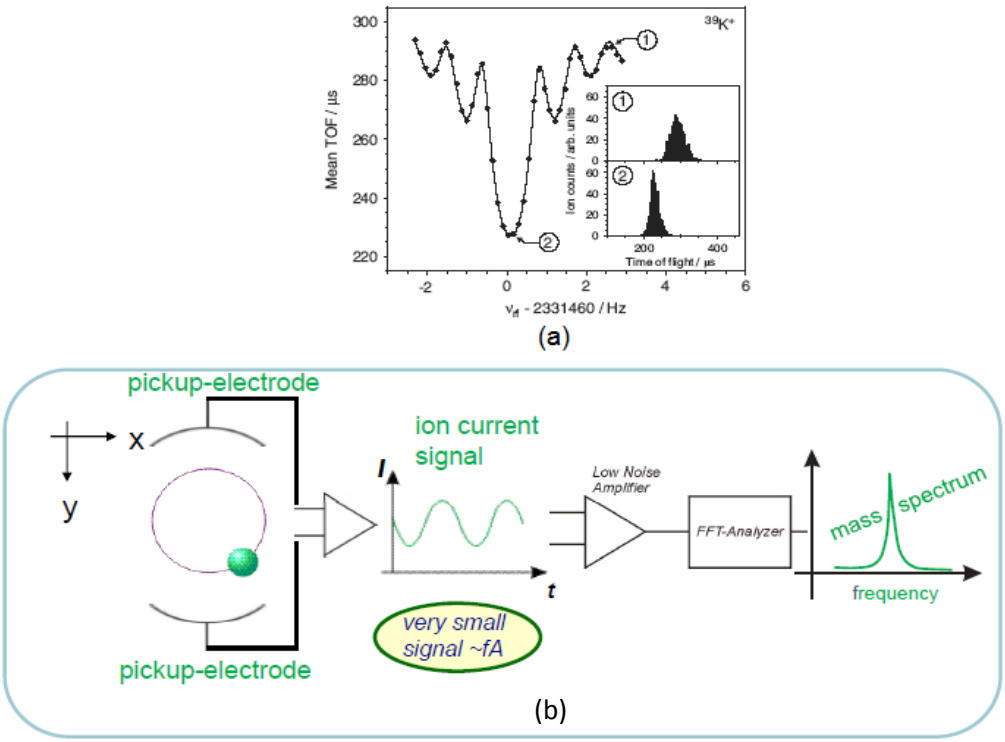

Fig. 4. Determination of the cyclotron frequency in the ion trap: a – dependence of the TOF of singly charged ions (from the trap to the outside detector MCP) on the external *rf* field, and fragments of the TOF spectrum [6]; b – principle for determination of the resonance frequency in the Fourier Transformation method (FT – ICR) [1]

The principle of mass determination is the same for these two methods of measurements. The mass of an ion with the known charge can be easily found if the magnetic field is known. The latter can be determined in similar measurements with the ions of nuclides whose mass is well known. The atomic mass M is determined from the expression:

$$M = (\omega_{cal} / \omega)(M_{cal} - m_e) + m_e,$$

where ω_{cal} and ω are the measured cyclotron frequencies of the calibrant and investigated singly charged ions, respectively; M_{cal} is the mass of the calibration ion, and m_e stands for the electron mass.

4. Individual units of the MATS Complex (with the responsibility of PNPI)

4.1. Ion-optical channel

After the LEB cryogenic gas cell, the ions should be collected into a beam and transported over a distance of about ten metres to the MATS installation. For these purposes, thermal ions are accelerated to several keV, and the ion beam is bent by a dipole magnet for additional mass separation and for guiding in the required direction. Next, the focused ion beam, assembled into ion groups by means of a gas-filled *rf* quadrupole, is bent again electrostatically and forwarded towards the MATS set-up. In the MATS set-up, the ion guide starts with an electrostatic deflection. A gas-filled *rf* quadrupole, which is placed directly in front of the deflector, forms an ion beam at the exit with the emittance of 50 $\pi \cdot$ mm and with the energy of about 100 eV. In order to avoid substantial losses, the beam should be accelerated. A scheme with two doublets of electrostatic quadrupoles, placed symmetrically with respect to the bending dipole magnet, was chosen to transport the beam. Simulations with the SIMION code [8] showed that the optimal acceleration energy should be ~ 5 keV with the beam diameter increased to 14 mm and with the angular divergence approximately of ± 1 mrad. The overall scheme of this part of the set-up is shown in Fig. 5 (see also Ref. [9]). In order to trap ions, the energy of the entrance beam should not exceed several hundred eV. Therefore, it is necessary to stop the accelerated beam just in front of the ion trap. To do this, six cylindrical electrostatic lenses are proposed. The scheme was simulated by the SIMION code and is shown in Fig. 6.

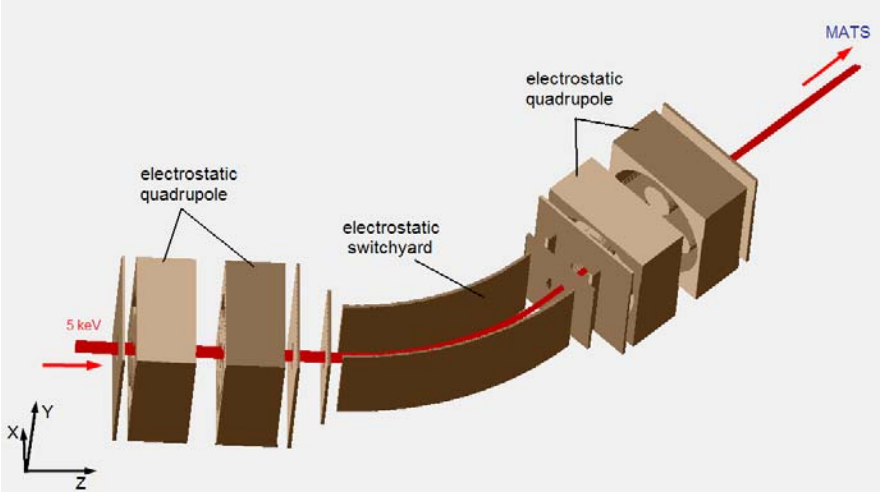

Fig. 5. Simulated arrangement of the ion-optical guide for bending and passage of the ion beam towards the MATS set-up [9]

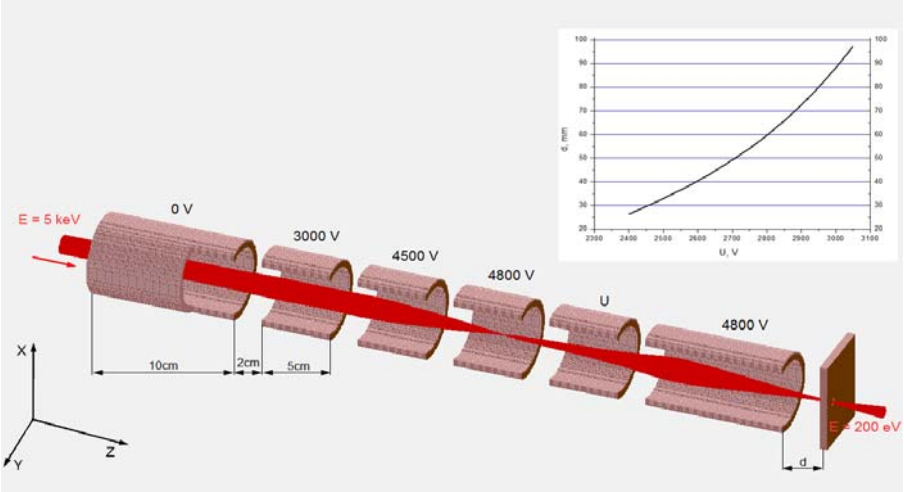

Fig. 6. System of cylindrical lenses for stopping and focusing the ion beam at the entrance of the Penning trap, and the dependence of the electrostatic potential on the focal distance *d* [9, 10]

4.2. Mass calibrator

High precision experiments for mass determination require careful calibration of the precision ion trap. Besides the necessity to eliminate temporal effects of magnetic field instabilities caused by different reasons [11], an important component of the experiments is the accuracy of the calibration mass. The relative accuracy of the masses of nuclides ^{23}Na, $^{85–87}$Rb, and ^{133}Cs most often used for calibration is $\delta m/m = (1–2) \cdot 10^{-10}$, which could be insufficient for ultraprecise measurements for nuclides far from the mass number of the calibration nuclides. For this reason, ^{12}C was proposed for calibration. This mass standard can be used in cluster compounds (of the fullerene type) to cover the extensive mass ranges of the chart of nuclides [12]. As can be seen in Fig. 2, the mass calibrator B2 can be used in coupled operations of both traps (B3 and B4). A scheme of the unit proposed by PNPI is shown in Fig. 7, which includes different types of ionizers (laser, surface, and electron impact). This versatile unit will cover different mass regions of the calibrants, and thus can be used for calibration of broad unknown mass regions.

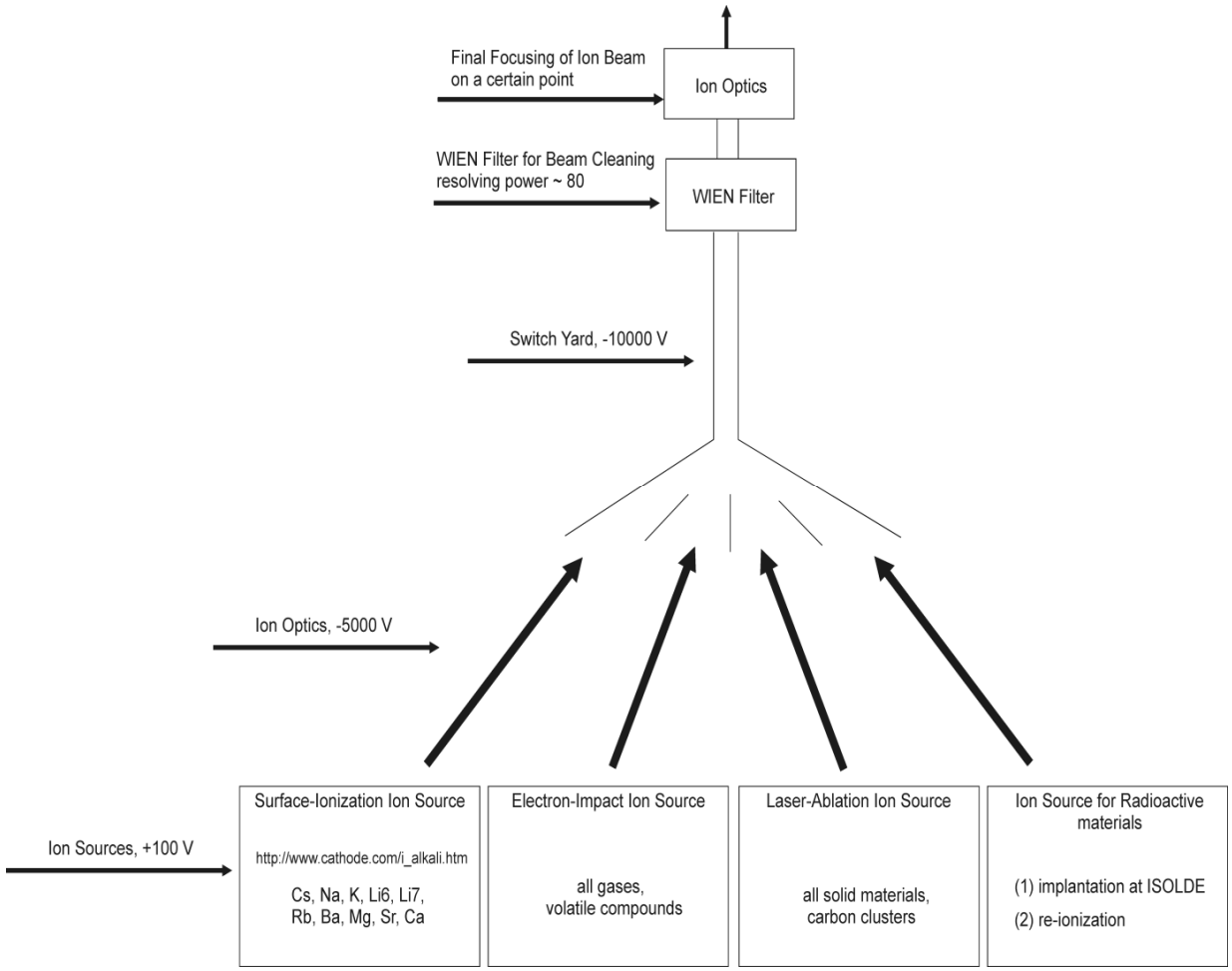

Fig. 7. Schematic diagram of the mass calibrator proposed by PNPI for the PTMS at MATS. Ions can be produced by ion sources of different type, then extracted and forwarded to the ion trap for mass measurements

4.3. Post- and in-trap spectroscopy

An ion trap is a very precision mass separator which confines nuclides of only one mass- and *Z*-number. The ions extracted from the trap fly in a magnetic field gradient and strike the substrate, which can be installed instead of MCP (usually used for PTMS). The particle and gamma radiation of the implanted nuclides with the specific values of *Z* and *A* then can be measured. Another important advantage is

the possibility to use a trap for the in-trap spectroscopy. The ions in a trap are held at rest without any corresponding carrier, which is a necessary component of any conventional radioactive source. The presence of a carrier leads to the problem of accurate determination of the energy of the very low-energy charge radiation (α, *p*, or *e*), which passes through the thickness of the substrate and therefore unavoidably loses energy. The α decay particles can be detected with silicon strip detectors surrounding the trap that simultaneously acts as a trap ring electrode to confine the decaying nuclei. This will allow to detect the momentum vector of α decay particles without energy losses. Thus, the properties of the excited states of exotic nuclides can be firstly investigated. The ion-optical simulations for the in-trap spectroscopy were performed at PNPI [12].

5. Conclusion

The MATS project is dedicated to precision mass measurements of exotic nuclides very far from the stability line. A dramatic increase of the production yields, which can be provided by the FAIR accelerator, makes it possible to measure masses of hundreds of new nuclides, some of which are still unknown. These global measurements will pave the way for the mass mapping and investigation of the landscape of exotic nuclides, which is very important for nuclear physics and astrophysics. A novel method of measurements of highly charged ions in combination with an advanced approaches in detection of single ions will allow one to reach the mass precision on the level of 10^{-9} for the nuclides with the half-lives even well below 1 s. MATS will be superior to all other existing and planned experimental installations for mass-spectrometry of radioactive nuclides. The Penning traps of the MATS project can in addition be used for post- and in-trap spectroscopy of very clean radioactive samples. PNPI is responsible for ion-optics simulations of the MATS system, for building of the mass calibration unit and for production of thin Si-detectors.

We would like to thank the members of the MATS project for very fruitful collaboration.

References

1. K. Blaum, Yu.N. Novikov, and G. Werth, Contemporary Phys. **51**, 149 (2010).
2. D. Rodriguez, K. Blaum, W. Nörterhauser, *et al.*, Eur. Phys. J. Special Topics **183**, 1 (2010).
3. G. Martinez-Pinedo (private communication).
4. L. Brown and G. Gabrielse, Rev. Mod. Phys. **58**, 233 (1986).
5. S. Eliseev, M. Block, A. Chaudhuri, *et al*., Intern. J. Mass Spectrometry **262**, 45 (2007).
6. M. König, G. Bolen, H.-J. Kluge, *et al*., Intern. J. Mass Spectrometry **142**, 95 (1995).
7. S. Eliseev, K. Blaum, M. Block, *et al.*, Phys. Rev. Lett. **110**, 082501 (2013).
8. D. Dahl, Inter. J. Mass Spectrometry **200**, 3 (2000).
9. Yu.N. Novikov, A.A. Vasiliev, Yu.A. Gusev, *et al*., Atomnaya Energiya **112**, 117 (2012) (in Russian).
10. D. Nesterenko, Report for FAIR-Russia Research Centre (2012).
11. Ch. Droese, M. Block, M. Dworzchak, *et al.*, Nucl. Instr. Meth. A **632**, 157 (2011).
12. K. Blaum, G. Bollen, F. Herfurt, *et al.*, Eur. Phys. J. A **15**, 245 (2002).

PNPI IN THE R3B PROJECT AT FAIR

PNPI participants of R3B Collaboration:
G.D. Alkhazov, D.V. Balin, A.V. Dobrovolsky, G.E. Gavrilov, V.L. Golovtsov, A.G. Inglessi, A.V. Khanzadeev, G.A. Korolev, A.G. Krivshich, E.M. Maev, D.A. Maysuzenko, G.E. Petrov, V.V. Sarantsev, L.N. Uvarov, V.V. Vikhrov, S.S. Volkov, V.I. Yatsoura, Yu.K. Zalite, A.A. Zhdanov

1. Introduction

A versatile reaction set-up R3B with high efficiency, acceptance, and resolution for kinematically complete measurements of reactions with high-energy radioactive beams is proposed [1] (Fig. 1). The set-up will be located at the focal plane of the high-energy branch of the Super-FRS. The experimental configuration is based on the concept similar to the existing Large Area Neutron Detector (LAND) reaction set-up at GSI introducing substantial improvements with respect to resolution and an extended detection scheme, which comprises the additional detection of light (target-like) recoil particles and a high-resolution fragment spectrometer. The set-up is adapted to the highest beam energies (corresponding to 20 Tm magnetic rigidity) provided by the Super-FRS capitalizing on the highest possible transmission of secondary beams. The experimental set-up is suitable for a wide variety of scattering experiments, *i.e.*, such as heavy-ion induced electromagnetic excitation, knockout and breakup reactions, or light-ion elastic, inelastic, and quasi-free scattering in inverse kinematics, thus enabling a broad physics programme with rare-isotope beams to be performed. The R3B programme will focus on the most exotic short-lived nuclei, which cannot be stored and cooled efficiently, and on reactions with large-momentum transfer allowing the use of thick targets.

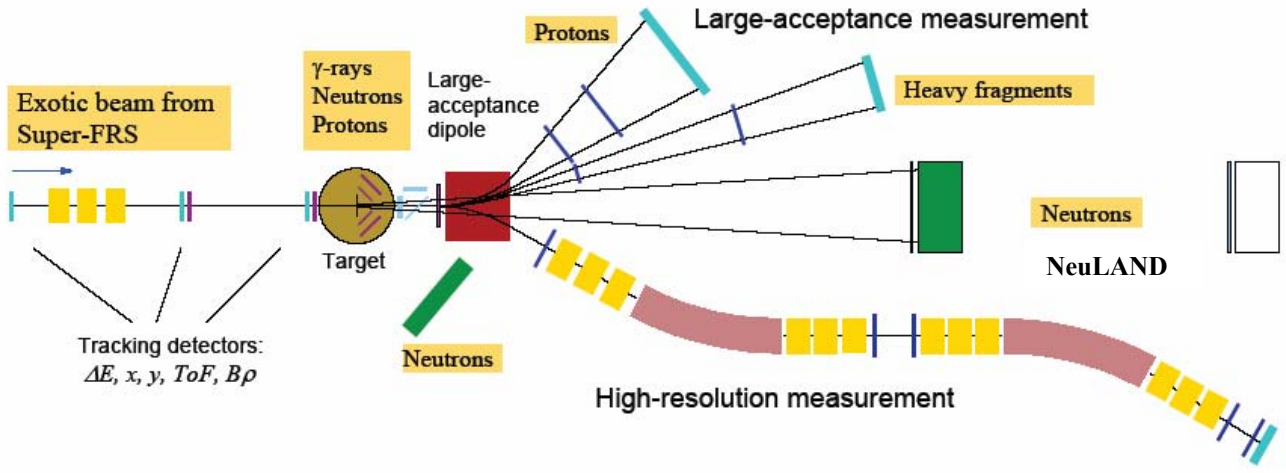

Fig. 1. Schematic drawing of the experimental set-up comprising γ-ray and target recoil detection, a large-acceptance dipole magnet, a high-resolution magnetic spectrometer, neutron and light-charged particle detectors, and a variety of heavy-ion detectors (two possible positions of NeuLAND are shown)

The incoming secondary beams are tracked and identified on an event-by-event basis. Measurements of the magnetic rigidity $B\rho$ (position measurement at the dispersive focus in the Super-FRS), Time-Of-Flight (TOF), and energy loss ΔE provide unique isotope identification and momentum determination. After the secondary target, the kinematically forward focused projectile residues are again identified and momentum analysed. The large gap of the dipole provides a free cone of ± 80 mrad for the neutrons, which are detected in forward direction by a new LAND (NeuLAND). The target is surrounded by a γ-ray spectrometer. For elastic, inelastic and quasi-free scattering experiments or charge-exchange reactions, liquid hydrogen or frozen hydrogen targets are considered. Recoiling protons and neutrons are detected by a Si-strip array and plastic scintillators, respectively. For measurements at low momentum transfer, the use of an active target is

foreseen. For most of the experiments envisaged, a high-efficiency total-absorption spectrometer (cooled CsI or NaI) is the optimum solution, which is also used to measure the energy of recoiling protons. For specific experiments requiring ultimate energy resolution for γ-detection, the germanium spectrometer AGATA might be used alternatively.

High beam energies, in the range of a few hundred MeV/nucleon, allow a quantitative description of the reaction mechanisms, while also having experimental merits, such as the possibility of using relatively thick targets (in the order of 1 g/cm^2). Moreover, due to the kinematical forward focusing full-acceptance measurements are feasible with moderately sized detectors. This makes it possible to gain nuclear-structure information from reaction studies even with very low beam intensities, as low as about 1 ion/s. R3B will cover experimental reaction studies with exotic nuclei far off stability, with emphasis on nuclear structure and dynamics. Astrophysical aspects and technical applications will be also concerned. A survey of reaction types and associated physics goals that can be achieved is given in Table 1.

Table 1

Reaction types with high-energy beams measurable with R3B and corresponding achievable information

Reaction type	Physics goals
Knockout	Shell structure, valence-nucleon wave function, many-particle decay channels, unbound states, nuclear resonances beyond the drip lines
Quasi-free scattering	Single-particle spectral functions, shell-occupation probabilities, nucleon-nucleon correlations, cluster structures
Total-absorption measurements	Nuclear matter radii, halo and skin structures
Elastic *p*-scattering	Nuclear matter densities, halo and skin structures
Heavy-ion induced electromagnetic excitation	Low-lying transition strength, single-particle structure, astrophysical *S*-factor, soft coherent modes, low-lying resonances in the continuum, giant dipole (quadrupole) strength
Charge-exchange reactions	Gamow – Teller strength, soft excitation modes, spin-dipole resonance, neutron skin thickness
Fission	Shell structure, dynamical properties
Spallation	Reaction mechanism, astrophysics, applications: nuclear-waste transmutation, neutron spallation sources
Projectile fragmentation and multifragmentation	Equation-of-state, thermal instabilities, structural phenomena in excited nuclei, γ-spectroscopy of exotic nuclei

PNPI physicists plan to participate in the R3B project in construction of the detector NeuLAND [2] and the detectors ACTAR, as well as in the physics program when the R3B set-up starts to collect data.

NeuLAND is the next-generation high-energy neutron detector (200 to 1000 MeV) designed for R3B, which meets all requirements defined by the ambitious physics program proposed for the R3B facility. NeuLAND features a high detection efficiency, a high resolution, and a large multi-neutron-hit resolving power. This is achieved by a highly granular design of plastic scintillators, avoiding insensitive converter material. The detector will consist of 3000 individual sub-modules with a size of 5 × 5 × 250 cm^3, arranged in 30 double planes with 100 submodules providing an active face size of 250 × 250 cm^2 and a total depth of 3 m. NeuLAND can be divided into two detectors for special applications and will be placed at different distances from the target, in order to meet specific experimental demands. The main design goals of NeuLAND comprise a one-neutron detection efficiency above 95 % in a wide energy range and a full acceptance corresponding to an angular coverage of 80 mrad. The desired resolutions for momenta and thus the excitation energies lead to the required spatial resolutions of ~ 1.5 cm and to a time resolution of ~ 150 ps for the standard distance between the detector and target of 15.5 m. When placed at a distance of 35 m, an excitation-energy resolution of better than 20 keV will be reached for an excitation energy of 100 keV above threshold for a beam energy of 600 A MeV. Apart from the excellent energy resolution, NeuLAND has an enhanced multineutron recognition capability with an efficiency of up to 60 % for reconstructed four-neutron events.

Several groups of the R3B Collaboration will contribute to the construction of the NeuLAND detector. The final assembly will take place at the GSI/FAIR site. The construction of the full detector will take about 3.5 years, allowing for first experiments with the complete detector in 2016. PNPI physicists plan to participate in assembling of the NeuLAND detector and in fabrication of the High Voltage (HV) sources for 6000 photomultipliers detecting light from the ends of the scintillation bars.

2. HV system for NeuLAND

In April 2012, PNPI physicists presented to GSI a proposal for designing and manufacturing a High Voltage Distribution System (HVDS) for the spectrometer NeuLAND. Advantages and disadvantages of three approaches for building such a system were considered in order to meet the requirements specified in the NeuLAND TDR [2].

1. A HV distribution option: the HV from a primary Power Supply (PS) unit is individually down-regulated and then distributed to each PhotoMultiplier Tube (PMT).

2. An integrated option with an analog interface: the HV is generated from a LV locally at the PMT base, control levels and voltage and current monitoring values being delivered to/from the PMT via an analog interface.

3. An integrated option with a digital interface: the same as above, but DAC and ADCs are located on each PMT base as well.

The proposal was further discussed in September 2012 at GSI. It turned out that the NeuLAND TDR requirement of 2.0 kV and 2.0 mA per PMT was a bit overkill, the actual requirement being closer to 1.5 kV and 0.5 mA (or even 0.3 mA). A cost estimate of circuit components for each option made by PNPI engineers revealed the expected result: the HV system options were listed above from the least to the most expensive. So, it was decided to pursue the first option, to try to further reduce the required current and to use an active divider developed at PNPI.

2.1. The HV system overview

The principle of operation of the proposed HVDS is individual down-regulation of the output voltage of a primary HVPS for each PMT (see Fig. 2).

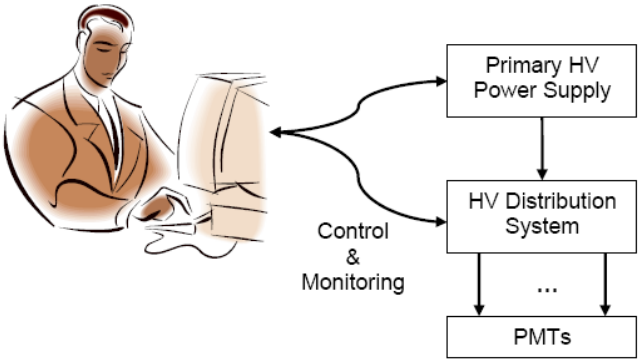

Fig. 2. HVDS for NeuLAND

The host computer controls HV settings of the primary PS and each out of 6000 down-regulators of the HVDS. It also monitors the actual HV applied to each PMT and the current drawn by it. All control and monitoring operations are executed over Ethernet. Given each PMT consumes 0.3 mA of current, a primary HVPS rated at 1 A can feed up to 3000 PMTs, or one half of the NeuLAND detector.

2.2. HV distribution details

The proposed HVDS details are shown in Fig. 3.

Each PMT is powered from an output of a separate regulator Reg_XX, where XX is a channel number spanning from 01 to 50. 50 regulators reside at a 50-channel Distributor Board (DB50). Only 4 DB50s are

needed for a double plane of scintillator bars (containing 100 scintillator bars), with 2 DB50s sitting at each top corner of the double-plane frame. A single primary HVPS rated at 1 A can feed up to 15 double planes or up to 60 DB50s.

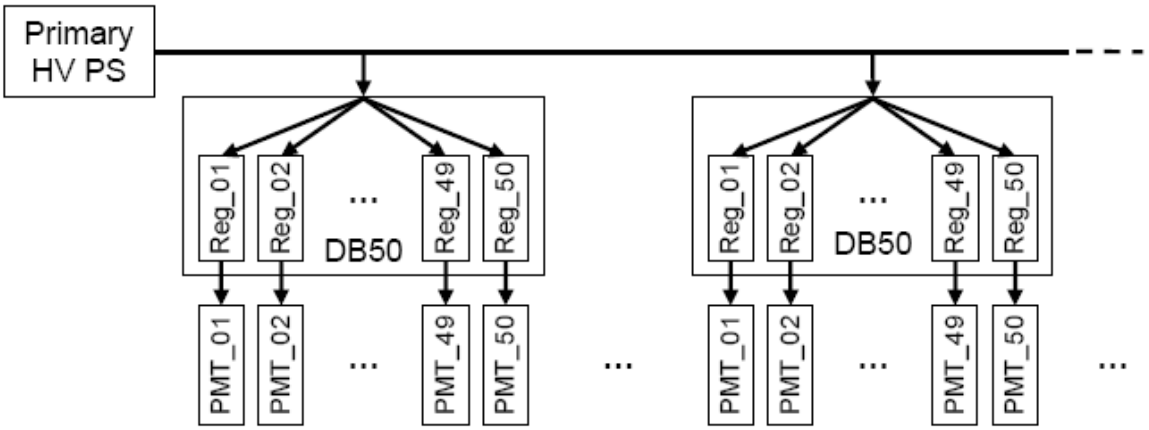

Fig. 3. HVD from a primary HVPS

2.3. HVDS control and monitoring

A host computer uses Ethernet to connect to the HV Control Board (HVCB) (see Fig. 4). The HVCB features 4 outputs with RJ-45s for connecting Control & Monitoring Buses (CMB). Each CMB is capable to control and monitor up to 16 DB50s. The HVCM serves up to 64 DB50s, which translates to 3200 PMTs. The CMB is implemented as a Cat 5 network cable with 4 pairs of wires. 2 pairs are used for downloading HV settings and 2 pairs – for receiving voltage and current monitoring data. Each DB50 has a pair of RJ-45s connected to the same bus. To add a new DB50 to the already existing bus, the user just needs to add a jumper cable from the last DB50 in the chain to a new one. Plugging in the CMB terminator in the last DB50 is optional and depends on the overall CMB length. The DB50 has a switch that sets its address (from 00 to 15 in decimal or from 0 × 0 to 0 × F in hex). Of course, all DB50s on the same CMB should carry exclusive addresses. The HVCB carries an FPGA that keeps the control and monitoring data for each HV regulator. There is also a sequencer that continuously updates control values in regulators and scans them for monitoring data.

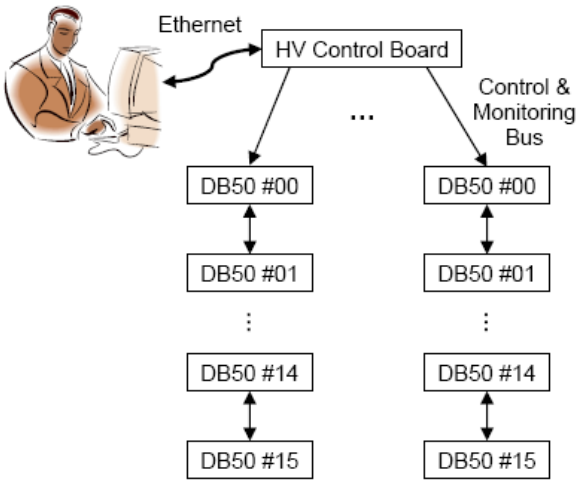

Fig. 4. HVDS control and monitoring

The output voltage is regulated from 0 to 1600 V by a 10-bit DAC. The voltage is monitored by a 10-bit ADC for the same range. The current is monitored by a 10-bit ADC with 1 nA resolution. The maximum output current into load is 0.5 μA. The system comes with a software package to perform control, monitoring and calibration tasks.

3. Active target

Nuclear sizes and the shape of the nuclear matter distributions are among the basic nuclear characteristics. Nuclear charge radii and nuclear charge density distributions can be determined by electron-nucleus scattering experiments. Precise information on nuclear charge radii is also obtained by means of laser spectroscopy of atoms of the nuclei under study. An effective method for studying radii and distributions of the total nuclear matter including nuclear protons and neutrons is proton-nucleus elastic scattering at intermediate energy. The successful use of intermediate-energy protons as probes for studying nuclear matter distributions is mainly due to the capability of the multiple-scattering theory in precisely describing the scattering process, thus permitting to correlate the measured differential elastic-scattering cross sections and the matter distributions in the studied nucleus in an unambiguous way. Stable nuclei are usually studied by proton-nucleus elastic scattering in the direct kinematics, that is when intermediate-energy protons are scattered on the target nuclei. As for exotic short-lived nuclei, which are obtained in small quantities, the experiments can be performed in the inverse kinematics, that is when a beam of the intermediate-energy nuclei is scattered on target protons.

Some years ago, PNPI physicists proposed to measure differential cross sections for proton-nucleus elastic scattering at small momentum transfers with the help of an active target – ionization chamber IKAR [3]. Note that the proton-nucleus cross sections in the region of small momentum transfers contain important information on the spatial structure of halo nuclei, which have extended nuclear matter distributions, since the contribution to the cross section from the scattering on the halo nucleons is concentrated just at small scattering angles, *i.e.* at small momentum transfers. The active target detector is a relatively novel gas detector concept where the gas constitutes both the target and the detector medium. It allows to measure differential cross sections for elastic proton-nucleus scattering for very short-lived nuclei at small momentum transfers. The ionization chamber IKAR was successfully used at GSI to measure differential cross sections for elastic scattering of ~ 0.7 GeV protons on neutron enriched nuclei of isotopes of He [4], Li [5], Be [6], C [7], and on the neutron deficient nucleus ^{8}B [7]. Important information on the sizes of the core, halo and total nuclear matter was extracted from the measured cross sections.

Ionization chamber IKAR consists of six in-line identical axial ionization chambers, which have a 2π acceptance in the azimuthal angle for the recoil proton ionization. Each IKAR module has a cathode electrode, an anode electrode and a grid, all placed perpendicular to the direction of the beam. The IKAR chamber is filled with hydrogen at a pressure of 10 bar. The beam of the studied nuclei passes through the chamber where interaction of the beam particles with the hydrogen gas takes place. The recoil protons produce ionization. The electrons which are freed in the process of ionization are collected on the anodes. The anode signals, the size of which is proportional to the collected charge, give information on the energy of the recoil protons, that is on the value of the momentum transfer. In more details, the construction of IKAR and how it works is described in Ref. [8].

It is expected that an Active Target (Actar1, Fig. 5) will become an essential subdetector of the R3B experimental complex, which will extend the possibilities of R3B in studies of nuclear structure of light and middle-weight exotic short-lived nuclei. As a matter of fact, Actar1 is a new version of the IKAR chamber designed specially for investigation of proton-nucleus elastic scattering in inverse kinematics at small momentum transfers in the case of middle-weight nuclei. As it was said before, IKAR had been used to study proton-nucleus scattering for very light nuclei: He, Li, Be, B, and C. It is problematic to use IKAR for investigation of exotic nuclei with $Z > 6$. This occurs because the studied nuclei passing through the active volume of the chamber also produce ionization which masks the signals from the recoil protons. In order to exclude the contribution of the ionization produced by the beam particle, the anodes of Actar1 are segmented (Fig. 6), so that most of the charge produced by this particle is collected on an inactive central electrode of small diameter. Of course, a small part of the ionization produced by the recoil proton will also be collected

on this electrode and will not be registered. However, the amount of the lost charge can be rather accurately estimated if we know the transverse coordinates of the interaction point and the azimuthal angle of the recoil proton. The transverse coordinates of the interaction point can be determined with the help of tracking detectors placed before and after the chamber Actar1. The azimuthal angle can be estimated due to angular segmentation of the anodes. Note that segmentation of the anodes allows also to reduce the contribution of energetic delta electrons produced by the beam particles.

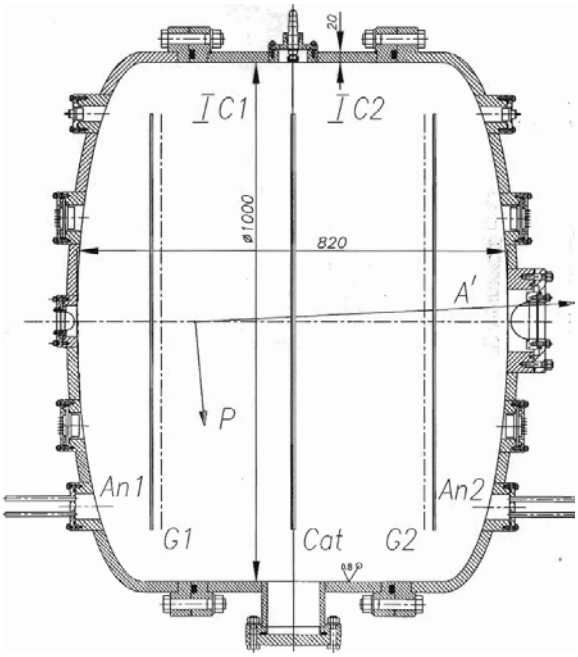

Fig. 5. Cross section of the proposed chamber Actar1. An1 and An2 – two anodes at zero potential; G1 and G2 – two grids, and Cat – common cathode at a negative potential

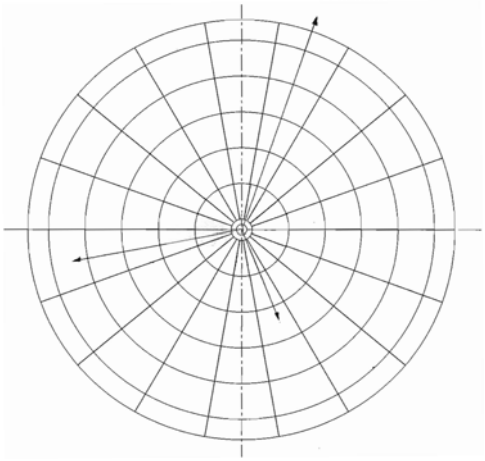

Fig. 6. A version of division of the Actar anodes on segments

Figure 5 shows the vertical cross section of the proposed chamber Actar1. It consists of two identical modules. In distinction from IKAR, it has a larger diameter (1 m) and can be filled with hydrogen at a pressure up to 20 bar, which allows to investigate proton-nucleus cross sections to higher values of the momentum transfer. The measurement of the drift time of electrons of the recoil proton tracks to segmented rings of the anode allows one to determine the polar angle of the recoil protons. This angle is different for elastic and inelastic scattering events, which allows one to select the elastic scattering events from the inelastic ones, provided the energy of excitation to the lowest levels of the studied nuclei is sufficiently large. The energy of the recoil protons whose tracks are shorter than the radius of the outer anode segments will be measured with an accuracy better than 100 keV. The polar angle of the recoil protons whose tracks are close to or larger than the radius of the outer anode segments will be measured with an accuracy of 4–6 mrad, which is sufficient to separate the elastic scattering events from the inelastic ones for several nuclei of interest, such as ^{56}Ni or ^{132}Sn.

PNPI physicists were also proposed to fabricate a small active target Actar2 (a prototype of such a chamber is shown in Fig. 7) for studying inelastic ^{4}He-nucleus scattering in inverse kinematics. This chamber will be filled with helium under pressure of up to 10 bar. It will be placed inside the gamma-spectrometer CALIFA (Fig. 8). The recoil ^{4}He particles in ACTAR2 will be registered in coincidence with signals from the spectrometer CALIFA, which will measure the energy and the azimuthal and polar angles of gamma-rays emitted from the excited states of the studied nuclei. A prototype of the chamber Actar2 (Fig. 7) is under preparations for testing in a GSI ion beam.

Fig. 7. Prototype of the chamber Actar2 to be placed inside the gamma-spectrometer CALIFA

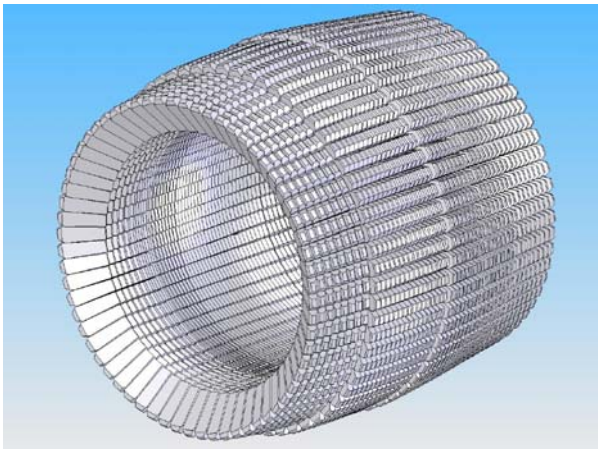

Fig. 8. Spectrometer CALIFA inside which the active target Actar2 will be inserted

4. Concluding remarks

The experiment R3B at FAIR is devoted to the study of the nuclear structure of exotic nuclei using a universal experimental set-up with high efficiency, acceptance, and resolution for kinematically complete measurements of reactions with high-energy radioactive beams. PNPI physicists plan to participate in construction of this set-up by fabricating the high-voltage system for the NeuLAND detector, by assembling the scintillator bars of this detector, by designing and building an active target (Actar1) for studying elastic proton-nucleus scattering (in inverse kinematics) and an active target (Actar2) for studying inelastic ^{4}He-nucleus scattering. Also, a possibility to fabricate proton tracking detectors based on straw tubes is under discussion.

The experiment R3B will be the only facility worldwide providing the capability for kinematically complete measurements of reactions with relativistic heavy-ion beams of short-lived nuclei up to about 1 A GeV. The experimental results which will be obtained with the R3B set-up are expected to be very important for theory of the nuclear structure and for solving open questions of modern astrophysics.

References

1. http://www.gsi.de/r3b
2. NeuLAND Technical Design Report: http://www.faircenter.de/fileadmin/fair/experiments/NUSTAR/Pdf/TDRs/NeuLAND-TDR-Web.pdf
3. A.A. Vorobyov, G.A. Korolev, V.A. Schegelsky, *et al.*, Nucl. Instr. Meth. **119**, 509 (1974).
4. G.D. Alkhazov, A.V. Dobrovolsky, P. Egelhof, *et al*., Nucl. Phys. A **712**, 269 (2002).
5. A.V. Dobrovolsky, G.D. Alkhazov, M.N. Andronenko *et al.*, Nucl. Phys. A **766**, 1 (2006).
6. S. Ilieva, F. Aksouh, G.D. Alkhazov, *et al*., Nucl. Phys. A **875**, 8 (2012).
7. IKAR Collaboration, to be published.
8. S.R. Neumaier, G.D. Alkhazov, M.N. Andronenko, *et al*., Nucl. Phys. A **712**, 247 (2002).

Methodical and Applied Research

PROTON RADIOSURGERY AT THE PNPI SYNCHROCYCLOTRON

PNPI participants: Yu.A. Gavrikov, E.M. Ivanov, V.I. Lazarev, V.V. Lysenko, Yu.A. Malov, G.A. Ryabov, D.M. Seliverstov

RSCRST participants: D.L. Karlin, T.V. Pushkareva, R.A. Shalek, A.A. Shtyrkova, N.A. Skugareva, V.M. Vinogradov, M.V. Zhydkov, O.M. Zhydkova

1. Introduction

Radiosurgery is a one-time exposure of small pathological formations to high doses of radiation. Since April 1975, it has been systematically carried out at the PNPI synchrocyclotron medical proton complex SC-1000. The exposure technique is described in detail in Refs. [1, 2]. In total, 1386 patients have received a stereotactic radiosurgery by January 1, 2013.

Several upgrades of the installation, as well as of its system to control the exposure parameters, have been performed during 40 years of operation of the Pilot Medical Proton Complex (PMPC). In 1990, a lock-head device of the third generation was built, and the process to control the exposure parameters was computerised. In 2002–2004, with the support of the Government of Leningrad region, the PMPC was upgraded. In particular, new systems for monitoring the supplied doses and scanning, as well as for controlling the proton beam parameters, were built, some worn-out elements were replaced, and the automation of the beam output was performed.

2. Modernisation of the medical proton complex

In the period after 2005, the worn-out measuring systems were replaced, the software was changed, and some work to ensure the reliability of the system operations was carried out. In particular, to ensure the stability against noise, a photocoupler isolation of the local manual control of the installation for the exposure of patients was added.

A new temperature control unit was fabricated in the installation for the thermoluminescence dosimetry, which also increased the reliability of its operation.

The performance of the TLD-100 detectors of the “Harshaw” company was studied with respect to the parameters presented below, with the aim to use these detectors in clinical dosimetry instead of LiF detectors.

2.1. Dependence of the light yield on the radiation dose

One can see in Fig. 1 that the obtained data are in good agreement with those in the literature.

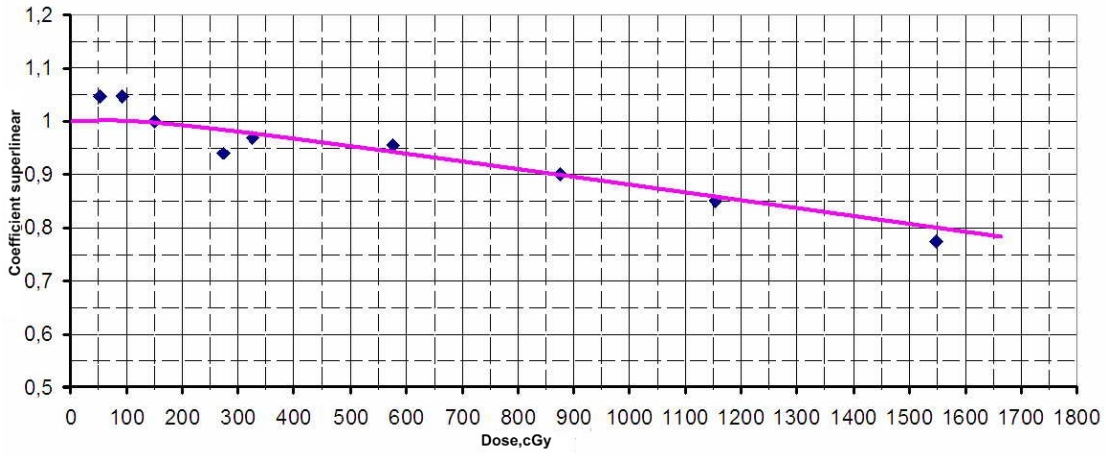

Fig. 1. Superlinearity curve for the TLD-100 detectors

2.2. Spontaneous loss of the information on the accumulated dose over time

Such a characteristic as the loss of the detector information (fading) is very important. While fading occurs even in normal conditions, its influence can be reduced by using special modes of the TLD preparation to reading, *e.g.*, by their pre-exposure to certain temperatures for a certain time. Providing that the reading regimes are standard and preparing them to be read, one can apply the corrections for fading, which is a function of the time passed after the previous reading or the moment of exposure. The results of the fading effect are given in Fig. 2.

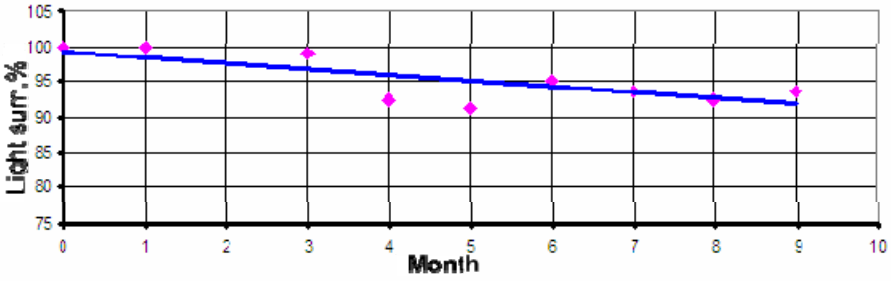

Fig. 2. Information loss of the irradiated TLD-100 versus the storage time

For the TLD-100, the fading for the first three months (the typical control period) was about 3 %. After the period of four months, the fading did not exceed more than 7.5 %. The obtained results are in good agreement with the published data on the dependence on the storage time of the information loss of the irradiated TLD.

2.3. Reproducibility of dosimeter readings

In clinical dosimetry, including the construction of dose distributions and fields, the reproducibility of the detectors – the ability of the dosimeters to show the same value of a dose in the same experimental conditions – is very important. For clinical dosimetry, the detectors are considered to be acceptable when the difference in readings of two measurements does not exceed 5 % (2 divisions on the device frame). The number of suitable TLD-100 detectors with the difference in readings between the first and the second measurement equal to 0, 1, 2 divisions was 155, or 78.7 % of the total number (197) of the detectors (Table 1).

Table 1

Reproducibility of dosimeter indications

Difference in the dosimeter readings between the 1-st and 2-nd measurements	Number of TLD	% of the total number
0	41	20.8
1	61	31
2	53	26.9
3	23	11.7
4	12	6.1
5	3	1.5
6	1	0.5
7	2	1
9	1	0.5
0–2	**155**	**78.7**

2.4. Dose measurements and construction of the dose fields and distributions

Two cassettes *XY* and *ZY* with the thermoluminescence detectors (by the "Harshaw" company) were prepared to measure the doses and to construct the dose fields. The measurements were performed using a homogeneous phantom of the human head made from plexiglass in the shape of a sphere of 160 mm in diameter. Before the irradiation, the phantom was centred on the rotation pole. During the period of the irradiation, the loch-device made 14 passes over ± 36º, the treatment table – 14 passes in one direction, the radiation dose being 6.56 Gy.

The calculations were made using Microsoft Office Excel, and the dose distributions and the dose fields were built in the PUSK application hosted inside MATLAB 5.5.0. The flowchart of the application used to build the dose distributions and fields is given in Fig. 3.

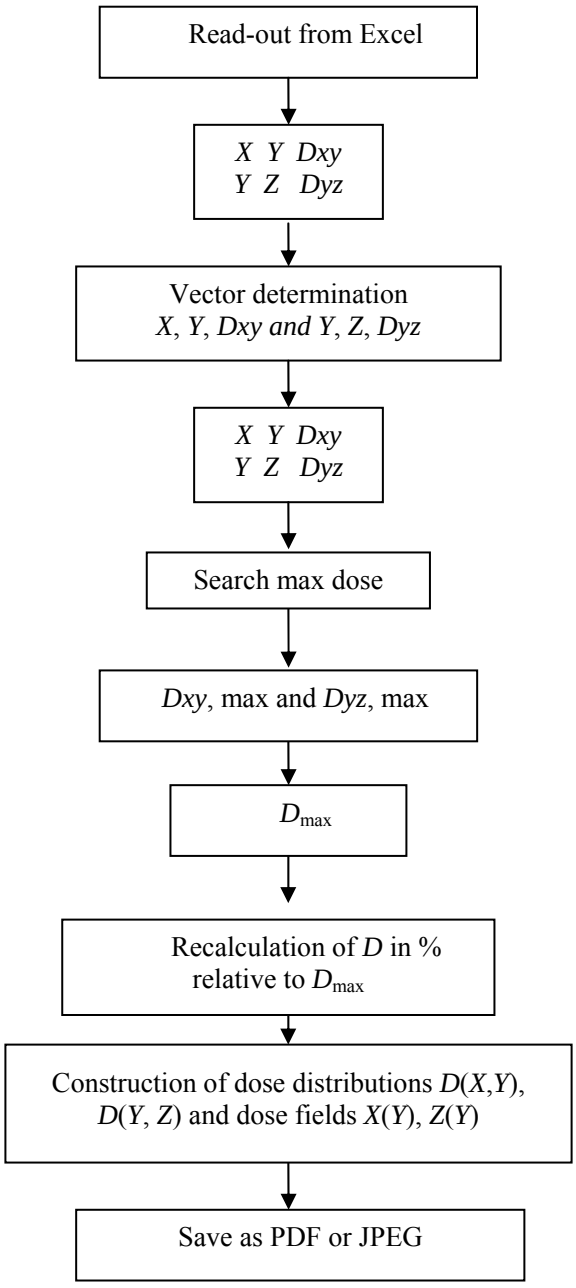

Fig. 3. The flowchart of the used application

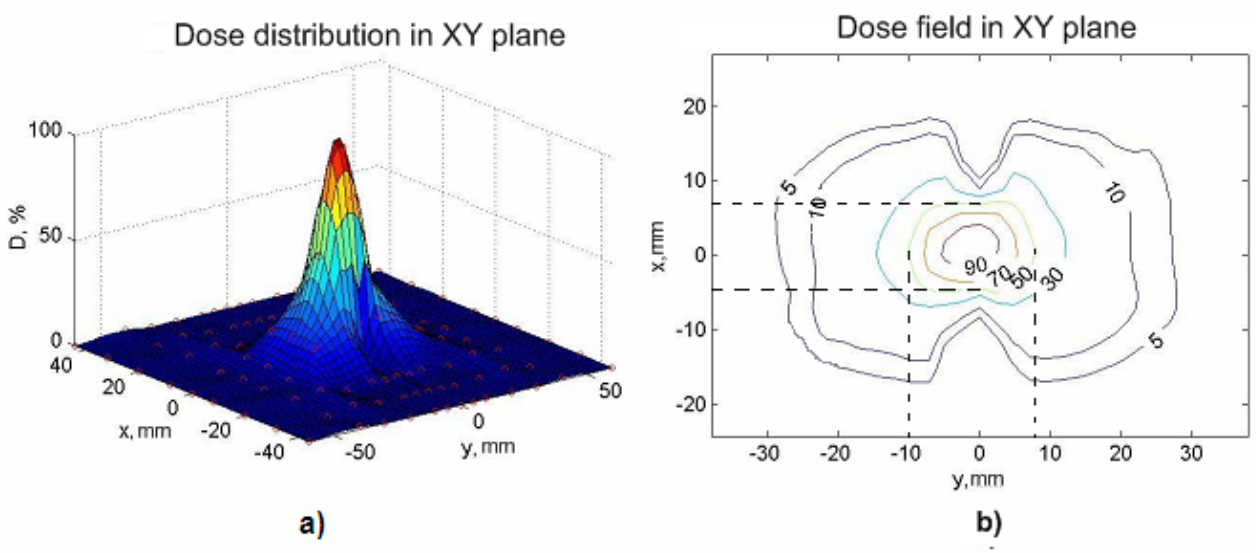

Fig. 4. Result of the PUSK application. a – the dose distribution and b – the field in the *XY* plane with mobile proton beam irradiation. The beam dimensions are Δx = 12 mm and Δy = 18 mm

The result of the PUSK application is presented in Fig. 4a, b, which shows the result of the connection to 50%-isodoses of two fields with the dimensions Δx = 6 mm, Δy = 8 mm, Δz = 6 mm. The docking of the fields is necessary for the irradiation of complex configuration targets, *e.g.*, cerebral ArterioVenous Malformation (AVM). The distance between the centres of the fields is selected according to the form and the size of the irradiation field, which was measured in a tissue-equivalent on the phantom and obtained at mobile proton beam irradiation with the dimensions Δx = 12 mm and Δy = 18 mm (50 % isodose). Note that the rotation pole and the phantom centre coincide. The measurements were performed with the thermoluminescent dosimeters that were 3 mm in diameter and 1 mm thick. Such a representation of the depth dose field clearly shows a high degree of localization of the absorbed energy in the centre of rotation.

3. Proton radiosurgery

The experience of proton radiosurgery performed at the SC-1000 is summarized in Table 2.

Table 2

Proton radiosurgery of FSBI RSCRST at the PNPI synchrocyclotron from 2007 to 2012

Irradiation of pituitary – hypophysectomy	50
Pituitary adenomas	12
Mammary cancer	18
Prostate cancer	20
Irradiation of brain	10
Arteriovenous malformation	10
Total Of these repeated	60 2

In detail, in the cases of prolactin-secreting adenoma, clinical remission was observed in 80 % of the patients and stabilization – in 15 % of the cases. 21 female patients could become pregnant and gave birth to healthy children (4 patients – twice). The complete clinical remission was observed in 92 % of the Icenko – Cushing's disease cases and, in the long-term period, this figure was equal to 96 %. This was manifested in

disappearance of the diabetes, normalization of the blood pressure and regression of the pathological obesity. In the long-term period, the sustained recovery and full normalization of the growth hormone was observed in 86 % of the patients with acromegaly. In this case, the overwhelming majority of the patients were not marked by development of the secondary hormone deficiency. The clinical cure with hormonally inactive adenomas was 95 %. The treatment with the proton irradiation did not cause any serious threatening complications.

Figure 5 shows photographs of a patient before and after the irradiation. The patient had the Icenko – Cushing's disease causing obesity, diabetes, high blood pressure, calcium loss from bones, fractures, and impotence. The results of the proton therapy speak for themselves: 2 years after the therapy – the blood pressure became normal, there was no diabetes, the patient had daily 2 km runs; 3 years after the therapy – the patient got married; 4 years later – he became father.

Fig. 5. Patient before (left) and after (right) the irradiation

Figure 6a shows the arteriovenous malformation of patient L., who previously had a stroke, before the Proton Therapy (PT) and 3 years after the PT. Figure 6b shows patient L. after the PT.

A year after the proton therapy, L. had a child and moved to a village to work as a postman. She drives a car and gives an interview to a TV reporter.

Our work is still in progess…

Fig. 6. a – the AVM of patient L. before the PT (left) and the AVM of this patient 3 years after the PT (right); b – patient L. several years after the proton therapy

References

1. N.K. Abrossimov *et al.*, Abstracts of XI Meeting on Applied Accelerators (ICAA 05), SPb. (2005).
2. N.K. Abrossimov *et al.*, Synchrocyclotron Journal of Physics: Conference Series **1**, 424 (2006).

DESIGN FEATURES OF THE 80 MeV H^- ISOCHRONOUS CYCLOTRON IN GATCHINA

PNPI participants: S.A. Artamonov, E.M. Ivanov, G.F. Mikheev, Yu.T. Mironov, G.A. Riabov.
D.V. Efremov NIIEFA participant: V.G. Mudrolubov

1. Introduction

The synchrocyclotron for acceleration of proton beams up to the energy of 1000 MeV is in operation in Gatchina since 1970. During this time, several reconstruction projects were proposed, but none of them was financially supported. As a result, it was decided to concentrate on a cheaper project and to construct an isochronous cyclotron for acceleration of protons up to 80 MeV. The cyclotron complex is designed for fundamental and applied researches – production of medical isotopes, beam therapy of eye melanoma and surface types of cancer.

To minimize the expenditures while designing the cyclotron, an attempt was made to use at most the existing synchrocyclotron infrastructure, *i.e.* the building, the bridge crane for 30 ton, the electric power system, the water cooling system, the ventilation system, *etc*. The iron yoke of the magnet model of the existing synchrocyclotron was taken for the cyclotron magnet system.

Acceleration of H^- ions has obvious advantages: a possibility for 100 % extraction of the beam with high intensity and variable energy. On the other hand, it requires a special source of H^- ions, high vacuum, and what is most important, the magnetic field strength in the magnet sector should not exceed in our case 17 kGs to prevent H^- electromagnetic dissociation.

The designing and construction of the H^- isochronous cyclotron were in progress several years, and the drawings for the main accelerator subsystems were completed in 2010 [1–3]. The cyclotron magnet was designed, produced, commissioned and put into operation, and full scale magnetic measurements were started. The main problem by that time became a purchase of industrially and commercially produced equipment that was realized in the frame of the nuclear medicine program of the National Research Centre "Kurchatov Institute". Starting from September 2010, the cyclotron and the beam transport line equipment have been mounted in the experimental hall.

2. General description

Main parameters of the cyclotron are presented in Table 1.

Table 1

Main parameters of the cyclotron

MAGNET	
Pole diameter	2.05 m
Valley gap	386 mm
Hill gap (min)	164 mm
Number of sectors	4
Spiral angle (max)	65 degrees
Field in the centre	1.352 T
Flutter (max)	0.025
Ampere-turns	3.4×10^5
Power	120 kW
Weight	250 t
HF SYSTEM	
Frequency	41.2 MHz
Potential	60 kV
Harmonics	2
HF power	2 × 40 kW

VACUUM Pressure 2 cryogenic pumps 1 turbo-molecular	 10^{-7} Torr 2 × 3500 l/s (H_2)
H^- source Multipole Injection energy	 1.5 mA 26 keV
AXIAL INJECTION Transport system: solenoid lens, solenoid, inflector	
EXTRACTION SYSTEM Stripping method Energy range	 40–80 MeV

3. Features of the magnetic system

The magnet and the magnetic system are the most important and expensive parts of the cyclotron, and a considerable attention was paid to their design. The cyclotron magnetic field should meet several requirements. The magnetic field rigidity at the final orbit must reach Br = 13.2 kGs · m, which corresponds to 80 MeV energy of the proton beam. For insuring the isochronism, the magnetic field averaged over the azimuth when going from the centre of the magnet to the final orbit should increase by 8.5 %. The azimuthal variation of the magnetic field should provide the vertical and horizontal transversal focusing. Some room should be left for a high frequency system: the gap between the shims should be wider than 140–150 mm. In distinction from a standard cyclotron, there is an additional and essential requirement for an H^- machine – to keep H^- losses due to dissociation less than 5 %. There are two main problems related to the design of the magnetic field of an isochronous cyclotron. The first one is a selection of the magnetic field structure that would provide both the highest possible energy of the accelerated H^- ions for the given magnet and the beam losses below 5 %. The second problem is the determination of the pole tips geometry that would provide the desired field structure.

3.1. H^- losses and the magnetic structure

Two alternative versions of the magnetic structure have been examined. The first one has the flutter (the mean square relative variation of the magnetic field along the path of the particle under acceleration) F = 0.04, the spiral angle (the angle between the radius vector at the radius r and the tangent to the median line of a sector at the same radius) γ = 55°, the harmonic amplitude A_4 = 4.15 kGs, and the second one has F = 0.025, γ = 65°, and A_4 = 3.28 kGs at the final radius. Both versions provide about the same net axial focusing and differ by the field in the hill regions. Figure l presents the beam losses due to electromagnetic dissociation for these two versions of the magnetic structure. The second version, with a low flutter and a high spiral angle, was selected for the Gatchina cyclotron since it provides beam losses less than 5 %.

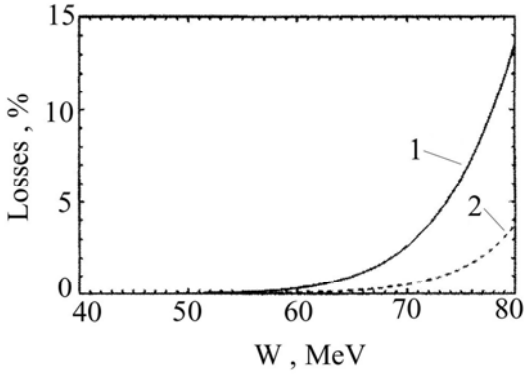

Fig. 1. H^- losses due to electromagnetic dissociation for two versions of the magnetic structure

3.2. The magnetic structure with a high spiral angle

Figure 2 presents a top view of the pole tips of the magnetic system. With the use of the Novosibirsk MERMAID code, which accounts for the iron saturation and permits to use up to 20×10^6 nodes, the profile of the iron shims was determined. More detailed information on the formation of the magnetic field is in a special report in this book. The distribution of the magnetic field in the full scale magnet was measured using a measuring system based on twenty NMR calibrated Hall probes and an automated coordinate system, which could position probes in the cylindrical coordinate system with an accuracy of 0.1 mm along the radius and azimuth at the radius of 100 cm. The achieved precision was equal to 2×10^{-2} % with the total time of measurements of 6–8 hours. Disagreement between the measurements and calculations did not exceed 20 Gs. The final distribution of the magnetic field was measured with 2–5 Gs precision.

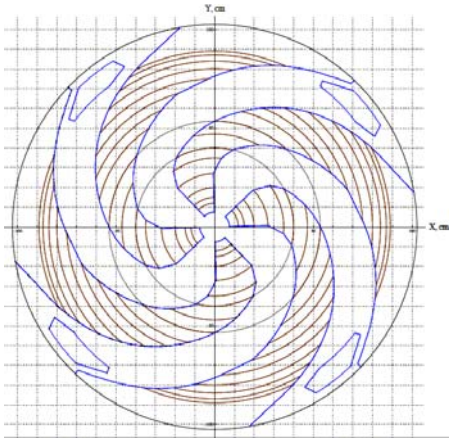

Fig. 2. Top view of the pole tip

3.3. The flutter versus the radius for straight sectors

The needed sizes of the valley and hill gaps were estimated by calculations of the flutter in a straight sector structure. An estimation of the flutter value, which defines the azimuthal variation of the magnetic field at different radii, requires three dimensional calculations even for straight sectors. Such calculations presented a real problem quite recently. For this reason, approximate methods were developed to analyze the problem. Approximate calculations cannot give quantitative results, but allow us to analyze qualitatively the relations between different parameters of the magnetic structure. In [4], under an assumption of a uniform magnetization of the magnet sectors, the value of the main harmonics of the magnetic field variation in an isochronous cyclotron is determined as:

$$B_N = 8\, M \sin(2\pi a / d) \exp(-2\pi g_h / d),$$

where $2a$ is the sector width along the azimuth for a given radius, $2g_h$ is the hill gap, d is the structure period equal to the sum of widths of the valley and the hill, and $4\pi M = 21$ kGs. From this expression one can see that for an isochronous cyclotron with $d = 2\pi r/N$, where $N = 4$ is the number of sectors, the azimuthal widths of the valley and hill being equal, the flutter increases with the radius as:

$$F \sim B_N^2 \sim \exp(-2/x),$$

where $x = r/Ng_h$. The flutter increases when the hill gap is decreased and decreases with the growth of the number of sectors. The maximum value of the flutter corresponds to the case when the sector and valley widths are the same. In this case, $a = 0.25d$, and $\sin(2\pi a / d) = 1$. For the case of $x < 0.5$, which corresponds to the range of radii $r < 0.5 \cdot Ng_h$, the value of the flutter rapidly decreases, and the edge focusing becomes ineffective. For C-80, this effect takes place at radii $r < 15$ cm. These qualitative results are supported with more exact calculations. The precisely calculated flutter versus the radius is presented in Fig. 3 for two variants of the magnetic structure.

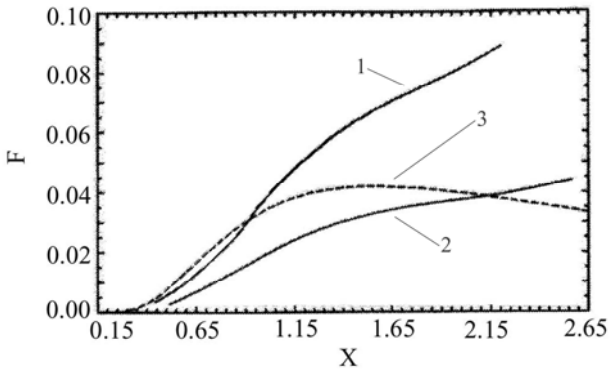

Fig. 3. Flutter as a function of the non-dimensional parameter $x = r / Ng_h$: 1 – $2g_v$ = 386 mm, $2g_h$ = 170 mm; 2 – $2g_v$ = 284 mm, $2g_h$ = 145 mm; 3 – approximation of the sector uniform magnetization for the case 1. Here, g_v is a half of the valley gap

3.4. The effect from the spiral pole tips

For acceleration of H^- ions, it is advantageous to use a highly spiraled magnetic structure and small variation of the magnetic field from hill to valley. The presence of high spiral angles leads to an increase of the vertical focusing and provides an extra focusing due to angular focusing. It is a standard practice to estimate an increase of the flutter by using the following factor:

$$S(r, \gamma) = 1 + 2 \tan^2 \gamma(r),$$

where γ(r) is the spiral angle at the given radius. However, in the real life for a spiral structure with high values of γ and especially for the central region, the benefit in focusing is smaller than it could be expected from this expression. This is explained by a drop of the flutter at small radii and a difference between the spiral angle for the pole tips and that for the magnetic field. The drop of the flutter due to introduction of the spirality can be understood on the basis of simple geometrical considerations [5]. At large values of the spiral angle, the difference between the sector width along the azimuth (AB in Fig. 4) and the sector width A_1B_1 determined along the perpendicular to the middle line, becomes substantial. In the case of straight sectors, the flutter is defined by the edge effect along the azimuth. With introduction of the spirality, the distance between sectors along the line perpendicular to the middle line of a sector becomes smaller than the distance along the azimuth. It leads to a decrease of effective sector and valley widths, and as a consequence to a decrease of the flutter. At middle and large radii, the total effect from the spirality of the magnetic structure connected with an increase of the edge focusing and a decrease of the flutter leads to an increase of focusing. However, the spirality of the magnetic structure decreases the effective width of the sectors and may result at small radii in a drop of the flutter and to a decrease of focusing. The influence of the spiral angle on the flutter value can be estimated with calculations of the flutter for a straight sector (see Fig. 4) if one makes the following replacement: $x_{\text{eff}} = x \cos\gamma$. The total effect from the spiral angle can be characterized with the parameter which is a product of the flutter F and the value of $S(r, \gamma)$. Since the flutter rapidly decreases at $x_{\text{eff}} < 0.5$, the spirality can result in a decrease of focusing. For each value of the radius and the parameter x, there is a critical spiral angle that results in an increase of focusing from introduction of the spirality. For the spiral angles more than the critical value the vertical focusing decreases. The value of the critical angle for each value of x can be found as a root of the following equation:

$$U(x, \gamma) = (F(x \cos\gamma) / F(x)) \cdot (1 + 2 \tan^2 \gamma) - 1 = 0,$$

where $F(x)$ is a function similar to that shown in Fig. 3.

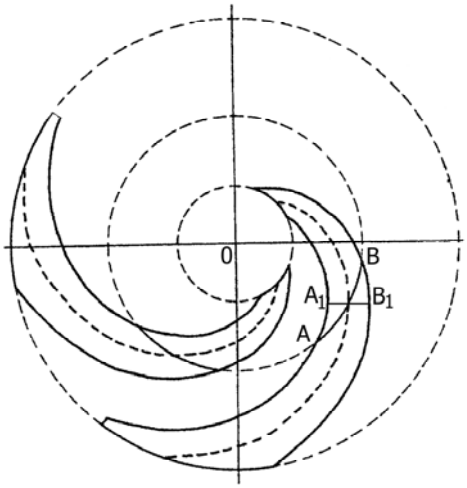

Fig. 4. The difference between the sector width along the azimuth and an "effective" width at large spiral angles. AB – width of a sector along the azimuth; $A_1B_1 \approx AB\cos\gamma$ – an effective width of a sector along a perpendicular to the middle sector line

Figure 5 shows the critical spiral angle versus the radius for the considered accelerator C-80. According to the plot, the spiral structure with high spiral angles has an advantage at $r > 35$ cm, whereas at radii $r < 15$ cm it becomes ineffective. Therefore, it is necessary to use a straight sector structure in the central region, a highly spiraled structure like the spiral of Archimedes being ineffective in this region.

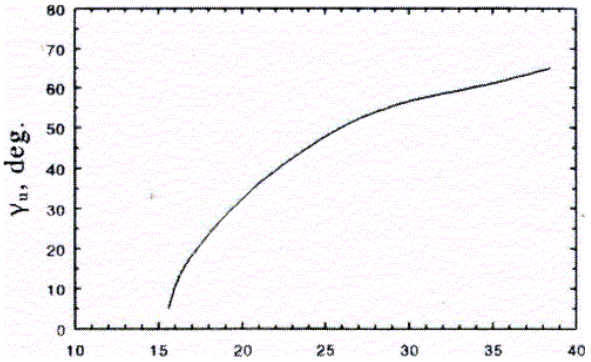

Fig. 5. The critical spiral angle in dependence on radius for $2g_v = 386$ mm, $2g_h = 170$ mm, $r = N \cdot g_h x_{eff,}$, $N = 4$

Another effect, which has been already mentioned, is related to a mismatch of the geometrical and magnetic field spiral angles. For C-80, the maximum mismatch between the magnetic field and geometrical spiral angles is about 7°, which results in a reduction of the edge focusing by up to 30 % at the angles of 65–70°. This effect was noted in [4], and it needs to be taken into account in a design of the magnetic structure of the cyclotron.

4. Features of the chamber and vacuum system

The chamber for the C-80 cyclotron has an unusual design. As has been noted before, successful acceleration of H^--ions requires high vacuum of 10^{-7} Torr in the chamber. To achieve such high vacuum, the pumping system involves two cryogenic and one turbo molecular pumps, an external ion source being used. Moreover, in the adopted design the magnetic system with correction shims is placed outside of the vacuum volume. The upper and lower lids of the chamber are attached to the poles of the magnet. Thus, two walls of the chamber (2 × 16 mm) occupy about 10 % of the magnet gap, which has required to increase the ampere-turns of the magnet winding and the power of the magnet.

5. Beam extraction

The beam extraction is realized with a stripping method. Due to acceleration of H^- ions, it is possible to extract 100 % of the beam with intensity of 100 μA and implement a variation of the extracted beam energy from 40 to 80 MeV. The scheme of the extraction system is shown in Fig. 6.

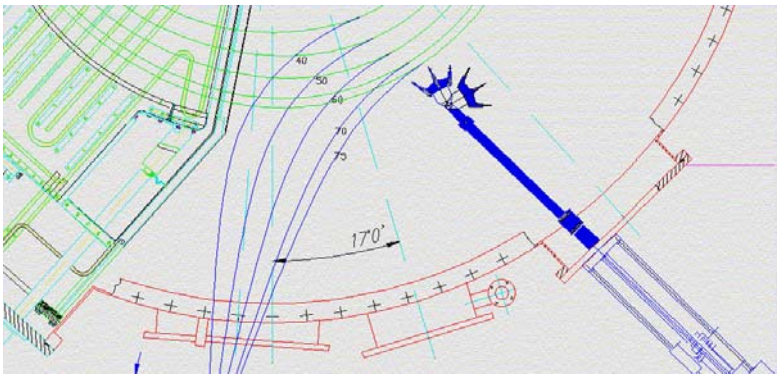

Fig. 6. Schematic view of the extraction system

As is shown in Fig. 6, rays of the extracted beams of different energies come together to a focus point outside of the vacuum chamber in the centre of the correction magnet. This magnet provides matching of the extracted beam with the transport beam line. Figure 7 shows the calculated parameters of the extracted beam. This information can be used as input data to design the beam transport lines.

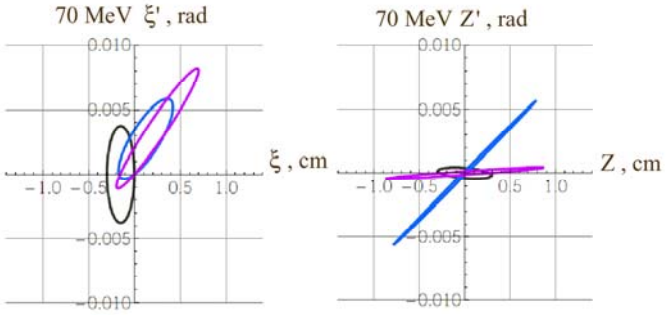

Fig. 7. Phase space ellipses of the extracted beam: black is at the stripping foil, blue is at the input of the correction magnet, and lilac is at the exit of the correction magnet. Here, ζ (ζ') is the horizontal coordinate (angle), Z (Z') is the vertical coordinate (angle)

6. The experimental area

The multy-purpose experimental complex consists of targets of different specialization and beam transport lines. A beam of high intensity is transported to the basement, where three stationary targets are installed for production of medical radioisotopes and pharmaceutical medications: two targets are intended for radiochemical separation methods, and the third target is to be used for separation with the electromagnetic separator as is shown in Fig. 8.

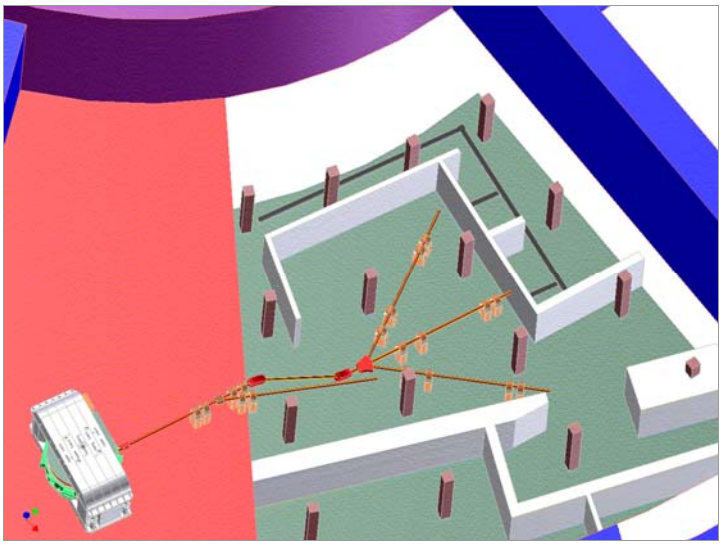

Fig. 8. Transport lines to the targets for production of medical radioisotopes

On the ground floor are disposed an ophthalmology facility with a low intensity beam line and a facility for radiation tests of electronics components with the beam of energies from 20 to 80 MeV.

7. Conclusion

By present, the repair and modernization work of the experimental hall for installation of the cyclotron complex has been completed. The installation and commissioning of the main equipment of the cyclotron is in progress: a power system, a high-frequency generator, a vacuum chamber, an axial injection system and a source, beam probes with a beam diagnostic system, an extraction system with a stripping probe and a correction magnet, and a control system of the cyclotron. Designing and manufacturing of the elements of the beam transport system are in progress. According to the plans, the first beam is expected to be in the end of 2012 or in the beginning of 2013.

References

1. N.K. Abrossimov *et al*., *Proc. XIII Intern. Conf. on Cycl. and Their Applic.*, Vancouver, Canada, 54 (1992).
2. N.K. Abrossimov *et al*., RUPAC-XIII, Russia, Dubna **2**, 205 (1993).
3. N.K. Abrossimov *et al*., RUPAC-XIV, Russia, Protvino **4**, 5 (1994).
4. V.I. Danilov, Preprint JINR-R-**409**, Dubna (1959).
5. N.K. Abrossimov *et al*., *Proc. XV Intern. Conf. on Cycl. and Their Applic.*, Caen, France, 58 (1997).
6. H.G. Blosser and D.A. Jonson, NIM **121**, 301 (1974).

3D MODELING AND FORMATION OF THE MAGNETIC FIELD IN THE C-80 ISOCHRONOUS CYCLOTRON

S.A. Artamonov, E.M. Ivanov, G.A. Riabov

1. Introduction

The isochronous cyclotron C-80 which is under construction at PNPI is planned to be used for fundamental researches in nuclear physics, solid state physics and biology, as well as for an applied program – production of medicine isotopes for therapy of eye melanoma and surface forms of cancer. As a first approximation, the magnetic system of the cyclotron C-80 was designed a few years ago on the basis of 2D calculations by using the POISSON program and measurements on two small models [1, 2].

A rather complicated magnetic structure with high spiral angles and a set of 17 correction shims in each of 8 sectors is used in the H^- ion isochronous cyclotron C-80. The 3D Novosibirsk code MERMAID was applied to optimize the geometry of the sectors and shims in the hill and valley regions. A precision finite-element model allows taking into account the iron non-linear effects and the detailed magnet geometry. The MERMAID code makes use of about 20.5 million nodes and provides magnetic field calculations with an accuracy of 10–20 Gs. The integral magnetic field parameters (isochronism, transversal motion frequency, H^- ion electromagnetic dissociation) have been optimized by using a trajectory analysis. The MERMAID program provides a significant reduction of time and efforts for determination of necessary shims, as compared with a trial-and-error method.

The final version of the C-80 magnetic structure optimized with 3D calculations using the MERMAID program is presented in this report.

2. Main calculation problems

One of the central problems for every isochronous cyclotron is to form the radial and azimuthal magnetic field distribution with required properties. A well designed cyclotron magnet should ensure isochronism for particle acceleration, the magnetic field that provides axial (vertical) and radial (horizontal) focusing of the beam during acceleration, the magnetic field that guarantees an operation point (for cyclotrons it looks like an operation curve) away from dangerous resonances or a fast passage of the beam through the resonance zones, and last, but not least, a possibility to install all cyclotron subsystems.

It is always worth to reduce the number of nodes in the 3D model magnet, which consequently reduces also the time of calculations. This can be done by application of all possible symmetries of the cyclotron magnet. Some magnet details can also be neglected since their influence on the magnetic field in the median plane is very small (*e.g.*, holes for screws on the outer side of the return yoke necessary to handle and fix other cyclotron subsystem elements). Unfortunately, the full model is always required when one wants to study the influence on the magnetic field of different imperfections, such as, for example, a shift and/or rotation of the upper part with respect to the lower part of the cyclotron, a shift and/or rotation of one of the coils with respect to the median plane of the cyclotron, some mechanical defects of one or more poles, *etc*.

Another problem is related with acceleration of H^- ions. To reduce H^- dissociation losses, a magnetic structure of C-80 with high spiral angles was proposed [3]. Note that the spiral structure provides vertical beam focusing.

It is also necessary to mention an essential mathematical nonlinearity of the problem. In the isochronous C-80 cyclotron, three types of steel are used for the magnetic structure. The main magnet yoke is constructed from a set of two types of steel: steel 3 with the permeability $\mu_3(B)$ (see Fig. 1) and steel 10 with $\mu_1(B)$. The poles are constructed from steel 10 with $\mu_1(B)$. The spiral sectors, 17 correction shims in each of 8 sectors, and the valley shims are constructed from steel 10 with $\mu_2(B)$. In Fig. 1, it is seen that the values of $\mu(B)$ very strongly differ in the working range of magnetic fields of the cyclotron (11000–18000 Gs). It is obvious that this gives rise to additional calculation difficulties and problems for making a 3D model.

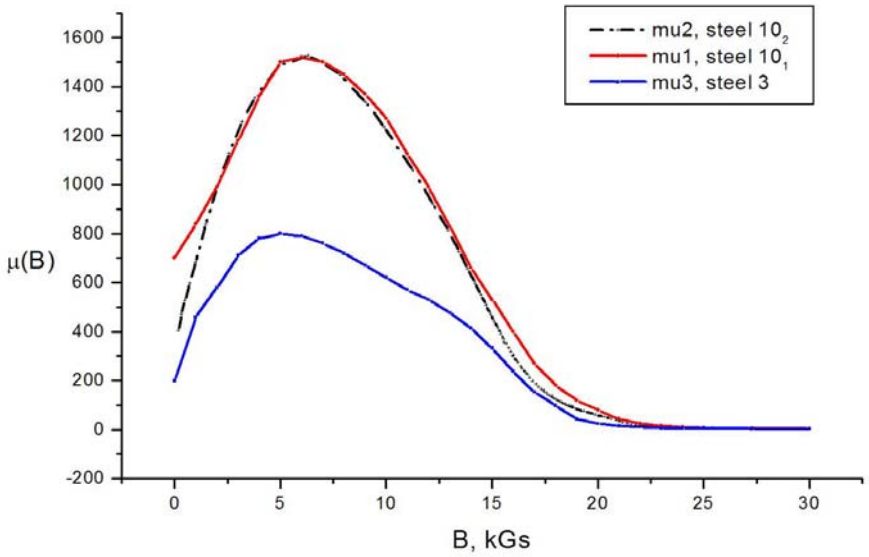

Fig. 1. Permeability curves μ(B) for the steel used in C-80

3. Magnetic field formation

The selection of magnetic structure parameters and the necessary magnetic field formation for C-80 was accomplished step by step using the program MERMAID [4].

At the first stage, the geometry and the key parameters of the magnetic system for C-80 [5] were fixed. It was supposed that the height of each of the sectors is equal to 90 mm, and during further optimization was not changed. For obtaining the required isochronism, the height of the correction sector shims was varied. The initial height of these shims was selected equal to 20 mm. Besides, in the course of the optimization, a special constrained condition was imposed. It was required that the amplitude of the 4-th field harmonic should not exceed ~ 3000 Gs, and the field near the extraction radius r = 90 cm should be $B \leq 17000$ Gs. Under these conditions, the H^- dissociation is below 5 % [3]. For these purposes, additional valley shims were introduced into the magnetic system, and their geometrical parameters were also varied. Thus, the formation of the demanded isochronous field was carried out only by changing the iron shim geometry without using correction coils.

At the second stage, a 3D model of the magnetic system of C-80 was developed and constructed (see Fig. 2). It reproduces accurately the geometry of the magnet yoke, of the sectors (4 pairs), sector shims (17 correction shims in each sector), of the valley shims, the coils current, and the external boundaries. It also takes into account nonlinear magnetic properties of the used electrotechnical steels.

As a rule, 1/8 or 1/4 part of the magnet with the periodic symmetric boundary conditions is used in 3D calculations. Such a model essentially reduces the number of nodes and increases the accuracy of the calculations. In our case, it is impossible to use this approach. Because of a big angular extension of the spiral sectors in C-80, it was necessary to use a half of the magnet with the corresponding symmetry boundary conditions in our calculations. The external boundary of the area where the calculations were performed was chosen rather far to get rid of its influence on the magnetic field in the working region and to determine correctly the fringe field. The fringe field should be taken into account for correct calculations of the extraction beam optics.

Thus, for the description of the magnetic structure of C-80 using the MERMAID program, about 20.5 million direct prisms were required, which allowed us to reach the necessary precision of 10^{-3}–10^{-4} in the calculation of the magnetic field.

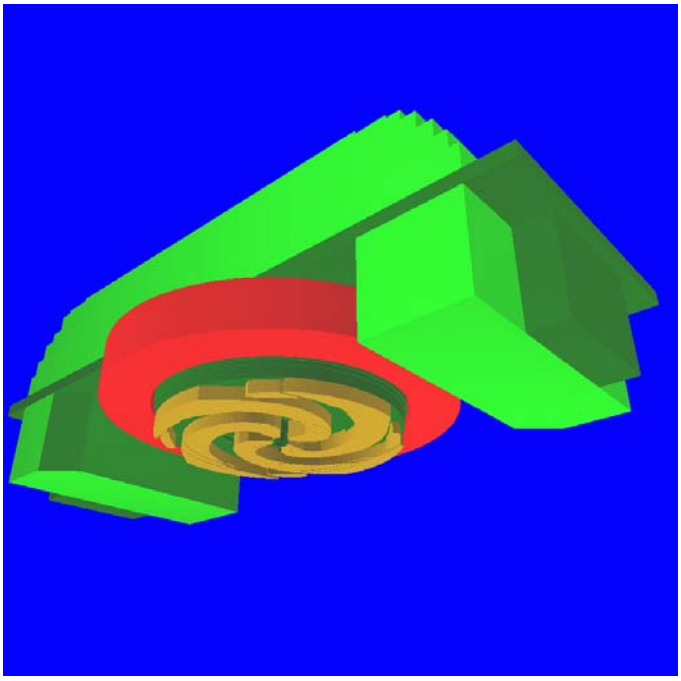

Fig. 2. MERMAID model of C-80

Our three-dimensional model is close to the reality. Therefore, the results of magnetic field measurements are expected to be close to the results of calculations. Our experience is that using the MERMAID software one can expect a difference of 10–20 Gs between the calculated and measured magnetic field values. These field differences can be explained by not sufficient precision of the software, by uncertainties in the permeability curves $\mu(B)$, and by some small geometrical differences between the model and the real cyclotron magnet.

4. Algorithm of optimization

The developed computing model was used for simulations of the necessary spatial distribution of the C-80 magnetic field $B_z(z,r,\theta)$ and for its subsequent analysis. As is well known, the cyclotron magnetic field at the given radius r, having the N-fold rotational symmetry, can be presented as a Fourier series

$$B_z(z=0,r,\theta)=\overline{B}(r)\left\{1+\sum_{n=1}^{\infty}\left[a_n(r)\cos(nN\theta)+b_n(r)\sin(nN\theta)\right]\right\}=$$

$$=\overline{B}(r)\left\{1+\sum_{n=1}^{\infty}A_n(r)\cos nN\left[\theta-\psi_n(r)\right]\right\},$$

where N is the number of symmetry periods of the cyclotron ($N = 4$ in our case),

$a_n, b_n, A_n=\sqrt{a_n^2+b_n^2}$ are the coefficients of the Fourier series,

$\psi_n(r)=\frac{1}{n}\operatorname{arctg}\frac{b_n(r)}{a_n(r)}$ is the phase of the n-th harmonic,

$\overline{B}(r)=\frac{1}{2\pi}\int_0^{2\pi}B_z(r,\theta)d\theta$ is the magnetic field averaged over the azimuth.

The magnetic field flutter F at the radius r can be defined as

$$F=\frac{\overline{B^2}-\overline{B}^2}{\overline{B}^2}=\frac{1}{2}\sum_{n=1}^{\infty}A_n^2,\quad \overline{B^2}=\frac{1}{2\pi}\int_0^{2\pi}B_z^2(r,\theta)d\theta\,.$$

The procedure of the magnetic field optimization was divided into two stages. At the first stage, the isochronous field (the averaged over the azimuth magnetic field necessary for isochronous particles acceleration) and the betathron frequencies were estimated using analytical formulas from [6]. Namely, the betathrone frequencies were approximated by the following equations:

$$\nu_z^2 = -k + F + \frac{1}{2(N^2-1)}\left[A_N^2(1+(2N^2-1)\mathrm{tg}^2\gamma) - A_N A_N' - A_N'' A_N\right] + \frac{(A_N')^2}{2N^2},$$

$$\nu_r^2 = 1 + k + \frac{1}{2(N^2-1)(N^2-4)}\left[6N^2F(1+\mathrm{tg}^2\gamma) + (5N^2-8)A_N A_N'\right] + \frac{A_N'' A_N}{2(N^2-1)} + \frac{(A_N')^2}{2(N^2-4)},$$

where ν_z is the axial (vertical) betathron frequency, ν_r is the radial (horizontal) betathron frequency, $k = \frac{r}{\overline{B}(r)}\frac{d\overline{B}(r)}{dr}$ is the radial field index, $A_N' = r\frac{dA_N}{dr}$ and $A_N'' = r^2\frac{d^2A_N}{dr^2}$ are the first and second derivatives of the A_N harmonic amplitude, $\mathrm{tg}\gamma = r\frac{d\psi_N(r)}{dr}$, γ is the sector spiral angle (the angle between the radius vector at radius *r* and the tangent to the pole tip edge at this radius).

Ions motion should be synchronized with a given phase of the cyclotron RF system during acceleration. Therefore, the magnetic field in the cyclotron should ensure a constant rotation period of ions $T = 2\pi/\omega_0$. As was mentioned above, the magnetic field with this feature is called isochronous. This field can be approximated by the following equation:

$$\overline{B}_{\mathrm{isochr}}(r) = \frac{B_0\tau(r)}{\sqrt{1 - \frac{r^2\tau^2(r)}{R_c^2}}},$$

where

$$\tau(r) = 1 - \sum_{n=1}^{\infty}\frac{A_{Nn}^2 + A_{Nn}A_{Nn}'}{\left[(Nn)^2 - 1\right]},$$

$R_c = c/\omega_0 = \mathrm{const}$, c is the light velocity, $\omega_0 = \frac{qB_0}{m_0c}$, q is the particle charge (in units of the electron charge), B_0 is the magnetic field in the centre of the cyclotron, m_0 is the rest mass of the particle under acceleration.

The aim of the magnetic field optimization is to make the value $\Delta B = \overline{B}(r) - \overline{B}_{\mathrm{isochr}}(r)$ as small as possible at each radius *r*. For the purpose of receiving the minimum difference between the calculated average field $\overline{B}(r)$ and the estimated isochronous field $\overline{B}_{\mathrm{isochr}}(r)$, some geometrical changes were made in the 3D model (with a control of other required characteristics of the cyclotron). Such an approach is rather simple and fast, but it doesn't possess the sufficient accuracy for an isochronous cyclotron.

At the second stage, a full particle trajectory analysis was carried out. Namely, we solved numerically the relevant nonlinear equations describing the particles movement:

$$r'' = r + 2\frac{r'^2}{r} + \frac{q\sqrt{r'^2+r^2+z'^2}}{\sqrt{E^2-E_0^2}}\left[B_z\left(r+\frac{r'^2}{r}\right) - B_r\frac{r'z'}{r} - B_\theta z'\right],$$

$$z'' = 2\frac{r'z'}{r} + \frac{q\sqrt{r'^2+r^2+z'^2}}{\sqrt{E^2-E_0^2}}\left[B_z\frac{r'z'}{r} - B_r\left(\frac{z'^2}{r}+r\right) + B_\theta r'\right],$$

$$B_r = \int_0^z\frac{\partial B_z}{\partial r}dz = \frac{\partial B_z}{\partial r}z,$$

$$B_\theta = \frac{1}{r}\int_0^z\frac{\partial B_z}{\partial\theta}dz = \frac{\partial B_z}{\partial\theta}\frac{z}{r}.$$

Here E and E_0 are the total energy and the rest mass of the particle (in MeV); r', r'', z' and z'' are derivatives of r and z over θ. The orbit will be an equilibrium one if the periodic initial conditions are as follows:

$$r_{eq}(2\pi) = r_{eq}(0), \quad r'_{eq}(2\pi) = r'_{eq}(0).$$

In the first approximation, an analytical formula from [6] was used for $r_{eq}(\theta)$ near $r = r_k$:

$$r_1(\theta) = r_k \left\{ 1 + \sum_{n=1}^{\infty} \frac{A_{Nn}}{(Nn)^2 - (1+k)^2} \cos Nn[\theta - \psi_{Nn}] - \right.$$
$$\left. - \sum_{n=1}^{\infty} \left[A_{Nn}^2 \frac{3(Nn)^2 - 2}{4[(Nn)^2 - 1]^2} + \frac{A_{Nn} A'_{Nn}}{2[(Nn)^2 - 1]} \right] \right\}.$$

The expression for $r_1'(\theta)$ can be received from $r_1(\theta)$ if one differentiates it over θ.

A special procedure allowed us to determine the so-called static equilibrium orbits, more precise values of the time of particle revolutions at different radii, the betathron frequencies, the H^- ions losses due to electromagnetic dissociation, and the value of the isochronous field (details see in [7]). This new more precise value of the isochronous field was compared with the magnetic field averaged over the azimuth. If it was necessary, geometrical corrections of the magnetic structure were repeated in order to minimize the difference between the calculated average and the isochronous fields. Such iteration procedures were repeated until the difference between the average 3D field and the isochronous one (calculated at the second stage) became less than 20 Gs.

The C-80 magnet structure optimization was realized for a number of minimum magnet gaps: 146, 156, 170, 176 and 164 mm.

5. Main results of the calculations

The final version of the magnetic structure for the isochronous cyclotron C-80 was chosen for a minimum gap equal to 164 mm. The optimum 3D magnetic field is presented on Fig. 3.

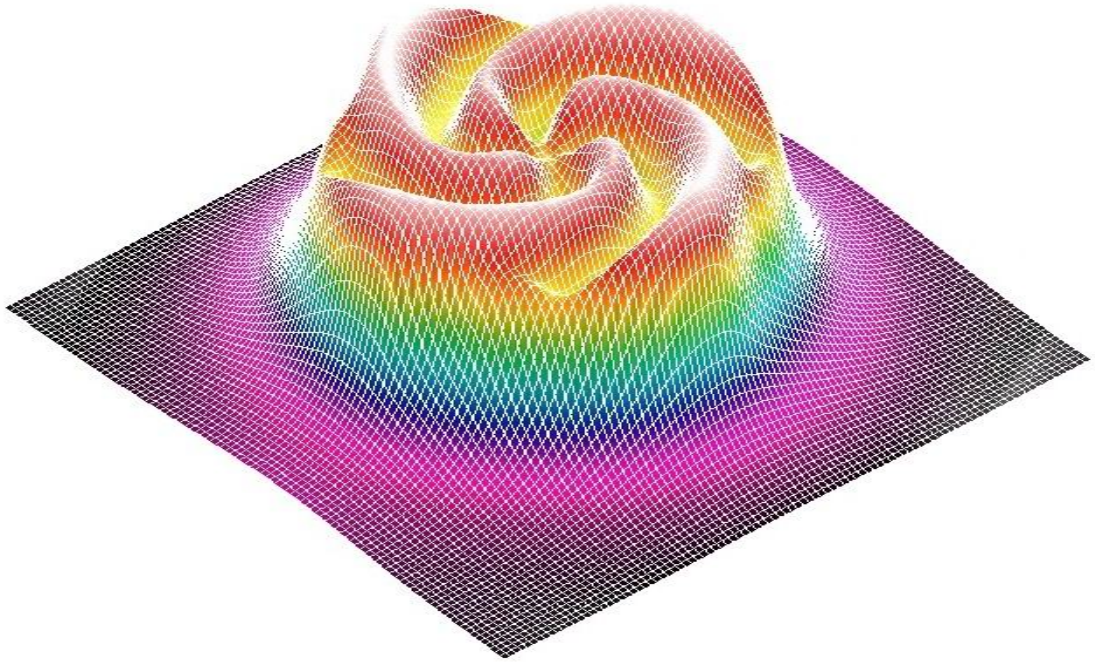

Fig. 3. 3D MERMAID magnetic field for C-80

The results of 3D magnetic field calculations provide information about the magnetic field in any point of the model and around it. Very often they are used to make magnetic field maps in the cyclotron magnet median plane or in three dimensions around this plane. Such a magnetic field map becomes a part of the input data for programs calculating the trajectories of particles and for programs calculating properties of the magnetic field, for example, the equilibrium orbit codes [7].

Briefly, we will enumerate main modifications of the initial magnetic system [1, 2] executed on the basis of 3D simulations. The direct sectors were prolonged from the radius of 27 cm to the radius of 40 cm, but with two turns at fixed angles, keeping the previous sector widths along the azimuth the same (see Fig. 4). It led to blocking of an uncontrollable penetration of the magnetic spiral angle to the area near the central region. Thereby, a growth of the amplitude of the main harmonic was provided which led to stable motion of particles in this area. For reduction of the number of valley shims, the azimuthal expansion of the sectors was made by ~ 20 mm from the radius of 70 cm to the final radius of 102.5 cm (see Fig. 4). It allowed to reduce the number of the valley shims in each valley from four in the initial magnetic system to one in the final version.

The dashed and solid blue lines in Fig. 4 show the old and new geometry of a C-80 sector, respectively. The red line is the central line of the sector. The central region was changed in the 3D C-80 model so that to consider the real geometry of the system with an axial injection. Besides, by means of a magnetic plug, a necessary fall of the magnetic field in the central region was ensured.

It is necessary to emphasize that the proposed modification of the magnetic system allowed to receive stable axial and radial motion of the accelerated ions in all working area of the C-80 cyclotron. A preliminary numerical study of resonances in the cyclotron acceleration system has also been performed. For this purpose, the data presented in Fig. 5 were used. The operation point (ν_r, ν_z) moves as the particle kinetic energy increases and can cross the resonance curves shown in Fig. 5. Resonances are dangerous when the crossing of these resonances is slow (when the kinetic energy gain per turn is small). On the other hand, if the passage through the resonance zones is fast, then the quality of the beam becomes only slightly worse.

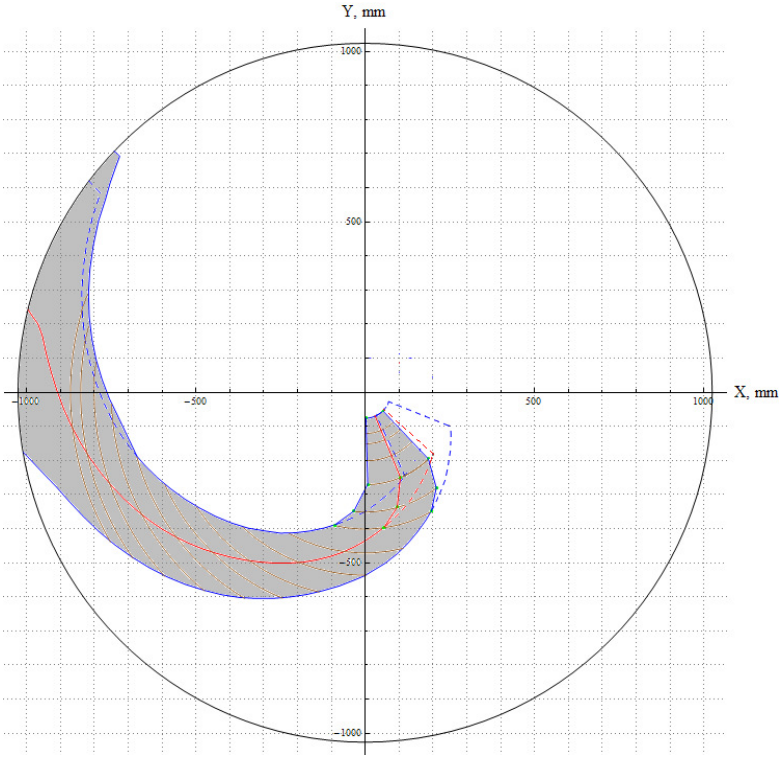

Fig. 4. Modification of C-80 sectors

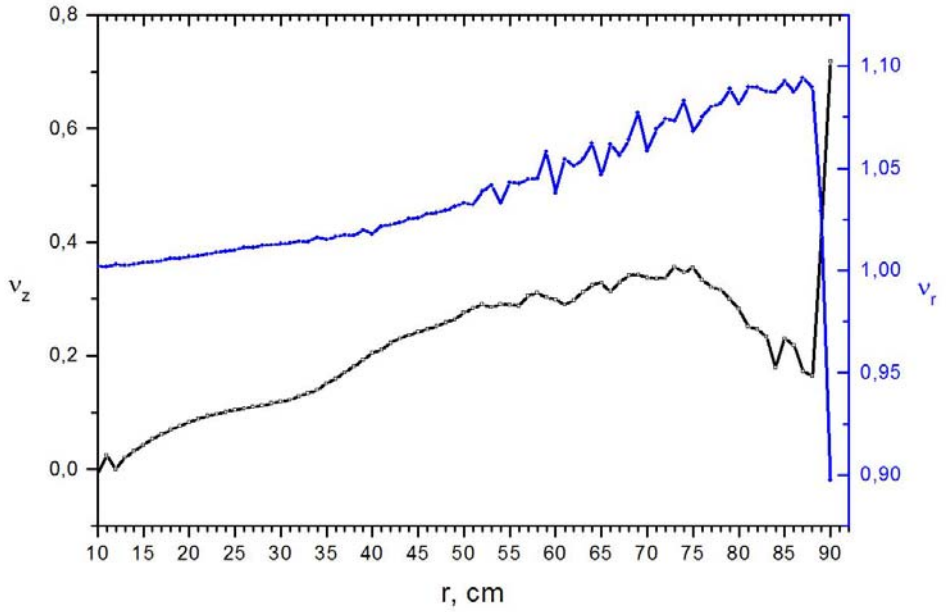

Fig. 5. Horizontal ν_r (the upper curve) and vertical ν_z betathron frequencies (the numbers of oscillations per turn) in C-80

The performed changes of the magnetic structure led also to a decrease to 2.2–2.5 % of losses of the H^- ions dissociation in the course of acceleration. The final proposed magnetic structure for the C-80 cyclotron is shown in Fig. 6.

Fig. 6. View of the pole tip for the cyclotron C-80

6. Conclusion

A careful analysis of the 3D data on the magnetic field, performed with the method described in detail in [7], has shown that practically all problems of the isochronous cyclotron C-80 under construction have been overcome. The betathrone frequencies are acceptable in all working area of the cyclotron. However, most likely, small corrections of the isochronous field will be required, depending on the measurements to be done. The final distribution of the magnetic field is planned to be measured with a 2–6 Gs precision when the sectors will be mounted.

According to the results of simulations of the 3D magnetic field and particles trajectory calculations, it is possible to state that the last version of the magnetic structure of the isochronous C-80 cyclotron meets all design requirements.

References

1. N.K. Abrossimov, S.A. Artamonov, V.A. Eliseev, G.A. Riabov, "Design and Optimization of the Magnet and Magnetic Structure for the 80 MeV H^- Isochronous Cyclotron", Proceeding of the Second International Workshop: Beam Dynamics & Optimization – BDO, 1995, St.-Petersburg, Russia, 7 (1995).
2. N.K. Abrossimov, S.A. Artamonov, V.A. Eliseev, G.A. Riabov, "Design and Modelling of the Spiral Magnetic Structure for 80 MeV H^- Isochronous Cyclotron", Proceeding of the XV International Conference on Cyclotron and Their Application, Caen, France, 518 (1998).
3. N.K. Abrossimov, S.A. Artamonov, V.A. Eliseev, G.A. Riabov, "Losses of H^- Ions Due to Electromagnetic Dissociation and Their Effect on Selection of Isochronous Cyclotron Magnetic Structure", PNPI Research Report 1994–1995, Gatchina, 275 (1996).
4. S.N. Andrianov, S.A. Artamonov, A.N. Dubrovin, V.A. Eliseev, "Computer Simulation of the 3D Magnetic Field of the PNPI Isochronous Cyclotron" (in Russian), Vestnik SPbSU, ser. 10, iss. **3**, 12 (2008).
5. G.A. Riabov *et al*., "Design Features of the 80 MeV H^- Isochronous Cyclotron in Gatchina", these proceedings.
6. Yu.G. Basargin, V.P. Belov, "Some Problems of Particle Motion Dynamic in Cyclotrons with Spatially Variable Fields", Electrofisicheskaya Apparatura (in Russian), **3**, Moscow, Atomizdat, 3 (1965).
7. S.N. Andrianov, S.A. Artamonov, "Optimal Algorithm for Forming an Isochronous Magnetic Field in Accelerators with Azimuthal Variation" (in Russian), Vestnik SPbSU, ser. 10, iss. **2**, 3 (2009).

DEVELOPMENT OF TARGETS FOR THE RIC-80 PROJECT

V.N. Panteleev, A.E. Barzakh, D.V. Fedorov, A.M. Filatova, V.S. Ivanov, K.A. Mezilev, F.V. Moroz, P.L. Molkanov, S.Yu. Orlov

1. Introduction

The rapidly growing studies in nuclear physics, developments of experimental methods and implementation of very sensitive and effective detectors have provided a very good possibility for development of a completely new direction in medical diagnostics and therapy of diseases, which is presently known as nuclear medicine. The exceptional ability of nuclear medicine methods is based on the possibility to detect and treat a large set of diseases at a very early stage, saving human lives and reducing expenses for treatment. The technology of nuclear medicine used for diagnostics and therapy is based on employing radioactive isotopes with selected properties. The common methods in nuclear diagnostics use the technology of marking medications by specific radionuclides. By measuring the distribution of radioisotopes in the human body, it is possible to observe the functions of the investigated organs or their parts. Similar methods are used for treatment of malignant tumors. In this case, the compounds containing radioactive isotopes are absorbed by malignant formations, which leads to their local irradiation and subsequent destruction. The main advantage of nuclear radiomedicine methods is that the diagnostics and treatment can be carried out at very early stages of the disease.

This work is the first part of the program of the target development for the new project of RIC-80 (Radioactive Isotopes at the cyclotron C-80) [1], which is presently being carried out at PNPI. The main task of this work is the development of methods of production and separation of the isotope-generator ^{82}Sr, which is used for PET diagnostics of heart diseases, and also of some other isotopes used for diagnostics and therapy. The methods are worked out using a 1 GeV proton beam of the synchrocyclotron with the aim to use the developed target prototypes at the new radioisotope facility RIC-80 with the proton energy of 80 MeV and the beam intensity of up to 200 μA.

2. Description of the experiment and experimental results on production of ^{82}Sr

In the first experiments, niobium foils were used as target material for production and yield measurements of ^{82}Sr. This nuclide with the half-live $T_{1/2}$ = 25.55 days is the generator for its daughter isotope ^{82}Rb ($T_{1/2}$ = 1.25 min), which is widely used in PET diagnostics.

A stack of niobium foils of 16 g/cm^2 thickness was placed into a Ta-W container which was designed as a prototype of the target device for production of ^{82}Sr at RIC-80. Results of FLUKA [2, 3] calculations of the ^{82}Sr activity produced in the irradiated Nb and Zr targets are presented in Fig. 1.

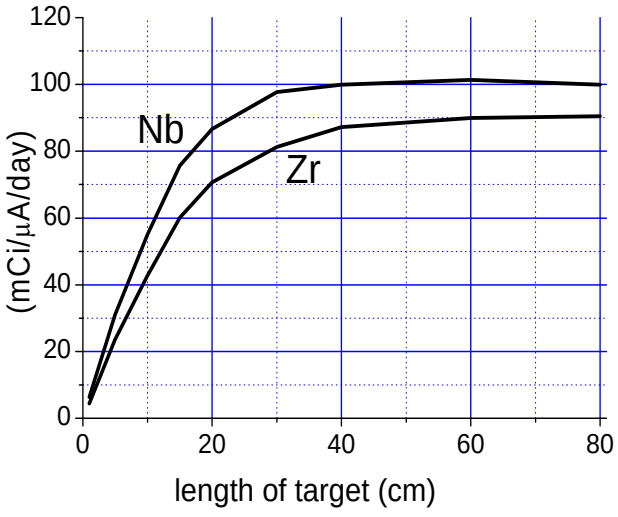

Fig. 1. ^{82}Sr radioactivity produced in the Nb or Zr foil target *vs* target length. The activity value is in mCi; the proton energy is 1 GeV; the proton beam intensity is 1 μA; the irradiation time is 24 hours

One can see in Fig. 1 that even with a rather low current of the PNPI synchrocyclotron (up to 1 μA), it is possible to obtain about 0.5 Ci of ^{82}Sr after 5 day irradiation of a target of the appropriate length of 30 cm.

For irradiation and target heating tests, the target prototype was manufactured with the parameters close to those specified for the target of the RIC-80 facility, which were the following: the target material – Nb foils of 25 mm in diameter; the target thickness – 16 g/cm^2; the length of the target container – 200 mm; the cylindrical container of Ta-W alloy – 30 mm in diameter. A target prototype (shown in Fig. 2) was fabricated for irradiation by the proton beam to accumulate ^{82}Sr in the target material.

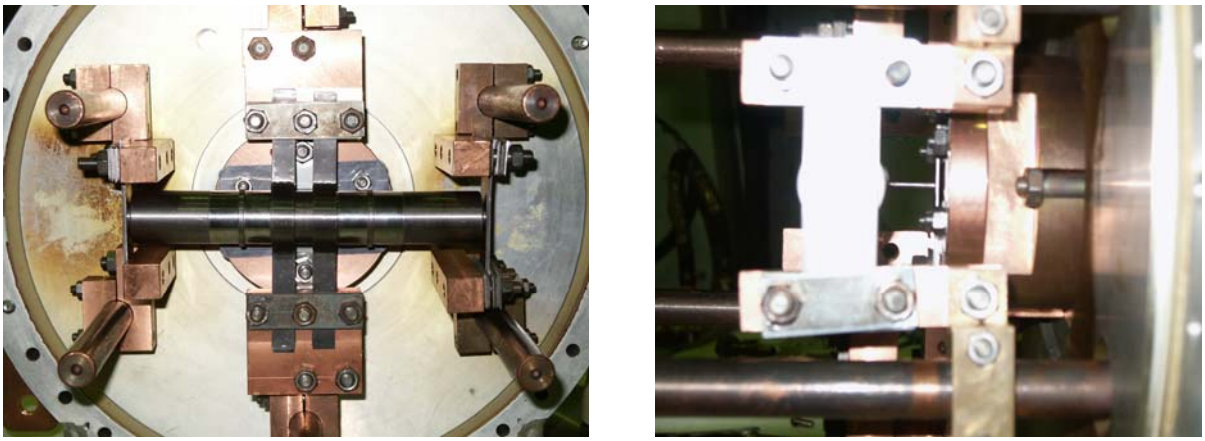

Fig. 2. Target prototype constructed for tests of production and thermal extraction of the generator isotope ^{82}Sr from the irradiated niobium foil target

The proton beam was directed along the target container with a stack of niobium foils. In the central part, the target container was connected to a tungsten tube with a hole of 2 mm in diameter. The radioactive nuclides accumulated in the target material were evaporated through this tube in the course of the target heating up to 2100 °C and were absorbed by the tantalum foil collector, which was placed in contact with the copper flange cooled by water. For the tungsten tube, along which the evaporated nuclides passed through, the same method of heating was used as that for the target container. Before irradiation by the proton beam, the container was installed and tested at a test bench. The target was heated up to its working temperature of 2000–2100 °C and subsequently cooled down, and this procedure was repeated many times under vacuum of 10^{-5} Torr.

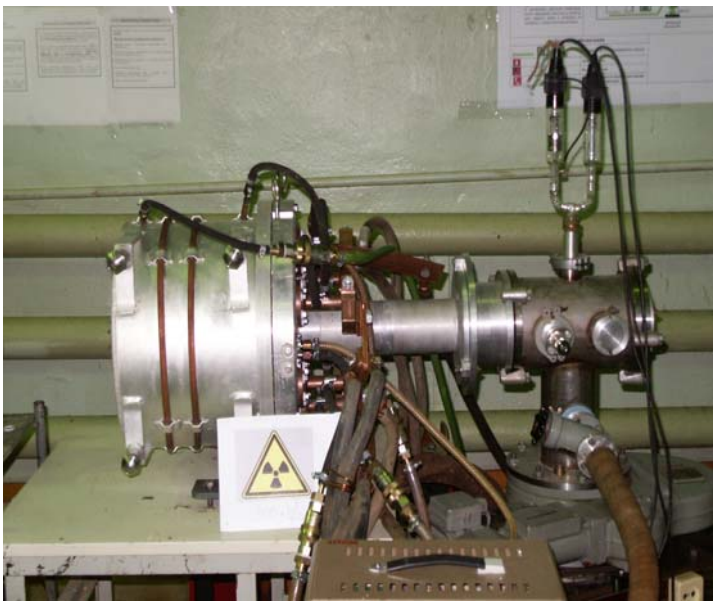

Fig. 3. Vacuum test bench with the investigated target installed. The target itself is inside of the water cooled aluminum vacuum container

The target heating tests demonstrated that the repeated process of target heating and cooling had not caused any noticeable changes of such target parameters as the shape of the target container, its position and electric resistance. The thermal investigations of the target confirmed the results of our earlier tests with high-temperature and high-density uranium carbide target units investigated in the same temperature conditions [4]. Figure 3 shows the vacuum test bench constructed for testing high-temperature targets with the heating power of up to ~ 9 kW. The parameters of the test bench heating system are the following: the current through the target is up to 1100 A; the voltage drop on the target container is up to 8 V; the target heating power is up to 8.8 kW. This target construction provides production and extraction of radionuclides from diverse target materials such as refractory metal foils, refractory metal carbides and liquid metals.

The constructed target device was installed in the PNPI synchrocyclotron proton beam for irradiation with the beam intensity of 0.1 μA during 24 hours. After two weeks of radiation cooling (the time interval for decay of short-lived isotopes), the target unit was transported to the experimental hall of the IRIS facility and placed on the test bench for ^{82}Sr extraction by target heating. Figure 4 presents the gamma-spectrum measured by an ultrapure germanium detector placed at a three-meter distance from the irradiated target before its heating started.

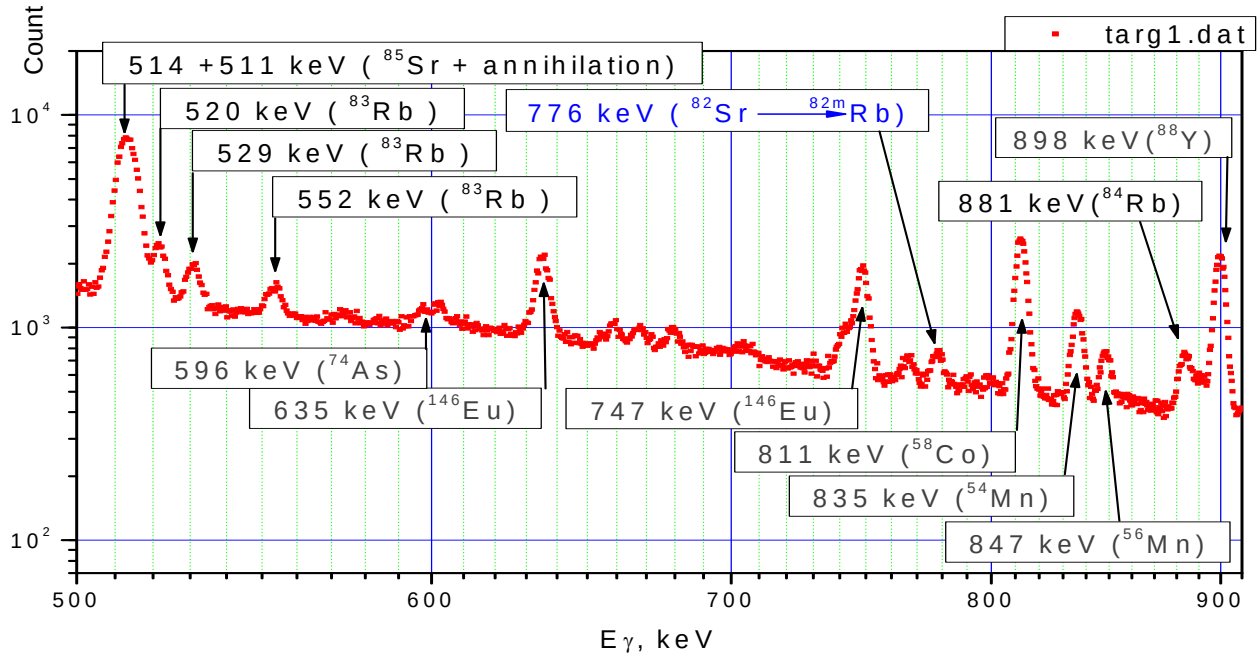

Fig. 4. Gamma-spectrum of the irradiated niobium foil target. The gamma-line of 776 keV belongs to the decay of ^{82}Sr daughter isotope ^{82}Rb used for PET diagnostics

To extract the radioactive species produced in the target material, there were several stages in the process of target heating in high vacuum. Since strontium is released from the target by relatively slow diffusion and effusion processes, the target heating was started at low temperatures of 1500–1800 °C to evaporate Rb, Mn and other radionuclides with low values of diffusion-effusion parameters. The gamma-spectrum of the radioactive species extracted from the target during two hours of heating at 1500 °C and deposited on a tantalum collector is shown in Fig. 5.

One can see in Fig. 5 that only the isotopes of easily diffusing and volatile elements (Rb, Mn) escape the target at the temperature of 1500 °C. The gamma-spectrum of radioactive species collected at the tantalum foil is shown in black; the red points show the gamma-spectrum of these radioactive species washed out of the foil-collector by alcohol. The efficiency of washing out Rb and Mn from the surface of the tantalum foil collector by alcohol was about 30 %. In the collected radioactive matter, no traces of ^{82}Sr are seen. It means that at this temperature all volatile species can be removed from the target in a rather short time (6–8 hours) without losses of strontium. After that, strontium can be selectively extracted by heating the target to higher temperatures.

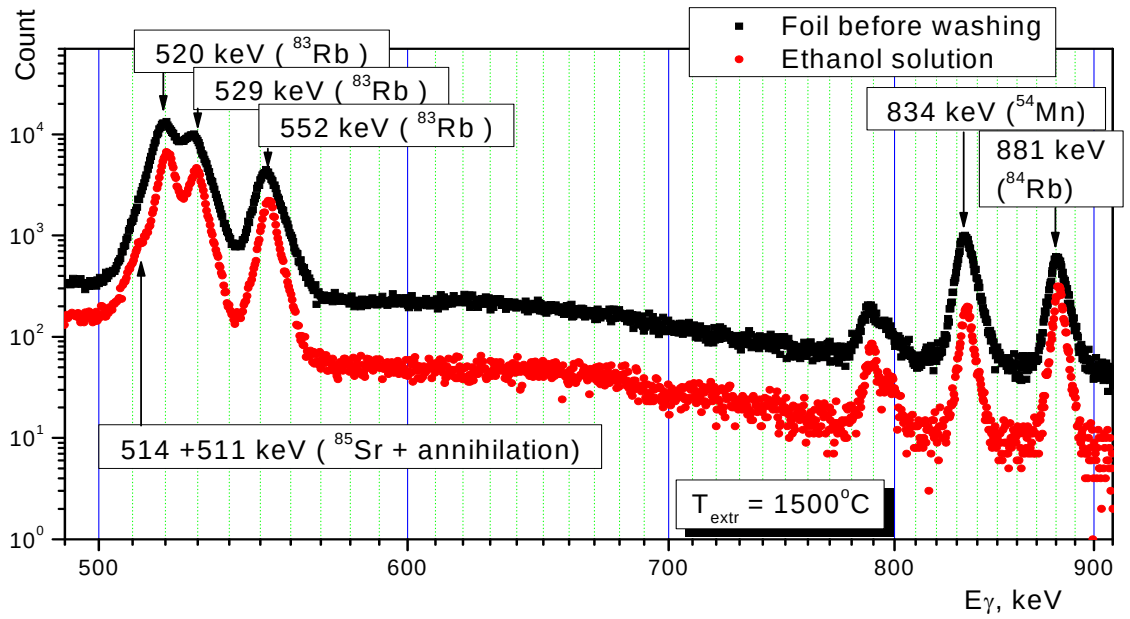

Fig. 5. Gamma-spectra of the radioactive species extracted from the target during two hours of heating at 1500 °C and deposited on a tantalum collector

The gamma-spectrum of the species collected at the temperature of 2000 °C after the target heating during 8 hours at the temperature of 1500–1600 °C is shown in Fig. 6. As one can see, all the radioactive species were finally evaporated from the irradiated target, except for strontium. The efficiency of washing out strontium from the tantalum foil collector by a solution of HNO_3 acid was 70 %. During the target heating at the temperature of 2000 °C, 93 % of ^{82}Sr was removed from the target in ten hours, with 65 % collected on the tantalum foil and 70 % transferred to the acid solution. Thus, we can estimate that the integral efficiency of our first experiment on ^{82}Sr production was 42%.

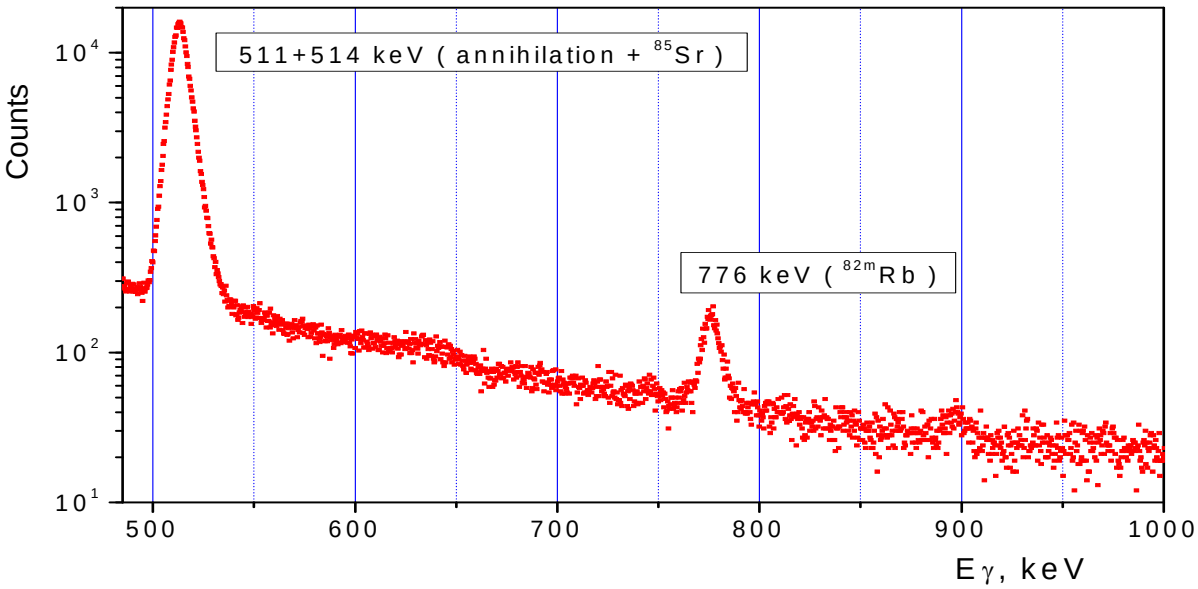

Fig. 6. Gamma-spectrum of the species collected at 2000 °C after target heating for 8 hours at 1500–1600 °C to evaporate the volatile species. During this heating process, the gamma spectrum of the collected active matter was measured every 2 hours to control that strontium did not escape

3. Production of thallium isotopes from a Pb target

The radionuclide ^{201}Tl ($T_{1/2}$ = 3.04 d) is used for diagnostics of myocardial diseases. It can be effectively produced from lead targets of natural or enriched abundance. The cross section for production of ^{201}Tl from a lead target is presented in Fig. 7.

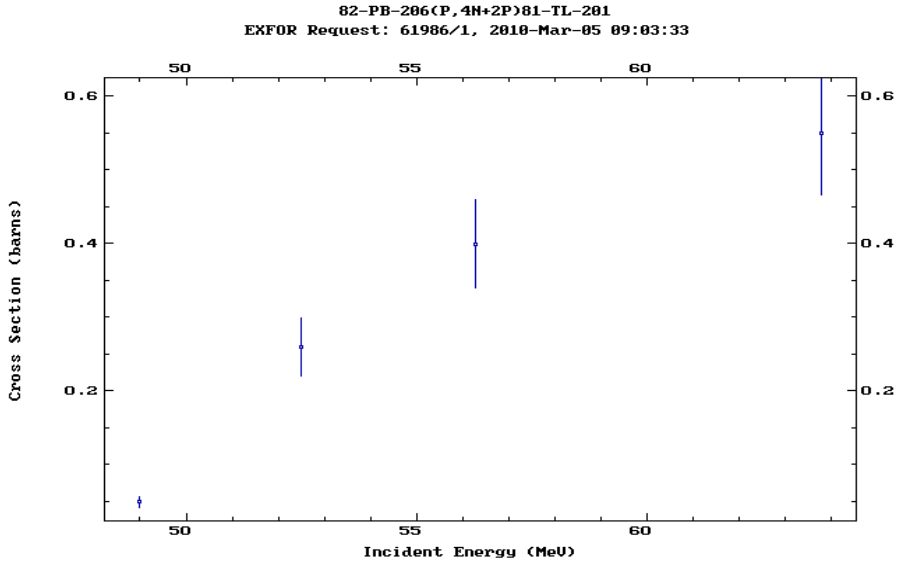

Fig. 7. Dependence of the cross section for production of ^{201}Tl from ^{206}Pb on the incident proton beam energy

One can see in Fig. 7 that the production cross sections are very high and, hence, this method can be used for effective production of ^{201}Tl. The only problem is the admixture of the neighbour isotopes with similar half-lives, ^{200}Tl ($T_{1/2}$ = 1.09 d) and ^{202}Tl ($T_{1/2}$ = 12.23 d). In this case, the mass-separator method of production of high purity ^{201}Tl can be used.

In the experiment on production and extraction of thallium isotopes, the target of 1 g lead of natural abundance was irradiated by the 1 GeV proton beam of the PNPI synchrocyclotron for 24 hours. After 10 days of cooling, it was transported to the experimental hall of the IRIS facility and was placed on the vacuum test bench into a tungsten container to be heated. The gamma-spectrum of the irradiated lead sample before its heating is shown in Fig. 8.

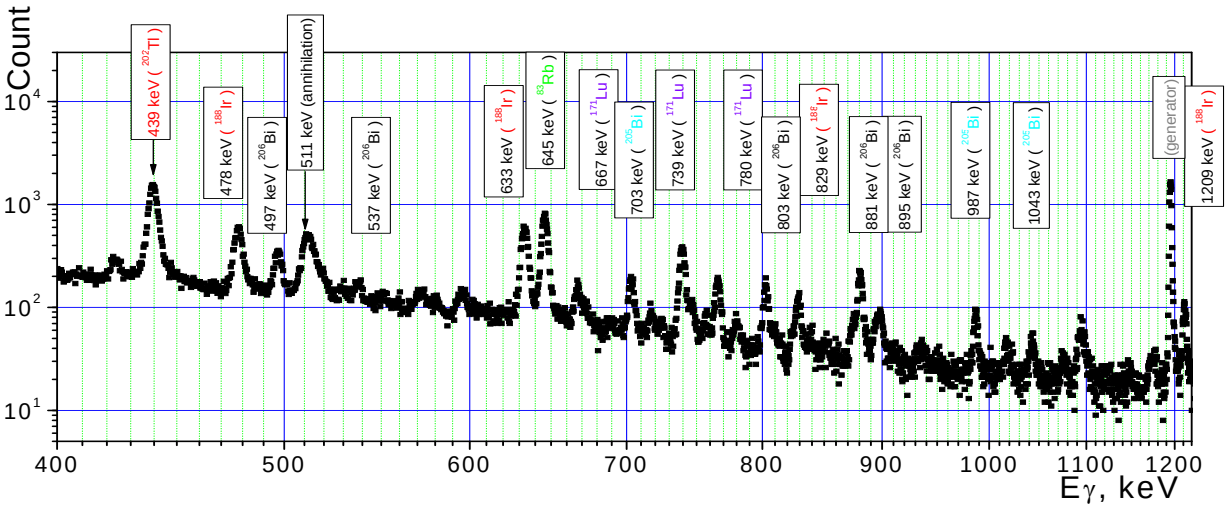

Fig. 8. Gamma-spectrum of the irradiated 1 g lead sample of natural abundance after 10 days of radiation cooling. The gamma-line of 439 keV is from the decay of ^{202}Tl ($T_{1/2}$ = 12.23 d)

The main goal of the first experiment on Tl isotopes production from a lead target was to figure out the heating conditions for selective Tl extraction from the irradiated lead sample. It was expected that thallium, which is a very volatile element, has the rate of evaporation from the melted lead target material exceeding that of other radioactive species. Since the melting point of lead is 327 °C, the extraction was carried out at 400 °C to make sure that the lead sample was completely melted. The gamma-spectrum of the species evaporated at 400 °C from the lead sample and deposited onto the cooled tantalum collector is shown in Fig. 9.

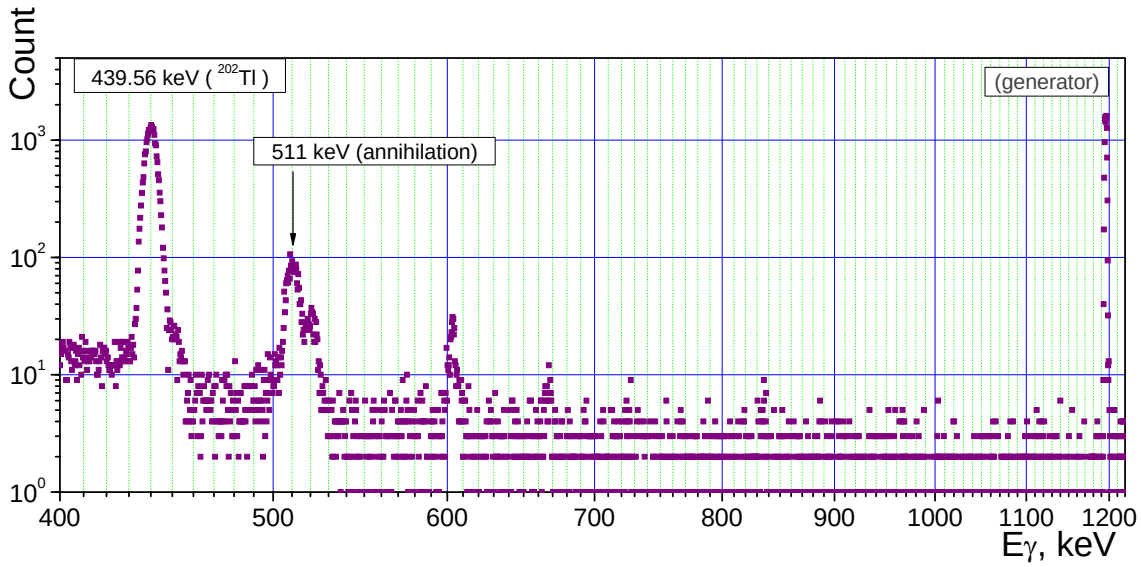

Fig. 9. Gamma-spectrum of the species evaporated at 400°C from the lead sample and condensed on a cooled tantalum collector. The time of evaporation was 2 hours

Comparing the gamma-spectra in Figs. 8 and 9, we see that the selective evaporation of thallium from the melted lead target is very fast. In two hours of heating, about 80 % of ^{202}Tl escaped from the target and was absorbed by the collector. In this case, the situation is very different from the case of strontium extraction, where the target material (niobium foils or yttrium carbide for RIC-80) had to be heated up to 2000 °C.

4. Production of alpha decaying radium isotopes from a uranium carbide target

Radionuclides decaying by alpha particle emission can be a very effective tool for therapy of malignant tumors at very early stages of their formation. The main advantage of alpha particles (the so called “alpha-knife”) is their very short range (60–80 μm) in biological tissue, which is very important for treatment of small malignant formations. The action of radionuclides emitting alpha particles is very effective, as it is very local and does not destroy the surrounding tissues. Among the alpha decaying radionuclides that can be used for therapy, there are two isotopes – ^{223}Ra ($T_{1/2}$ = 11.4 d) and ^{224}Ra ($T_{1/2}$ = 3.66 d) – that can be effectively produced by proton irradiation of uranium or thorium targets. The cross section for ^{227}Th production from a thorium target [5] is presented in Fig. 10.

This nuclide has a rather high value of the cross section for production in the spallation reaction for the case of a natural ^{232}Th (100 %) target and the proton beam with the energy close to 80 MeV. The subsequent alpha decay of ^{227}Th produces ^{223}Ra:

$$^{227}\text{Th}(18.7\text{ d}) \rightarrow {}^{223}\text{Ra}(11.4\text{ d}) \rightarrow {}^{219}\text{Rn}(3.96\text{ s}) \rightarrow {}^{215}\text{Po}(1.8\text{ ms}) \rightarrow {}^{211}\text{Pb}(36.1\text{ min}) \rightarrow$$

$$\rightarrow {}^{211}\text{Bi}(2.14\text{ min}) \rightarrow {}^{207}\text{Tl}(4.77\text{ min}) \rightarrow {}^{207}\text{Pb}(\text{stable}). \quad (1)$$

In the decay chain presented above, the decay of the selected ^{223}Ra produces three alpha particles and considerably increases the efficiency of therapy.

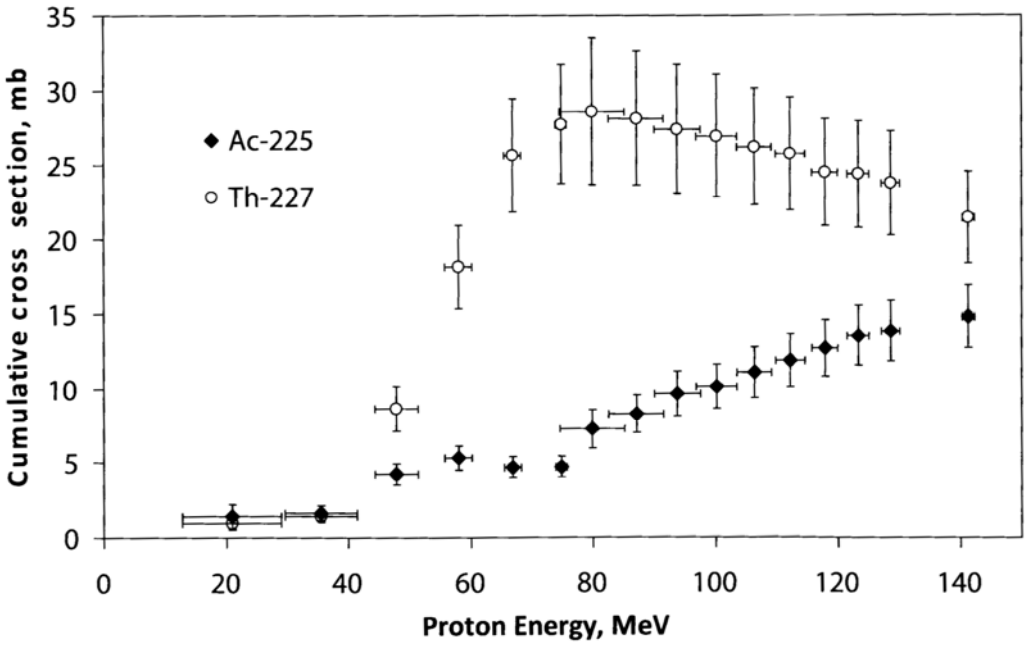

Fig. 10. Cross sections for ^{227}Th production in a thorium target *vs* the energy of protons. The open circles show the cross section for ^{225}Ac production

In our experiments, we used a ^{238}U target (uranium monocarbide of high density [6]) for production and high temperature extraction of radium isotopes. The Uranium Carbide (UC) target with the density of 11 g/cm^3 was irradiated by the proton beam with the intensity of 0.1 μA for 24 hours at the PNPI synchrocyclotron. The target mass was about 1 g. After two months of radiation cooling, the target was placed into the heating tungsten container on the vacuum test bench. The radium isotope extraction was carried out at the temperature of about 2400 °C, which is close to the melting point of the uranium monocarbide target material (2500 °C). The alpha-spectrum of the species evaporated at 2400 °C from the UC target and deposited on a cooled tantalum collector is shown in Fig. 11.

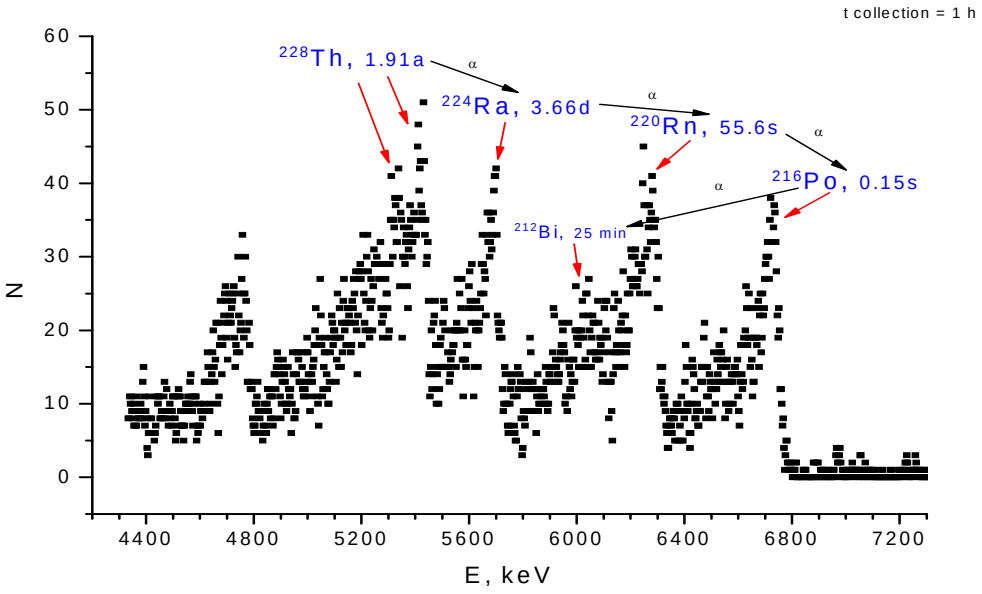

Fig. 11. Alpha-spectrum of species evaporated at 2400 °C from the UC target and deposited on a cooled tantalum collector

As the irradiated target was cooled down during a rather long period, we detected the alpha particles emitted only by the long-lived ^{228}Th ($T_{1/2}$ = 1.9 y). In Fig. 11, we can see the chain of alpha lines after the decay of the extracted ^{228}Th:

$$^{228}\text{Th}(T_{1/2} = 1.9\text{ y}) \rightarrow {}^{224}\text{Ra}(T_{1/2} = 3.66\text{ d}) \rightarrow {}^{220}\text{Rn}(T_{1/2} = 56\text{ s}) \rightarrow {}^{216}\text{Po}(T_{1/2} = 145\text{ ms}) \rightarrow$$

$$\rightarrow {}^{212}\text{Pb}(T_{1/2} = 10.6\text{ h}) \rightarrow {}^{212}\text{Bi}\ (T_{1/2} = 25\text{ min}) \rightarrow {}^{208}\text{Tl}(T_{1/2} = 3\text{ min}) \rightarrow {}^{208}\text{Pb(stable)}. \quad (2)$$

The experiment on ^{224}Ra production demonstrated the principal possibility to obtain alpha emitting radium radionuclides from high density UC targets. There is also a possibility to increase the yields of Ra isotopes by more than an order of magnitude with a ThC target instead of the UC target. The technology of ThC targets has already been developed. Next year, we plan to test this target material for production of radium and other alpha emitting isotopes for medicine.

5. Conclusion

This work can be considered as the first stage of developments of targets for production of several radionuclides from a large set of isotopes for nuclear medicine planned to be produced at the RIC-80 facility. In our tests, several kinds of target materials were explored. The tested target materials will be used for manufacturing of real target prototypes for the PNPI radioisotope complex. All these target materials can be also used to construct the mass-separator targets for production of radioisotopic medical beams of high purity at RIC-80. The following stage will be the construction of a target unit prototype with the amount of the target material of 5–10 g for medical radionuclide production at the RIC-80 complex.

References

1. V.N. Panteleev *et al*., Abstracts of 7th Int. Conf. on Isotopes, 4–8 Sept. 2011, Moscow, p. 35.
2. G. Battistoni *et al.*, *Proc. of the Hadronic Shower Simulation Workshop 2006,* Fermilab, 6–8 Sept. 2006, Eds. M. Albrow and R. Raja, AIP Conference Proceeding **896**, 31 (2007).
3. A. Fassò *et al.*, CERN-2005-10 (2005), INFN/TC_05/11, SLAC-R-773.
4. V.N. Panteleev *et al*., Eur. Phys. **150**, 297 (2007).
5. V. Chudakov *et al.*, Absracts ICI7, 4–8 Sept. 2011, Moscow, p. 42.
6. V.N. Panteleev *et al*., Eur. Phys. A **42**, 495 (2009).

NEW EXPERIMENTAL METHOD FOR INVESTIGATION OF THE NUCLEON POLARIZABILITIES

G.D. Alkhazov, V.P. Chizhov, E.M. Maev, E.M. Orischin, G.E. Petrov, V.V. Sarantsev, Yu.V. Smirenin

1. Introduction

The electric α and magnetic β polarizabilities are basic structure constants of the nucleon, which characterize the response of the internal nucleon structure to the action of external electric and magnetic fields. The knowledge of α and β provides a stringent test of models describing the quark-meson structure of the nucleon, *e.g.*, in Chiral Perturbation Theory [1]. These polarizabilities are found by measuring Compton scattering cross-sections as a function of the photon energy and scattering angle and by a best fit using a theoretical description with the quantities of interest as open parameters. Experiments focus on photon energies below the pion mass because at these energies the Compton scattering cross-sections can be related model-independently to the polarizabilities through a Low Energy Theorem [2], which takes into account the proton structure in lowest order and shows that the scattering amplitude of Compton scattering off a system with spin ½ can be expanded in powers of E_γ.

Recent experiments on Compton scattering to measure the polarizability of the proton and the deuteron were mostly performed using quasi-monoenergetic photons from bremsstrahlung tagging (see review of Shumacher [3]). The photons were scattered on liquid hydrogen or deuterium, and the scattered photons were detected under one or several scattering angles with NaI or BaF_2 spectrometers. These experiments provided the four-vectors p_i and the numbers of the incoming and scattered photons. A disadvantage of this method is a limited photon flux a tagger system can provide. To increase the luminosity, thick liquid targets were used.

In contrast to the above experiments, in the method proposed in [4] and developed at the Superconducting Darmstadt Electron Accelerator S-DALINAC, bremsstrahlung photons produced by an electron beam are used, and not only the angle and energy of the scattered photons but also the angle and energy of the recoiling protons (deuterons) are measured. This approach (sketched in Fig. 1) increases the luminosity and lowers the background considerably, especially below 50 MeV.

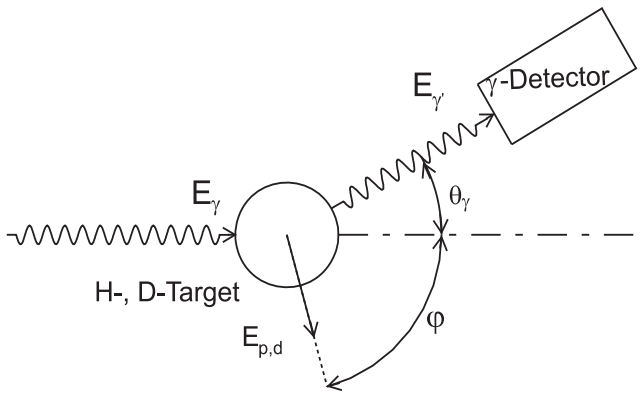

Fig. 1. Experimental method (schematic). A photon beam with a full bremsstrahlung spectrum is scattered from a gaseous hydrogen/deuterium target inside a high pressure ionization chamber, the energy of the scattered photons is determined in a γ-detector under a certain angle. By detecting the scattered bremsstrahlung photon in coincidence with the recoiling proton (deuteron) in the ionization chamber the incoming photon energy is determined

In this report, we describe the new method and a new experimental set-up for measuring the nucleon polarizabilities, and the performed test experiments. The photons scattered off protons in the ionization chambers are detected under two angles, 90° and 130°, by means of 10×14 in^2 NaI(Tl) detectors. The energies of the scattered photons are measured with the NaI(Tl) detectors, while the energies of the scattered recoil protons are measured with the ionization chambers (ICs), which serve simultaneously as targets and detectors.

2. Bremsstrahlung photon facility

A high-energy bremsstrahlung photon facility was built at the S-DALINAC [5]. The aim was to generate a high-intensity, nearly background-free photon beam. In this facility, a fully controlled electron beam is transformed into a photon beam by passing through a 0.3 mm thick (corresponding to 0.1 radiation lengths) bremsstrahlung-radiator made of gold. After the passage through two lead collimation systems into a 3 m concrete wall, the photon beam enters the experimental hall, where the Compton scattering set-up is installed. The position and intensity of the photon beam is measured downstream from the experiment by means of two special ionization chambers placed inside a hole in a concrete wall directly in front of the γ-beam stop for background minimization. The first chamber has segmented anode and cathode plates and allows an online determination of the photon beam position. In future experiments, the position of the electron beam on the radiator target, and therefore the position of the photon beam will be steered with the help of the output signals of this detector. The second ionization chamber is the so called Gaussian quantameter [6]. It allows to measure the γ integrated beam power in a wide energy range from 10 MeV up to several GeV.

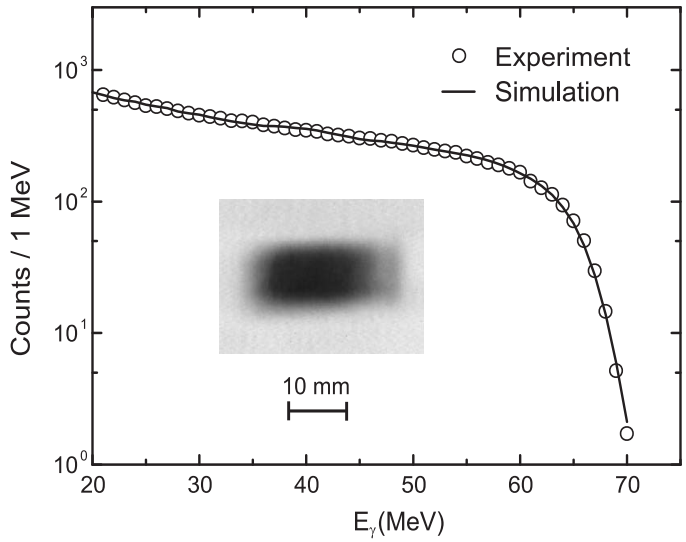

Fig. 2. Bremsstrahlung spectra and a part of a colour inverted Polaroid picture of the collimated bremsstrahlung beam approximately 3 m behind the bremsstrahlung target: Areas with high beam intensity are dark, with low intensity are grey. Circles correspond to the measured bremsstrahlung spectrum. The curve shows a folded simulation spectrum

In order to determine the absolute cross-sections for the Compton scattering off the proton (deuteron) with the reported technique, it is essential to know not only the integral intensity of the photon beam measured with the above-mentioned quantameter, but also the shape of the energy spectrum of the beam. The shape of this spectrum is determined with two additional 10×10 in^2 NaI-spectrometers, which detect Compton scattered photons from the atomic electrons in the exit beryllium window of the ionization chambers. They are placed approximately 10 m downstream from this window under angles of 1.89° and 2.42°, respectively. Photons Compton scattered from electrons under these angles have the same energies as photons Compton scattered off the proton in the ionization chambers at 90° and 130°. The 10×10 in^2 spectrometers are equipped with the same active and passive shielding as the main γ-spectrometers. With the knowledge of the response functions of the NaI(Tl) crystals it is possible to evaluate the intensity as well as the shape of the energy spectrum of the incoming bremsstrahlung beam. Figure 2 shows the energy spectrum of the bremsstrahlung beam measured with the above-mentioned γ-spectrometer in comparison with the results of GEANT4 calculations. Excellent agreement is observed. A colour-inverted Polaroid picture of the collimated γ-beam cross-section obtained 3 m behind the bremsstrahlung target is also shown as insert in this figure. The beam spot size at this position corresponds to a size of 20×10 mm^2 inside the ICs.

3. γ-ray spectrometers

All NaI(Tl) photon spectrometers for detecting the scattered photons are items on loan from the Institute of Nuclear Physics of the Johannes Gutenberg-Universität, Mainz. Those used to detect the photons scattered from protons (deuterons) are 10×14 in^2 in size. Compton scattered photons from the ionization chambers enter these γ-spectrometers through collimation systems, which determine a solid angle of about 10 msr. With this collimator system only the inner part of the γ-detectors is hit, which reduces the low-energy tails in the response functions. An energy calibration was achieved up to $E_\gamma = 4.44$ MeV with the help of standard γ-sources. At higher energies, the energy calibration was performed by using an electron beam with the known energy, and detecting electrons scattered from an aluminum target replacing the hydrogen ionization chamber. According to GEANT4 simulations, the response functions of the detectors for photons and electrons are practically identical. An extrapolation of the energy calibration parameters to the low-energy region shows good agreement with the results of the γ-source measurements. Since these detectors work as trigger detectors and the dead time of the ionization chamber is rather long (about 4 μs), it is essential to minimize their background counting rate. Therefore, the NaI(Tl) crystals are well shielded.

4. High pressure ionization chambers

The detector of recoil protons (deuterons) consists of two ionization chambers combined in one volume. The incident photons scattered on the filling gas of the first (second) chamber are detected under the angle of 90° (130°). Both chambers have a cathode, a grid and an anode divided in strips (Fig. 3).

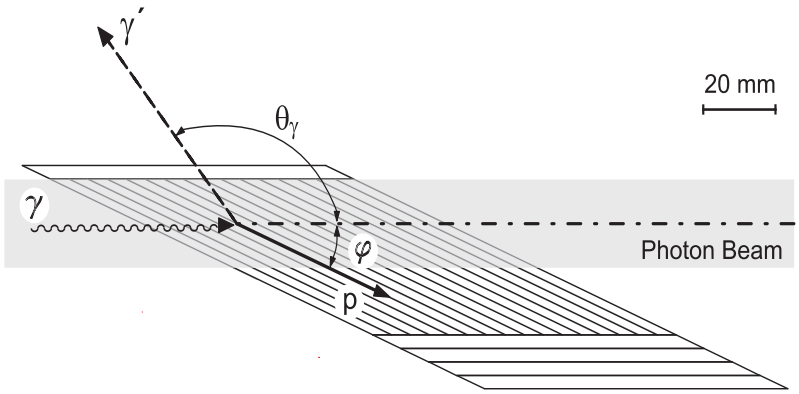

Fig. 3. Top view on a multi-strip anode: the 2 cm broad photon beam enters the volume of the IC from the left side. In the case a photon is scattered under the angle θ = 130°, the scattered proton gets a momentum along an anode strip (at φ = 22°)

The body of the chamber is made of stainless steel with a wall thickness of 14 mm. The photon beam enters (leaves) the chambers through 6 mm (7 mm) beryllium windows. This material was chosen in order to minimize the absorption of photons and production of e^+e^--pairs. The Compton scattered photons on hydrogen at these selected angles ($\theta_\gamma = 90° \pm 4°$ and $\theta_\gamma = 130° \pm 3°$) leave the IC's through 9 mm beryllium windows to the γ-spectrometers. The ICs operate in the electron collection mode, *i.e.* the signals result from the electrons collected after ionization produced by protons. The applied high voltages are –40 kV on the cathode and –3.5 kV on the grid, the anode being at zero potential. The electron drift times are 3.5 and 0.12 μs for the cathode-grid and grid-anode distances, respectively. To select the recoiling proton, a special geometry of the IC anode is used. It is designed to detect tracks of recoiling protons in a background of tracks of Compton scattered electrons and secondary electron-positron pairs. The anode of the IC consists of several strips aligned along the direction of the recoil protons. In particular, in the case of Compton scattering under θ = 130°, the proton recoil angle φ is 22°. Along its path, the proton ionizes hydrogen molecules. As schematically shown in Fig. 4a, ionization electrons drift towards the anode and are collected there on one or two anode strips. When Compton scattered electrons and electron-positron pairs are formed, they have angles different from that of the recoil protons. The charges released by them are collected by several strips and produce only small signals on a single strip. In Fig. 4b, different simulated proton pulse forms are shown. At an azimuthal angle 0° (the proton track is parallel to the anode), the pulse lengths have a

minimal value and are equal for all energies. For protons with higher energies and at larger azimuthal angles, the pulse shape becomes wider and asymmetric.

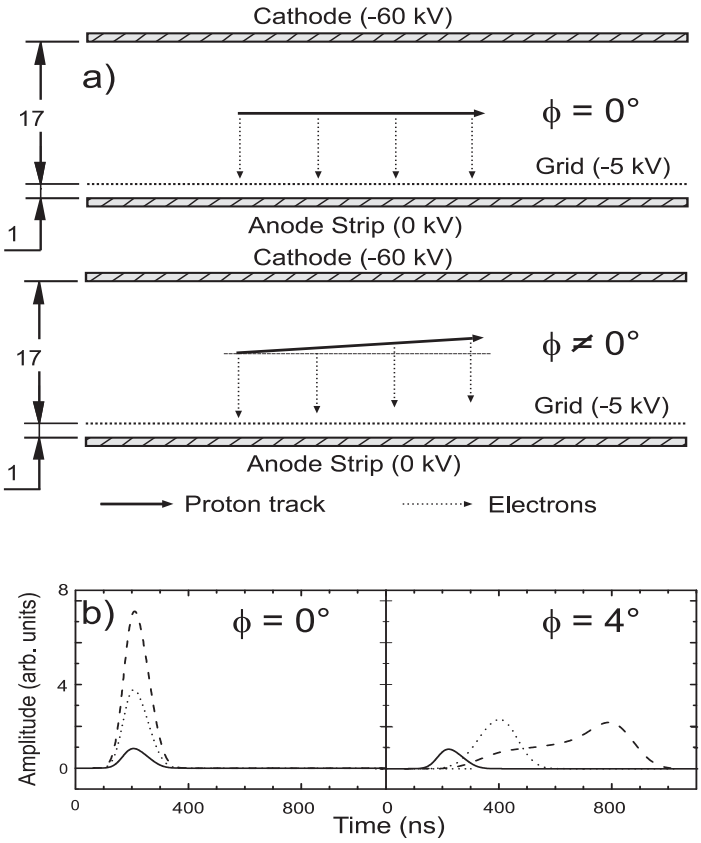

Fig. 4. a – side view of the chamber electrodes. The upper part shows a track of a proton, parallel to the anode. The lower part demonstrates a track of a proton under a finite angle. Dimensions are in mm; b – simulated pulse form for different azimuthal angles and for different proton energies: 1 MeV (solid line), 4 MeV (dotted line) and 8 MeV (dashed line)

Due to high hydrogen pressure in the ICs (75 bar), the effect of recombination of the electrons and positive ions formed by an ionizing particle becomes significant. The effect of recombination was studied for α-particles with a ^{237}Pu source (E_α = 5.15 MeV) mounted on the IC cathodes. It was found to be rather large, reducing the registered signals by about 30 %. The effect of recombination in case of ionizing protons is expected to be noticeably smaller. According to [7], the collected charge produced by protons with energies $E_p \geq 0.5$ MeV in hydrogen at the conditions of our experiment can be estimated by the following empirical formula: $Q = e\,K\,(E_p - E')\,/\,W$, where E' = 0.15 MeV, K = 0.9, e is the electron charge, and W = 36.3 eV is the energy for electron-ion pair production in hydrogen. The proton recoil energy is thus

$$E_p = E' + QW\,/\,eK. \quad (1)$$

Another process that might cause a reduction of the registered signals is the attachment of electrons to electronegative impurities (such as O_2 and H_2O) in the working gas of the chambers. To reduce the amount of gas impurities, the chambers were heat trained under vacuum pumping. The hydrogen used for experiments contained less than 1 ppm impurities. Signals from a ^{237}Pu α-source were used for checking the gas quality. During the test experiments, the position of the energy peak of the 5.15 MeV α-particles decreased by ~ 5 % per week, indicating slow evaporation of contaminants from the chamber walls. As simulations have shown, a noticeable amount of electrons (on the level of 0.1 %) appears in the photon beam in the active regions of the ionization chambers due to interaction of photons with the working gas of the chambers. To exclude registration of scattered electrons in the γ-ray spectrometers, anticoincidence scintillation counters, the so-called veto detectors, were placed in front of the NaI detectors.

5. Electronics

The electronics used in the data acquisition consisted mostly of standard NIM, CAMAC and VME components. The signals on the anodes of the ICs were registered by special low-noise preamplifiers, amplifier-discriminators and 14-bit 100 MHz Flash ADCs (FADCs). The FADCs digitize the analog signal in 10 ns steps continuously and hold the values for 4.5 μs in a ring buffer memory. This is necessary, since the signals from ICs are delayed relative to the trigger pulse of the NaI(Tl) detectors by the drift time of electrons produced by recoil protons in the Compton scattering event. The trigger signals define a time window of 4.5 μs, in which the proton pulse is expected to take place. The current on the IC anodes is always recorded within this window by the FADCs when a trigger signal is generated. Figure 5 shows an example of a recoil proton signal, registered by a FADC, in comparison with a GEANT4 simulation. The results of the measurement and the simulation are in good agreement.

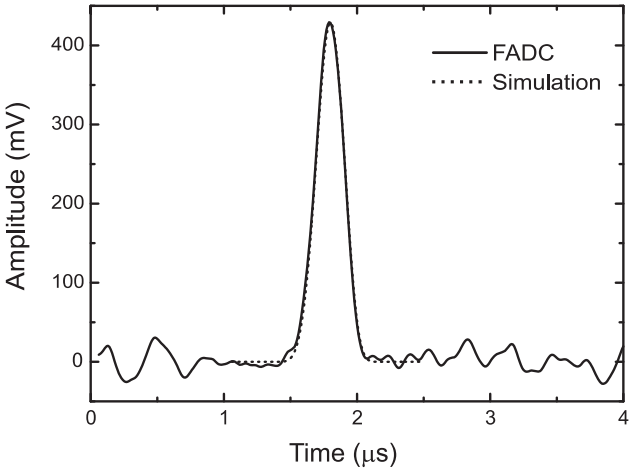

Fig. 5. Example of a signal in the IC from a 4 MeV recoil proton, registered by a FADC, compared to a GEANT4 simulation

The channels of the FADC have to be read out for each IC, which takes quite a long time (about several μs) making it necessary to minimize the trigger rate. In order to improve the signal-to-noise ratio, the registered signals can be treated off-line with digital filters. A preliminary energy calibration of the amplifier channels was performed by inserting calibrated charges through a small capacitance to the anodes of the ICs. The NaI(Tl) detectors, which act as trigger detectors, are operated in anticoincidence mode with the surrounding plastic detectors. The signal is split in two: one signal starts the whole readout from the trigger module, the second signal is delayed by 4.5 μs and stops the recording of the FADCs, which are then read out. This trigger unit also starts the readout of the ADCs, which digitize the NaI(Tl) energy pulses. In addition to the energy signals from the main γ-detectors (for registering γ*p*-scattering) and the pulses on the anode strips of the ICs, data of other detectors like the quantameter, the position detectors, the Faraday cup and the signals from the γ-detectors for the beam monitoring are continuously read out and written onto tape or disk using the MBS data acquisition system.

6. Test experiments

Test experiments were performed at the S-DALINAC using bremsstrahlung photon beams with endpoint energies of 60 and 79.3 MeV. Electron beam currents ranged from 1 to 5 μA. The ICs were filled with hydrogen gas of high purity (99.9999 %) at a pressure of 75 bar. The gas pressure was measured with a precision of about 0.5 %. In these test experiments about 5000 Compton scattered events in total were collected in coincidence with recoil protons. Figure 6 shows a typical drift-time distribution of signals which appeared at the IC anodes. This distribution reflects the γ*p*-interaction points in the vertical direction. The width of this distribution corresponds to a vertical photon beam size of about 1 cm. It is seen that the position of the photon beam was not in the middle of the gap between the IC grid and the cathode, but closer to the grid. The number of events in the drift time interval from 2.5 to 3.5 μs is small demonstrating that

the coincidence between the signals from the γ-spectrometers and the ionization chambers suppresses the background very efficiently. At the same time, one can see some events in the drift time interval of 0–0.5 μs and 2–2.5 μs. Presumably, these events appear due to some halo of the photon beam.

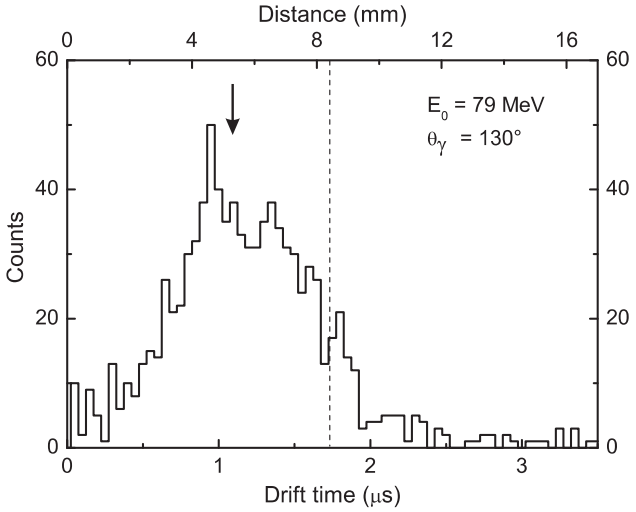

Fig. 6. Drift-time distribution of proton signals in an IC. The dashed line denotes the centre of the active volume between electrodes. The actual location of the photon beam is indicated by the arrow

The measured energy correlation between the scattered photons and recoiled protons is shown in Fig. 7 for the data taken at E_0 = 60 MeV, θ_γ = 130° and energies E_γ > 20 MeV, E_p > 1 MeV. The experimental data are in good agreement with the expected kinematical relation. This figure also demonstrates that the background is rather small. Events on the left side of the (E_γ, E_p) correlation curve are partly due to tails of the γ-response function and partly due to background, which may be reduced in the future by building additional shielding for the γ-spectrometers.

The cross sections obtained in the experiments at E_0 = 60 and 79.3 MeV are shown in Fig. 8. The overall normalization of the (γ, *p*) cross sections measured as a function of the photon energy was performed with the help of the theoretical curve with α = 11.8, β = 2 (dashed line). The resulting cross sections are in good agreement with a previous measurement [8] at comparable photon energies.

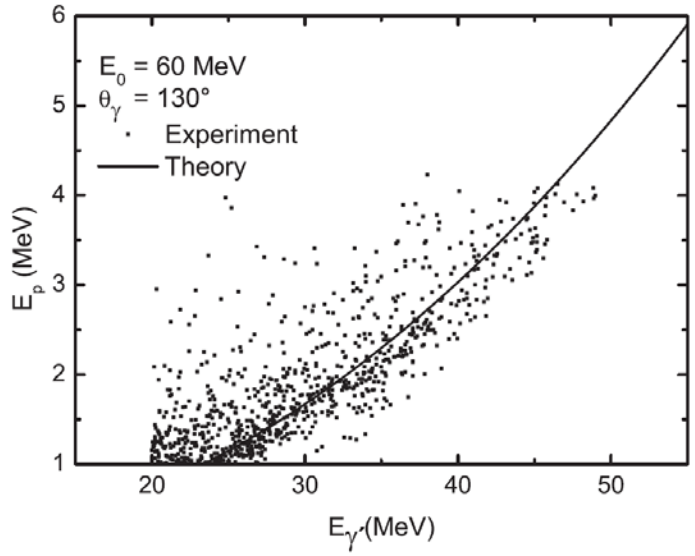

Fig. 7. Measured energy correlation of the scattered photons (E_γ > 20 MeV) and recoil protons (E_p > 1 MeV) in comparison with the expected kinematic relation for E_γ and E_p (solid curve) for the data taken at E_0 = 60 MeV and θ = 130°. The proton recoil energies are determined from the measured charges, collected on the IC anodes, with the help of Eq. (1)

Of course, the low statistics collected in the test experiment is not sufficient to extract meaningful results on the proton polarizabilities. From those measured values and the range of results from theoretical calculations [2] it has been estimated that in order to determine the values of α and β for the proton with a precision of Δα = 0.3 and Δβ = 0.4 with this technique it is necessary to perform measurements at a 100 MeV

electron beam (to increase the photon flux per incident electron) with an integrated beam current of 2.5×10^4 μAxh. The proposed new experimental method and the results of two test runs have shown that future high-statistics experiments to determine α and β are indeed feasible.

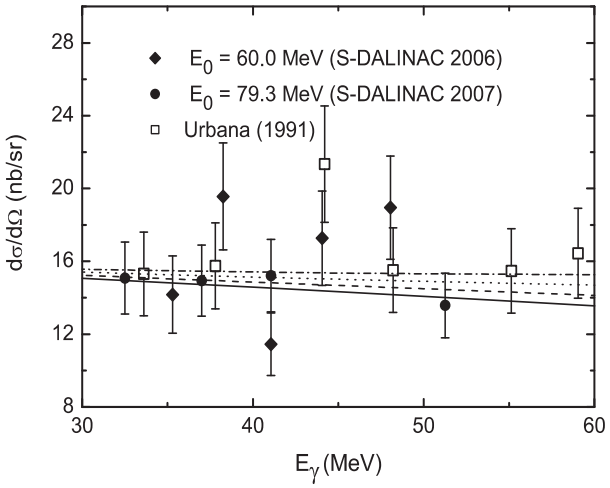

Fig. 8. Differential cross sections for Compton scattering on the proton obtained in the experiments at the S-DALINAC at $E_0 = 60$ MeV (full diamonds) and $E_0 = 79.3$ MeV (full circles) at an angle θ = 130°. Data from [8] in the same energy region and at an angle of 135° are given as squares. The lines correspond to calculations for different values of α and β: α = 13.8, β = 0 (solid line), α = 11.8, β = 2 (dashed line), α = 9.8, β = 4 (dotted line), α = 7.8, β = 6 (dashed-dotted line). The error bars include statistical contributions only. The data from the S-DALINAC are normalized with the theoretical curve shown as dashed line

7. Conclusion

A new method for measurements of the electric and magnetic polarizabilities (α and β) of the proton and deuteron has been proposed and tested. The new approach for determination of α and β is based on Compton scattering of untagged bremsstrahlung photons and registration of the recoil protons (deuterons) with special high-pressure hydrogen ionization chambers, which serve as targets and detectors. The scattered photons are registered with NaI(Tl) spectrometers. Test experiments have shown that the whole set-up functions in the expected way. The new experimental set-up for measuring the electric and magnetic nucleon polarizabilities is described in more detail in [5].

This work was performed in collaboration with O. Yevetska, S. Watzlavik, P. von Neumann-Cosel, J.-M. Porté, A. Richter, and G. Schrieder (Institut für Kernphysik, Technical University Darmstadt, Germany).

References

1. V. Bernard, N. Kaiser, U.-G. Meissner, Int. J. Mod. Phys. E **4**, 193 (1995).
2. A.I. L'vov, V.A. Petrun'kin, M. Schumacher, Phys. Rev. C **55**, 359 (1997).
3. M. Schumacher, Prog. Part. Nucl. Phys. **55**, 567 (2005).
4. D.V. Balin, M.J. Borkowski, V.P. Chizhov, G.A. Kolomensky, E.M. Maev, D.M. Seliverstov, G.G. Semenchuk, Yu.V. Smirenin, A.A. Vasiliev, A.A. Vorobyov, N.Yu. Zaitsev, Preprint PNPI-**2104**, Gatchina (1996).
5. O. Yevetska *et al*., Nucl. Instr. and Meth. A **618**, 160 (2010).
6. A.P. Komar, S.P. Kruglov, I.V. Lopatin, Nucl. Instr. Meth. **82**, 125 (1970).
7. V.A. Volchenkov, E.M. Maev, V.P. Maleev, G.A. Ryabov, G.G. Semenchuk, Preprint PNPI-**1368**, Gatchina (1988).
8. F.J. Federspiel, R.A. Eisenstein, M.A. Lucas, B.E. MacGibbon, K. Mellendorf, A.M. Nathan, A. O'Neill, D.P. Wells, Phys. Rev. Lett. **67**, 1511 (1991).

GAS-FILLED POSITION-SENSITIVE THERMAL NEUTRON DETECTOR

V.A. Andreev, G.A. Ganzha, E.A. Ivanov, D.S. Ilyin, L.M. Kochenda, S.N. Kovalenko, M.R. Kolkhidashvili, A.G. Krivshich, A.V. Nadtochy, A.I. Okorokov, V.V. Runov, G.D. Shabanov, V.A. Solovei

1. Introduction

Multi-wire proportional chambers filled with the $^3He + CF_4$ gas mixture with a delay line readout are widely used for thermal neutron detection, especially in Small-Angle Neutron Scattering (SANS) instruments [1–3]. The purpose of the discussed work was to find a set of strongly interrelated detector design parameters with the aim to improve the detector performance. After careful consideration of important detector parameters, such as the space resolution, the efficiency and differential and integral nonlinearity, a satisfactory solution was found. In order to guarantee a reliable and optimal operation of the neutron detector, a wide range of scientific and technological investigations was carried out to:

- improve and optimize the detector mechanical characteristics, simulations of the detector pressure behavior up to 10 bar were performed;
- minimize the detector outgassing, a new technology for fabrication of the detector electrodes was successfully developed. It has opened a way to improve the gas purity by a few orders of magnitude;
- minimize the gas leakage to a level smaller than 0.03 % per day, the detector gas sealing technology was improved.

This paper describes general approaches and technological solutions that have allowed us to develop thermal neutron detectors for the SANS diffractometers “Vector” and “Membrana-2” at the VVR-M reactor of PNPI. The required parameters of the detector are listed in Table 1.

Table 1

The required characteristics of 2D-detectors

Characteristic	Diffractometer	
	“Membrana-2”	“Vector”
Neutron wave length, Å	3	9
Entrance window $X \times Y$, mm^2	200 × 200	300 × 300
Neutron efficiency, %	≥ 70	≥ 70
Position resolution $X \times Y$, mm^2	2 × 2	2 × 2
Counting capability, kHz	≤ 100	≤ 100
Intrinsic noise, Hz	< 0.5	< 0.5
Life time, years	≥ 5	≥ 5

2. Detector design principles

2.1. Thermal neutron detection

Neutrons are detected by their capture in the ^3He gas according to the nuclear reaction

$$^3He + n \rightarrow p + {}^3H + 764 \text{ keV}. \quad (1)$$

Achieving the highest detector efficiency was one of the first problems to be solved by detector construction. From this point of view, ^3He is very convenient gas to use because it has a large cross-section for capture of thermal neutrons, 26500 b for 9 Å neutrons.

2.2. Detector construction

Several model calculations (ANSYS 8.1) of different versions of the mechanical design of the neutron detector have been carried out using the finite-element method. The most successful design was chosen from the point of view of minimal deformations of the entrance window under internal pressure. The chamber

prototype was constructed from the aluminum alloy AMg5. This alloy has the most suitable combination of the mechanical strength and good neutron transmission properties. Moreover, as it was measured, this material has a minimal cross section for neutron small-angle scattering compared to other investigated materials for detector construction.

To ensure uniformity of the detector efficiency across the detector entrance window, it was necessary to avoid deformations of the entrance window under gas pressure. After improvements of the detector design it became possible to minimize deformations of the entrance window (of 10 mm thickness) to 0.2 mm.

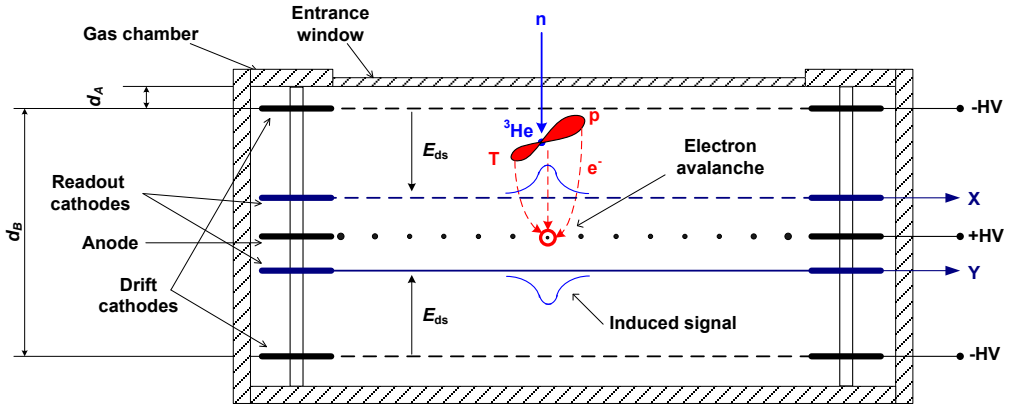

Fig. 1. Schematic diagram of the 2D-detector: E_{dr} – direction of the electric field in the drift gaps, d_A = 1.5 mm – the gap between the entrance window and the plane delimiting the detector sensitive volume (detector insensitive zone), d_B = 32 mm – the thickness of the sensitive volume, +HV and –HV – the potentials applied to the anode and the drift electrodes, respectively

The detector design (Fig. 1) was based on a Multi-Wire Proportional Chamber (MWPC). It has a conventional design with two orthogonal cathode grids symmetrically located about the central anode grid. The anode consists of gold plated tungsten wires with the diameter 25 μm, the wire spacing being S = 4 mm. The anode-cathode distance is L_c = 4 mm. The cathode wires diameter is 55 μm, the wire spacing is 1 mm. Every three wires are connected together into one strip, which is connected to a delay line with an impedance of 100 Ohm with a specific delay of 6 ns per strip. So, the strip pitch is w = 3 mm. In order to increase the detector efficiency, there were two 12 mm absorption/drift regions, which were adjacent to both cathodes of the MWPC. In this way, the detector active thickness was 32 mm.

In order to achieve the best physical parameters of the detector, it was necessary to optimize the anode signal transmission to cathode strips. For this purpose, some other geometrical parameters of the MWPC were selected close to the optimum condition: $w/L_c \approx 0.8$, which provided both high amplitude of signals induced on the cathode, Q_c, and a minimal level of the differential nonlinearity.

Because of a high cost of the ^{3}He gas, much attention was paid to the problem of gas leakage from the chamber volume. At the stage of the detector design, significant efforts were undertaken to decrease the gas leakage. To evaluate the final value of this parameter, the temperature and pressure of the gas mixture were measured in the chamber during a period of about 400 days. The time dependence of the relative density of the gas mixture was calculated. It was shown that the leakage rate was about 0.03 % per day.

2.3. Neutron efficiency

The efficiency of a neutron detector is determined by a set of factors such as the partial pressure of ^{3}He, the construction and material of the gas chamber, the geometry of the MWPC, and its location in the chamber. Special attention was paid to inevitable losses of neutrons both in the entrance window and in the intermediate gas gap between the entrance window and the first drift cathode (Fig. 1). The efficiency of the detector was calculated as

$$\varepsilon = \exp(-\mu_{Al} d_{Al}) \times \exp(-\mu_A d_A) \times [1 - \exp(-\mu_B d_B)], \quad (2)$$

where $\mu = n \times \sigma$; n is the gas atomic concentration, σ is the neutron capture cross-section, d_{Al} is the entrance window thickness, d_A is the gap thickness between the entrance window and the upper drift cathode, d_B is the thickness of the detector active area.

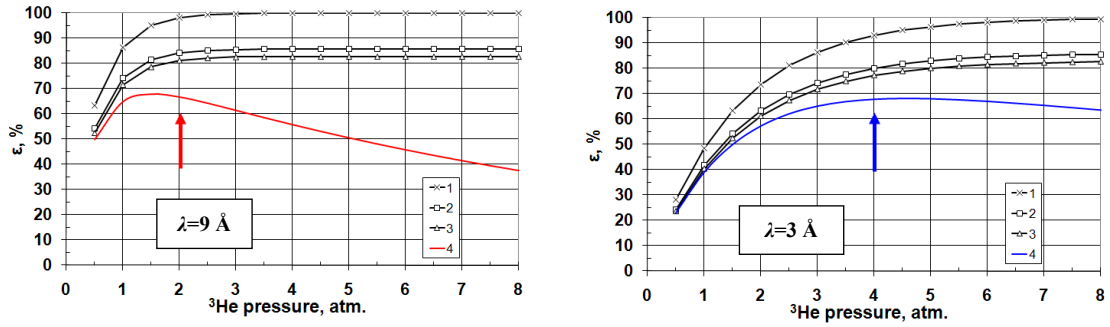

Fig. 2. Calculated efficiencies of the neutron detectors for the spectrometers "Vector" (left) and "Membrana-2" (right). (1) – neutron conversion efficiency without attenuation factors; (2) – the same as (1) with neutron losses in the entrance window; (3) – the same as (2) with losses in the upper drift electrode; (4) – the same as (3) with losses in the gap between the entrance window and the sensitive volume. This is the final detector efficiency

To achieve the required efficiency $\varepsilon \geq 70$ % (Table 1), the gap between the entrance window and the upper drift cathode was reduced to $d_A = 1.5$ mm. The drift electrode was made of thin (2.5 mm) plane of quartz glass with metallic coating 15 μm thick.

The detectors were designed for different wavelengths of neutrons. The 2D-detector for the diffractometer "Vector" ($< \lambda > = 9$ Å) has achieved efficiency $\varepsilon \approx 70$ % at the partial ^{3}He pressure $P(^3\text{He}) = 2$ bar, and the 2D-detector for the diffractometer "Membrane-2" ($< \lambda > = 3$ Å) has achieved the same efficiency only at $P(^3\text{He}) = 4$ bar, Fig. 2. To keep the detector efficiency stable for a long time and to make it insensitive to possible gas leakage from the gas volume, the working pressure of the ^{3}He gas was chosen on the plateau, indicated by arrows in Fig. 2.

2.4. Design of the electrodes

The neutron detectors are closed in a sealed gas-filled volume. To guarantee long-term detector performance and to prevent degradation of the energy resolution, it is necessary to maintain a high level of the gas mixture purity. In other words, the detector must be fabricated from the materials which can be pumped to high vacuum and heated up to at least 100 °C. To minimize outgassing of the detector inner parts, we have developed a new technology of fabrication of the detector electrodes. Now, all electrodes are fabricated from quarts glass and are subject to high vacuum pumping and heating up to 130 °C. The properties of the deposited printed circuits are staying constant even after heating of the frame up to 150 °C. The wire soldering is done by a solder with the melting point at 280 °C. This technology has opened a way to improve the gas purity by several orders of magnitude. No glues are used in the detector construction.

The new technology has provided an increased lifetime and stable operation of the detectors since 2007 without refilling the gas.

3. Experimental results

3.1. Detector efficiency

To measure the detector efficiency, a reference proportional counter filled with the ^{3}He gas under 10 bar pressure intended for thermal neutron detection with the efficiency of about 100 % was used. Our detector of neutrons and the proportional counter were irradiated by a collimated neutron beam independently. The ratio of the counting rates demonstrated us that our detector has the efficiency about $\varepsilon = 70$ %, which is in good matching with the results of calculations (see section 2.3). The neutron beam flux density was 1.7×10^4 s^{-1}cm^{-2}.

3.2. Differential nonlinearity

The differential nonlinearity is the derivative dx_m/dx of the position calibration curve $x_m = f(x)$, where x_m is the measured neutron position and x is the true position. A measure of the differential nonlinearity is prompted by the flat response of a uniform illumination spectrum. Any nonuniformity of the detector efficiency is also encompassed by this spectrum. Figure 3 shows a uniform illumination spectrum along the anode wires (X-axis) obtained with a wide beam of thermal neutrons. The differential nonlinearity of this measurement is very small and does not exceed ± 7 %. This parameter is very sensitive to boundary discontinuities between the two multi-pin connectors transferring the signals from the cathode strips. There was no indication of discontinuities at the section boundaries.

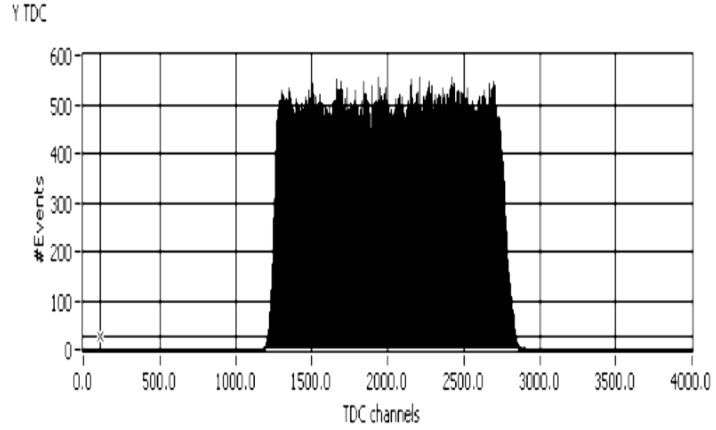

Fig. 3. Uniform illumination spectrum along the fine resolution axis (parallel to the anode wires)

3.3. Position resolution

We point out three more important parameters, which are directly related to the detector position resolution: the ranges of particles produced in the reaction (determining the physical limit of the detector position resolution); the geometrical structure of the MWPC, and the intrinsic resolution of the detector.

3.3.1. The range of primary particles

The physical limit of the detector position resolution is determined by the particle ranges from reaction (1) and their ionization losses. The proton and the triton are emitted in opposite directions from the point of the nuclear reaction, the emission being isotropic. The centroid of the ionization charge is displaced with respect to the point of the nuclear reaction due to different ionization losses of protons and tritons. The loci of the centroids for many neutrons are uniformly distributed on the surface of a sphere. The resulting probability distribution along any axis is rectangular. According to Ref. [1], the spheroid diameter is $D_{sph} = 0.7 \times R_p$, where R_p is the proton range.

The gas ^{3}He has low stopping power, and that is why CF_4 was used as a stopping gas to reduce the particle ranges. It localizes the electron avalanche near the anode wire in the point of its formation, and it has good quenching properties.

The position resolution of the detector is limited to D_{sph}, it is determined by the pressure $P(CF_4)$ of CF_4:

$$D_{sph} = 0.7 \times R_p \approx 2.8 \text{ mm} / P(CF_4) \text{ [bar]}. \quad (3)$$

So, the physical limit for the space resolution will be about 1.4 mm under the CF_4 pressure of 2 bar.

3.3.2. Readout method

The cathode strip Delay Line (DL) readout method was chosen to acquire the signals from the MWPC. It provides a high position precision and high integral counting capability (limited by the DL length, typically $T_{DL} < 1$ μs) with the minimum number of electronic channels – only five.

The induced pulses come from the ends of a DL to a charge-sensitive PreAmplifier (PA), Fig. 4. The zero-crossing method was used to fix the signal arrival time to the PA. The time delay between the arrival of signals to the PAs was determined by the coordinate of the electron avalanche

$$x = \left(1 - \frac{t_2 - t_1}{T_{D\ L}}\right)\frac{L_{d\ e}}{2}. \tag{4}$$

Here t_1 and t_2 are the times of arrival of signals at the ends of the DL, T_{DL} is the time length of the DL (ns), L_{det} is the geometric length of the cathode sensitive area along the coordinate X.

The structure of the MWPC and the readout method determine the measurement of coordinates. The coordinate spectrum along the X-axis (perpendicular to the anode wires) is discrete. The position resolution along the X coordinate ($FWHM_X$) is determined by the anode pitch S if the condition $D_{sph} < S$ is satisfied. The coordinate spectrum along the Y-axis (parallel to the anode wires) is continuous. The position resolution along the coordinate Y ($FWHM_Y$) does not depend on the anode pitch. It is determined by the value D_{sph} and the intrinsic resolution of the detector ($FWHM_{int}$):

$$\mathrm{FWHM}_Y = \sqrt{D_{sph}^2 + \mathrm{FWHM}_{int}^2}. \tag{5}$$

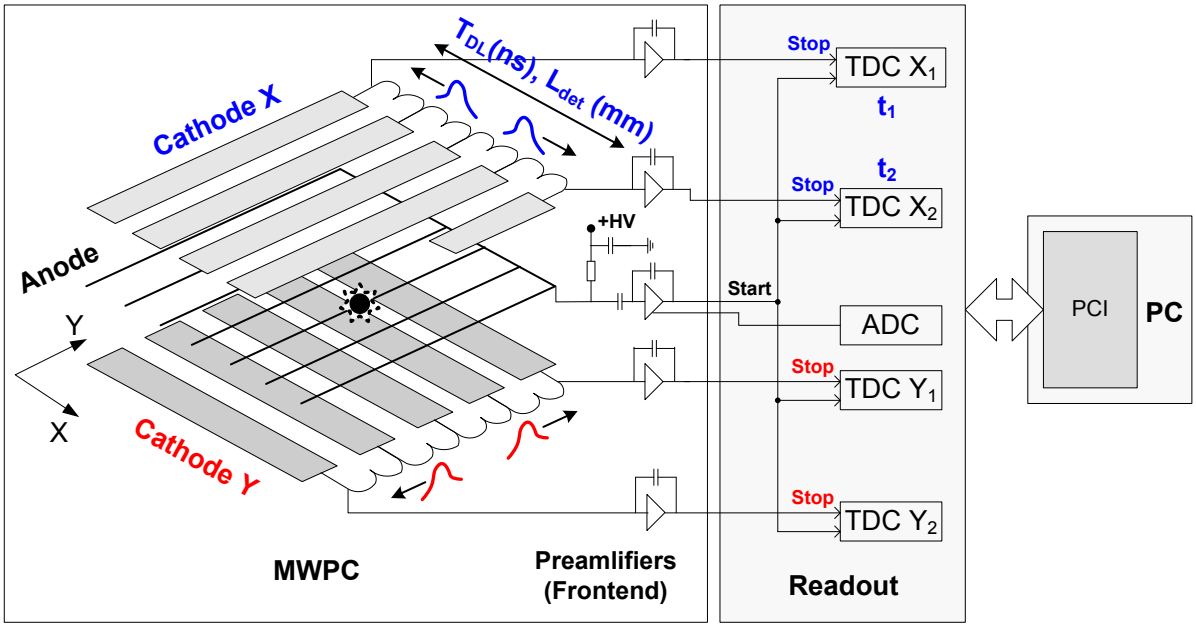

Fig. 4. Scheme of information readout from the MWPC. The cathode strips with a DL (Z = 100 Ohm), cathode preamplifiers (PAs with the input impedance R_in = 100 Ohm), Time-to-Digital Converters (TDCs), Analog-to-Digital Converters (ADCs), and the computer (PC) with a PCI-interface card are shown

The intrinsic resolution of the MWPC is determined by its design, by induced charge amplitudes, by the signal transmission quality of the DL, and by the noise level of the front-end electronics. In practice, the intrinsic position resolution $FWHM_{int}$ is limited by the noise generated in the termination of the DL with the PA:

$$\mathrm{FWHM}_{int} \cong \frac{1}{\theta}\frac{e_n}{ZQ_c}\sqrt{\tau}. \tag{6}$$

Here $\theta = T_{DL}/\tau$ is the "quality" factor of the DL, τ is the dispersion of a signal in the DL, e_n is the noise spectral density ($V/Hz^{1/2}$).

To achieve the best physical parameters of the detectors, it was necessary to reach the required intrinsic resolution at the minimal gas gain. This regime is characterized by a lower level of the high voltage noise of the MWPC, a higher level of the gas gain uniformity and a higher amplitude resolution.

The designs of the DL and preamplifiers were refined in the detector prototype. In order to reach the value $FWHM_{int} \leq 1$ mm, the impedance of the DL was chosen as high as possible, $Z = 100$ Ohm. To minimize the electronic noise, the input impedance of the cathode preamplifiers was chosen the same as the DL impedance $R_{in} = Z$ (the "electronic cooling" mode). In the result, the intrinsic resolution of the detector has reached the value $FWHM_{int} \leq 1$ mm at the gas gain $M \geq 130$ and $FWHM_{int} = 0.5$ mm at $M = 200$.

3.3.3. Position readout in the direction perpendicular to the anode wires (*Y*-axis)

As one can see from the differential nonlinearity presented in Fig. 3, the uniform illuminated spectrum has a flat response, and no edge effects in this spectrum are observed, which usually manifest themselves as a rise of the local intensity at the spectrum edges. This means that the absolute position error in the *X*-direction is small.

Figure 5 shows the uniform illumination spectrum as seen in the *Y*-direction. One can see good shaped independent peaks with the modulation period of the anode wire spacing. Because the peak positions are determined by the gas avalanches surrounding the anode wires, it allows us to conclude that the integral nonlinearity along the *Y*-direction is less than 0.4 % (this is the measured absolute position error).

Generally speaking, it is possible to state that the absolute position error in both *X*- and *Y*-directions is small and considerably smaller than the space resolution determined by physical reasons.

It is essential to note that the width (FWHM) of these peaks means the real (intrinsic) resolution of the detector, which is affected by the electronic noise, the DL quality, the electric field structure, *etc*. The obtained results are presented in Fig. 6. As one can see, the intrinsic resolution of the detector is 0.6 mm, which is several times better than the physical limit D_{sph}.

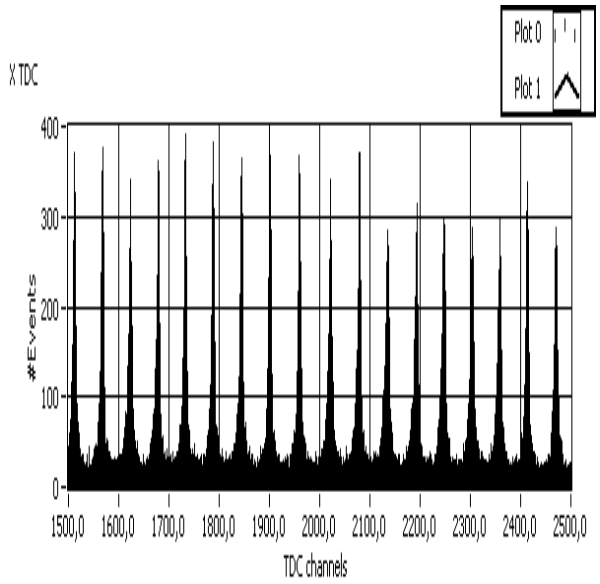

Fig. 5. Uniform illumination spectrum along the discrete axis (perpendicular to the anode wires)

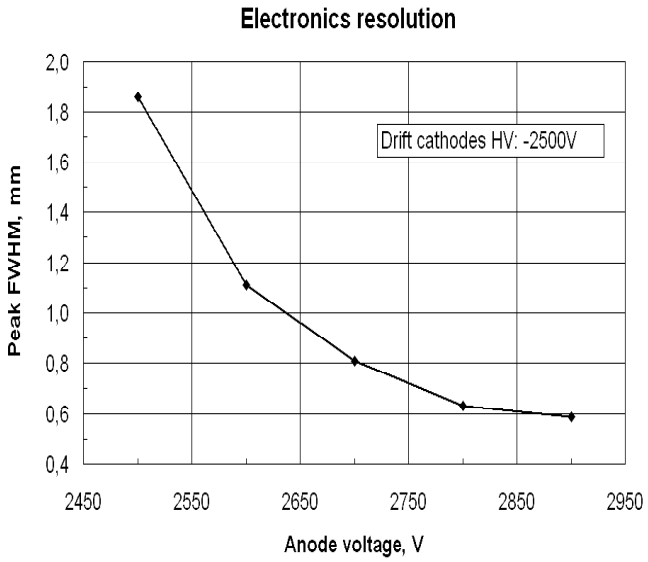

Fig. 6. Intrinsic resolution of the detector *vs* high voltage

3.3.4. Position resolution in the direction along the anode wires (*X*-axis)

To measure the space resolution, the detector was irradiated by a narrow neutron beam with its width being discretely changed in the range from 4.0 to 0.5 mm by cadmium collimators. A typical view of the obtained spectra is shown in Fig. 7. As one can see from the obtained data in Fig. 8, the detector spatial resolution is about FWHM = 1.5 mm.

This is in good matching with the expected neutron resolution.

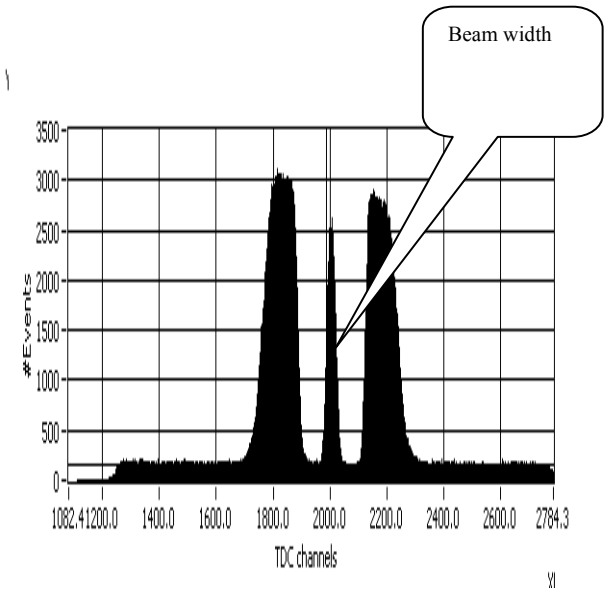

Fig. 7. Experimental method of the neutron position response measurement along the fine resolution axis

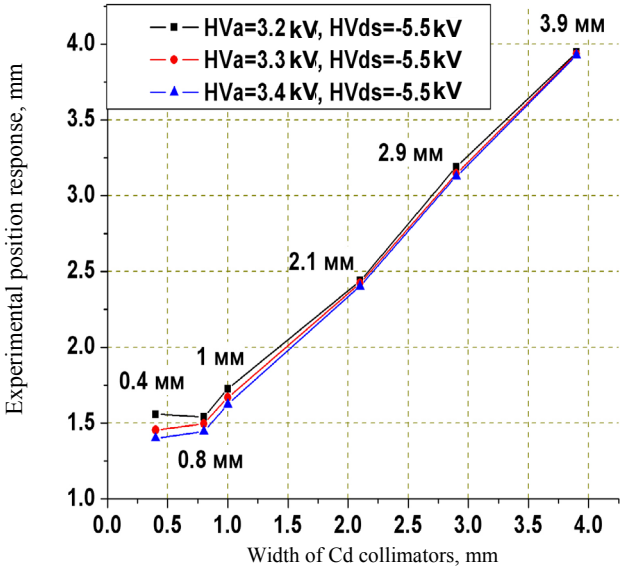

Fig. 8. Results of measurements of the spatial resolution of the detector

3.4. Energy spectra

The shape of the amplitude spectra is an important characteristic of the neutron detector. It is determined by the gas composition and its purity, the gas pressure, the gas gain and its uniformity along the detector window, the applied anode and cathode voltages.

3.4.1. Amplitude spectra of the neutron detectors and the standard neutron counter

The pulse height spectra dependence on the anode high voltage and the electric field in the drift regions was investigated. It was shown that the neutron detector spectra (Fig. 9b) are very similar to those obtained with the reference proportional counter with the gas pressure of 10 bar and look like a “dark body” for thermal neutrons, Fig. 9a.

The energy spectrum has a well-defined peak corresponding to the energy released in reaction (1). There are bumps corresponding to the energies of the proton (573 keV) and the triton (191 keV). Some distinctions are due to the fact that the detectors were filled with different gas mixtures (various concentrations of ^{3}He and CF_4 in the gas mixtures and different pressures) and that the 2D-detector is a multi-wire detector consisting of several hundred of anode wires.

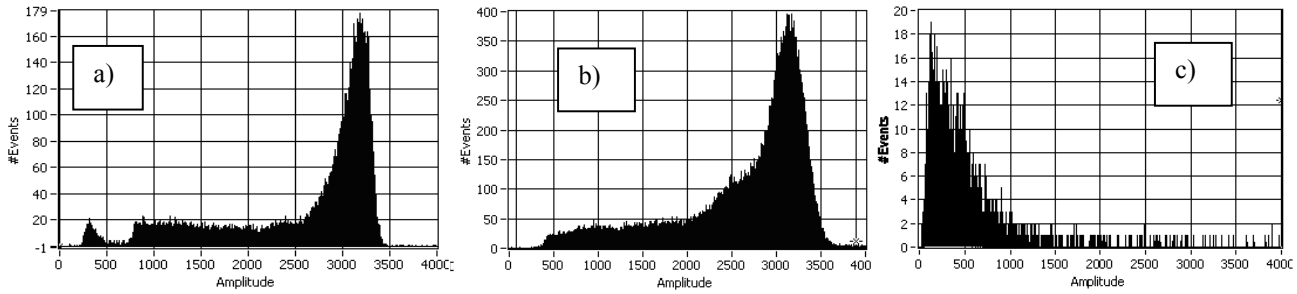

Fig. 9. Amplitude spectra measured with the neutron detectors. a – standard neutron counter SNM-50, high voltage was 2.0 kV; b – neutron detector, anode high voltage is H_A = 2.6 kV, cathode high voltage HV_{DS} = –2.5 kV. The intrinsic noise of the detector was rejected by the PA threshold; c – intrinsic noise of the neutron detector. The PA threshold is about zero

The intrinsic noise and the background spectrum of the neutron detectors are located in the low-amplitude part of the spectrum (Fig. 9c). Therefore, a correct choice of the events discrimination threshold can provide a minimal level of noise, keeping the neutron efficiency value constant. It corresponds approximately to the triton energy E_T =191 keV or ¼ of the peak amplitude of the total energy.

3.4.2. Amplitude spectra and background discrimination

An investigation of γ-sensitivity of the detectors has shown that amplitudes of events caused by registration of γ-rays are rather small. Therefore, if necessary, a rejection of low-amplitude events can provide very low γ-sensitivity of the detectors, $\varepsilon_\gamma \approx 1.8 \times 10^{-8}$ with small reduction of the neutron detection efficiency, < 5 % (Fig. 10). This feature allows to effectively register thermal neutrons in a high background of γ-quanta.

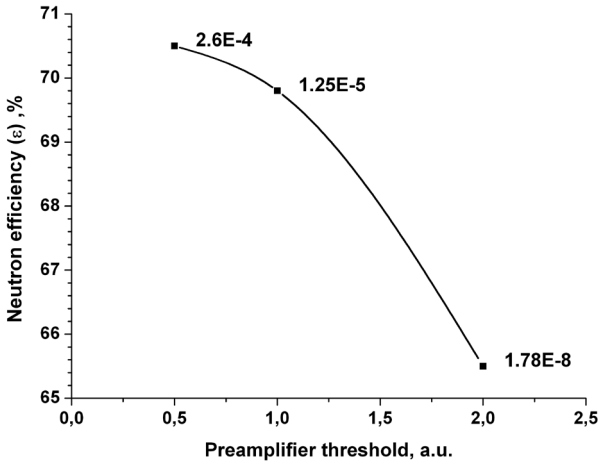

Fig. 10. Neutron- and γ-sensitivity of the detector with the entrance window 200 × 200 mm^2 *vs* the preamplifier threshold. The γ-source ^{137}Cs: A = 80 MBq, E_γ = 0.662 MeV

3.4.3. Gas purity control

Insufficient purity of the working gas dramatically affects the operation of the detector. It leads to violation of the operating parameters and makes impossible to ensure the correct functioning of the detector. Therefore, at the stage of the gas filling of each detector, the amplitude spectra were measured with the proportional counter SNM-50. Typical spectra are shown in Fig. 11.

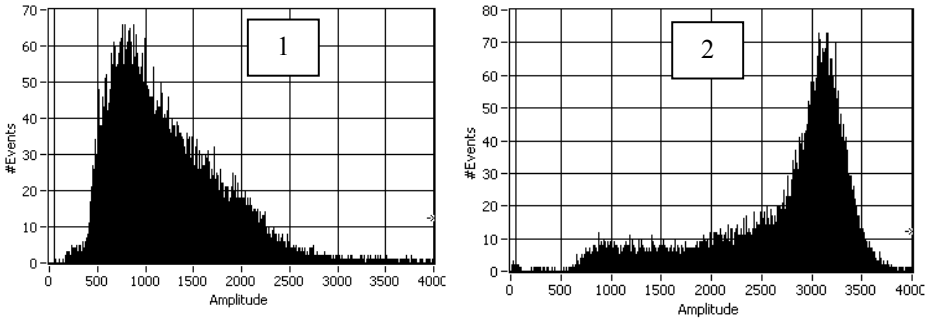

Fig. 11. Amplitude spectra measured by the neutron counter SNM-50 filled with the investigated gas. 1 – before ^{3}He cleaning. Gas mixture: (4 bar ^{3}He + + 100–300 ppm of O_2) + 2 bar CF_4; 2 – after ^{3}He cleaning. Gas mixture: 4 bar ^{3}He + 2 bar CF_4

4. Conclusion

Thermal neutron detectors for the diffractometers “Vector” and “Membrana-2” have been designed, constructed and successfully tested [4]. All required parameters have been achieved, as in Table 2. These detectors were successfully used in neutron diffraction experiments at the reactor VVR-M of PNPI.

Table 2

Working characteristics of the designed detectors

Characteristic	Diffractometer	
	"Membrana-2"	"Vector"
Neutron wave length, Å	3	9
Entrance window, mm	200 × 200	300 × 300
Gas mixture (^{3}He + CF_4), bar	4 + 2	2 + 2
Gas leakage, %/year	< 7	5
Neutron efficiency, %	70	72
Position resolution ($FWHM_{X, Y}$), mm	1.6 × 2.0	1.5 × 2.0
Plateau voltage range, kV	HV_A = + (2.9–3.4) HV_{DS} = – (1.0–6.0)	HV_A= + (2.9–3.3) HV_{DS}= – (1.0–6.0)
Intrinsic noise, Hz	< 0.2	< 0.3
Maximum counting rate (limited by the readout electronics; 10%-level of miscalculations), kHz	125	125
γ-sensitivity (^{137}Cs)	$< 2 \times 10^{-8}$	$< 2 \times 10^{-8}$

The approaches applied for optimization of the detector parameters have allowed us not only to achieve the required set of the detector characteristics, but also to ensure stable operation of the detectors over a wide voltage range, with very low noise and high stability of their characteristics. The technology developed for fabrication of the detector electrodes opens a way to improve the level of gas purity in the detectors by a few orders of magnitude and provides a longer detector lifetime in comparison with similar devices.

References

1. V.A. Andreev *et al.*, Nucl. Instr. Meth. A **581**, 123 (2007).
2. V.A. Andreev *et al.*, Bull. RAS: Physics **72**, 1001 (2008).
3. V.A. Andreev *et al.*, Preprint PNPI-**2780**, Gatchina (2008).
4. V.A. Andreev *et al.*, Phys. Solid State **52**, 1029 (2010).

TESTS OF THIN-WALL DRIFT TUBES DEVELOPED FOR PANDA TRACKERS

A.P. Kashchuk, O.V. Levitskaya

The PANDA experiment will be carried out at the international FAIR facility in the GSI laboratory (Darmstadt, Germany). According to the Technical Design Report, the Forward Tracker (six stations FT1–FT6) [1] and the Central Straw Tube Tracker (STT) [2] will be composed from thin-wall drift tubes (called straw-tubes below) in large quantities, 13500 and 4600 tubes, respectively. The straw-tubes used here were produced by winding and gluing two Mylar aluminized films of 12 μm thickness (the wall thickness including the glue was ~ 27 μm). The tube wall was used as a cathode (R_{tube} = 5 mm), and the coaxial gold-plated W-Re wire was used as an anode of the counter (R_{wire} = 10 μm). The Mylar material was preferred to the Kapton one because of its better mechanical properties – a higher Young's modulus and tensile strength. The drift tubes are filled with two-component gas mixture Ar(90 %) + CO_2(10 %) at the 1 bar overpressure, *i.e.* at the 2 bar absolute gas pressure. The overpressure stretches the tube and prevents the wire sagging. The detector plane consisted of two mono-layers of drift tubes shifted by the radius R_{tube}, see Fig. 1a. The radiation length of a single tube X is characterized by X/X_0 = 0.05 %, where X_0 is the media radiation length. As a calculation shows, the maximum sag of a 20 μm wire inside of a 1.5 m long horizontal straw tube due to its weight is smaller than 35 μm at the wire tension of 50 g.

In this report, we summarize various laboratory measurements made on straw tubes of 0.75 m and 1.5 m lengths (Fig. 1a), as well as on two module prototypes. The experimental set-up is shown in Fig. 1b. The modules were installed horizontally (as in the STT) and also vertically (as in the FT).

An intense 1.3 GBq ^{137}Cs γ-source (660 keV) was used for gas gain measurements, because a very low ionization current (pA) had to be detected. A low intensity ^{55}Fe X-ray source producing a point-like ionization in only one straw tube within the module was used for gas gain uniformity tests and to investigate the counting characteristics and cross-talks. A collimated ^{90}Sr β-source (emitting electrons of ≤ 2.3 MeV) with the intensity 11 MBq was used for efficiency measurements and for estimation of the spatial resolution of a single straw tube within the straw-module prototype.

The gas gain measurements were performed in order to specify the operational voltage at the 2 bar absolute gas pressure and to study the gas gain variations versus voltage, pressure, temperature and wire diameter. The ionization current corresponding to the unity gas gain was measured using the intense 1.3 GBq ^{137}Cs γ-source. In order to eliminate offsets in measurements of very small currents, we used batteries (as a floating voltage source) at both positive and negative voltages applied to the anode wire with respect to the cathode. The auto-ranging Keithley-485 pico-ammeter with the sensitivity of 0.1 pA was connected between the cathode and the ground. The ionization current $I_0 = 1.68 \pm 0.17$ pA was measured at ± 50 V and $I_0 = 1.73 \pm 0.12$ pA at ± 100 V. The resulting value of $I_0 = 1.70 \pm 0.21$ pA was obtained by averaging the partial results. The gas gain at any voltage V was calculated as the ratio I/I_0, where I was the current corresponding to the voltage V. Now the voltage was incremented in the range 1000–1900 V and the corresponding gas gain changed from 10^2 to 10^5, see Fig. 2a.

The gas gain versus voltage at several gas overpressures (above the atmospheric pressure) at fixed temperature is presented in Fig. 2b. The results of measurements were fitted by the Diethorn formula with two parameters, $E_{\min}$ and ΔV [3]:

$$G(V,\rho) = \left[\frac{V}{a \ln(b/a) \cdot E_{\min} \dfrac{\rho}{\rho_0}} \right]^{\dfrac{V}{\Delta V} \cdot \dfrac{\ln 2}{\ln(b/a)}}. \qquad (1)$$

Here, a and b are the radii of the anode wire and cathode tube, respectively, $E_{\min}$ is the minimal electric field needed for ionization, ΔV corresponds to the minimal voltage difference required to produce free electrons in an avalanche; $\rho/\rho_0 = (P/T)/(P_0/T_0)$ and P/T are the ratios of gas density, pressure and temperature at the real conditions to the reference ones P_0 = 1000 mbar, T_0 = 293 K, respectively.

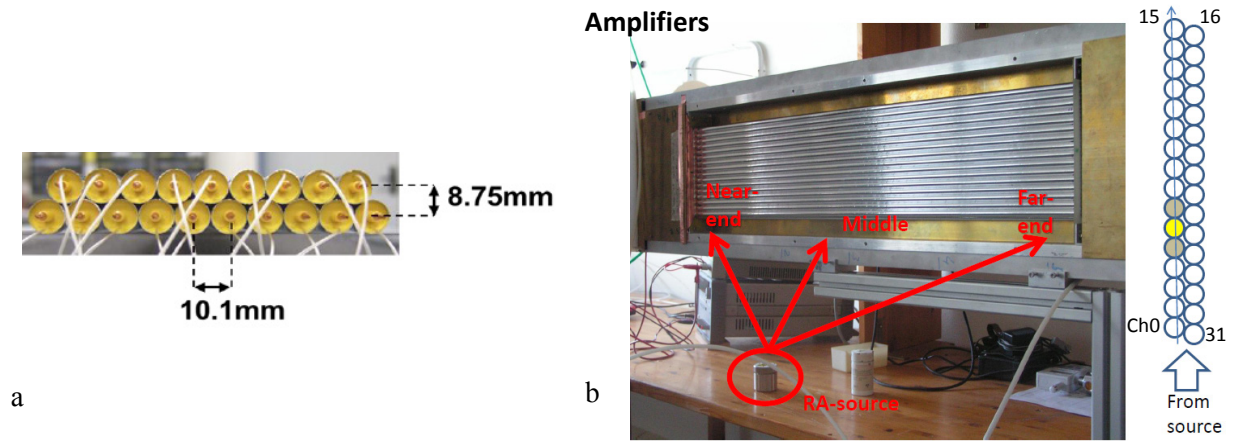

Fig. 1. Two mono-layers of thin-wall drift tubes filled with Ar(90 %) + CO_2(10 %) mixture at the 2 bar absolute gas pressure (a) and double layer 32-straw module prototype used in laboratory tests with various radioactive sources (b)

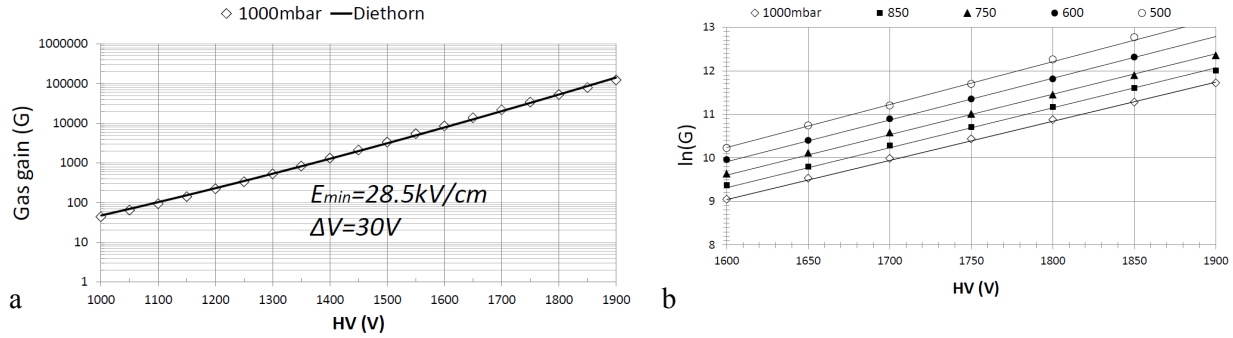

Fig. 2. Gas gain *vs* voltage for Ar(90 %) + CO_2(10 %) gas mixture at the 1000 mbar overpressure, (at the 2 bar absolute gas pressure) and the Diethorn parametrization of the measurement results (a). The gas gain *vs* voltage at various gas overpressures ranged from 1000 mbar down to 500 mbar (b). The points correspond to the measurements, the lines – to the parameterization function

Tests with the ^{55}Fe-source were performed to find a set of characteristics. In these measurements, the straw-tube impedance was terminated with the amplifier impedance via a 350 Ohm resistor connected in series to the amplifier, while the far-end of the straw-tube was un-terminated [4]. In Fig. 3a, a typical amplitude spectrum is presented, which was used to verify the gas gain uniformity along the straw-tube. In the case of an individual straw tube, the sag can modify the gas gain dramatically in the middle of the tube. But for the 32-straw module where the tubes were arranged in double layer and glued together, the gas gain is rather uniformly distributed. In this case the gas gain non-uniformity in the middle of any tube within the module is below 1 %, as it is shown in Fig. 3b.

Figure 4a shows three typical regions observed in the counting characteristics measured with the ^{55}Fe-source: the beginning of the plateau (the point corresponding to 5.9 keV), the constant rate region (the plateau) and the region of increasing counting rate above the end of the plateau. The measurements show rather similar counting rates for all straw tubes within the 32-straw module in all regions mentioned above: at the near-end (at the amplifier side), in the middle and at the far-end. The rise of the counting rate correlates with the growth of the dark current and appearance of two and more pulses (cross-talks). The position of the plateau end strongly depends on the quality of straw-tube production. The ^{55}Fe *X*-ray source produces point-like ionization in the gas and generates signals in one and only one straw tube. This feature makes possible to measure the cross-talks in any pair of tubes within the module. As is shown in Fig. 4b, typical cross-talks were observed on the level of 0.2 % in a wide range of voltages up to 1900 V in some cases, and only near the end of the plateau they could reach 10 % and even 100 %.

The efficiency of particle detection was measured with the collimated ^{90}Sr-source with the aim to specify the operational voltage for registration of MIPs (minimum ionizing particles). The particles emitted by the ^{90}Sr-source cross many tubes, as illustrated in Fig. 5a. A set of three neighboring tubes was used to find the efficiency of the inner tube with respect to the outer tubes. The efficiency was measured at both ends and in the middle of the tube. Figure 5a shows the efficiency versus voltage at a fixed threshold of 10 fC. Figure 5b shows the dependence of the efficiency on the threshold for several voltages.

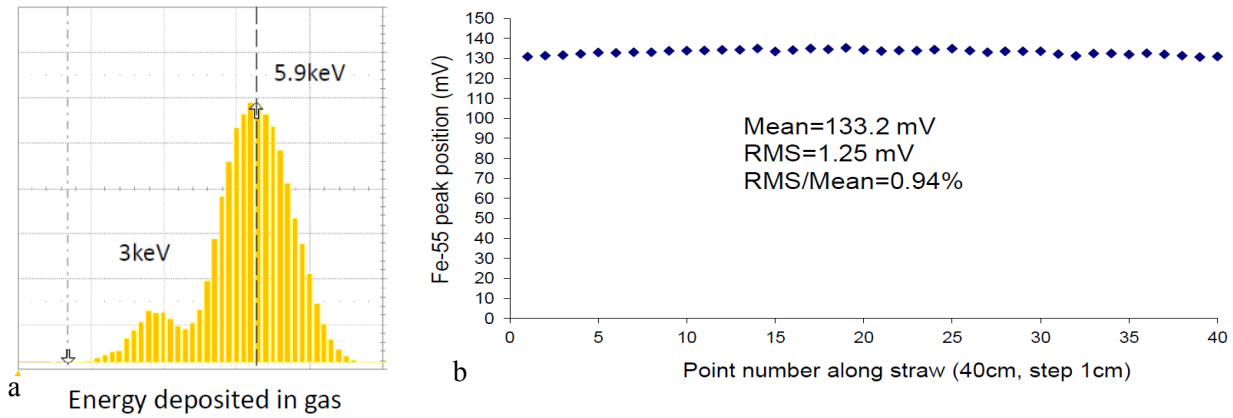

Fig. 3. Typical amplitude spectrum measured with the ^{55}Fe-source in a single tube within a 32-straw module (a). Gas gain variation in the tube measured as the position of the 5.9 keV peak along the distance of 40 cm in the middle of the tube (b)

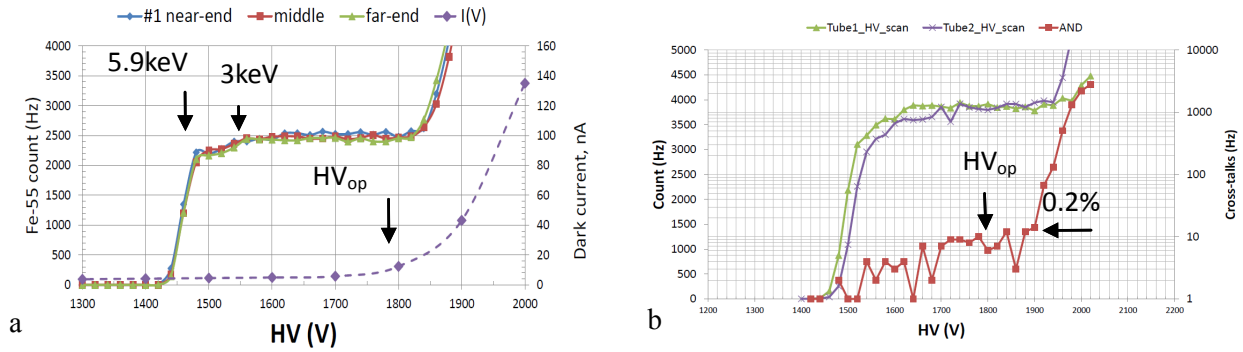

Fig. 4. Counting characteristics measured with the ^{55}Fe-source at a sequence of points along a 0.75 m straw tube filled with Ar(90 %) + CO_2(10 %) mixture at the 2 bar absolute gas pressure (a). The cross-talks measured with the ^{55}Fe-source between two straw tubes of 1.5 m length (b). HV_{op} = 1800 V is indicated as the operational voltage for registration of MIPs

We have compared the results of the efficiency measurements obtained with the ^{90}Sr-source and with Cosmic Rays (CR), performed at large statistics, collected for many days, for all straw tubes within the 32-straw module. The measurements with CR were made at the HV = 1800 V (Fig. 6a) and HV = 1700 V (Fig. 6b). One can notice that the results obtained with ^{90}Sr and CR are consistent. Comparing the data in Figs. 5a, b and 6a, b we see that the operational voltage should be at least 1800 V. According to Fig. 2a, the gas gain at the HV = 1800 V is equal to 5.5×10^4. A similar gas gain at the HV = 1800 V was obtained in a cross-check using the ^{55}Fe-source by measuring both the rate (see the plateau in Fig. 4a) and the current. If the gas gain is known, we can map the threshold of 10 fC to 10 p.e. (primary electrons). Then, the efficiency with such a threshold has to be better than 95 % at 200 p.e./cm, which is the total number of primary electrons formed along the track of a MIP at the 2 bar absolute gas pressure, assuming a uniform distribution of primary clusters along the track. In reality, the efficiency will be better and close to 100 % in a 2-layer detector.

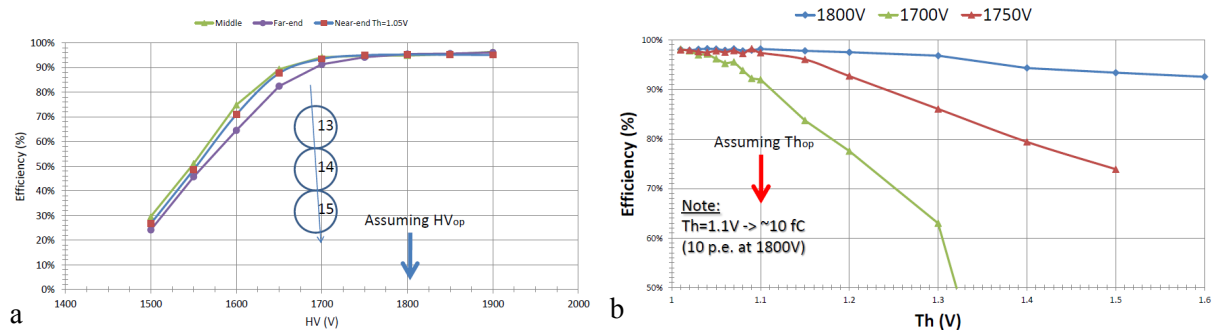

Fig. 5. Efficiency *vs* voltage at a fixed threshold for various points along a straw tube (a), and efficiency *vs* threshold at fixed voltages at the wire (b). Both characteristics were obtained in few minutes with the ^{90}Sr-source using the "three neigbouring tubes" method

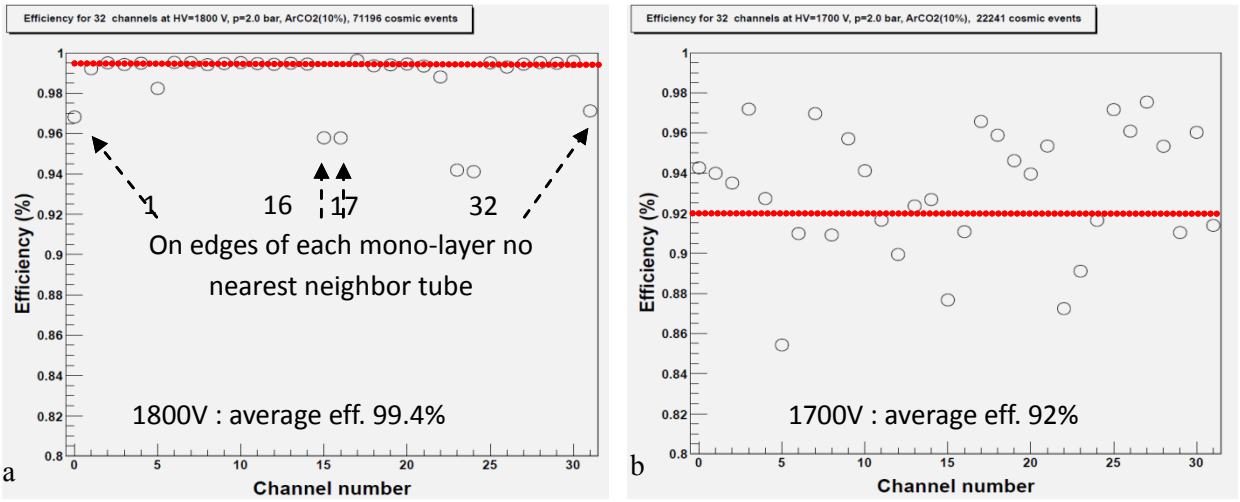

Fig. 6. Efficiency of straw tubes within a 2-layer (16 + 16 = 32 straw) module at the HV = 1800 V (a) and HV = 1700 V (b) obtained with CR with large statistics collected for many days

Further tests were performed to estimate the single-straw spatial resolution by observation of time spectra. The time-to-digit conversion was made with a 128-channel CAEN TDC module V1190A with the time resolution 100 ps/bin. Our ^{90}Sr source of charged particles for laboratory tests is a unique one, it allows to obtain large statistics in a few minutes (10^5 events in 20 min), while many days are required with CR. Nevertheless, this source in not appropriate for accurate measurements of the spatial resolution due to low energies of electrons (maximum 2.3 MeV), because significant multiple scattering in the gas and material of the detector deteriorates its spatial resolution.

Measurements of TDC-spectra with ^{90}Sr were carried out at the operational voltage of 1800 V and threshold 10 p.e. As one can see in Fig. 7a, b, primary electrons drift without multiplication practically through all the distance R_{tube}. Avalanches in the gas start at the distance $r \approx 102$ μm from the anode wire, at the electric field $E_{\text{min}} = 28.5$ kV/cm, as is shown in Fig. 2a.

Raw TDC-spectra measured with the ^{90}Sr-source are "corrupt" due to two main processes. The first process is clusterization of primary ionization along the track, the second is multiple scattering of low energy electrons emitted by ^{90}Sr. As it is illustrated in Fig. 8a, b, many primary electrons drift to the wire from the track with different starting velocities, and they can produce two or more pulses (hits). The first pulse is used as a rule to determine the spatial coordinate. However, the second pulse from the same track (or even the 3-rd) can be also registered with a multi-hit TDC. As one can see in Fig. 9a, b in the two-dimensional plot and its projections, low energy electrons scattered in the gas, on the wall and also on the glue can randomly "deform" the shape of the TDC-spectrum. In such a case, the 1-st pulse can be wrong, *i.e.* it can be not related to the closest electron cluster to the wire.

The spatial resolution of a single straw-tube was obtained using the so-called "auto-calibration" technique described in detail in [2]. Parameters of the TDC-spectrum and the corresponding $r(t)$-relation (Fig. 10a, b) for each channel were derived from a fit performed with the following empirical function:

$$\frac{\mathrm{d}n}{\mathrm{d}t} = p_1 + \frac{p_2[1 + p_3 \exp((p_5 - t)/p_4)]}{[1 + \exp((p_5 - t)/p_7)][1 + \exp((t - p_6)/p_8)]}. \quad (2)$$

Here, dn is the number of events within the time bin dt in the TDC-spectrum, the parameters p_5 and p_6 are the values t_{min} and t_{max}, their difference being the maximum drift time in the straw-tube; other parameters describe the spectrum shape.

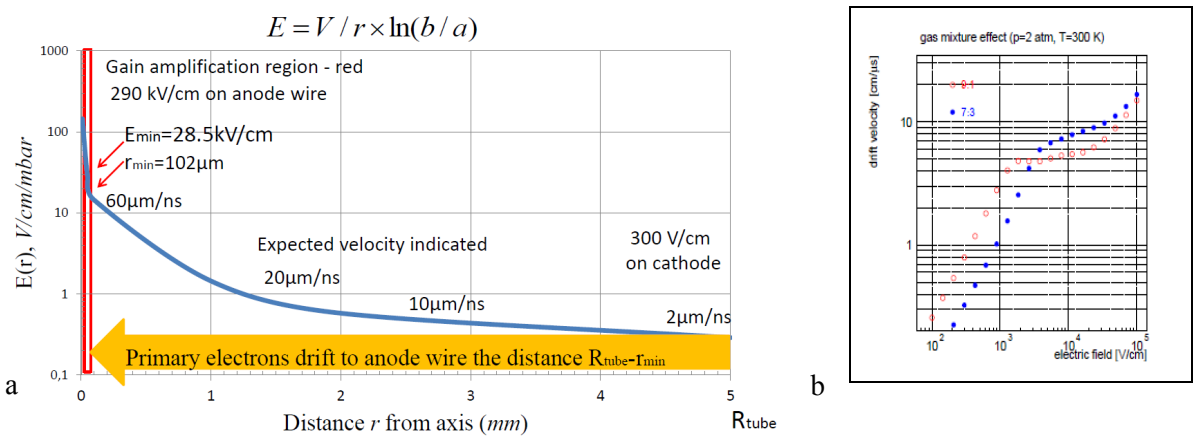

Fig. 7. Electric field strength in a tube at 1800 V with indication of the electron drift velocities at certain field values (a). Electron drift velocity *vs* electric field for two-component gas mixtures Ar + CO_2 at the 2 bar gas pressure [2]: open red points – our case of Ar(90 %) + CO_2(10 %), blue points – Ar(70 %) + CO_2(30 %) (b)

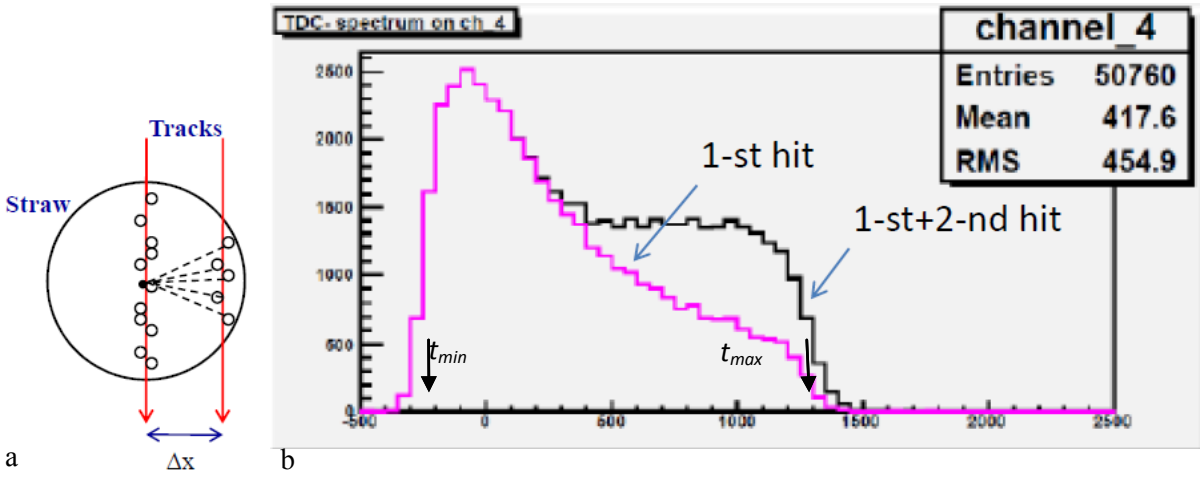

Fig. 8. Origin of multiple pulses due to clusterization of primary ionization along the track (a); TDC-spectrum measured with the ^{90}Sr-source including only the 1-st pulse and a sum of the 1-st and 2-nd pulses (b). With multiple scattering, the 1-st pulse can be generated by a cluster not nearest to the wire. The time scale is in the TDC sampling units, one histogram bin containing 50 sampling units

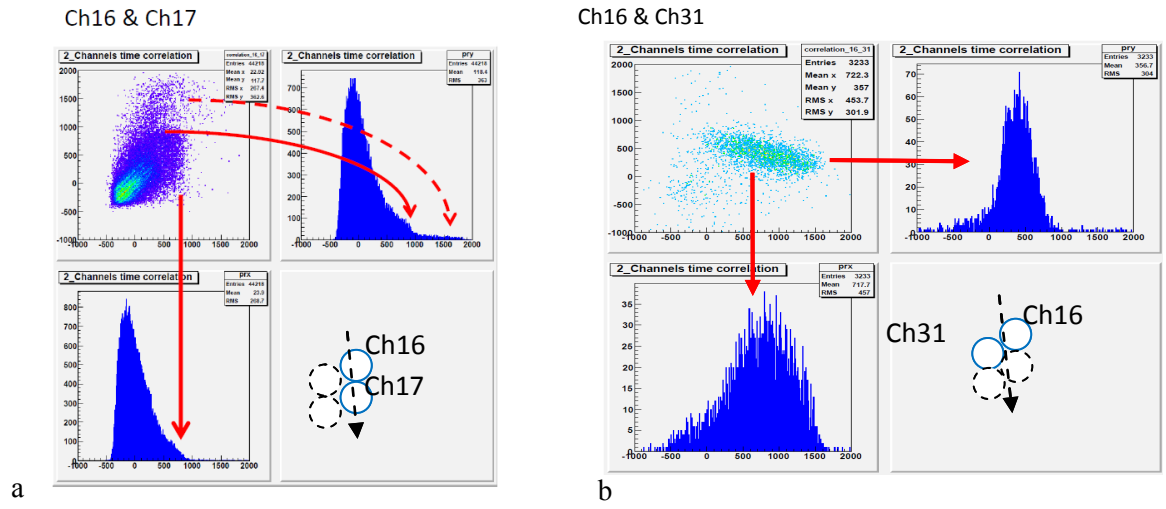

Fig. 9. 2D plot of the correlation between two time intervals for two tubes Ch16 and Ch17 from the same straw monolayer, measured with the ^{90}Sr-source with TDCs, and the 1D TDC-spectra obtained as its projections (a). The same plot for another pair of tubes Ch16 and Ch31 taken from different monolayers (b). The tails, as well as spurious hits on the level of ~ 20 % in the TDC-spectra, appear due to multiple scattering. To obtain correct TDC-spectra and the $r(t)$-relation, a special hit selection is provided in the event analysis

The $r(t)$-relation has been found from the TDC-spectrum with N_{tot} entries using the following formula:

$$r(t) = \int_{t_{\min}}^{t_{\max}} \frac{\mathrm{d}r}{\mathrm{d}t} \cdot \frac{\mathrm{d}n}{\mathrm{d}n} = \frac{R_{tube} - R_{wire}}{N_{tot}} \int_{t_{\min}}^{t_{\max}} \frac{\mathrm{d}n}{\mathrm{d}t} \approx \frac{\sum_{i=1}^{i=i_t} n_i}{N_{tot}} \cdot (R_{tube} - R_{wire}). \quad (3)$$

For further conversion from the measured time to spatial coordinate, the $r(t)$-relation was parameterized by the Chebyshev polynomial of the 5-th order:

$$r(t) = q_0 + q_1 t + q_2(2t^2 - 1) + q_3(4t^3 - 3t) + q_4(8t^4 - 8t^2 + 1) + q_5(16t^5 - 20t^3 + 5t). \quad (4)$$

Here, t is the time interval measured as the radius of an isochrone, *i.e.* the distance from the primary cluster to the wire; the parameter q in Fig. 10b has been replaced by p.

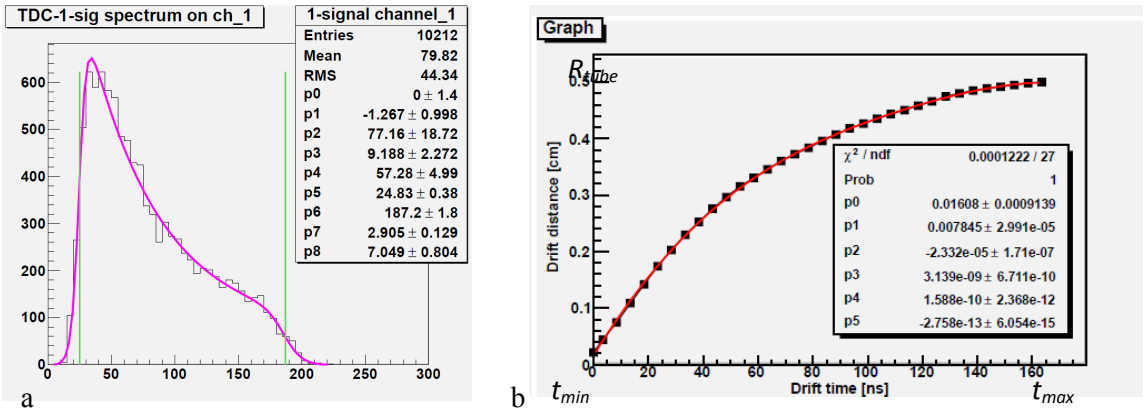

Fig. 10. TDC-spectrum measured with the ^{90}Sr-source for one straw tube (time in ns) (a), and the corresponding $r(t)$-relation with the parameters (b)

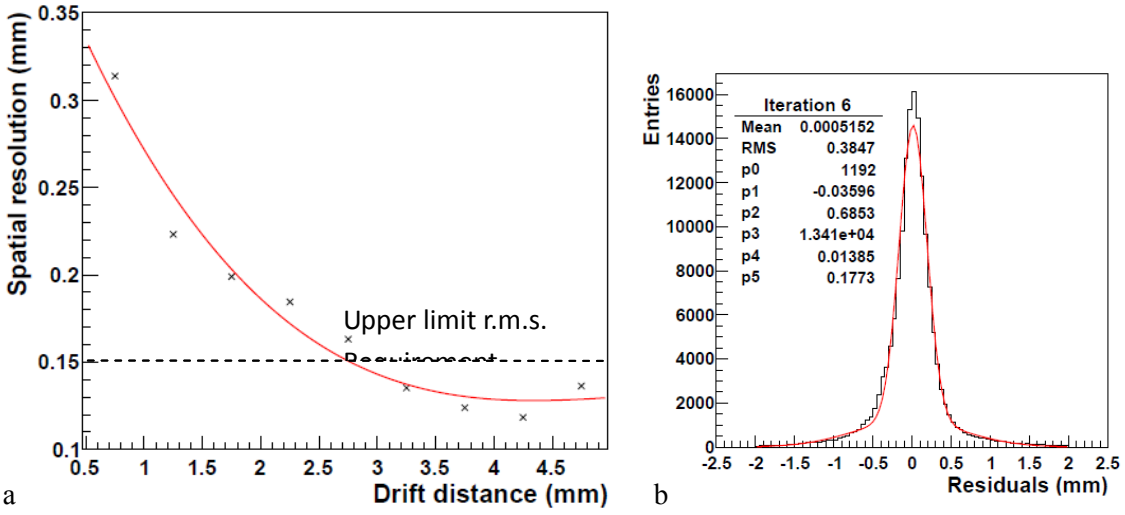

Fig. 11. Spatial resolution measured with the ^{90}Sr-source as a function of the distance between the track and the wire (a). The averaged distribution of residuals and its r.m.s., p5 = 177.3 μm (b). The spatial resolution specified for the PANDA experiment is indicated by the dashed line

According to the auto-calibration, the final $r(t)$-relation is obtained sequentially by iterations using various hit selection criteria. The residuals, which are the differences between the best track and $r(t_i)$, are minimized by this iterative procedure (t_i is the measured time interval in the i-th TDC-channel).

As one can see in Fig. 11a, a much better spatial resolution is obtained in the region from $R_{\text{tube}}/2$ to R_{tube} within each mono-layer shifted by R_{tube} if the data are not averaged over the full interval R_{tube}. Using this effect, one can combine the data properly from two independent monolayers in order to improve the spatial resolution.

The upper limit of the spatial resolution specified for the PANDA experiment is 150 μm (r.m.s.). According to the TDR, the resolution like that will provide the momentum resolution of the order of 1 %.

A large spread of the parameters of Eq. (2) describing the TDC-spectra of the 32-straw module was observed due to multiple scattering of low energy electrons, emitted by ^{90}Sr in a wide energy range around 2 MeV. As could be expected, this explains why the spatial resolution measured with the ^{90}Sr-source is worse than that predicted by simulations, see Figs. 11a, b and 12a, b, c.

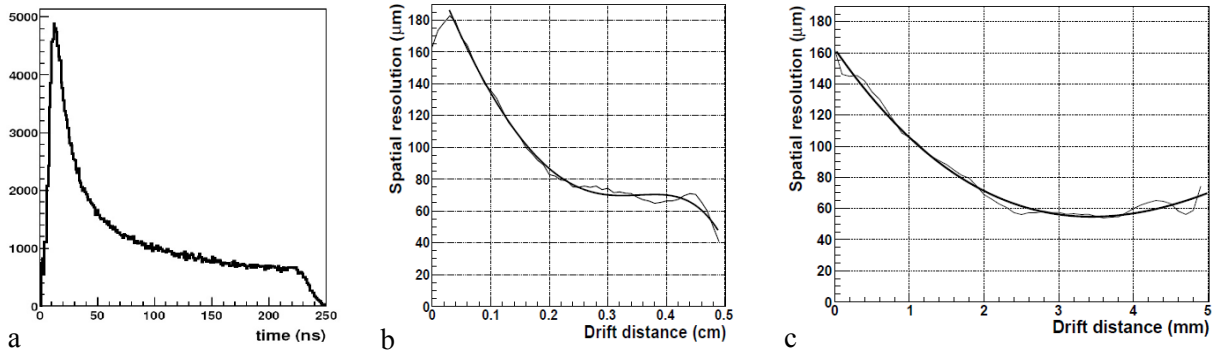

Fig. 12. Simulation of a TDC-spectrum for MIP particles. As the simulation shows, the magnetic field extends the drift time to 220 ns (a). Single straw-tube spatial resolution (r.m.s.) *vs* distance to the wire found without a magnetic field (b) and with a magnetic field (c). In the range between $R_{\text{tube}}/2$ and R_{tube}, the resolution is around 70 μm (r.m.s.). These results were taken from [2, 5]

Our goal at present is to prepare the apparatus, technique and software for beam tests with high energy particles at various rates with and without magnetic fields and to compare the results of measurements with

simulations. Note that tests with radioactive sources are good tools for straw-tube quality control at the mass production and provide feedback on possible improvements of the module assembly procedures.

This work was performed in collaboration with P. Gianotti and M. Savrie.

References

1. PANDA Forward Tracking System. Technical Design Report (in preparation).
2. PANDA Central Straw Tube Tracker. FAIR/Pbar/Technical Design Report, Darmstadt (2012), http://panda-wiki.gsi.de/pub/Tracking/WebHome/panda_tdr_trk.pdf
3. P. Gianotti, A. Kashchuk… O. Levitskaya *et al*., Note LNF-**11/05** (P), Frascati (2011).
4. A.P. Kashchuk… O.V. Levitskaya *et al*., Phys. of Particles and Nuclei Letters **8**, 40 (2011).
5. S. Costanza… A. Kashchuk… O. Levitskaya *et al*., Nuovo Cim. **34** C, 94 (2011).

CBM RICH PROTOTYPE GAS SYSTEM

L.M. Kotchenda, P.A. Kravtsov

1. Introduction

The Compressed Baryonic Matter (CBM) experiment is a heavy-ion experiment at the future FAIR facility being designed to explore the intermediate range of the QCD phase diagram in the beam energy range from 10 to 45 A GeV. With its physics program, CBM will investigate properties of the dense baryonic matter and the expected phase transition between the hadronic and partonic matter. Among the key observables are the low-mass vector mesons and the charmonium decaying into lepton pairs. In CBM, electrons with energies lower than 8 GeV/*c* will be identified by a RICH detector, which is being developed at several laboratories. In addition, the detector will improve the kaon/pion separation at the momenta higher than 4 GeV/*c*.

The concept of the RICH detector involves CO_2 as the radiator gas, spherical glass mirrors reflecting the Cherenkov radiation to an array of Multianode Photomultipliers as photo detectors. The CO_2 gas has been chosen because it has the Lorentz factor of 33.3, the radiation length of 183 m and the pion momentum threshold for Cherenkov light production of 4.65 GeV/*c*, thus representing a very good compromise to fulfill the CBM RICH requirements.

The RICH detector requires stable differential pressure of the CO_2 gas above the atmospheric pressure, as many of gaseous detectors, which requires to ensure mechanical stability of the detector volume. The radiator gas must be free of moisture and oxygen. Additional measurements should be carried out to investigate temperature influence on the detector performance.

2. Gas system design

The primary purpose of the CBM RICH Prototype gas system (Fig. 1) [1] is to provide pure CO_2 gas to the RICH prototype at the correct differential pressure. Its design is based on the gas systems for the STAR and PHENIX experiments at BNL [2–4]. The system operates nominally as a closed circuit gas system with the majority of gases recirculating through the prototype. During the normal operation, the fresh gas is added with a Burkert 8711 mass flow controller FM1. To support constant differential pressure at the 2 mbar level measured with the pressure transmitter PT4, the control system will change the flow through the FM1 controller. If the differential pressure is increasing, the gas flow through FM1 will be reduced. And vice versa, in the case of a differential pressure drop, the flow through FM1 will be increased. The gas system can be operated in an open configuration for purging.

A bypass valve (BMV1) is manually adjusted to enable the optimum flow rate through the prototype. The purity of the recirculating gas is monitored using Panametrics Oxygen (O2X1) and Humidity (MMS35) analysers. A fraction (up to 30 %) of the recirculating gas can be passed through the purifier and dryer to remove oxygen and moisture. There is a possibility to check the gas purity with the analysers after the purifier and dryer to determine their saturation.

The Purifier is filled with active copper. Its operating and regenerating temperature is 220 °C. A Temperature Indicating Controller TIC1 supports this temperature level. The mixture CO_2 + 5 % H_2 can be used to regenerate the Purifier. The oxygen content after the purifier is about 2–3 ppm. The Dryer is filled with NaX (13X) molecular sieves. Its normal operating temperature is 22 °C. The water content at this temperature is 1–2 ppm in the Dryer output flow. The regeneration of the Dryer is performed at 350–400 °C supported with the TIC2.

A computer driven data acquisition/control system monitors all the process variables and provides stabilization of the RICH prototype differential pressure. The computer system flags the quantities which fall outside of the predefined limits and initiates corrective actions. Using data from the TT1, PT4 and BP (Barometric Pressure) sensors, the computer system estimates the value of the CO_2 refraction index.

The gas system is assembled in a single 19″ rack and can be easily transported with the RICH prototype. It can also be used in the future for the complete RICH detector with minor changes.

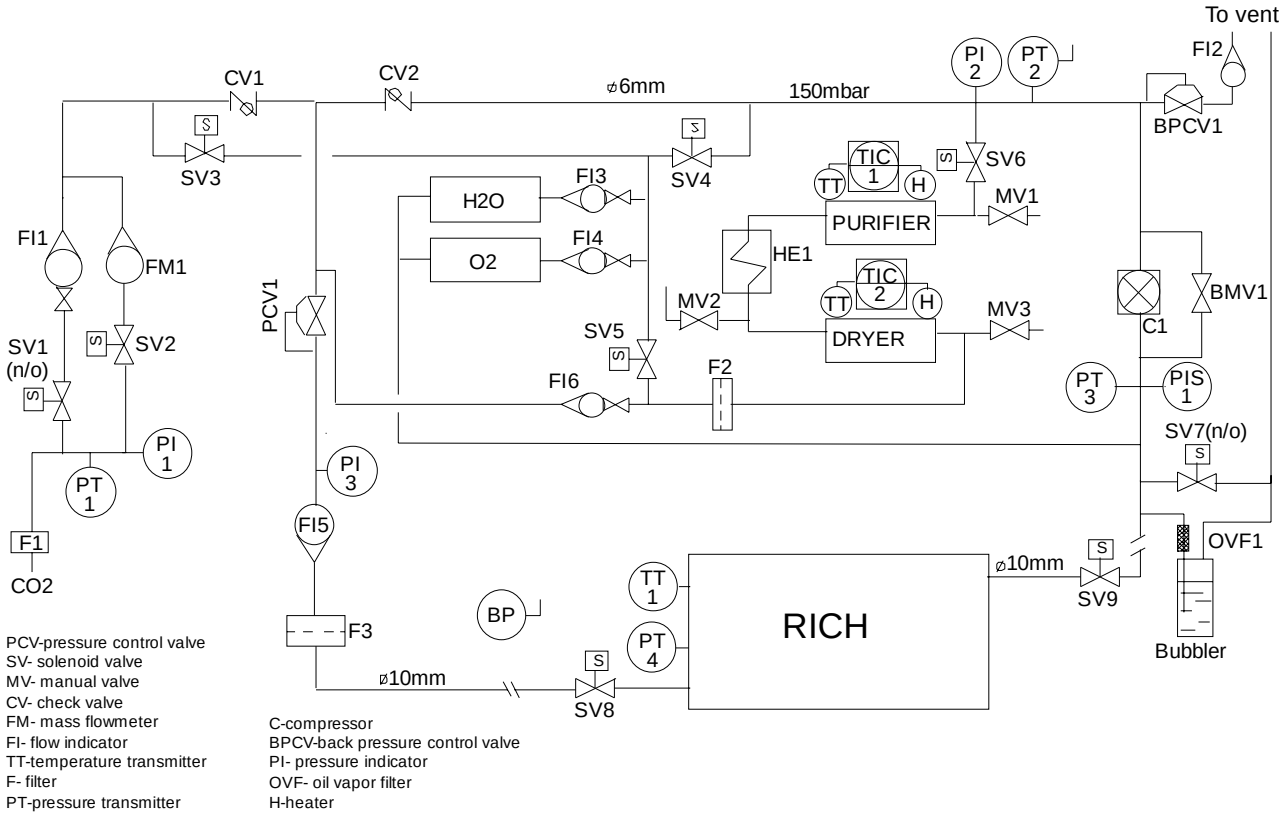

Fig. 1. CBM RICH Prototype gas system

3. Slow control subsystem

The CBM RICH gas system is controlled by a custom slow control subsystem [5] that is based on the data acquisition DAQ32 module [6]. This module was designed for controlling small cryogenic and gas supply systems. It provides reading of up to 32 sensors with industrial standard voltage or current outputs. The device precision is 0.004 % of the measurement scale, which can be selected from the range of +(0–4) V, ± 5 V, +(0–10) V, ± 10 V. The module is also equipped with 16 buffered digital outputs to control acting devices like solenoid valves or compressors, and 4 analog voltage outputs for flow controllers or heaters. Such input-output channel density allows to control small systems like the CBM RICH gas system with a single module.

The variety of data exchange interfaces simplifies the connection of the instrument to an external control system or to a computer. Flexible controller firmware allows implementing the necessary control algorithms like the PID regulation, directly in the firmware. Two of these modules (one working and one spare) are mounted in the gas system rack.

Control computer software [7] has been developed for the Windows platform. It provides reliable data acquisition, automated handling of alarm conditions and manual control of the gas system. All the alarm events and system variables are logged into a database. The software is split into multiple processes that communicate, making use of special operating system kernel objects.

The main process reads all the sensor values and passes them to other processes. In order to make the software more reliable, it has been divided into two threads: one for the Graphical User Interface (GUI) and one for the data acquisition. The GUI thread shows all the gas system parameters including the valve states in the main window. The operator can also use the controls to manage the system manually, as well as adjust the alarm parameters.

The DAQ thread acquires all the process variables, writes them into shared memory and checks the alarm conditions. Every alarm setting contains an alarm threshold, an alarm message and a control template. The template indicates the alarm set and the release actions for every controlled device, *e.g.*, a valve or a

compressor. The system makes corrective actions automatically and alerts the operator about the problem. Alarm control templates provide the user with a high degree of flexibility when setting up the system. All the process variables are written into the MS Access database with a specified period. In the case of an alarm trigger, the current values are written out in turn. All the alarm events and software messages are logged into the same database.

It is also useful to have a fast access to particular data and to plot the results during the gas system operation. A special tool (DBViewer) has been developed to work with the gas system database. It provides visualization of the data for any gas system process variable and exports the data from the database to an MS Excel file or tab-delimited text file for further analysis.

One more program has been designed for visualization of the actual state of the system. This program (Charts) displays up to ten selected parameters in the time chart format. Besides, it can be used for a tabular display of the process variables, with extra alarm signals for every parameter in the table. In addition, the TCP/IP client/server is implemented in the Charts software so that it can be used remotely to monitor the system under control.

The gas system control software was successfully used in nine gas systems [2, 3] for several detectors in the STAR and PHENIX experiments at RHIC.

4. Test beam results

During the test beam run in October 2011 at CERN, we had a good opportunity to test the gas system. The major task was to check the differential pressure stability of the RICH prototype in the recirculation mode during stable operation. Figure 2 features the results of our pressure regulation. Obviously, the differential pressure of the RICH prototype was stable at 2.0 ± 0.1 mbar, although the barometric pressure PTB varied in the range of 22 mbar. We can see the same results for the STAR and PHENIX gas systems [2–4], in spite of different control technique. For the STAR and PHENIX gas systems, mass controllers were used to prepare a fresh mixture with a very stable content. The fresh mixture was added to the system gas at a constant flow, and therefore the pressure of the detector was stabilized using a dedicated PID-controller in the recirculation mode.

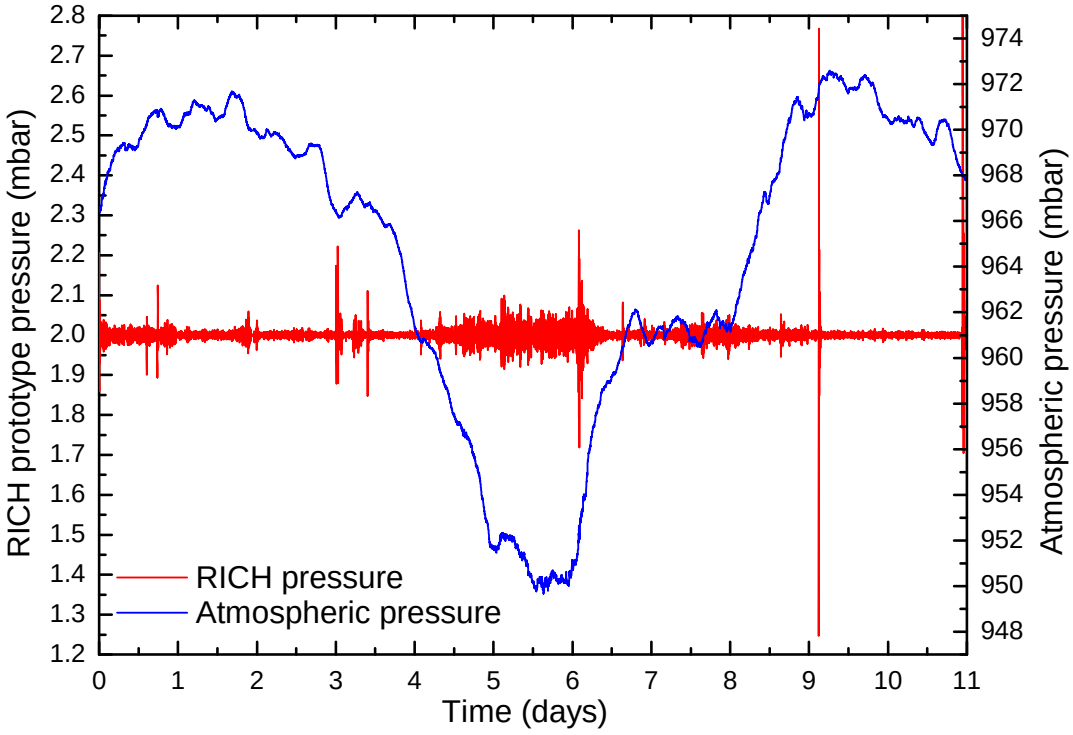

Fig. 2. Detector differential pressure (red line) and the atmospheric pressure (blue line)

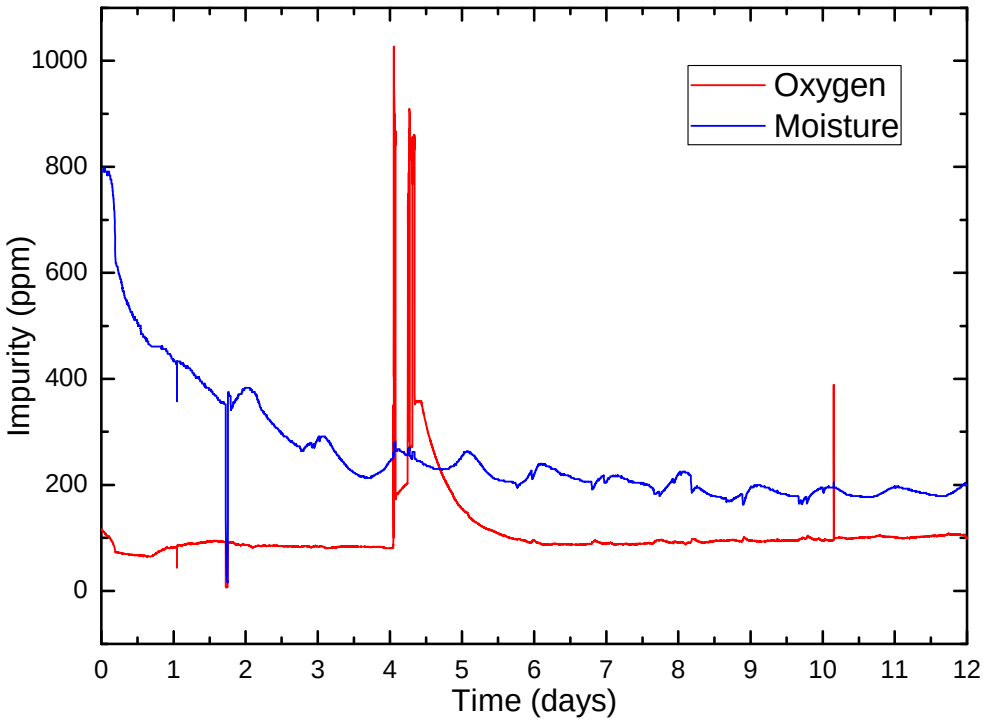

Fig. 3. Oxygen (red line) and moisture (blue line) content

The efficiency of the gas system Dryer and Purifier was also checked. Test results are shown in Fig. 3. It should be mentioned that the inner RICH prototype surface was not treated with a special cleaning process, and we had a lot of water and oxygen adsorbed by the walls of the RICH vessel and the inner structure elements. Even at these conditions, both the Dryer and Purifier had enough efficiency to remove moisture and oxygen to the required level.

The gas system was also used to add a certain amount of oxygen in order to check the detector operation at a higher oxygen content (the spikes in the oxygen line on the fourth day in Fig. 3). The oscillations of the moisture content are caused by daily temperature changes in the hall.

In general, the gas system provided stable operation with stabilization of all the required gas parameters in the RICH prototype. It was reliably operated by the control system, providing all the system parameters to the external slow control system. The RICH prototype vessel (3.5 m^3) was checked for leaks prior to the beam time. Measuring the pressure decrease in the vessel, we have estimated the leak rate to be below the sensitivity of the gas system ($\leq$ 50 sccm).

References

1. L. Kotchenda *et al.*, CBM Progress Report, Darmstadt (2010).
2. L. Kotchenda *et al.*, STAR TPC Gas System, NIM A **499**, 703 (2003).
3. L. Kotchenda *et al.*, PHENIX Muon Tracking Detector Gas System, NIM A **578**, 172 (2007).
4. L. Kotchenda *et al.*, Preprint PNPI-**2712**, Gatchina (2007).
5. P. Kravtsov *et al.*, CBM Progress Report, Darmstadt (2010), p. 32.
6. P. Kravtsov and V. Trofimov, Preprint PNPI-**2723**, Gatchina (2007).
7. P. Kravtsov, Preprint PNPI-**2593**, Gatchina (2005).

RECOVERY OF AGED ANODE WIRES IN PROPORTIONAL COUNTERS USING A NEGATIVE CORONA DISCHARGE IN 80 % CF_4 + 20 % CO_2

G.E. Gavrilov, A.G. Krivshich, D.A. Maysuzenko, A.A. Fetisov, N.Yu. Shvetsova

1. Introduction

During last few years, large-scale studies of the radiation hardness of gaseous detectors were carried out in preparation for LHC experiments. Today, most of the factors affecting the aging rate of these detectors are well defined [1].

The "classical aging effects" are the result of chemical reactions occurring in the avalanche plasma near anode wires leading to formation of deposits on the electrode surfaces. This mode of aging is extremely sensitive to various additives and contaminants in the gas and materials used in contact with the gas. The most harmful chemical element, which is systematically detected in analyses of wire deposits, is silicon. Si compounds are found in gas-system components, sealant Room Temperature Vulcanizing Silicone Rubber, silicon-based lubricant, *etc*. Usually, Si deposits appear at the accumulated charges much below 1 C/cm per wire. That is why most of the materials used for construction of the detectors have to be tested to address their safety from the aging point of view.

Due to the need for radiation hardness, a broad list of conventional working gas mixtures was narrowed down to Ar(Xe) + CO_2 + CF_4. These mixtures block the negative influence of silicon deposits, preventing the anode aging. However, at the accumulated doses above 1 C/cm per wire, there exist aging effects that are not related to polymerization.

Anode wires are commonly made of gold-plated tungsten. It has been found that oxygen and other active radicals produced in avalanches penetrate through the pores and micro-cracks in the gold-plating and react with tungsten [2]. This process results in swelling of the wires because the forces within a wire break the gold-plating, and tungsten oxides (WO_x) appear on the wire surface. The aim of the present work was to demonstrate recovery of an aged anode wire in a proportional counter by treating it with a negative corona discharge in a 80 % CF_4 + 20 % CO_2 gas mixture.

2. Test set-up

Aging tests of straw-tubes were carried out using three ^{90}Sr β-sources mounted in a line with a total rate at one straw of 15 MHz. The beam profile of the irradiated zone was uniform with the width about 35 mm. Two straw-tubes used in our investigations had 0.4 cm diameter, and the anodes were made of 50 μm gold-plated tungsten wires. The gas flow rate was 0.5 cm^3/min, which was equal to four straw volumes per hour. To avoid both air and water vapor penetration into the straws from the outside, a set of straws was placed in a sealed box blown over by argon. Measurements of the straw tube properties were performed regularly each day after every charge accumulation increment of about 0.13 C/cm during the exposure [3, 4].

To monitor the gas gain, the photo peak position of a collimated ^{55}Fe *X*-ray source (E_γ = 5.9 keV) in the amplitude spectrum was measured at different test points along the irradiated straw. During the aging tests, we chose several working points of the high voltage to achieve gas gains and irradiation currents over a wide range: 2×10^4, 5×10^4, 1×10^5 and 0.38 μA/cm, 0.97 μA/cm, 1.98 μA/cm, respectively. This has covered the gas gains commonly used in gaseous wire detectors.

An analysis of the anode surface after the aging procedure was performed using a scanning electron microscope with *X*-ray emission (0–10 keV) spectroscopy (SEM/XEM).

3. Aging test results

Usually after accumulation of the total charge of about 1.5–1.8 C/cm at the rate of 0.13 C/cm per day, the wire degradation resulted in the gas gain reduction of about 10–15 %. The results of the SEM/XEM analysis of the aged anode wire in the centre of the irradiated zone (the gas gain being $G = 5 \times 10^4$) are presented in Fig. 1. As one can see, the gold coating was broken, and the tungsten oxide compounds

penetrated through the cracks in the gold layer and almost covered the surface of the swollen wire. As a result, the wire diameter increased by 6 % from 50 to 53 μm.

In principle, one known way to clean the wire surface from Si compounds and extend the operational lifetime of a straw detector non-invasively is to etch the wires by using a high current gas discharge in gas mixtures with CF_4 [5, 6]. We have applied this technique to WO_x cleaning, too.

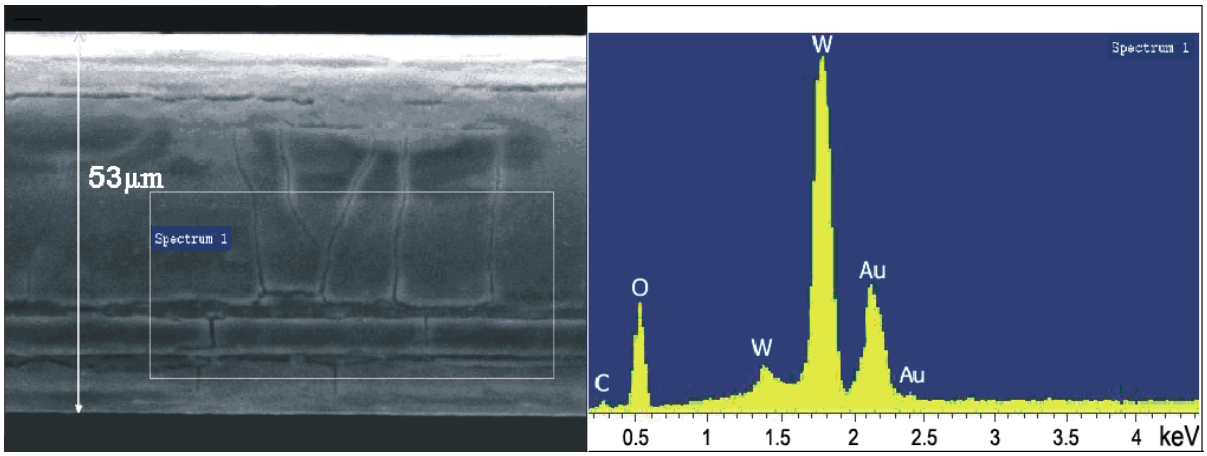

Fig. 1. SEM micrograph of the anode wire surface in the centre of the irradiated zone after the charge accumulation of Q = 1.53 C/cm (left) and XEM spectra (right) of the area that is denoted at the SEM micrograph by the rectangle

4. Task-setting

4.1. Glow discharge and integrated circuits production

Plasma chemistry is extensively applied in fabrication of semiconductor devices for microelectronic industry, which typically makes use of a glow discharge, which represents a low-pressure (< 1 Torr, RF-13.6 MHz) plasma. The glow discharge (DC, RF-plasma) in CF_4/O_2 gases is widely used in integrated circuits production for etching of silicon and tungsten compounds [7–9]. Our idea was to use this experience for removing tungsten oxides from the anode wire surface.

4.2. Corona discharge in wire chambers

The dominant parameter of a wire chamber is a strong non-uniform electric field around an anode wire. A classical corona discharge occurs in gases in regions of high electric field near sharp corners, edges of metal surface, including small diameter anode wires of MWPCs under atmospheric pressure. A start of a corona discharge in a straw (or MWPC) manifests itself with a sharp current increase.

It was observed that the gaseous products formed in avalanches in a proportional counter are qualitatively the same as expected under assumption that the chemical mechanisms in the avalanches are similar to the mechanisms of a low-pressure glow discharge [10–14]. On the other hand, because of strong non-uniform electric field around an anode wire, the spatial dimensions of the zone where chemical radicals, associated with the glow discharge processes are generated, is small and, according to our evaluation, does not exceed several tens of microns.

That is why it is important to find experimental evidence that the negative corona discharge can generate a considerable amount of chemical products usually associated with the glow discharge, which is enough to carry out effective etching of silicon and tungsten compounds in a proportional counter. If it is so, then one can use the principles of traditional plasma chemistry of a glow discharge (low pressure, RF) to predict the plasma chemistry of a corona discharge in the wire chambers (at 1 atm, DC).

5. Recovery of the aged anode wires

The wire etching is a rather complex chemical process. To obtain a general picture of the wire etching, it is necessary to identify the dominant processes occurring in the gas phase and at the gas/surface interface, resulting in formation of active chemical species (radicals, ions, *etc*.). The avalanche environment is plasma of ions and neutral radicals, and thus the wire etching process should be studied in the framework of the plasma chemistry. The intensity of ion and radical production depends on pressure, power density, detector irradiation rate, electric field strength, gas gain, materials of electrodes, gas composition including the presence of *ppm*-level impurities, *etc*.

5.1. Choice of the gas mixture

The discretion whether the etching or the yield of deposits will occur in CF_4 depends on plasma properties, although the F / C ratio model predicts that an effective etching gas mixture has the ratio of fluorine (F) to carbon (C) atoms in the range of $0.8 < F/C < 4.0$, and strong etching takes place at $F/C = 4$ [11]. On the other hand, the etching ability of tungsten compounds is more effective in CF_4/O reactive etching plasma [7–9]. To prevent the damage of carbon coating on the straw (cathode) wall during the recovery treatment, the oxygen in the etching gas mixture was replaced by CO_2. The needed oxygen radicals were mostly generated due to dissociation of CO_2 in collisions with the avalanche electrons near the wire. To optimize the recovery processes, the following gas mixture was chosen: 80 % CF_4 + 20 % CO_2 with the ratio $F/C = 3.2$ [15].

5.2. Etching process

The glow discharges media used in the plasma processing are partially ionized gases containing ions, electrons and neutral species in both ground and excited states. The degree of ionization is small, typically about 10^{-5} of all species, but the degree of dissociation can be quite large, sometimes exceeding 10^{-1} of all the species. Because of their higher concentration, neutrals (radicals) are the primary chemical species responsible for deposition and etching processes.

Due to a significant difference in mobility between the ions and electrons, the surfaces in contact with plasma generally acquire negative potential with respect to the plasma. As a result, positive ions are accelerated to the surface, and they can have a synergistic effect on the etching chemistry. This process is distinctly different in a wire chamber operating under atmospheric pressure, where the ionized gas contains electrons with a moderate energy of 5–10 eV, low-energy negative ions < 1 eV, and near-thermal positive ions [11].

To etch the tungsten or silicon compounds in a glow discharge (DC, RF-plasma), a negative potential was applied to the substrate that was in electric contact with the wafer. The etching process was carried out at a normalized electric field of 10–50 V/cm · Torr. The molecular dissociation leading to neutral radicals can be attributed to electrons with the energy in the range of 4–6 eV.

In a wire chamber (with a corona discharge, at 1 atm), the normalized electric field in vicinity of the wire surface is about 300–400 V/cm · Torr, which is enough to accelerate electrons up to the energy 5–10 eV. This energy is sufficient to break chemical bonds of the gas molecules and to start both molecular dissociation and other processes associated with the etching processes in a low-pressure glow discharge.

The mechanism of the etching process development can be considered to have four sequential steps:

- generation of active radicals $F^{\bullet}$, $O^{\bullet}$, $CF_3^{\bullet}$ in the gas discharge;
- their penetration through the wire gold coating;
- chemical interaction between the absorbed radicals and the wire materials leading to formation of tungsten compounds and their deposition on the wire surface;
- chemical interaction between the absorbed radicals and tungsten compounds leading to formation of volatile components and their desorption from the wire.

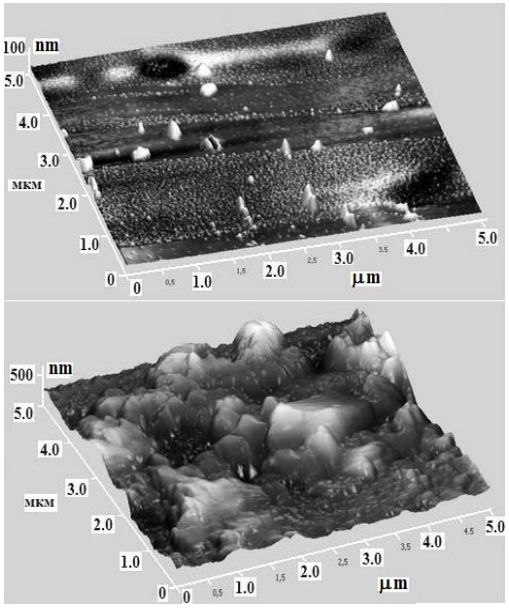

Fig. 2. Scanning Force Microscopy (SFM, solvent P47, cantilever HA-NC) images of both the non-irradiated wire surface (top) and the aged wire surface after irradiation (bottom)

To make the corona discharge recovery processes more stable, the damaged zone of the wire was irradiated with a low intensity 3.5 kHz ^{55}Fe *X*-ray source. Photons effectively stabilize the ionized plasma, supporting the etching conditions and breaking chemical bonds of the compounds coating the wire.

The wire surface in the centre of the irradiated zone is the main source of ionizing electrons because it is covered with irregular spikes of 100–400 nm height with the radii smaller than 1 μm, Fig. 2. The electric field on the tops of the spikes can be estimated as $E_{\max} \approx 2U/r \cdot \ln(2R/r)$, where $r \sim 0.5$ μm is the spike radius, $R = 2000$ μm is the straw radius, and $U \approx 2700$ V is the applied high voltage. As it follows from this formula, the electric field on the wire surface is about $E \approx 2.5 \times 10^5$ V/cm, and at least two orders of magnitude higher on the top of a spike, $E \sim 10^7$ V/cm. Therefore, a layer of tungsten oxides can be an additional source of electron current due to high field emission. Of course, such a wire surface damage stimulates micro-discharges and fast rising up of the corona discharge current, which results in production of radicals and ions in the vicinity of the wire surface.

The electrons formed in the ionized gas move in an intense electric field and obtain sufficient energy to break chemical bonds of the gas molecules. Thus, due to electron impact dissociation of CO_2 (the dissociation energy is $E_d = 5.5$ eV) and CF_4 around the anode wire, oxygen ions and radicals are produced, and many different active species, as well:

$$e^- + CF_4 \rightarrow CF_3^- + F^\bullet; \quad (1)$$

$$e^- + CF_4 \rightarrow CF_3^\bullet + F^\bullet + e^-; \quad (2)$$

$$e^- + CF_4 \rightarrow CF_2^{\bullet\bullet} + 2F^\bullet + e^-; \quad (3)$$

$$e^- + CO_2 \rightarrow CO^\bullet + O^\bullet + e^-. \quad (4)$$

The reactive gas fragments are transported in the electric field to the wire surface where they can be absorbed. The etching refers to a complex set of sequent chemical processes in which the gas-phase species interact with the tungsten-oxide compounds, which are placed both inside of the gold coating cracks and over the wire surface, the volatile products (↑) being evacuated through the gas. The most important plasma-chemical reactions for our gas mixture and their corresponding active radicals are the following:

$$W + O^\bullet \rightarrow WO_x\downarrow; \quad (5)$$

$$2WO_x + 10F^\bullet \rightarrow WF_6\uparrow + O_2\uparrow + WOF_4\downarrow; \quad (6)$$

$$2WOF_4 \rightarrow WO_2F_2\downarrow + WF_6\uparrow; \quad (7)$$

$$3WO_2F_2 \rightarrow WF_6\uparrow + 2O_2\uparrow + 2WO\downarrow; \quad (8)$$

$$WO \rightarrow W + O^\bullet; \quad (9)$$

$$W + 6F^\bullet \rightarrow WF_6\uparrow. \quad (10)$$

The average energy of positive ions in the gas discharge is almost thermal due to multiple elastic collisions with surrounding atoms and molecules. In contrast to electrons, ions do not store the energy obtained in the electric field: it is lost in each collision. The optimal etching conditions are fulfilled mainly in the peaks of the tungsten oxide compound where the electric field is high enough.

5.3. Choice of the working point for the negative corona discharge treatment

As it was mentioned above, a corona gas discharge occurs in high non-uniform electric fields surrounding anode wires. The tungsten-oxide deposits, which are placed both on the wire surface and inside of the cracks of the gold layer (see Fig. 2), will stimulate fast rising up of the corona discharge current because of their sharp shapes. Just in these points, chemical radicals generation associated with glow discharge processes becomes maximal, which results in intensive plasma-chemical etching of the tungsten-oxide peaks. As a result, the current of corona discharges falls down in time. That is why we performed the high voltage regulation every 30–40 min to compensate corona current decreases from 5 to about 1 μA.

In order to achieve the maximum etching rate, it was necessary to increase the current of corona discharges as high, as possible. This forced us to use a negative corona discharge because it has the following advantages in comparison to a positive corona discharge:

- this discharge is more stable and, consequently, it can generate a higher current;
- the mobility of negative ions is only half of that of positive ions.

Usually, the corona discharge in a straw manifests itself as a sharp current increase from 20–50 nA at the HV = –2500 V to 4–6 μA at the HV = –2650 V. The last potential was taken as the working point in the beginning of the recovery procedure.

5.4. Experimental results of recovery of aged wires

The progress of the wire recovery in terms of the gas gain along the straw is shown in Fig. 3a, b. Since the ^{55}Fe source spectrum has a sufficiently narrow peak in the 80 % CF_4 + 20 % CO_2 gas mixture, it was used to monitor the gas gain during the recovery process. The efficiency of the wire recovery procedure is presented in Fig. 3a. Such measurements were carried out every two hours. The gas gain distribution measured with the regular working gas mixture (60 % Ar + 30 % CO_2 + 10 % CF_4) before and after the recovery procedure is shown in Fig. 3b. As one can see, after six hours of the negative corona discharge treatment, the gas gain along the wire becomes the same as it was before irradiation.

Figure 4 shows results of SEM/XEM examinations of a restored anode wire surface in the centre of the irradiated zone in comparison with a non-irradiated wire surface. The total accumulated charge on a wire was 3 C/cm.

These results lead us to the conclusion that the proposed wire recovering procedure is very promising. The following processes are associated with the etching occurring after application of this procedure:

- the etched wire surface in the centre of the irradiated zone looks smooth and without any traces of deposits (tungsten-oxides compounds);
- the cracks formed by tungsten-oxides compounds in the gold layer (Fig. 1) have tightened. It means that etching of tungsten-oxides compounds occurs not only on the wire surface but also inside of the cracks and underneath the gold layer, too;
- the swollen wire diameter has decreased from 53 μm to the nominal value of 50 μm.

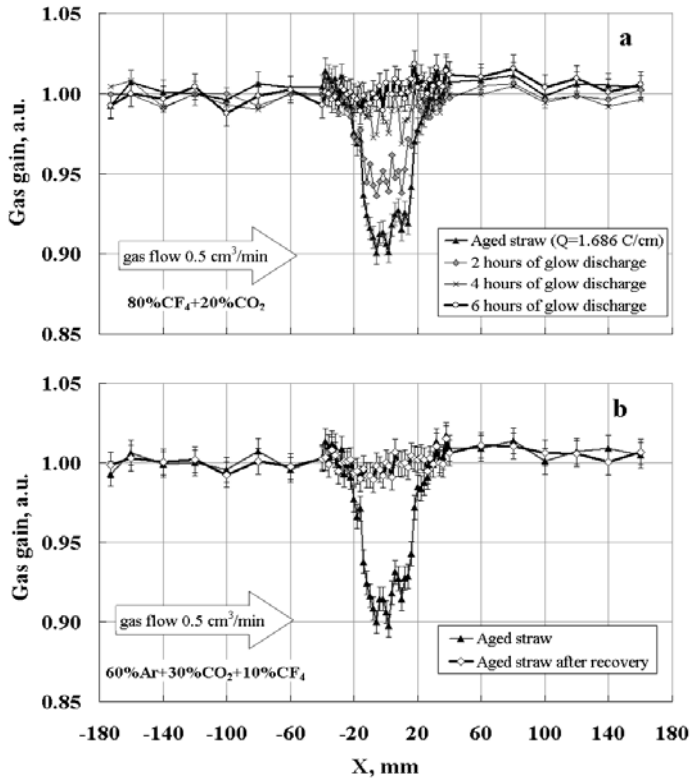

Fig. 3. a – gas gain behaviour along the straw during application of the wire recovering procedure. These measurements were carried out every two hours; 80 % CF_4 + 20 % CO_2 gas mixture, negative corona discharge; b – gas gain distribution along the straw before and after application of the wire recovering procedure; 60 % Ar + 30 % CO_2 + 10 % CF_4 working gas mixture

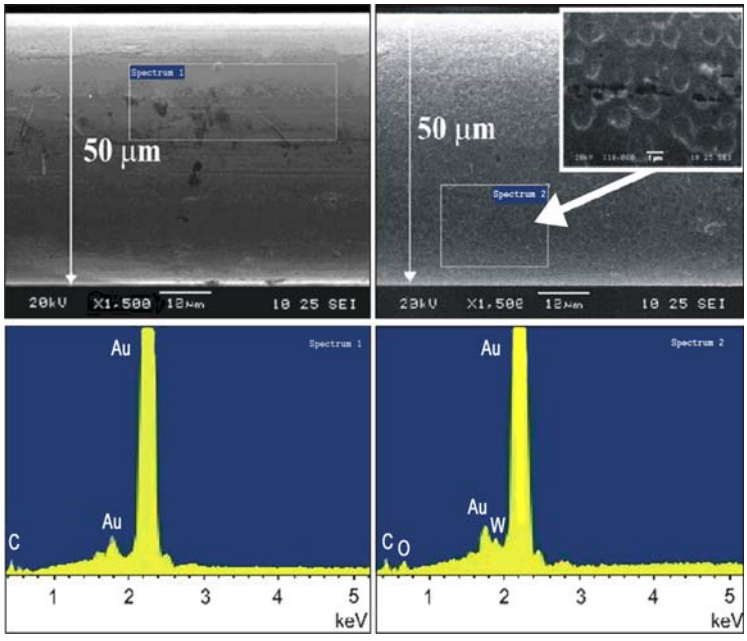

Fig. 4. SEM micrograph and the corresponding XEM spectra of the non-irradiated part of an anode wire surface (left) and in the centre of the irradiated zone of the wire after applying of recovery procedures (right). Both XEM analysis areas are denoted at the SEM micrograph by rectangles

6. Multiple recovery of aged anode wires

In order to confirm both the reliability and the reproducibility of the wire-recovering processes, multiple recoveries of the anode wires were performed. Our aim was to realize several cycles of an "aging-recovery" sequence during the continuous session of measurements.

The wire aging was carried out with a 60 % Ar + 30 % CO_2 + 10 % CF_4 gas mixture, and the recovery procedure was performed with an 80 % CF_4 + 20 % CO_2 mixture.

Two "aging-recovery" runs were performed. In the first run, the degradation of the gas gain in each cycle was 3 %, and in the second run in each cycle it was 6 %. During the first run, four cycles of the "aging-recovery" session were carried out, and during the second run three cycles were done. The total charge accumulated in each run was 3 C per 1 cm of the wire length.

The obtained data clearly demonstrate the efficiency of the proposed wire recovery method, see Fig. 5. As one can see, the application of a negative corona discharge to aged wires allows us to restore initial characteristics of a wire chamber several times. In other words, the lifetime of a straw detector can be increased by a few times. It is especially important when the wire detector is intensively irradiated with the irradiation current of about 1 μA/cm.

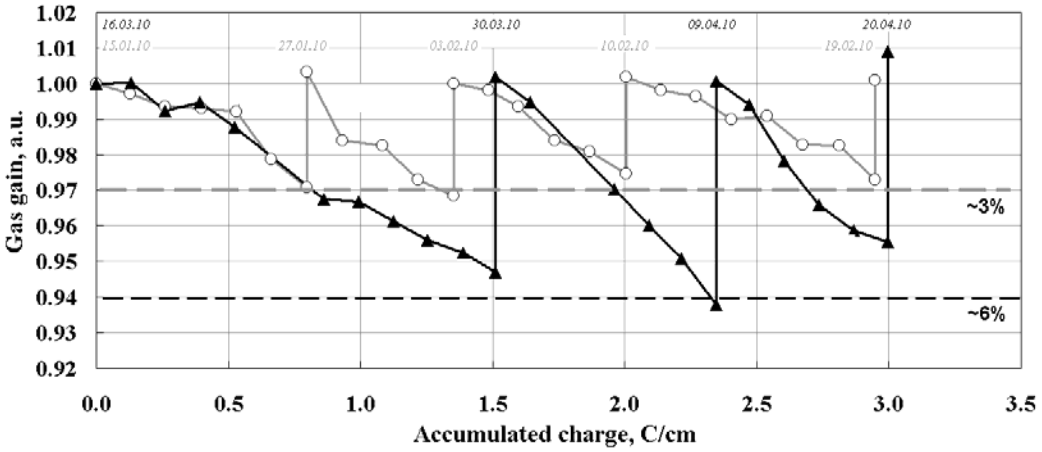

Fig. 5. Relative gas gain in the irradiated zone *vs* accumulated charge per unit of the wire length. The grey curve corresponds to the "aging-recovery" session with about 3 % of the maximum amplitude drop. The black curve corresponds to the "aging-recovery" session with about 6 % of the maximum amplitude drop due to wire swelling

Results of SEM examinations of anode wire surfaces in the centre of the irradiated zone after four cycles of "aging-recovery" session are shown in Fig. 6. As one can see, the wire surface is almost smooth and practically undamaged. Only some traces of WO_x compounds were found on the wire surface. This result looks almost similar to that of once-recovered wire, see Fig. 4. The wire diameter has decreased to the nominal value of 50 μm.

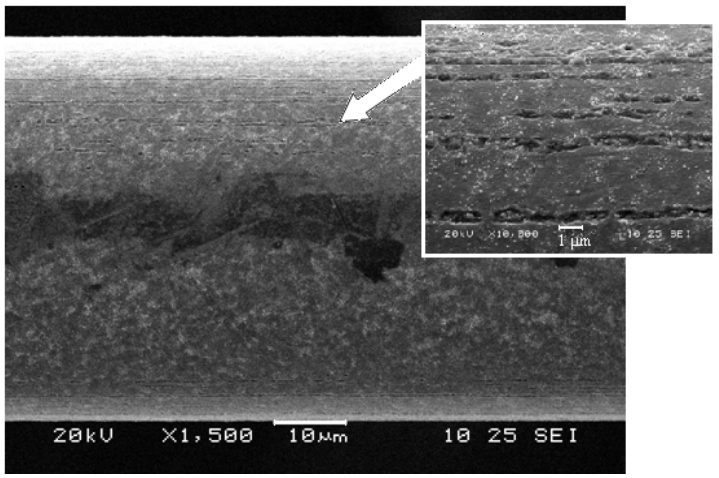

Fig. 6. SEM micrograph of the wire surface after applying of four cycles of the wire recovering procedure (see Fig. 5). The "aging-recovery" session with about 3 % of the maximum amplitude drop. The total accumulated charge was about 3 C/cm

7. Conclusion and outlook

1. A method for recovery of swollen anode wires in proportional counters by using a negative corona discharge treatment (with the current density about 3 μA per cm of the wire length) in 80 % CF_4 + 20 % CO_2 gas mixture has been proposed, successfully developed and tested. This method can remove from the surface of anode wires tungsten containing deposits which are accumulated there due to swelling effects.

2. Using this method, we have been able to recover a swollen wire multiple times, extending significantly the detectors lifetime. The proposed recovery mechanism is running "softly" and reliably.

3. We suppose that the application of the proposed method is more effective at the beginning of the detector degradation, when the gas gain drop does not exceed several percent (up to 9 %), and the total accumulated charge is smaller than 2 C/cm. For more aged wires, the wire degradation process becomes irreversible because of a high risk of formation of blisters and even ripping off fragments of the gold coating from the wire surface.

4. All the mentioned above experimental results allow us to conclude that the negative corona discharge can generate a considerable amount of chemical products usually associated with the glow discharge, which permit to carry out an effective etching of tungsten compounds in a proportional counter. This means that the principles of the traditional plasma chemistry of the glow discharge (low pressure, RF) can be used to explore the plasma chemistry of the corona discharge in wire chambers (1 atm, DC).

The authors thank I. Parchenko and E. Ivanov (PNPI) for assistance in manufacturing of the detectors.

References

1. M. Hohlmann *et al*., Nucl. Instr. Meth. Phys. Res. A **494**, 179 (2002).
2. T. Ferguson *et al*., Nucl. Instr. and Meth. Phys. Res. A **488**, 240 (2002).
3. T. Ferguson *et al*., Nucl. Instr. and Meth. Phys. Res. A **515**, 266 (2003).
4. D.A. Aksenov, G.E. Gavrilov, A.G. Krivchitch, D.A. Maysuzenko, A.A. Fetisov, Preprint PNPI-**2830**, Gatchina (2010).
5. R. Openshaw *et al*., Nucl. Instr. Meth. Phys. Res. A **307**, 298 (1991).
6. S. Belostotski *et al*., Nucl. Instr. Meth. Phys. Res. A **591**, 353 (2008).
7. I.C. Plumb, K.R. Ryan, A Model of the Chemical Processes Occurring in CF4/O2 Discharges Used in Plasma Etching, Plasma Chem. and Plasma Process. **3**, 6 (1986).
8. R. d'Agostino, F. Fracassi, R. Lamendola, The Chemistry of Etching and Depositing Processes, Pure&Appl. Chem. **66**, 1185 (1994).
9. T.D. Bestwick, G.S. Oehrlein, Tungsten Etching Mechanisms in CF4/O2 Reactive Ion Etching Plasmas, J. Appl. Phys. **66**, 10 (15 November 1989).
10. J. Va'vra, Nucl. Instr. Meth. A **252**, 547 (1986).
11. J. Wise, J.A. Kadyk, D.W. Hess, M.C. Williams, IEEE Trans. Nucl. Sci., NS-**37**, 470 (1990); J. Wise, Vs Thesis, LBL-**29033**, University of California, Berkeley (1990).
12. M.E. Fraser, D.A. Fee and R.S. Sheinson, Plasma Chem. and Plasma Process. **5**, 163 (1985).
13. D.E. Tevault, Plasma Chem. and Plasma Process. **7**, 231 (1987).
14. S. Kanazawa, M. Kogoma, T. Moriwaki and S. Okazaki, J. Phys. D **1**, 838 (1988).
15. D.A. Aksenov, Yu. Dikarev, V.M. Vakhtel, G.E. Gavrilov, A.G. Krivchitch, D.A. Maysuzenko, A.A. Fetisov, Preprint PNPI-**2842**, Gatchina (2010).

UF/PNPI HIGH VOLTAGE SYSTEM IN THE LHCb MUON DETECTOR

N.F. Bondar, S.V. Bondarev, N.B. Isaev, O.E. Maev, A.V. Mylnikova,
E.M. Orischin, L.O. Sergeev, S.S. Volkov

1. MUON detector in LHCb

The muon system [1], shown in Fig. 1, consists of five stations (M1–M5) of rectangular shape, placed along the beam axis. Each Muon Station is divided into four regions, R1 to R4 with the distance increasing from the beam axis. The full system comprises 12 pairs of triple GEMs (M1R1), 264 double-gap MultiWire Proportional Chambers (MWPC) in M1/R2–R4 and 1104 four-gap MWPCs in M2–M5.

All the muon stations, including the iron f lters, are separated into two halves called A(access)-side and C(cryogenic)-side, which can move on rails away from the beam pipe for maintenance and installation. For M2–M5 stations, two large support structures built from iron beams accommodate the suspensions for the four chamber support walls and have platforms for electronics racks (4 racks on each side) and a gas system (2 racks on a side). The cable chains provide unbreakable connections of all the cables, optic f bers and pipes with the movable sides of the detector. Special racks with patch panels are located near each side of the detector as terminals of the cable chains. Station M1 has an independent support structure.

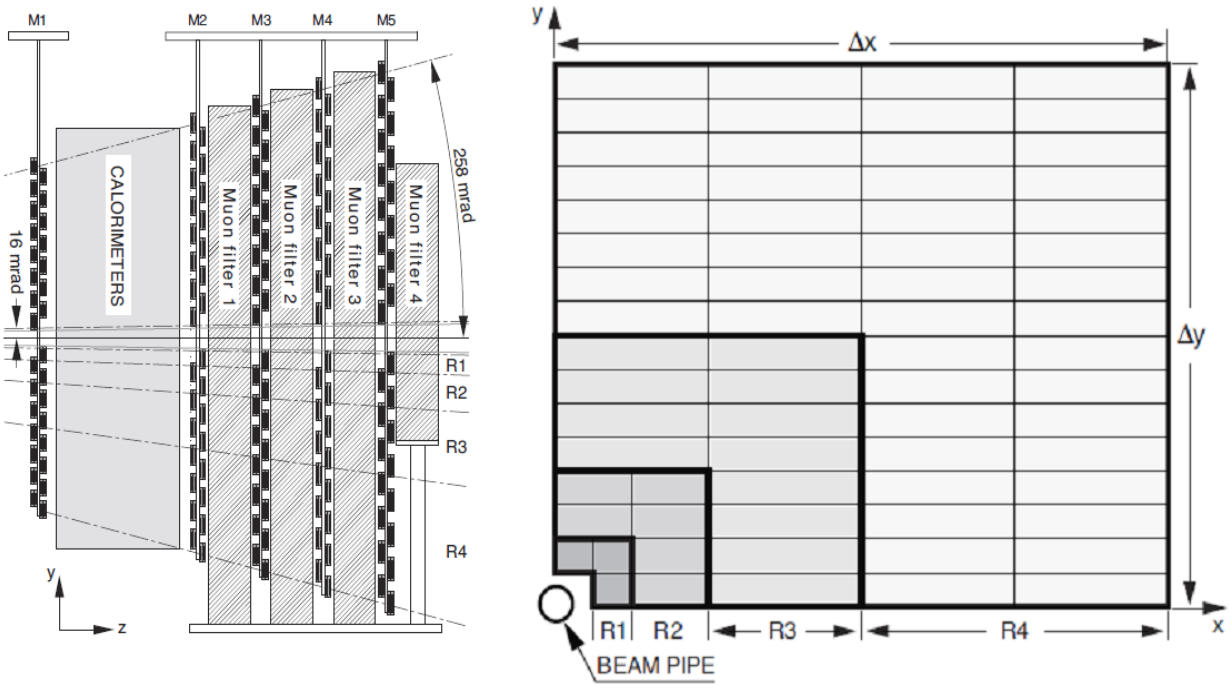

Fig. 1. Left – side view of the muon system. Right – front view of a quadrant of a muon station. Each rectangle represents one chamber, each station contains 276 chambers

2. Selection of a HV system

Due to great variations in technical requirements to HV parameters within the stations and regions in the MUON detector and taking into account the limited budget of LHCb, the choice of a HV system was a really big issue. Finally, the gas gain in MUON is now controlled by three independent HV systems: the INFN HV system was specially developed to control the gas gain in 72 HV channels of GEMs (M1R1), the CAEN system is serving R2–R4 regions in M1 and R1–R2 in M2–M5 – with 1104 channels, and the UF/PNPI HV system has been chosen for R3–R4 in M2–M5 with 3840 channels.

Initially, this multi-channel High Voltage Distribution and Monitoring System (HVDMS) was designed and produced by UF/PNPI collaboration for the End-cap Muon detector of the CMS project, and it met most of the LHCb requirements. To fit the LHCb chambers, special “LHCb-type” HV connectors were installed on the distribution boards [2]. A two stage configuration was selected for the LHCb muon detector.

The total number of HV channels is 3840. Taking into account the granularity of the HV system and the detector configuration we had to produce 4032 HV channels. To minimize initial price of the HV system, the production was divided into two stages. At Stage 1, all the chamber gaps of R3 are fed individually. Some of the gaps of the R4 chambers are connected in parallel in groups of four via the patch panels. The gaps connected in parallel always belong to different chambers to minimize losses of the efficiency. At Stage 2, all the chambers should be fed individually.

This solution allowed us to produce only half of the channels – 2016. Also, we have designed and produced a relatively cheap splitting device called “HV Patch Panel” (HV PP) for other 2016 channels.

At Stage 1, we produced:

- PCI card of the System Interface/Buffer (Host Card) – 6 modules plus 2 spares;
- 8-channel Master Distributor Board (MB) – 8 modules plus 2 spares;
- 36-channel radiation hard Remote Distributor Board (RDB) – 56 modules plus 10 spares;
- 320-channel HV Patch Panel – 8 units.

As a primary HV power supply, the Matsusada AU-5P60-LF was selected – 2 units plus 1 spare. Also, for a low voltage power supply, the WIENER type VEP 6021-LHC was selected – 1 unit.

For Stage 2, we had to produce additional 56 RDB modules and 8 MB modules to replace 8 units of the HV PP.

3. UF/PNPI HV layout in LHCb

The HV system layout is presented in Fig. 2. To follow the LHCb structure, the HV system is also divided into two independent parts, for the A-side and C-side. Each part has a complete set of equipment: a computer with 3 host cards, a Primary HV power supply and an individual crate with 4 Master Distributor boards. The low voltage power supply has 5 output channels. It allows to feed independently Remote Distributors on each side with +/– 8 volt power and to supply all the Master Distributors with 12 volts.

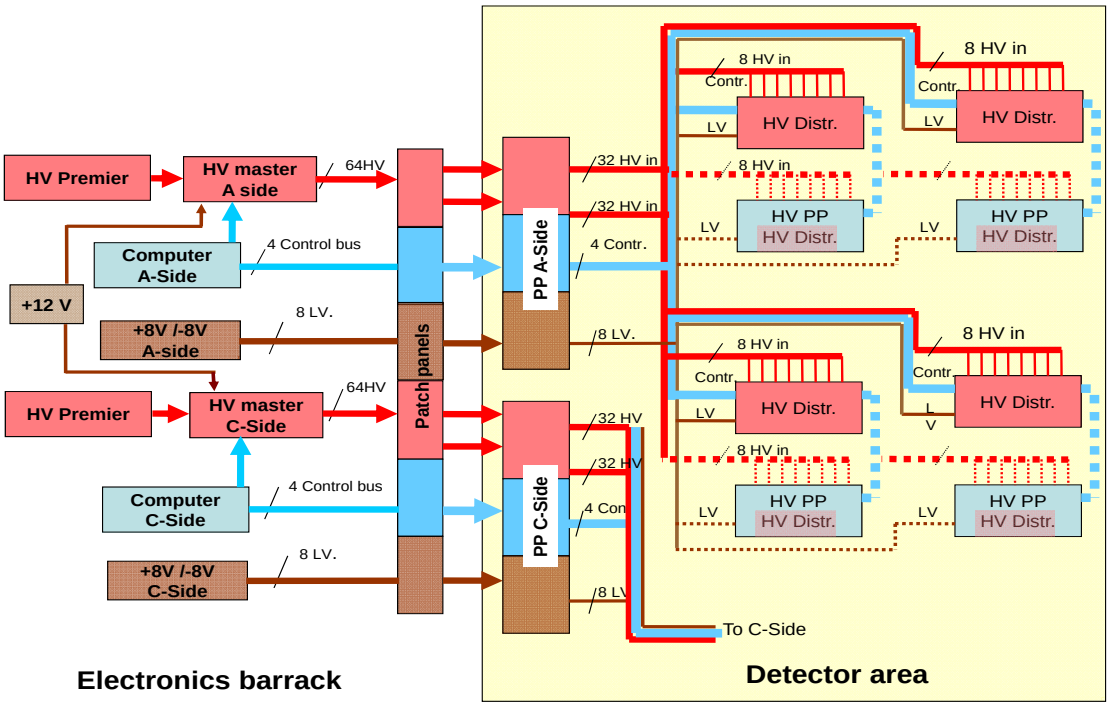

Fig. 2. UF/PNPI HV system layout of the LHCb muon detector. The remote distribution part is presented for the A-side

All the components including 2 computers, 2 Matsusada power supplies, 2 crates with 4 MB in each, and the low voltage WIENER power supply were assembled in one rack. The rack was installed in the electronics barrack away from the detector, so that it was always accessible even during the beam time. The cables for the low and high voltage, the signal cables for the final system layout were placed between the rack and two patch panels in the detector area. All the voltages and control signals were delivered from these patch panels to the Remote Distributors crates with flexible cables. The total length of the cables was more than 100 meters. The voltage drop and the signal cable skew was taken into account.

Since one control line can serve only up to 16 RDB modules, for the maximum number (56) of the RDB modules on each side we had to put 4 control lines per side. Currently, for Stage 1 we are using half of the RDB modules (28 at one side) and only 2 control lines per side.

In Fig. 2, the red boxes "HV Distr." are the crates with the RDB modules, and the blue boxes "HV PP/HV Distr." are the HV Patch Panels. These Panels have the same size as the RDB crate, so to implement Stage 2 we should replace these Patch panels with the RDB crates and reconnect some HV cables to chambers and rearrange the control lines. All the signal cables, the HV and power cables are now installed for the final version of the UF/PNPI HV system.

4. Improvement of the system parameters on the base of the operation experience

The first two years of operation were like a burn-in time for the system. There were quite a large number of failures that required a lot of attention, and changes to improve the system reliability and the precision of the specified and measured parameters.

First, it was found that the output voltage in some channels drifts, and biases in several channels were observed in both directions. Therefore, a procedure of calibration of the sensor output voltage was introduced to all channels directly in the detector. The reason for the voltage instability was low reliability of the 1 GigaOhm resistors in the HV divider circuits, which were used in each channel of the voltage stabilizer and also used as sensors of the output voltage. During a shutdown, these resistors were replaced by more reliable resistors in all the RDB and MB modules.

The second problem we faced in Stage 1 was a high level of the output current noise in some channels of the RDB and MB. Sometimes, this noise led to false alerts of the overcurrent protection circuit during ramping up of the output voltage, which impeded severely setting up of the system into the operation mode. The main reason of this excess noise was found to be some instability of the voltage regulators in these channels. The replacement of the 1GigaOhm resistors of the HV dividers improved the noise performance significantly. Also, we tuned the stabilizer parameters in all the RDB channels. Finally, we have reached the resolution of the current sensors for all the RDBs better than one ADC step.

The voltage regulator of the MB has four FETs connected in series. This solution allows to make a 4 kV stabilizer using 1.0 kV transistors. Unfortunately, this circuit is not very stable, in particular, during ramping up the output voltage. By selecting parameters of the transistors, we were able to assemble quite stable voltage regulators for the MB. Unfortunately, these regulators tend to aging, their stability being decreased. Now, there is a new commercially available transistor with the working voltage of 1.5 kV. We have designed a new version of the MB regulator specified for 3 kV with 2 transistors. This regulator is simpler and more stable, and can be used for the LHCb muon chambers since the HV in these chambers is lower than 2.8 kV.

There is a proposal to improve the temperature stability of the current sensors up to 1.5 nA/10 °C. This modification will be implemented in new modules.

One channel of the MB can supply up to 36 gas gaps through the RDB. In the case of a short circuit in any gap or in an RDB channel, all the 36 outputs will be tripped. To keep the maximum efficiency of the muon detector, a special remotely disconnecting fuse is installed in the output of every RDB channel. It allows to disconnect a failed channel during the beam time, when the LHCb cavern is closed for access. Because of large cable lengths and small wire cross sections, this procedure was not reliable enough. To improve it, we have increased the burning voltage up to 60 V.

According to the LHCb specifications, the HV control system must be USB controllable. This work is in progress, a new control system will be implemented during the 2013 shutdown.

5. HV system performance

Since 2009, the HV system is working under option “Stage 1” [3]. The main task of the system is to keep the output voltage within the specified limits to provide a homogeneous and stable gas gain in MWPCs. The system has a very useful feature, which apparently is a great competitive advantage over most commercial HV-systems. It is the ability to control and monitor the precision of the output voltage censors and to recalibrate them if necessary. The procedure is as follows: we set the HV-transistors to the fully open state and measure the voltage set on the primary power supply with the RDB voltage sensors. To have this option precise, we need properly calibrated primary power supplies, which are always accessible, only two of them being in the system.

This procedure allows us to sustain the output voltage with the precision of +/– 5V (Fig. 3). The system has the current measurements resolution about 1 step of an ADC. The average quantity of faulty channels per year is less than 5 out of 2000. The average quantity of disconnected channels is about 3 per year.

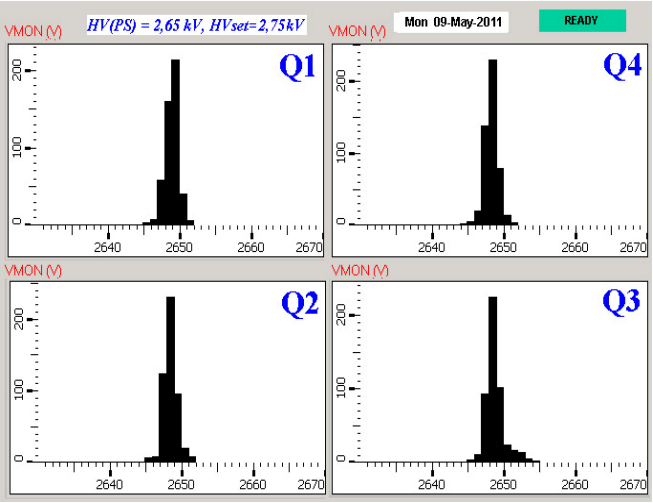

Fig. 3. Typical distribution of the measured voltages at the RDB outputs

After the period of 3 year maintenance and modifications described above, the HV system behaves very stable and reliable. Stage 2 is in progress, and the complete system must be commissioned and put into operation after the long shutdown in 2013–2014.

The authors thank Genakh Mitcelmakher, Alex Madorsky and Victor Barashko for technical support and useful consultations during the period of installation and commissioning of the HV system in the MUON detector.

Referenses

1. The LHCb Detector at the LHC/ LHCb Collaboration 2008, J. Instrum. **3** (2008).
2. S.V. Bondarev, N.B. Isaev, V.I. Lazarev, A.V. Mylnikova, L.O. Sergeev, S.S. Volkov, Multi-Chanel High Voltage Distribution and Monitoring System for LHCb Muon Chambers in *PNPI High Energy Physics Division, Main Scientific Activities 2002−2006*, Gatchina, 2007, p. 335.
3. A.A. Vorobyev *et al*., Experiment LHCb at the LHC, this issue.

CROS-3B – COORDINATE READOUT SYSTEM (NEW DRIFT CHAMBER VERSION)

V.L. Golovtsov, E.M. Spiridenkov, L.N. Uvarov, S.L. Uvarov, V.I. Yatsura

The Radio Electronics Laboratory of the High Energy Physics Division of PNPI continues developing a series of Coordinate ReadOut Systems – the so called CROS-3 series, which was first described in [1] and consists of 3 types of cards: Digitizer, Concentrator and System Buffer. Here we present the CROS-3B version targeted for instrumentation of large-size Drift Chambers (DCs) built at PNPI and designed for using as a tracking detector of the magnetic forward spectrometer for the BGO-OD experiment [2] at the Electron Stretcher Accelerator (ELSA) [3] facility at the Physics Institute of the University of Bonn, Germany.

The CROS-3B retains common features of the CROS-3 series.

- The CROS-3 basic setup consists (see Fig. 1) of 3 types of cards: System Buffer, Concentrator and Digitizer. The cards make use of high-speed serial 2.0 Gb/s fiber and 100 Mb/s copper links to transfer control, trigger and readout data. The cards functionality is based on a firmware loaded into FPGAs.
- The System Buffer provides interfaces to the host computer and trigger logic.
- The Concentrator collects event fragments from the Digitizers in parallel, builds an event and sends it to the System Buffer.
- The Digitizer amplifies, discriminates and continuously digitizes input signals, stores data in the digital pipeline for the trigger decision time and encodes arrival time and positions of hits in a programmable readout gate upon receiving a trigger.

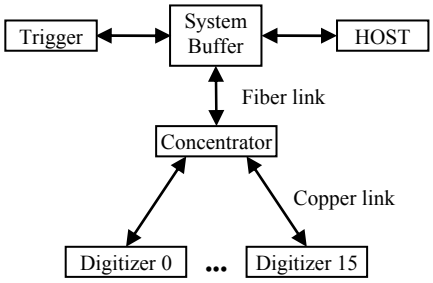

Fig. 1. CROS-3 basic setup

There are new features, specific only to the CROS-3B version. The amplifier input impedance and integration constant are optimized to get the best possible time resolution for large-size DCs with a rather big wire capacitance. The system setup is extended by adding a Low-Level Concentrator. So, the System Buffer is now able to control and collect data from up to 4096 channels, 16 times more channels than before. The built-in error detection logic allows to terminate gracefully the readout process in case of hardware failures.

1. Drift chambers

PNPI has designed and built 8 DCs for the BGO-OD experiment. The DCs will be used for tracking of charged particles behind a spectrometer magnet. They are grouped into 2 stations. Each station consists of 4 (*X*, *Y*, *U*, and *V*) DCs with sensitive areas of approximately 1.2×2.4 m^2, 1.3×2.4 m^2, 1.8×2.7 m^2, and 1.8×2.7 m^2. All chambers feature similar design and contain a double layer of hexagonal drift cells as shown in Fig. 2, where black dots are sense (anode) wires and white dots are field (cathode) wires. Sense wires are spaced at 17 mm, so the maximum drift distance for tracks perpendicular to the chamber plane (vertical tracks in Fig. 2) is about 8.5 mm. The chambers operate with the standard 70/30 Ar/CO_2 gas mixture. The high voltage of –(2.9÷3.2) kV is applied to cathode wires, anode wires being at 0 V for the signal readout.

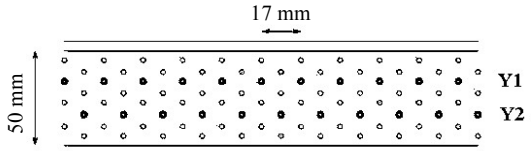

Fig. 2. Drift Chamber cell structure, sense wires are shown as black dots, and field wires – as white dots

The *X*, *Y*, *U*, and *V* chambers have 160, 288, 320, and 320 sense wires correspondingly, totaling to 2176 sense wires for the entire system of two stations. The space resolution requirement for the experiment is 300 μm, the trigger rate being about 1 kHz.

2. Amplifier optimization

The basic amplifier structure shown in Fig. 3 was used as a starting point for optimization. The structure features 3 independent, but equal, RC circuits that integrate the input current signal *I*. The first trans-impedance amplifier stage K_R is implemented as a common base transistor with low input noise. The amplifier input impedance (including a protection circuit) and the sense wire impedance are well matched.

The second stage K_V is a voltage amplifier with the 500 MHz bandwidth. *D* stands for a differential discriminator with a threshold voltage TH applied to its positive input and an amplified and integrated input signal to its negative input. The goal of the optimization was to choose the RC time constant that would result in the best time/space resolution for the given cell geometry.

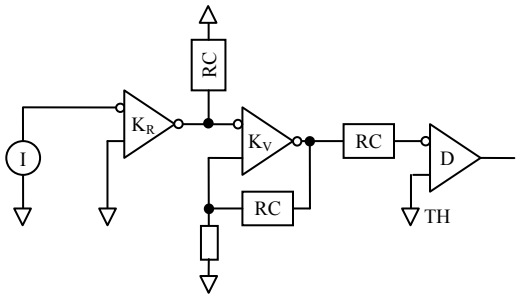

Fig. 3. Basic amplifier structure

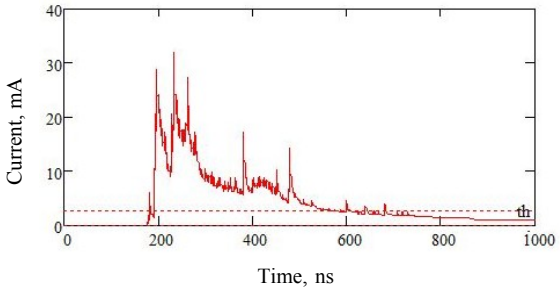

Fig. 4. Drift chamber anode current produced by a track

The DC model used assumes each primary electron in the track is independently amplified by a random factor distributed exponentially [4]. Figure 4 shows an example of the anode current produced by a charged particle which traversed the drift cell perpendicular to the chamber plane. The tracks were generated using HEED [5], a program that computes in detail the energy loss of fast charged particles in gases. The simulated tracks in turn were used in GARFIELD [6] to calculate drift times of electrons or, in other words, the arrival time of amplifier input signals.

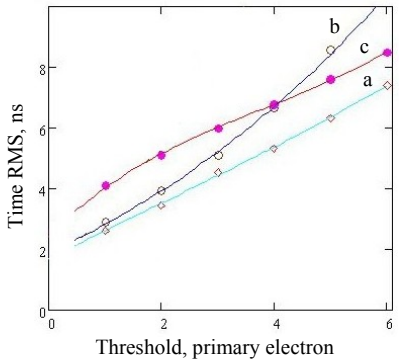

Fig. 5. Calculated DC time resolution for the amplifier with: the response as a step function (curve a); 2 ns time constant (curve b); 10 ns time constant (curve c)

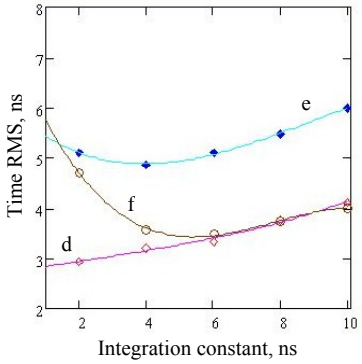

Fig. 6. Calculated DC time resolution at the threshold set to: 1 primary electron (curve d); 3 primary electrons (curve e); 5σ (curve f), where σ – noise standard deviation

Figure 5 demonstrates the calculated DC time resolution as a function of the threshold for 3 different ways of processing the anode signal. Ideally, an amplifier with the response as a step function for each primary electron (curve a) gives the best time resolution, which can be called an intrinsic DC resolution. 2 other curves are for the basic amplifier structure with 3 independent integration circuits. The time constant of each circuit is either 2 ns (curve b) or 10 ns (curve c). The smaller time constant is preferred for lower thresholds, while for thresholds above 4 primary electrons the bigger time constant yields better resolution.

The calculated DC time resolution as a function of the integration constant for different threshold settings is presented in Fig. 6. There is almost a linear dependence for 1 primary electron threshold (curve d). At the threshold of 3 primary electrons the best resolution is achieved with the integration constant of 4 ns (curve e). However, both curves do not take into account the input noise of the amplifier. If it is taken into account, the dependence has a distinct minimum at 6 ns for the threshold equal to 5 standard deviations of the input noise (curve f). So, the integration time constant of 6 ns was chosen.

Figure 7 demonstrates the calculated DC space resolution as a function of the track distance from an anode wire at the threshold set to 1 primary electron for an amplifier with the response as a step function (curve g) and for the implemented amplifier (curve h). The space resolution in the second case is only slightly worse than in the first one. The average space resolution is better than the required 300 μm.

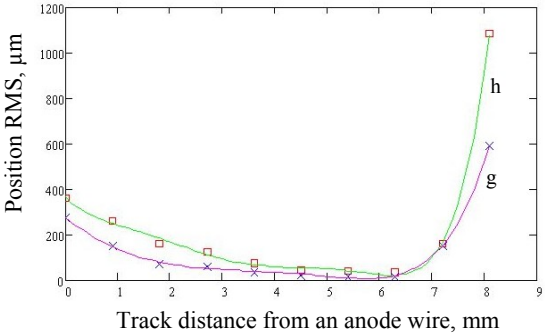

Fig. 7. Calculated DC space resolution at the threshold set to 1 primary electron for: an amplifier with the response as a step function (curve g); the implemented amplifier (curve h)

3. CROS-3 extended setup

An evaluation of the data payload for copper and fiber data links under the expected occupancy and the trigger rate for the BGO-OD experiment revealed a possibility of merging more data into a single data stream by implementing a setup with 2 Concentrator levels.

A newly developed CROS-3 extended setup, shown in Fig. 8, consists of the same 3 types of cards: System Buffer, Concentrator and Digitizer, but there are two kinds of Concentrators. The regular Concentrator interfaces with the System Buffer over a fiber link as it does in the CROS-3 basic setup. But now, instead of Digitizers, it serves up to 16 Branches consisting of a Low-Level Concentrator with up to 16 Digitizers linked to it. 1 Branch serves an *X* DC, and 2 Branches serve *Y*, *U*, and *V* DCs, the total number of Branches being 14 for the entire system. Each Low-Level Concentrator interfaces with the upstream Concentrator over a copper link. Both Concentrators utilize the same printed circuit board. Though, the boards are differently stuffed and run under different firmwares. The CROS-3 extended setup retains the backward firmware and program compatibility with the CROS-3 basic setup, but serves up to 16 times more channels than before.

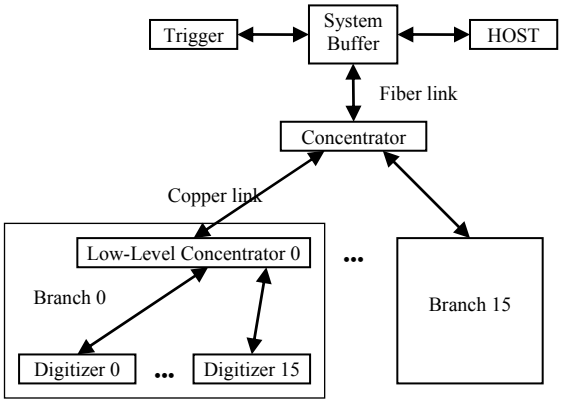

Fig. 8. CROS-3 extended setup

4. CROS-3B features

The CROS-3B version makes use of the extended setup and includes the following cards:

- CSB-B as the System Buffer, Fig. 9;
- CCB16-B as the Concentrator, Fig. 10;
- CCB10-B as the Low-Level Concentrator, Fig. 11;
- AD16-B as the Digitizer, Fig. 12.

The CSB-B complies with the PCI/PCI-X Local Bus Specifications and supports linear burst reads. The CCB10-B is a ten-port version of the sixteen-port CCB16-B card. The built-in error detection logic can be activated in the CSB-B, CCB16-B, and CCB10-B cards. It gracefully terminates the readout and reports the encountered problem(s) to the HOST in case of the hardware failure.

The AD16-B main features are:

- 16 input channels;
- an effective digitization frequency of 400 MHz or 2.5 ns per time bin;
- an 8-bit programmable threshold;
- an 8-bit programmable pipeline delay in 10 ns steps;
- an 8-bit programmable gate width with 2.5, 5, 10, or 20 ns programmable binning;
- 4 modes of operation with different output formats:
  - in the “Leading-Edge Raw” mode a 2-dimensional array (time bin #, channel #) of the leading edge transitions (hits) of the discriminator outputs is returned;

– in the “Leading-Edge Encoded” mode a list of encoded hits (time bin #, channel #) is returned;
– in the “Time-Over-Threshold” mode a 2-dimensional array (time bin #, channel #) of the discriminator outputs is returned;
– in the “Threshold Curve” mode a threshold scan is performed. For each channel at each step a sum of noise and test pulse hits is counted up, and an array of counter values is returned. The initial threshold, the threshold step and the number of generated test pulses (exposure window) are programmable.

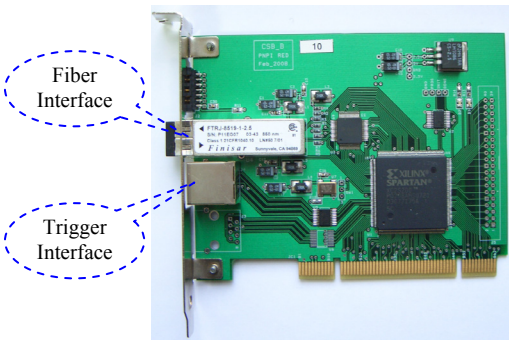

Fig. 9. CSB-B – the CROS-3B System Buffer

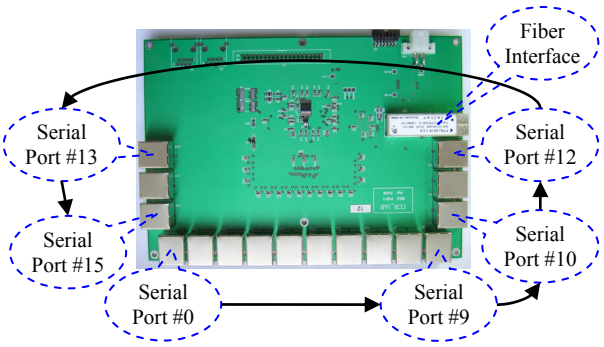

Fig. 10. CCB16-B – the CROS-3B Concentrator

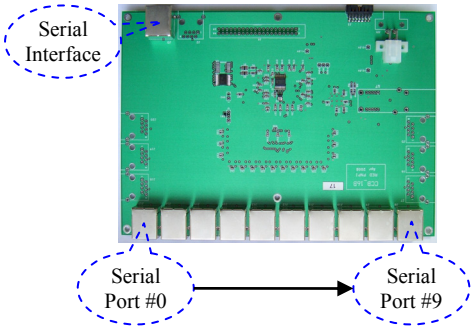

Fig. 11. CCB10-B – the CROS-3B Low-Level Concentrator

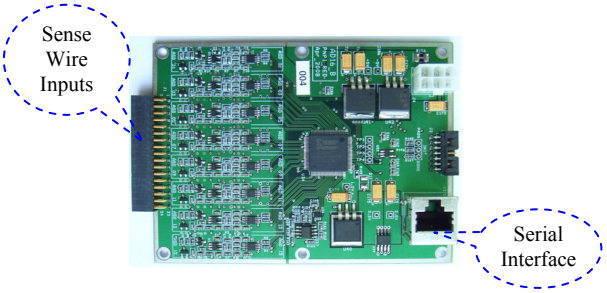

Fig. 12. AD16-B – the CROS-3B Digitizer

The CROS-3B command library provides an access to all CROS-3B registers. Examples of the system configuration and the data taking algorithms can be found in the CROS-3B Reference Guide [7]. A user is supposed to create his/her own code based on the above library and algorithms to effectively exploit all CROS-3B features.

References

1. N.F. Bondar, V.L. Golovtsov, A.G. Golyash, E.A. Lobachev, L.N. Uvarov, S.L. Uvarov, V.I. Yatsura, Third Generation Coordinate Readout System – CROS-3, *PNPI High Energy Physics Division, Main Scientific Activities 2002–2006*, Gatchina, p. 335.
2. http://bgo-od.physik.uni-bonn.de
3. http://www-elsa.physik.uni-bonn.de/elsa-facility_en.html
4. L. Kudin, V. Sedov, E. Spiridenkov, Electronics Noise and Time Resolution of the Multiwire Proportional Chamber, LHCb Note 99-039, MUON.
5. I.B. Smirnov, Modeling of Ionization Produced by Fast Charged Particles in Gases, Nucl. Instr. and Meth., A **554**, 474 (2005); the HEED Latest Developments Can Be Found at http://ismirnov.web.cern.ch/ismirnov/heed
6. R. Veenhof, GARFIELD, Recent Developments, Nucl. Instr. and Meth. A **419**, 726 (1998); the GARFIELD Latest Developments Can Be Found at http://garfield.web.cern.ch/garfield/
7. http://red.pnpi.spb.ru/~uvarov/BONN/CROS-3B.htm

CROS-3L – COORDINATE READOUT SYSTEM (LHCb TEST STAND VERSION)

V.L. Golovtsov, E.M. Spiridenkov, L.N. Uvarov, S.L. Uvarov, V.I. Yatsura

The design and development of the CROS-3 series is in the scope of interest of the LHCb Test Stand, which is constructed specially for tests of LHCb muon chambers [1]. We present a CROS-3L version, which has been designed and used for the LHCb Test Stand.

The block-diagram of the system is illustrated by Fig. 1 and includes:

- 4-channel front-end digitizer (ADF-L);
- 16-channel concentrator (CCB16);
- system buffer (CBS-B).

The analog part of the ADF-L is based on discrete elements performing chamber signal amplification and shaping, as well as pulse discrimination with peaking time 15 ns and operational threshold ≤ 15 fC. The digital part is implemented in a Xilinx Spartan-3 FPGA that performs both the time digitization and readout tasks. The delay range compensates trigger latency of up to 2.5 μs in 10 ns steps. The finest time bin resolution is 2.5 ns, the maximum number of time slices being 255. The amplitude digitization per each channel is performed by 10-bit ADC at a 100 MHz rate. The readout is performed over a STP CAT5 cable at a 100 Mb/s rate.

The CCB16 collects data from up to 16 digitizers into temporary buffers, which are read out to the CBS-B via an optical fiber at a 2.0 Gb/s. The CBS-B is implemented as a universal PCI card. The electronics modules of the system are illustrated by Figs. 2–4. Figure 5 shows the LHCb muon chamber equipped by CROS-3L electronics.

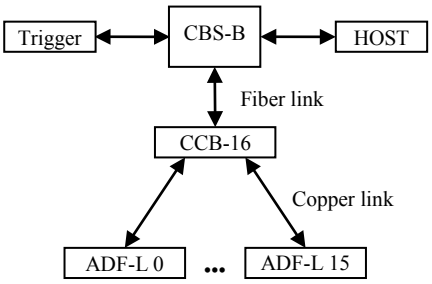

Fig. 1. CROS-3L set-up

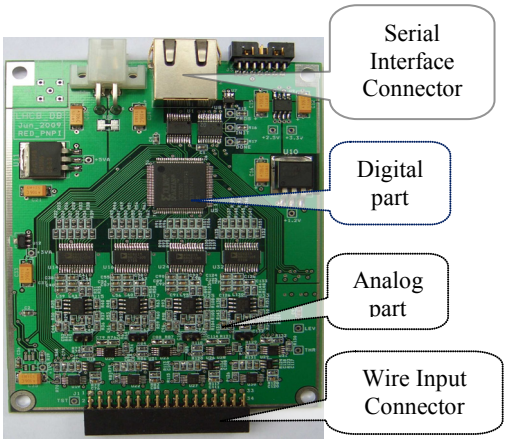

Fig. 2. ADF-L digitizer module

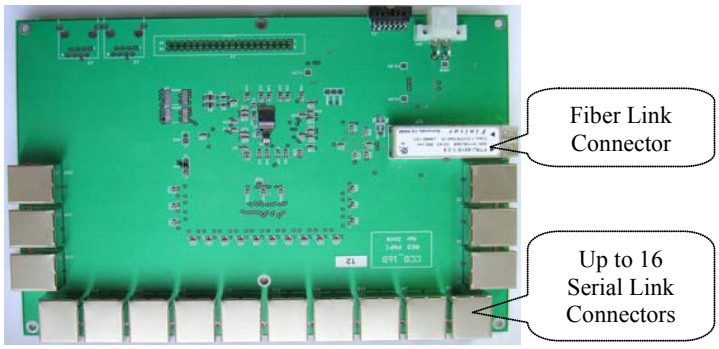

Fig. 3. CCB-16 concentrator module

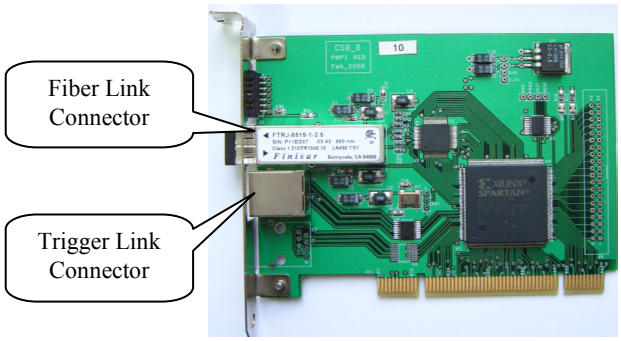

Fig. 4. CBS-B system buffer module

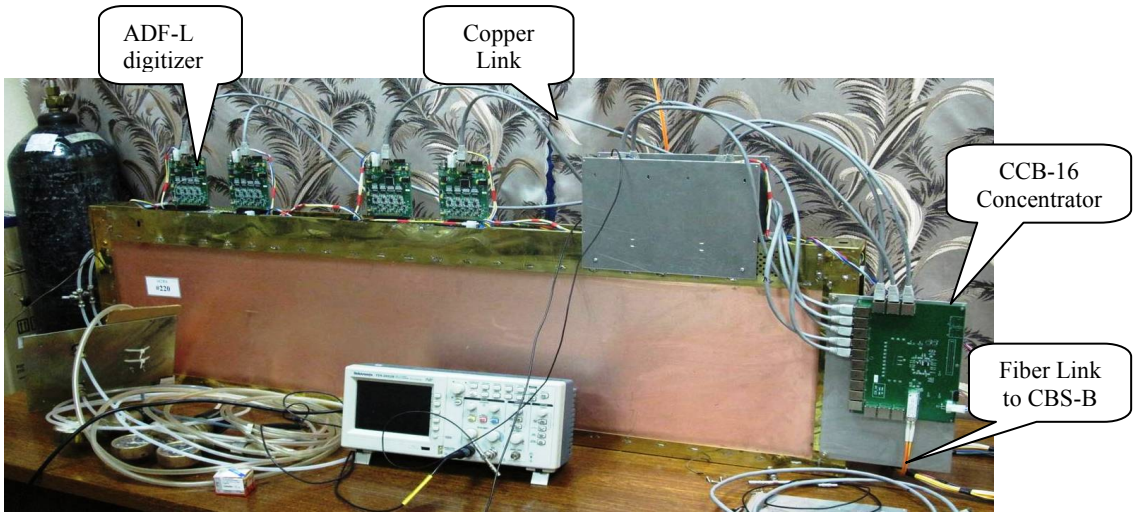

Fig. 5. LHCb muon chamber equipped by CROS-3L electronics at the Test Stand

The CROS-3L modules have the following features:

- the digitizers and the concentrator are mounted directly on the chamber;
- each digitizer amplifies, discriminates and pipelines input signals in parallel at a 100 MHz rate;
- when the system trigger occurs, the sparse encoding within the gate is started at a 400 MHz rate to collect data in parallel into a temporary buffer located in the digitizers;
- when the sparse encoding is over, the readout process is started over serial links at a 100 Mb/s rate to collect the sparse compacted data into a temporary buffer located in the concentrator;
- finally, the data are collected into the system buffer over the fiber link at a 2 Gb/s rate;
- fiber and copper links are used for the system trigger to be sent and the system constants such as the delay and gate values to be downloaded into the digitizer.

Reference

1. High Energy Physics Division, Main Scientific Activities 2002–2006, Gatchina (2007).

SCINTILLATION PROPERTIES OF BaF_2:Cd, BaF_2, BaF_2:Ce, BaF_2:Sc, BaF_2:Tm CRYSTALS AND CERAMICS; NEW PHOTOSENSORS FOR THE VACUUM ULTRAVIOLET REGION

Yu.I. Gusev, S.V. Kosyanenko, D.M. Seliverstov, V.M. Suvorov

1. Introduction

Research and development of new scintillation materials is mainly triggered by the growing needs of modern medical imaging, high energy and nuclear physics.

Pure BaF_2 crystals are widely applied as scintillation material because of its high density, high radiation resistance and good time resolution due to the fast component (< 1 ns) appearing in the emission bands around 220 and 195 nm. This fast component luminescence is called Auger-free luminescence or cross-luminescence, and it is attributed to the radiative recombination of the F-2*p* valence band electrons with the outmost holes of the Ba-5*p* core band.

However, in addition to the fast component, the BaF_2 crystal has a slow component at 300 nm with a decay time of about 700 ns, which causes deterioration of the time resolution at high counting rates. Suppression of the slow component is a crucial key when applying this crystal to high counting rate experiments in such fields as high energy physics and nuclear medicine.

This work is aimed to develop specimens of BaF_2-based crystals and ceramics doped with different elements in order to improve the light yield of the fast component and to suppress the slow part of the luminescence.

2. Experimental method

BaF_2 crystals were grown by the Stepanov – Stockbarger method, which provides high light transparency in the Vacuum UltraViolet (VUV) region. The optical transparency of our samples was measured with a SF-26 spectrophotometer in the wavelength range from 190 to 600 nm. We used an improved method of ceramics production from the BaF_2 powder with 40 to 60 nm nano particles by hot pressing in the CF_4 environment at a temperature of 1050 °C and under pressure of 200 MPa. The transparency of ceramics at 220 nm is only 11 % lower in comparison to that of single crystals, allowing to use them for measurements in the VUV region. However, such transmittance is insufficient for 20 mm length specimens and requires further improvements.

The luminescence spectra were measured under constant *X*-ray (40 kV) excitation. The registering equipment consisted of a MDR-2 monochromator and a FEU-106 photomultiplier. The obtained spectra were corrected for decreasing of the PMTs sensitivity in the wavelength range from 200 to 600 nm. In measurements of the luminescence kinetics, a pulsed *X*-ray (30 kV) source was used with the pulse duration shorter than 1 ns and a repetition rate of 12 kHz. The registering equipment was arranged according to the standard “start-stop” scheme, the time resolution of the system being better than 50 ps.

3. Results of measurements of optical properties of BaF_2 crystals and ceramics

3.1. Cd-doped BaF_2 crystals

The transmission curves within the range of 200–600 nm for pure BaF_2 and BaF_2:0.1%CdF_2 crystals are identical within the experimental error of 1 % (here and in the following, the percentage of the doped element is given in mol/%). In the case of ceramics, a slight decrease of the transparency in the UV range (200–300 nm) at a level of 3–5 % is observed. Increasing the Cd concentration to 0.3 % has virtually no effect on the sample transparency. The transparency of the BaF_2:0.1%CdF_2 sample is higher by 30 %, relative to that of the BaF_2 single crystal. A comparison of the total *X*-ray luminescence light yield for BaF_2:0.1%CdF_2 crystals and the corresponding ceramics shows that the light yield is 15 % higher in ceramics. A discovery of the strong dependence on the Cd concentration of the light yield in ceramics (clearly visible in Fig. 1) is a subject of interest. Changing the Cd concentration from 0.1 to 0.3 % in the

ceramics reduces the light yield by a factor of 5.4, while in the doped crystal it falls by a factor of 1.3 only. The optical parameters of the BaF_2:0.1%CdF_2 crystals and ceramics, which we determined for the first time, make these scintillators promising from the standpoint of obtaining high light yield for the fast component and reducing the intensity of the slow component relative to that of single BaF_2 crystals [1].

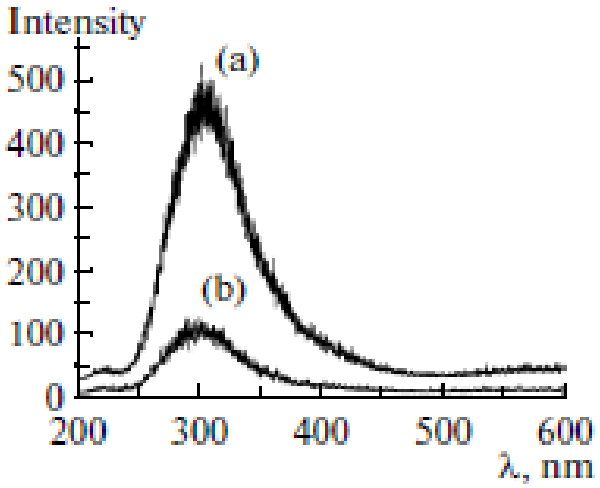

Fig. 1. Influence of Cd doping on the light yield of BaF_2:CdF_2 ceramics: a – 0.1%CdF_2; b – 0.3%CdF_2

3.2. BaF_2 single crystals and ceramics

A comparison of *X*-ray luminescence spectra for single BaF_2 crystals and ceramics shows an increase of the fast component yield in ceramics (as compared to BaF_2 single crystals) of about 12 % and a reduction of the slow component yield by a factor of 3.6 (Fig. 2a, b), which is observed for the first time. We suppose that the suppression of the slow component is caused by the non-irradiative annihilation of excitons on boundaries of nano particles in ceramics. Fitting the experimental data with two exponential decay curve $LY(t) = A_1\exp(t/\tau_1) + A_2\exp(t/\tau_2)$ gives $\tau_1 = 1.77 \pm 0.12$ ns and $\tau_2 = 493 \pm 6$ ns. A similar reduction of the time decay exciton component is observed in BaF_2 crystals doped with Cd [1, 2].

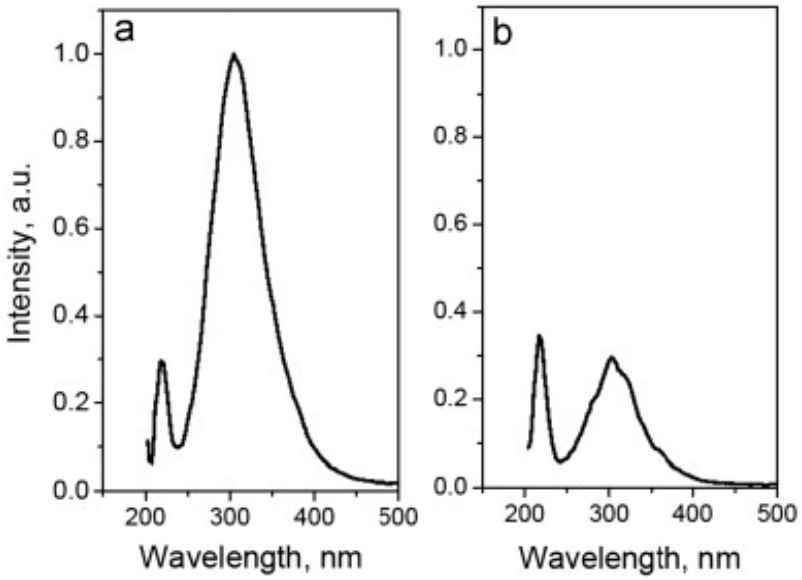

Fig. 2. *X*-ray luminescence spectra of a single BaF_2 crystal (a) and of ceramics (b)

3.3. Sc-doped BaF_2 single crystals and ceramics

BaF_2 single crystals and ceramics were doped with 0.5, 1.0 and 2.0 % Sc. The transparencies of $5 \times 10 \times 15$ mm^3 BaF_2:0.5%Sc and BaF_2:2.0%Sc crystals are close to that of single BaF_2 crystals with a slight absorption line at 290 nm. An increase of the Sc concentration from 0.5 to 2.0 % reduces the transparency at 220 nm by 8–10 %, which does not affect significantly other optical properties of the crystals. Doping the crystals with scandium (1%Sc, Fig. 3a, b) and annealing in CF_4 increase the relative light yield of the fast component by a factor 2.6, in comparison with that of single BaF_2 crystals.

Doping the BaF_2 crystals with scandium (1.0 and 2.0 %) does not change the decay time of the fast component ($\tau_1 = 2.0 \pm 0.5$ ns). The dependence of the light yield upon annealing in the CF_4 atmosphere of ceramics samples of dimensions $4 \times 4 \times 15$ mm^3 with the concentration 0.5 and 2.0 % of Sc was studied. Relative measurements showed an increase of the ratio of the fast to slow components yield by a factor from 1.7 to 2.5, as compared with single crystals [2].

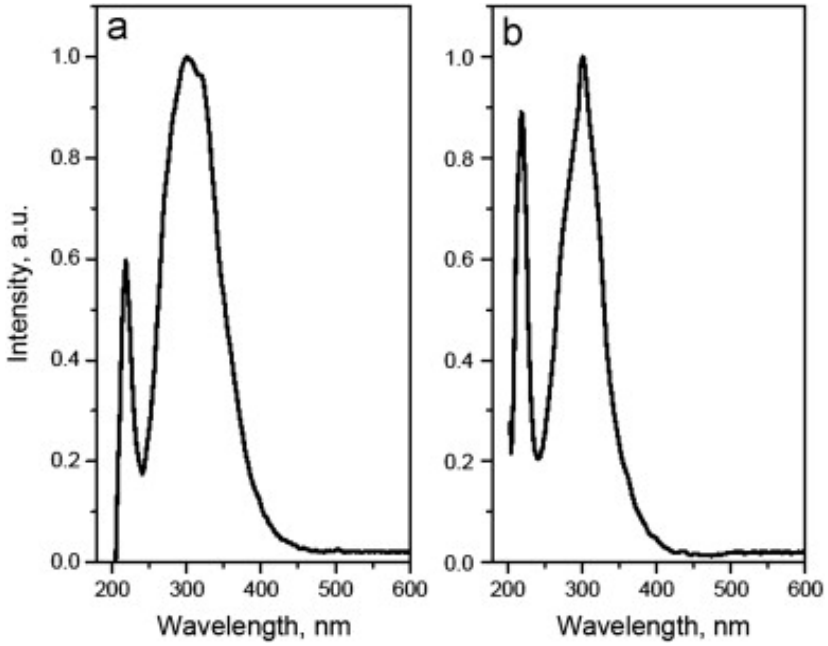

Fig. 3. Light yields of a single BaF_2 crystal without annealing in CF_4 (a) and of a BaF_2 crystal doped by 1%ScF_2 with annealing in CF_4 (b)

3.4. Tm-doped BaF_2 crystals

The main objective of our investigation of BaF_2 crystals doped with 0.5, 1.0, 2.0 and 3.0 % Tm was the development of crystal production technology and then its application to ceramics with the possibility of a four-fold increase of the fast component yield and accordingly a significant reduction of the slow component.

The transmission spectrum of BaF_2:3%Tm is more complicated than a similar BaF_2:Sc spectrum. The spectrum is characterized by three main bands of absorption caused by 4*f*–4*f* transitions in Tm^{3+} ions.

Figure 4 presents *X*-ray luminescence spectra of BaF_2 single crystals, pure and doped with Tm at a concentration of 0.5 %. One can observe an increased yield of the fast component and the corresponding suppression of the slow one, which is typical for all the studied samples. Fitting the experimental data with two exponential decay curve gives $\tau_1 = 1.34 \pm 0.06$ ns and $\tau_2 = 534 \pm 7$ ns [2].

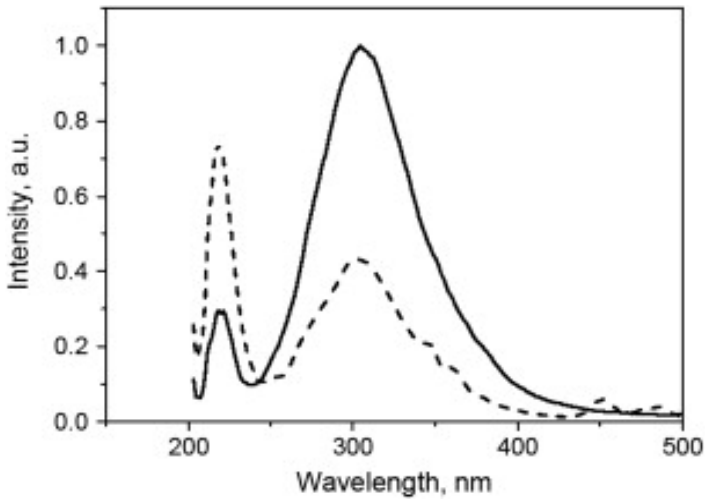

Fig. 4. *X*-ray luminescence spectra of a single BaF_2 crystal (solid line) and a crystal of BaF_2 doped with Tm (dash line). The BaF_2:0.5%Tm crystal has the light yield of the 0.9 ns component 2.4 times larger than that of a single BaF_2 crystal and the slow component yield smaller by the same factor

3.5. Ce-doped BaF_2 crystals

Emission spectra of BaF_2 single crystals and those doped with 0.1 % of CeF_3 are shown in Figs. 4 and 5. The spectrum of the pure BaF_2 ceramics (as well as of the crystals) exhibits a wide band with a maximum near 300 nm, which is caused by self-trapped excitons and a weak band 220 nm relating to the core-valence transitions. In BaF_2:Ce^{3+}, two bands at 308 and 323 nm, typical for Ce^{3+} ions, have been detected.

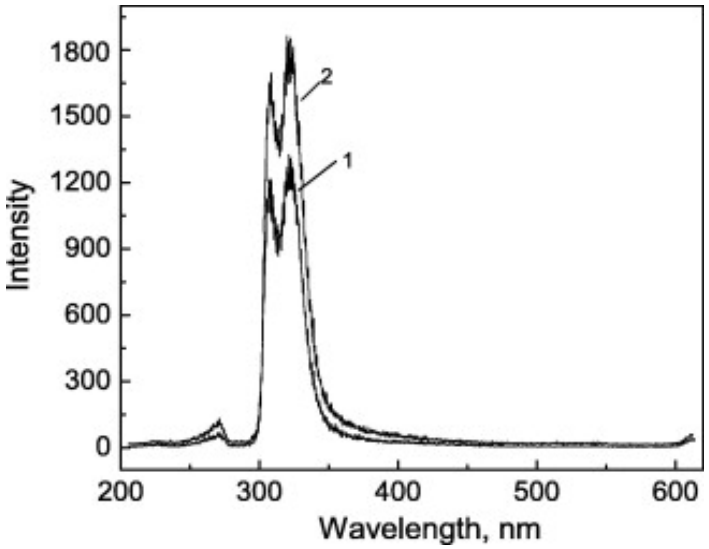

Fig. 5. *X*-ray induced emission spectra: 1 – BaF_2:Ce (0.1 %) single crystal and 2 – BaF_2:Ce (0.1 %) ceramics

It is worth noting that the intensity of the ultrafast component in BaF_2:Ce^{3+} ceramics is slightly larger than that in the standard BaF_2 crystals [3].

4. Photodetectors with AlGaN photocathodes

New photodetectors with photocathodes operated within the VUV spectral range have been developed. $Al_xGa_{1-x}N$ epitaxial films within a full range of composition (x = 0–1) and AlGaN-based heterostructures were grown by plasma-assisted molecular-beam epitaxy. The samples were grown on the annealed and

nitridated c-sapphire substrates, the growth temperature being varied within the range of 650–740 °C. The RF-power in the plasma source, changed within the range of 115–150 W at a constant nitrogen mass-flow of 5 sccm, allowed the *N*-limited growth rates from 0.25 to 0.5 μm/h, respectively. All the heterostructures had 1–1.6 μm-thick AlGaN buffers and *p*-type 20-nm-thick GaN:Mg top layers doped with solid-state Mg effusion cells. To control the AlGaN growth, a phenomenological approach based on simultaneous *in-situ* measurements of the laser interference and high energy electron diffraction followed by *ex-situ* electron probe micro-analysis was used. When the photocathode was grown, it was activated with Cs. The structural and optical properties of the structures were analysed using the scanning electron microscopy, the transmission electron microscopy, the *X*-ray diffraction and photoluminescence spectroscopy.

The Quantum Efficiency (QE) spectrum has an abrupt threshold at the photon energy equal to the GaN band gap. Changing the band gap value, it is possible to suppress the QE in the range of the BaF_2 slow luminescence component. The maximal value of the QE of 0.14 was measured at the wavelength of 230 nm [4].

5. Conclusion

1. The BaF_2 ceramics with the transmission at the wavelength 220 nm close to that of monocrystals can be obtained.
2. The BaF_2 ceramics luminescence spectrum demonstrates stability of the fast component and suppression of the slow one as compared to that of monocrystals.
3. Doping the BaF_2 crystals and the ceramics with different elements causes suppression of the slow component.
4. A photocathode with the quantum efficiency of 0.14 at 220 nm has been developed. The photocathode has an abrupt threshold about the slow luminescence component.

References

1. E.A. Garibin *et al*., Bull. Rus. Acad. Sci., Phys. **75**, 1011 (2011) (translated from Izvestiya Rossiiskoi Akademii Nauk., Ser. Fiz. **75**, 1066 (2011)).
2. D.M. Seliverstov, A.A. Demidenko, E.A. Garibin, *et al*., Nucl. Instr. Meth. A **695**, 369 (2012).
3. A.A. Demidenko, E.A. Garibin, S.D. Gain, *et al*., Opt. Materials **32**, 1291 (2010).
4. G. Benemanskaya, E. Garibin, Yu. Gusev, *et al*., Nucl. Instr. Meth. A **610**, 335 (2009).

COMPUTING FACILITIES FOR SMALL PHYSICS ANALYSIS GROUPS: EXAMPLES AND CONSIDERATION

A.Y. Shevel

1. Introduction

A small physics group (3–15 persons) might use a number of computing facilities for analysis/simulation, developing/testing, teaching. The most recent instances of small clusters for the Nuclear Chemistry Group at the State University of the New York campus, Stony Brook (http://www.sunysb.edu) and for the High Energy Physics Division at the Petersburg Nuclear Physics Institute (http://hepd.pnpi.spb.ru/) are briefly described here. Different types of computing facilities are discussed: collaboration computing facilities, local group computing clusters (including colocation), and cloud computing. A growing variety of the computing options and the growing role of the group-owned computing clusters of micro size are emphasized.

The members of a physics group usually have their computer accounts on large computing facilities, which are supported by institutional collaborations. Such facilities have certain rules: who can access the computing installation, in what scale, and for what purpose. As a result, the registration procedure takes some time. On the other hand, short-term students and/or visitors might need a computer account just temporarily. Finally, a physics group needs in addition to the institutional computing infrastructure a more agile and flexible computing infrastructure completely under group's control for several purposes:

- to keep common group data (papers, drafts, programs, fractions of experimental data, *etc.*);
- to test new/modified simulation or/and analysis software/algorithms;
- to provide an account for short-time visitors/students who need to do something in data analyses;
- for any other possible purpose, in particular, as a good gateway to remote large computing clusters.

We have to take into account the growth of the computing power of Computer Processing Units (CPU) every year. If we pay attention not only to CPU but to the whole computing power of a cluster, we can find, for example, such an estimation: "...DOE (U.S. Department of Energy) centres have historically delivered average improvements in computing capability of 40–80 % per year with relatively flat budget" [1]. This means that dozens of modern computing nodes in 2012 are more powerful than hundreds of servers in 2002.

Obviously, such a small computing installation is a good complement to large computing facilities. The computing needs can be considered in various ways (from the point of view of a small group):

- to use a big[1] centralized cluster (we mean a collaboration cluster);
- for cloud computing;
- as a group owned local cluster (might be in two instances):
  - location of the group computing cluster in the group office space with all responsibilities for air conditioning, electric power, hardware support, *etc.*;
  - colocation of the groups cluster hardware somewhere else [2].

Many pros and contras for each of the above listed options were discussed earlier [3]. Here it is assumed that the physics group uses more than one cluster to get the computing task done. Within the scope of papers, such group owned computing clusters are referred to as clusters Tier[2]-3 [4]. In the following in this paper, we will analyse our own local computing cluster and cloud computing facilities: now and in the nearest years.

Usually, a small physics group has limited financial resources. This fact does impose many restrictions on the cluster architecture. The cluster has to be:

- cheap (a useful consideration on the true cluster ownership cost is in Ref. [5]);
- composed of reliable hardware;
- not demanding for intensive supervision/maintenance.

[1] The cluster sizes: big, large – more than 1000 machines; middle size – up to 1000; small – up to 100; micro – around 10.

[2] In the grid, like the computing infrastructure around the LHC, several Tiers are defined: Tier-1, Tier-2, Tier-3, and so on. The difference is mainly determined by expected functionality (ability to accept and maintain the policy of Virtual Organization (VO), implement distinguished service for different VOs, availability of backup facilities, *etc.*).

Other requirements are the implications of the desire to reduce the maintenance efforts: compatibility (architecture and base OS) with the collaboration cluster environment (*e.g.*, as in the ATLAS or CMS and other CERN Collaborations), in particular, with the same set of application software, as in the collaboration cluster.

From the above, we see that a group-owned computing cluster cannot be large or even mid-range, it is quite small, a micro cluster. A good configuration of a group-owned cluster might consist of 5–15 modern machines (multicore CPUs, 2–3 GB of the main memory per core, 10–20 TB or more of the disk space per machine). It is better to use a 10 Gbit network switch. Such a group cluster can help to get more flexibility when using several remote computing facilities: the collaboration cluster(s), public/private cloud computing, *etc*.

The situations in different physics groups might differ from each other. Here, we shall discuss the particular group cluster solutions for the Nuclear Chemistry Group (NCG) at SUNYSB/Chemistry and for the High Energy Physics Division (HEPD) at PNPI.

2. Local computing cluster at SUNYSB/Chemistry

The computing cluster in the NCG was organized in 2000, or a bit earlier. At that time, all the machines (30+) had 512 MB of the main memory and Dual 500 MHz CPUs. This cluster was used for program developments, test analyses, students work, *etc*. There were more than 70 registered users, and about 3–5 of them were quite active. More detailed information about the cluster is available in Ref. [3].

To reduce the downtime of the cluster, it is good to buy and install special equipment – a KVM switch over the Internet Protokol [6] to do many control actions (switching on and off any machine in the cluster, to get access to the console of any machine, *etc*.) remotely over Internet. So, the group might use a remote help from external experts. However, in the cases described here the idea has not been implemented yet.

For the batch system, we use a pair of torque/maui from http://www.supercluster.org. Due to security reasons, the regular maintenance of the cluster is available only from specifically defined network domains. Because the cluster is located in a relatively large room with good ventilation, there is no need for air conditioning. After years of experience, we conclude that the University electric power supply is quite stable.

The basic OS (Scientific Linux with the same Red Hat Package Manager set as on the RHIC&ATLAS Computing Facility at BNL) installation procedure and the basic configuration are semiautomatic: there are a couple of scripts which use the kickstart as the initial step, and another step consists of a script for a post kickstart configuration. No virtualization technique was used in the cluster.

In our circumstances, the users mailing list does form a kind of a thinking engine for various methods how to use the cluster for concrete tasks. The mailing list is located in the Google.com (*i.e.* somewhere in a “cloud”).

3. Local computing cluster at the High Energy Physics Division of PNPI

The computing cluster at the HEPD stemmed from a very small cluster consisting of three servers in February 1998. Details of the initial implementation are available in Ref. [7]. The cluster passed through multiple upgrades in hardware and software, though it remained quite small, or micro size. Now, the cluster consists of 5 hardware servers with 20 virtual machines (completely virtualized) and has around 16 TB of the disk space. The OS is Scientific Linux 5.7. There are about 150 registered users on the cluster; about 50 users logged many times per month, and about 15 persons use the cluster every day. Virtual tools permit to use specific configurations for specific user needs, *e.g.*, it is possible to use the CERNVM for a range of physics collaborations.

There is a custom-made backup scheme for user home directories (not for the data). One experienced person spends part of his/her time to keep the cluster running. The cluster room is equipped with air conditioner, UPSs, and UDP.

In the two computing cluster examples for High Energy Physics (at SUNYSB and PNPI) we can see the main similar trend: to reduce the cluster Total Cost of Ownership (TCO). It includes everything: the cost

of hardware and deployment, electric power, manpower, software and hardware support, any operation cost, cost of upgrades, *etc*. In this context it is not bad to have a look at the "cloud" computing.

4. Cloud computing

The cloud computing is a hot topic in the information technology for about 5 years. Many successful experiments with clouds were carried out (see Refs. [8–10]). It is not quite a common paradigm, though it has a lot of examples in government and private sectors. The quote below is a part of the most consistent cloud computing definition copied from Ref. [11].

Cloud computing is a model for enabling convenient, on-demand network access to a shared pool of configurable computing resources (*e.g*., networks, servers, storage, applications, and services) that can be rapidly provisioned and released with minimal management effort or service provider interaction. This is just the beginning of the definition[3], but it gives the main idea. Scores of cloud services are available with a small difference in character and style of service and in policy of payment for the service, *e.g.* [12, 13].

Some physicists are afraid to use public cloud computing service because the public cloud is out of their control (for instance, the service could be down forever due to business or/and political issues). That is true. On the other hand, we can consider the control capability as the reliability of the access to the cloud. Can we think that public cloud service is 100 % reliable all the time? The right answer is "no". Unfortunately, we have to say the same about any other case of computing service of any kind. At the same time, small groups often have not so reliable local computing, which depends on unstable enthusiast activity. In many cases during even medium time frame (2–5 years), a local computing service is most probably less reliable than a public cloud computing service. If you are worrying about reliability of your data being safe, the obvious solution is to use all of the mentioned options.

Several successful testbeds with using the cloud computing for production simulation in HEP were carried out, *e.g.*, in ATLAS [12] and STAR [9]. The latter work has many deep and smart observations of the experience with computing in grid and cloud computing environments. The success does depend on a lot of details, in particular on the computing infrastructure components and their parameters which are "under hood" of the computing cloud. The authors of Ref. [14] were urged to do additional conversions of virtual machine images, may be for lack of open standards in the field. In other cases [9, 10], the authors found that the tested public cloud had not so good computer hardware parameters, as they expected. Also, the computing cloud initiatives and the government plans are to be taken into account [15].

5. Conclusion

Small computing/information installations are already on the way to use the clouds. For a small physics group, moving to the cloud does eliminate the cluster hardware maintenance task, but not the application software and data structure maintenance. Also, to achieve the maximal effect of using the cloud one should not ignore good understanding of the cloud hardware, architecture, and OS details.

We are emphasizing specifically the clusters of micro size, because if we take a look at a range of all size clusters, we might see more servers in the cluster, more spendings and efforts to support it. With a more powerful cluster, you need additional staff and additional activity to meet more complicated conditions including stronger regulations from the public authorities: fire safety, information security, insurance, *etc.*; all these factors increase the TCO significantly. There are many reasons for the TCO of midrange computing clusters to grow faster with the number of hardware servers than the total cost of the servers in the cluster, that is the relative TCO (per server) is less for micro size clusters and for huge clusters (due to the large scale) than for midrange clusters (see Fig. 1). This leads to the idea, that two main types of computing clusters will have long life: the huge clusters with many thousands of servers, often referenced as data centres which have a lot of users (actually such clusters are used as computing clouds), and micro clusters, which can be deployed in almost any office and used by a small group of users.

[3] The whole definition is explained on two pages or so.

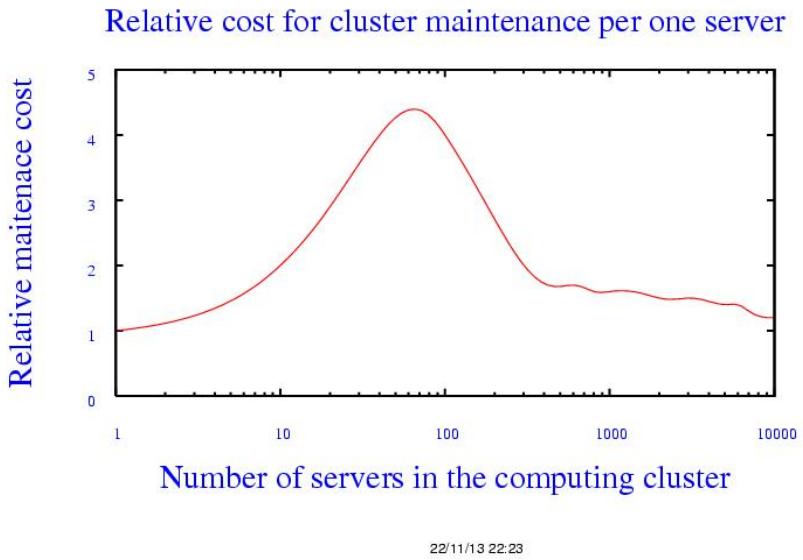

Fig. 1. Estimate of the relative maintenance cost per serever

In the light of the above experience, a group-owned cluster is to be used as an important gateway to public or private (*i.e*. collaborational) cloud computing. The number of public and private cloud computing instances is growing significantly every year. This means that the importance of suitable gateways to different clouds for small physics group is growing, as well.

References

1. The Magellan Report on Cloud Computing for Science – U.S. DOE, Office of Advanced Scientific Computing Research, December, 2011, p. 125; http://www.science.energy.gov/~/media/ascr/pdf/program-documents/docs/Magellan_Final_Report.pdf
2. Colocation Centre, http://en.wikipedia.org/wiki/Colocation_centre
3. Damian Reynolds, Andrey Y. Shevel, PHENIX Technical Note tn-452.0, http://www.phenix.bnl.gov/phenix/WWW/publish/shevel/tech-reports/ClusterPaper-2011-04-11.pdf
4. OSG Tier3 Twiki, https://twiki.grid.iu.edu/bin/view/Tier3/WebBook
5. The True Cost of HPC Cluster Ownership, http://www.clustermonkey.net//content/view/262/1/
6. KVM Switch, http://en.wikipedia.org/wiki/KVM_switch
7. Batch Computing Facility Based on PCs, http://hepd.pnpi.spb.ru/CSD/CSDPublications/proc_043.pdf
8. Jan-Philip Gehrcke *et al*., ATALS@AWS, http://iopscience.iop.org/1742-6596/219/5/052020
9. Jerome Lauret *et al*., From Grid to Cloud: STAR Experience, http://computing.ornl.gov/workshops/scidac2010/papers/data_j_lauret.pdf
10. Keith R. Jackson *et al*., Performance Analysis of High Performance Computing Applications on the Amazon Web Services Cloud, http://www.lbl.gov/cs/CSnews/cloudcomBP.pdf
11. NIST Definition of Cloud Computing, http://www.nist.gov/itl/cloud/upload/cloud-def-v15.pdf
12. Dropbox, http://www.dropbox.com/
13. ADrive, http://www.adrive.com/
14. Jerome Lauret *et al*., Contextualization in Practice: the Clemson Experience, http://pos.sissa.it/archive/conferences/093/027/ACAT2010_027.pdf
15. Vivek Kundra, U.S. Chief Information Officer, Federal Cloud Computing Strategy, http://www.cio.gov/documents/Federal-Cloud-Computing-Strategy.pdf

CONTENTS

NUCLEAR AND ATOMIC PHYSICS

NEW PROJECTS

METHODICAL AND APPLIED RESEARCH

High Energy Physics Division
MAIN SCIENTIFIC ACTIVITIES
2007–2012

Отпечатано в издательско-полиграфическом отделе
ФГБУ «ПИЯФ» НИЦ «Курчатовский институт»
на Konica Minolta bizhub C552

188300, Гатчина Ленинградской обл., Орлова роща
Зак. 347, тир. 50, уч.-изд. л. 51; 29.11.2013 г.